10th NAVY SYMPOSIUM on AEROBALLISTICS

LEVEL II

VOLUME 2

15-16-17 JULY

SPONSORED BY THE

NAVY AEROBALLISTICS ADVISORY COMMITTEE

NAAC

HOSTED BY

NAVAL SURFACE WEAPONS CENTER

DAHLGREN LABORATORY, DAHLGREN, VA.

HELD AT THE

SHERATON MOTOR INN

FREDERICKSBURG, VA.

AD063354

(11)

(6)

PROCEEDINGS OF THE TENTH NAVY SYMPOSIUM ON AEROBALLISTICS (U)

~~VOLUME 2~~

~~15-16-17 JULY 1975~~

HELD AT THE SHERATON MOTOR INN
FREDERICKSBURG, VIRGINIA, on
15-16-17 July 1975. Volume 2. (U)

SPONSORED BY THE NAVY AEROBALLISTICS
ADVISORY COMMITTEE NAAC

17 Jul 75

12 1/2 p.

411 022

78 11 16 03

FOREWORD

These ***Proceedings***, published in four volumes, comprise the 45 papers presented at the Tenth Navy Symposium on Aeroballistics held at the Sheraton Motor Inn, Fredericksburg, Virginia, 15, 16 and 17 July 1975.

This symposium was the tenth in a series begun in 1950 under the sponsorship of the then Bureau of Ordnance Committee on Aeroballistics, and currently conducted by the Naval Aeroballistics Advisory Committee as sponsoring committee for the Naval Air Systems Command and the Naval Ordnance Systems Command. The continuing purpose of the symposiums has been to disseminate the results of aeroballistics research and to bring the research findings of industry, the universities, and government laboratories to bear upon the Navy's aeroballistic research and development programs.

Over 160 research scientists representing 56 organizations attended this tenth symposium. Session I covered the subjects of missile stability and performance; Session II was concerned with missile stability and performance/launch dynamics; Session III dealt with heat transfer; Session IV covered inlets and diffusers/gas dynamics; and Session V presented aero-elasticity and structures.

The papers in these ***Proceedings*** have been reproduced in facsimile. They appear in the order of presentation except that all classified papers have been taken out of sequence and grouped together as Volume 4, a confidential volume. Volumes 1 through 3 are unclassified. This is Volume 1.

Requests for or comments on individual papers should be addressed to the respective authors.

THOMAS A. CLARE
General Chairman
Symposium Committee

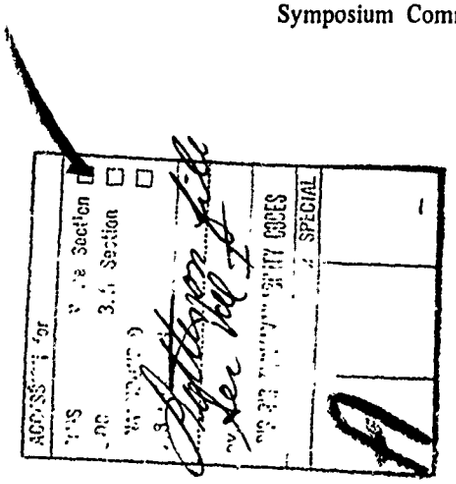

CONTENTS

CONTENTS (Continued)

Volume 1

Volume 2

CONTENTS (Continued)

Volume 2

CONTENTS (Continued)

Volume 2

Volume 3

CONTENTS (Continued

Volume 3

CONTENTS (Continued)

Volume 3

Volume 4
(Classified Papers)

CONTENTS (Continued)

Volume 4
(Classified Papers)

AUTHORS

GREETINGS

The Navy Aeroballistics Advisory Committee (NAAC) provides valuable assistance to the Naval Air and Naval Sea Systems Commands. It is extremely active in promoting the exchange of technical information among Naval activities, Navy contractors, and other government agencies. It also provides effective guidance by recommending aeroballistics research investigations and identifying the new aeroballistic facilities necessary for future weapons development. We hope that this Symposium, as in the past, will provide for a stimulating exchange of information and will be of value to all participants. Best wishes for a successful Symposium.

A. B. McCaulley
Captain, USN
Assistant Commander
for Research & Technology
Naval Air Systems Command

R. W. King
Rear Admiral, USN
Deputy Commander
for Research & Technology
Naval Sea Systems Command

WELCOME

On behalf of the Dahlgren Laboratory of the Naval Surface Weapons Center, we are pleased to welcome you to the Tenth U. S. Navy Symposium on Aeroballistics.

The Navy Aeroballistics Advisory Committee, established jointly by the Naval Air Systems Command and the Naval Sea Systems Command, has prepared an excellent program covering diverse technical disciplines in the field of aeroballistics. It is noted that the Symposium brings together speakers and guests with special competence in aeroballistics from the Navy, Air Force, Army, other government agencies, universities and from industry. It is our hope that we can provide a pleasant atmosphere for you during the Symposium.

C. J. Rone
Captain, USN
Commander
Naval Surface Weapons Center

U S. NAVY SYMPOSIUMS ON AERODALLISTICS

FIRST SYMPOSIUM – NOVEMBER 1950
Hosted by . . . . . Defense Research Laboratory
Held at . . . . . University of Texas
Austin, Texas

SECOND SYMPOSIUM – MAY 1952
Hosted by . . . . . Naval Weapons Center
Held at . . . . . Huntington Hotel
Pasadena, California

THIRD SYMPOSIUM – OCTOBER 1954
Hosted by . . . . . Applied Physics Laboratory
The Johns Hopkins University
Held at . . . . . Applied Physics Laboratory
The Johns Hopkins University
Silver Spring (Howard County Location), Md.

FOURTH SYMPOSIUM – NOVEMBER 1957
Hosted by . . . . . Naval Weapons Laboratory
Held at . . . . . Department of Commerce Auditorium
Washington, D. C.

FIFTH SYMPOSIUM – OCTOBER 1961
Hosted by . . . . . Naval Ordnance Laboratory
Held at . . . . . Naval Ordnance Laboratory
White Oak, Md.

SIXTH SYMPOSIUM – OCTOBER-NOVEMBER 1963
Hosted by . . . . . Naval Ship Research and
Development Center
Held at . . . . . National War College
Fort McNair, Washington D. C.

SEVENTH SYMPOSIUM – JUNE 1966
Hosted by . . . . . Naval Missile Center
Held at . . . . . Naval Missile Center
Point Mugu, Calif.

EIGHTH SYMPOSIUM – MAY 1969
Hosted by . . . . . Naval Weapons Center
Held at . . . . . NWC Corona Laboratories
Corona, Calif.

Vol. 2

NINTH SYMPOSIUM – MAY 1972

Hosted by . . . . . Applied Physics Laboratory
The Johns Hopkins University

Held at . . . . . Applied Physics Laboratory
The Johns Hopkins University
Silver Spring (Howard County Location), Md.

TENTH SYMPOSIUM – JULY 1975

Hosted by . . . . . Naval Surface Weapons Center
Dahlgren Laboratory
Dahlgren, Virginia

Held at . . . . . Sheraton Fredericksburg Motor Inn
Fredericksburg, Va.

NAVAL AEROBALLISTICS ADVISORY COMMITTEE

MEMBERS AND ALTERNATE MEMBERS FOR 1975

Members	Alternate
S. de los Santos, Chairman (NSRDC)	S. Gottlieb
L. Schindel (NAVSURFWPNCEN/WOL)	K. Enkenhaus
L. L. Cronvich (APL/JHU)	E. T. Marley
R. D. Cuddy (NAVSURFWPNCEN/DL)	F. G. Moore
J. W. Rom (NMC)	M. R. Marson
R. W. Van Aken (NWC)	R. E. Meeker
W. A. Langan (NADC)	V. C. Dailey

ASSOCIATES

W. C. Volz, Executive Secretary (NAVAIRSYSCOM)
H. Andrews (NAVAIRSYSCOM)
L. Pasiuk (NAVSEASYSCOM)
C. Wheeler (NAVSEASYSCOM)

NAAC PANELS AND PANEL CHAIRMAN FOR 1975

Aeroelasticity and Structures	E. L. Jeter (NWC)
Air Inlets and Diffusers	R. L. Rumpf (APL/JHU)
Gas Dynamics	G. Pick (NSRDC)
Heat Transfer	W. C. Lyons (NSWC/WOL)
Missile Stability and Performance	T. A. Clare (NSWC/DL)
Launch Dynamics	G. Cooper (NMC)

PAST NAAC CHAIRMEN

Feb 1949-Nov 1949	CDR H. M. Mott-Smith (BuOrd)
Dec 1949-Oct 1950	CDR L. G. Pooler (BuOrd)
Oct 1950-Feb 1953	CDR L. G. Pooler (NOL)
Mar 1953-Jul 1953	A. I. Moskovits (Acting) (BuOrd)
Sep 1953-Jul 1955	E. A. Bonney (APL/JHU)
Aug 1955-Aug 1957	H. H. Kurzweg (NOL)
Sep 1957-Jul 1959	W. R. Haseltine (NWC)
Aug 1959-Jul 1961	R. A. Niemann (NSWC/DL)
Jul 1961-Jan 1963	R. E. Wilson (NOL)
Jan 1963-Jan 1965	S. T. de los Santos (NSRDC)
Jan 1965-Jan 1967	R. H. Peterson (NMC)
Jan 1967-Jan 1969	W. A. Kemper (NSWC/DL)
Jan 1969-Jan 1971	L. L. Cronvich (APL/JHU)
Jan 1971-Jan 1973	W. R. Haseltine (NWC)
Jan 1973-Jan 1975	R. E. Wilson (NAVSURFWPNCEN/WOL)

PAPER SELECTION COMMITTEE

R. W. Van Aken, Chairman . . . . . NWC
T. C. Tai . . . . . NSRDC
R. Rumpf . . . . . APL/JHU
L. Schindel . . . . . NAVSURFWPNCEN/WOL
F. G. Moore . . . . . NAVSURFWPNCEN/DL
J. Rom . . . . . NMC
W. C. Volz . . . . . NAVAIRSYSCOM
L. Pasiuk . . . . . NAVSEASYSCOM

ACKNOWLEDGEMENTS

Thanks to all who have contributed to the Tenth Navy Symposium on Aeroballistics:

The host organization, the Department of the Navy of the Naval Surface Weapons Center.

Dr. T. A. Clare, Chairman of the Symposium; and Mrs. Mitzi Lumpkin and Miss Virginia Scott of NAVSURFWPNCEN/DL for their administrative and secretarial assistance.

Mr. E. T. Marley (A[illegible]), Mr. W. C. Volz (NAVAIRSYSCOM), Mr. L. Pasiuk (NAVSEASYSCOM) for their advice and assistance regarding arrangements and technical matters relating to the Symposium.

Mr. R. W. Van Aken, Chairman of the paper selection committee, and the committee members for their efforts in paper selection and session organization.

Mr. Amos Clary, Public Affairs Director at the Dahlgren Laboratory, Mr. C. Philbrick, Director of Security for the Symposium, and Mrs. Judy Kinnaman, Sheraton Fredericksburg Motor Inn, for their assistance in arrangements for the Symposium.

Session chairman, opening speakers and honored guests, for their contributions to the Symposium.

And, finally, the authors and presenters of the technical papers, without whom the Symposium would not be possible, for their excellent literary and oral presentation of technologies in the field of Aeroballistics.

SYMPOSIUM ATTENDEE LIST

ANDERSON, C. W., JR.
Atlantic Research Corp.
Gainesville, VA 22065
(703) 754-4111 – Ext. 279

ATHA, L. C.
Ballistic Missile Defenses
Advanced Technology Center
P. O. Box 1500
Huntsville, AL 35807
(205) 895-3431

BAILIE, J. A.
Lockheed Missiles & Space Co.
D81-12, B154
Box 504
Sunnyvale, CA 94088
(408) 742-9226

BARNARD, H. R.
Texas Instruments
P. O. Box 6015
M/S 96
Dallas, TX 75222
(214) 238-3582

BAUER, R. L.
Raytheon Co.
Missile Systems Division
Hartwell Road
Bedford, MA 01730
(617) 274-7100 – Ext. 2849

BECKER, M.
Naval Surface Weapons Center
Dahlgren Laboratory
Code DK-21
Dahlgren, VA 22448
(703) 663-8107

BELL, R. W.
Naval Postgraduate School
Dept. of Aeronautics
Monterey, CA 93940

BELSKY, R. C.
Naval Surface Weapons Center
Dahlgren Laboratory
Code DK-70
Dahlgren, VA 22448
(703) 663-8835

BENSIMON, M.
NASA-Goddard Space Flight Center
Code 742
Greenbelt, MD 20771
(301) 982-4865

BERGSTEN, B.
Wright-Patterson AFB, OH 45433
(513) 225-2449

BOLICK, R. G.
Naval Surface Weapons Center
Dahlgren Laboratory
Code DG-40
Dahlgren, VA 22448
(703) 663-7646

BOURGEOIS, B. M.
Naval Surface Weapons Center
Dahlgren Laboratory
Code DN-10
Dahlgren, VA 22448
(703) 663-8565

BRAZZEL, C. E.
AMSMI-RDK
Bldg. 5400
Redstone Arsenal, ALA 35809
(205) 876-7276

BRIGGS, M. M.
McDonnell Douglas Astronautics Co.
Dept. A3-203, M/S 11-2
5301 Bolsa Ave.
Huntington Beach, CA 92647
(714) 896-3352

SYMPOSIUM ATTENDEE LIST

BROOKS, W. B.
McDonnell Douglas Astronautics Co.
P. O. Box 516
Dept E241, Bldg. 10614, M/S 39
St. Louis, MO 63166
(314) 232-7479

BROWNE, P. E.
LTV Aerospace Corp.
Vought Systems Division
Unit 2-53364
P. O. Box 5907
Dallas, TX 75222
(214) 266-3237

BRUCE, C. F.
MIT-Lincoln Laboratory
Rm. D-382
P. O. Box 73
Lexington, MA 02173
(617) 862-5500 – Ext. 7872

BRUNSVOLD, R. S.
Naval Surface Weapons Center
White Oak Laboratory
Silver Springs, MD 20910
(202) 394-2080

BURNS, G. P.
Naval Surface Weapons Center
Dahlgren Laboratory
Code DK-22
Dahlgren, VA 22448
(703) 663-8368

CARTER, S. K.
Naval Weapons Center
Code 4063
China Lake, CA 93555
(714) 939-2627

CAVALLERI, R.
Atlantic Research Corp.
5390 Cherokee Avenue
Alexandria, VA 22314
(703) 354-3400 – Ext. 288

CAYWOOD, W. C.
Johns Hopkins University
Applied Physics Laboratory
8621 Georgia Avenue
Silver Spring, MD 20910
(202) 953-7100 – Ext. 7408

CHALK, J. B.
Naval Intelligence Support Center
4301 Suitland Road
Washington, D. C. 20390

CHAPMAN, G. T.
NASA – Ames Research Center
Moffet Field, CA 94035

CLARE, T. A.
Naval Surface Weapons Center
Dahlgren Laboratory
Code DK-20
Dahlgren, VA 22448
(703) 663-8829

COOPER, G. F.
Pacific Missile Test Center
Code 1241
Point Mugu, CA 93042
(805) 982-8941

CORLETT, W. A.
NASA-Langley Research Center
Mail Stop 406
Hampton, VA 23665
(804) 827-3181

CRESCI, R. J.
Polytechnic Institute of N. Y.
Route 110
Farmingdale, NY 11735
(516) 694-5500

CRONVICH, L. L.
Johns Hopkins University
Applied Physics Laboratory
8621 Georgia Avenue
Silver Spring, MD 20910
(202) 953-7100 – Ext. 7475

SYMPOSIUM ATTENDEE LIST

CURRY, W. H.
Sandia Laboratories
Division 5625
Albuquerque, NM 87115
(505) 264-8500

DAHLKE, C. W.
U. S. Army Missile Command
AMSMI-RDK
Redstone Arsenal, AL 35809
(205) 876-7753

DAILEY, V. C.
Naval Air Development Center
Warminister, PA 18974
(215) 672-9000 – Ext. 2316

DANIEL, D. C.
AFATL/DLDL
Eglin AFB, FL 32542

DANIELS, P.
Naval Surface Weapons Center
Dahlgren Laboratory
Code DK-21
Dahlgren, VA 22448
(703) 663-8107

DE LOS SANTOS, S.
Naval Ship Research & Development Center
Carderock Laboratory
Aviation & Surface Effects Dept (1606)
Bethesda, MD 20084
(202) 227-1463

DENYSYK, B.
Naval Surface Weapons Center
Dahlgren Laboratory
Code DK-55
Dahlgren, VA 22448
(703) 663-8615

DEVAN, L.
Naval Surface Weapons Center
Dahlgren Laboratory
Code DK-21
Dahlgren, VA 22448
(703) 663-8107

DILLENIUS, M. F.
Nielsen Engineering & Research, Inc.
510 Clyde Avenue
Mountain View, CA 94043
(415) 968-9457

DRAGOWITZ, C. J.
Grumman Aerospace Corp.
Dept. 393, Plant 35
Bethpage, NY 11714
(516) 575-3671

DUNBAR, L.
Science Applications, Inc.
101 Continental Bldg.
Suite 310
El Segundo, CA 90245
(213) 640-0480

DUP. DONALDSON, C.
Aeronautical Research Association
of Princeton, Inc.
50 Washington Rd.
P. O. Box 2229
Princeton, NJ 08540
(609) 452-2950

EAVES, R. H., JR.
ARO, Inc.
VKF-Tunnel F Bldg.
Arnold Air Force Station, TN 37389
(615) 455-2611 – Ext. 650

ENKENHUS, K.
Naval Surface Weapons Center
White Oak Laboratory
Flight Measurement Div.
Bldg. 430-109
Silver Spring, MD 20910
(202) 394-1939

FARLEY, H. C.
Naval Surface Weapons Center
Dahlgren Laboratory
Code DG-44
Dahlgren, VA 22448
(703) 663-7481

SYMPOSIUM ATTENDEE LIST

FELDHUHN, R. H.
Naval Surface Weapons Center
White Oak Laboratory
Aerodynamics & Structural Branch
WA-21
Silver Spring, MD 20910
(202) 394-1675, 2890

FIDLER, J. E.
Martin Marietta Aerospace
Orlando Division
P. O. Box 5837, MP-88
Orlando, FL 32805
(305) 352-2204

FISHER, P. D.
Atlantic Research Corp.
P. O. Box 38
Gainesville, VA 22065
(703) 754-4111 – Ext. 258

FORTUNATO, E.
Naval Surface Weapons Center
White Oak Laboratory
Code 312
Silver Spring, MD 20910
(202) 394-2070

FRIERSON, J. L.
Naval Surface Weapons Center
Dahlgren Laboratory
Code DG-44
Dahlgren, VA 22448
(703) 663-7481

GARNER, J. P.
Naval Surface Weapons Center
Dahlgren Laboratory
Code DK-21
Dahlgren, VA 22448
(703) 663-8107

GILLERLAIN, J. D.
Naval Surface Weapons Center
White Oak Laboratory
Silver Spring, MD 20910
(202) 394-2086

GIRAGOSIAN, P. A.
Wright-Patterson AFB, OH 45433

GNAGY, J. R.
Pacific Missile Test Center
Code 1241
Point Mugu, CA 93042
(805) 982-8941

GORECLAD, A. J.
Naval Surface Weapons Center
White Oak Laboratory
Silver Spring, MD 20910
(202) 394-1651

GOTTLIEB, S. M.
Naval Ship Research & Development Center
Bethesda, MD 20084

GRACEY, C.
Naval Surface Weapons Center
Dahlgren Laboratory
Code DK-21
Dahlgren, VA 22448
(703) 663-8107

GRAFF, G. Y.
Naval Surface Weapons Center
Dahlgren Laboratory
Code DG-44
Dahlgren, VA 22448
(703) 663-7481

GUIOU, CAPT M.
Arnold Air Force Station
AEDC/DYR
Arnold AFS, TN 37389
(615) 455-2611 – Ext. 7834

GURKIN, L. W., III
NASA – Wallops Island Flight Cntr.
Wallops Island, VA 23337
(804) 3411 – Ext. 2566, 2200

SYMPOSIUM ATTENDEE LIST

HALDEMAN, C. W.
Massachusetts Inst. of Technology
560 Memorial Drive
Cambridge, MA 02139
(617) 253-2602

HALL, R. B.
Naval Weapons Center
Code 4576
China Lake, CA 93555
(714) 939-7395

HARRIS, T. B.
General Electric Company
Valley Forge Space Techn. Center
Rm. U-3217
King of Prussia, PA 19406
(215) 962-1340

HARTLEY, R. M.
Naval Ship Research & Development Center
Code 166
Bethesda, MD 20084

HASTINGS, S. M.
Naval Surface Weapons Center
White Oak Laboratory
Silver Spring, MD 20910
(202) 394-1669

HAYES, C.
NASA – Langley Research Center
Mail Stop 406
Hampton, VA 23665
(804) 827-3181

HERRON, R. D.
ARO, Inc.
PWT-4T
Arnold Air Force Station, TN 37389
(615) 455-2611 – Ext. 7150, 7433

HESSMAN, F. W.
Rockwell International
Missile Systems Division
4300 East Fifth Avenue
Columbus, OH 43216
(614) 239-2667

HOLESKI, D. E.
Pacific Missile Test Range
Code 1232
Point Mugu, CA 93042
(805) 982-8403

HUANG, S. L.
Naval Air Development Center
Code 3033
Warminster, PA 18974
(215) 672-9000 – Ext. 2041

HUMPHREYS, D. E.
Naval Coastal Systems Laboratory
Code 710.2
Panama City, FL 32401
(904) 234-4213

INGALLS, R.
Pacific Missile Test Center
Point Mugu, CA 93042
(805) 982-8941

INGRAM, C. W.
Systems Research Lab., Inc.
28000 Indian Ripple Rd.
Dayton, OH 45440
(513) 426-8961

JENKINS, B. Z.
U. S. Army Missile Command
AMSMI-RKD
Redstone Arsenal, AL 35809
(205) 876-7278

SYMPOSIUM ATTENDEE LIST

JOHNSON, G. G.
LTV Aerospace Corp.
Unit 2-53363
P. O. Box 5907
Dallas, TX 75222
(214) 266-7494

KALIVRETENOS, C. A.
Naval Surface Weapons Center
White Oak Laboratory
Silver Spring, MD 20910
(202) 394-4267

KATZ, W. M.
Naval Surface Weapons Center
Dahlgren Laboratory
DK-21
Dahlgren, VA 22448
(703) 663-8107

KAUFMAN, L. G., III
Grumman Aerospace Corp.
Research Dept. – Plant 35
Bethpage, NY 11714
(516) 575-2323

KEARNS, J. P.
Johns Hopkins University
Applied Physics Laboratory
8621 Georgia Avenue
Silver Spring, MD 20910
(202) 953-7100 – Ext. 646

KEMPER, W. A.
P. O. Box 129
Dillon, Colorado 80435

KING, RADM R. W.
Naval Sea Systems Command
SEA 03
Washington, D. C. 20362
(202) 692-8696

KRENS, F. J.
Naval Surface Weapons Center
Dahlgren Laboratory
Code DG-40
Dahlgren, VA 22448
(703) 663-7646

KUSTER, F. A.
Advanced Missile Project Office
Naval Air Development Center
Code 30P4
Warminister, PA 18974
(215) 674-9000 – Ext. 2574

KUTSCHINSKI, C. R.
Hughes Aircraft Co.
8433 Fallbrook Avenue
Bldg. 265/X35
Canoga Park, CA 91304
(213) 883-2400 – Ext. 3618

KYRISS, C. L.
General Electric Co.
Room U-3217, VFSTC
P. O. Box 8555
Philadelphia, PA 19101
(215) 962-5725

LA GRANGE, D. E.
Naval Ammunition Depot
Code 5041
Crane, IN 47522
(812) 854-1603

LANDO, D. W.
Naval Surface Weapons Center
Dahlgren Laboratory
Code DK-55
Dahlgren, VA 22448
(703) 663-8359

LARSEN, K. A.
Pacific Missile Test Center
Code 1241
Point Mugu, CA 93042
(805) 982-8941

SYMPOSIUM ATTENDEE LIST

LEE, K. W.
Naval Air Development Center
AVTD-3014
Warminister, PA 18974
(215) 672-9000 – Ext. 2344 or 2166

LEWIS, C. H.
Virginia Polytechnic Inst. &
State University
214 Randolph Hall
Blacksburg, VA 24061
(703) 951-6126 – Ext. 6742

LINDORM, C. A.
Naval Surface Weapons Center
Dahlgren Laboratory
Code DN-30
Dahlgren, VA 22448
(703) 663-8731

LUCERO, E. F.
Johns Hopkins University
Applied Physics Laboratory
11100 Johns Hopkins Road
Laurel, MD 20810
(301) 953-7100 – Ext. 7450

LYNCH, J. P., III
Naval Surface Weapons Center
Dahlgren Laboratory
Code DG-50
Dahlgren, VA 22448

MADDOX, A. R.
Naval Weapons Center
Code 40604
China Lake, CA 93555
(714) 939-2935

MARKARIAN, C. F.
Naval Weapons Center
Aerothermodynamics Branch
Code 4061
China Lake, CA 93555
(714) 939-2824

MARLEY, E. T.
Johns Hopkins University
Applied Physics Laboratory
11100 Johns Hopkins Road
Laurel, MD 20810
(301) 953-7100 – Ext. 7477

MAYER, W. E.
Boeing Aerospace Corp.
Seattle, WA 98124
(206) 655-3479

MATTHEWS, M. L.
Boeing Aerospace Corp.
P. O. Box 3999
Seattle, WA 98124
(206) 773-1525

MCCABE, E. F., JR.
Naval Ship Research & Development Center
Code 166
Bethesda, MD 20084
(202) 227-1670

MARSHALL, J. R.
Naval Weapons Center
Code 4063
China Lake, CA 93555
(714) 939-2820

MCCAULLEY, CAPT H. B./USN
Assistant Commander for Research
and TEchnology
AIR-03
Naval Air Systems Command
Washington, D. C. 20361
(202) 692-7439

MASON, L. A.
Naval Surface Weapons Center
Dahlgren Laboratory
Code DK-21
Dahlgren, VA 22448
(703) 663-8107

SYMPOSIUM ATTENDEE LIST

MASSEY, J. M.
Naval Surface Weapons Center
Dahlgren Laboratory
Code DK-63
Dahlgren, VA 22448
(703) 663-8468

MEEKER, R. E.
Naval Weapons Center
Code 4063
China Lake, CA 93555
(714) 939-2820

MATTHEWS, M. L.
Boeing Aerospace Corp.
P. O. Box 3999
Seattle, WA 98124
(206) 773-1525

MILTON, J. E.
University of Florida
Graduate School
P. O. Box 1918
Eglin AFB, FL 32542
( ) 882-5614

MOFFAT, R. J.
Leland Stanford Junior University
Dept. of Public Safety
711 Serra Street
Stanford, CA 94305

MOGAVERO, M. A.
Computer Science Center
221-C Preston Court
Baltimore, MD 21228
(301) 788-5832

MONTAG, W. H.
NASA-Goddard Space Flight Center
Code 742
Greenbelt, MD 20771
(301) 982-4865

MORRISSETTE, R. C.
Naval Surface Weapons Center
Dahlgren Laboratory
Code DG-30
Dahlgren, VA 22448
(703) 663-8411

MOORE, F. G.
Naval Surface Weapons Center
Dahlgren Laboratory
Code DG-40
Dahlgren, VA 22448
(703) 663-7481

MURPHY, C. H.
Aberdeen Proving Ground
Exterior Ballistics Laboratory
R. H. Kent Bldg. (120)
Aberdeen Proving Ground, MD 21005
(301) 278-3109

NARDACCI, J. L.
McDonnell Douglas Astronautics Co.
5301 Bolsa Avenue
Huntington Beach, CA 92647
(714) 896-5223

NESTLER, D. E.
General Electric Company
P. O. Box 8555
Philadelphia, PA 19101
(215) 962-6090

NEWQUIST, J. C.
Naval Surface Weapons Center
Dahlgren Laboratory
Code DG-50
Dahlgren, VA 22448
(703) 663-8586

NIELSEN, J. N.
Nielsen Engineering and
Research, Inc.
510 Clyde Avenue
Mountain View, CA 94043
(415) 968-9457

SYMPOSIUM ATTENDEE LIST

OBERKAMPF, W. L.
University of Texas at Austin
Austin, TX 78712
(512) 471-4585

OHLMEYER, E. J.
Naval Surface Weapons Center
Dahlgren Laboratory
Code DG-40
Dahlgren, VA 22448
(703) 663-7481

OSBOURNE, B. P., JR.
Defense Research & Engineering
Rm. 3D1089
The Pentagon
Washington, D. C. 20301
(202) OX-5-0552

OSKAY, V.
Director, U. S. Army Ballistic
Research Laboratories
Attn: AMXBR-EB
Aberdeen Proving Grounds, MD 21005
(301) 278-3405

O'CONNER, J. S.
Johns Hopkins University
Applied Physics Laboratory
Johns Hopkins Road
Laurel, MD 20810
(301) 953-7100 – Ext. 7416

ON, T. J.
Naval Surface Weapons Center
Dahlgren Laboratory
Code DK-21
Dahlgren, VA 22448
(703) 663-8107

PARRY, E. M.
Naval Surface Weapons Center
Dahlgren Laboratory
Code DG-30
Dahlgren, VA 22448
(703) 663-8411

PASIERB, J. J.
Johns Hopkins University
Applied Physics Laboratory
8621 Georgia Avenue
Silver Spring, MD 20910
(301) 953-7100 – Ext. 3260

PASIUK, L.
Naval Sea Systems Command
SEA-03513
Washington, D. C. 20362
(202) 692-1151

PEPITONE, T. R.
Naval Surface Weapons Center
Dahlgren Laboratory
Code DK-21
Dahlgren, VA 22448

PERPER, D. N.
Hughes Aircraft Co.
Missile Division
Bldg. 268/W83
Canoga Park, CA 91304
(213) 883-2400 – Ext. 1294

PICK, G. S.
Naval Ship Research & Developm. Cntr.
Code 1660
Bethesda, MD 20084
(202) 227-1670

PLATZER, M. F.
Naval Postgraduate School
Dept. of Aeronautics
Monterey, CA 93940
(408) 646-2944

RAUSCH, J. R.
General Dynamics Corporation
5001 Kearny Villa Road
P. O. Box 80847
San Diego, CA 92138

SYMPOSIUM ATTENDEE LIST

REDING, J. P.
Lockheed Missiles & Space Co.
Dept. 81-11, Bldg. 154
P. O. Box 504
Sunnyvale, CA 94088
(408) 742-1944

ROM, J. W.
Pacific Missile Test Center
Code 0101
Point Mugu, CA 93042
(804) 982-7831 – Ext. 7833

RUMPF, R. L.
Johns Hopkins University
Applied Physics Laboratory
8621 Georgia Avenue
Silver Spring, MD 20910
(202) 953-7100 – Ext. 7440

SANDERS, D. K.
Naval Ammunition Depot
Code 5041
Crane, IN 47522
(812) 854-1603

SCHINDEL, L. H.
Naval Surface Weapons Center
White Oak Laboratory
Silver Spring, MD 20910
(202) 394-1245

SCHMIDT, L. V.
Naval Air Systems Command
Code AIR-3200
Washington, D. C. 20361
(202) 692-7417

SHEA, G. C.
Naval Surface Weapons Center
Dahlgren Laboratory
Code DN-30
Dahlgren, VA 22448
(703) 663-8731

SHEETZ, N.
Naval Surface Weapons Center
White Oak Laboratory
Code 323
Silver Spring, MD 20910
(202) 394-2323

SINGLETON, R. E.
U. S. Army Research Office
Box 12211
Research Triangle Park, N. C. 27709
(919) 549-0641

SLYKER, R. W.
Pacific Missile Test Center
PMTC 2144
Point Mugu, CA 93042
(805) 982-8063

SMITH, R. E.
Naval Weapons Center
Code 4063
China Lake, CA 93555
(714) 939-2477

SMITH, R. H.
NASA OAST Headquarters
600 Independence Avenue
Washington, D. C. 20546
(202) 755-2383

SOKOL, C. R.
Naval Surface Weapons Center
Dahlgren Laboratory
Code DG-40
Dahlgren, VA 22448
(703) 663-7481

SOLIS, R. E.
Naval Surface Weapons Center
Dahlgren Laboratory
Code DK-21
Dahlgren, VA 22448
(703) 663-8107

SYMPOSIUM ATTENDEE LIST

STEVENS, F. L.
Naval Surface Weapons Center
Dahlgren Laboratory
Code DK-21
Dahlgren, VA 22448
(703) 663-8107

STOEHR, G.
Naval Surface Weapons Center
Dahlgren Laboratory
Code DK-55
Dahlgren, VA 22448
(703) 663-8359

SUN, J.
Naval Surface Weapons Center
Dahlgren Laboratory
Code DK-21
Dahlgren, VA 22448
(703) 663-8107

SWANSON, R. C.
Naval Surface Weapons Center
Dahlgren Laboratory
Code DG-10
Dahlgren, VA 22448
(703) 663-7561

TAI, T. C.
Naval Ship Research & Developm. Center
Code 1606
Bethesda, MD 20084
(202) 227-1462

TALBOT, J. F.
Naval Ship Research & Developm. Center
Bethesda, MD 20084
(202) 227-1670

TISSERAND, L. E.
Johns Hopkins University
Applied Physics Laboratory
11100 Johns Hopkins Road
Laurel, MD 20810
(301) 953-7100 – Ext. 7452, 7477

VAN AKEN, R. W.
Naval Weapons Center
Code 406
China Lake, CA 93555
(714) 939-3374

VAN TUYL, A. H.
Naval Surface Weapons Center
White Oak Laboratory
Code 331
Silver Spring, MD 20910
(202) 394-2265

VAS, I. E.
Gas Dynamics Laboratory
Forrestal Campus
Princeton University
Princeton, NJ 08540
(609) 452-5135

VOISINET, R. L. P.
Naval Surface Weapons Center
White Oak Laboratory
Silver Spring, MD 20910
(202) 394-2061

VOLZ, W. C.
Naval Air Systems Command
AIR-320C
Washington, D. C. 20361
(202) 692-7417

WERBACK, W. J.
Naval Weapons Center
Code 4062
China Lake, CA 93555
(714) 939-3348

WILSON, G. G.
Sandia Laboratories
Division 5625
Albuquerque, NM 87115
(505) 264-3939

SYMPOSIUM ATTENDEE LIST

WING, L. D.
NASA-Goddard Space Flight Center
Code 742
Greenbelt, MD 20771
(301) 982-4865

XERIKOS, J.
McDonnell Douglas Astronautics, Co.
Space Systems Center
5301 Bolsa Avenue
Huntington Beach, CA 92647
(714) 896-3563

ZIEN, T. F.
Naval Surface Weapons Center
White Oak Laboratory
Bldg. 402, Rm. 204
Silver Spring, MD 20910
(202) 394-2082

PAPER NO. 16

STORE SEPARATION STATE-OF-THE-ART REVIEW

G. F. COOPER
PACIFIC MISSILE TEST CENTER
POINT MUGU, CALIFORNIA

A. R. MADDOX
J. R. MARSHALL
NAVAL WEAPONS CENTER
CHINA LAKE, CALIFORNIA

E. F. McCABE
NAVAL RESEARCH & DEVELOPMENT CENTER
BETHESDA, MARYLAND

I - INTRODUCTION

An enormous amount of material exists on the subject of store separation. Notable previous surveys by McKinney and Polhamus (Reference 1) in 1966 and Ryan (Reference 2) in 1973 contain extensive bibliographies of data and techniques up to the respective dates. Other extensive bibliographies are by Marsden and Haines (Reference 3) in 1962 and Knutsen (Reference 4) in 1968. These references are essential to an overall view of the subject of store separation. The purpose of this paper is to briefly review developments since the last of the above surveys and to attempt to show the interaction of many of the diverse elements. References cited in the above surveys will not be cross-referenced again except where a particular point or comparison is to be made.

Generally speaking the whole subject of store separation can be sub-divided into three separate but definitely interacting sub-areas of analytical mechanics, simulations and full scale flight testing. The analytical techniques for mathematically modeling the store/aircraft combination have steadily improved to the point where the aerodynamics can be calculated for many relatively complex store aircraft configurations at least for subsonic flows. Supersonic techniques are well along in principle, but they are not as far along as the subsonic models in a general correlation and implementation. Transonic mathematical models are less well developed.

The wind tunnel is the prime simulator of the store separation problem, and various wind tunnel tests of different configurations make up the largest amount of the material available on this subject. The bulk of this testing is very small scale, generally in the

neighborhood of five percent. Only recently have systematic tests been undertaken to determine the effects of scale and other related features. It appears that these effects can be large at times, and they must be taken into account.

Full scale flight tests present a unique situation in that they constitute the real world environment in which the store is to be used, but additional features to be considered such as elastic structures, ejectors and the lack of control in the full scale 'laboratory' all lead to few legitimate correlations of the make-up of the aerodynamic contributions to the performance of an airborne weapons delivery system. An overriding feature of full scale work is the safety of flight, and, as a result, most testing is oriented toward definition of a condition of minimal store activity. Likewise, in the event of a catastrophic occurrence, the thrust of subsequent work is not likely to dwell on correlations. These features combined with the difficulty in fully instrumenting full scale flight tests have led to the situation that few if any comprehensive tests have been carried out to correlate the use of small scale and mathematical simulations.

II ANALYTICAL MECHANICS

General Development

In this section, techniques that calculate flow fields and associated store loads for complex aircraft/store configurations are discussed. Previous surveys, such as References 1 and 2, list at length the many reports written in this technical area and those lists will not be repeated here. Emphasis in this report is placed on the comparison of two current subsonic methods with each other and with experimental data. The first of the methods was developed by Fernandes at General Dynamics reported in Reference 11, and the other was developed at Nielsen Engineering and Research, Incorporated, by Goodwin, Dillenius and Nielsen and is reported in Reference 8. The NEAR method has been improved to alleviate two important restrictions. The non-circular fuselage was treated in Reference 9, and the pylon model was improved in Reference 10. Comparisons here are made in regions where the restricted NEAR model is expected to apply. The General Dynamics model also includes a capability of predicting loads for supersonic flight, but no general correlation has been conducted with that model, and it will not be discussed at this time.

Both the computational techniques of the General Dynamics and NEAR models are similar in that they solve the potential flow problem with no viscous effects for the store loads. This potential flow problem represents two distinct calculations, and for ease of discussion they will be treated separately. The first calculation is associated with solving the non-uniform flow field which the store experiences. The second determines the loads on the store from that flow field.

Solution to the Flow Field.

Both the NEAR and the General Dynamics methods solve a potential flow problem using discrete singularities, the major differences being in the interaction of components. The NEAR method allows the lifting surfaces (wing, pylon) to be influenced by the thickness effects of bodies (fuselage, rack, stores) in the configurations; however the bodies are not influenced by lifting surfaces. The body thickness is represented by axial sources calculated independently of the lifting surfaces in the given freestream. The General Dynamics method considers the effect of each configuration component separately. The effect of the mutual interference between components, particularly a store and wing, can be significant near the mate position. This is the region which has been shown to affect the resultant store motion the most and should be modeled properly.

Both methods model the wing-pylon with a vortex lattice which allows for most conventional wing characteristics except for discontinuities in the chord. Wing-pylon thickness is modeled by source strips which are three-dimensional surface source singularities thin in the axial dimension. The NEAR model uses an externally determined, discrete source distribution to account for all body volume effects and a two-dimensional upwash to account for fuselage angle of attack. The General Dynamics method uses line source and doublet singularities to represent fuselage volume and angle of attack effects.

Both methods allow the flow field to be calculated at any point in the aircraft flow field. The main limitation in both models is that bodies such as the rack that are very near the store are modeled as axisymmetric shapes. The improved non-circular fuselage model that was

developed at NEAR, Inc. can represent a realistic fuselage; however the rack models look nothing like a conventional rack shape.

The first comparison was made using the theory and data presented in Reference 8. The configuration involved a test at Mach number 0.25 of a simplified model of a circular fuselage with a constant sweep wing which was used in a component build-up in support of the development of the NEAR model. The General Dynamics method was also applied to the model of Reference 8, and the perturbation velocities are plotted in Figures 1 and 2, along the centerline of the position the store would occupy. In general, it can be seen that both methods produce nearly the same trends of the data; however, the magnitudes are more nearly matched by the NEAR method. Figure 1 shows the effect of the pylon, and both potential techniques overpredict the pylon effect, probably a result of the discrete nature of the vortex lattice. Figure 2 shows the effect of a rack and stores at two vertical positions. At the carriage position or Z/D = 0, the General Dynamics method, which allows for no interaction between the stores and the lifting surfaces, is drastically inaccurate. The inaccuracy in the NEAR method is probably due mostly to the lack of interference between the stores, including the rack, and the fact that the rack is represented as an axisymmetric body. At Z/D = 1 the NEAR method is more accurate, as would be expected.

The second comparison was made using the theory and data from Reference 5, and is presented in Figures 3 and 4. Here the downwash and sidewash flow angles have been measured beneath another circular fuselage constant sweep wing model. The method of Alford is compared with the NEAR method and data for the model at various lift coefficients. Alford used a rectangular vortex lattice for lifting effects and the

method of Kuene for thickness. Kuene's method basically uses two-dimensional airfoil theory applied to a swept wing by considering the wing section perpendicular to lines of constant percent thickness. Both methods generally predict the trends of the data very well. It can be seen that at $C_L = 0$ the downwash flow angle magnitudes predicted by Alford are in better agreement with the data. This indicates that the thickness model Alford used, the Kuene method, is better than the thickness strips (source strips) used in the NEAR method. At $\alpha = 4^o$ Alford has the advantage of the known lift on the wing to generate the circulation strengths in the vortex lattice. This provides a good comparison in Figure 3 of the downwash angles, perhaps better than the NEAR method directly beneath the wing. However, Figure 4 shows that the rectangular lattice used by Alford poorly predicts sidewash flow angles, whereas the swept lattice used by the NEAR method provides very good predictions here. At $\alpha = 8^o$ both methods are departing from the data due to non-linear and perhaps viscous effects.

The third comparison was made between the NEAR method and the data presented in Reference 6. This data for an F-4C aircraft flow field was taken for the clean aircraft; aircraft with pylon; aircraft pylon and rack; and the aircraft with pylon, rack and stores. This allows the analysis for the theory with a build up of various components for a real configuration similar to the procedure with the simple configuration reported on in Reference 8. The data and theory are presented in Figures 6 to 13. Figure 5 illustrates the positions beneath the F4 aircraft model at which the data was taken and the sign convention of the flow angles. This is the most extreme flow conditions to which the NEAR model was applied. Very rapid flow angularity changes that are visible

in the data indicate that the existence of compression and rarefaction waves are probably present in this high subsonic Mach number. This effect can be seen in Figures 6, 7 and 12. Also at locations close to the fuselage the magnitudes are not well predicted due to the non-circular shape of the fuselage model tested in the wind tunnel. The first series of Figures 6 to 9 shows the flow field beneath the wing-fuselage only. Chordwise plots of downwash and sidewash flow angles are shown at different spanwise stations and different vertical positions beneath the wing. Agreement can generally be seen to be poor except for the sidewash in cases below MWL of -3. The downwash predictions are not able to make the rapid changes exhibited in the data, even relatively far from the fuselage as in Figure 8. The predictions do approach the data in a qualitative sense as the distance from the fuselage is increased. This is to be expected since the effects of the non-circular fuselage become more source-like with distance. However, Figures 6 and 8 show that the downwash flow angles are also not well predicted quantitatively, indicating the wing model is not accurate at this Mach Number.

Figures 10 and 11 present the results of the NEAR theory for the F4 wing-fuselage model with an inboard pylon attached. It can generally be seen that, considering the previously mentioned disadvantages to which the model is subjected, the trends of the data are quite well accounted for excepting, perhaps, the sidewash flow angles near the downstream side of the flow investigation region. The qualitative agreement and the substantial difference in the flow field created by the pylon, e.g. compare Figures 9 and 11, indicate that the theory is properly accounting for the interfering effect of the pylon. This is true both inboard, MBL = 3, and outboard of the pylon, MBL = 5.

The last flow field comparison, Figures 12 and 13, represents the most realistic configuration which a store might experience. The model tested in the wind tunnel consisted of the F-4 fuselage-wing-pylon with a TER rack. Inboard of the pylon/store combination at MBL = 3 and MWL = -3, the flow is poorly predicted, where the flow angle is not varying rapidly. Directly below, at the centerline store position on the TER rack, MBL = 4 is the position in the flow field which the store would occupy. Here the theory is in much better agreement with the data, although it cannot match the rates of flow angle change. MBL = 5 is the position outboard of the pylon/rack combination. The flow at this position has smoothed out considerably and the theory is in good agreement.

The comparison of the NEAR potential model with the AEDC test data at M = 0.85 for the F-4 model provides some insight into the extent to which the theory applies. As would be expected at some distance away the non-circular fuselage can be modeled with simple sources. The complex interaction of multiple stores also appears tractable. Yet in the same comparison it is very evident that regions exist which cannot be modeled by the NEAR theory of Reference 8. More calculations and comparisons with data are necessary to build up a complete understanding of the limits of this theory.

The surveys of the theories and data here lead to the conclusion that the NEAR model is more accurate in predicting the flow field than the General Dynamics model as a result of the mutual interaction of the aircraft components. The non-circular fuselage modification should be used for stores close to the fuselage, but this will introduce the very complex

problem of modeling the engine inlets along with flow spillage. The General Dynamics model actually makes an attempt at this. Another possible modification should include mutual interference between the stores and rack on multiple carriage configurations.

Calculation of Loads on a Store in Non-Uniform Flow

Slender body theory has been used extensively to formulate the calculation of the store loads in the influence of a non-uniform flow field produced by the parent aircraft in both the General Dynamics and NEAR methods.

The General Dynamics method, although generally derived from slender body theory, was developed for complicated store configurations and coefficient slopes derived from any source, such as experimental data. The store body including the fin section is broken into axial sections, and a coefficient slope is required for each, and slender body theory wing-body interference factors are used to complete the configuration aerodynamics. Although being able to input the loading slopes may enhance the accuracy if they are well known, this requirement becomes difficult if the aerodynamics of the configuration are not known. The buoyancy term assumes a linear static pressure gradient across the store and the velocities are calculated at surface points to determine the gradient.

The NEAR method calculates all the aerodynamics internally and is all based on slender body theory except for a viscous cross flow and a buoyancy term. The slender body theory for the body loads does not require any aerodynamic inputs; however the results are limited by not taking advantage of experimental data when it is available. Only

cruciform or planar tail surfaces are allowed by this method. The viscous cross flow term is difficult to use because not much is known about flow separation on bodies in non-uniform flow, and a downwash field under a wing could inhibit lee side separation on a body. The buoyancy term is derived from two-dimensional flow considerations assuming that the static pressure gradient is linear and just equal to the centrifugal force created by the curvature of the streamlines. Thus, the buoyancy term looks exactly like the slender body term due to axial rate of change of perturbation velocities.

The NEAR load calculations appear to be a well formulated, unified approach for non-uniform flow and the method is presented in References 7 and 8. However, as a unified approach the approximations seem inconsistent between the slender body and the buoyancy calculations. The slender body approximation takes the boundary condition to the centerline of a body by assuming that changes across the radius can be neglected. The buoyancy term assumes that these changes are significant and is the largest component of the calculated load in the vicinity of the carriage position.

Comparison of Load Calculations with Data

A limited amount of aerodynamic load data was considered here; however, several conclusions can be drawn from these calculations. The incremental load due to the presence of the parent aircraft is assumed to combine linearly with the freestream quantity. Therefore only that increment is considered here. Two store shapes were considered, the MK-83 which is slender, and the M-118 which is not so slender. The data was taken from Reference 13 and is presented here

in Figures 16, 17 and 19. The parent aircraft was an F-4C model at a Mach Number of 0.6. All load calculations were made using the NEAR method.

The pitch plane aerodynamics of the MK-83 store is presented in Figures 16 and 17 for different vertical positions beneath the carriage location. Qualitatively the theory predicts the trend of the data very well, and if the 10% data were adjusted for an apparent flow angle, the theory would predict the magnitude of the data well all the way to the carriage position. This indicates great promise for the use of completely potential models for predicting complex flow situations.

The incremental normal force and pitching moment coefficients are presented in Figure 19 for the M-118 store. Here it appears the data and theory differ substantially through the vertical range of consideration. It also should be noted that the two data sets also disagree and thereby add some question as to its validity.

One important feature of the potential model exhibited here is the monotone decreasing nature of the loads with vertical distance away from the mate position. This will always be observed in the theory since the velocities vary as 1/R, where R is the distance from store to any singularity of which the parent aircraft is composed. More simply stated, as the store moves uniformly away from the aircraft the perturbation velocities die out which in turn uniformly decreases the loads. There have been numerous examples in the data where this is not true most likely for a fat store carried in close to other surfaces. This leads to the conclusion that there is an inconsistency in the buoyancy term which must be resolved.

Slender body theory may lack the ability to model general body shapes as well as the ability to consistently predict loads close to the aircraft. It is suggested here that a computational technique which employs surface singularities and surface load calculations should be utilized for these difficult conditions.

III - SIMULATION

Background

The wind tunnel is the prime simulation device for the store/aircraft aerodynamics and hence the store separation problem, and this is likely to remain the case for some time. The bulk of these simulations have been at the relatively small scale of five percent with the main objective of determining that a given store will clear the aircraft upon ejection. Little attention has been paid to the effects of scale not only on the aerodynamics but on the hardware aspects of mounting the configuration, and, in general, scale corrections have not been made to the data. At about the same time, researchers in the Air Force as well as the Navy began to view this situation with some concern. Dix in Reference 12 first outlined a comprehensive program at Arnold Engineering Development Center (AEDC) to investigate some of the effects for several stores mounted on an F-4C. The test program proposed an investigation of the effects of the presence of a sting and its size as well as the scaling of the gap between the store and the mounting for both pylon-mounted and rack-mounted stores. Also to be considered was the effect of altering the store afterbody to accommodate the sting.

Arnold Engineering Development Center Test Program

The test was conducted essentially as proposed with some expansion of interest such as the inclusion of another store of mutual interest to both the Air Force and the Navy. The results of this test pointed out a secondary factor often ignored but frequently a hindrance in a store separation investigation. The plethora of data created not only a massive data handling problem in the reduction but also an in-depth analysis

of the large amount of data that can nearly overwhelm an investigator. Results of the first phase of this series of tests will be reported by Dix in Reference 13, but some of the preliminary data is shown in Figures 14 and 15 provided by AEDC.

The effect of the sting presence as well as the afterbody modification is small at least on the finned bodies where the fins dominate the loading. On unfinned bodies where only the body loading is important, the sting presence has a larger effect not generally dependent on the sting size within the limits tested here. The effects also seem to peak in the transonic Mach range. Effects on other coefficients show a similar pattern, but it should not be concluded that a large effect in the pitch plane signifies a large effect in the yaw plane at the same time. The effects are a little more subtle. Examination of the effects of the sting on the store on the outboard station in Figure 15 as compared with the same store on the inboard station reveals a much larger effect on the outboard station. This would be mysterious until a check on the flow field data of Reference 6 shows the fin region, when the store is on the outboard station, is in a much more severe flow gradient than when the same store is on the inboard station, and small changes in the flow should have more effect when the gradients are large. This same situation generally holds true for other configurations and has led to the formulation of the following conclusion in conjunction with AEDC investigators:

> "If the sting affects the measurement of loads and moments on a store in a free stream environment without the aircraft present, then the effect of mutual interference between the store and aircraft will be to exaggerate the sting effect depending on the severity of the flow gradient over the affected regions of the store."

All the effects and trends pictured in Figures 14 and 15 are clouded by the fact that the data uncertainty is so large, but it should be noted

that the larger increments in coefficients shown here constitute on the order of thirty percent of the absolute coefficient level. Similar data for a smaller family of stores on the A-7 aircraft was taken by Hill and reported in Reference 14. A similar qualitative correlation of this data with A-7 flow field data reported in Reference 15 reveals the same conclusion regarding sting effects.

Naval Ship Research and Development Center Test Program

To contribute to the development of a store separation technology development, the Naval Ship Research and Development Center (NSRDC) conducted tests to complement the prior sting-effect tests at AEDC. Parameters considered were Mach Number, Reynolds Number and store attitude, and position relative to the parent aircraft. Two AEDC store configurations were considered as follows:

1. M-118 3000 lb. General Purpose Bomb.
2. Mk-83 Low Drag 1000 lb Bomb

In the second case, the TER was loaded with stores in both of the other positions. Some overlap of test conditions of AEDC was made to establish mutual confidence in the data.

Six-component loading on the store was determined by the Modified Grid Method utilizing the Captive Trajectory System for traversing the aircraft flow field in the 7 by 19 foot Transonic Wind Tunnel at NSRDC. Data for the Modified Grid Method was acquired by the automatic traversing through a predetermined grid of X and Z tunnel positions when the store was manually set in a given alpha, beta and phi attitude and Y tunnel position. Only one or two manual settings were required for

each automatic traverse (one data run). Configurations evaluated were as follows:

1. M-118/F-4, 5% scale, mounted left inboard pylon
2. Mk-83/F-4/TER Sta. 1, 5% scale, other stations occupied
3. Mk-83/F-4/TER Sta. 1, 10% scale, other stations occupied

The 5% M-118 and 5% Mk-83 balances, and stings were identical to those used at AEDC. In fact, many components were simply borrowed. The geometry of the M-118 tail cone was modified to accommodate the sting such that it corresponded to afterbody #2 of the AEDC tests. The Mk-83 afterbody was the same as the AEDC tests. The NSRDC 5% F-4 model employed was a complete model whereas the AEDC model lacked the tail section. The NSRDC 5% model also had closed inlets (no flow through), while the AEDC model had flow through inlets. In the case of the M-118 tests, all five parent pylons were present on the aircraft at the conventional stations. These same pylons were present for the Mk-83 tests, but a Triple Ejector Rack (TER) was mounted on the left inboard pylon with both shoulder stations filled with Mk-83 shapes.

The 10% Mk-83 model and associated sting were exact duplicates of the 5% configurations scaled up by a factor of two. This provided the same base to sting relationship and reproduced the tail geometry of the 5% tests. A 10% M-118 model was also fabricated to duplicate that portion of the 5% tests, but tunnel time was exhausted before this test could be done. The 10% F-4 model was actually a "B" model as opposed to the Air Force "C" model, but the main external difference is in the nose section. This was not expected to affect the flow in the vicinity of the inboard wing pylon. It also had flow through inlets.

In order to facilitate traversing the store model in close to the aircraft model, a special six-inch offset sting was used with the mounting

TABLE 1 - PARAMETERS INVESTIGATED
(Nominal Values)

CONFIGURATION	MACH NUMBER		REYNOLDS NUMBER $\times 10^6$/ft	ATTITUDES-(DEGREES) PITCH	YAW	ROLL	POSITION (INCHES) LONGITUDINAL	LATERAL	VERTICAL	TOTAL RUNS
5% M11°	0.600	2.0	3.6	-10→30	-15→15	-22.5→0	2→-16	-10→0	11→0	53
	0.800	2.0	3.6	-10→30	0	0	2→-16	-4	11→0	5
5% Mk 83	0.600	2.0	3.5	-10→30	-15→15	-22.5→0	2→-16	-8→0	11→0	65
	0.865	2.0	3.5	-10→10	0	0	2→-16	-4	11→0	3
10% Mk 83	0.600	2.0	4.2	-10→15	-15	15→-22.5→0	4→-16	-12→-2	11→0	49
	0.700	1.0	5.5	0	0	0	4→-16	-8	11→0	1

TABLE 2

REFERENCE INFORMATION

Model Scale

ITEM MODEL	5% MK 83	10% MK 83	5% M118	5% F4C	10% F4C
Area (Ft^2)S	.002673	.01069	.007933	1.325	5.30
Span (In)B	.700	1.400	1.206	23.0445	46.089
Chord (In)C	.700	1.400	1.206	9.624	19.248
Length (In)	5.725	11.453	9.113	-	-
Diameter (Max) (In)	.700	1.400	1.206	-	-
Moment Ref Sta (Inches from Hose)	2.525	5.05	2.81	17.68	35.36
(Full Scale Equivalent)	(50.5)	(50.5)	(56.2)	(353.6)	(353.6)

as shown in Figure 20. No artificial transition strips were applied to any of the models used, and no base pressure corrections were applied to the data. The investigations were conducted with the aircraft angle of attack set to represent a level flight condition for the particular Mach Number. This led to approximately 2^{o} at the lower speed and 1^{o} at the higher speed. As a result of angular offsets of various components the store was nearly zero with respect to the free stream at the lower speed and approximately -1^{o} at the higher speed. A total of 176 runs were made over a Mach Number range of 0.6 to 0.865 and Reynolds Numbers from 3.6×10^{6} to 5.5×10^{6} per foot. The range of all parameters investigated is summarized in Table 1.

Data was acquired continuously during a traverse and was eventually recorded as z increments ranging from 0.1 inches near the aircraft to 2.4 inches or greater at large distances from the aircraft. The end result is an average of three readings taken 20 milliseconds apart with 5-hertz filters. Reference dimension information is given in Table 2, and the final data is reduced to conventional body-axis coordinates.

Comparison of Test Results

A general comparison of the results is shown Figures 16 through 19. Figure 16 shows the normal force from several sources on the Mk-83 as a function of normalized z-distance from the attached position. The angle of attack of the store is or should have been "0", and this coefficient is the increment due to mutual interference. Upon examination of this data, it is gratifying to see that data from the NSRDC 5% tests generally agree with the AEDC 5% test. The scatter of the

data is quite large even after averaging three points in recording and plotting only about every other point. Readily apparent is the data shift for the 10% data. Two factors are involved. First there is an obvious small angularity in at least the NSRDC tests. It appeared to exist at least at times in the AEDC data too, but testing was not carried out far enough from the aircraft to be definitive. An approximation to the free stream can be made by examining the asymptotic behavior of the store. A large amount of the data far removed from the aircraft was averaged together to form an apparent free stream for the tunnel environment at NSRDC and is shown in Figure 18. The store normal force coefficients in the tunnel free stream are in relatively good agreement for the 5% and 10% tests, but they lead to discrepancies in flow angle as large as 2^{o}. It is easy to see that such discrepancies could occur with alignment not taking into account any asymmetrical blockage effects of the massive dual sting apparatus and possibly some component misalignment on the model. 2^{o} does not seem large and does not seem a large factor here, but small angular discrepancies appear much more significant later for the M-118 store. It should also be noted that the discrepancy between the 5% and 10% tests and the best estimate of the true store characteristics as reported in Reference 16 can be roughly attributed to the reduction in the fin area aft end of the store to accommodate the sting.

Shifting the data such that all of it decays in a consistent manner does not affect the agreement of the 5% data sets, but the 10% data, at least for the near position, is still considerably different revealing the second factor, probably a Reynolds Number effect. Examination of the drag data, not shown here, tends to confirm that this data shift is

due to Reynolds Number.

To complete the picture here, the NEAR mathematical model results are also shown. It was originally thought that this model represented rather poorly the 'close-in' loading, but the data here indicates a good overall agreement even with the close-in position when the larger scale data is considered.

Similar data is shown in Figure 17 for the moment, and the conclusions are the same as for the force data. Equivalent free stream data for the moment coefficient is also shown in Figure 18, and again angular discrepancies as large as 2^{o} appear in the moment coefficient. Furthermore there is a marked difference in characteristics of the equivalent free stream aerodynamics between the 5% and 10% data. Conversations with AEDC researchers indicate that this is not unusual in tests at this scale; in fact it is the usual case. If this is the case then small scale data should be used very cautiously in defining mutual interference data. Rather than use the data in its absolute form, it should be viewed as a change from the equivalent free stream of the tunnel and then combined with the real free stream environment. The 10% data has the same characteristics as the estimated full scale, and again the discrepancy existing can be attributed to the change in fin region to accommodate the sting.

Data comparable to the Mk-83 was taken for a single M-118 store on the left inboard pylon of the F-4, and this is shown in Figure 19. Unfortunately 10% data was not available for this test, and the AEDC data is of limited extent. The results are not of interest operationally because this configuration cannot be flown, but they do reveal several

shortcomings of both the wind tunnel simulations as well as the mathematical model. Results of the normal forces from the AEDC and NSRDC 5% tests appear to be very much in disagreement, but it can be seen that the asymtotic values again indicate some flow misalignment. Shifting the NSRDC data so that the asymtotic data decays toward zero tends to give an approximate value of zero for the initial position values of the NSRDC data but would not lead to a reversal of sign that exists in the AEDC data. This feature will be the subject of future analysis, but it should be noted that one apparent difficulty which may be un-resolvable is that data of this level is nearly within the accuracy of the system.

Also shown in Figure 19 are the NEAR mathematical model results for this configuration, and they are generally in disagreement with everything. This illustrates the problem alluded to before that a strictly potential solution of this type cannot produce a force that changes sign, and the use of slender body theory breaks down in close where a 'buoyancy-like' term must dominate. Furthermore the M-118 store is far from a slender body and may in itself violate the model. Lastly, just as the test data is approaching the limit of accuracy possible, the model itself may be doing likewise. Preliminary analysis of the data indicates that at larger angles of attack, where the force levels are larger, both AEDC and NSRDC data are in closer agreement with each other as well as with the NEAR model.

Examination of the moment coefficients for this configuration reveals that the same arguments apply. Shifting the NSRDC data for a consistent decay value tends to give it the same general trend as the AEDC data, but there is still a large disagreement for the rack position. The NEAR model now has the same trend as the data, but this is considered

fortuitous in view of the lack of correlation with the force data.

Use of the moment and force data from the different sources shown in Figure 19 would clearly give different results for store motion. There have been, from time to time, various comparisons of the store motion close to the aircraft as a result of inaccuracies in the data. This is only half of the problem. If the store-aircraft interference is ever to be used in conjunction with aiming information, the effect of various inaccuracies in the data must be carried to some impact point. A broad general comparison of this was done by Maddox in Reference 17, but the fictitious store/aircraft interactions were in general too large. Further studies along this line using levels in agreement with loads shown in Figures 16, 17 and 19 are called for to determine how good wind tunnel or mathematical model data must be. Trajectory comparison tests then should ideally accompany most wind tunnel investigations to verify if the test data is conclusive.

The use of a wind tunnel to simulate store separation requires a large number of detailed considerations especially if the resulting data must be accompanied with trajectory studies involving perturbations. The wind tunnel data techniques usually fall into two conflicting schools of thought. One technique referred to as the Point Prediction Technique, or in some cases the Captive Trajectory Sting, allows a store to "fly" a limited trajectory in the tunnel in which each point is computed from the simulated loads as seen by the model. The final result, in this case, is a trajectory. On the other hand, there is a technique which might be called a Field Array technique which seeks to map the flow field or perhaps the loads on some store as a function of position and attitude in the vicinity of the aircraft. The result is a set of aerodynamics at discrete points in the combined flow field which must be

used with separate programming to generate a trajectory.

Generally speaking, wind tunnel installations have tended toward the PPT/CTS approach partly as a result of the neat concise form of the final answer and certainly because of the unquestionable cost effectiveness of generating a single trajectory. On the other hand, field installations have tended toward a preference for the Field Array data largely because of the data flexibility through which it can be manipulated to apply to different flight conditions, different initial conditions or even different stores. Other important attributes of the Field Array approach are the ability to make necessary corrections to the data such as that for scale, ready integration of data from multiple sources and the small effort required to extend the trajectory to an impact.

It would be most advantageous to the technical community at large to try to retain both techniques which at first glance appear mutually exclusive. This is an expensive proposition, however, to simultaneously develop and keep current procedures and software for two separate techniques. Bamber, in References 18 and 19, foresaw some of these problems and suggested, as an alternative, some sort of combined system capable of doing both techniques. The numerical techniques developed there are quite bulky especially in view of some current unpublished work, but the comparison of systems is valid, and the conclusion has considerable merit in future wind tunnel simulations.

IV - FULL SCALE TESTING

Background

Carefully structured testing both in flight and on the ground serves to verify the functioning of an airborne weapon delivery system. Marginal aerodynamic performance areas are usually identified by wind tunnels or theoretical models. All reasonable failure modes, including instrumentation systems, are anticipated with estimates made of their probabilities of occurrence and of the consequences. Validated simulations are of great value here and allow a quantitative analysis of worst-case failure modes. This includes the concern for range safety under some conditions. Separations ranging from jettison through possible launch failures (i.e. week ejection, control failure, and etc.) to perfect launches are all analyzed before a new store/aircraft combination can be accepted for flight test. Finally, the concern is for success of the test and acquisition of engineering data. Table 3 lists the engineering information that is sought in normal flight testing. An evaluation is made as to the items that are nearly always obtained and those which are more difficult to instrument and are thus acquired only in special cases.

An example of a program which includes most all of these considerations is the recent missile development program for the Air Launched Low Volume Ram Jet (ALVRJ), and a brief description of the separation investigation of this vehicle may serve to illustrate the interlocking nature of various features of this type of launch certification. The missile was developed by Vought Systems Division of LTV Aerospace Corp. as a propulsion test bed and had a critical separation phase requiring launch within narrow Mach Number and angle-of-attack limits at the performance limit of the A-7 launch aircraft. With fixed fins, it is statically unstable at launch

TABLE 3

ENGINEERING DATA ACQUIRED DURING SEPARATION PROGRAMS

	Typical Status	
	Determined Prior to Flight	Instrumented During Flight
Aircraft Related Variables:		
Mach No.		2
Altitude		2
Normal G-Load		3
Lateral G-Load		3
Angle-of-Attack		4
Angle-of-Side Slip		5
Trajectory Vertical Angle		3
Pitch Attitude		3
Roll Attitude		4
Store Station	2	
Adjacent Store Loading	3	
Local Flow Field -- Infl. Coef.	3	
Local Flow Field -- Angularity	4	6
Ejector Support Struct. Compliance	5	6
Ejected Related Variables:		
Mass	1	
CG Position	2	
Moments of Inertia	3	
Free Stream Aerodynamic Char.	3	
Control Characteristics	3	
Thrust Characteristics	2	2
Structural Vibration Char.	3	4
Translation Rel. to Aircraft		3
Body Angular Rate History		3
Angular Attitude Rel. to Aircraft		3
Body Accelerations		3
Control History		3
Store Related Variables:		
End-of-Stroke Velocity	2	4
End-of-Stroke Pitch Rate	2	4
Stroke Position History	4	4
Stroke Force History	4	4
Cartridge Loading	1	
Plumbing Initial Temperature		4
Sway Brace Pre-Load	5	
Stow Loads	4	5
Piston Gas Pressure History	3	5
Ejector Pitch Rate History	4	4
Cartridg-Related Tolerances	3	

Legend:

1 - Always, 2 - Usually, 3 - Sometimes, 4 - rarely, 5 - very rarely, 6 - Never

and it must be stabilized. Tenth scale captive rig model tests in the NSRDC tunnel indicated a strong pitch-down flow field throughout the planned launch envelope; thus a modified single piston ejector was positioned to apply the ejection force aft of the missile CG off-setting the pitch-down flow field for a limited flight range. In addition to the above constraints, the booster motor was an experimental design so that ignition was delayed until 5 seconds after separation.

Considerable simulation of the separation phase was undertaken using various control and ejector failure modes. Fixed fin and hard-over fin as well as weak and overly strong ejector impulses were tried. In addition, ejections at the instant of aircraft response to an air gust were simulated. Three fixed fin unthrusted versions of the ALVRJ were launched at progressively greater Mach Numbers at the planned altitude. These were known as the STV (Separation Test Vehicle) one, two,and three. As dynamic pressure increased, their transition into tumbling occurred sooner after launch in accordance with predicted behavior. Table 4 compares predicted and test results from Reference 21 for the three STV's.

The first real ALVRJ launched was the DTV No. 1 (Demonstration Test Vehicle No. 1) shown in Figure 21. Comparisons of predicted and actual separation dynamics are shown in Figures 22, 23, and 24. Both pre-flight and post-flight predictions are made. The pre-flight prediction assumed a standard atmosphere and the launch aircraft flying at the planned launch condition. The post-flight prediction was initiated with the actual atmospheric condition and the launch aircraft flight condition. The post-flight prediction allows validation of the simulation. Since the three STV's were unguided and unthrusted, only the first fraction of a second of their separation trajectory afforded data for validation of the simulation.

TABLE 4

STV NUMBERS 1, 2 AND 3 TEST RESULTS

Launch Conditions:

STV NO	DATE	ALTITUDE	MACH NO.	DYNAMIC PRESSURE
1	10 May 1974	13,000	.6	326
2	6 June 1974	13,000	.77	536
3	13 June 1974	13,000	.84	627

Summary Results at 0.5 sec. After First Motion:

	PREDICTED VALUE	TEST DATA
Vertical Clearance	9 to 12 ft.	9 to 12 ft.
Pitch Attitude	$+1^{o}$ at low Mach No.	-2^{o} at low Mach No.
	-16^{o} at high Mach No.	-12^{o} at high Mach No.
Roll Attitude	-2^{o} (ejector on CL)	-7^{o} to -12^{o}
	-27^{o} (ejector 1/8 in. left of C/L)	

This sort of analysis represents a formidable undertaking for a single store/aircraft combination in a limited flight range. Similar undertakings for all store/aircraft/flight conditions constitute an impossible task. On the other hand, traditional test techniques involving starting from an obviously safe condition and gradually progressing through the flight environment also represents an ineffective procedure. Some combined use of theoretical models, simulations, data from other tests and limited flight tests must be brought together in a simple effective analysis of the separation process.

Measurement of Stowed Loads

Most local flow fields are at their greatest intensity at a nominal missile-stowed position and decay monotonically with distance below the aircraft to the free stream. Thus, measurement of the air loads acting on the store while in the stowed position is beneficial. The local flow field air loads are separated from the total air loads by using the known free-stream aerodynamic characteristics of the store by post-flight computer processing of the data. "On line" computation would require high capacity machines; however simplified data libraries could be used for approximate "on line" determination of the local flow field. This could be of considerable value in conducting an extensive flight test program by directing the test pilot toward (or away from) the most critical portion of a flight envelope.

Once the stowed loads are determined, wind tunnel grid surveys for the store determine the rate of attenuation of influence air loads with vertical distance. Use of only the stowed-loads influence field coefficients has led to good results in some cases as described in Reference 22. Grumman Aerospace Corp. used both the stow-loads-determined influence field coefficients and captive rig grid-survey-determined influence coefficients

in its separation math model for predicting AIM-7 separation from the F-14. The best results were obtained with the stow-loads-determined coefficients in the subsonic and transonic speed regimes and the grid-survey-determined influence coefficients in the supersonic regime.

Unfortunately there are a number of situations where stowed-loads do not accurately indicate the influence field at positions below the stow position. This is true where shock waves emanate at acute angles from major launch aircraft components at supersonic speeds, as shown in Figure 25 from Reference 23. Abrupt changes in influence coefficients can be expected when traversing downward through such shock waves. Anomalous flow conditions at certain flight and adjacent store loading combinations can even strongly vary the influence field even within the stroke distance of an ejector. In Reference 24 it is reported that the AIM-7E at station 4 (fuselage aft centerline station) of the F-14 experiences an increasingly strong nose-up pitching moment from the stowed position to end of stroke at high dynamic pressure transonic speeds; however, Reference 24 goes on to say "by Mach 1.2 the trajectories match the strong nose-down predictions indicated by wind tunnel and installed loads flight tests". Figure 26, Reference 24, shows predicted and flight test results compared for station 4 separations within the transonic regime. Another instance during stowed loads flight testing of the F-14 in which measured stow loads lead to an erroneous prediction of separation trajectory was in the case of a small bomb carried on a forward left hand station. The local flow field at this one station experienced an anomalous preturbation due to outflow from a vent on the underside of the F-14. Maddox, in Reference 17, stressed the strong effect that the close-in gradients of the influence force field can have on the separation trajectory. This situation can be aggravated in the

case of an unstable missile such as the AIM-7E which is statically unstable at subsonic speeds and small angles of attack.

In response to the need to measure full scale stowed air loads in flight, a number of force balance configurations have been devised. One technique is to instrument an operational rack with strain gages. Two such racks, the MAK-79 and the BRU-10, were used in the program described in Reference 25 with the F-14 external stores certification program to measure the stowed loads on a variety of air-to-ground stores. As a result of the great number of external store combinations only the worst flight conditions and store loadings were flown. By "on line" processing of the telemetered data from the F-14, it was possible to alter the flight conditions during testing thus allowing optimum use of flying time to evaluate the many combinations of external store loads.

Hooton in Reference 26 describes a similar instrumented TER rack. All standard racks of this type must be strong enough to hold a heavy store under maximum expected stowed loads; thus the separation of air loads becomes a difficult calibration problem with very large tares. As a result, such racks frequently have limited ranges and/or do not measure full six-degree-of-freedom loadings. Smith, in Reference 22, describes the use of another type of device that still has difficult calibration features but has lower tares. The device incorporates a balance designed to go inside a lightweight shell. It can be used with any configuration for which a dummy shell to represent the store will fit over the balance. The most extensive use of this device has been with a Rockeye II store, but the results were inconclusive because of an inability to make a confident correlation between aircraft flight conditions and wind tunnel conditions.

In addition to the instrumented racks and more sophisticated airborne balances, the quest for reliable large scale loading has even led

investigators to attempt extendable load measuring devices, but the hardware and other associated problems have kept this device from becoming a practical reality.

Ejector Characteristics

The ejector plays a key role in intiating the separation trajectory, and studies such as Reference 17 have shown the ejection event can have a strong effect on the separation motion near the aircraft as well as the impact point for unguided stores. In addition, the ejection can also strongly affect the structural integrity of light weight structure stores. Included in the factors that affect the ejector characteristics are the mass properties of the store itself, air loads on the store, compliance of the supporting structure of the ejector, and the cartridge burning and internal gas dynamics in the case of the hot gas ejector. Characteristics for an ejector are usually determined experimentally in what is sometimes called a "pit" test where the ejector is mounted on a rigid support and physically ejects a body of dynamic properties similar to desired stores. The body is sometimes rigged with some sort of elastic restraints to simulate aerodynamic loads. Results of such a test are shown in Figure 27 from Reference 29 and in Figure 28 from Reference 30. Repeatability of these results under operational conditions as well as the effect of the crudely simulated air loads have both raised serious doubts of the meaning of such results,and especially of the use of fixed end-of-stroke condition as an input.

The interaction between the ejector and the supporting structure has recently been investigated by Devan as reported in References 27 and 28. Military Specifications require that ejection racks must be qualified by structural testing to loads 100% in excess of worst expected loads, and one would expect the result to be a fairly rigid structure. On the other

hand, store release films, particularly for the Multiple Ejection Rack, clearly show considerable vibrational excursions in many cases. The representative case examined by Devan was a MER on the center wing pylon of an A-7D and loaded with M-117 bombs. Second, fourth and sixth release stations were considered for a dive angle of 30° at 10,000 feet and a Mach Number of 0.9. Aircraft pull-up rate in the vertical plane was varied between 0 and .1 rad/sec., and representative air loads from 5% wind tunnel testing were used. General computational results illustrated in Figure 29 are summarized as follows:

(1) Ejection velocities, mainly vertical component, deviate by 15 percent or less from the rigid case.

(2) Ejection pitching and rolling rates are affected significantly by flexibility. For the second bomb in the normal release sequence at .1 rad/sec. aircraft pull-up rate, the increment is about 35 percent of the rigid case.

(3) Ejection yawing rate is insignificantly affected by flexibility.

Finally, in recognition of the variability of current ejector characteristics to various factors, a number of adaptive or "smart" ejectors have been developed in conceptual or prototype form such as described by Maestri and Schindel in Reference 20 to use various levels of feedback of aerodynamic information to place the store in a more predictable condition outside the interference flow field of the aircraft. No known flight testing or ground simulation of these concepts is available at this time.

Comparison of Separation Prediction and Testing Results

Even with limited knowledge about most flow fields, separation prediction has in most cases become sufficiently accurate to define safe or unsafe launch conditions when backed up by wind tunnel testing and sufficient

analysis particularly parametric studies to reveal especially sensitive conditions. The separation perturbation on aiming of a free fall store has not yet been introduced into use except through a large sample statistical approach. As indicated previously, the ALVRJ did have considerable initial testing to define its separation characteristics, and the comparisons of pre-flight prediction, flight test and post-flight corrected prediction are shown in Figures 22,23, and 24. The AIM-7 on the F-14 is less well defined even with considerable background investigation. The results of this store separating from a semi-submerged fuselage station at high dynamic pressure and low G-load are shown in Figure 26.

Agreement between wind tunnel derived interference effects and flight test results is achieved by treating the wind tunnel data as a library of interference influence coefficients and by adjusting the library to agree with flight tests as more experience is obtained. Such adjustment would account for scale effects such as shown in the Simulation Section or any other effect not covered by the wind tunnel testing, but it is generally an empirically determined adjustment. Once predictions agree with one or more flight test separations, the library is assumed trustworthy enough to predict separations of that particular store under similar conditions. Figure 30 taken from Reference 31 is an example of such an adjustment but care must be taken to guarantee that such a representation is not misleading. For instance, the results of Reference 31 are for an inactive store and hence the correlation is probably not at all general.

Instrumentation and Data Reduction

Adequate validation of an empirical separation math model is predicted upon accurate and complete instrumentation of flight test separations.

By math model in this sense, the meaning, as opposed to the theoretical math model outlined in the Analytical Section, is essentially a trajectory program with a library of aerodynamic functions which represent the configuration in question. The extent to which a separation math model can be forced to fit observed data is limited not only by the library but also by the data accuracy. As indicated in Table 3, time and cost preclude instrumenting for many variables to describe fully a store separation unless the separation is of critical importance.

Inertial instrumentation (accelerometers and rate gyros) is particularly useful in analyzing the first motions of an ejected store, and in one program it was found that a double time integration of accelerometer data agreed closely with onboard camera data. Accelerometer data has been used exclusively between hook opening and end of stroke to determine initial loads on the missile. Photographic data has generally been too slow during this period, and second time derivatives of its data resulted in erroneous accelerations. Accelerometer data has been continually telemetered because of its high frequency content, while other variables were sampled as higher rates.

Photographical coverage of store separations is most useful in determining clearance with other stores and aircraft. Onboard cameras, providing timing marks on the film to aid synchronization, are carefully located and boresighted to produce accurate store separation kinematic data. Reduction of movie films to extract relative store/aircraft kinematics is done by tracking reference points on the store images. Triangulation from several different cameras allows construction of the store trajectory in the aircraft coordinate system. A new faster variation of this technique has been developed at Point Mugu as the Photo Data Analysis System (PDAS) employs a television mixing system to superimpose an image. The system is

described in greater detail in Reference [32]. Achievable accuracies with good lighting and proper positioning of onboard cameras are 0.1 ft. in position and 1^{o} in angle.

Ground based theodolites furnish separation data up to several thousand feet above ground as well as subsequent trajectory information, but airborne theodolites, which are dependent on highly stabilized optics, are still under development. Radar coverage of store separation from ground tracking radar is of limited usefulness because of the inability to distinguish two separate bodies until they are some distance apart, but radar is most useful in tracking after the separation phase.

V - CONCLUSIONS/RECOMMENDATIONS

Operational techniques for mathematically modeling the store/aircraft flow field now allow at least one class of bodies (slender) to be treated even in complex configurations. There are some improvements still necessary in simulating the various component interactions for the flow field and for dealing with some of the more complex relationships in body loading such as the buoyancy component. A large improvement is probably possible by employing the more complex models which use surface singularities.

Wind tunnel simulations show the sting to be less a problem than anticipated. There is, however, a large scale effect in evidence, and additional work is required on this effect. Flow angle anomalies were observed, and in one case a large blunt store gave very erratic results in two different facilities particularly in close to the attached position. This region of erratic behavior in wind tunnel simulations coincides with the region where mathematical models also produce questionable results. Equivalent free stream conditions for the wind tunnel create a problem in interpreting the results.

Store separation, when backed up by adequate wind tunnel simulation and analysis, can be predicted for many cases, but the typical operational test or certification for flight of a utility pod does not rate sufficient back-up information. In addition, much of the data on separation produced by research facilities is not in a format that is easily used by field facilities. Theoretical mathematical models would be most effective for field activity use if the internally generated aerodynamics were capable of being supplemented or revised

by empirically observed conditions. Likewise, the most useful wind tunnel information is the basic aerodynamic information corrected for scale effects in some form of array as opposed to a store trajectory. The latter imposes the inverse problem of extracting the basic aerodynamics from kinematic data, while the former provides a vehicle for transforming the results to other conditions. Cheaper more effective instrumentation is desirable as well as ground equipment to evaluate system performance such as an ejectory dynamometer to determine ejector output under various conditions.

REFERENCES

1. McKinney, Linwood W. and Polhamus, Edward C. "A Summary of NASA Data Relative to External-Store Separation Characteristics" NASA Technical Note TN D-3582, November 1966

2. Ryan, E.M. "Analytical Techniques for the Determination of Flow Fields about Aircraft-Store Combinations" Technical Note 4061-167, Naval Weapons Center, China Lake, California, April 1973

3. Marsden, P. and Haines, A.B. "Aerodynamic Loads on External Stores: A Review of Experimental Data and Method of Prediction" A.R.A. Report No. 5, Aircraft Research Association, Ltd., Manton Lane, Bedford, November 1962 (Confidential Report)

4. Knutsen, Dale E. "Determination of Captive Flight Loads and Separation Trajectories of Airborne Stores" TP-4328, Naval Weapons Center, China Lake, California, June 1968

5. Alford, W.J. "Theoretical and Experimental Investigation of the Subsonic-Flow Fields beneath Swept and Unswept Wings with Tables of Vortex-Induced Velocities" NACA Report 1327, 1957

6. Hill, D.W. "Investigation of the Flow Field beneath the Wing of the F-4C Aircraft with Various External Stores at Mach Number 0.85" AEDC TR-72-92, Arnold Engineering Development Corporation, June 1972

7. Goodwin, Frederick K. ; Nielsen, Jack N. and Dillenius, Marnix F.E. "A Method for Predicting Three-Degree-of-Freedom Store Separation Trajectories at Speeds up to the Critical Speeds" AFFDL-TR-71-81, November 1974, (see also NEAR Report TR-26, Nielsen Engineering & Research, Inc., Mountain View, California)

8. Goodwin, Frederick K.; Dillenius, Marnix F.E. and Nielsen, Jack N. "Prediction of Six-Degree-of-Freedom Store Separation Trajectories up to the Critical Speed - - Volume I, Theoretical Methods and Comparisons with Experiment" AFFDL-TR-72-83, October 1974, (see also NEAR Report TR-37)

9. Dillenius, Marnix F.E.; Goodwin, Frederick K. and Nielsen, Jack N. "Extension of the Method for Predicting Six-Degree-of-Freedom Store Separation Trajectories at Speeds up to the Critical Speeds to Include a Fuselage with Noncircular Cross Section - - Volume I, Theoretical Methods and Comparisons with Experiment" AFFDL-TR-74-130, November 1974, (see also NEAR Report TR-60)

10. Dyer, C.L. "An Investigation into Flow Field Prediction with Multiple Pylon Models" AFFDL TM-74-105-FGC, October 1973

11. Fernandes, F. Dan "Theoretical Prediction of Interference Loading on Aircraft Stores - - Part I, Subsonic Speeds" NASA CR-112065-1, June 1972, General Dynamics, Electro Dynamic Division, Pomona, California

12. Dix, Richard E. "A Review of Methods of Measuring Aerodynamic Forces and Moments Acting on Captive Stores in Wind Tunnel Tests" AEDC-TR-72-108, August 1972, Arnold Engineering Development Corporation

13. Dix, Richard E. "Effects of Sting Presence on Measurements of Aerodynamic Loads Acting on Captive Stores in Wind Tunnel Tests" AEDC-TR-..., AFATL-TR-..., (to be published) Arnold Engineering Development Corp.

14. Hill, D. W. "Investigation of Factors affecting the Wind Tunnel Measurements of Carriage-Position Air Loads on External Store Models at Transonic Mach Numbers" AEDC-TR-75-12, AFATL-TR-75-22, Arnold Engineering Development Corporation, February 1975 (see also Arnold, R. J.; Braud, S. C. and Hill, D.W. "An Investigation of Factors Affecting the Accuracy of the Captive Trajectory Wind Tunnel Technique" JTCG/ALNNO Aircraft/Stores Compatibility Symposium Proceedings from Sacramento, Calif. 18-20 September 1973)

15. Carman, J. B. "An Investigation of the Flow Field of the A-7D Aircraft with Several External Store Loadings at Mach Numbers 0.70 and 0.95" AEDC-TR-75-15, AFATL-TR-75-21, Arnold Engineering Development Center, April 1975

16. Piper, W.D. and DeMeritte, F. J. "Summary of the NOL Investigations to Date of the Aerodynamic Characteristics of the Navy Low Drag Bomb" NAVORD Rept. 5679, Naval Ordnance Laboratory, February 1960

17. Maddox, A. R. "A Parametric/Sensitivity Study of Store Separation" Procedings of Aircraft/Stores Compatibility Symposium Sponsored by Joint Technical Coordinating Group for Air-Launched Non-Nuclear Ordnance, Sacramento, Calif., 18-20 September 1973

18. Bamber, Millard J. "Two Methods of Obtaining Aircraft Store Trajectories from Wind Tunnel Investigations" Aero Rept. 970, David Taylor Model Basin, Washington, D. C., January 1960

19. Bamber, Millard J. "Store Separation Investigations by Grid Method Using Wind Tunnel Data" Report 2202, David Taylor Model Basin, Washington, D. C., January 1960

20. Maestri, Raymond R. and Schindel, Leon H. "Self-Compensating Store Ejection" NOLTR 74-32, Naval Ordnance Laboratory, White Oak, Maryland, 5 February 1974

21. Tetens, R. C. "ALVRJ Monthly Technical Report for July 1974" LTV Aerospace Corp., Dallas, Texas, July 1974

22. Smith, R. E., "Prediction of Store-Separation Motion Using Initial Captive Loads" NWC TP-5261, Oct 1971, Naval Weapons Center, China Lake, Calif.

23. Forsmo, D. P. "Simulation of Missile Trajectories in Proximity of the Launching Aircraft and Comparison with Flight Test Data" presented at the Seventh U.S. Navy Symposium on Aeroballistics, Point Mugu, California, 7-9 June 1966, PP 21-37

24. Johnson, R. "F-14/Separation Analysis Correlation for Station 4 Sparrow 'Delta' Program: Memorandum: Rpt. A51-234-DR-74-8, 25 July 1974, Grumman Aerospace Corporation, Flight Acceptance Dept., Structural Sciences Section Data Release No. A51-234-DR-74-8 (above R. Johnson memo portion of Rpt. is dated 19 June 1974, Rpt. No. A51-335-1-74-18)

25. Grumman Aerospace Corporation "Air-to-Ground Stores Net Loads Survey" Report No. FAD-303-1-9-Va. 1306, 11 Feb 1975, Flight Dynamics and Loads Section Data Release, Flight Acceptance Dept.

26. Hooton, J. "Flight Test Results for an Instrumented TER-9 Bomb Rack" AFATL-TR-73-111, Eglin Air Force Base, May 1973

27. Devan, L. "An Estimate of the Effect of MER Structural Dynamics on Store Separation" NWL Technical Report TR-3097, Naval Weapons Laboratory, February 1974

28. Devan, L. "An Estimate of the Effect of Multiple Ejection Rack Flexibility on Six-Degree-of-Freedom Store Ejection Conditions" NSWC/DL Technical Report No. TR-3252, Naval Surface Weapons Center, Dahlgren Laboratory, March 1975

29. Kyle, Robert L. "Suspension Equipment Considerations" McDonnell-Douglas Aircraft Co., Long Beach, Calif., Proceedings of JTCG-ALNNO Aircraft/Stores Compatibility Symposium, Sacramento, Calif., 18-20 Sept. 1973, Sponsored by JTCG/ALNNO AP-12-2

30. McQuiston, George "LAU-92 Test Results" (informal memo), Missile Systems Division, Raytheon Co., Bedford, Massachusetts, March 1975

31. Black, Robert I. "High-Speed Store Separation -- Correlation between Wind-Tunnel and Flight-Test Data" JOURNAL OF AIRCRAFT, Vol. 6, No. 1, Jan-Feb 1969, pp. 42-45

32. Cooper, G.R. and Kingery, R.W. "Naval Missile Center Photo Data Analysis of Store Separation Films" Tech. Publication TP-73-57, Naval Missile Center, Point Mugu, Calif., 17 January 1974

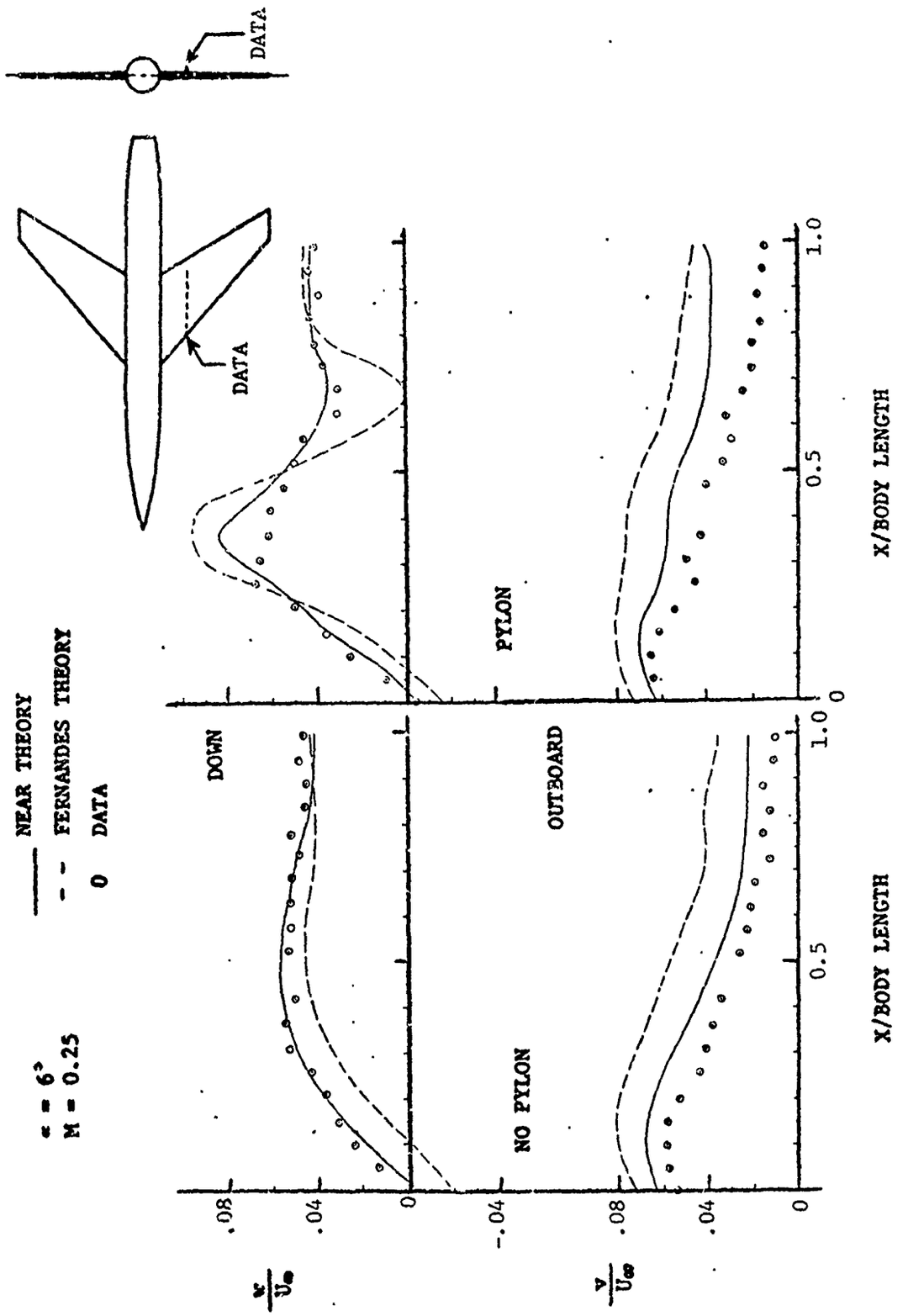

FIG. 1. COMPARISON OF NEAR AND GENERAL DYNAMICS METHODS WITH DATA

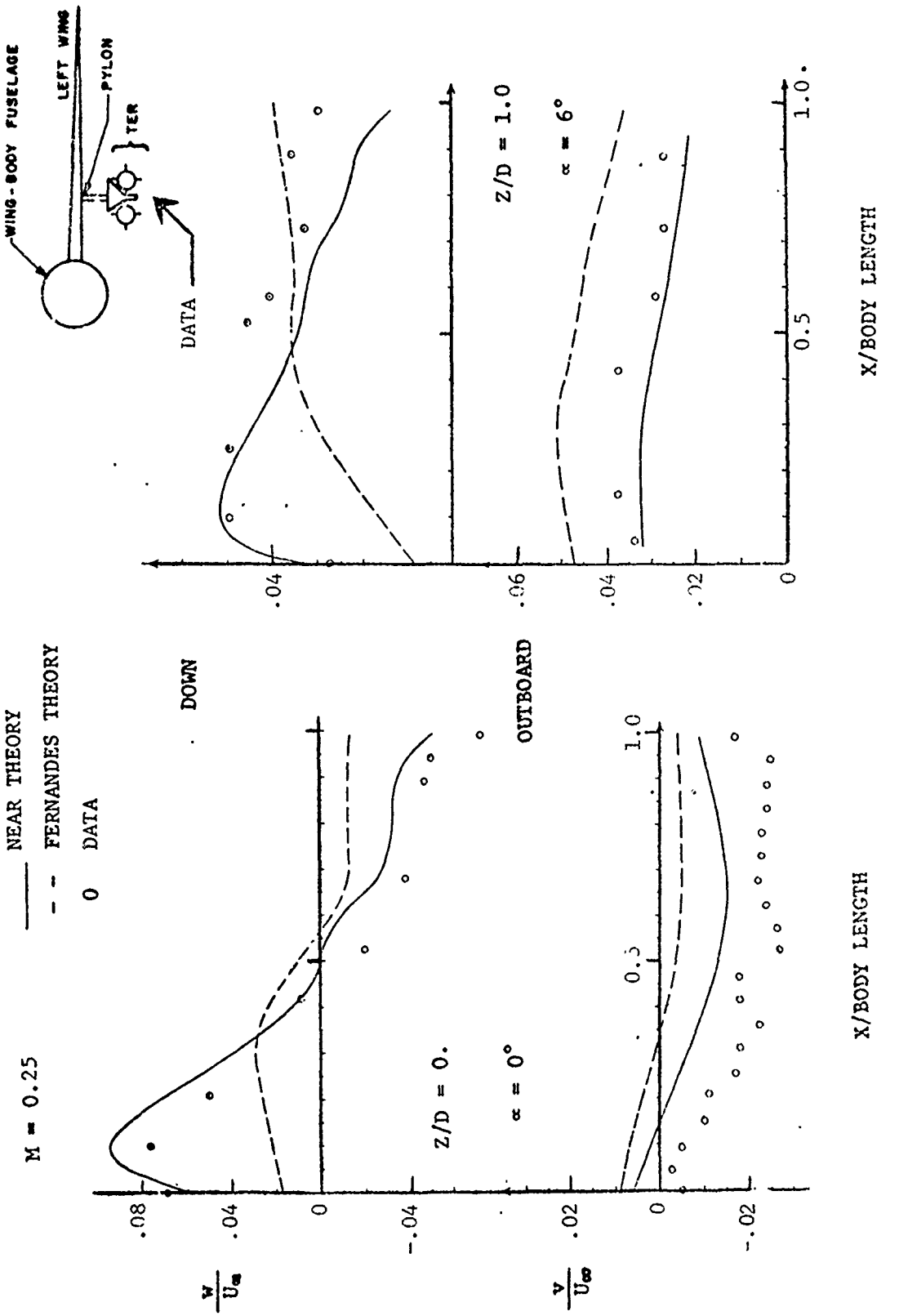

FIG. 2. COMPARISON OF NEAR AND GENERAL DYNAMICS METHODS WITH DATA

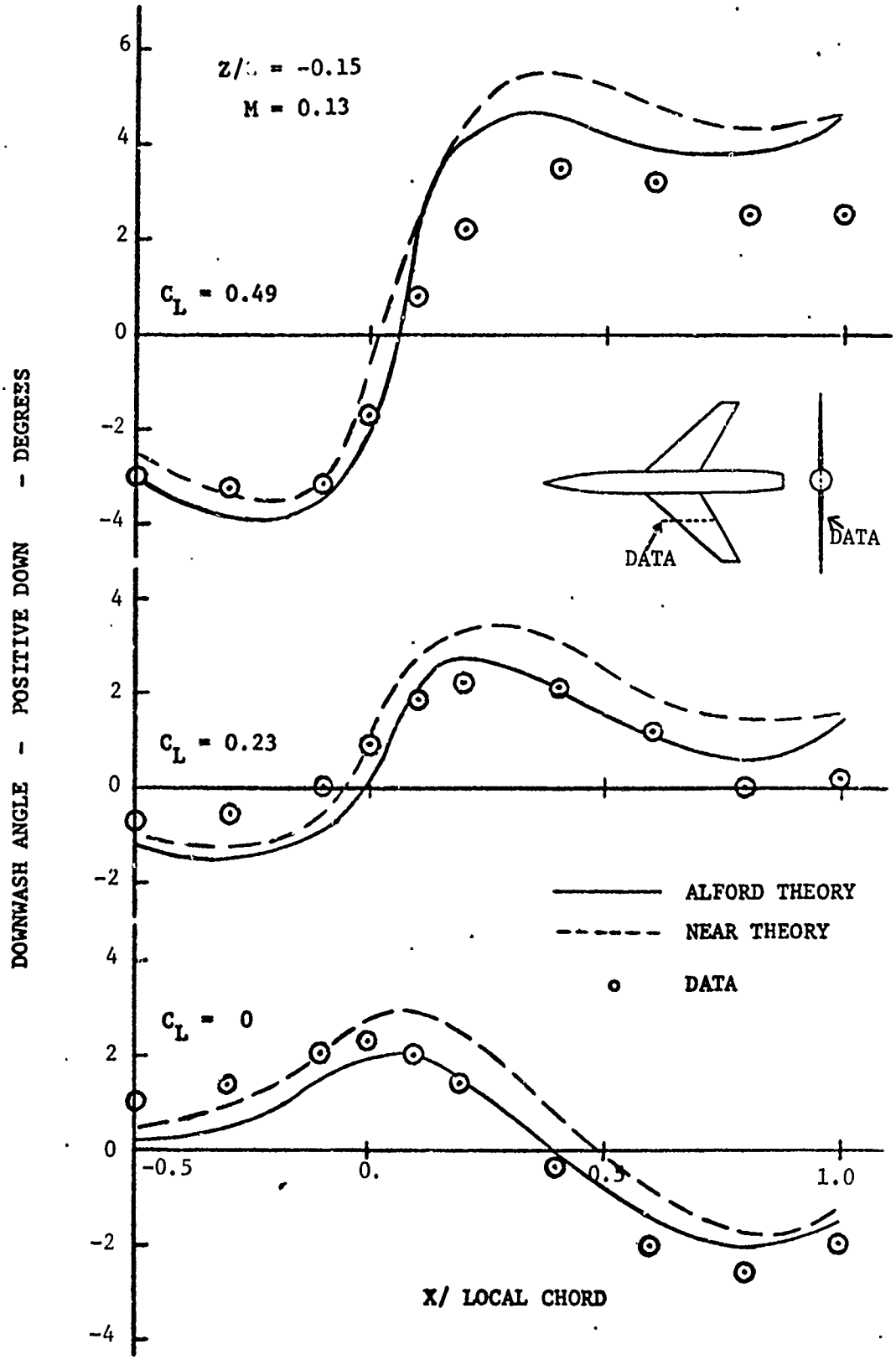

FIG. 3. COMPARISON OF ALFORD AND NEAR METHODS WITH DATA

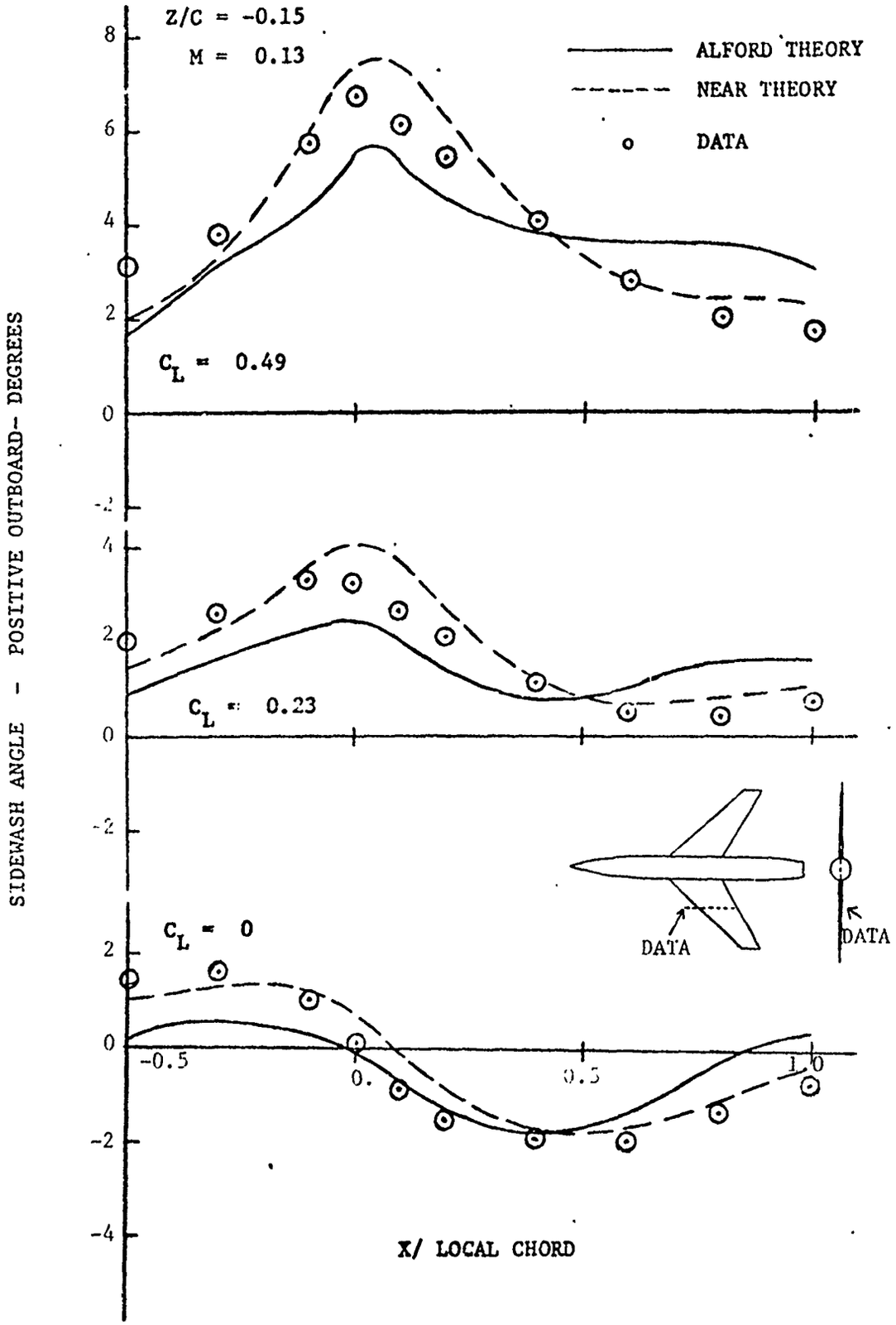

FIG. 4. COMPARISON OF ALFORD AND NEAR METHODS WITH DATA

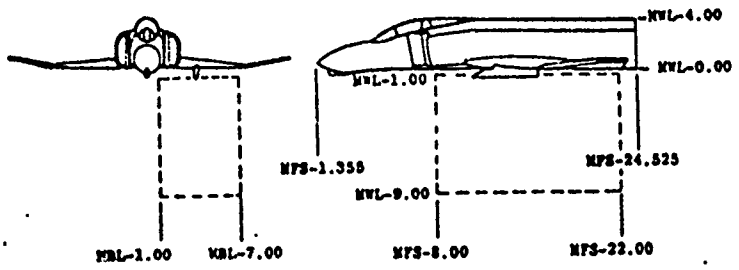

a. Region of Inboard Survey

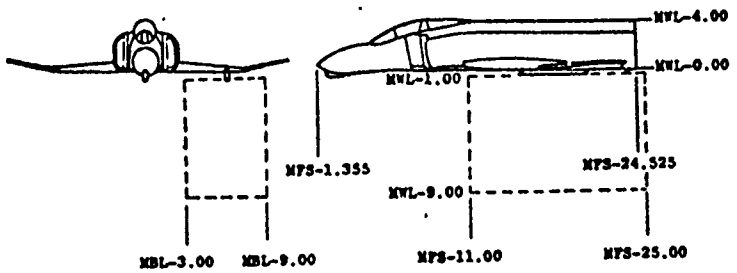

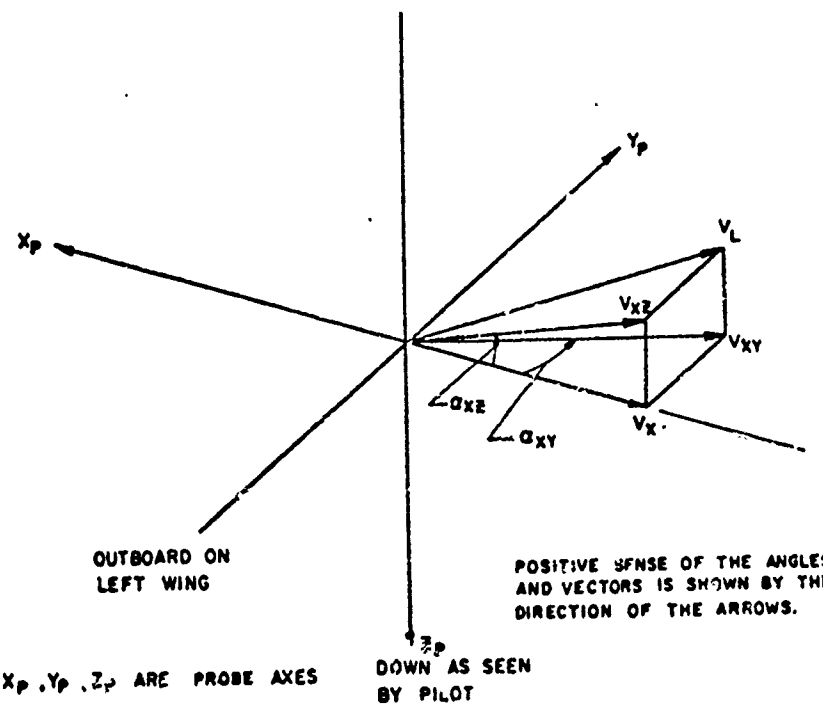

FIG. 5. LOCATIONS AND CONVENTIONS FOR AEDC DATA COMPARISON

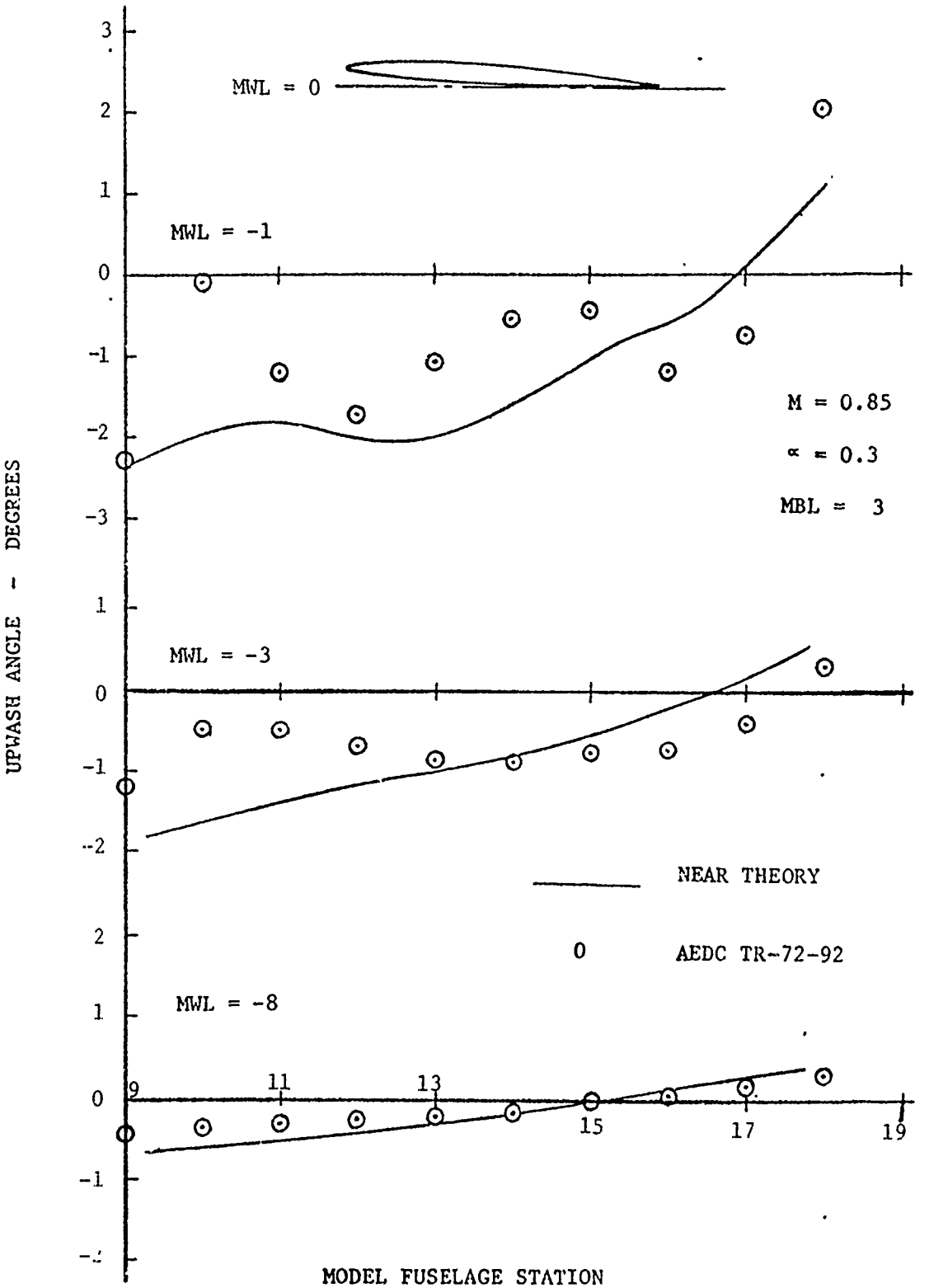

FIG. 6. UPWASH ANGLE COMPARISON - NEAR THEORY WITH DATA, F-4C FUSELAGE-WING

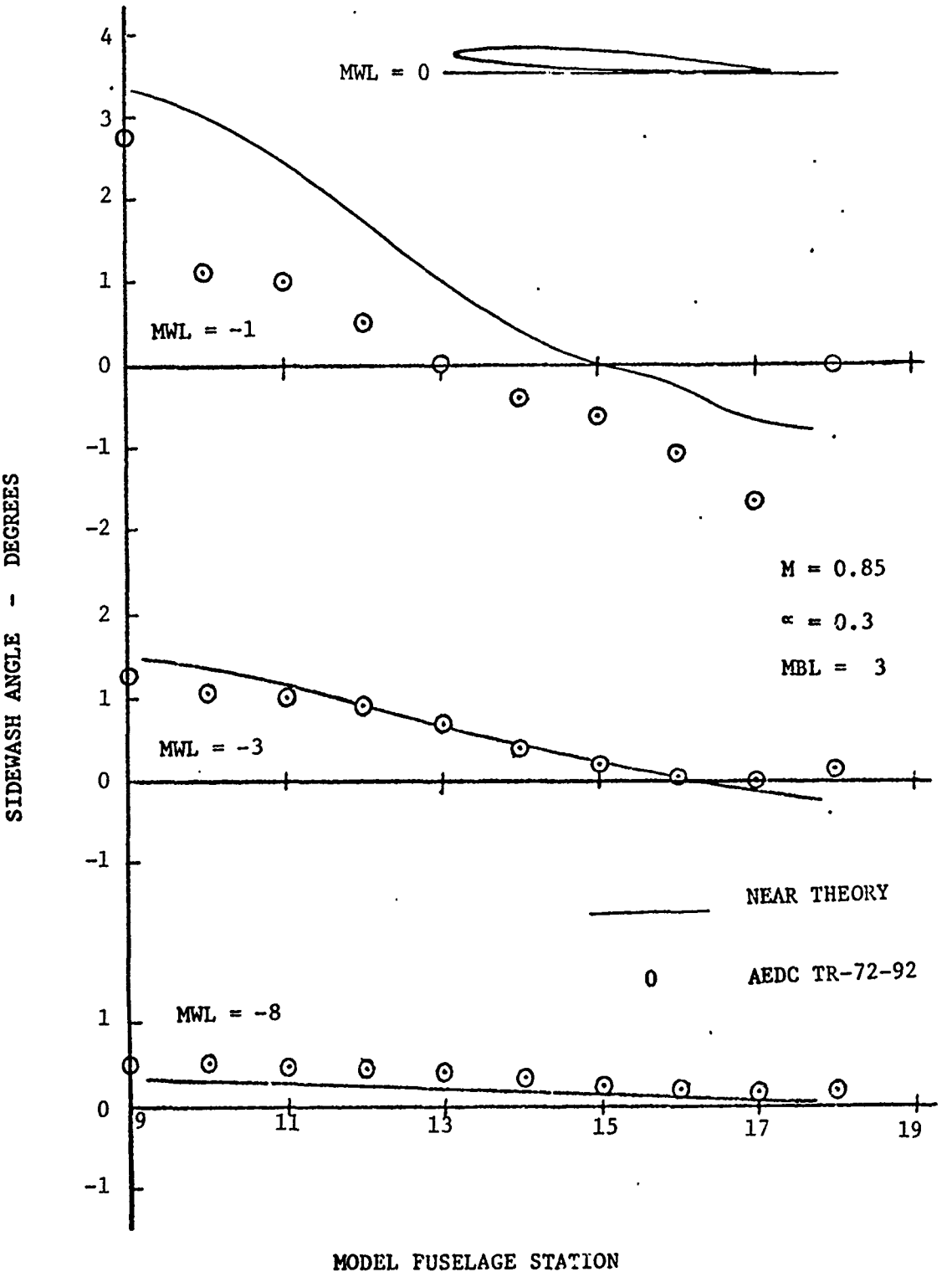

FIG. 7. SIDEWASH ANGLE - COMPARISON OF NEAR THEORY WITH DATA, F-4C FUSELAGE-WING

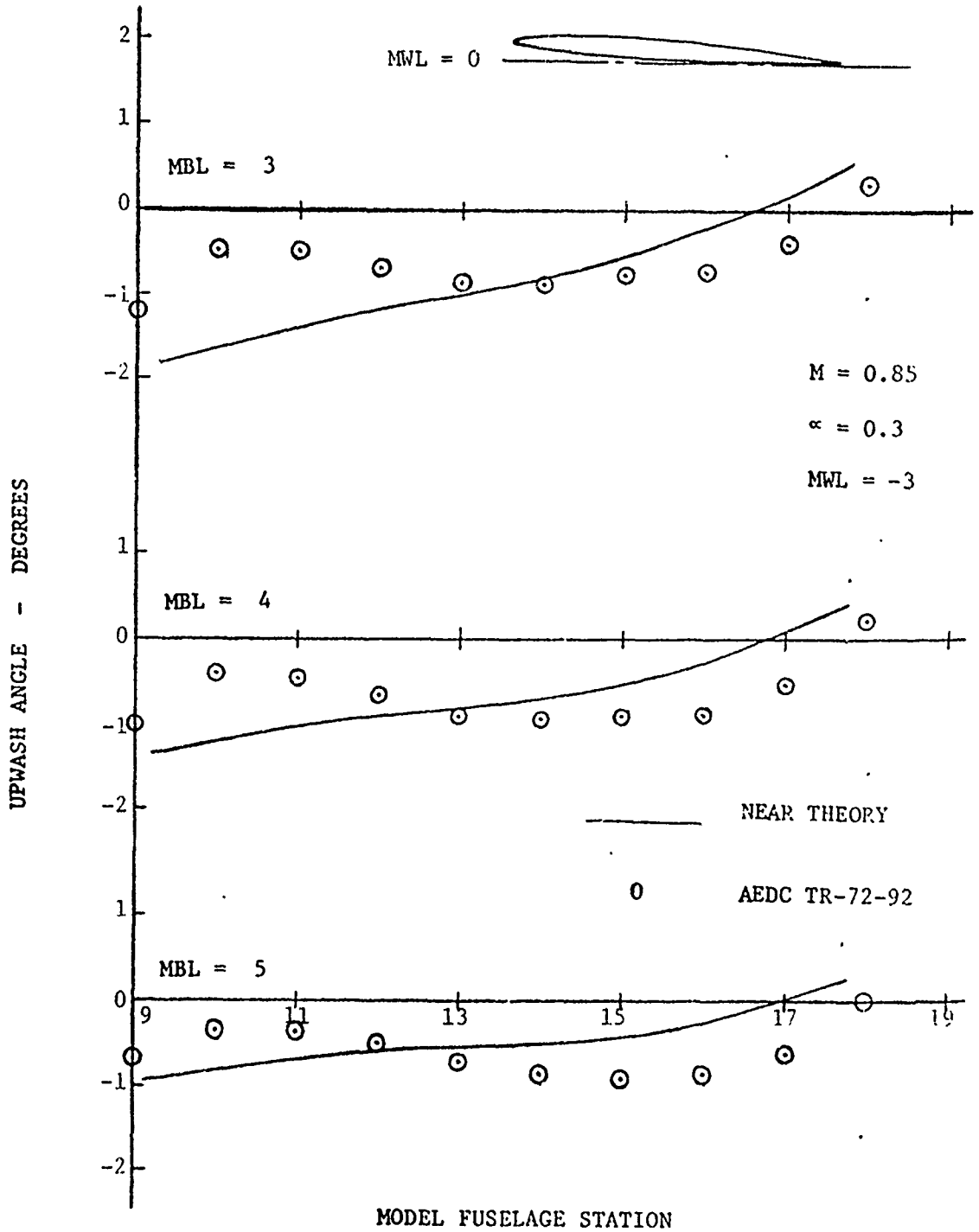

FIG. 8. UPWASH ANGLE - COMPARISON OF NEAR THEORY WITH DATA F-4C FUSELAGE-WING

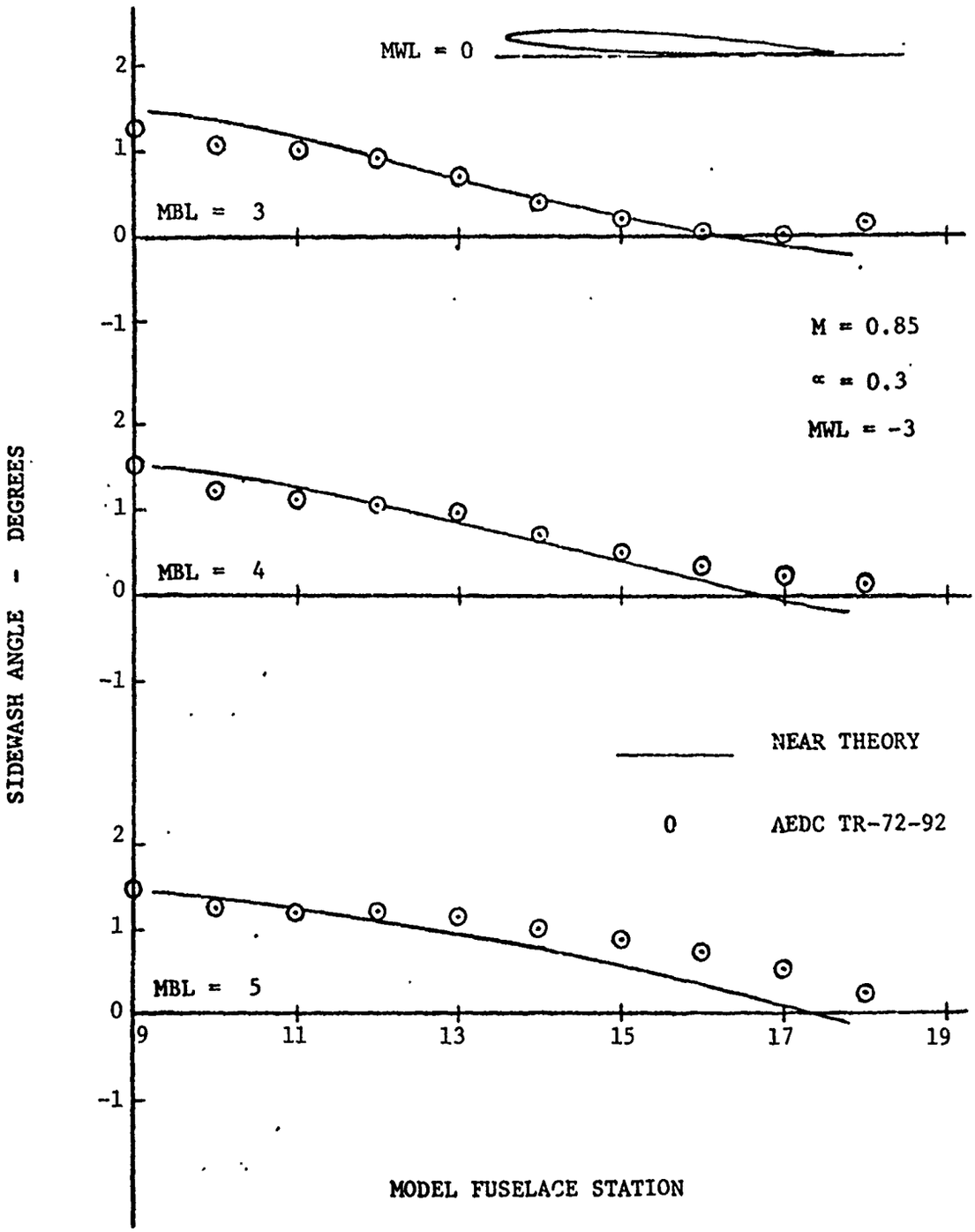

FIG. 9. SIDEWASH ANGLE - COMPARISON OF NEAR THEORY WITH DATA, F-4C FUSELAGE-WING

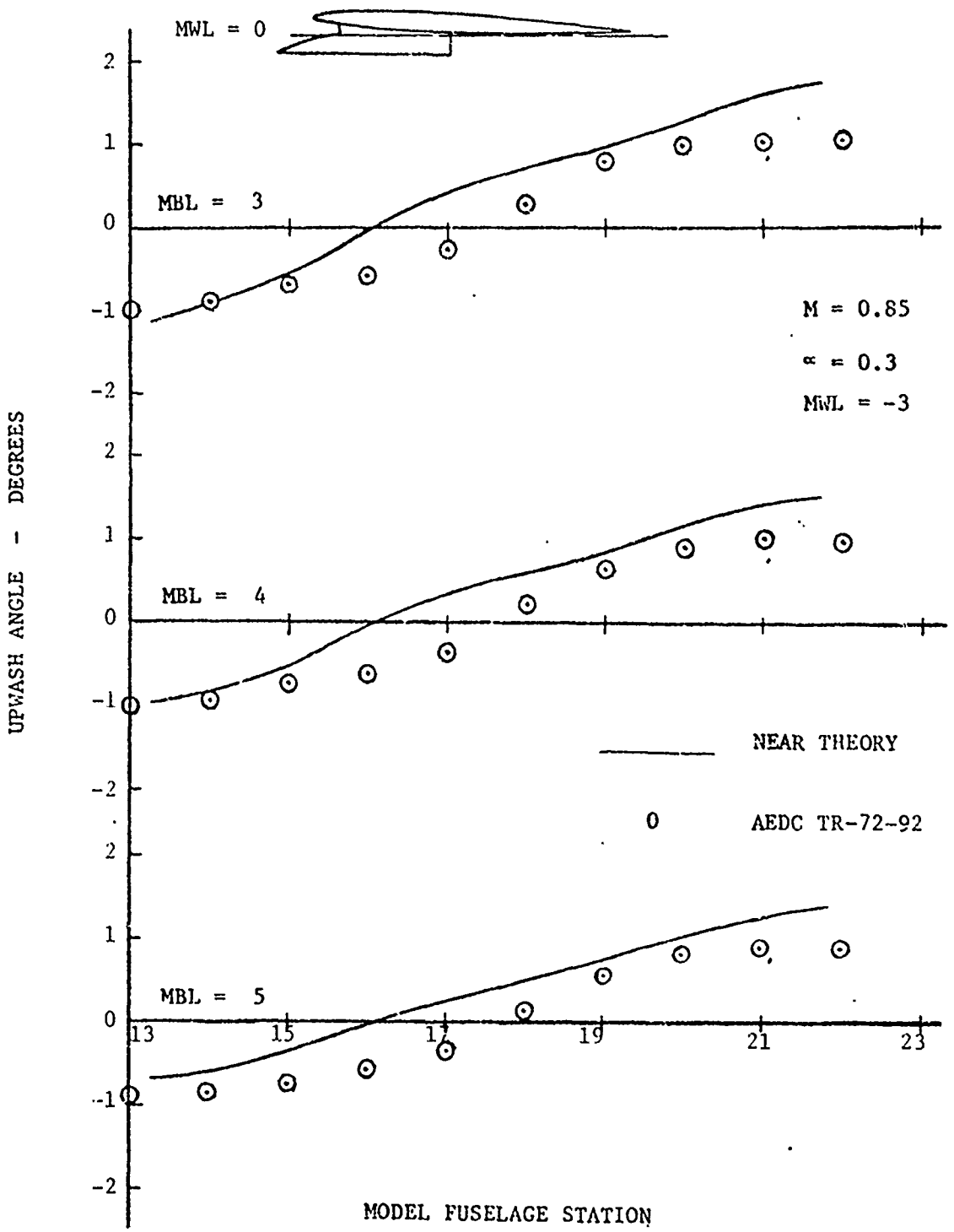

FIG. 10. UPWASH ANGLE - COMPARISON OF NEAR THEORY WITH DATA, F-4C FUSELAGE-WING-PYLON

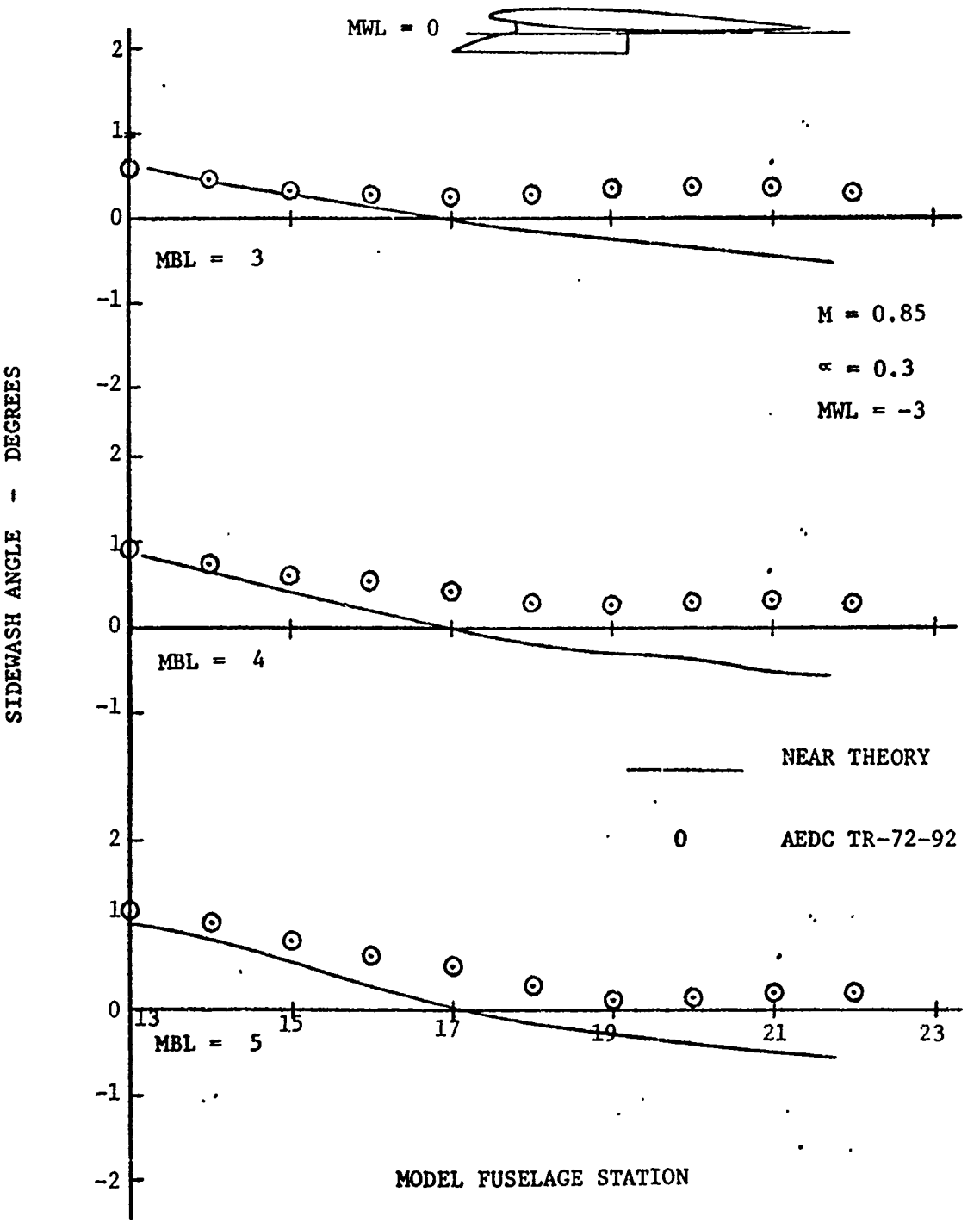

FIG. 11. SIDEWASH ANGLE - COMPARISON OF NEAR THEORY WITH DATA, F-4C FUSELAGE-WING-PYLON

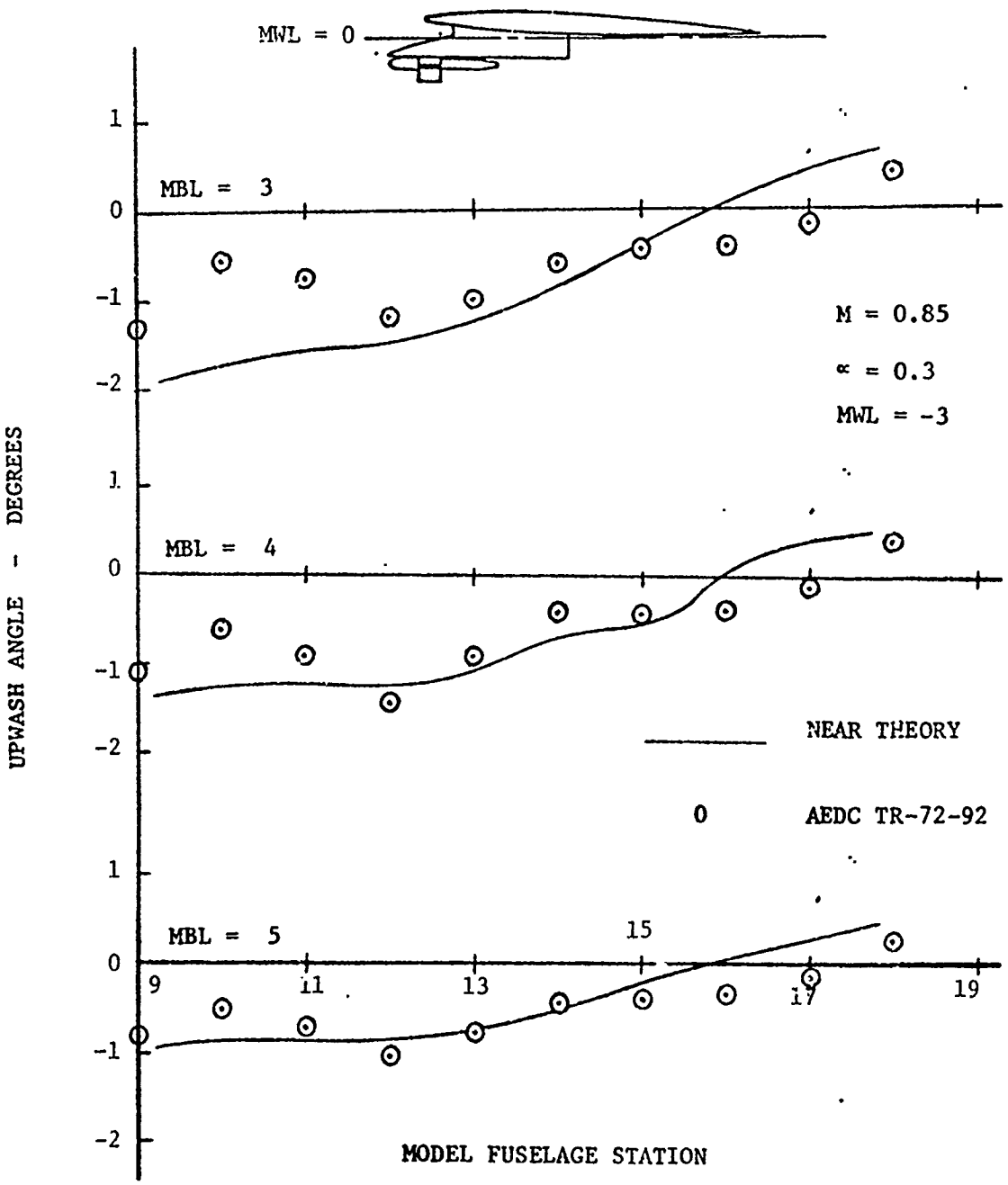

FIG. 12. UPWASH ANGLE - COMPARISON OF NEAR THEORY WITH DATA, F-4C FUSELAGE-WING-PYLON-RACK

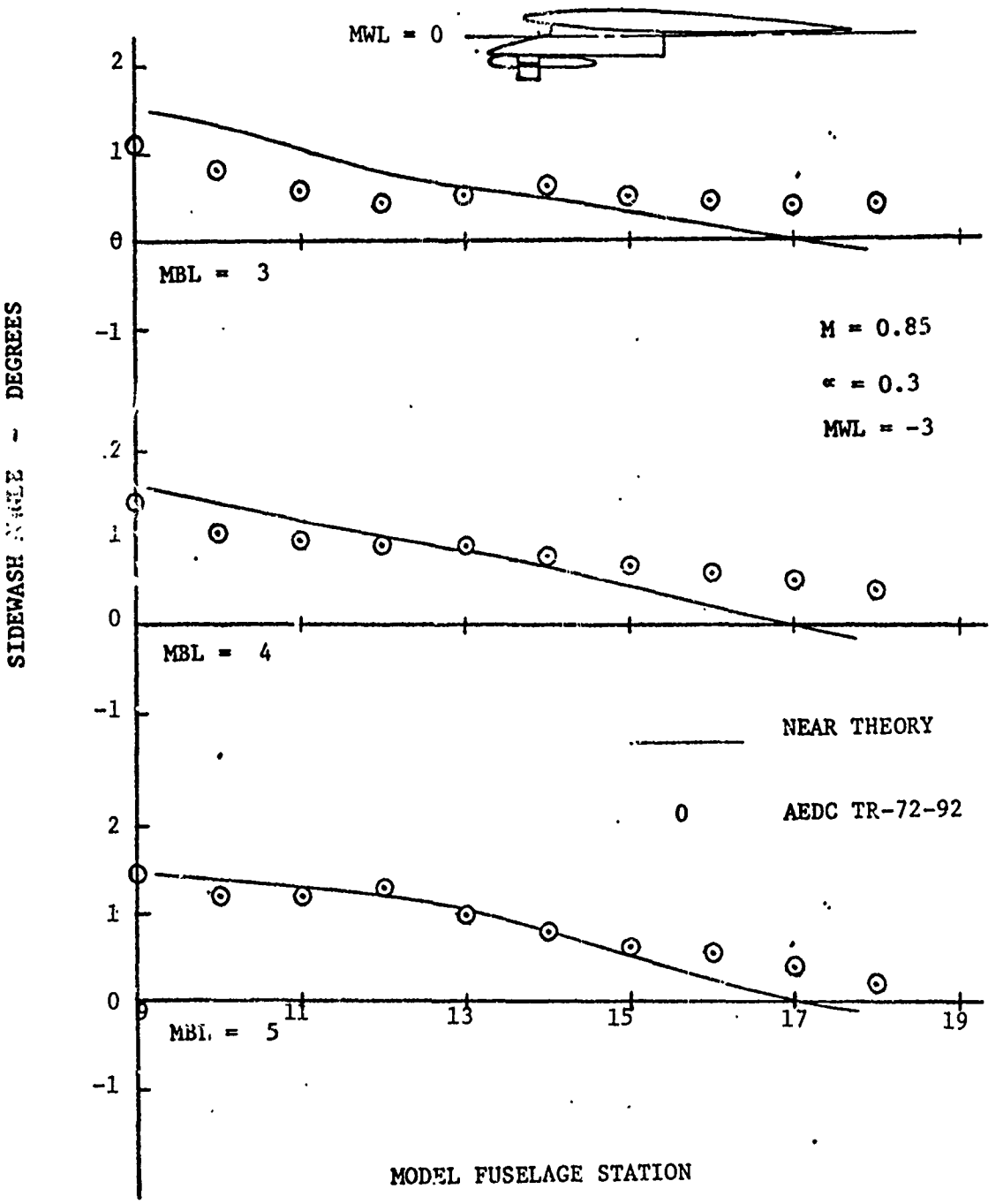

FIG. 13. SIDEWASH ANGLE - COMPARISON OF NEAR THEORY WITH DATA, F-4C FUSELAGE-WING-PYLON-RACK

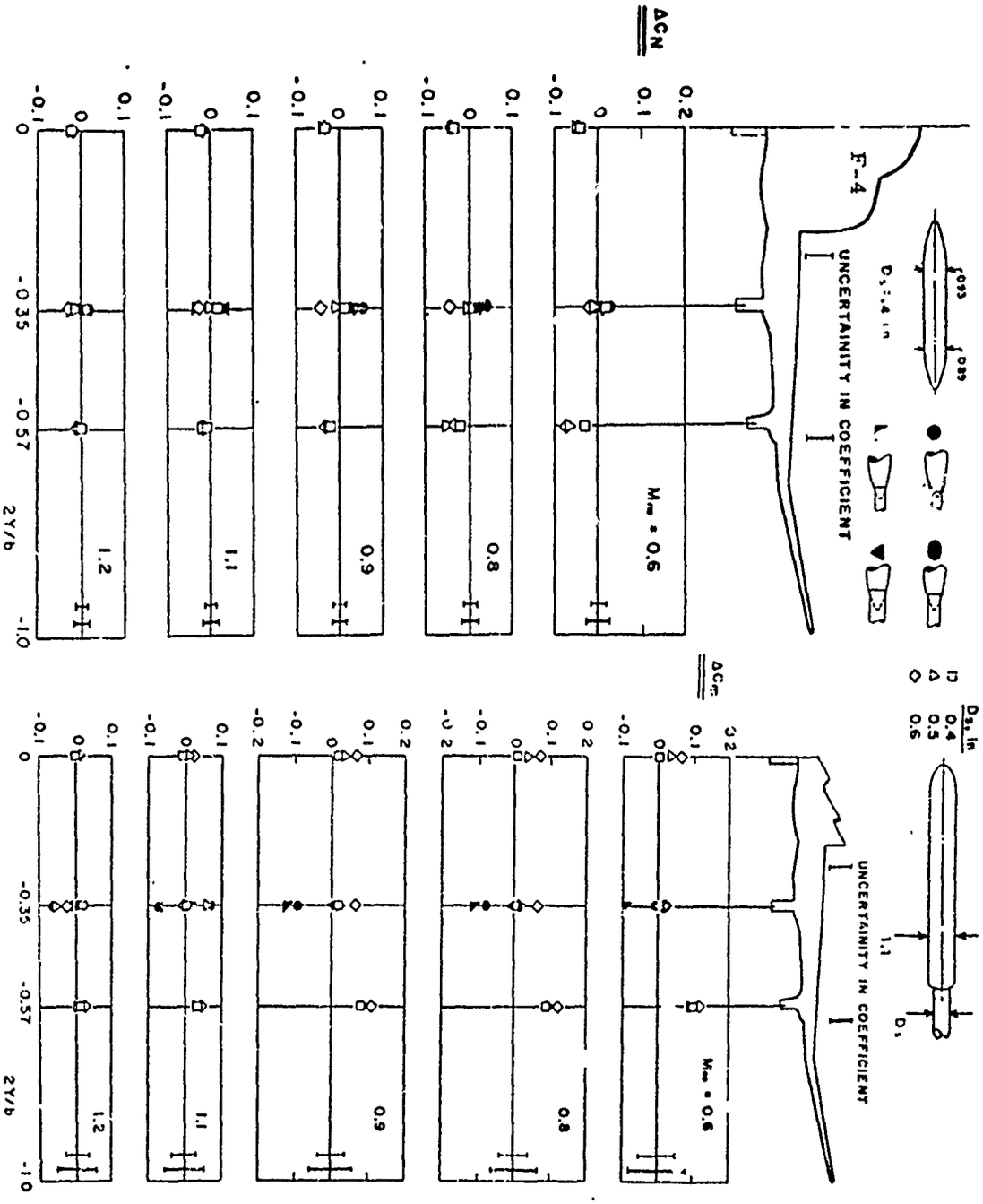

Figure 14 - Sting Effects (Unfinned Bodies) Increments due to Presence of Dummy Sting
Courtesy AEDC

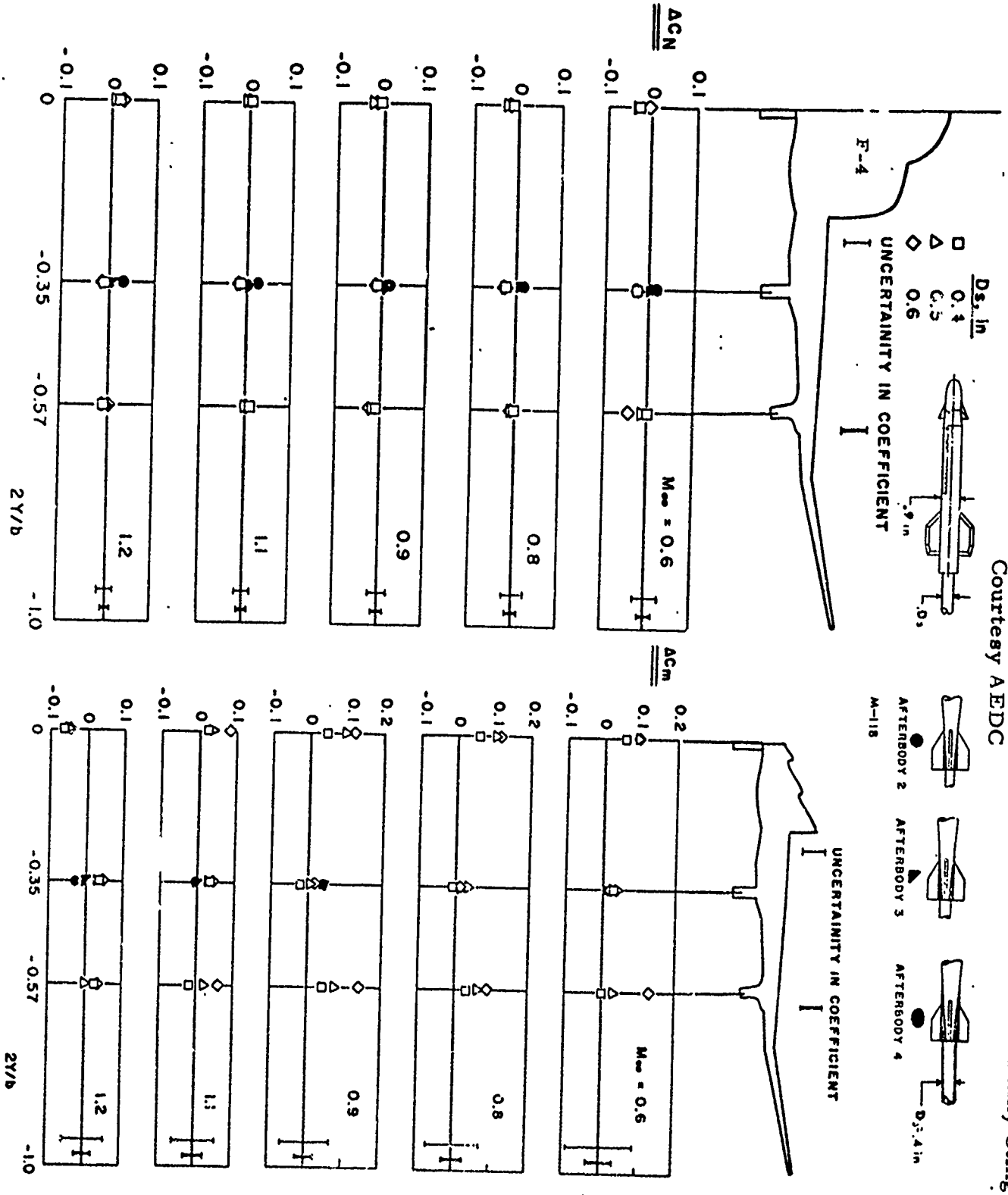

Figure 15 - Sting Effects (Finned Bodies) Increments due to Presence of Dummy Sting
Courtesy AEDC

Figure 16

STORE INTERFERENCE LOADING - F4 $^{B}_{C}$

MK-83 LIP X=0 Φ=0 $\alpha \cong 0$

M=0.6

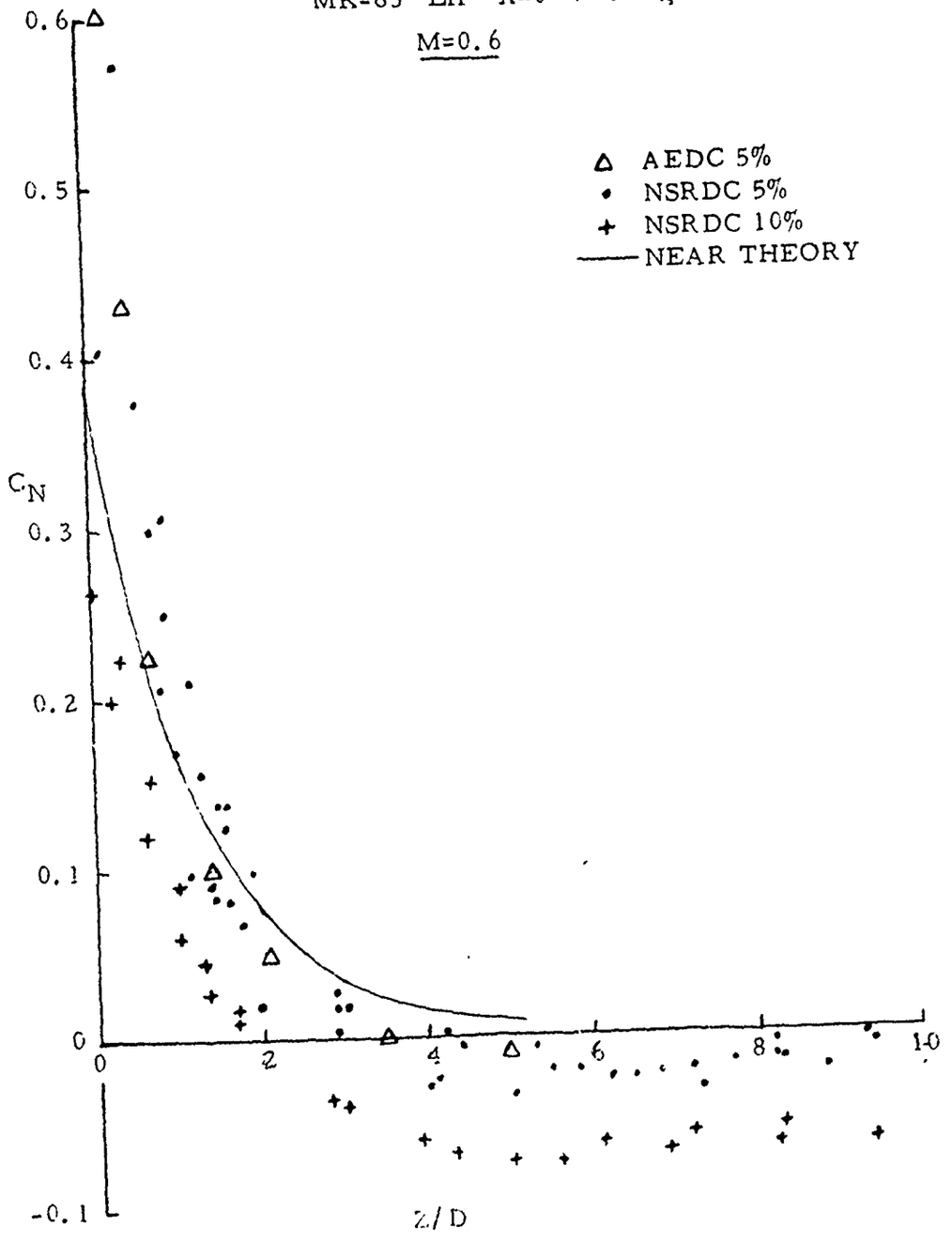

Figure 17
STORE INTERFERENCE LOADING - F4 Bc

MK-83 LIP X=0 Ø=0 $\alpha_s \approx 0$

M = 0.6

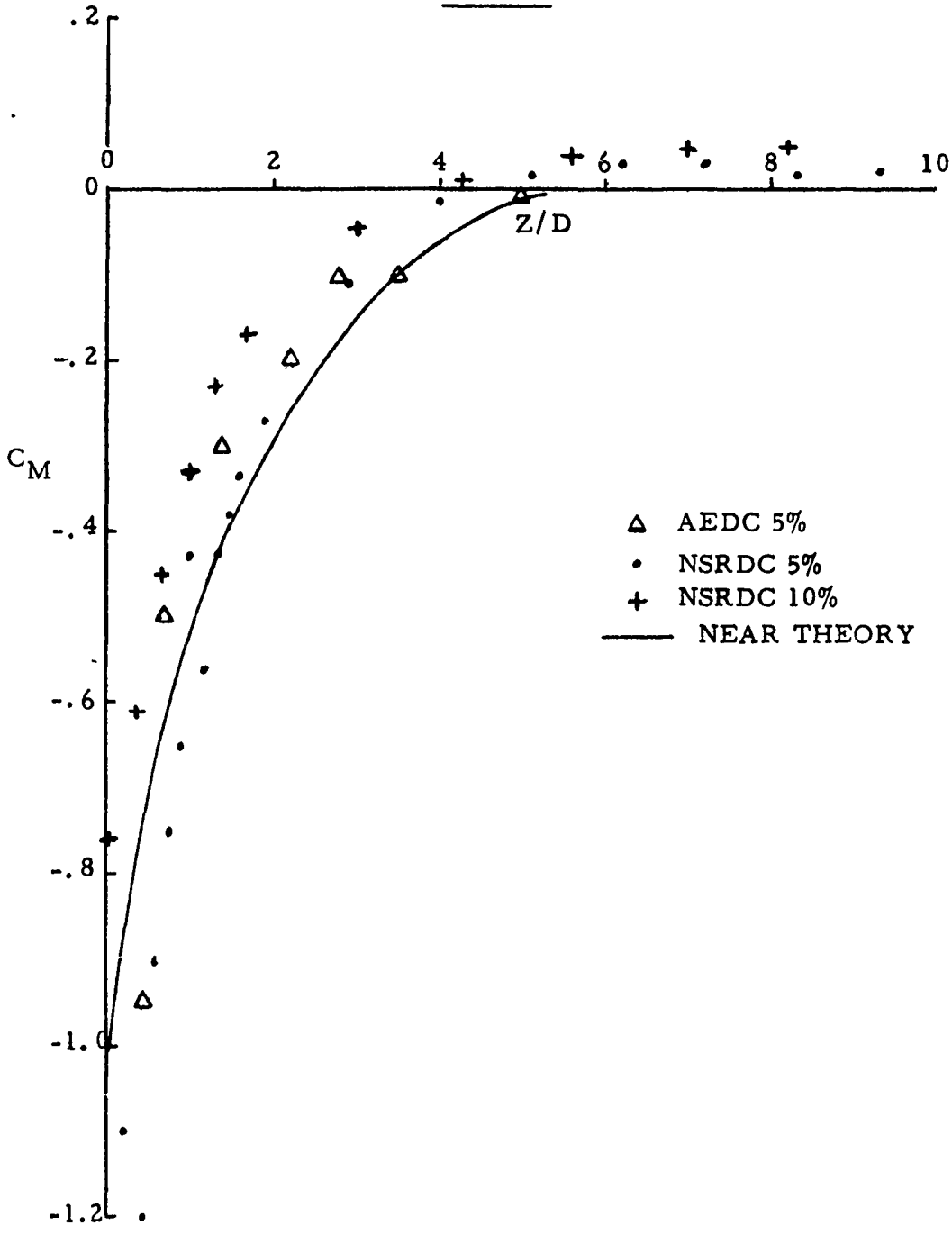

Figure 18

FREE-STREAM AERODYNAMICS
MK-83
M=0.6

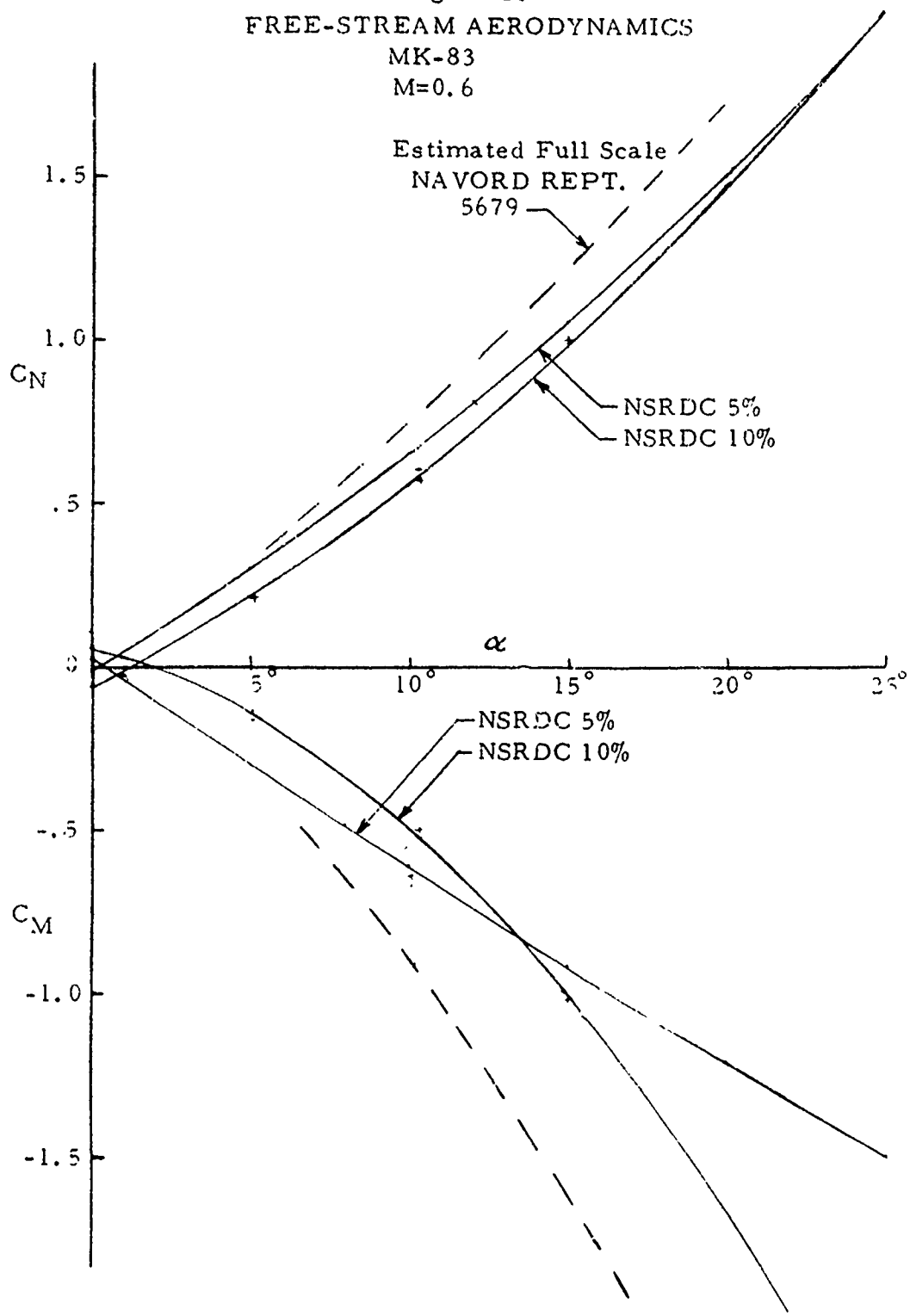

Figure 19

STORE INTERFERENCE LOADING - F4 $^{B}_{C}$

M-118 LIF X=0 ϕ=0 $\alpha_s \approx 0$

M= 0.6

△ AEDC 5%
• NSRDC 5%
—— NEAR THEORY

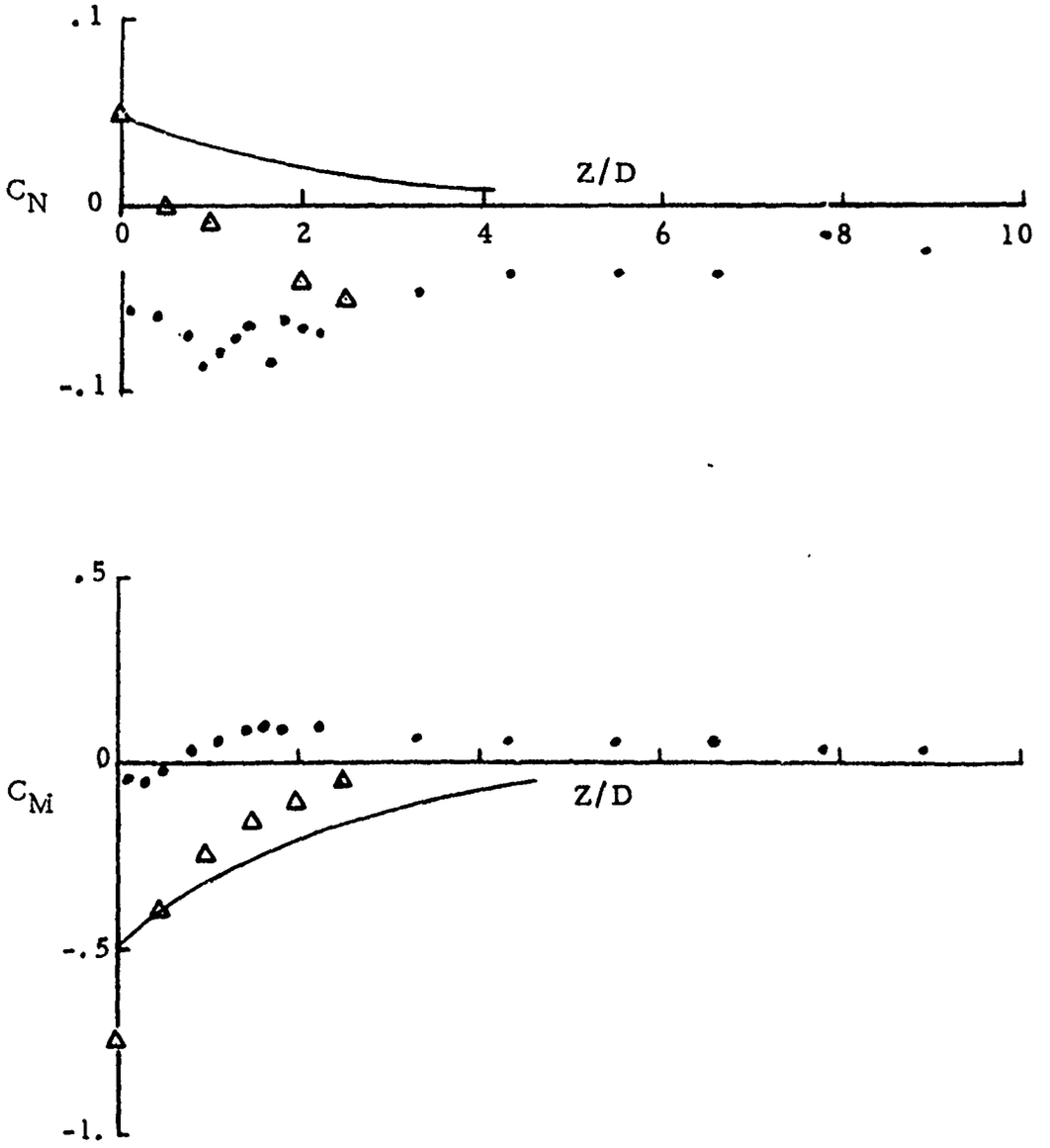

Figure 20

NSRDC TEST INSTALLATION

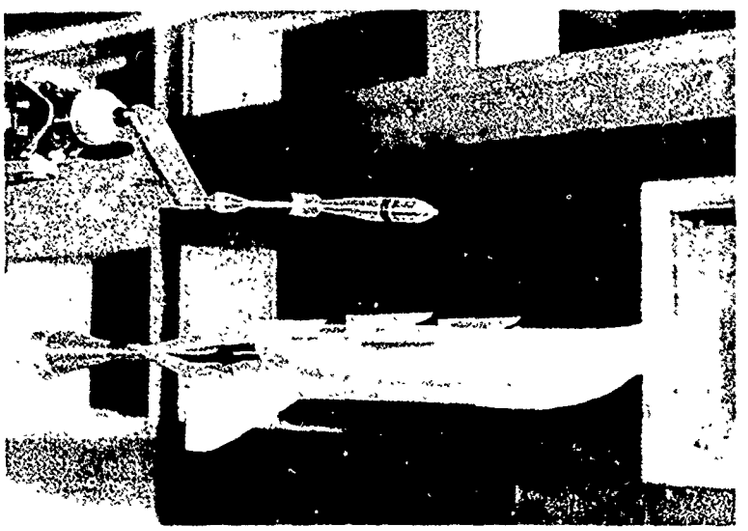

M - 118
(offset sting)

MK-83

Figure 21
ALVRJ TEST VEHICLE INSTALLED ON A-7

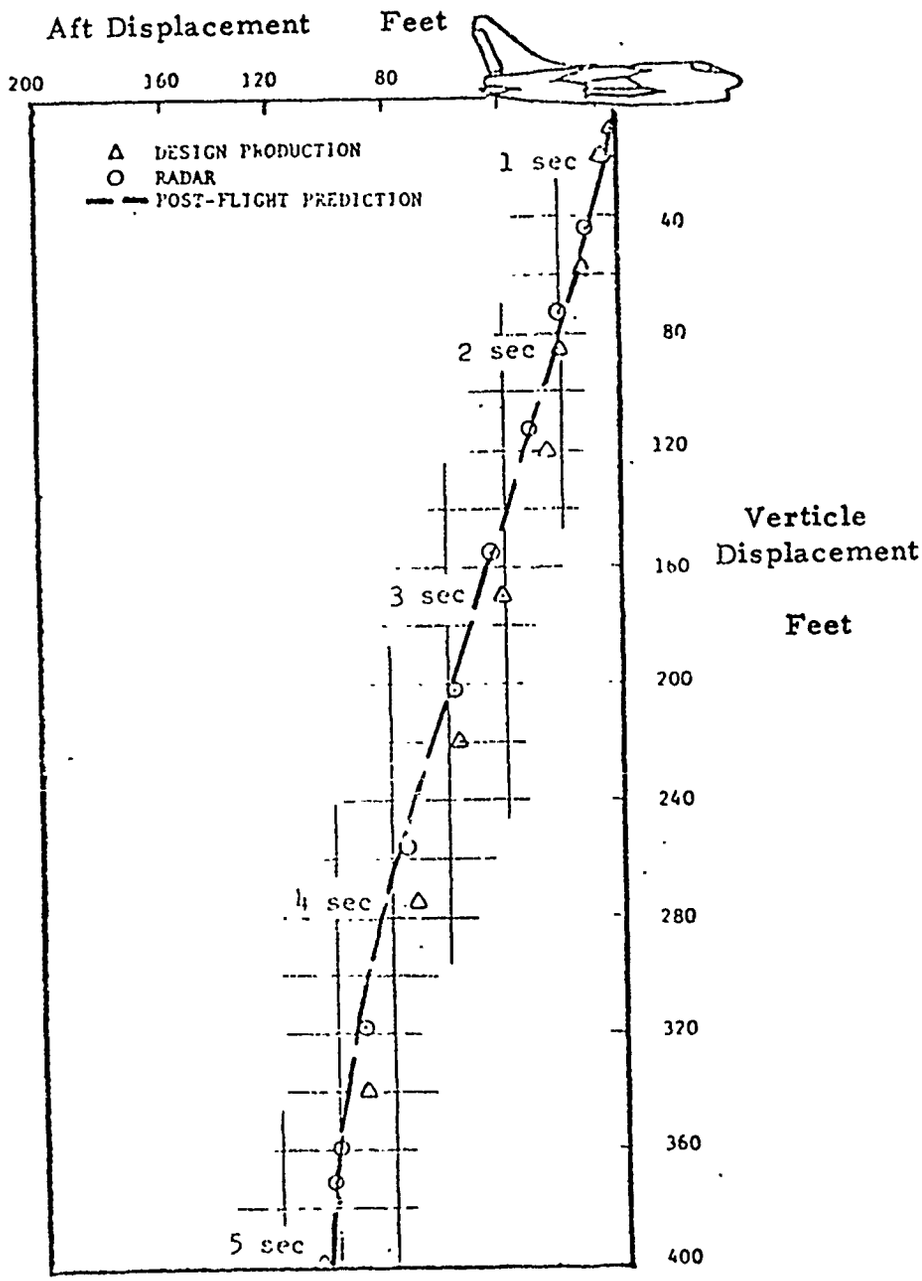

Figure 22 - ALVRJ DTV #1, Comparison of Flight Test and Predictions

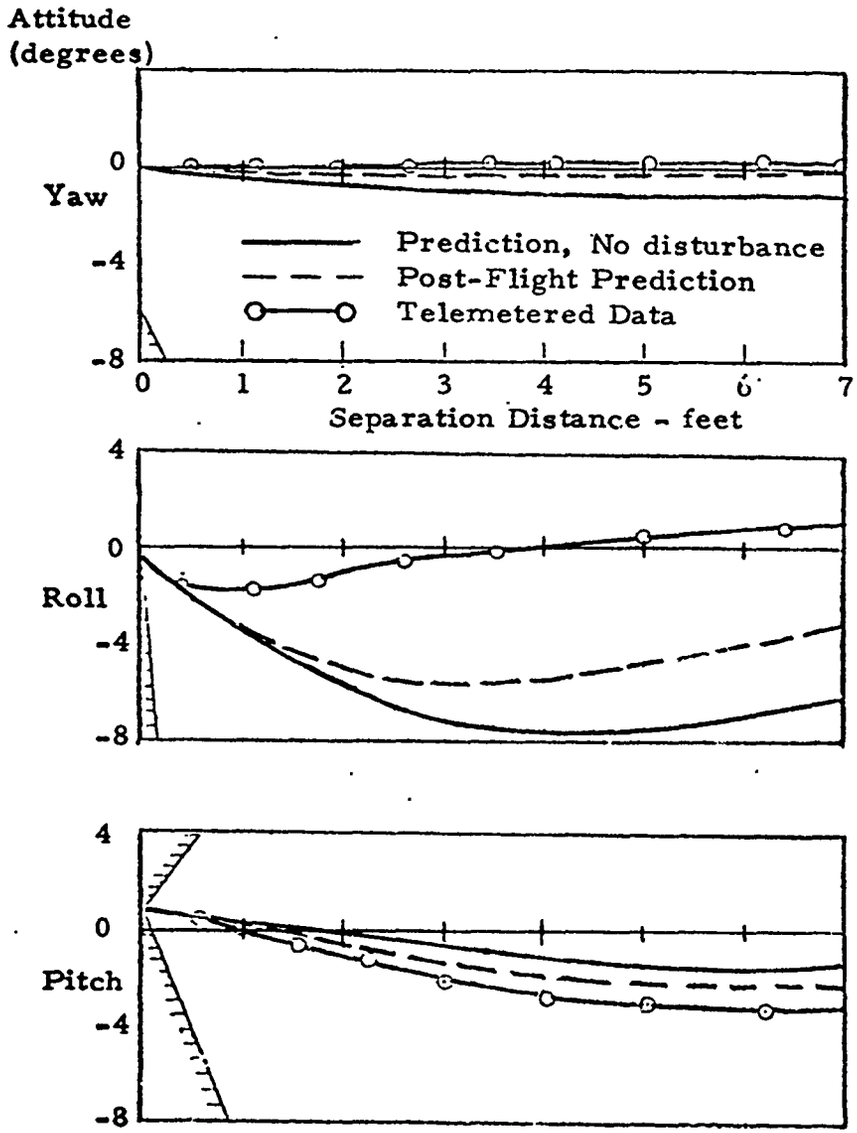

Figure 23 - ALVRJ DTV #1, Comparison of Clearance from Flight Test and Predictions

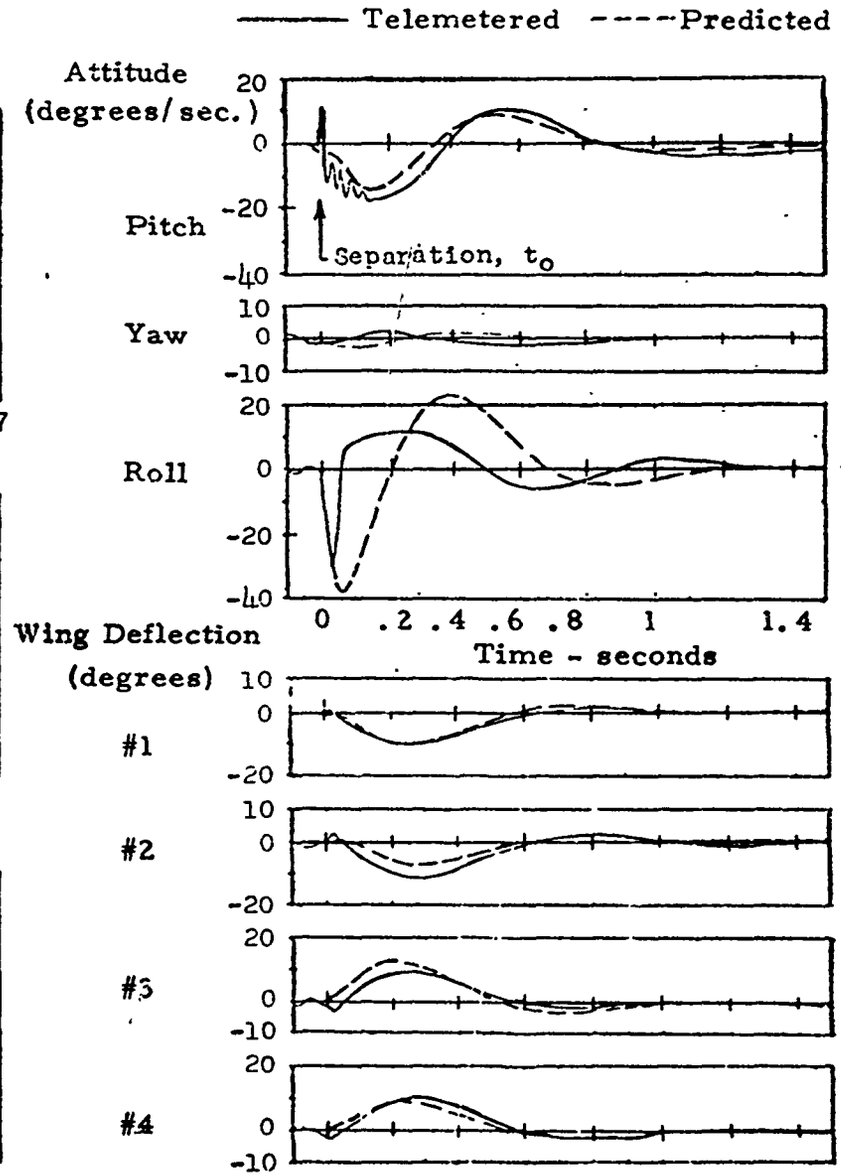

Figure 24 - ALVRJ DTV #1, Comparison of Control Response from Flight Test and Predictions

Figure 25 - Typical Influence Field (Supersonic Speeds)

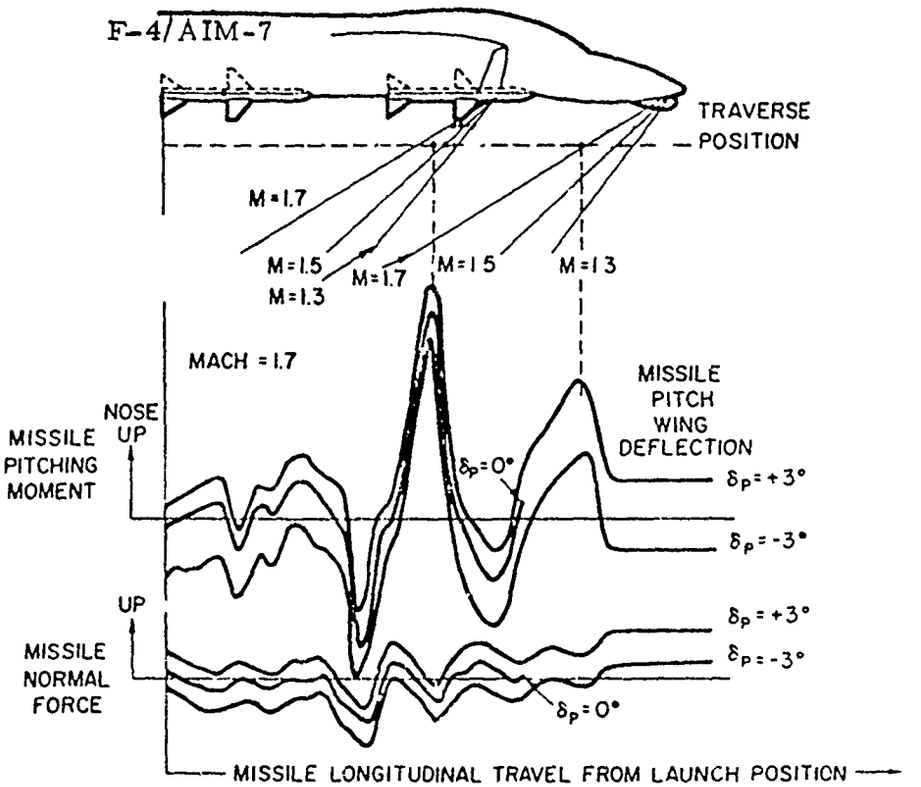

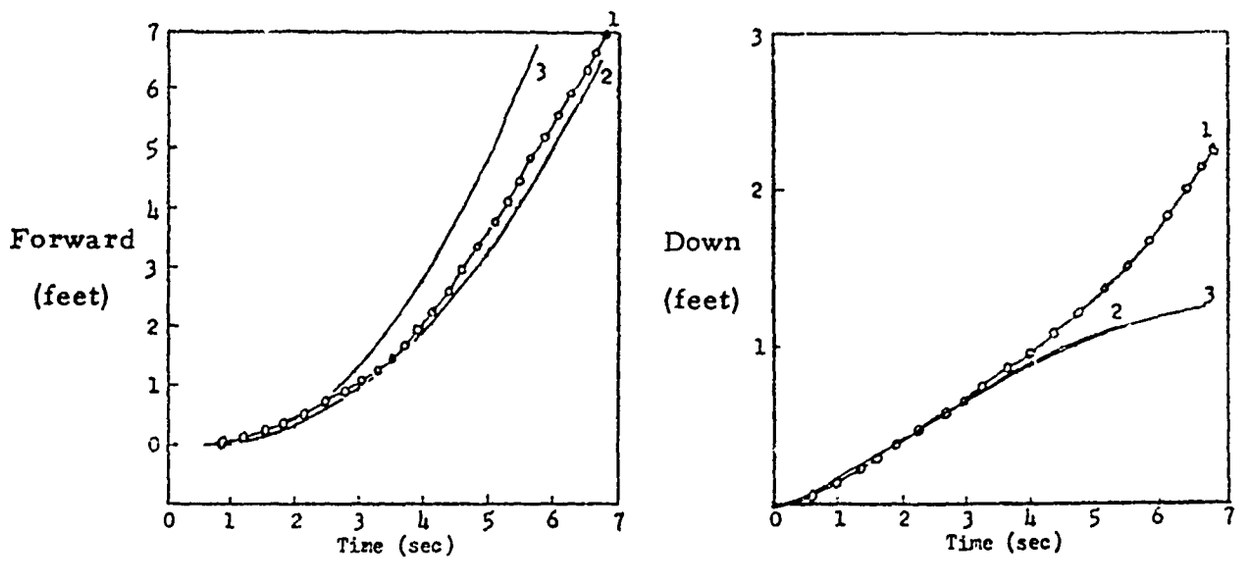

Legend: 1. Flight Test 2. Simulation (Mk-58 / early ignition)
3. Simulation (Mk-38)

Figure 26 - Comparison of Flight Test and Simulations
F-14/AIM-7

Figure 27 - Pit Tested Ejector Characteristics
Comparison of Theoretical Model and Experiment

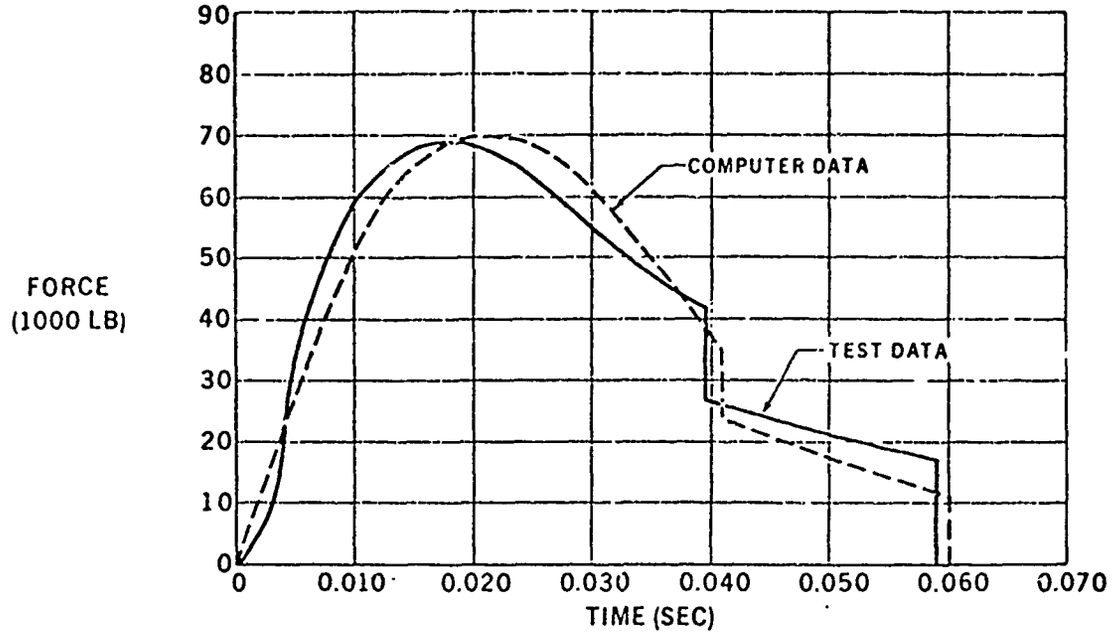

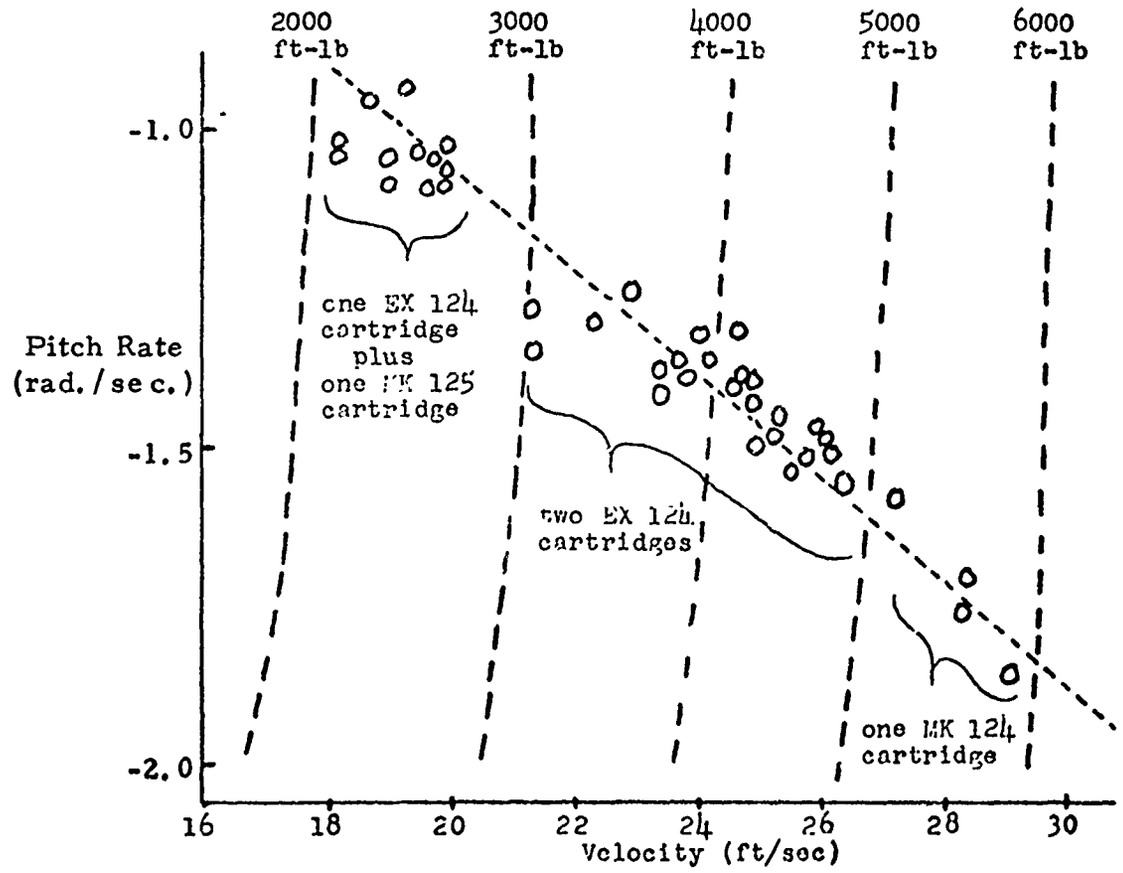

Figure 28 - Pit Tests of LAU-92 Launcher

Figure 29 - Rack Flexibility Increment of Ejection Pitch Rate

A-7D/MER/6 M-117

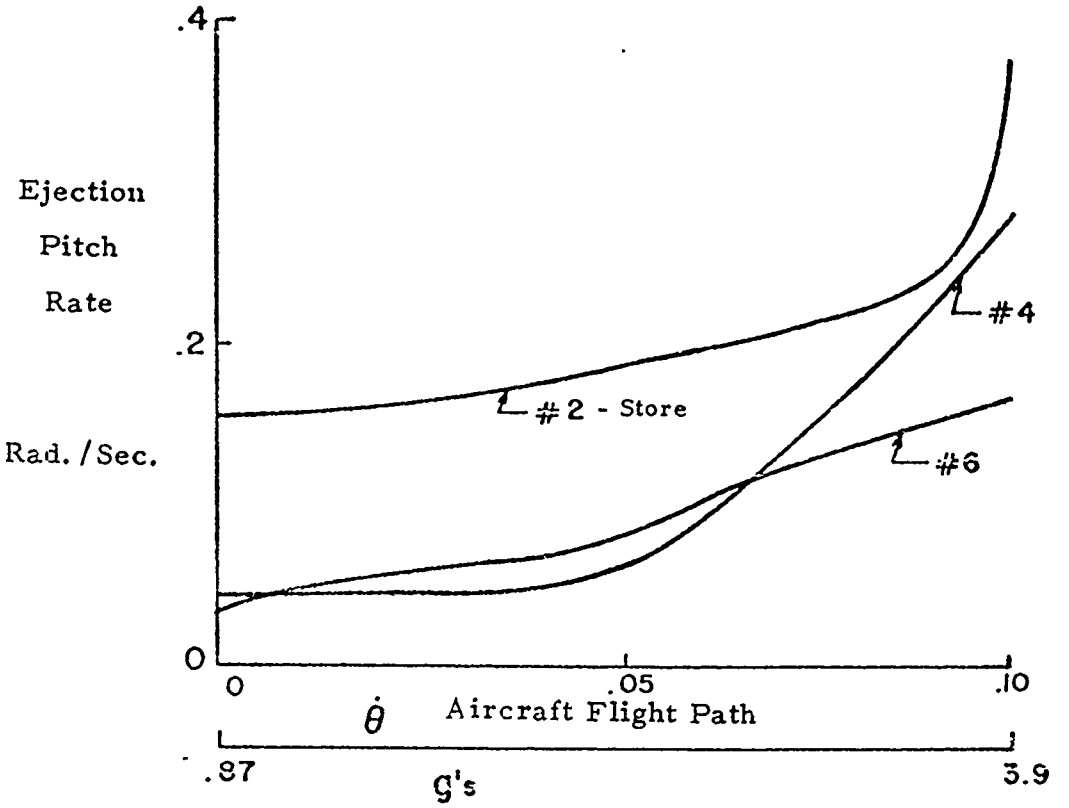

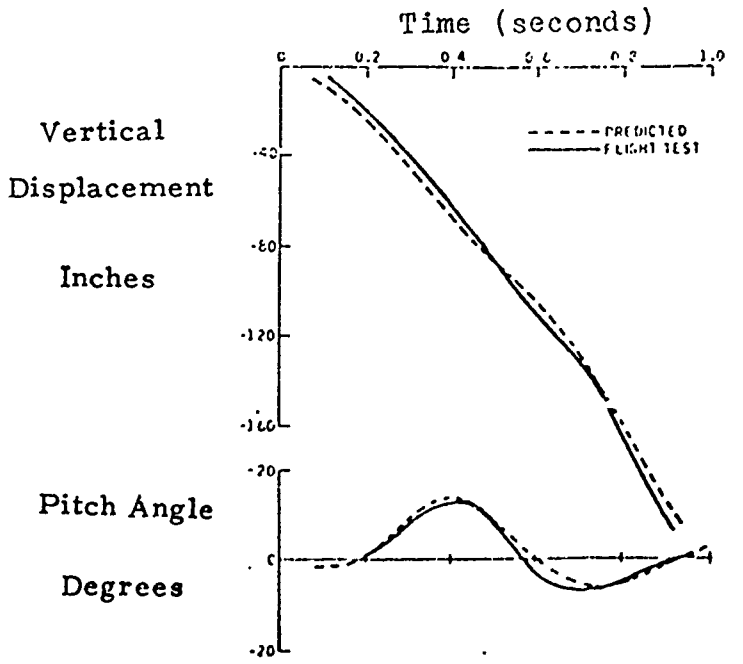

Figure 30 - Comparison between Flight Test and Adjusted Library Model

PAPER NO. 17

AN ESTIMATE OF THE EFFECT OF MULTIPLE EJECTION RACK FLEXIBILITY ON SIX-DEGREE-OF-FREEDOM STORE EJECTION CONDITIONS

by

Leroy Devan

Naval Surface Weapons Center

Dahlgren Laboratory

Dahlgren, Virginia

ABSTRACT

A theoretical structural dynamic model of a MER (Multiple Ejection Rack), based upon ***Bernoulli*** pitch and yaw bending deflections and torsional rotation, is developed. Six-degree-of-freedom store ejection conditions are predicted.

Sample computations were made for a M-117 bomb and constant aircraft pull-up rates corresponding to up to a 3.9 "g" normal acceleration. The computations were for the second, fourth, and sixth bombs dropped in the normal release sequence from an A-7D right wing center pylon station.

Ejection velocities computed do not deviate more than 15% from the rigid case. Ejection pitching and rolling rates are affected more significantly by flexibility. However, the pull-up maneuver alone affects the ejection conditions to a greater extent than flexibility for most ejection variables and "g" values greater than 2.

I. INTRODUCTION

Structural flexibity of multiple ejection racks has been recognized as being an important factor in predicting the dynamic response of aircraft carrying external stores in References 1 and 2.

In Reference 3, the effect of MER flexibility (not including aircraft structural modes) was considered. This report is an extension of the work presented in Reference 3, in which the detailed development was limited to MER pitch plane bending and pitch plane motion of the released store. Here, MER pitch plane and yaw plane bending and torsional deformation are considered together with 6-D store ejection dynamics.

II. STRUCTURAL DYNAMIC MODEL

Major assumptions and features of the model were given in Reference 3. The assumptions are repeated below:

(1) Wing, pylon, hanger, shoulder pad, and ejector unit deformations are neglected.

(2) Coriolis and centripetal accelerations induced by deformations are neglected.

(3) ***Bernoulli*** beam pitch and yaw deflections are considered. Torsional deformation is assumed to induce no longitudinal stresses. Longitudinal oscillations are neglected.

(4) Lug connections from the parent rack to the MER are assumed to be pinned. Parent rack sway brace reactions are assumed to be spring forces. It is assumed that the sway braces do not break contact with the MER during deformation.

(5) Static and dynamic aeroelastic forces on the MER are neglected due to lack of experimental data.

(6) Kinematics of the ejector foot and in-carriage store c.g. are computed from beam deflections and rotations at beam-ejector unit connection cross sections using linear interpolation relations.

(7) For a given cartridge, a single ejection force-time function is assumed for all store loads. Ejector force dynamics are assumed to be independent of beam motion.

(8) Beam motion acceleration, aircraft acceleration, ejection force, and aerodynamic loads for in-carriage stores are translated into beam loads by statically determinant computations.

(9) For the applications given, all stores in-carriage are identical.

In Figure 1 are shown coordinate systems used. x,y,z is a right-handed coordinate system embedded in the rigid MER beam. x coincides with a line of shear centers. y and z are parallel to the aircraft symmetry plane. X,Y,Z is parallel to x,y,z and embedded in the rigid aircraft frame with origin at the initial rigid c.g. location of the store being released. x′, y′, z′ is a right handed set of body coordinates with origin at the translating store c.g.

A. Structural Model and Influence Coefficients

Parent rack lugs are assumed to be pinned connections for the purpose of computation of all reaction force components. Sway brace arms are assumed to be springs. Figure 2 shows some of the force and geometric relations.

At the lug cross section, a rigid rotation about the lug centerline is assumed.

$$\eta + d_2\phi = 0 \tag{1}$$

η is the yaw deflection and ϕ the torsional rotation.

At sway brace cross sections, the forces P_ℓ and P_r are assumed to be proportional to the displacement along the line of action. From this assumption and the yaw, pitch, and rotation deformations, η, ζ, and ϕ one can obtain (see Figure 2)

$$P_r = k[d_1\phi \sin\epsilon - \eta\cos(\epsilon+\gamma) - \zeta\sin(\epsilon+\gamma)] + P_0 \tag{2}$$

$$P_\ell = k[-d_1\phi \sin\epsilon + \eta\cos(\epsilon+\gamma) - \zeta\sin(\epsilon+\gamma)] + P_0 \tag{3}$$

If the preload, P_0, is large enough P_r and P_ℓ do not go to zero (break of contact). If P_0 is very small, one can assume contact is broken immediately upon deflection. Intermediate values of P_0 lead to nonlinear forces which are not considered. Beam loads in the z and y directions and beam torque are computed from Equations 2 and 3 and the geometry of Figure 2.

$$F_z = -ck\zeta\sin^2(\epsilon+\gamma) \tag{4}$$

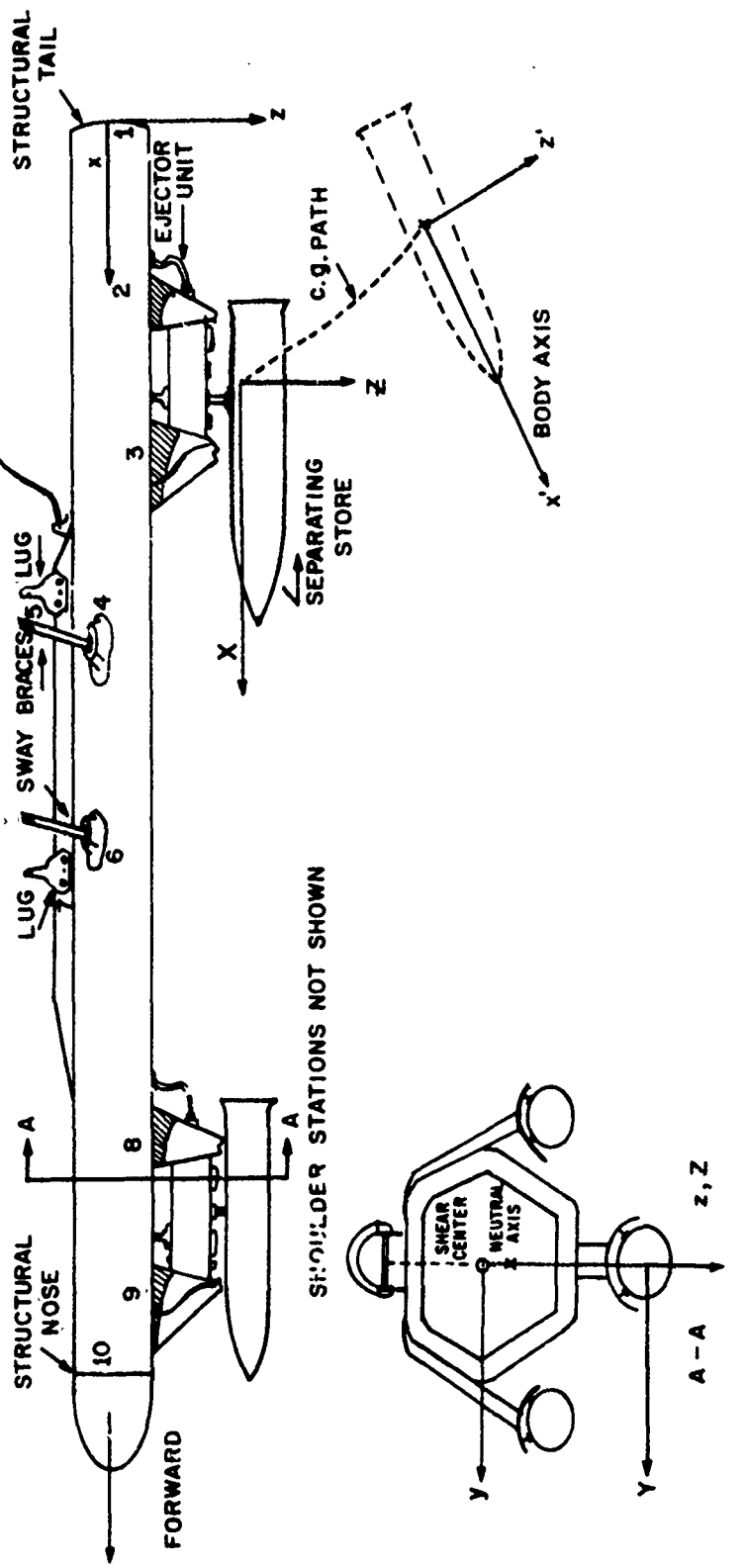

FIG. 1 EJECTION FROM A FLEXIBLE MER EJECTOR BEAM

P_l , P_r - LEFT AND RIGHT SWAY BRACE FORCES

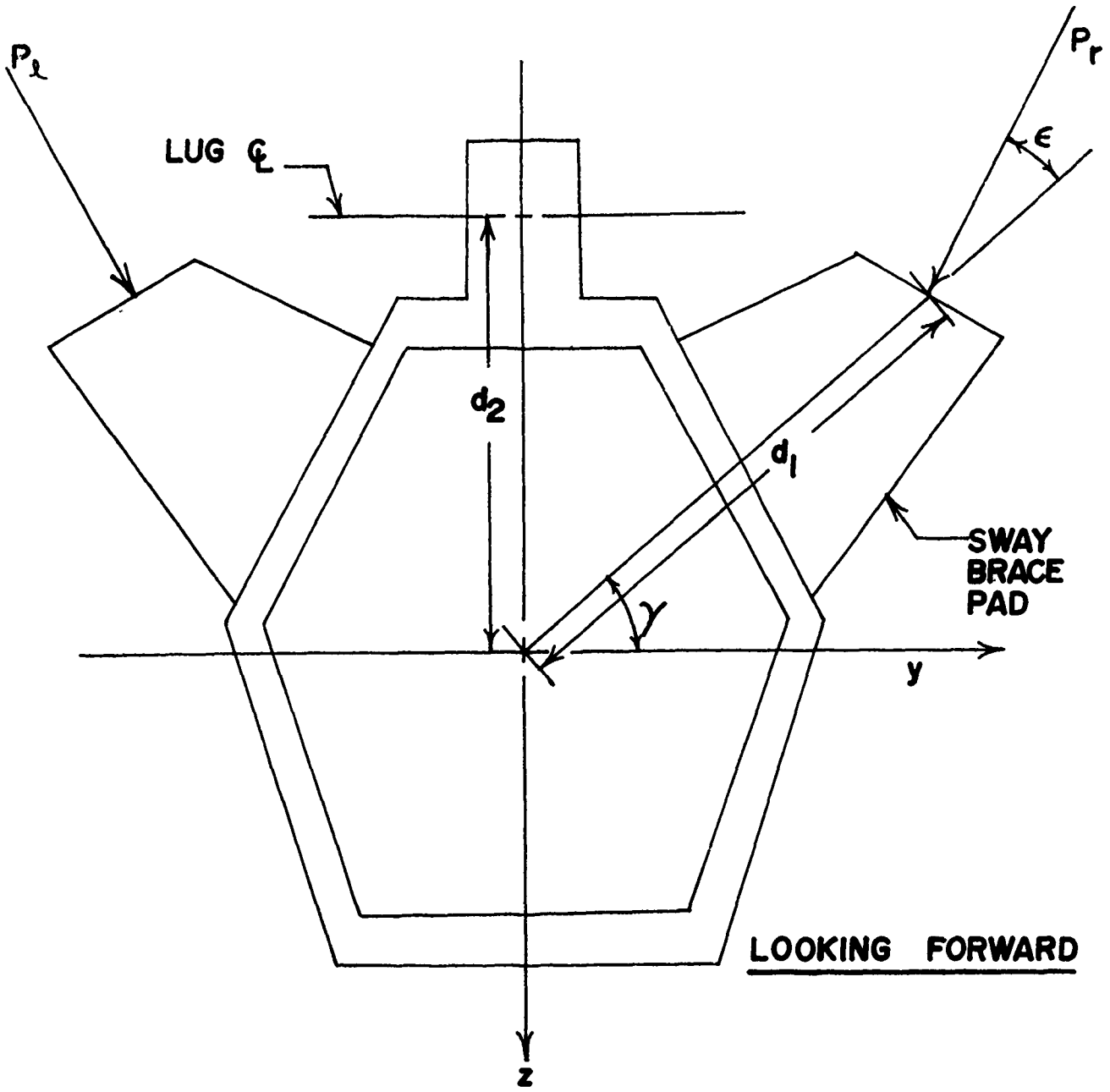

FIGURE 2
SWAY BRACE FORCE SYSTEM AT A MER SWAY BRACE CROSSECTION

$$F_y = - ck \cos(\epsilon + \gamma)] [\eta \cos(\epsilon + \gamma) - d_1 \phi \sin \epsilon] \quad (5)$$

$$M_x = - ck \sin \epsilon d_1 [d_1 \phi \sin \epsilon - \eta \cos(\epsilon + \gamma)] \quad (6)$$

c is 2 for P_0 large (no break of contact) and c = 1 for P_0 small (immediate break of contact).

Determination of influence coefficients leads to three subproblems. For the first problem, unit forces in the ż direction are applied at collocation points j and ζ deflections computed at i (see Figure 1). The bending deflection equations in the z direction may be obtained from

$$\zeta_i = C_{ij}^{z} F_{zj} \quad (7)$$

For the second and third problems, unit y forces and unit torques are applied and η and ϕ are computed. The coupled yaw plane bending and torsion equations of motion may be obtained from

$$\eta_i = C_{ij}^{y} F_{yj} + C_{ij}^{y\phi} M_{xj} \quad (8)$$

$$\phi_i = C_{ij}^{y\phi} F_{yj} + C_{ij}^{\phi} M_{xj} \quad (9)$$

Longitudinal forces contribute to moments M_y and M_z which lead to negligible deformations.

Distributed loads due to gravity, aircraft normal acceleration, and structural dynamic acceleration act along the beam. Beam inertia distribution is approximated by point masses and point rotational inertia.

Much larger loads act at the in-carriage bomb centers of gravity. Aerodynamic loads as well as the loads which act on the beam are also considered.

During store release, a reaction to the ejector force also acts on the beam.

B. Natural Frequencies and Normal Modes

The MER beam contributes much smaller inertial terms than the stores. Displacements at the store centers of gravity are assumed to be linear interpolations of displacements at aft and forward hanger cross sections (e.g., points 8 and 9 in Figure 1). The inertial loads at store centers of gravity are translated into beam loads by statically determinate computations.

For a store with c.g. located at $(\bar{y}, \bar{z})$ inertial loads at the c.g. are given by expressions like

$$\bar{F}_z = -M_s(\ddot{\bar{\zeta}} + y\ddot{\bar{\phi}}) \tag{10}$$

$$\bar{F}_y = -M_s(\ddot{\bar{\eta}} - \bar{z}\ddot{\bar{\phi}}) \tag{11}$$

$$\bar{M}_y = \frac{-I_p[\ddot{\zeta}_a - \ddot{\zeta}_f + \bar{y}(\ddot{\phi}_a - \ddot{\phi}_f)]}{x_h} \tag{12}$$

$$\bar{M}_z = \frac{I_p[\ddot{\eta}_a - \eta_f - \bar{z}(\ddot{\phi}_a - \ddot{\phi}_f)]}{x_h} \tag{13}$$

where

$$\bar{\zeta} = \frac{x_f\zeta_a + x_a\zeta_f}{x_h},$$

$$\bar{\eta} = \frac{x_f\eta_a + x_a\eta_f}{x_h},$$

$$\bar{\phi} = \frac{x_f\phi_a + x_a\phi_f}{x_h}$$

The c.g. loads are converted to beam loads by solving the statically determinant problems for the forces at the connection points between the ejector units and the beam (see Peference 3). Substitution of these forces and the smaller inertial forces associated with the beam into Equations (7)-(9) leads to the eigenvalue problem.

Release of the first, second, and sixth (rear $\mathcal{L}$, forward $\mathcal{L}$, and forward right shoulder, respectively) in the normal MER release sequence (see also Table 2)

leads to two separate eigenvalue problems. In this case, there is no mass unbalance (after release). One problem leads to modes associated with ζ motion. The other problem is associated with η, ϕ coupled motion.

For the mass unbalance cases (after release) of third, fourth, and fifth bombs (rear left shoulder, forward left shoulder, and rear right shoulder, respectively) released ζ, η, and ϕ motions all are coupled. Difficulties were associated with these cases in solving for the eigenvalues and resultant dynamic responses. For an unbalanced mass configuration, a variable transformation from ζ, η, ϕ to $\zeta + \bar{y}\phi$, $\eta - \bar{z}\phi$, ϕ for an unbalanced mass would probably resolve the problems encountered. Time did not permit reformulation.

The general formulation is non self-adjoint except for the case of the sixth bomb ejection (MER beam only).

The normal modes and eigenvalues are applied to the solution of the equations of motion in the next section.

C. Dynamic Response of MER Beam to Store Ejection

For the mass balanced cases (after 1st, 2nd, and 6th bomb released) the general equations of motion are

$$\zeta_i = -K^z_{ij} m_j \ddot{\zeta}_j + L^z_i - K^z_{ei} F_e(t) \tag{14}$$

$$\begin{Bmatrix} \eta_i \\ \phi_i \end{Bmatrix} = -\left[K^{y\phi}_{ij}\right] \begin{Bmatrix} m_j \ddot{\eta}_j \\ i_j \ddot{\phi}_j \end{Bmatrix} + L^{y\phi}_i - K^{y\phi}_{ei} F_e(t) \tag{15}$$

Solution of (14) and (15) may be obtained by expanding in the eigenvectors and using orthogonality between the eigenvectors and their adjoint eigenvectors. For the first and second bombs released, cases $K^{y\phi}_{ei} = 0$.

For the mass unbalanced case, the general equations of motion are given as

$$\begin{Bmatrix} \zeta_i \\ \eta_i \\ \phi_i \end{Bmatrix} = -\left[K^{yz\phi}_{ij}\right] \begin{Bmatrix} m_j \ddot{\zeta}_j \\ m_j \ddot{\eta}_j \\ i_j \ddot{\phi}_j \end{Bmatrix} + L^{yz\phi}_i - K^{yz\phi}_{ei} F_e(t) \tag{16}$$

III. EJECTION PHASE STORE DYNAMICS

A. Ejection Kinematics

The kinematic problem consists of finding the intersection between the straight line associated with the ejector foot and the cylindrical surface of the ejecting store. No friction between the bomb and the ejector foot is considered (bomb is free to slide).

The point, P (Figure 3), is located where the ejector foot exits from the ejector unit. Some of the geometry for in-carriage conditions are shown also in Figure 3.

Coordinates of the point P in X, Y, Z coordinates are computed from the initial rigid geometry and beam deformation. Deformation coordinates of the point P are compatible with the assumption of linear interpolation between forward and aft ejector unit connection point deformations.

$$X_p = X_{po} + z_h\left[\theta_p \pm \frac{\bar{y}(\phi_a - \phi_f)}{x_h}\right] \pm y_h - \psi_p\left[-\frac{\bar{z}(\phi_a - \phi_f)}{x_h}\right] \tag{16}$$

$$Y_p = \mp(\bar{y} - y_p) + \eta_a + x_p\psi_p - z_p\phi_p \tag{17}$$

$$Z_p = -(\bar{z} - z_p) + \zeta_a - \theta_p x_p \pm y_p\phi_p \tag{18}$$

where

$$\theta_p = \frac{\zeta_a - \zeta_f}{x_h},$$

$$\psi_p = \frac{\eta_f - \eta_a}{x_h}, \text{ and}$$

$$\phi_p = \frac{(x_h - x_p) + \phi_f x_p}{x_h}$$

θ_p, ψ_p, and ϕ_p may be considered to be a local set of Euler angles associated with the deformation of a set of axes with origin at P and parallel to X, Y, Z. ± signs are associated with right and left (looking forward) shoulder stations, respectively. X_{po} is the initial piston moment arm from the store c.g.

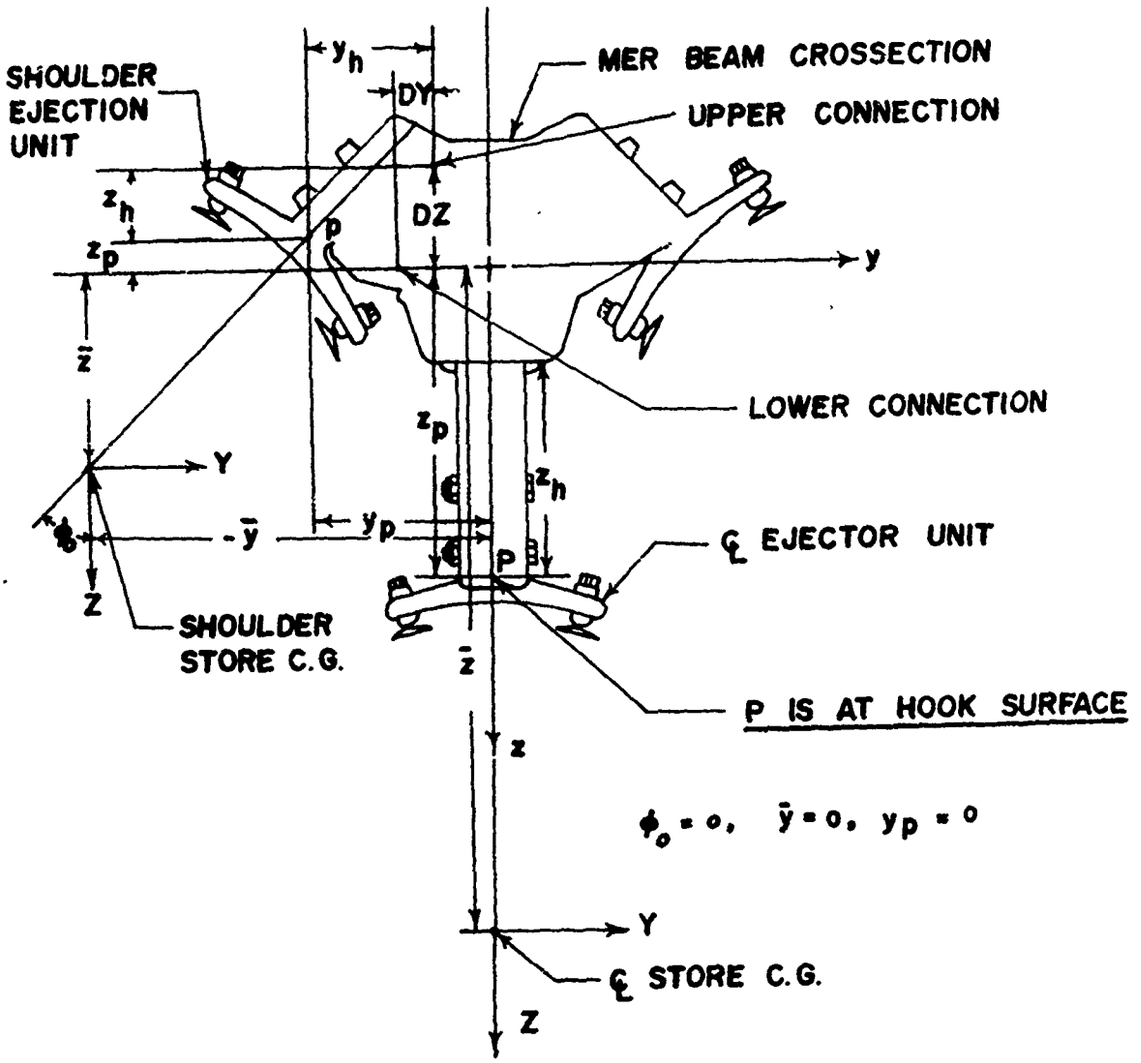

FIGURE 3(a)

MER BEAM IN-CARRIAGE GEOMETRY

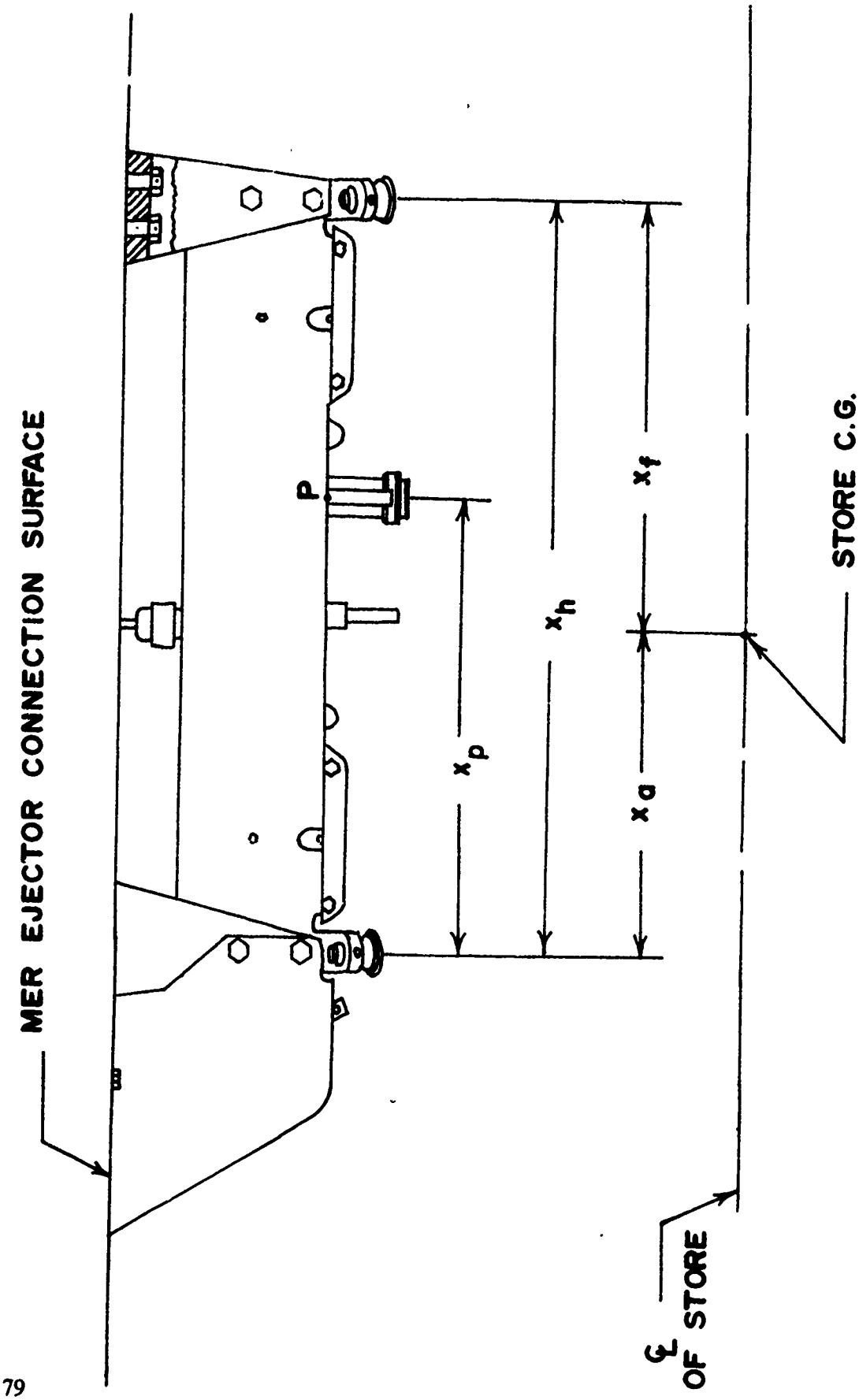

FIGURE 3 (b)

IN-CARRIAGE EJECTOR GEOMETRY

Initial conditions for the store c.g. in-carriage are given by similar expressions.

$$\theta_s(o) = \theta_p(o), \quad \phi_s(o) = 0, \quad \psi_s(o) = \psi_p(o) \tag{19}$$

$$X_s(o) = (z_h + \bar{z} - z_p)\left[\theta_p \pm \frac{\bar{y}(\phi_a - \phi_f)}{x_h}\right] \pm (y_h + \bar{y} - y_p)\left[-\psi_p - \frac{\bar{z}(\phi_a - \phi_f)}{x_h}\right] \tag{20}$$

$$Y_s(o) = \eta_a - x_a\psi_p(o) - \bar{z}\bar{\phi}(o) \tag{21}$$

$$Z_s(o) = \zeta_a - x_a\theta_p \pm \bar{y}\bar{\phi}(o) \tag{22}$$

At later times, the six-degrees-of-freedom are determined by store dynamics.

From $(X_p, Y_p, Z_p, \phi_p, \psi_p, \theta_p)$, $(X_s, Y_s, Z_s, \phi_s, \psi_s, \theta_s)$, the store diameter, and the assumption for small angles one can obtain the coordinates of the point of intersection of the ejector foot with the cylindrical surface of the bomb. Subsequently, one can compute ejector force moment arms and ejector foot displacement needed for store dynamics.

B. Ejection Dynamics

Release conditions for a bomb are at an elevation angle of θ_o, constant pull-up rate of $\dot{\theta}_o$, Mach number M_o, and angle-of-attack α_o.

Store aerodynamic loads are assumed to be a perturbation of in-carriage values (C_{No}, C_{yo}, C_{mo}, C_{no}). For small angles and short ejection times

$$C_N = C_{No} + C_{N\alpha}(\alpha_o)(\alpha - \alpha_o)$$

$$C_Y = C_{Yo} - C_{N\alpha}(o)\beta$$

$$C_m = C_{mo} + C_{m\alpha}(\alpha_o)(\alpha - \alpha_o)$$

$$C_n = C_{no} - C_{m\alpha}(o)\beta \tag{23}$$

$$\alpha - \alpha_o = \theta_s + \frac{W_s - \dot{\theta}_o x_o}{V_o} \tag{24}$$

$$\beta = -\psi_s + V_s/V_o \tag{25}$$

The perturbation terms are given by free stream aerodynamics using local slopes. Functional values of α_o and 0 indicate what angles of attack are used for computing local slopes.

Dimensionless aerodynamic forces for the body axes are

$$\frac{F'_z}{Q_o S} = -C_{No} - C_{N\alpha}(\alpha_o)(\alpha - \alpha_o)$$

$$\frac{F'_y}{Q_o S} = C_{Yo} - C_{N\alpha(o)}\beta$$

$$\frac{F'_x}{Q_o S} = -C_D$$

$$\frac{M'_z}{Q_o SD} = C_{no} - C_{m\alpha}(o)\beta + C_{nr}\frac{rD}{2V_o}$$

$$\frac{M'_y}{Q_o SD} = C_{mo} + C_{m\alpha}(\alpha_o)(\alpha - \alpha_o) + C_{mq}\frac{qD}{2V_o}$$

$$\frac{M'_x}{Q_o SD} = C_{\ell o} + C_{\ell p}\frac{pD}{2V_o} \tag{26}$$

$C_{\ell p}$, C_{mq}, C_{nr} are nominal values and do not greatly affect the solution.

The translational equations will be written in terms of coordinates relative to X, Y, Z coordinates. For small angles and linear aerodynamics, the equations are linear as in Reference 3. The rotational equations of motion remain nonlinear.

The direction cosines of the ejector foot are given by

$$\ell = \mp \sin\phi_o\ \psi_p + \cos\phi_o \theta_p$$

$$m = \pm \sin\phi_o - \cos\phi_o \phi_p$$

$$n = \pm \sin\phi_o \phi_p + \cos\phi_o \tag{27}$$

Contact point of the ejector foot with the bomb surface in terms of coordinates $\bar{X}$, $\bar{Y}$, $\bar{Z}$ with origin at the store c.g. but parallel to X, Y, Z are given by

$$\frac{\bar{Z}^2}{n^2} + \bar{Z}[-2(X_s - X_p)\theta_s + 2\psi_s(X_s - X_p)\frac{m}{n}$$

$$+\frac{2m^2}{n^2}(Z_s - Z_p) - 2\frac{m}{n}(Y_s - Y_p)] - R^2$$

$$+\frac{2\psi_s m}{n}(X_s - X_p)(Z_s - Z_p) - 2\psi_s(Y_s - Y_p)(X_s - X_p)$$

$$+\frac{m^2}{n^2}(Z_s - Z_p)^2 + (Y_s - Y_p)^2 - \frac{2m}{n}(Y_s - Y_p)(Z_s - Z_p) = 0$$

$$\bar{Y} = \frac{m}{n}(\bar{Z} + Z_s - Z_p) - (Y_s - Y_p)$$

$$X = \frac{\ell}{n}(Z + Z_s - Z_p) - (X_s - X_p) \qquad (28)$$

The root for $\bar{Z}$ with the negative sign is the proper one. The ejector throw length from point P at anytime is given by

$$\ell_{pt} = \frac{Z + Z_s - Z_p}{n} \qquad (29)$$

Approximate equations of motion are given as

$$\dot{U}_s = \frac{Q_o S}{M_s}[-C_{D_o} - \psi_s C_{y_o} - \theta_s C_{N_o}]$$

$$- \dot{\theta}_o[2W_s + V_o\alpha_o - \dot{\theta}_o x_o] + \frac{F_e \ell}{M_s} - g\sin\theta_o$$

$$\dot{V}_s = \frac{Q_o S}{M_s}[C_{yo} - C_{N\beta}\beta - C_D\psi_s + \phi_s C_{No}] + \frac{F_e m}{M_s}$$

$$\dot{W}_s = \frac{Q_o S}{M_s}[-C_{No} - C_{N\alpha}(\alpha - \alpha_o) + C_D\theta_s + \phi_s C_{Yo}]$$

$$+\dot{\theta}_o V_o + \frac{F_e n}{M_s} + g\cos\theta_o$$

$$\dot{p} = \frac{Q_o SD}{I_r}\left(C_{\ell o} + C_{\ell p}\frac{pD}{2V_o}\right)$$

$$+\frac{F_e}{I_r}[(X_s - X_p)(n\psi_s + m\theta_s) + n\bar{Y} - m\bar{Z}]$$

$$\dot{q} - pr\left(1 - \frac{I_r}{I_p}\right) = \frac{Q_o SD}{I_p}\left[C_{mo} + C_{m\alpha}(\alpha - \alpha_o) + C_{mq}\frac{qD}{2V_o}\right]$$

$$+\frac{F_e}{I_p}[-\phi_s m(X_s - X_p) + \bar{Z}\ell - n\bar{X} + \psi_s(m\bar{Z} - n\bar{Y})]$$

$$\dot{r} + pr\left(1 - I_r/I_p\right) = \frac{Q_o SD}{I_p}\left[C_{mo} + C_{m\alpha}(\alpha - \alpha_o) + C_{mq}\frac{qD}{2V_o}\right] +$$

$$\frac{F_e}{I_p}[-\phi_s n(X_s - X_p) + m\bar{X} - \ell\bar{Y} + \theta_s(n\bar{Y} - m\bar{Z})]$$

$$\dot{\phi}_s = p + r\theta_s$$

$$\dot{\theta}_s = q - r\phi_s - \dot{\theta}_o$$

$$\dot{\psi}_s = r + q\phi_s \qquad (30)$$

Computations begin at the in-carriage position and end when the store breaks contact with the foot (end of stroke) at time, $t = t_c$.

The three ejection velocity components are defined as

$$U_e \approx U_s(t_e)$$

$$V_e \approx V_s(t_e)$$

$$W_e \approx W_s(t_e) - \dot{\theta}_o V_o t_e \tag{31}$$

The above are the velocity components relative to the initial velocity vector of the store (wind axis components). $W'_e = (W_e^2 + V_e^2)^{1/2}$ is usually defined as the ejection velocity

IV. ANALYSED COMPUTATIONS

A. Input Data Generation

The model developed in the sets of equations in Sections II and III were programmed for the CDC 6700 with general input variables.

Bending stiffnesses for the MER beam were estimated with the aid of Reference 4. Torsional stiffness and shear center location were computed from the St. Venant theory of torsion[5] and agree to within 20% of the simpler shear flow estimates of Bredt.[6] Inertial properties of the beam were estimated from cross section geometry and material densities. The parent rack was taken as the AERO-7. H. Washmuth[7] indicates that the AERO-7 sway brace pad deflects .1" for a 2000 pound load. In the sample computations presented herein, only one pad at a time was assumed to be in contact (the most flexible condition possible). MER beam and ejector geometry were taken from Reference 8.

Tables 1 and 2 summarize input variables used for the sample computation given below.

As in Reference 3, an ejection force-time curve was assumed to be a mean curve for the MER ejector unit with a MK 2-1 cartridge.

In-carriage loads for all stores carried was available for the M-117 bomb from Reference 9. Hence, all computations were based upon these data. These loads are typical of the center wing pylon on the A-7D (right wing) at $M_o = .9$.

Free stream static aerodynamic data are taken from References 10 and 11. Dynamic aerodynamic data are from Reference 12.

TABLE 1

SAMPLE COMPUTATION INPUT VARIABLES

MER DATA

Material Properties (7075 Aluminum alloy)

$E = 3.9 \times 10^6$ psi $G = 10.4 \times 10^6$ psi

Sway Brace Variables

$d_1 = 5.5$ in, $d_2 = 4.0$ in, $\gamma = 51°$, $\epsilon = 9°$

$k = 2000$ lb/in, $c = 1.$

Second Moments of Area

On strongback: I_{zz} (pitch plane bending) $= 43.1$ in^4,

I_{yy} (yaw plane bending) $= 18.06$ in^4

J (Torsion) $J = 42.62$ in^4

Off Strongback: $I_{zz} = 27.1$ in^4, $I_{yy} = 17.93$ in^4

$J = 38.92$ in^4

Collocation Point Geometry and Inertial Data (MER Beam)

j (Collocation Point number)	1	2	3	4	5	6	7	8	9	10
x_j (in)	0.0	13.0	33.25	45.75	50.75	70.75	75.75	91.25	106.75	127.00
m_j (lbs)	5.4	36.0	36.80	8.70	12.40	12.40	10.10	15.40	38.30	34.10
i_j (lb-ft^2)	.24	4.96	5.02	.42	.60	.60	.50	.75	5.09	4.87

Ejector unit connections at j = 2, 3, 9, 10

Lug connections at j = 4,7

Sway braces at j = 5,6

Ejector Unit Geometry

$x_h = 20.25$ in, $x_p = 8.25$ in, $\phi_o = 45°$

ℓ_{pt} (end of ejection) $= 4.2$ in

Centerline unit: $y_h = 0$, $z_h = 5.75$ in, $y_p = 0$, $z_p = 8.25$ in,

Shoulder unit: DZ = 2.88 in, DY = 1.0 in, $y_h = 3.31$ in,

$z_h = 1.9$ in, $y_p = 5.0$ in, $z_p = -1.0$ in

TABLE 2

SAMPLE COMPUTATION INPUT VARIABLES

M-117 AND RELEASE CONDITION DATA

Store c.g. Location Geometry

x_a = 7.95 in.

Centerline store: $\bar{y}$ = o, $\bar{z}$ = 17.5 in.

Shoulder store: $\bar{y}$ = 11.6 in, $\bar{z}$ = 5.5 in.

Store Inertia and Geometry

D = 16 in., M_s = 824 lbs, I_p = 1609 lb-ft^2

I_r = 148 lb-ft^2

Normal MER Release Sequence (Looking Forward)

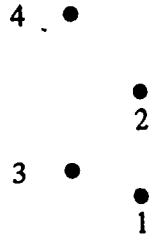

Forward

Aft

Number, N, refers to store being released.

Configuration just before release consists of stores, $N \leq M \leq 6$ in-carriage.

Store Dynamic Aerodynamic Coefficients

$C_{\ell p}$ = -1 C_{mq} = -1.3 C_{nr} = -4.3

Aircraft Release Conditions

H = 10,000 ft, M_o = .9, θ_o = -30°

$\dot{\theta}_o$, the pull-up rate of the aircraft, was varied from 0 to .1 rad/sec, corresponding to normal accelerations of .9 g to 3.9 g. The store angle-of-attack, α_o, was assumed to vary linearly between .5° and 7° in the interval for $\dot{\theta}_o$.

B. Discussion of Results

Computations for rigid and flexible cases for the second, fourth, and sixth store are summarized in Figures 4-13. Δ indicates flexible minus rigid values.

For the second store, 4 pitch-plane bending and 4 torsional-yaw plane bending modes were used. For the fourth bomb, 3 modes were used. For the sixth bomb, 5 pitch plane bending and 3 yaw plane bending-torsional modes were used. The number of modes chosen is compatible with the accuracy of the approximate computation.

The case of the second store dropped was computed in Reference 3 for 3-D dynamics. As noted in Reference 3, structural loading increases with the pull-up rate of the aircraft, $\dot{\theta}_o$, but the effect of pulling-up is more import: than flexibility in decreasing the ejection velocity. Here, the ejection velocity has a small y component. Maximum percent difference for the ejection velocity is about 11% or slightly larger than for the planar case. Rolling rates are insignificantly affected by flexibility. The pitching rate is significantly affected by flexibility as noted in Reference 3; this is primarily due to a change in initial orientation of the bomb with respect to the free stream (static aecroelastic effect). It is anticipated that the actual static aeroelastic effect is somewhat smaller. The lower yawing rates are affected by flexibility to a lesser extent since the loading in the yaw direction is less.

The case of the fourth store released is considerably different. Ejection velocities are affected to a lesser extent, 5% or less, since part of the initial stored potential energy and ejection force work is translated into rotational kinetic energy. Pitching and yawing rate are affected to a lesser extent. Roll rate is significantly affected. Computations show that pull-up alone affects the roll rate more significantly than flexibility.

For the sixth store beam frequencies are much greater since after release only the MER beam constitutes the structural dynamic system. Ejection velocity effect is somewhat less than for the centerline release. Yawing and pitching rates are slightly affected. Pitching rates are affected slightly less than for the fourth bomb release case.

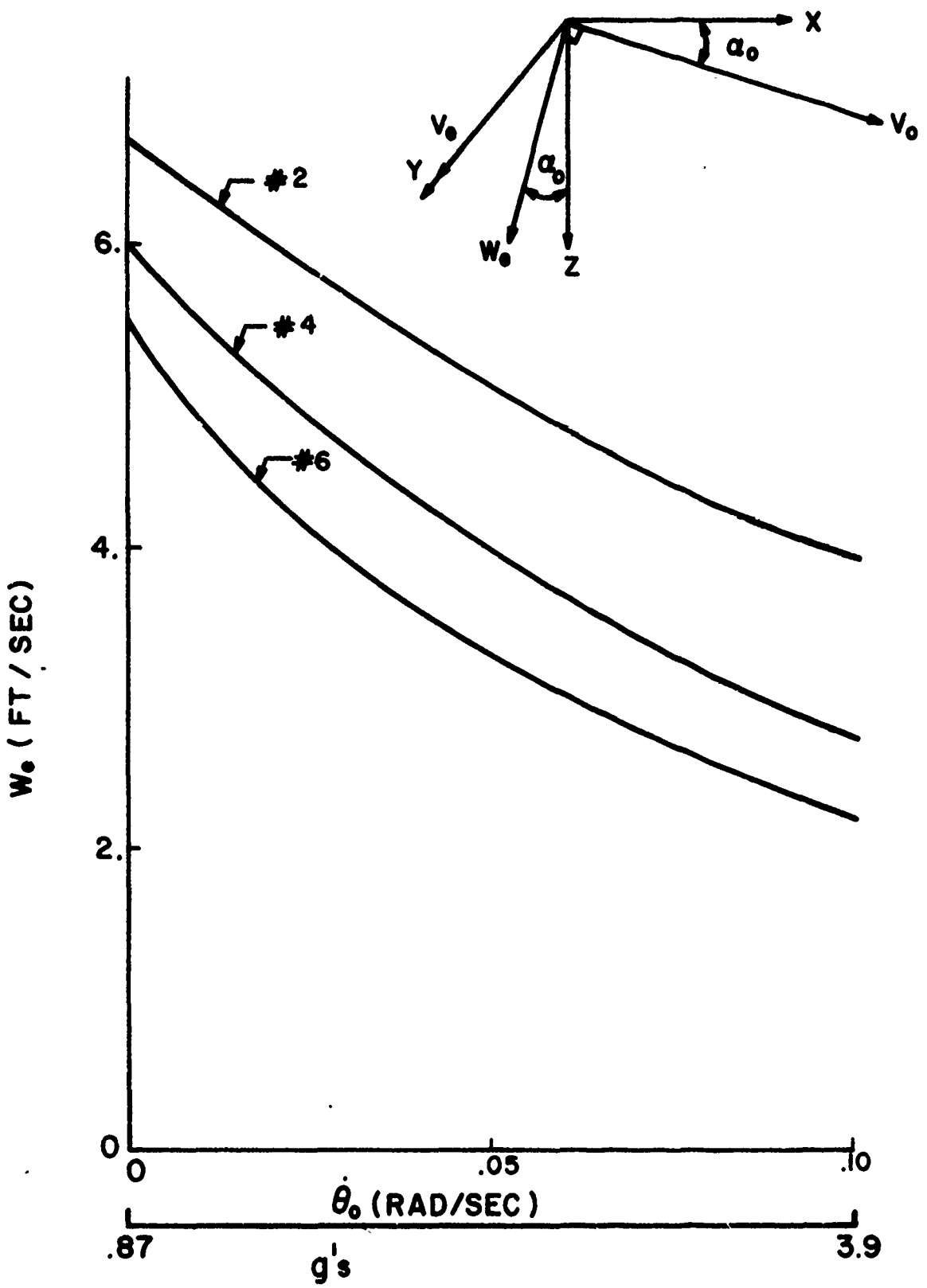

FIGURE 4

VERTICAL PLANE EJECTION VELOCITY COMPONENT

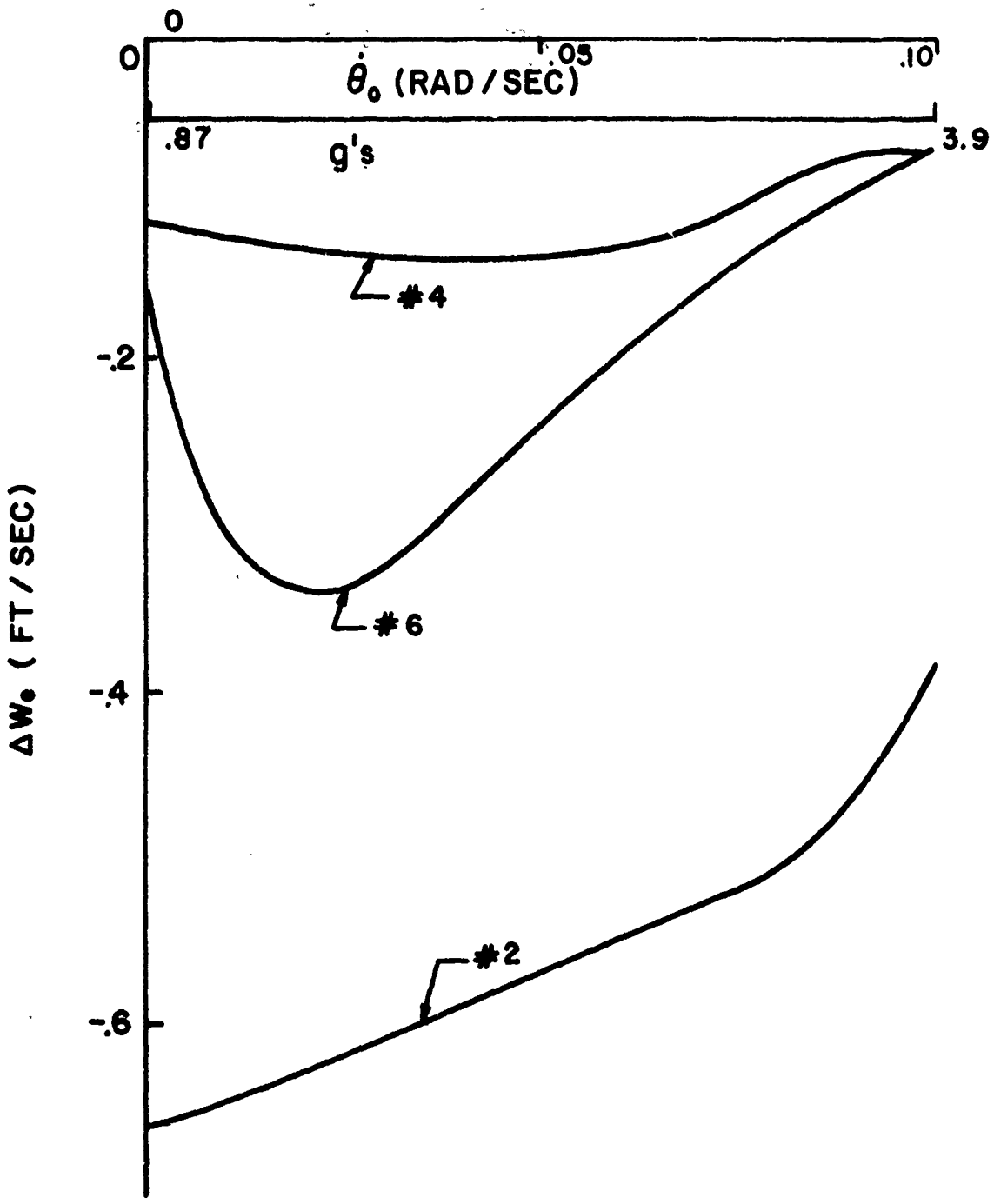

FIGURE 5

FLEXIBILITY INCREMENT OF VERTICAL EJECTION VELOCITY COMPONENT

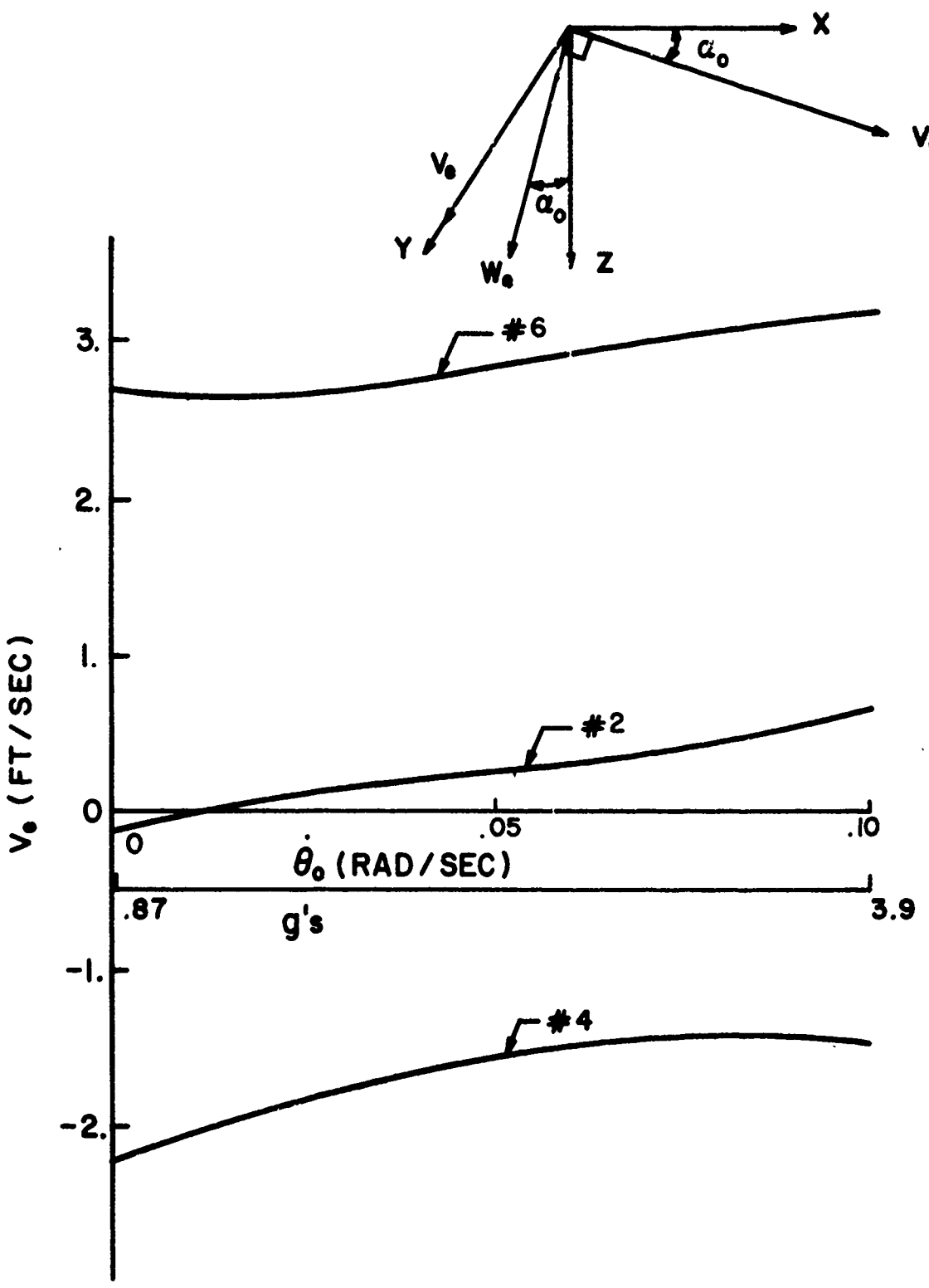

FIGURE 6.

HORIZONTAL PLANE EJECTION VELOCITY COMPONENT

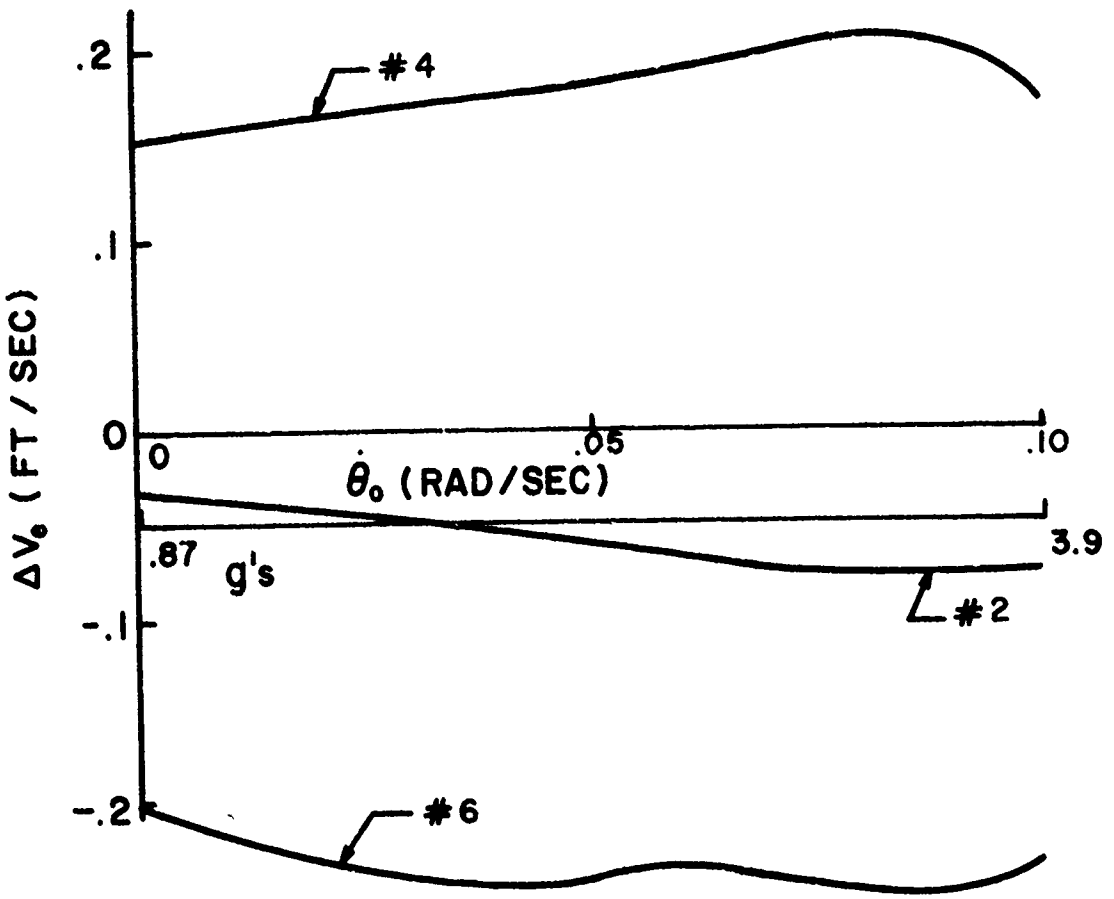

FIGURE 7

FLEXIBILITY INCREMENT OF HORIZONTAL EJECTION VELOCITY COMPONENT

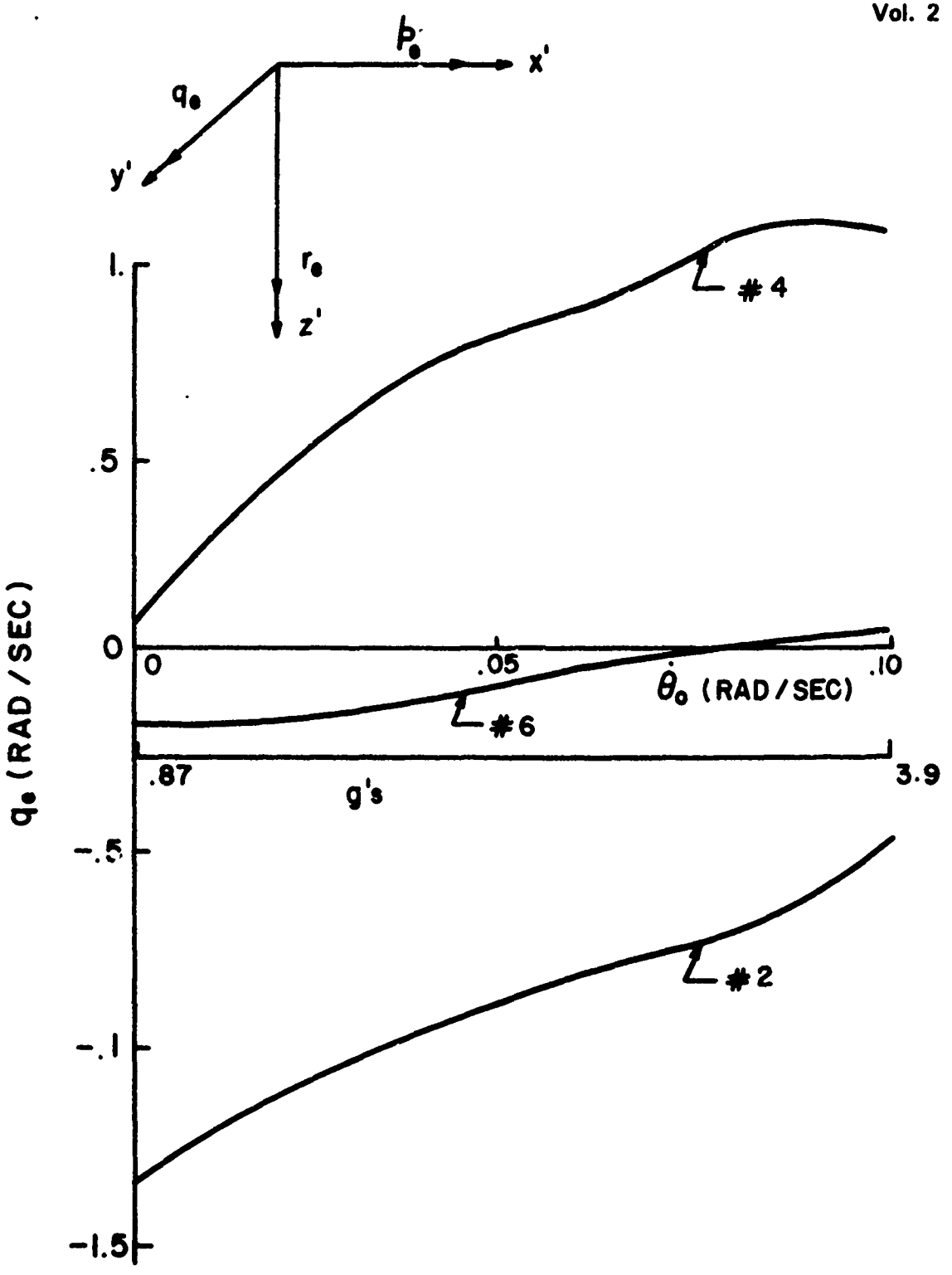

FIGURE 8

EJECTION PITCH RATE

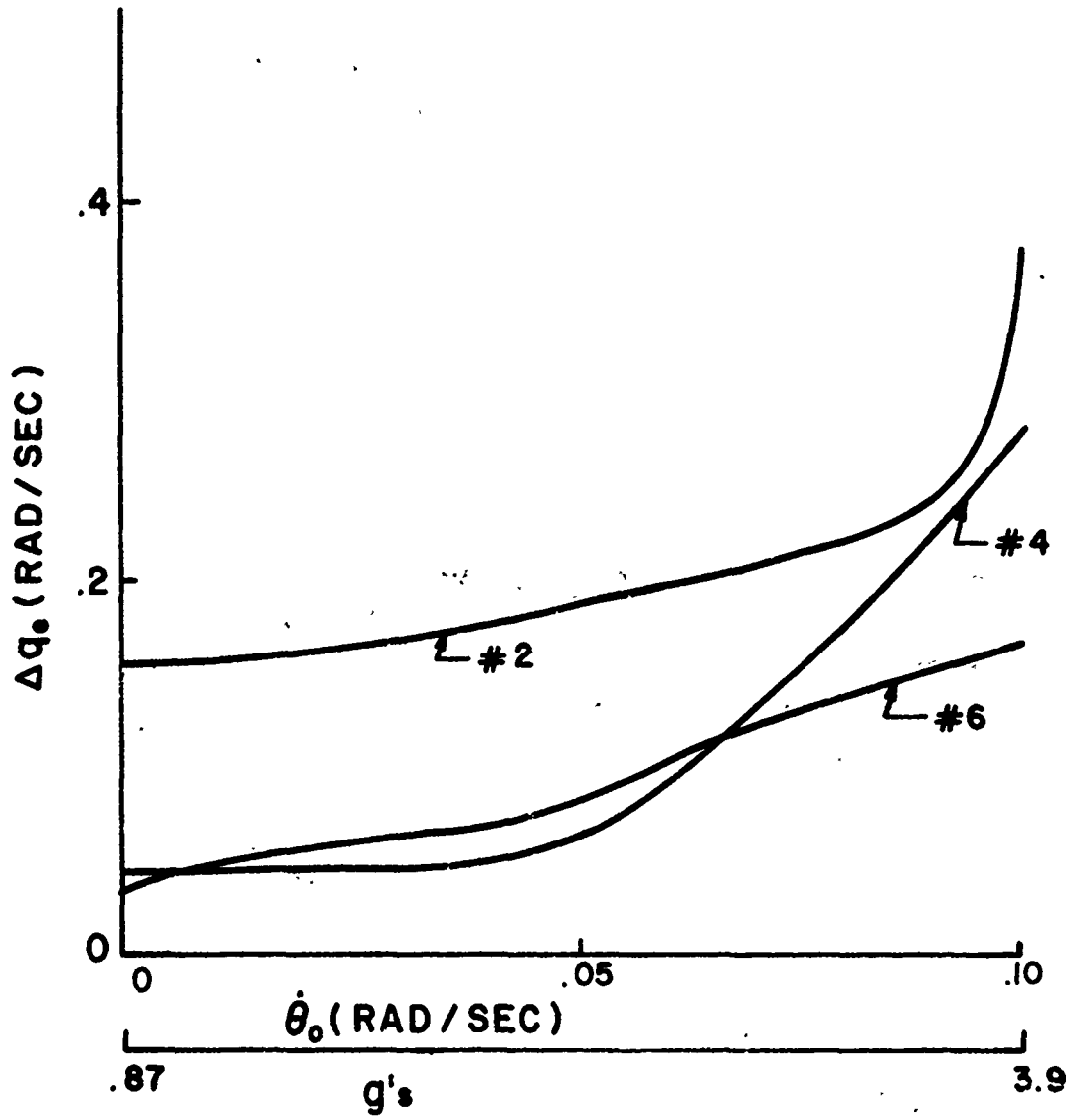

FIGURE 9

FLEXIBILITY INCREMENT OF EJECTION PITCH RATE

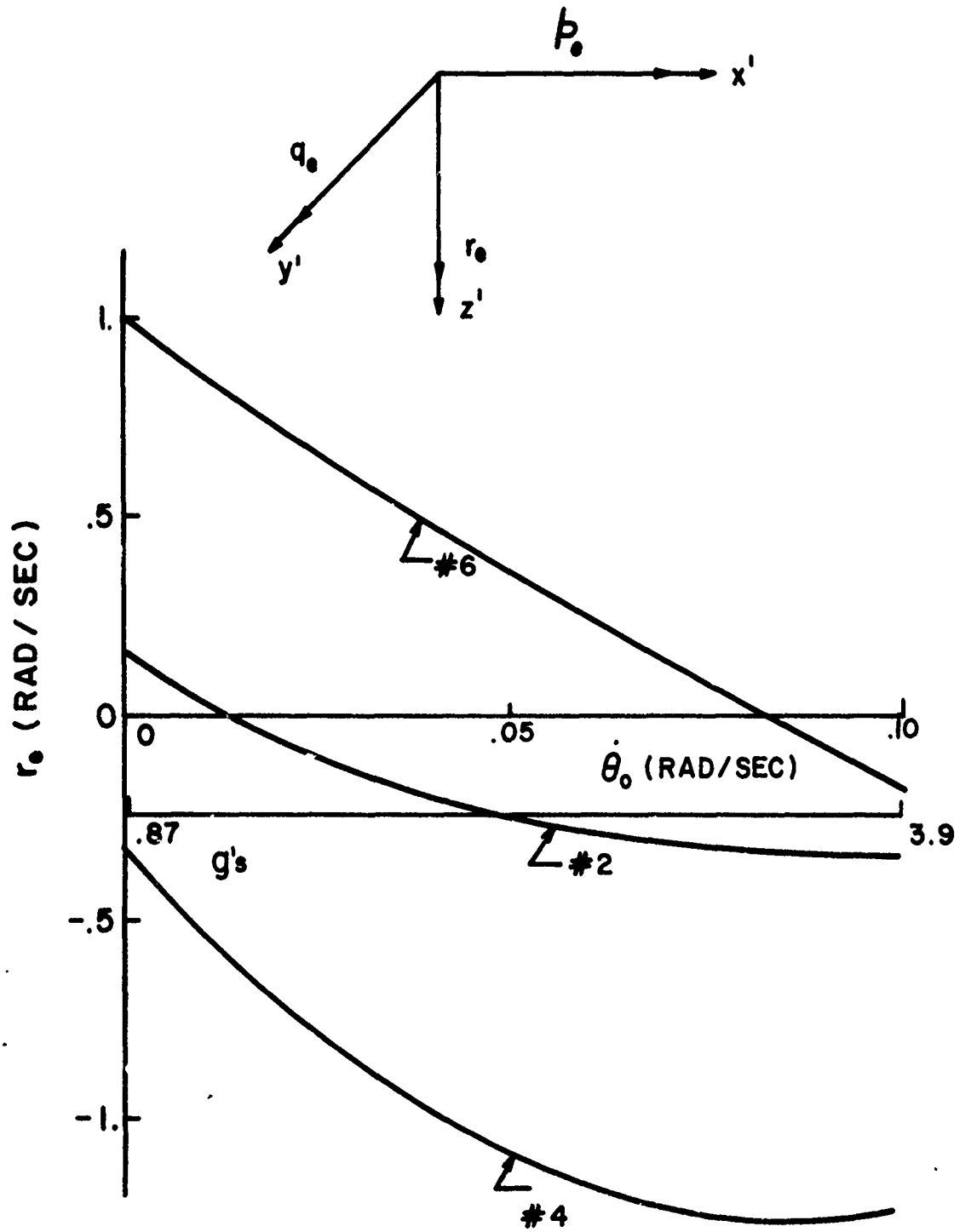

FIGURE 10

EJECTION YAW RATE

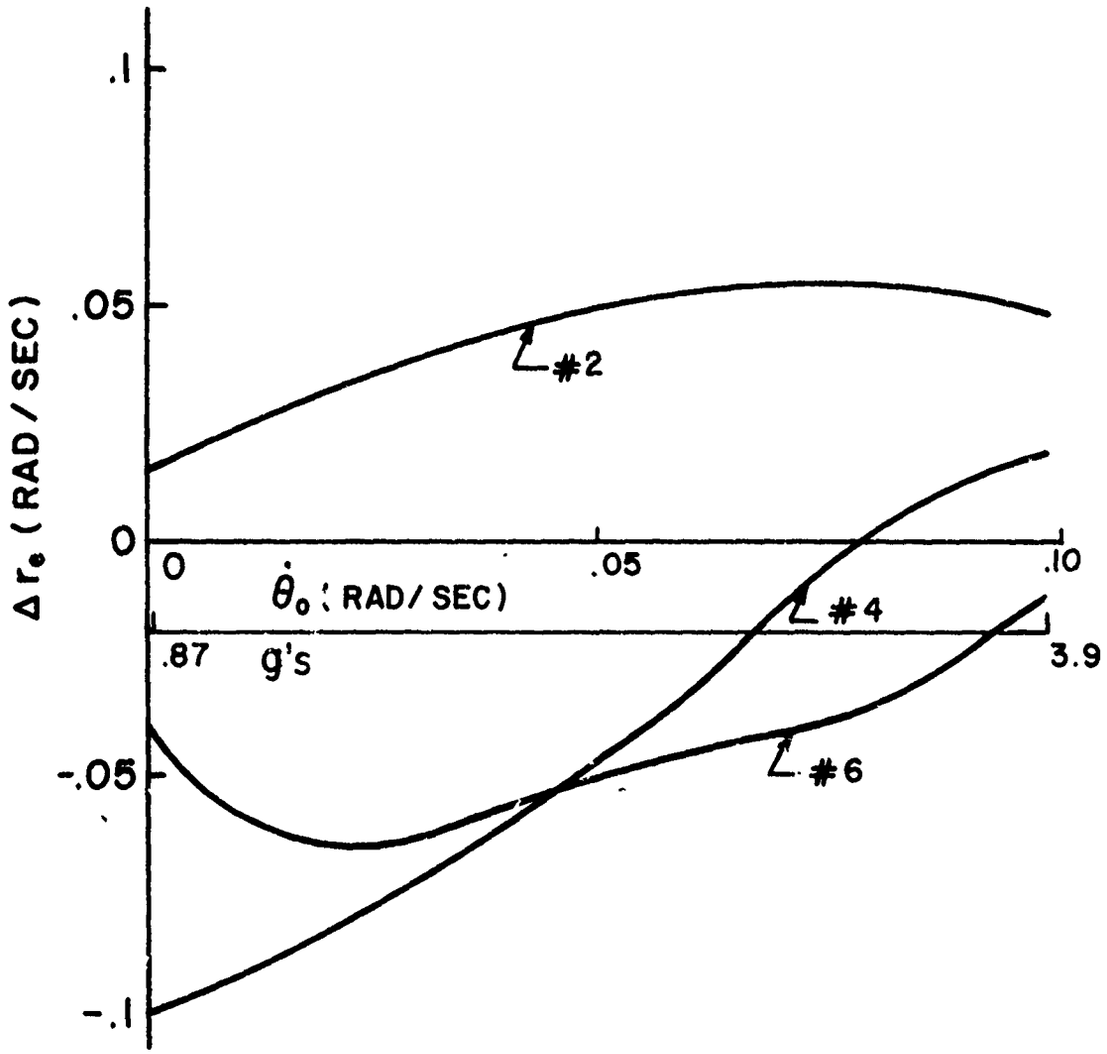

FIGURE 11

FLEXIBILITY INCREMENT OF EJECTION YAW RATE

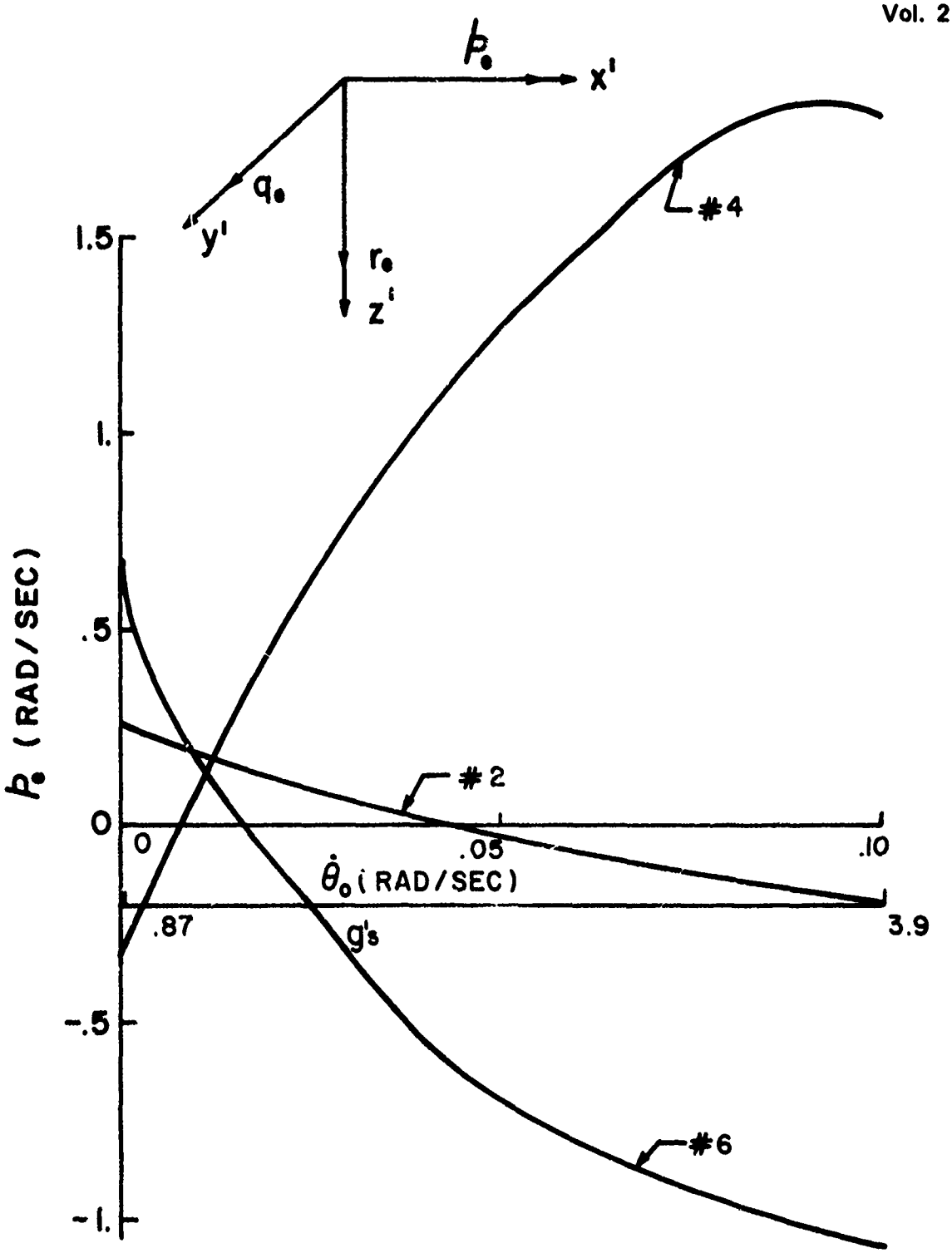

FIGURE 12

EJECTION ROLL RATE

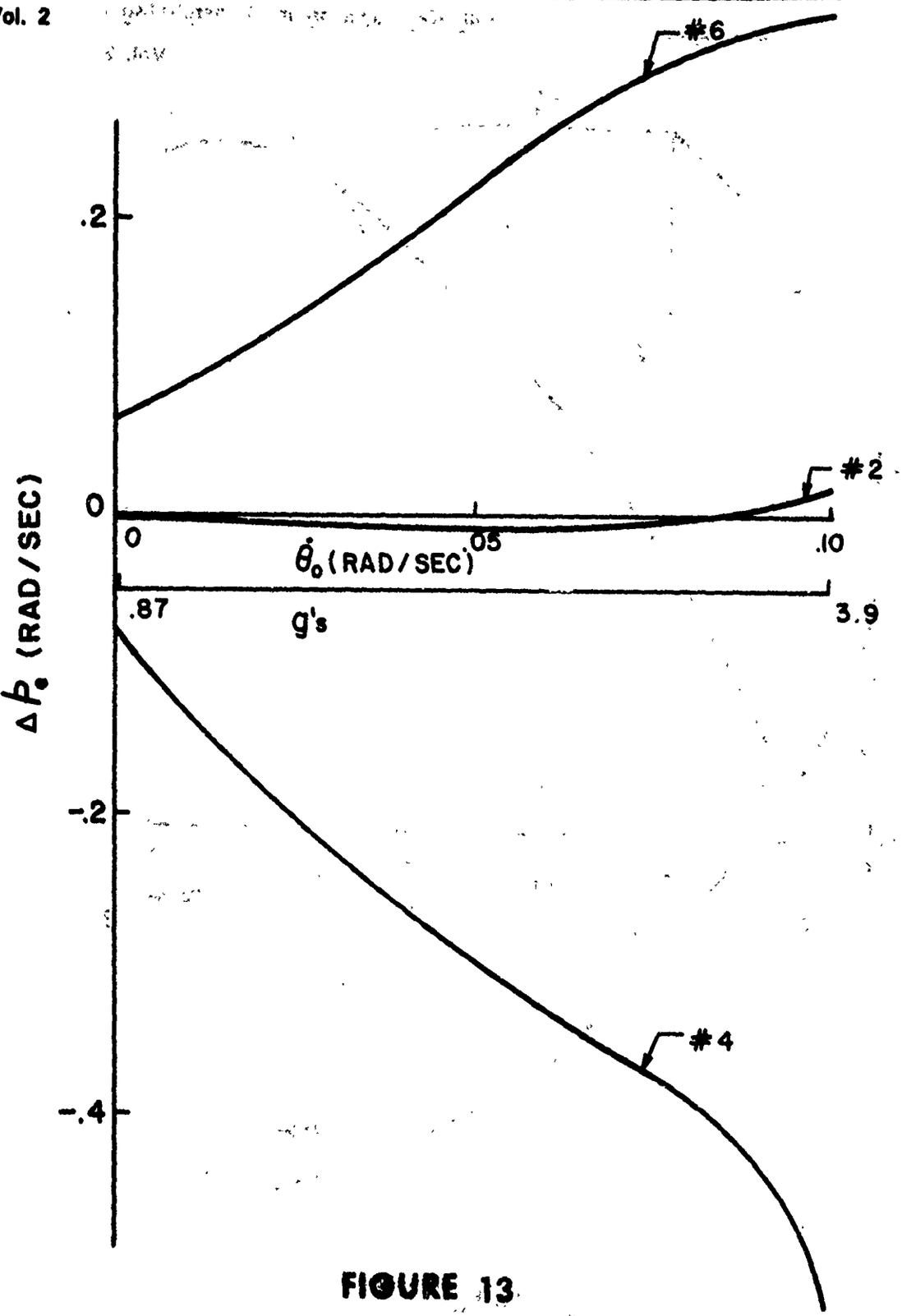

FIGURE 13

FLEXIBILITY INCREMENT OF EJECTION ROLL RATE

Differences between the effect on the pitching rate between the three cases is due to differences in initial deformation. For second, fourth, and sixth bombs, 3, 2, and 1 bomb loads, respectively, are present in the forward carriage positions before release.

The effect of pull-up rate alone affects all release variables to a greater extent than flexibility above a certain break-even value of $\dot{\theta}_o$ as was shown in Reference 3 except for q_e for the second store where the break even value is at $\dot{\theta}_o$ = .10 (rad/sec).

V. CONCLUDING REMARKS

A three-degree-of-freedom model has been extended to the prediction of six-degree-of-freedom ejection conditions of a store due to gravity, pull-up maneuver, ejector, and aerodynamic in-carriage loads acting on a flexible MER beam.

The ejection velocity is probably decreased by no more than 15 percent for the heaviest stores. The one new effect due to flexibility for a shoulder release is for the ejection roll rate. Again, the effect of pull-up rate alone is more significant.

The effect of initial deformation (due to aircraft g's) on the ejection pitch rate may be of importance. Aircraft wing torsion is probably important as well as MER deformation. Wind tunnel captive store trajectory tests with flexible models might decide this question.

The effect of flexibility/aircraft pull-up maneuver on weapon impact point, must be determined by extending calculations through the interference flow-field to target altitude. Such computations are the object of subsequent work.

REFERENCES

1. Storey, W. W., ***A-7 Flutter Model Results, Comparison of Low Speed, High Speed, Full Span, and Semi Span Results With Flight Test Results***, Aircraft/Stores Compatibility Symposium Proceedings, Held at Dayton, Ohio, December 1971, AFFDL TR-72-67, Vol. III, pp 3-22, Air Force Flight Dynamics Laboratory, August 1972.
2. Aaron, N. E. and W. W. Storey, ***An Investigation of the Dynamic Response of the A-7 Aircraft to Store Ejection Loads***, Aircraft/Stores Compatibility Symposium Proceedings, JTCG/ALNNO, WP-12-2, Vol. I, pp. 239-265, Sacramento Air Material Area/Air Force Logistics Command, September 1973.

3. Devan, L., *An Estimate of MER Structural Dynamics on Store Separation*, NWL Technical Report TR-3097, Naval Weapons Laboratory, February 1974.
4. Bruce, R. D., *Stress Analysis of the Multiple Ejector Rack III*, Rpt. No. LB-31414, Douglas Aircraft Co., May 1961.
5. Timoshenko, S., and J. N. Goodier, *Theory of Elasticity*, McGraw-Hill Book Co., 1951.
6. Peery, D., *Aircraft Structures*, McGraw-Hill Book Co., 1950.
7. Washmuth, H., Unpublished Data, Naval Weapons Center, China Lake, 1972.
8. Rack Assembly – Multiple Ejector Types 7 and 9, Douglas Drawing No. 5821500, Douglas Aircraft Co., July 1964.
9. LTV-VAC High Speed Wind Tunnel Test Facility (Transmitted by R. D. Gallagher), Selected A-7 Aircraft Individual Store Airloads, Vought Aeronautics Corp., November 1972.
10. Falkowski, E. W., *Transonic Characteristics of a Full–Scale M-117 Bomb With Three Fin Configurations*, TR-3785, Picatinny Arsenal, October 1968.
11. Transmitted by Falkowski, E. W., Supplementary Data to Reference 10, Picatinny Arsenal, January 1973.
12. Kukainis, J., and R. H. Roberts, *Separation Characteristics of Six Stores From the A-7D Aircraft at Mach Numbers From .42 to .95*, AEDC-TR-70-19, Arnold Engineering Development Center, January 1970.

APPENDIX A

LIST OF SYMBOLS

LIST OF SYMBOLS

c	Coefficient determining level of parent rack swaybrace preload; 1 for very low preload; 2 for large preload.
C_D	Bomb drag coefficient.
C_{ij}^{y}	MER beam y deflection at i^{th} collocation point due to unit force in y direction applied at j^{th} collocation point (ft/lb).
$C_{ij}^{y\phi}$	MER beam rotation at i^{th} collocation point due to unit force in y direction applied at j^{th} collocation point (rad/lb).
C_{ij}^{z}	MER beam z deflection at i^{th} collocation point due to unit force in z direction applied at j^{th} collocation point (ft/lb).
C_{ij}^{ϕ}	MER beam rotation at i^{th} collocation point due to unit torque applied at j^{th} collocation point (rad/ft-lb).
$C_{\ell p}$	Roll damping coefficient for a store.
$C_{\ell o}$	Store in-carriage roll moment coefficient.
C_m	Store pitching moment coefficient.
C_{mq}	Store pitch damping coefficient.
$C_{m\alpha}$	Store pitching moment coefficient α derivative.
C_{mo}	Store in-carriage pitching moment coefficient.
C_n	Store yaw moment coefficient.
C_{nr}	Store yaw damping coefficient.
C_{no}	Store in-carriage yaw moment coefficient.
C_N	Store normal force coefficient.
$C_{N\alpha}$	Store normal force coefficient α derivative.
C_{No}	Store in-carriage normal force coefficient.
d_1	Distance from MER shear center to sway brace contact point (ft).
d_2	Distance from MER shear center to MER lug centerline (ft).
D	Store diameter (ft).
E	Modulus of elasticity in tension (lb/ft^2).
F_e	Ejection force (lb).
F'_x	Store x' body axis force (lb).
F_y	Beam load in y direction (lb).
$\bar{F}_y$	Store in-carriage load in y direction (lb).

F'_y	Store y′ body axis force (lb).
F_{yj}	Beam load in y direction at j^{th} point (lb).
F_z	Beam load in z direction (lb).
$\bar{F}_z$	Store in-carriage load in z direction (lb).
F'_z	Store z′ body axis force (lb).
F_{zj}	Beam load in z direction at j^{th} point (lb).
g	Acceleration of gravity (ft/sec^2).
G	Modulus of elasticity in shear (lb/ft^2).
i_j	Beam point rotational inertia at j^{th} point ($slug\text{-}ft^2$).
I_p	Store pitch moment of inertia ($slug\text{-}ft^2$).
I_r	Store roll moment of inertia ($slug\text{-}ft^2$).
I_{yy}	Beam pitch plane second moment of area (ft^4).
I_{zz}	Beam yaw plane second moment of area (ft^4).
J	Beam torsion second moment of area (ft^4).
k	Sway brace stiffness coefficient (lb/ft).
$K_{ei}^{y\phi}$	Beam y deflection or rotation at i^{th} collocation point due to unit ejection force (ft/lb) or (rad/lb).
$K_{ei}^{yz\phi}$	Beam y or z deflection or rotation at i^{th} collocation point due to unit ejection force (ft/lb) or (rad/lb).
K_{ei}^{z}	Beam z deflection at i^{th} collocation point due to unit ejection force (ft/lb).
$K_{ij}^{y\phi}$	y,ϕ coupled flexibility matrix (ft/lb) or (rad/lb) or (rad/ft-lb).
$K_{ij}^{yz\phi}$	y, z, ϕ coupled flexibility matrix (ft/lb) or (rad/lb) or (rad/ft-lb).
K_{ij}^{z}	z flexibility matrix (ft/lb).
ℓ	X direction cosine for ejection force.
$L_i^{y\phi}$	y, ϕ coupled deflection due to constant forces (ft or rad).
$L_i^{y,z,\phi}$	y,z,ϕ coupled deflection due to constant forces (ft or rad).
L_i^{z}	z deflection due to constant forces (ft).
ℓ_{pt}	Piston throw length (ft).
m	Y direction cosine for ejection force.
M_o	Aircraft Mach number.
m_j	Beam mass at j^{th} point (slugs).
M_s	Store mass (slugs).

M_x	Beam x torque (ft-lb).
M'_x	Store x′ body axis torque (ft-lb).
M_{xj}	Beam x torque at j^{th} point (ft-lb).
M_y	Beam y torque (ft-lb).
$\overline{M}_y$	Store in-carriage pitch moment (ft-lb).
M'_y	Store y′ body axis torque (ft-lb).
M_z	Beam z torque (ft-lb).
$\overline{M}_z$	Store in-carriage yaw moment (ft-lb).
M'_z	Store z′ body axis torque (ft-lb).
n	Z direction cosine for ejection force.
p	Store roll rate (rad/sec).
P_ℓ	Left sway brace force (lb).
P_r	Right sway brace force (lb).
P_o	Sway brace preload (lb).
q	Store pitch rate (rad/sec).
Q_o	In-carriage dynamic pressure (lb/ft^2).
r	Store yaw rate (rad/sec).
S	Store cross-section area (ft^2).
t	Time (sec).
t_e	Ejection time (sec).
U_e	U_s at ejection (ft/sec).
U_s	X velocity component of store relative to aircraft (ft/sec).
V_s	Y velocity component of store.
V_o	Aircraft velocity (ft/sec).
W_e	W_s at ejection $- t_e\dot{\theta}_o V_o$ (ft/sec).
W'_e	$= (V_e^2 + V_e^2)^{1/2}$ (ft/sec).
W_s	Z velocity component of store relative to aircraft (ft/sec).
x	Coordinate along MER beam.
X	Coordinate parallel to x with origin at in-carriage c.g. position of store being released.
x′	Body axis along store centerline with origin at c.g.
$\overline{X}$	Axis parallel to X with origin at store c.g.
x_a	x distance from aft sway brace hanger (MER) to in-carriage store c.g. (ft).

x_f	x distance from forward sway brace hanger (MER) to in-carriage store c.g. (ft).
x_h	$= x_a + x_f$ (ft).
x_p	x distance from aft sway brace hanger (MER) to the point P where the ejector foot exits (ft).
X_p	X coordinate of point P.
X_{po}	Initial ejector foot moment arm (ft).
X_s	X coordinate of store c.g. relative to aircraft.
x_o	x distance of in-carriage store c.g. to aircraft c.g.
y	Coordinate perpendicular to x-z plane.
$\bar{y}$	y distance from in-carriage store c.g. to x axis.
y'	Transverse body axis.
Y	Coordinate transverse to X and parallel to y.
$\overline{Y}$	Coordinate parallel to Y but transverse to $\overline{X}$.
y_h	y distance from ejector unit connection point (to MER) to the point P (ft).
y_p	y distance from shear center to the point P (ft).
Y_p	Y coordinate of the point P.
Y_s	Y coordinate of the store c.g.
z	Coordinate transverse to x and lying in a vertical plane.
$\bar{z}$	z distance from in-carriage store c.g. to x axis.
z'	Transverse body axis.
Z	Coordinate transverse to X and parallel to z.
$\overline{Z}$	Coordinate parallel to Z but transverse to $\overline{X}$.
z_h	z distance from ejector unit connection point (to MER) to the point P (ft).
z_p	z distance from shear center to the point P (ft).
Z_p	Z coordinate of the point P.
Z_s	Z coordinate of the store c.g.
α	Bomb pitch plane angle of attack (rad).
α_o	Initial value of α (rad).
β	Bomb side slip angle (rad).
γ	See Figure 2 (rad).

ϵ	See Figure 2 (rad).
ζ	Beam z deflection (ft).
$\bar{\zeta}$	See definition below Eq. (13) (ft).
ζ_a	Beam z deflection at an aft ejector connection point (ft).
ζ_f	Beam z deflection at a forward ejector connection point (ft).
ζ_i, ζ_j	Beam z deflections at i,j collocation points (ft).
η	Beam y deflection (ft).
$\bar{\eta}$	See definition below Eq. (13) (ft).
η_a	Beam y deflection at an aft ejector connection point (ft).
η_f	Beam y deflection at a forward ejector connection point (ft).
η_i, η_j	Beam y deflection at i,j collocation points (ft).
θ_p	Mean beam deflection pitch slope at point P (rad).
θ_s	Pitch Euler angle of store relative to the aircraft (rad).
θ_o	Initial bomb orientation in pitch relative to earth axes (rad).
$\dot{\theta}_o$	Pitch up rate of aircraft (rad/sec).
ϕ	Beam rotation (rad).
$\bar{\phi}$	See definition below Eq. (13) (rad).
ϕ_a, ϕ_f	Beam rotations at aft and forward ejector connection points (rad).
ϕ_i, ϕ_j	Beam rotations at i,j collocation points (rad).
ϕ_p	Beam rotation at piston cross-section (rad).
ϕ_s	Roll Euler angle of store relative to the aircraft (rad).
ϕ_o	Angle between shoulder station piston axis and the vertical (rad).
ψ_p	Beam mean deflection yaw angle at point P (rad).
ψ_s	Yaw Euler angle of store relative to the aircraft (rad).

PAPER NO. 18

A STUDY OF VARIABLE ORIFICE CONTROLLED WEAPONS LAUNCHING

by

John Sun
NAVAL SURFACE WEAPONS CENTER
DAHLGREN LABORATORY
DAHLGREN, VIRGINIA 22448

ABSTRACT

A continuous Navy (and Air Force) problem is the safe and accurate delivery of air launched weapons to the intended target. This paper presents an approach to store separation which considers the aircraft, store-ejector and store as a single system rather than separate components. A concept has been developed for controlling store motion by using variable orifices which can be adjusted during flight.

This study also presents a simulation capability for aircraft store separation developed at the Naval Surface Weapons Center, Dahlgren Laboratory (NSWC/DL) and the analytical determination of the combined effects of ejector interior ballistics (using the high-low ballistic principle) and store exterior ballistics (including both the nonuniform and uniform flowfields). The numerical results show that the underestimation of the effects of interior/exterior ballistic interactions can lead to erroneous results in the study of launch dynamics. The study demonstrates that a dual-piston store ejector, having sufficient ballistic impulse and variable orifice capability, can compensate for or overcome the given in-carriage store pitching moments and loads, thus greatly enchancing safe store separation.

The results of limited ground tests, using an AERO 7/A Sparrow Missile Launcher modified to incorporate two variable orifices, indicate that weapon pitch rate and ejection velocity can be controlled.

INTRODUCTION

The problem of aircraft store separation dates back to the First World War. Recently, an intensive literature search and comprehensive study of this problem was conducted by the Navy (Reference 1). This study showed that many problem areas related to store separation have been investigated and defined. However, no solution to the overall store separation problem has been found.

It is well recognized that after ejection of a store from an aircraft, the free-fall trajectory is sensitive to the end of stroke pitch-rate, the ejection velocity, the pitch angle, and the time duration of the ejection process. These factors cause excessive ground impact miss distances (Reference 2). The problem becomes increasingly severe if the store is released at higher aircraft speed and lower ejection velocity and g-load. Relatively small pitching moment and slight changes in release condition can lead to radical changes in initial motion (Reference 3).

Current naval aircraft store ejectors (both missile launchers and bomb racks) utilize gas pressure supplied by ballistic cartridges to power ejector pistons. Ejection force, pitch rate, pitch angle, and initial velocity are controlled by metering the gases through orifices of fixed size. With these fixed size orifices, it is not possible to compensate for all combinations of flight parameters. These parameters include: aircraft speed, aircraft altitude, aircraft g-load, store type, store density (i.e., full versus empty fuel tank), store location (centerline, inboard, outboard, etc.), and in-carriage and interference aerodynamic forces. This inability to compensate for all flight conditions can lead to store-aircraft collisions and to the deviation of store trajectories from the desired ballistic trajectories. The fixed size orifices were selected from trial and error "ground" testing to satisfy acceleration, pitch rate, and separation requirements (Reference 4) imposed by a spectrum of aircraft flight regimes. It is hardly conceivable that the store would hit the target without proper consideration of the exterior ballistic effects during store ejection.

Wind tunnel tests conducted as part of the Navy conformal carriage program showed that stores released from different stations underneath an F-4B scale model had different amounts of pitch (Reference 5). The tests also showed that ROCKEYE II dispensers released at supersonic speeds underwent an unsafe noseup motion. These motions were corrected by selecting suitable orifice areas

(Reference 6). This suggests that variable control orifices could improve the trajectory accuracy and permit adjustments for station-to-station variation.

During prototype flight testing, the SUU-51A/B bomb dispenser experienced a separation problem when released from the centerline station of an inboard triple ejector rack (TER) on an F-4 aircraft at high subsonic speeds. A violent nose down pitch cause the tail of the weapon to rise and contact the tails of weapons on the adjacent shoulder stations. It was concluded that a dual piston, high impulse, tunable ejector system appeared to be the most promising solution to a long-range store separation problem (References 7 and 8).

The NSWC/DL computer data bank listed at least 81 store/aircraft collisions involving a variety of aircraft and stores during the period 1964-1973. The recent loss of a Navy F-14 aircraft was attributed to a missile colliding with the aircraft fuselage (Reference 9). The Hawker Siddley AV-8A HARRIER also encountered significant adverse store pitch motion at NATC (Naval Air Test Center), 1971-1973. The pitch down phenomenon caused a few MK 82 SNAKEYE finned bombs to tumble after release, a ROCKEYE II fin assembly to strike the gun pods and a SUU-44 flare dispenser to pitch up and nearly impact the aircraft (Reference 10). These facts demonstrate that the safety aspects must not be underestimated and intensive research should be conducted to develop a store ejector capable of controlling the store motion during store separation.

Kalivretenos, Schindel and Maestri have pioneered work in a self-compensating store ejection technique based upon relating the initial conditions to the in-carriage forces on the store (Reference 11). Store ejector racks can be instrumented to measure the in-carriage forces in a dynamic environment (Reference 12). However, the significance of the dynamic interior/exterior ballistics interactions, the orifice areas, and the detailed motion of the store during the ejection cycles and their overall effects on store separation have not been considered.

A study on energy sources for store ejection system (which included helical/cantilever springs, compressed gas blow-down, vented compressed gas, liquid monopropellant, bipropellant and solid propellant) was conducted by Edo Corporation under the sponsorship of the Air Force (Reference 13). The solid

propellant was considered to be the optimum energy source among the candidates investigated.

It has been shown that "fixed" orifices are capable of producing statistically repeatable ejection velocity, pitch-rate, and pitch angle (Reference 14). Therefore, it should be possible to design "variable" orifices and use cartridges (solid propellants) to control these factors in order to account for the wide range of flight conditions. It is, therefore, our objective to investigate the feasibility of a variable pitch-rate control system for store ejectors. The system concept is based on the principle that by appropriate orifice area selection, the pressure acting on the ejector pistons is controlled, thereby controlling the pitch-rate, pitch angle, ejection velocity and acceleration of the store.

ORIFICE CONTROL SYSTEM CONCEPTS

A. Possible Design Concepts

The general system concept (most complex) is shown in Figure 1. The flight parameters are obtained by the sensors and sent into the computer (fire control computer or mini computer). The sizes of the control orifices are determined by the computer as a function of flight parameters (aircraft dive angle, Mach Number, and density altitude). The computer signals are converted into mechanical signals by the processor. It then automatically actuates the orifice control mechanism (step motor or servomechanism) which adjusts the orifice sizes. The orifice sizes then remain constant during store ejection. The orifices are capable of controlling the ballistic gas pressure acting upon the forward and aft pistons which can impart the correct pitch-rate and ejector velocity to the store, resulting in a safe store separation and improved ballistic trajectory. If flight parameters exceed the launch capability (for instance, the ballistic force is not sufficient to push the store away from the aircraft) of the store ejector, a danger signal would be displayed on the instrumentation panel to indicate the possibility of a store-aircraft collision.

The system is divided into the five essential task areas indicated by dotted lines in Figure 2 and are as follows:

(1) Computer programming of a mathematical model which interfaces the

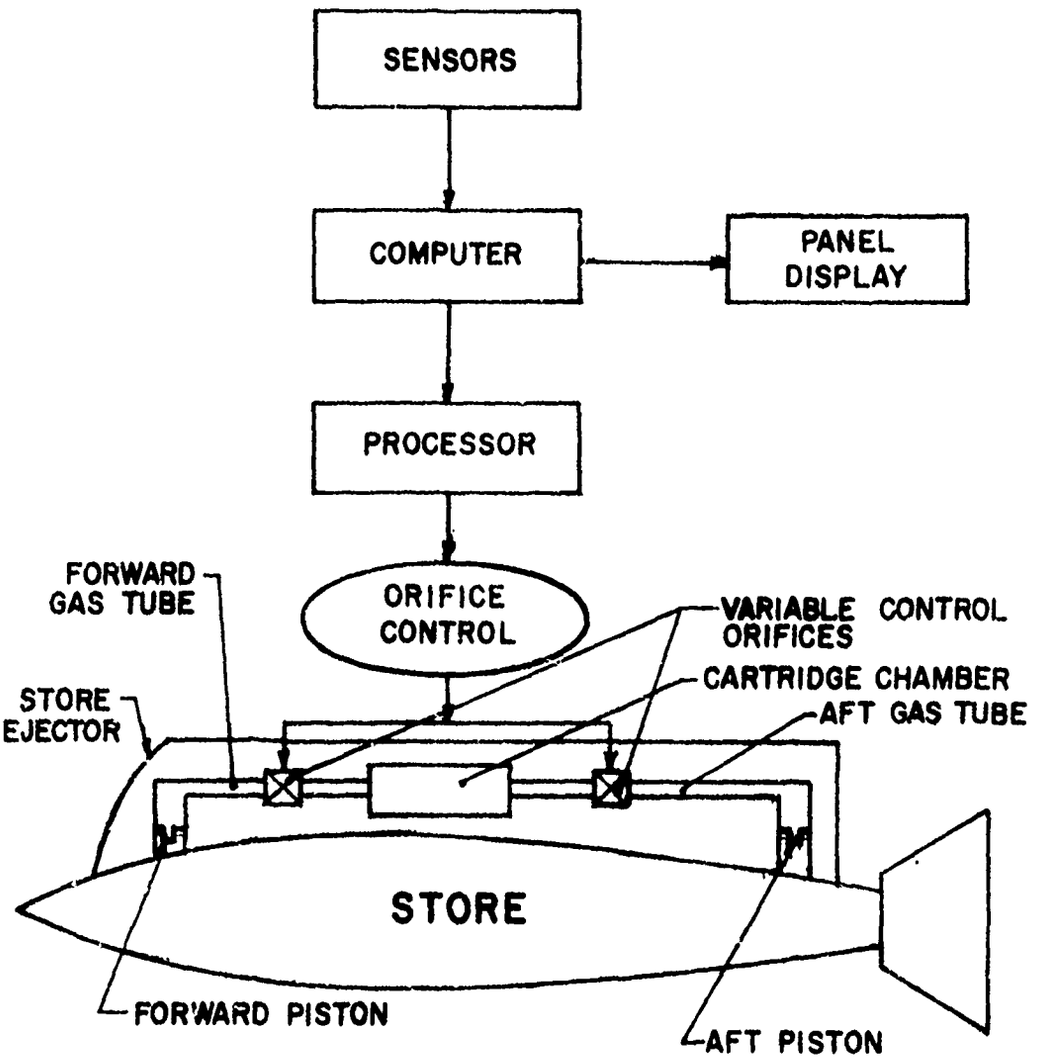

FIGURE 1

Schematic Diagram Showing the General System Concept

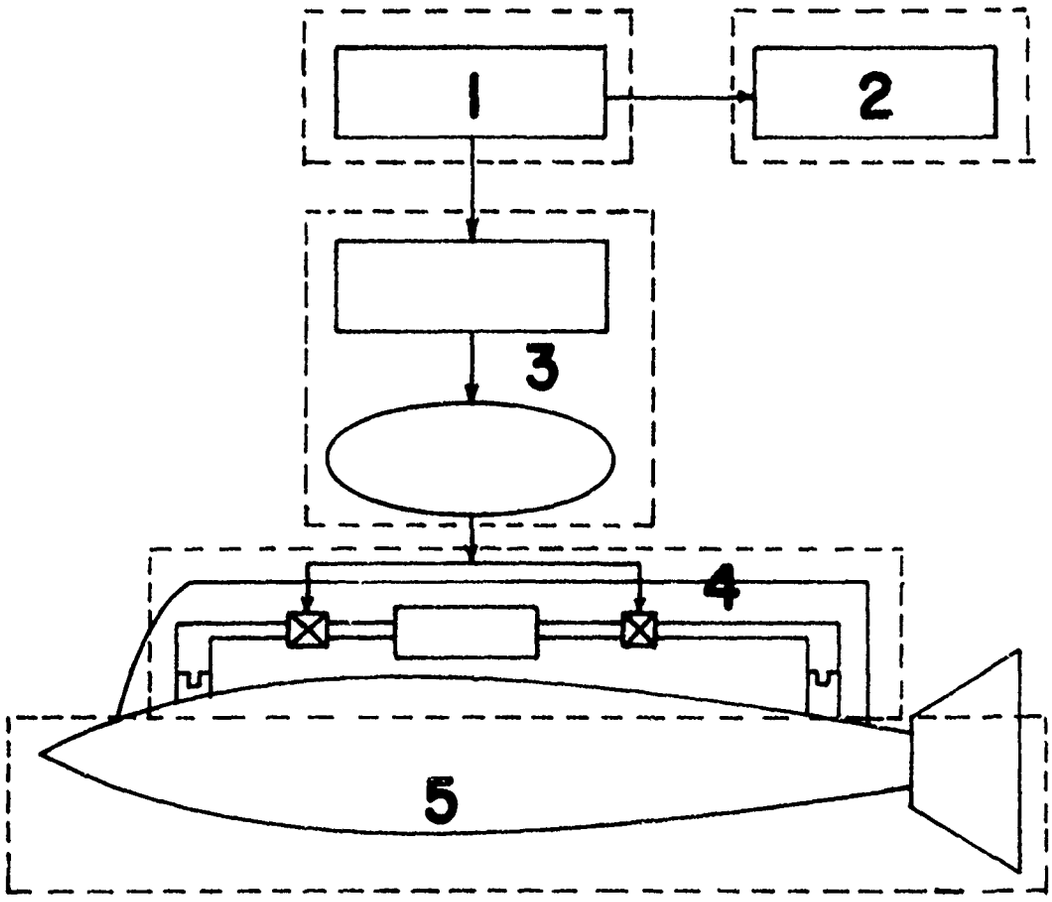

FIGURE 2

Task Areas of the General System

interior ballistics of the ejector, exterior ballistics of the store, flight parameters, and other related factors.

(2) Design of a display panel for warning signals.

(3) Design of a processor for converting computer signals to mechanical signals and the mechanical linkages to adjust the orifice size.

(4) Theoretical and experimental studies of the ballistic gas system.

(5) Aerodynamic, exterior ballistic and trajectory studies inside the nonuniform flowfield.

These areas must be investigated and interfaced to develop the entire system.

A less complex system would consist of areas (3), (4), and (5) as shown in Figure 3. The computer analysis, area (1), would generate discrete settings for the orifice adjustments, eliminating the need for a computer, processor and other electronic equipment. Each of these discrete settings would correspond to a given mode of operation.

Each mode (1, 2, 3, etc.,) represents the setting for either a standard tactical maneuver, an aircraft speed, or a variable store density. The pilot selects the particular mode that is needed and the mechanism will automatically adjust the orifice sizes. This will ensure safe store separation, improve the trajectory and provide operational flexibility.

The simplest system will also eliminate orifice control from the cockpit (Figure 4). Area (1) would again generate discrete settings for orifice adjustment. A variable orifice device will be installed in the store ejector to replace the conventional fixed size orifice. This device can provide infinite manual adjustment of orifice sizes. The setting required for the mission to be flown would be preset on the ground.

DEMONSTRATION HARDWARE AND RESULTS

A. Variable Control Orifice

An important part of this study is the design and evaluation of an adjustable orifice (Reference 15) which, when incorporated in a dual ejector rack or launcher, would provide the capability for controlling (give the controllability of) pitch-rate,

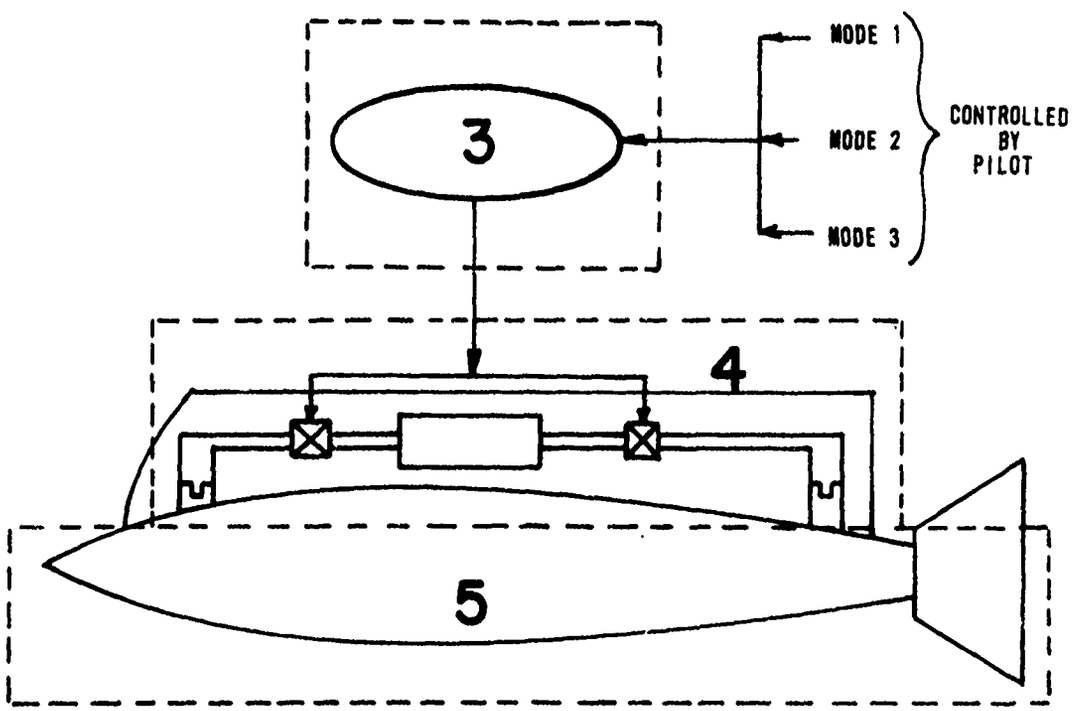

FIGURE 3

Task Areas of a Less Complex System

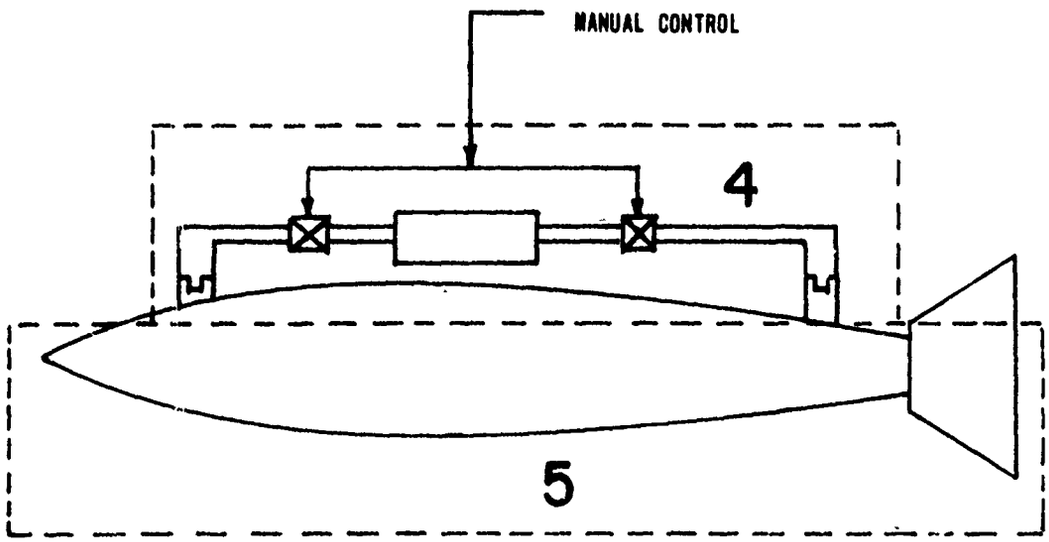

FIGURE 4

Task Areas of the Simplest System

ejection velocity, and pitch angle. This control orifice must provide infinite adjustability, permit straight-through flow and withstand high pressure, high temperature and erosive environments. The variable orifice design is shown in Figure 5. Orifice size is varied by turning the valve stem which moves the hemispherical tip in or out as required. The orifices areas can be determined as a function of the displacement of the valve stem.

The disc type conventional orifices were removed from an AERO 7/A SPARROW Missile Launcher and the variable orifices were installed as shown in Figure 6. The launcher was used to eject a simulated SPARROW, weighing 510 pounds, Missile vertically down. The instrumentation of the launcher and store are shown in Figure 7. Pressures were taken in the breech, before the forward and aft orifices, and in the forward and aft piston chambers. Acceleration and velocity were taken at points on both forward and aft parts of the test missile by using accelerometers and velocity tapes. The limited experimental results indicate that the pitch-rate and ejection velocity can be controlled by adjusting the variable orifices. Table 1 shows the experimental results taken from the end of strokes data and averaged through six rounds of testings. Typically, the ejection velocity and the pitch-rate vary between ±6% and ±10%, respectively. These variations can be attributed partially, if not totally, to cartridge variation. Positive values designate nose-up pitch and negative values designate nose-down pitch. Both orifices were examined for wear and accumulations of residue upon conclusion of the test series. Visual examination indicated that no visible erosion had occurred. Thus, less wear and maintenance may be expected with the hemispherical tip control orifices than with the conventional disc type orifices.

TABLE 1

MEAN PITCH-RATE AND EJECTION VELOCITY VERSUS ORIFICE AREAS

$A_{o_F}(in^2)$	0	0.0063	0.081	0.0124	0.024	0.024	0.081
$A_{o_A}(in^2)$	0.056	0.0133	0.056	0.0067	0.005	0.0035	0
$\dot{\theta}_B$(rad/sec)	3.13	1.72	0.81	0.74	0.1	- 0.11	-0.86
V_{cg}(ft/sec)	8.8	15.6	17.9	15.8	17.2	16.4	15.7

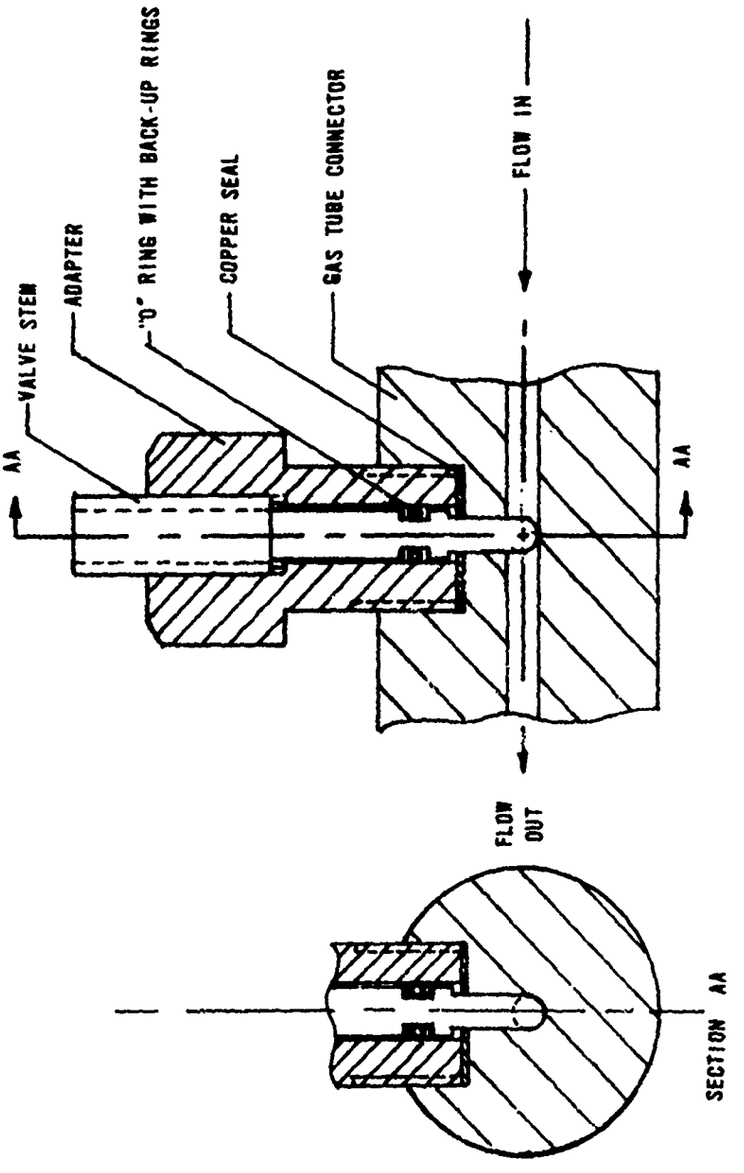

FIGURE 5
Variable Control Orifice

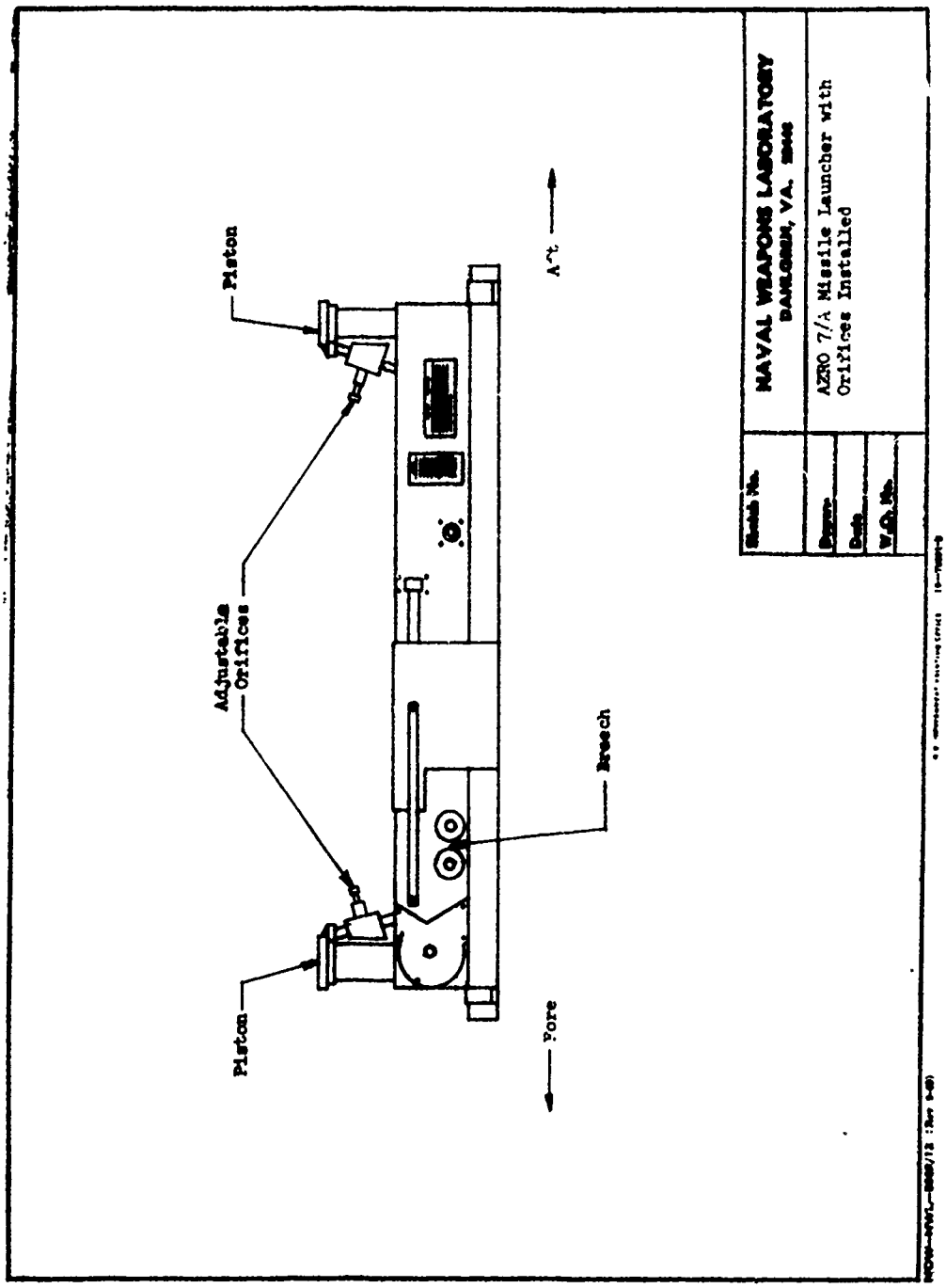

FIGURE 6

AERO 7/A Missile Launcher With Orifices Installed

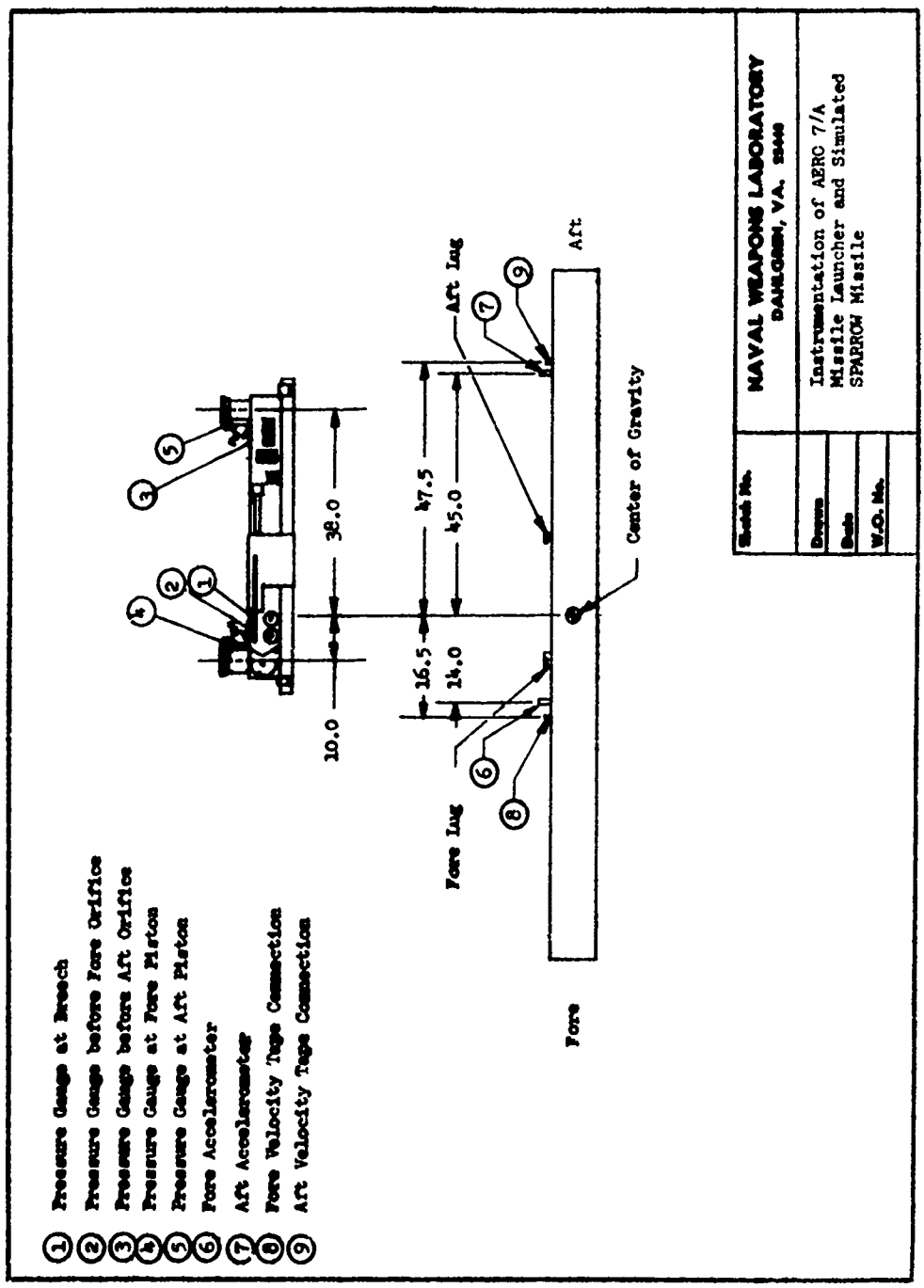

FIGURE 7

Instrumentation of AERO 7/A Missile Launcher and Simulated SPARROW Missile

THEORETICAL SIMULATION AND RESULTS

A. General

A unified mathematical model which treats the problem of aircraft store separation has been developed and implemented on the Hybrid Computer Facility (EAI 680 Scientific Computing System) at NSWC/Dahlgren Laboroatory. The problem is approached by considering the aircraft, store-ejector and the store as a system rather than separate efforts. This model includes both the interior ballistics of the store ejector gas system and the exterior ballistics of the store motion during and after the store separation phase. The interior ballisitcs theory is a generalized version of the high-low ballistic principle (see References 16 & 17) which can handle both dual and single piston store-ejectors. The exterior ballistic theory includes the aerodynamic effects of both the nonuniform and uniform flowfield in the pitch plane. This mathematical model was developed to achieve four objectives: (1) to demonstrate the variable orifice controlled store separation concept; (2) to investigate the dynamic interior/exterior ballistic interactions during the ejection cycle; (3) to furnish insight and understanding of the overall problem; and (4) to provide preliminary engineering estimates for the design of such a system.

B. Simulation

In essence, the computer program simulates three phases (see Figure 8) while an aircraft maneuvers with an angular rate (pullup, pushover, or horizontal flight) and the store is being launched from the store-ejector simultaneously (see Figure 9).

Phase 1: This phase includes the interval from the time $t = 0$, when the cartridge receives an ignition pulse from the pilot, to the time $t = t_s$, when both forward and aft pistons are fully extended with the store in direct contact with the pistons. During this phase the gas is metered by the control orifices thereby controlling the pressure at each ejector piston. The computer program takes into account the coupled effects of the interior ballistics of the ejector system and the exterior ballistics of the store in the nonuniform flowfield around the aircraft.

Phase 2: Immediately after the store separates from the ejector pistons, the

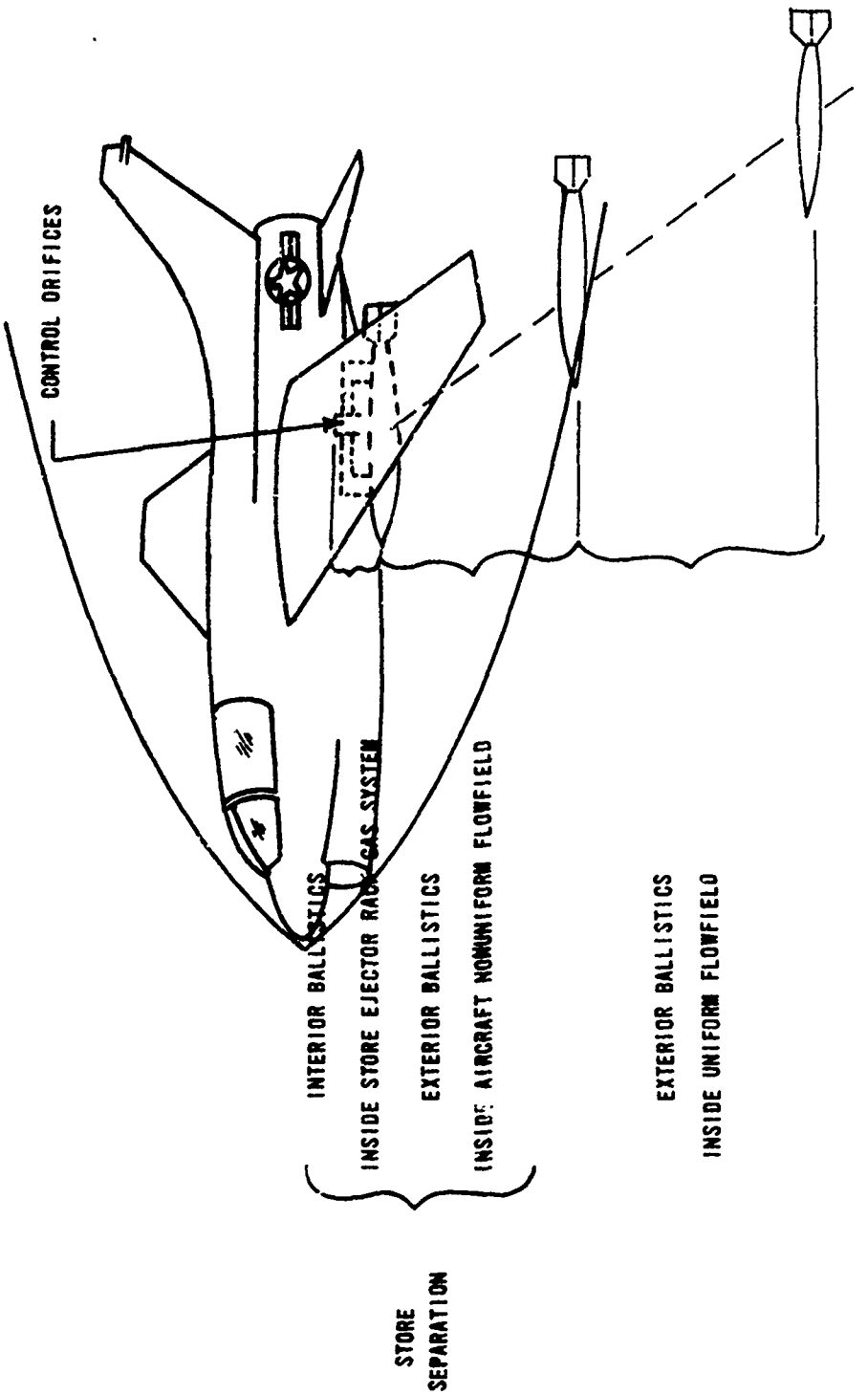

FIGURE 8

Schematic Diagram Showing Store Separation from Aircraft

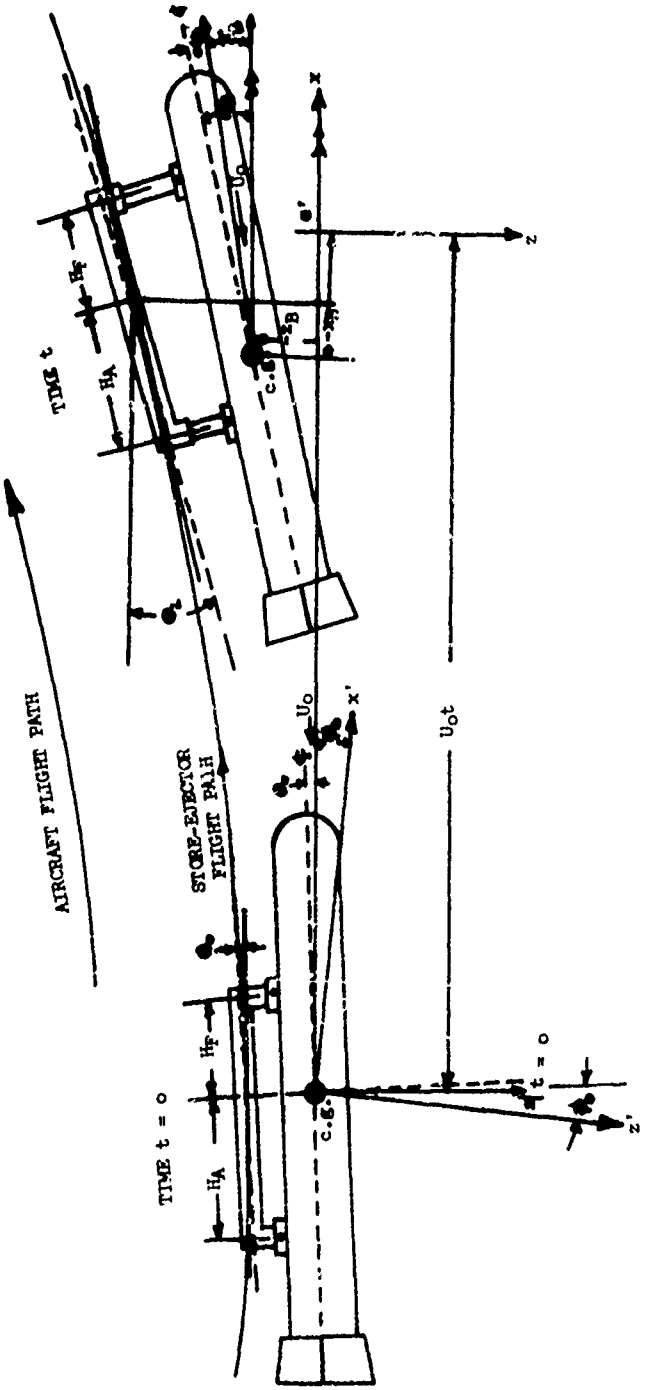

FIGURE 9

The Coordinate Axes and the Store Ejector Flight Path

force applied by the piston becomes zero and the only external forces are aerodynamic and gravitational. During this period, the computer calculates the motion of the store through the remaining nonuniform flowfield. For our demonstration, the aerodynamic characteristics of the nonuniform flowfield were simulated by the exponential decay law used by Maddox (see Reference 18). The loadings on a store, whether a moment or a force, are considered as coefficients representative of the store in the free stream in combination with perturbation coefficients. The perturbation coefficients decay exponentially with increasing distance from the in-carriage positions and represent the entire effect on the store of the mutual interaction between the store and the aircraft's nonuniform flowfield.

Phase 3: After the store escapes the nonuniform flowfield and enters the uniform flowfield, the computer will continuously calculate the store motion until ground impact.

C. Input

To initiate the computer program, we require the following input parameters as indicated in Figure 10.

Exterior Ballistics Input Parameters:

1. Aircraft flight parameters:
   aircraft speed, dive angle, air density, altitude, angle of attack, and number of g loading.
2. Store configuration:
   weight, pitch moment of inertia, center of gravity location, body length and reference cross-sectional area.
3. Nonuniform interference flowfield aerodynamic characteristics:
   in-carriage pitching moment and normal force coefficient of store, pitching moment and normal force coefficient of store at zero angle of attack inside aircraft influence flowfield as a function of position referenced to the store-ejector. The summation of these coefficients with corresponding uniform flowfiled aerodynamic characteristics give rise to the nonuniform interfence aerodynamic characteristics.
4. Uniform flowfield aerodynamic characteristics:

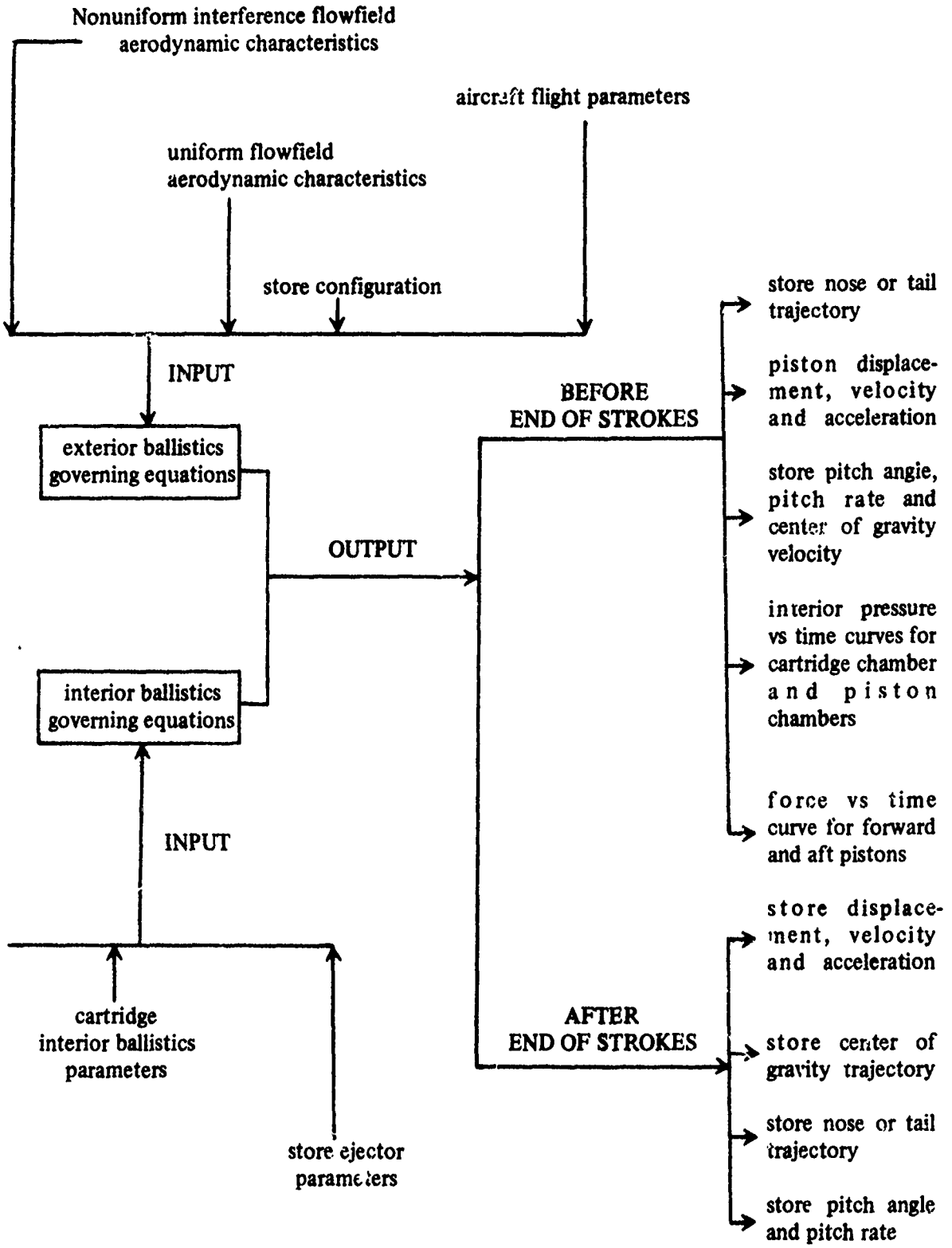

FIGURE 10

Store Separation Computer Simulation

pitching moment coefficient slope, normal force coefficient slope, axial force coefficient and pitch damping coefficient of store alone in free stream.

Interior Ballistics Parameters:

1. Store-ejector parameters:

   forward and aft orifice areas, forward and aft piston areas, forward and aft piston spring constants, frictional coefficient between pistons and store, forward and aft gas tube piston assembly volume available to gas at time t = o, cartridge chamber volume available to gas at time t = o, distance measured from the forward and aft piston feet to the store center of gravity at time t = o, angle measured between the store-ejector body axis and store-ejector flight path at time t = o, location and areas of forward and aft piston venting holes, cartridge chamber heat loss characteristics, forward and aft gas tube-piston assembly heat loss characteristics and stroke lengths for forward and aft pistons.

2. Cartridge interior ballistics parameters:

   cartridge type and classification, form function coefficients, propellant burning rate coefficient and exponent, total charge weight, propellant impetus, ratio of specific heats of propellant gas, covolume factor, density of propellant, molecular weight of propellant gas, constant volume flame temperature of propellant, total mass of gas present in cartridge chamber at time t = o, total mass of gas inside the forward and aft gas tube-piston assembly at time t = o.

D. Output

The results of the mathematical simulation can be directly displayed on the graphical terminal of the hybrid computer.

1. During the ejection cycle and before both the forward and aft pistons reach their end of strokes, we can obtain (but are not limited to) the following information:

   store nose or tail trajectory; piston displacement; velocity and acceleration; store pitch-angle, pitch-rate and center of gravity velocity; interior pressure versus time curves for cartridge chamber

and piston chambers; force versus time curve for forward and aft pistons.

2. After the store separates from the pistons, the following information can be obtained:

store displacement, velocity and acceleration; store center of gravity trajectory; store nose or tail trajectory; store pitch-angle and pitch-rate.

E. Numerical Results

This numerical study employs a conceptual dual piston ejector which closely follows the configuration of an AERO 7/A SPARROW launcher, using two MK 124 cartridges containing solid propellants, acting on a MK 82 low drag bomb. For the case of constant ejection force, the present analysis agrees quantitatively with that of Maddox (Reference 18). The present numerical results were obtained for the case of variable ejection force and dynamic interior/exterior ballistics interactions during store separation. It is assumed that the airspeed was 500 knots TAS and that the aircraft was at 5,000 feet altitude.

Figures 11 through 17 show the effect of one set of orifices on store separation for an aircraft in horizontal flight. The forward and aft orifices were set at $0.432 \times 10^{-5} m^2$ and $0.8194 \times 10^{-5} m^2$, respectively.

Figure 11 indicates the effect that the aerodynamic in-carriage force and moment have on the initial bomb trajectory. For the case considered here, the calculated ejection velocity at the center of gravity of the MK 82 bomb remains constant for different in-carriage moments. The end-of-stroke ejection velocity is approximately 5.49 m/sec (18 ft/sec). A positive in-carriage moment ($C_{m_o} = 1.5$) causes the store to fall more slowly than a store with negative moment ($C_{m_o} = -1.5$) due to a larger aerodynamic lifting effect. For a conventional fixed orifice store ejector with constant ejection velocity, the variation in the aerodynamic influence can lead to store dispersion in the ground impact points.

Figure 12 shows the forward and aft piston displacement versus time. It is found that the speeds of the forward and aft piston change when C_{m_o} is varied from +1 to -1. The negative moment tends to resist the aft piston and aid the

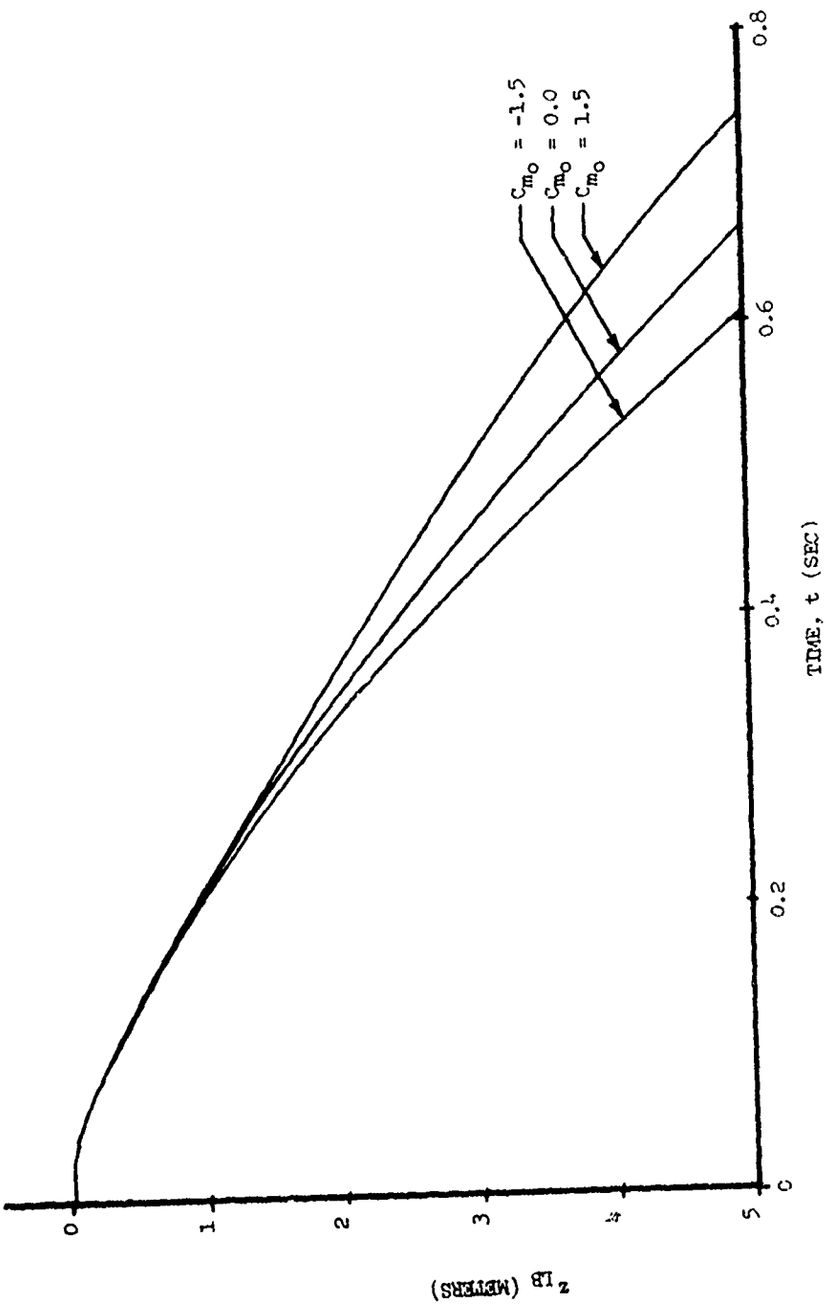

FIGURE 11

Time History of Store Displacement in z-Direction as a Function of Aerodynamic In-carriage Moment (C_{z_o} = -0.35)

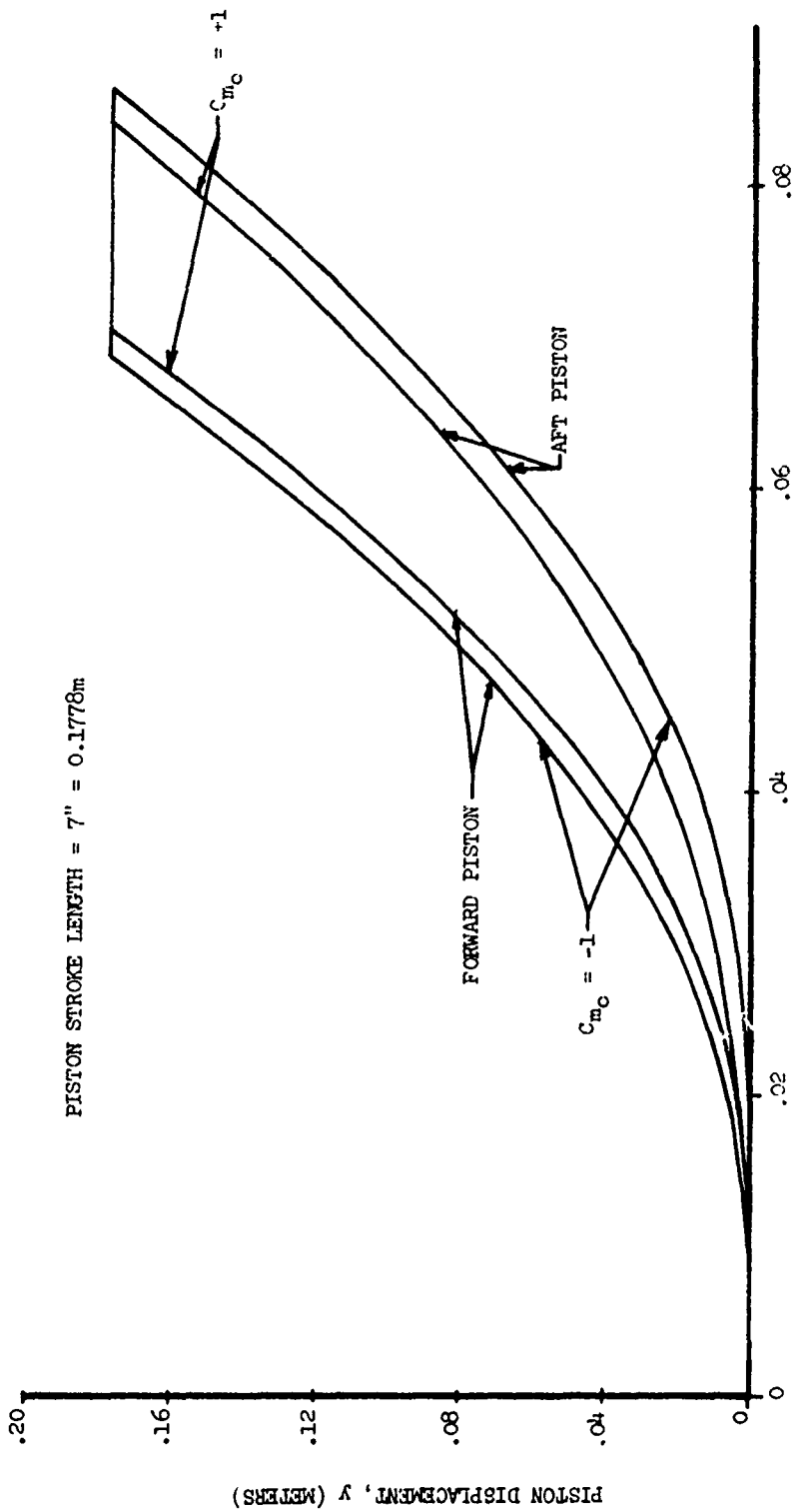

FIGURE 12

Forward and Aft Piston Displacement Versus Time as a Function of In-carriage Aerodynamic Moment (C_{z_o} = -0.35)

motion of the forward piston whereas this phenomenon is reversed with a positive moment. This explains the different pitch angle and pitch rate caused by the variation of in-carriage moment. It indicates that the dynamic interior/exterior ballistic interaction during the ejection cycle and the varying aerodynamic in-carriage loading can cause the speed of the pistons to vary.

Figure 13 shows the store pitch angle and angle of attack versus time. The store exhibits a nose down motion during the ejection phase. Immediately after separation from the forward and aft pistons, a positive aerodynamic moment forces the nose to pitch upward, while a negative moment assists in forcing the nose down. The trends found indicate that dynamic interactions during store separation is important and that an improper launch can cause unsafe store separation and inconsistent ballistic trajectories.

Figure 14 shows the variation of pitch rate as a function of time. It is interesting to find that the forward piston leads the aft piston slightly confirming the displacement difference noted in Figure 12. At approximately 0.07 seconds the forward piston bottoms and the aft piston catches up. This causes a rather abrupt change in pitch rate between approximately 0.07 and 0.08 second immediately before the store separates from the aft piston. The actual pitch rates at separation are approximately -0.25 radians/second (for $C_{m_o} = 1$) and -0.45 radians/second (for $C_{m_o} = -1$) rather than -1.3 radians/second (for $C_{m_o} = 1$) and -1.5 radians/second (for $C_{m_o} = -1$). Thus the piston motion during this period has a strong effect on pitch rate but a negligible effect on pitch angle (see Figure 13).

Figure 15 shows that different trends of pitch rates are obtained for $C_{m_o} = 1$ and $C_{m_o} = -1$ when the aft piston reaches the end of stroke. After the store separates from the store ejector, the aerodynamic moment continues to act on the store causing a change in pitch rate. Thus, it can be concluded that the aerodynamic moment is a significant part of the interior/exterior dynamic interaction and effects the store motion during and after the ejection cycle.

Figure 16 shows the variation of pressure inside the cartridge chamber and the forward and aft pistons versus time. The chamber pressure is generated by two MK 124 cartridges. The aft piston pressure is higher for $C_{m_o} = -1$ than $C_{m_o} = 1$ because the negative moment resists the aft piston motion causing a smaller rate of

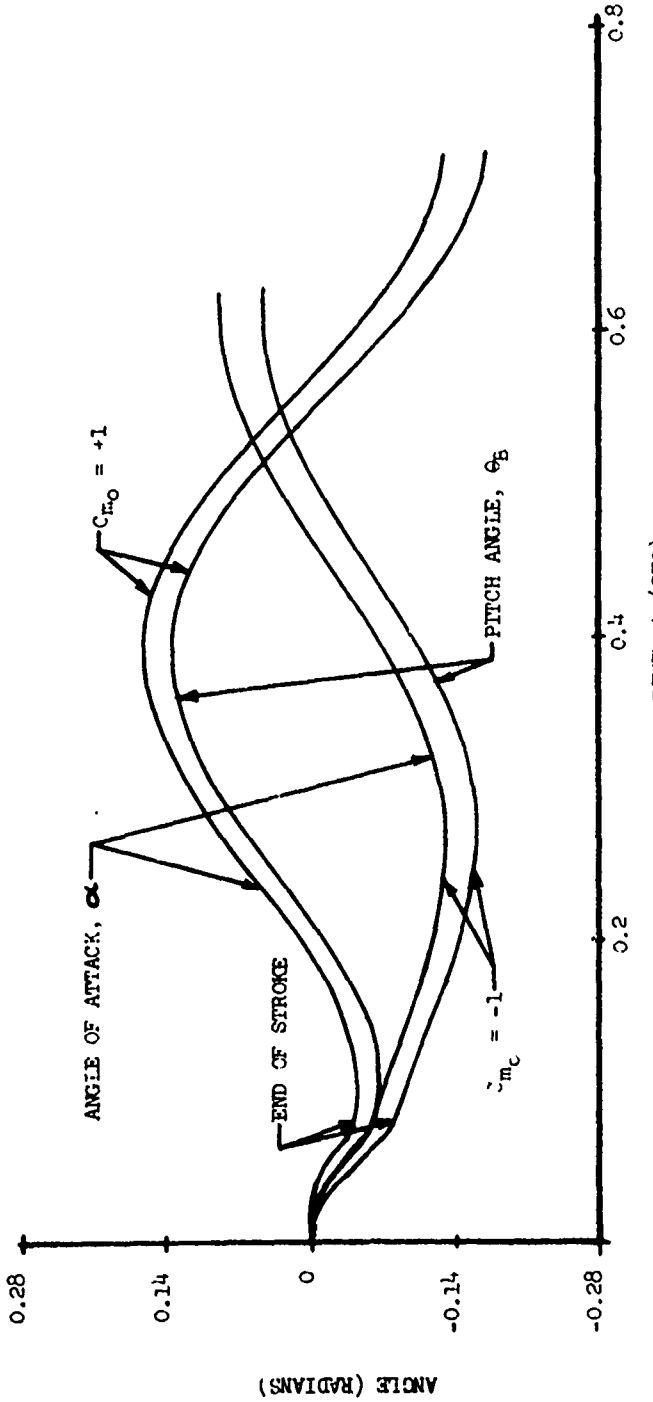

FIGURE 13

Pitch Angle and Angle of Attack Versus Time as a Function of Aerodynamic In-carriage Moment (C_{m_o} = -0.35)

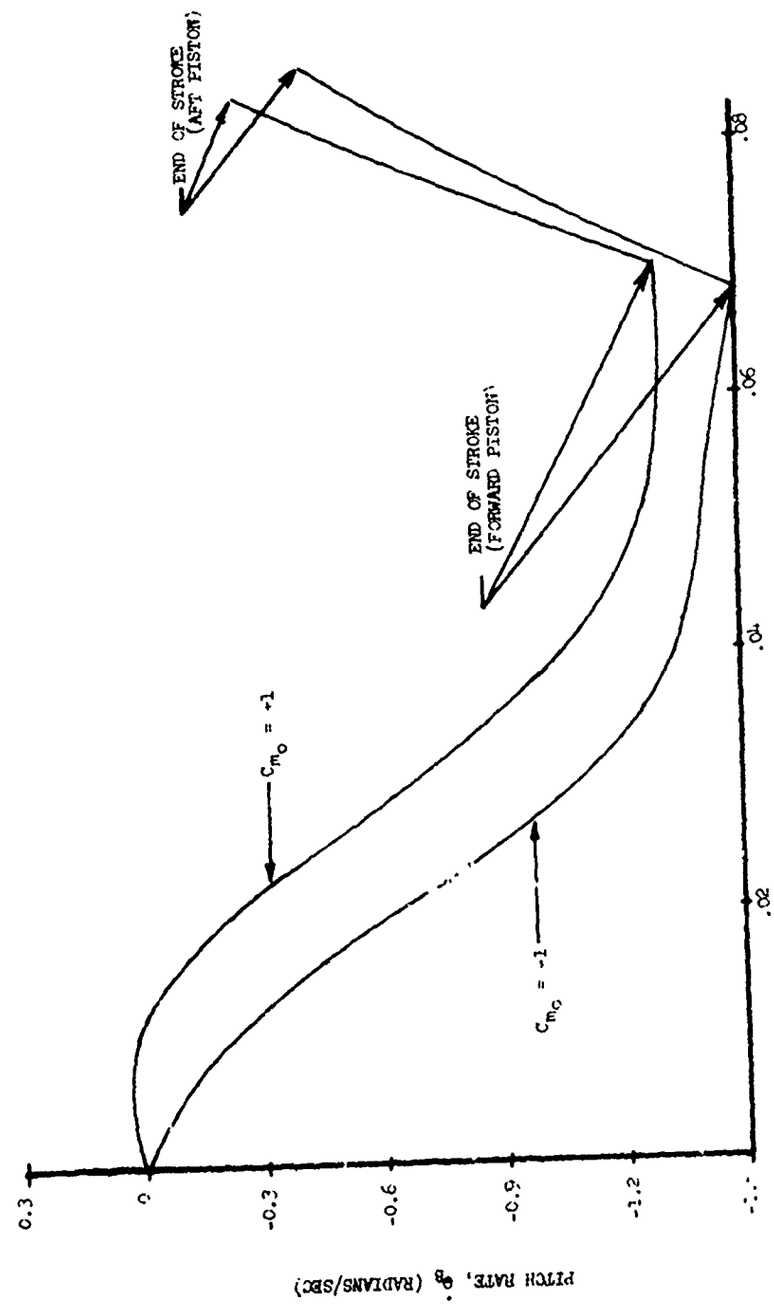

FIGURE 14

Variation of Store Pitch Rate Versus Time as a Function of Aerodynamic In-carriage Moment ($C_{m_o} = -0.35$)

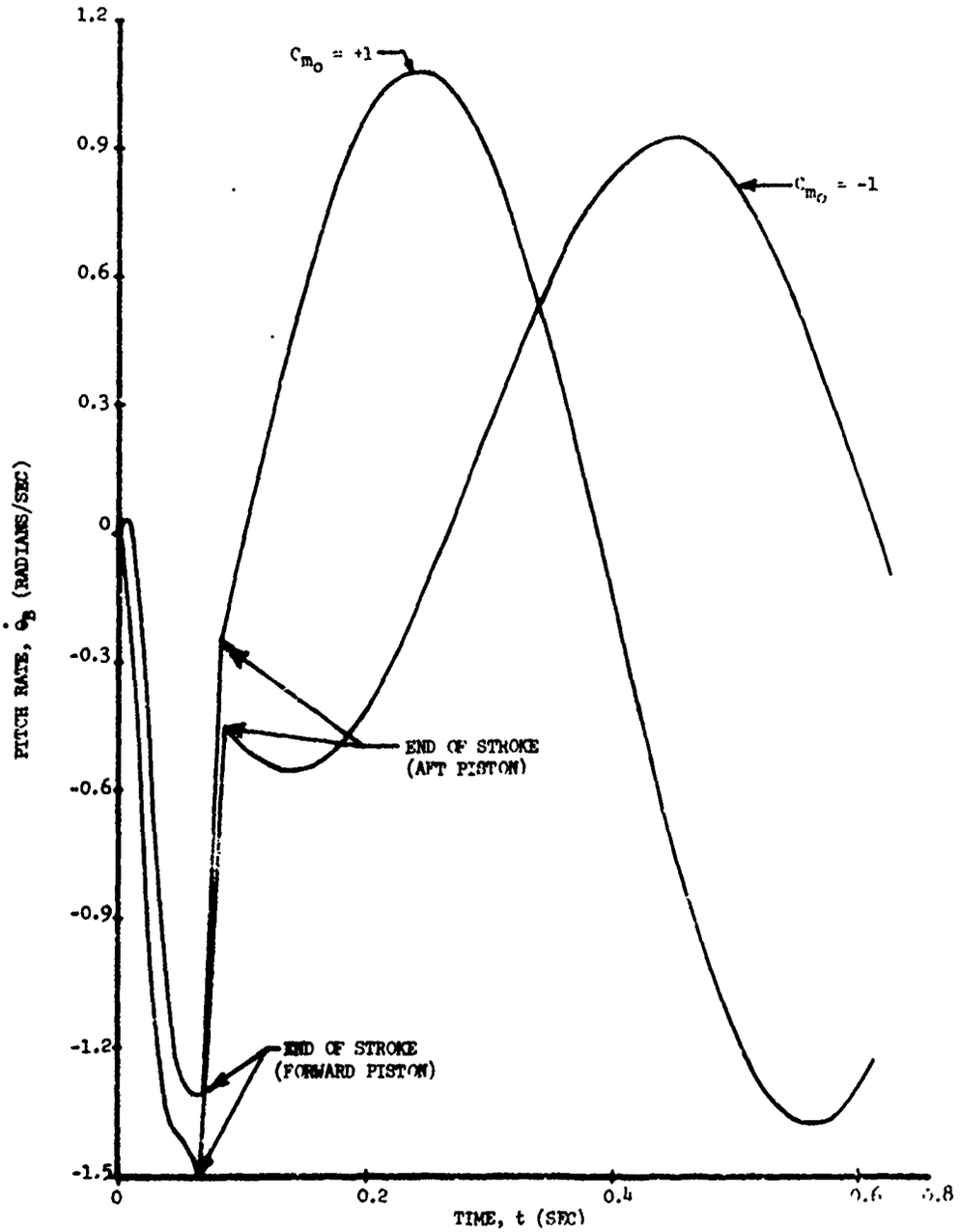

FIGURE 15

Pitch Rate of Store Versus Time as a Function of Aerodynamic In-carriage Moment ($C_{z_{o_o}}$ = -0.35)

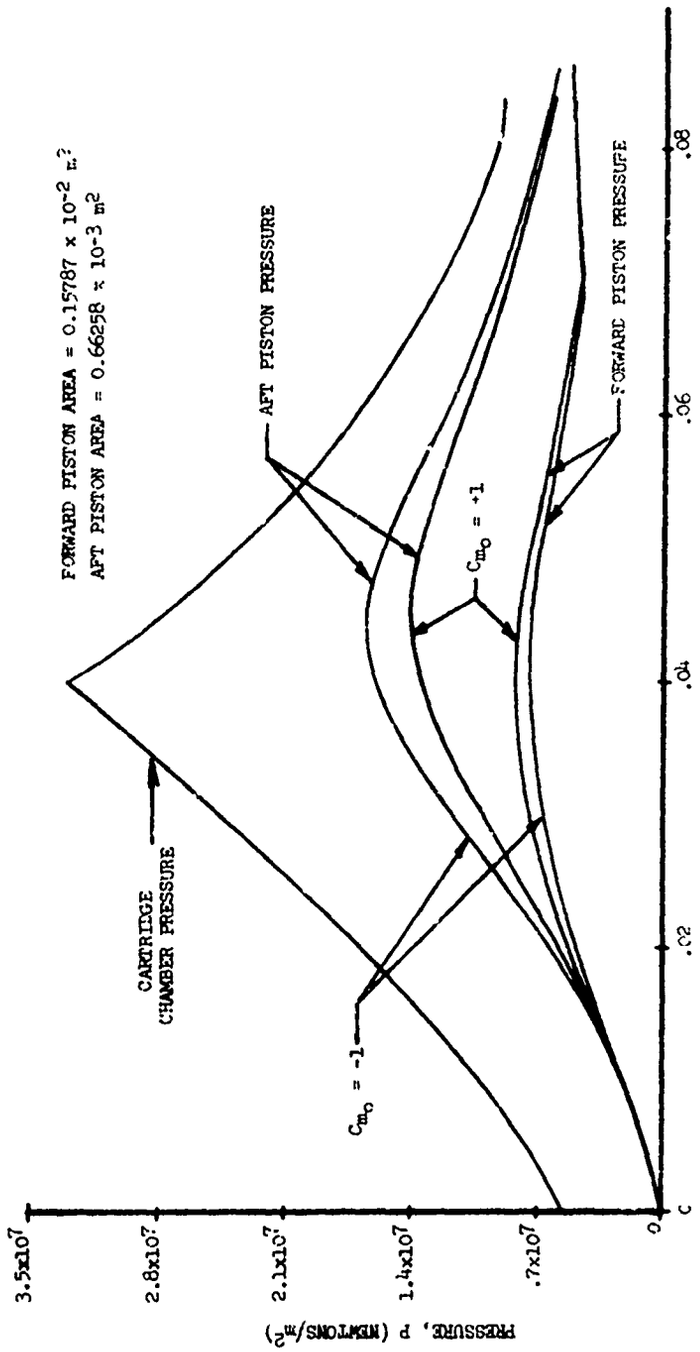

FIGURE 16

Variation of Pressure Versus Time as a Function of Aerodynamic In-carriage Moment (C_{m_o} = -0.35)

change in the piston volume and hence a larger increase in the aft piston pressure. The slighly higher pressure for the forward piston when comparing the cases between $C_{m_o} = 1$ and $C_{m_o} = -1$ can be explained in a similar manner. The foward piston arrives at the end of stroke before the aft piston. However, the propellant gas is still flowing into the forward piston which causes a slight increase in the pressure after t = 0.07 second approximately. This increase of pressure will not occur if venting is allowed at the end of stroke. This figure shows that aerodynamic loading is clearly affecting the interior gas pressure throughout the entire pressure-time history.

Figure 17 shows the variation of piston force versus time. The forward piston force is higher than the aft piston force. This is the reverse of the pressure versus time curves (Figure 21). The reversal is due to the fact that the forward piston area is more than twice as large as the aft piston area. Although the higher forward piston force causes the store to pitch nose down during the ejection cycle for both $C_{m_o} = 1$ and $C_{m_o} = -1$, this variation in aerodynamic moment does significantly change the ejection force throughout the ejection cycle. The greatest change is obtained in the peak ejection force region. This again confirms the importance of the interior/exterior dynamic interaction. The consequence of simulating a gas-powered ejector assuming a constant ejection force and underestimating the interior/exterior dynamic interaction could lead to erroneous results..

Figures 18 through 23 show the numerical results of store pitch angle, pitch rate and trajectory of an aircraft in a 60° dive (g = -0.05). In order to demonstrate the effect of variable orifices on store separation, we selected the three sets of orifices shown in Table 2. The difference in ejection velocity for the same orifice areas is due to the variation of in-carriage moment. The portion of the curves indicated by dotted lines (----) are the results obtained during the ejection phase, while the store is in direct contact with the ejector pistons. The termination of these curves corresponds to the time the store exits the nonuniform flowfield at five meters below the release plane (x-axis).

Figure 18 shows the effect of orifice area variation on the pitch angle for $C_{m_o} = 2, -2$ and $C_{z_o} = -0.35$. The smooth dotted lines indicate that there are no abrupt changes in pitch angle during the ejection cycle. However, when the forward

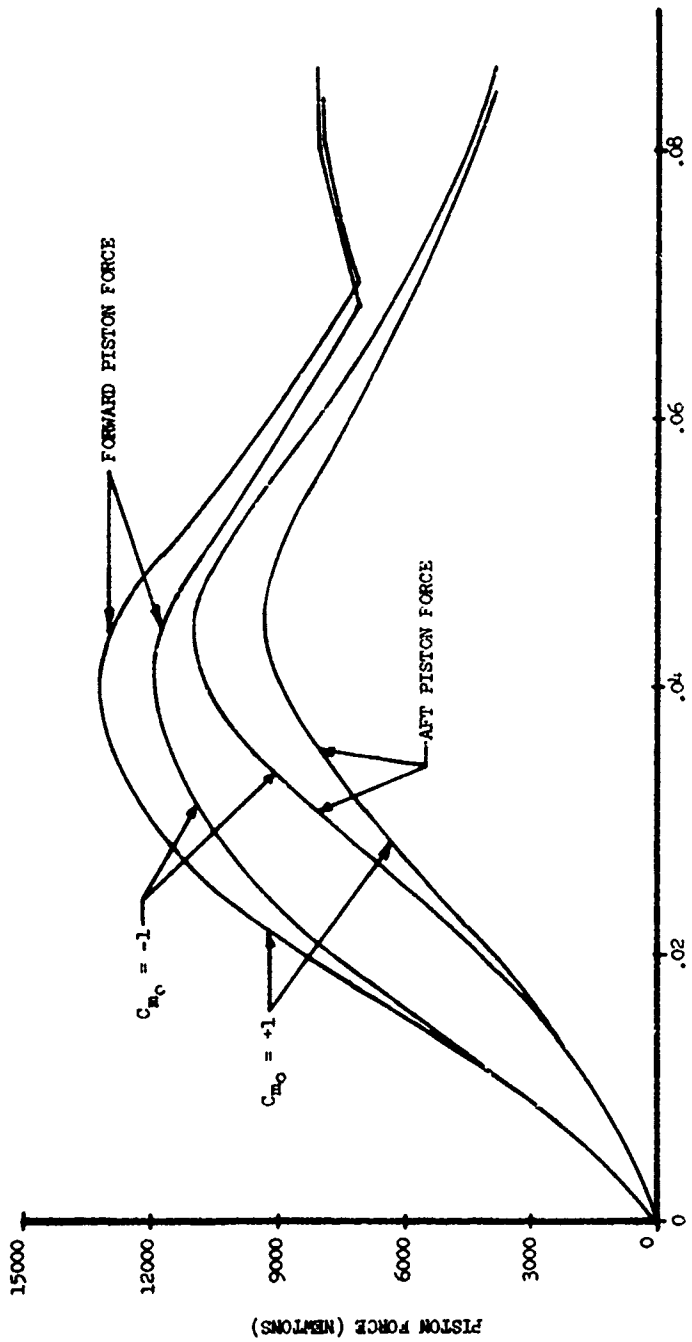

FIGURE 17
Variation of Piston Force Versus Time as a Function of Aerodynamic In-carriage Moment (C_{m_o} = -0.35)

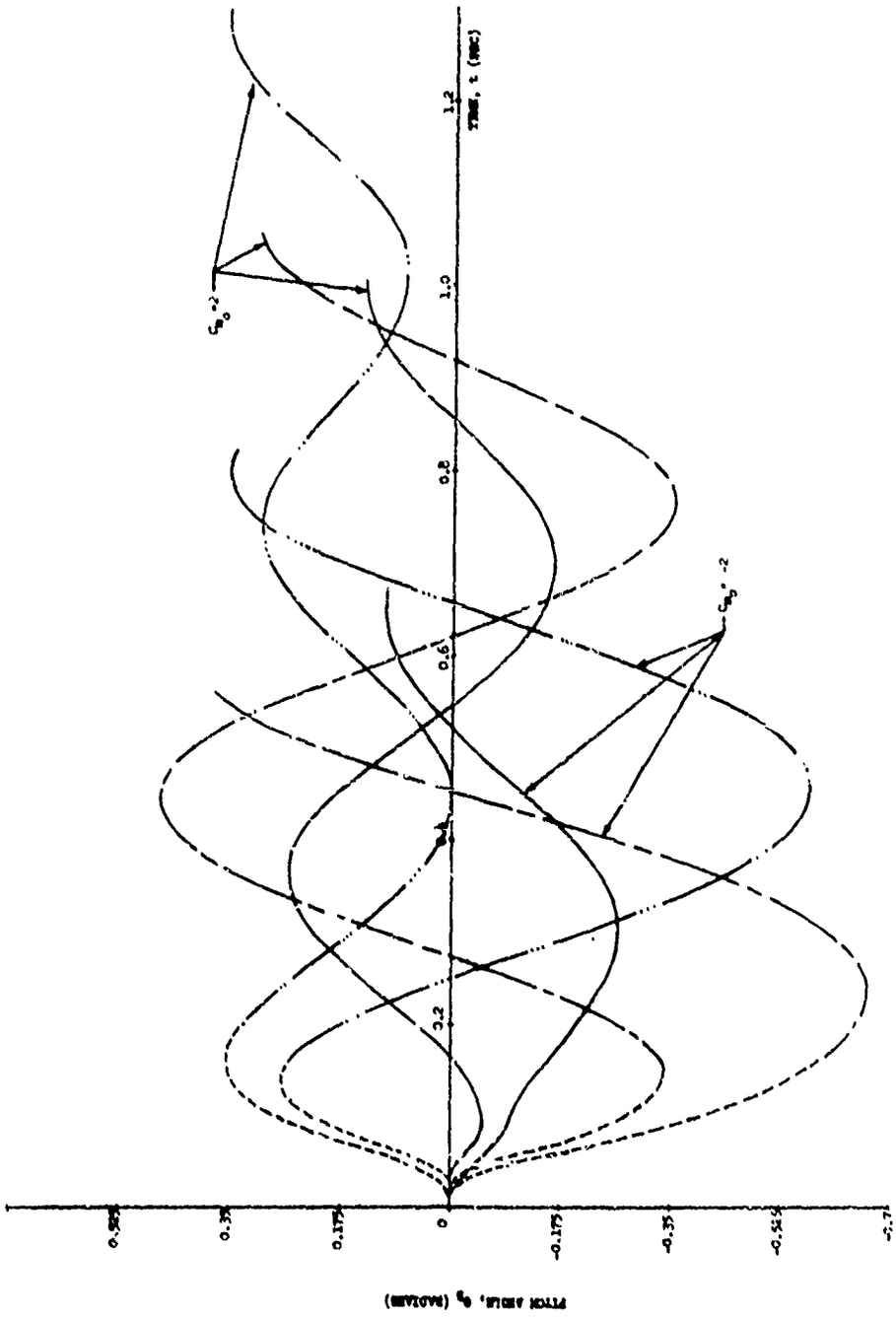

FIGURE 18

Pitch Angle of Store Versus Time as a Function of
Orifice Areas and Aerodynamic In-carriage Moments for Sixty Degree Dive

TABLE 2

DATA FOR LAUNCHING WITH VARIABLE ORIFICE AREAS

Symbol for Orifice Area Combination	In-carriage Pitching Moment Coefficient C_{m_o}	In-carriage Normal Force Coefficient C_{z_o}	Forward Orifice (m^2)	Aft Orifice (m^2)	End of Stroke Ejection Velocity (m/sec)
1. ———	2	-0.35	0.8194 $\times 10^{-5}$	0.4323 $\times 10^{-5}$	5.2
	0				5.2
	-2				5.2
2. —·—·—	2	-0.35	0.03277 $\times 10^{-5}$	0.4323 $\times 10^{-5}$	1.9
	0				2.4
	-2				2.8
3. — - —	2	-0.35	0.8194 $\times 10^{-5}$	0.03635 $\times 10^{-5}$	3.2
	0				2.9
	-2				2.6

orifice is small (A_{o_F} = 0.03277 X 10^{-5} m^2, A_{o_A} = 0.4323 X 10^{-5} m^2), the aft piston force imparts a large rotational motion and small translational motion to the store. This results in a large nose-up first pitch and a small end of stroke ejection velocity (v_s = 1.9, 2.4, 2.8 m/sec for C_{m_o} = 2, 0, -2, respectively). The trend in pitch is reversed when the aft orifice is small (A_{o_F} = 0.8194 X 10^{-5} m^2, A_{o_A} = 0.03635 X 10^{-5} m^2). However, a small nose-down motion and a large ejection velocity (v_s = 5.2 m/sec) at the end of stroke can be obtained by choosing an intermediate pair of forward and aft orifice sizes (A_{o_F} = 0.8194 X 10^{-5} m^2, A_{o_A} = 0.4323 X 10^{-5} m^2). This demonstrates that by varying the orifice size we can control the pitch motion and ejection velocity.

The store pitch rate versus time curves are shown in Figure 19 as a function of aerodynamic in-carriage moments and orifice areas. The abrupt changes in pitch rate during the ejection cycle indicate that one piston bottoms, then the other piston catches up rapidly. This jump phenomenon causes a significant variation in pitch rate. The termination of these curves at different times is due to the variation

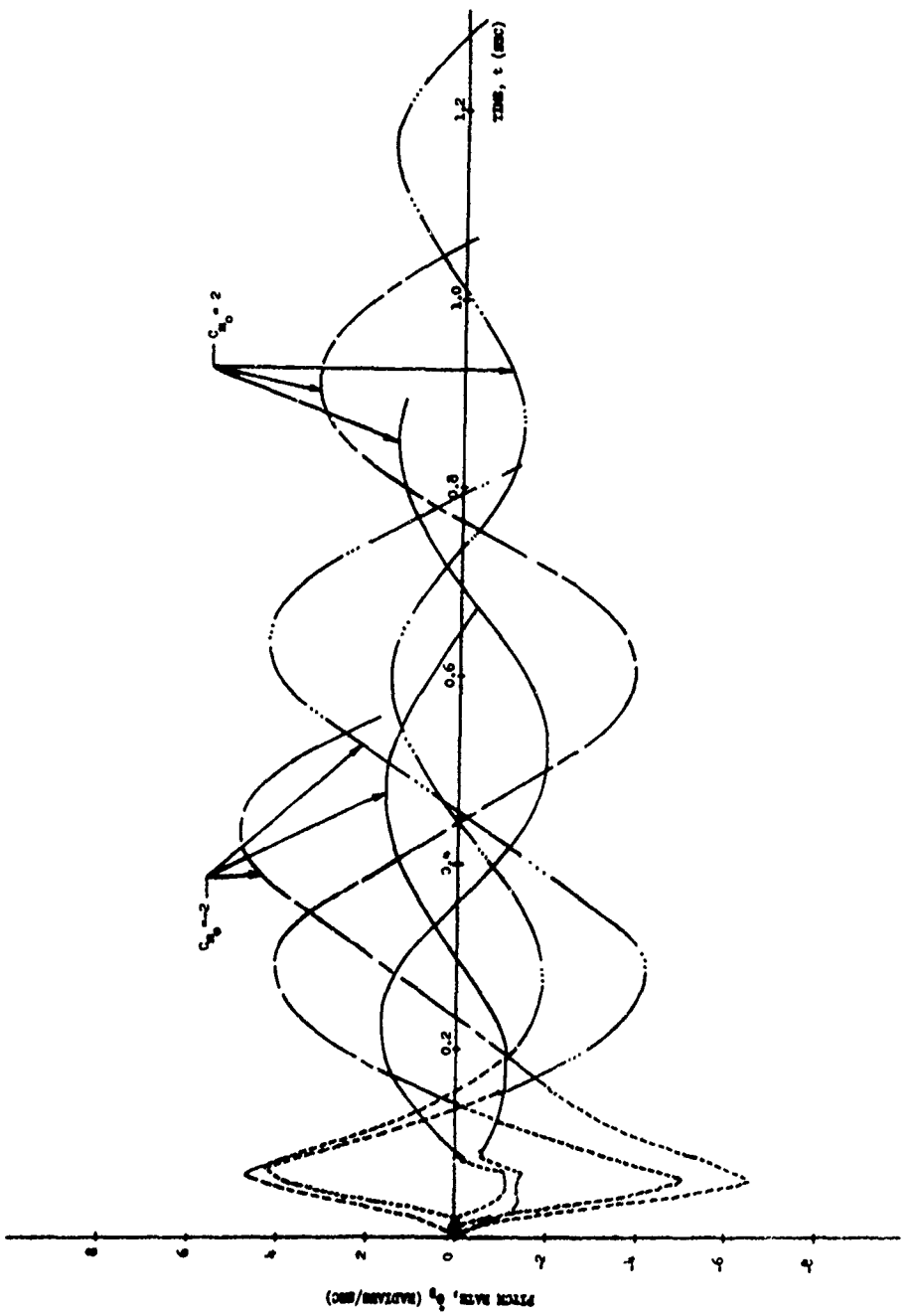

FIGURE 19

Pitch-Rate of Store Versus Time as a Function of Orifice Areas and Aerodynamic In-carriage Moments for Sixty Degree Dive

of aerodynamic loadings which causes the store to reach the end of the nonuniform flowfield at different times

During store separation, the store can rotate and rise through the release plane with either the store nose or tail striking the aircraft. The selection of appropriate orifice sizes is important for the elimination of these unsafe conditions. Figure 20 demonstrates the angular motion criteria by plotting the displacement of nose or tail as a function of in-carriage moments and orifice areas. The criteria for plotting either nose or tail is based on which end of the store is closer to the aircraft. It is found that the large nose up rotation for $C_{m_o} = 2$ causes the store nose to rise above the release plane during the ejection cycle and at time t = 0.8 sec. The large nose down motion for $C_{m_o} = -2$ causes the store tail to rise above the release plane and strike the aircraft. In agreement with Figure 18, the sharp changes in the curves occur at $\theta_B = 0°$. This is because the nose-tip plotting interchanges at $\theta_B = 0°$. An intermediate pair of orifice areas ($A_{o_F} = 0.8194 \times 10^{-5} m^2$, $A_{o_A} = 0.4323 \times 10^{-5} m^2$) ensures safe store separation under both $C_{m_o} = 2$ and -2.

Figure 21 shows the displacement of store center of gravity versus time as a function of aerodynamic in-carriage moments and orifice areas. The high nose-up moment of $C_{m_o} = 2$ and a small front orifice area ($A_{o_F} = 0.0328 \times 10^{-5} m^2$, $A_{o_A} = 0.4323 \times 10^{-5} m^2$) can cause the store center of gravity to rise above the release plane at time t = 1.14 seconds after the store nose rotates and rises above the release plane as described in Figure 24.

Figures 22 show the trends of the store center of gravity trajectories under a spectrum of aerodynamic in-carriage moments ($C_{m_o} = 2, 0, -2$) for three sets of orifice areas. During a 60° dive, the x-component of the gravitational force acting on the store overcomes the aerodynamic drag component. Except for the case of large initial nose pitch down caused by a negative moment and a small aft orifice area, all the store trajectories lead the store ejector in flight.

Figure 23 shows the store trajectory for and aircraft during 1 g horizontal flight. For the same orifice size combinations and aerodynamic in-carriage moments, all the trajectories lag the store-ejector since there is no x-component gravitational force and the aerodynamic drag is acting on the store.

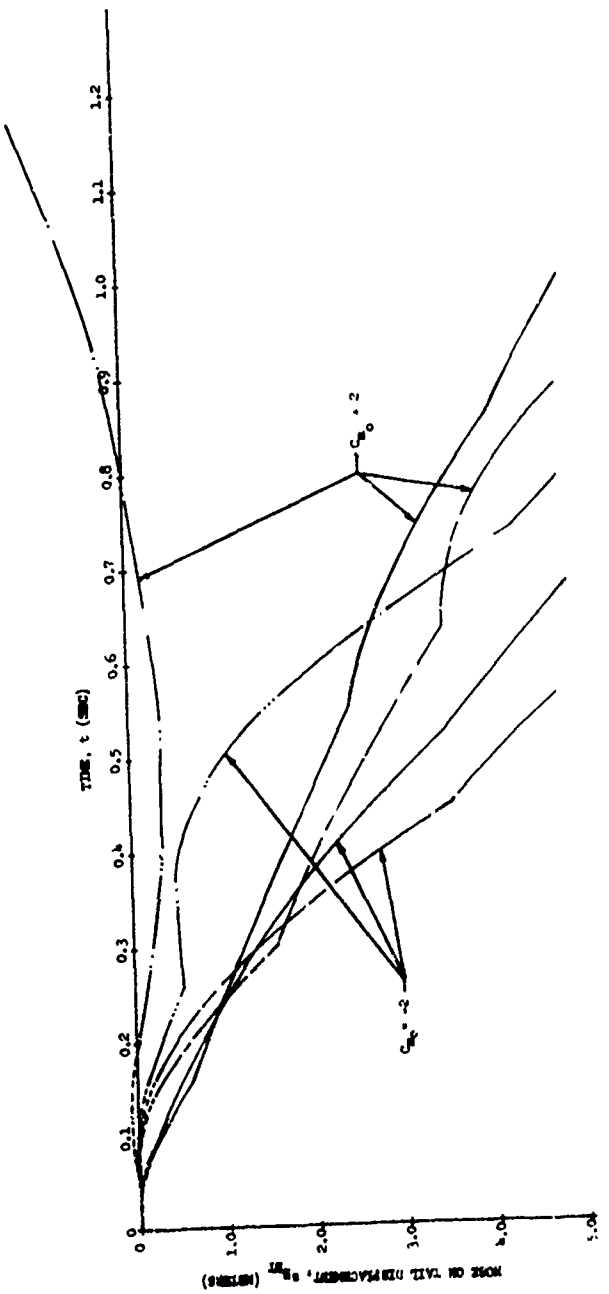

FIGURE 20

Nose or Tail Displacement Versus Time as a Function of Orifice Areas and Aerodynamic In-carriage Moments for Sixty Degree Dive

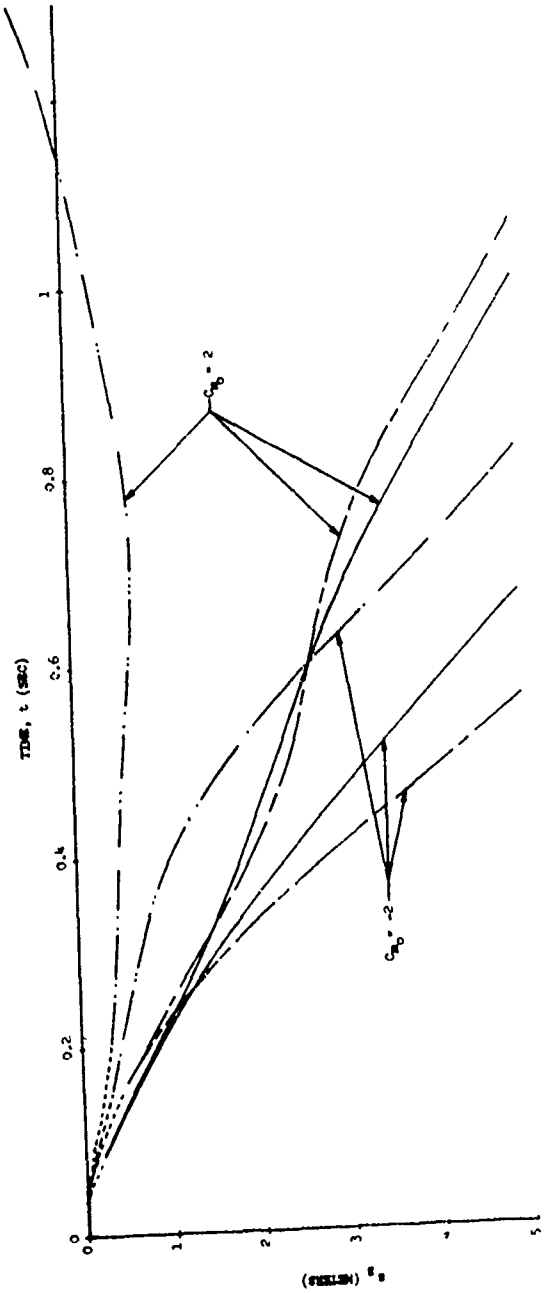

FIGURE 21

z-Direction Displacement of Store Versus Time as a Function of Orifice Areas and Aerodynamic In-carriage Moments for Sixty Degree Dive

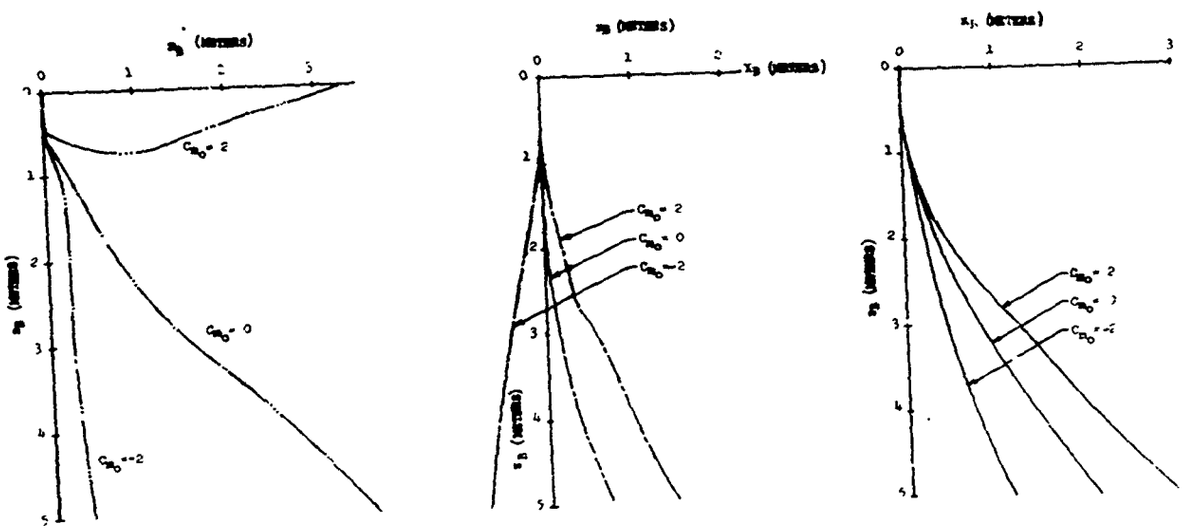

FIGURE 22

Store Trajectories as a Function of Aerodynamic In-carriage Moments for Three Sets of Orifice Areas and Sixty Degree Dive

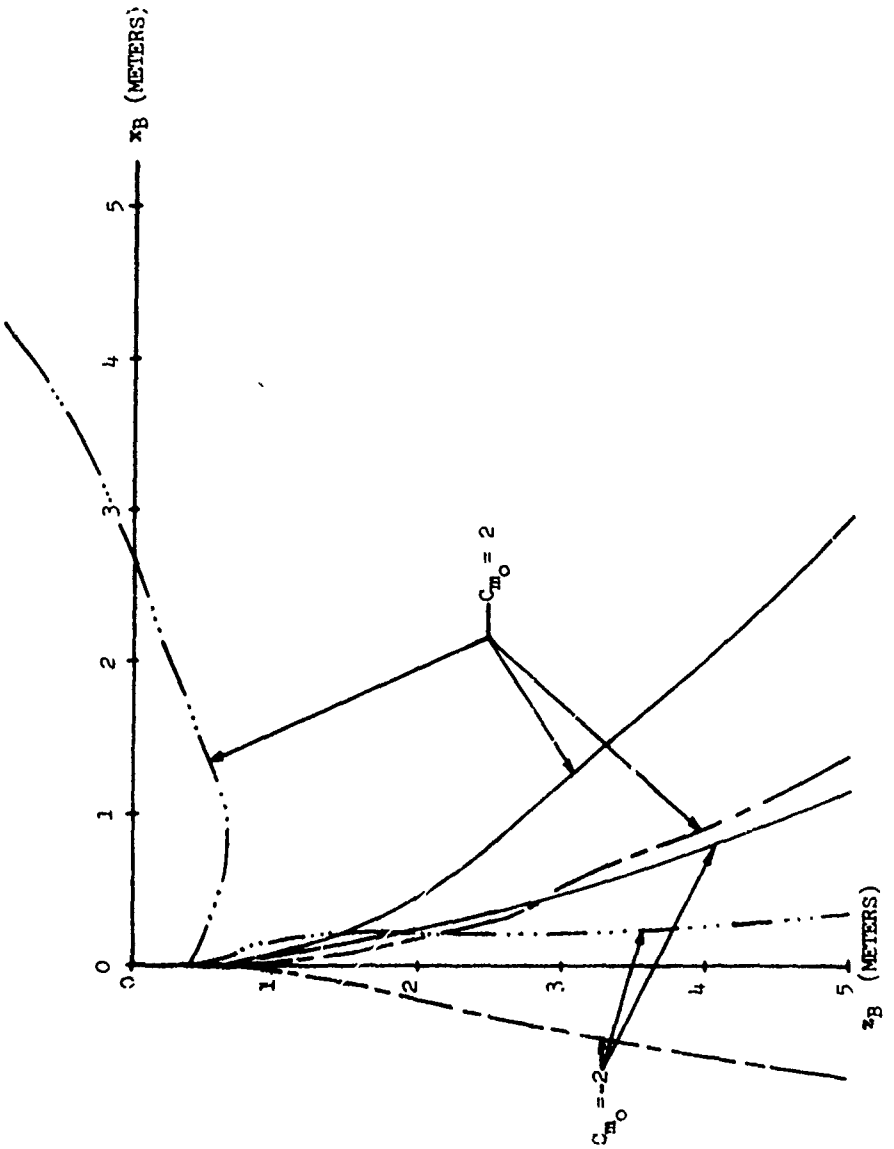

FIGURE 23

Comparison of Trajectories as a Function of Aerodynamic In-carriage Moments for Three Sets of Orifice Areas and Sixty Degree Dive

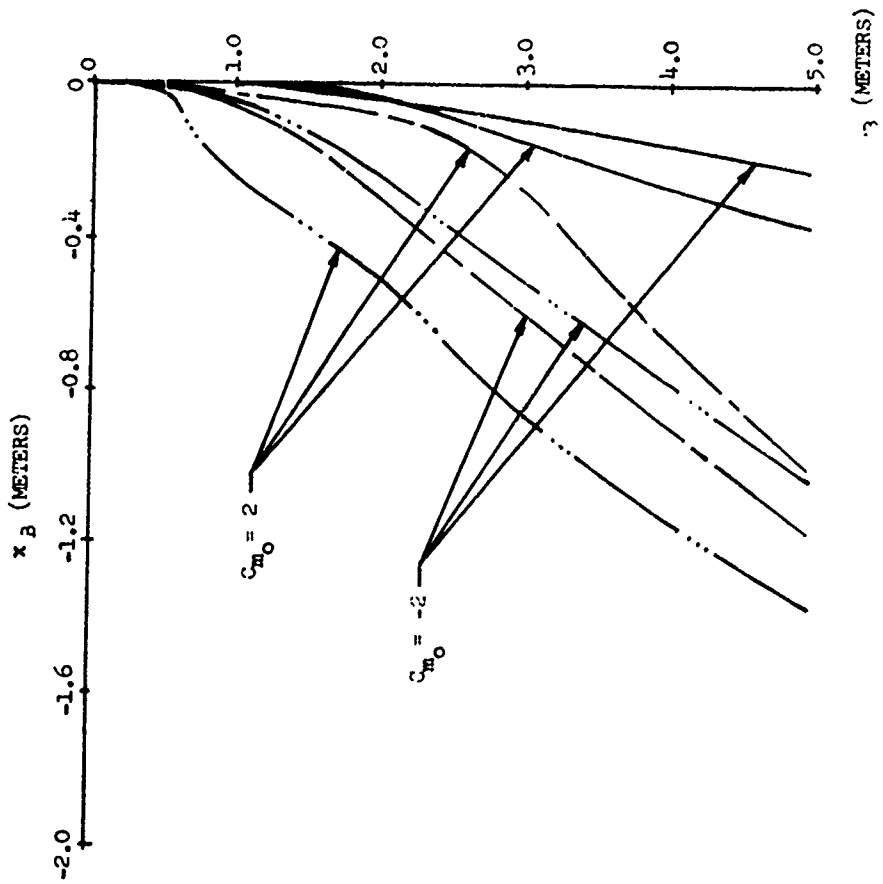

FIGURE 24

Comparison of Trajectories as a Function of Aerodynamic In-carriage Moments for Three Sets of Orifice Areas and Horizontal Flight

As a summary, it is demonstrated that the combination of orifice areas $A_{o_F} = 0.0327 \times 10^{-5} m^2$ with, $A_{o_A} = 0.4323 \times 10^{-5} m^2$ and $A_{o_F} = 0.8194 \times 10^{-5} m^2$, with $A_{o_A} = 0.03635 \times 10^{-5} m^2$, can result in undersirable situations during store separation. When one chooses $A_{o_F} = 0.8194 \times 10^{-5} m^2$ with $A_{o_A} = 0.432 \times 10^{-5} m^2$, the initial pitch angle and pitch rate are significantly decreased, and the ejection velocity is increased to 5.2 m/sec. The resulting oscillations are considerably smaller and the store safely clears the adverse influence of the aircraft nonuniform flowfield and enters the less violent environment of the free stream.

Therefore, the above studies indicate that by choosing appropriate orifice combinations and metering the gas pressure, it is possible to ensure safe store separation under given aerodynamic loadings. However, the remaining store oscillating motion can induce deviations from the desired ballistic trajectories. The goal of designing a conventional store ejector is to select "fixed" size orifices which can set the store on a trajectory calculated to avoid store/aircraft collision without significantly affecting the predetermined ballistic trajectories. The ever enlarging operational envelopes of present and future aircraft compound the complex problems of store release and delivery conditions. The appropriate variation in sizes is a necessary step to ensure safe store separation and improve trajectory under all aircraft flight conditions. The present approach is to set the store at an optimized trajectory with optimized angle of attack and pitch rate at the end of the aircraft flowfield. Thus, the store can clear the aircraft nonuniform flowfield with an improved trajectory. This could be achieved by using two variable orifices preadjusted during flight as described previously.

CONCLUSIONS

Based upon this preliminary study, the following are concluded:

1. The present study synthesized a system for controlling the store motion during the separation phase. The problem is approached by considering the store, store-ejector and aircraft submerged inside the nonuniform flowfield as a system rather than as separate components. Therefore, we

could combine the present analytical tools and experimental capabilities with existing technology to design a practical store separation system.

2. This study demonstrated that a dual-piston store ejector having sufficient ballistic impulse and variable orifice capability can compensate for, or overcome, the given in-carriage store pitching moments and loads, thus greatly enhancing safe store separation.
3. The effects of dynamic interior/exterior ballistic interactions imposed on an ejector in-flight have been ignored in the past. This study shows that the underestimation of these effects can lead to erroneous results in the study of launch dynamics.
4. The experimental results indicate that the infinitely variable orifice design is capable of controlling pitch rate and ejection velocity and reducing the maintenance required.
5. By providing sufficient ballistic impulse and adequately controlling the ejector movements using computer selected orifices, a system could be designed to launch a large variety of stores for various flight conditions. This would reduce the number of rack and launcher models required in service and improve operational flexibility.
6. Apart from the proposed system, the present theoretical model can be useful in the study of conventional store ejectors (when the ejector gas system design closely follows the basic high-low ballistic principle) and store separation problems. It can be used to simulate the overall effects of systematically varying the interior/exterior parameters and ejector design criteria which is not easily done in either wind tunnel or flight testing.
7. From both analysis and design view points, the present study may lead to the development of a theoretical-empirical package for solving future store-to-aircraft collision problems as well as the improvement of ballistic trajectories.

REFERENCES

1. Ryan, B. M., R. E. Meeker, and L. W. Seely, ***Store Separation State-of-the-Art Summary Report***, NWC TP5530, June 1973.
2. Gonzalez, J. M., ***Trajectory Sensitivity of the MK 82 Low Drag Bomb to Pertinent Delivery Parameters***, Armament Memorandum Report 69-20, Air Force Armament Laboratory, Air Force Systems Command. (1969)
3. Jones, D. A., III, ***Some Aspects of the Aircraft Store Separation Problem***, NWL Technical Report TR-2206, Naval Weapons Laboratory, Dahlgren. (1968).
4. Forrest, J. L., ***An Investigation of the Phoenix Launcher Gas System***, NWL Technical Report TR-2395, Naval Weapons Laboratory, Dahlgren, (1970).
5. Frank, L. A., ***Conformal Carriage/F-4 Compatibility Part 2 -- Subsonic Separation Characteristics of Conventional Weapons and Advanced High Density Bluff Weapons***, Evaluation Report AL-86, Naval Ship Research and Development Center, December 1972.
6. Smith, R. E., ***Conformal Carriage Flight Test Program***, Part 2, Weapon Separation, NWC-TP-5529, Part 2, Naval Weapons Center, China Lake, (1973).
7. Holmberg, John L., ***A Study of the SUU-51A/B Dispenser Munition's High Speed Separation Problem and Proposed Solutions***, AF-ATL-TR-73-114, Air Force Armament Laboratory, May 1973.
8. Holmberg, John L., ***Modifications of Triple Ejector Rack Geometry to Reduce Bottom Station Weapon Separation Perturbations at High Speeds***, AF-ATL-TR-73-171, Air Force Armament Laboratory, August 1973.
9. ***F-14A Crash***, Aviation Week and Space Technology page 25, June 1973.
10. Maughlin, R. K.,, and R. L. Hanle, Jr., ***A History of AV-8A (HARRIER) Weapon Compatibility Trials***, **Aircraft/Stores Compatibility Symposium Proceedings**, JTCGT/ALNNO WP-12-2, Volume 4 of Volume 4, pages 273-301. September 1973.
11. Kalivretenos, C. A., L. H., Schindel, and R. R., Maestri, ***Self-Compensating Store Ejection Technique***, Aircraft/Store Compatibility Symposium Proceedings, Volume 2 of 3, AFFDL-TR-72-67, August 1972.
12. Hooton, J., ***Flight Test Results for an Instrumented TER-9 Bomb Rack***, Technical Report AFATL-TR-73-111, Air Force Armament Laboratory, May 1973.

13. Miko, R. J., and Rutiglians, D., ***Advanced Concepts in Ejector Rack Design***, EDO Corporation, Interior Report 1, prepared for ADT/PPRN, Eglin AFB, Report No. 9939, May 1973.

14. EDO Corporation, ***Preproduction Test Report MXU-611/A Fuel Tank Release Mechanism***, Report 9575, SC-392 (1972).

15. Ramey, R. A., ***Design and Evaluation of an Infinely Variable Orifice***, NSWC/DL, Technical Note, (Being prepared for publication.)

16. Hedden, S. E., J. M., Massey, Jr., and P. N. Stamoules, ***An Evaluation of the High-Low Ballistic Principle for Cartridge Actuated Devices***, NWL Report Number 1964, Naval Weapons Laboratory, Dahlgren, (1965).

17. Sutton, G. P., ***Rocket Propulsion Elements***, (New York: John Wiley and Sons, Incorporated, 1957).

18. Maddox, A. R., ***A Parametric/Sensitivity Study of Store Separation***, Aircraft/Stores Compatibility Symposium Proceedings, JTCGT/ALNNO WP-12-2, Volume 3 of Volume 4, pages 105-133, September 1973.

ACKNOWLEDGEMENTS

The work described here was supported by Naval Air Systems Command under AIRTASK A350-350E/009B/4F54-546-504.

The author is indebted to Mr. J. Max Massey, Jr., Mr. R. C. Montgomery and Mr. R. D. Kilpatrick for their implementation of the complicated mathematical model on the NSWC/Dahlgren Laboratory hybrid computer. The author also wishes to thank Mr. R. A. Ramey for his efforts in the hardware demonstration.

PAPER NO. 19

THE AERODYNAMIC ENVIRONMENT OF ROCKETS LAUNCHED FROM HELICOPTERS

By

B. Z. Jenkins
U. S. Army Missile Command

1. Introduction

The Army is deeply committed to the concept of an attack helicopter - one which may be armed with conventional firearms as well as guided missiles or free rockets. A helicopter is not the most ideal launch platform for rockets and missiles due to the numerous launch transients involved. These transients, principally vibration, rotor downwash, and translation and rotation of the launch platform, have not been properly investigated as sources of rocket dispersion. In an effort to assess the importance of rotor downwash on the dynamics of the round during its first few feet of flight, it is first necessary to determine the induced velocity field about the helicopter in flight. Knowing the properties of the environment which the rocket must traverse, one may then use aerodynamic forces derived therefrom in simulating the rocket's trajectory. A theoretical capability to define the helicopter's downwash properties exists at MICOM through a computer program developed over the past eight years. In order to verify and supplement this, a flight test experiment was begun in 1973 and is still being carried out.

2. Description of Analytical Technique

The computer program being used at MICOM and the analysis upon which it is based are described in references 1, 2, and 3. Basically, the resultant flow in the domain of interest is assumed to be a superposition of three elements: the freestream, the fuselage represented by a distribution of sources and sinks, and the rotor wake represented by line vortices shed from each blade. (Figure 1 indicates these sources.) Obviously, the representation of the fuselage and the representation of the rotor downwash are interdependent and both should be periodic

functions of time. In the program, the initial representation of the wake is chosen to be helical (one for each blade) and slanted aft in accordance with momentum theory. The fuselage representation is initially taken to be that resulting from the freestream only. The rotor representation is then advanced by marching timewise for several revolutions of the rotor. The fuselage representation is then recalculated using the time averaged values for the downwash effect in accounting for flow nonuniformity. This procedure is then repeated until a nearly periodic flow is established - usually approximately four complete passes. It is seen that the solution found is not completely interactive - the fuselage representation resulting is the one that would result from the time average of the periodic flow. The influence of the fuselage is relatively small compared to the other sources and this shortcoming is not very important. There is another shortcoming which is potentially more serious. The shed vortex sheet from all along the blades is ignored or lumped into the vortex filaments being shed by the blade tips. More recent downwash simulation programs which account for this effect indicate that it is quite important.

Consideration of the model representation of the flow field reveals several important facets of the resulting flow:

a. Areas of strong velocity gradients and high velocities will occur near the vortices distributed through the flow.

b. The position of the boundaries of the rotor wake is strongly influenced by the aircraft's speed. For rockets launched from the helicopter in a conventional fashion, there exists a maximum airspeed for which the rotor downwash intersects the rocket's flight path.

c. The weight of the aircraft influences the vertical downwash component almost linearly.

d. The incidence of the rotor disk to the freestream, α_T, is quite important for characterization of the downwash properties and is largely determined by aircraft drag and weight.

3. Description of Experiments

The most direct quantities for defining the aerodynamic environment occurring about helicopters are the time dependent velocity components throughout the region of interest. This was undertaken, but for economy of effort the rotor wake boundary as a function of airspeed was first undertaken to fix the forward limit of the survey. Virtually all the experimental data shown here can also be found in reference 4.

a. Aircraft and Range

The flight tests were carried out by the US Army Aviation Engineering Flight Activity located at Edwards Air Force Base, California. Based primarily on aircraft availability, a UH-1M helicopter was selected as the test vehicle. A drawing of the aircraft showing the coordinate system used is presented in Figure 2.

b. Instrumentation and Procedure

The wake boundary surveys were made using an Elliott dual-axis low airspeed system. The Elliott system was mounted at Y = -65, Z = 29 for various X positions and at Y = -65, Z = 88 for various X positions. The flow angularity in the helicopter pitch plane was noted for various forward speeds of the aircraft. As the foremost boundary of the rotor wake passed the Elliott probe a pronounced change in the flow angularity occurred, allowing one to determine the X coordinate of the wake boundary as a function of airspeed for two outboard stations. This is

presented in Figure 3. It is seen that the weapon mount location, typically forward of fuselage station 120, will be free of downwash effects for true airspeeds greater than 45 feet per second.

The flow field velocity survey was carried out using an array of seven split film 3-component anemometers mounted linearly on a lateral rack (Figure 2) 8.5 inches apart. Plans were to make successive flights, repositioning the rack between flights until the entire volume of interest had been covered. During each flight a number of data records were to be taken at a predetermined set of flight conditions. The appendix briefly lists the instrumentation and data conditioning and collecting procedure. Complete descriptions and specifications are given in reference 1.

Unfortunately, the tolerance of the anemometers to vibration had not been determined and insufficient vibration isolation had been built into the support structure. The sensors failed subsequent to the first flight with the rack in the first position. The probe locations for the first rack position are given in Table 1. During this test flight, data were taken for a variety of forward velocities. As Table 1 indicates, only five of the seven sensors were fully operative throughout the flight.

TABLE 1. PROBE LOCATIONS

Probe No.	X (in.)	Y (in.)	Z (in.)	Comments
1	111.885	-109.56	58.928	
2	111.885	-101.06	58.928	Operative in one axis only
3	111.885	-92.56	58.928	
4	111.885	-84.06	58.928	
5	111.885	-75.56	58.928	Inoperative
6	111.885	-67.06	58.928	
7	111.885	-58.56	58.928	Data noisy (perhaps due to turbulence)

Flight data records were taken at airspeeds of approximately 8, 18, 54, 74, 393, 113, 135 and 153 feet per second. The helicopter was flying with zero sideslip, straight and level out of ground effect. Gross weight was 7400-7500 pounds and rotor speed was nominally 324 rpm.

c. Velocity Survey Results

Velocity-time curves for each component, sensor, and flight record are presented for the entire measurement interval in reference 1. This time interval is large compared to the period of the fluctuating velocity, making it hard to distinguish details of the curve shape over only one period (= 0.095 second). In reference 5, these data are re-presented over an interval of only six periods allowing the scatter in data, repeatability from cycle to cycle, and variability of data quality from flight record to flight record to be readily seen. One of these plots is shown

as figure 4. Note in particular:

a. The passage of the vortex filaments as indicated by the fast velocity change in all components but principally V_X and V_T.

b. The low amplitude of the fluctuations of vertical downwash component.

c. The weakness of the lateral component of velocity at this station. According to analysis, this is true even at station located near the wake boundaries.

d. The unusually high value for V_X (30 - 40 feet per second) is unrealistic for a forward velocity of only 7.7 feet per second. All theoretical methods indicate the mean value of V_X should be on the order of $7.7 + V \sin \alpha_T T = 7.7 + 75 \cdot \sin 2° = 10$ ft/sec. The measured values were repeatable between different data records of about 5 seconds each.

4. Comparison of Theory and Experiment

Theoretical simulations were carried out for several of the experimental flight records. One of the critical input variables is the incidence of the rotor tip path plane to the freestream (α_T). This quantity varies with airspeed and aircraft weight and center of gravity location and was not directly measured during the experiment but inferred from aircraft attitude measurements. Since rotor flapping angle was not measured, the angle of the tip plane relative to the aircraft coordinate system was unknown. For the values of α_T derived from experiment, the flapping angle was assumed to be zero; therefore, α_T may be in error by the amount of the true flapping angle. If one uses the available data for aircraft weight and drag, α_T may be calculated by balancing forces at the rotor hub. The comparison of the values obtained in these two different ways is presented in Figure 5. We may then expect

to find disagreements between theory and experiment which correspond to up to 4 degrees of flow incidence in the pitch plane.

a. Time Dependent Data Comparison

Since the period of the velocity fluctuations is governed by the rotation of the rotor, the time coordinate was replaced with rotor position. For a two-bladed rotor, such as that of the UH-1M, each blade contributes to the flow velocity experienced by a point in the wake, therefore, the period is 2 per revolution or 180 degrees of rotation of the rotor. Instead of plotting rotor position as an ever increasing angle for successive periods, it was plotted modulo 180 degrees. In this way all the periods are superimposed on each other in the same 0 to 180 degree range. This is called a folded plot. For flight record 1, the absolute value of rotor position was measured with 0 and 180 degrees corresponding to alignment of the rotor with the fuselage centerline. This measurement subsequently became inoperative; therefore, for the remaining flight records the experimental values for rotor position are known relative to each other but not with respect to any reference position as was the case for flight record 1. As a result, in comparing theory with experiment using Figures 6 through 8, one must realize that theory and experiment can be arbitrarily displaced relative to each other along the abscissa.

During the course of the experiment, the rotational velocity of the rotor was nominally 324 rpm which would correspond to a period of 0.0926 second. However, in plotting the folded data it was found that slightly higher values for the period gave much better results, in that there was less scatter in the data. The value used for the period is indicated on each graph of Figures 6 through 8.

Instead of plotting flow velocity components along the three coordinate axes (as in figure 4), velocity magnitude and direction are shown in figures 6 through 8. Θ_Y and Θ_Z are the angles between the flow velocity vector and the Y and Z axes respectively. In this manner differences in flow direction between theory and experiment are put in proper perspective whereas in plotting VX, VY, and VZ a small error in flow direction can overwhelm a small component, such as VY, making it scattered to the point of being useless.

The inconsistency mentioned earlier in velocity measurement shows in figure 8 as a 10-15 degree direction error. Since this occurred at the most outboard probe, flow interference is unlikely-deflection of the probe and for rack is more likely. These angular inconsistencies were present for most flight records and probes, increasing with proximity to the fuselage. The velocity magnitude error is considered less alarming.

c. Time Averaged Data

In many cases the frequency of the flow fluctuation (= 10Hz) is high enough that objects of interest which are immersed in the flow cannot respond to it. In this case time dependent details of the wake flow can be ignored and the time averaged flow velocity and direction can be used to determine the behavior of the object. Theoretical and experimental flow magnitude and direction were time averaged and plotted (figure 9) as a function of Y for fixed X and Z locations corresponding to the sensor rack position (Table 1). Gaps in the experimental data correspond to positions of the malfunctioning sensors numbers 2, 5, and 7.

5. Elaboration of a Typical Situation

Having devoted some time to qualitatively describing the flow field and justifying the application of our downwash computer program, typical conditions existing along the path of a rocket fired from the AH-1G wing will be presented, based on calculated results (figure 10).

Figure 11 shows the downwash velocity components as a function of displacement along the trajectory of a 2.75" rocket. The conditions used in generating the data for this plot along with implications are as follows:

a. The aircraft is hovering. Forward velocity would diminish the vertical downwash while enhancing the component along the trajectory, thus decreasing cross flow angles and increasing dynamic pressure. Moreover, the rocket would be immersed in the downwash over a shorter distance for higher airspeeds and be entirely free of it at about 36 knots.

b. The round is launched from a position at butt line 42, water line 55 and fuselage station 148 corresponding to an inboard launcher position. Changes in the velocity-position profiles resulting from changes in launcher position within reasonable limits are minimal at hover. Moving outboard or forward results in a quicker exit from the wake, moving downward tends to reduce crossflow somewhat. Incidentally, if ground effect were to be accounted for, the induced vertical velocity component would be somewhat less depending on hover altitude.

c. The quadrant elevation of the round is 9.8°. The influence of changes in this parameter is to increase time of immersal and intensity of downwash if increased and vice-versa.

d. The solid lines are drawn corresponding to an instantaneous rotor position of alignment with the fuselage; the dashed lines-time average velocities and the shaded areas, the limits for other instantaneous values at various rotor positions and for the other side of the helicopter. The regions of greatest fluctuations are associated with the zone of passage of the vortex filaments.

Figure 12 relates the information of the previous slide to the angles of attack in pitch and yaw experienced by the 2.75" rocket. In this case the instantaneous values of downwash are used which are calculated at the time when the rocket nose occupies that point whereas in figure 11 time is constant along the solid line and is averaged out for the dashed line. These curves are specific to the 2.75" rocket since its forward velocity and elapsed time at each point figure in the computation.

Finally, just to show the effect that this environment can have on the rocket dispersion, suppose that we compute the trajectory to impact, assuming the rocket is fired from 30 feet above the plain. Neglecting downwash entirely, the round impacts at about 12,000 feet with only 1-1/2 feet cross range deflection. If a constant downwash of 50 ft/sec over the entire rotor disk shadow is assumed, the round impacts at about 14,000 feet with less than 3 feet of cross range deflection. With the indicated profile (figures 11 and 12) the round impacts at near 14,000 feet but has flown to the left about 120 feet. In both cases of downwash assumptions, the rocket is high in the air (several hundred feet) when it is 12,000 feet down range.

If the trajectory is calculated with different phasing of the launch-rotor positions, little change results; only 10 to 25 feet in cross range or down range. It would suffice in the case of the 2.75" rocket to consider time average downwash properties. It was noted, however, that a constant downwash model cannot properly predict cross range effects. (These results are subject to mitigation by ground effect.)

6. Conclusions and Recommendations

The downwash can significantly affect the trajectory of rockets launched from rotary wing aircraft at low speed or hover, however, the magnitude of these effects in relation to other launch transients is unknown and are not readily separable in firing tests. In the past, firing techniques have emphasized deployment from a dive at sixty knots or so, but current emphasis is on fire and forget tactics making use of pop-up and shoot at near hover. The role of downwash, in fact all launch transients, must be effectively assessed.

Further trajectory simulation is required for rockets having different aerodynamic and dynamic properties. The moderating effect of ground proximity should be accounted for. Some account should be taken of the influence of drift and gusts as well.

When the aerodynamic environment is accurately known, the aerodynamic force calculations should allow for gross nonuniformity of the flow. The flow properties can change significantly over the length of the rocket.

Flight tests are in progress to survey the flow field about the AH-1G from the launcher attachment point to the nose of the aircraft. These data will be used to verify the analytical technique further and will provide better definition of the aerodynamic environment for further trajectory simulation.

REFERENCES

1. Crimi, Peter, Theoretical Prediction of the Flow in the Wake of a Helicopter Rotor, Part 1, September 1965, CAL Report No. BB-1994-S-1.

2. Crimi, Peter, Theoretical Prediction of the Flow in the Wake of a Helicopter Rotor, Part 2, September 1965, CAL Report No. BB-1994-S-2.

3. Crimi, Peter and Trenka, Andrew, Theoretical Prediction of the Flow in the Wake of a Helicopter Rotor, Addendum, August 1966, CAL Report No. BB-1994-S-3.

4. Boirun, Barclay, Jefferis, Robert, and Holasek, Ronald, Rotor Flow Survey Program UH-1M Helicopter, May 1974, Final Report on USAASTA Project No. 72-05.

5. Jenkins, B. Z. and Marks, A. S., Rotor Downwash Velocities About the UH-1M Helicopter - Flight Test Measurements and Theoretical Calculations, 1 January 1975, MICOM Technical Report RD-75-27.

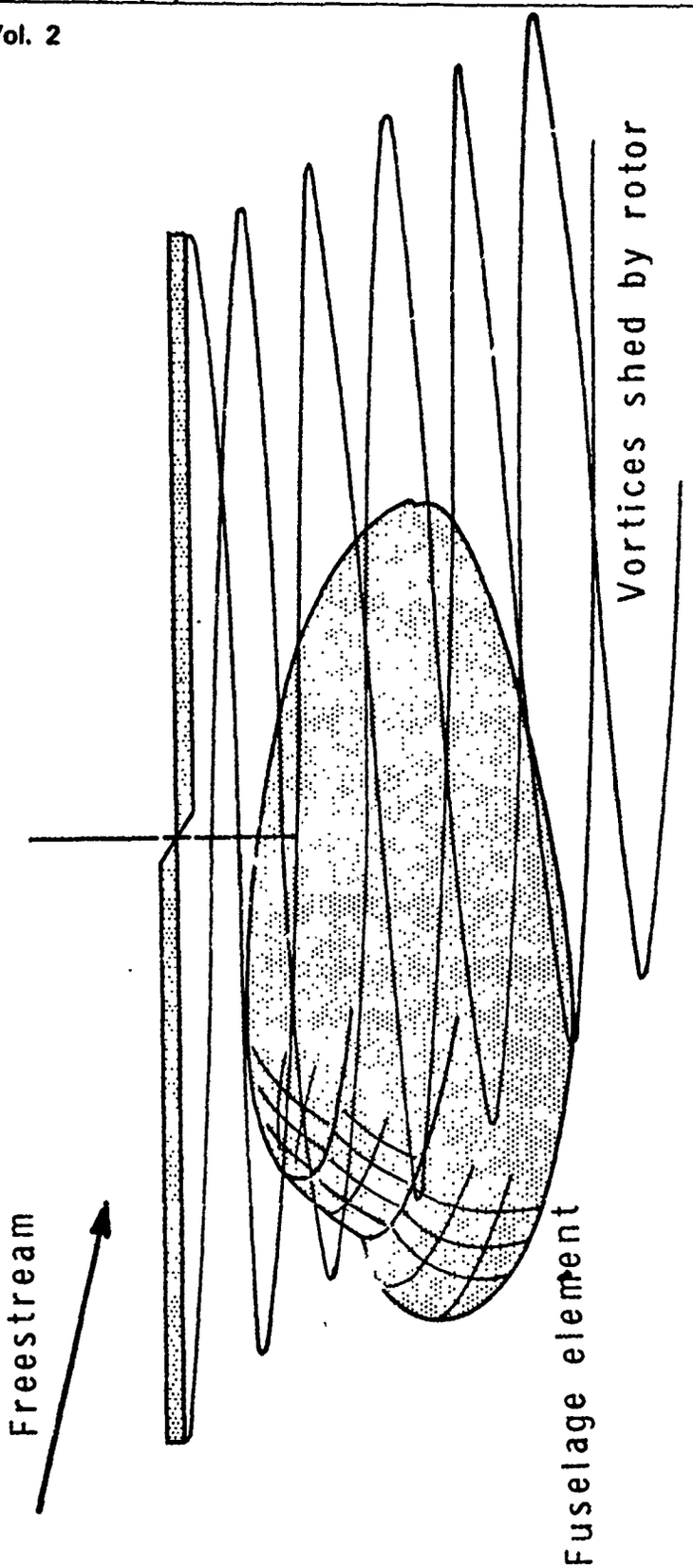

Figure 1. Schematic representation of flow field.

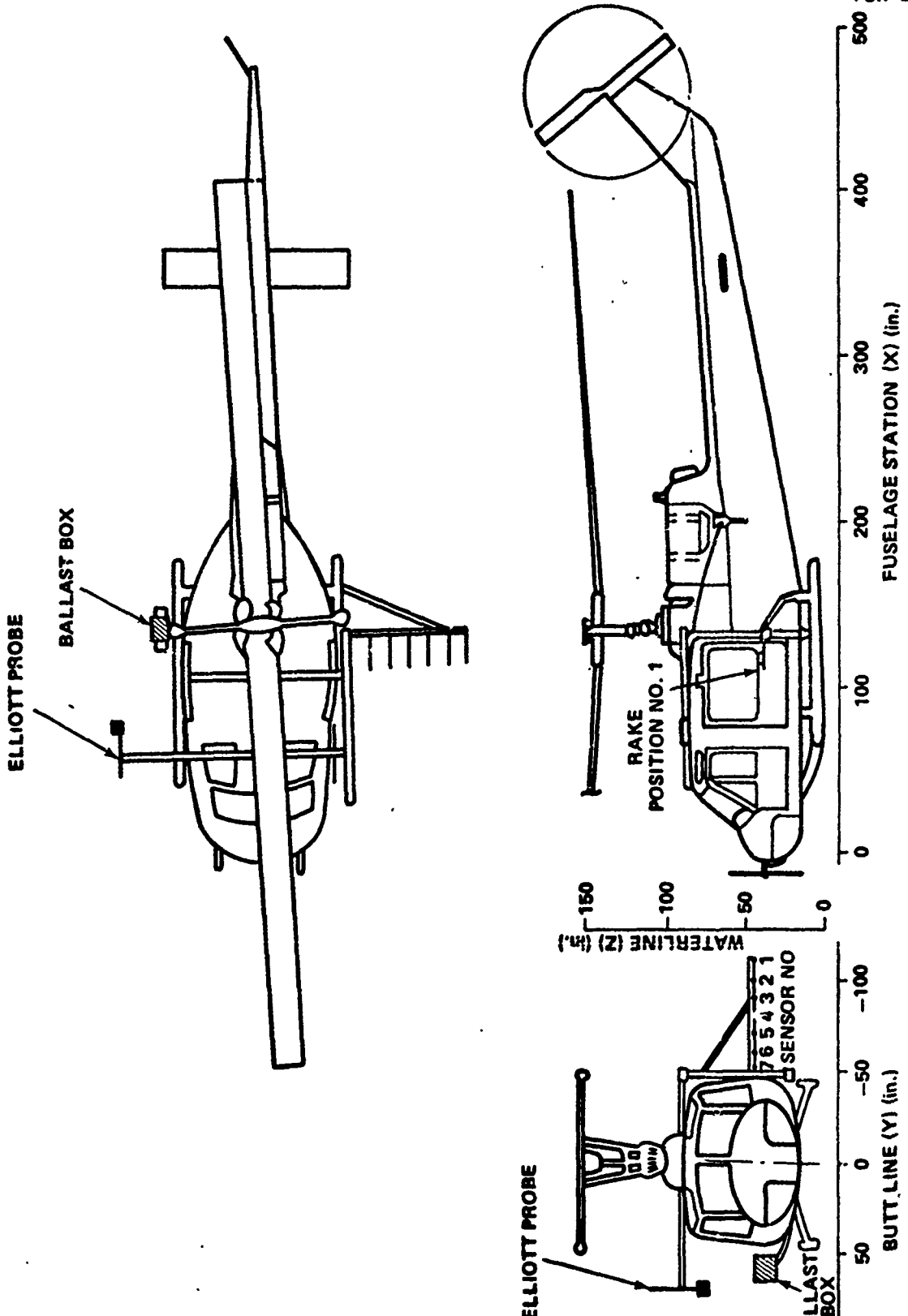

Figure 2. Aircraft coordinate system showing probe locations.

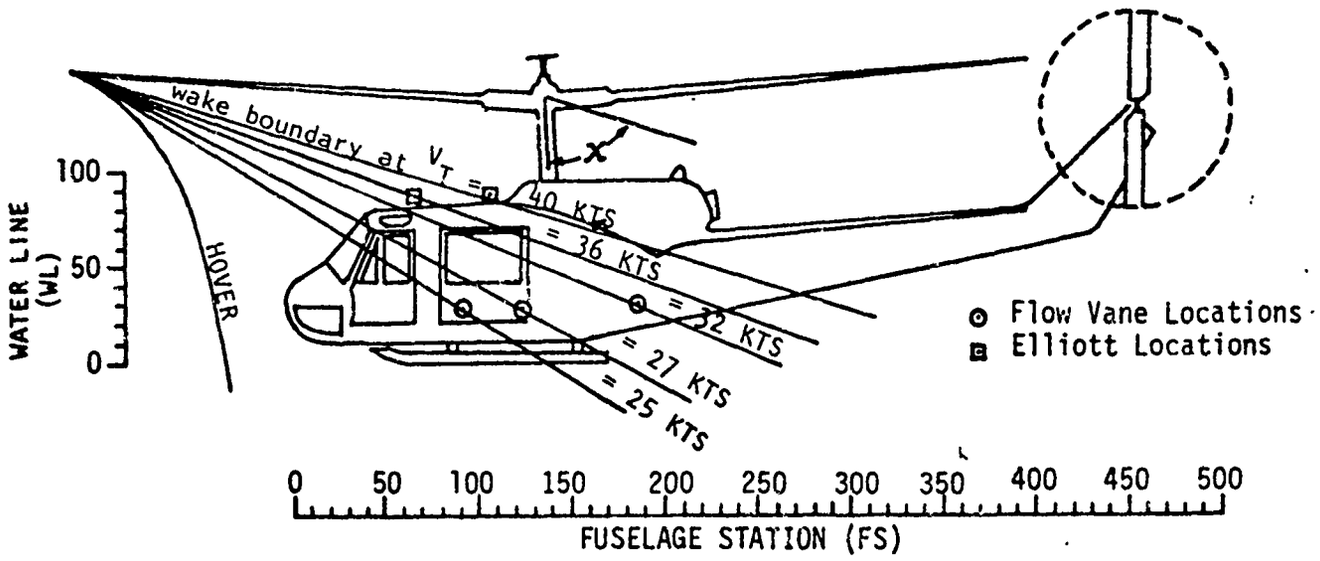

NOTES: 1. Data shown for buttline -65.
2. Data not corrected for displacement due to rotor flapping with increased forward speed.
3. Waterline stations are 83 and 29.
4. Average Conditions:
Gross Weight = 7500 pounds.
Density Altitude = 2500 feet.

Figure 3. Rotor wake boundaries in forward flight.

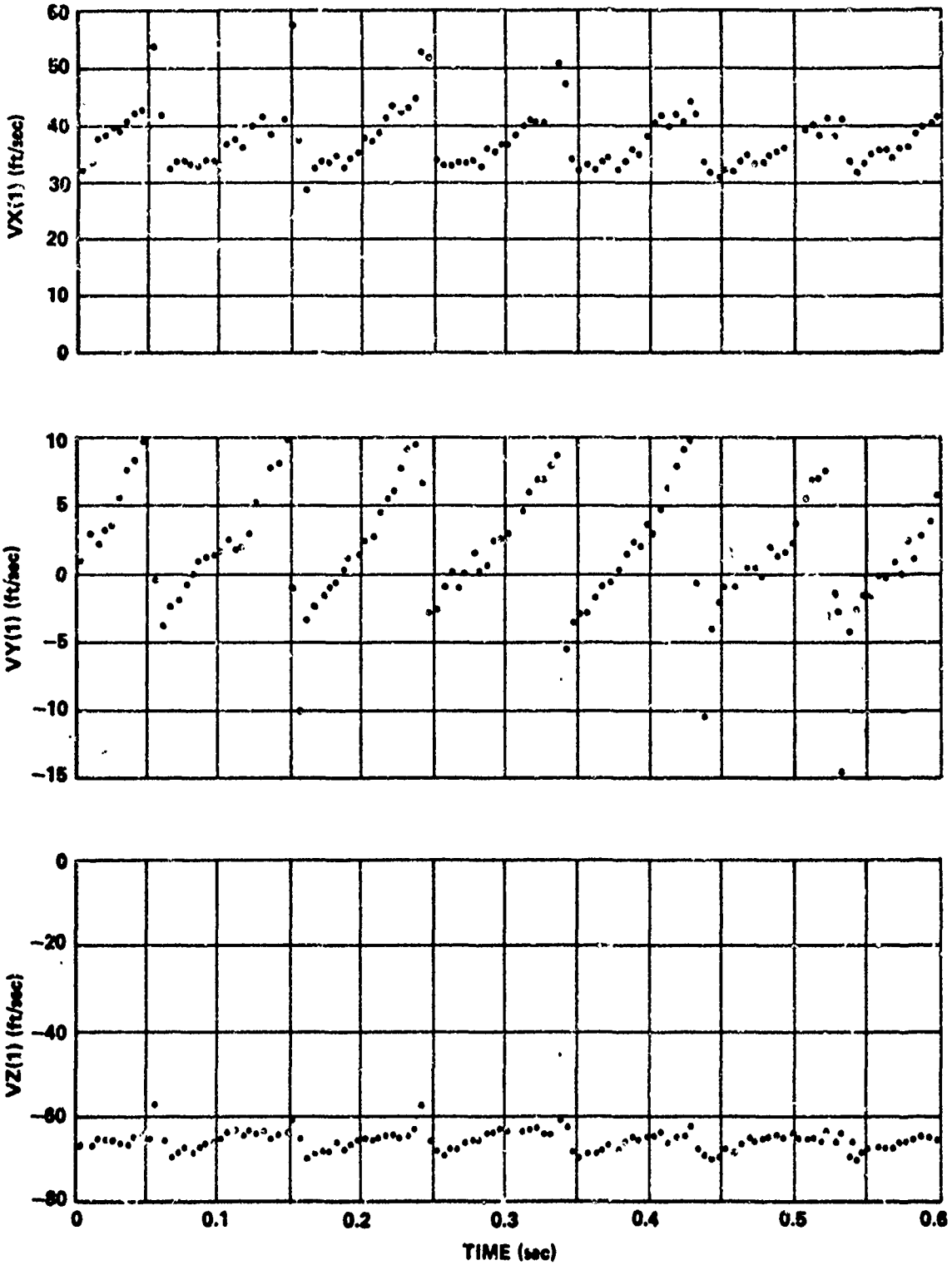

Figure 4. UH-1M helicopter flow field velocity components - 7.7 ft/sec airspeed, sensor No. 1.

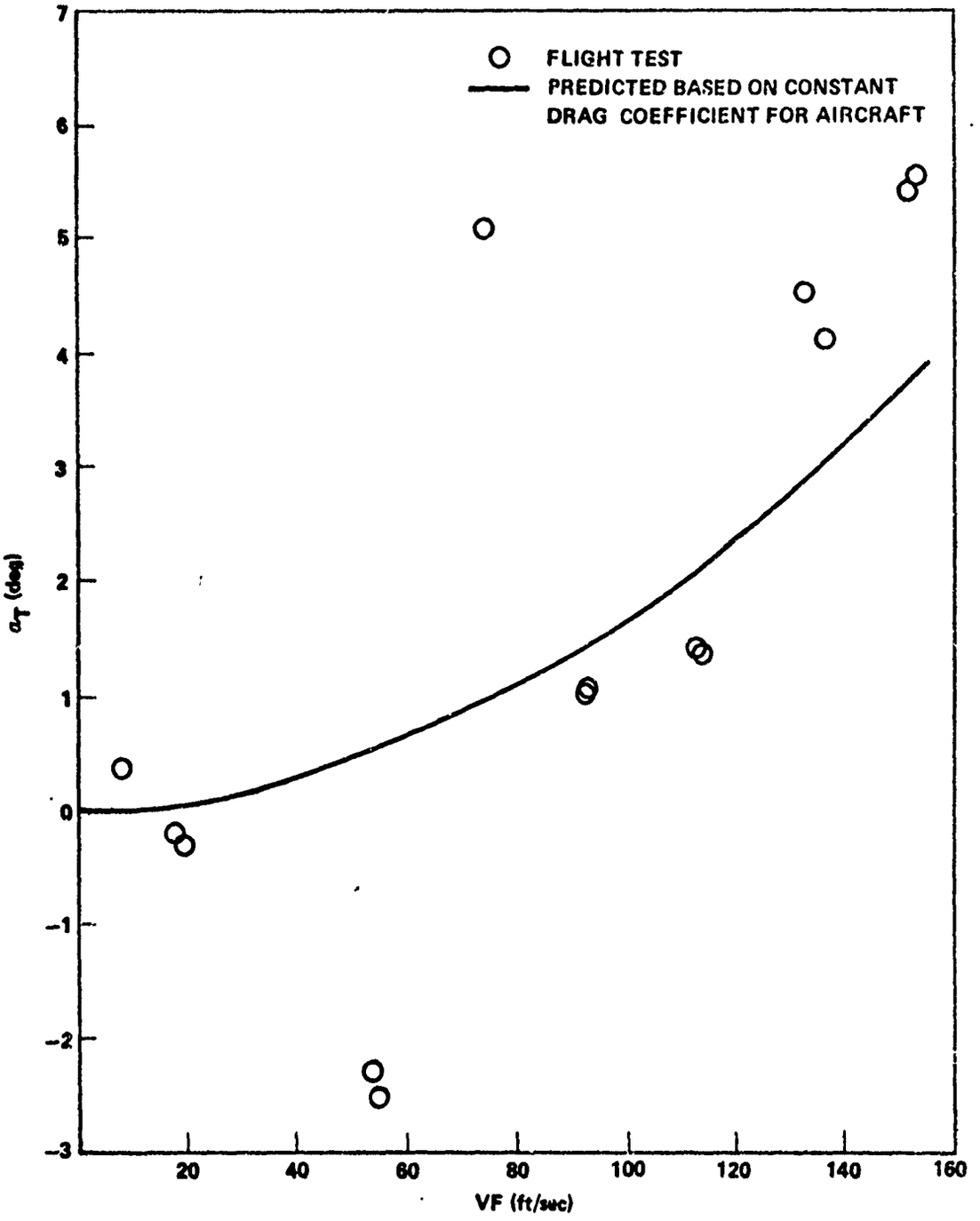

Figure 5. Variation of incliration of tip path plane of helicopter to freestream with helicopter airspeed.

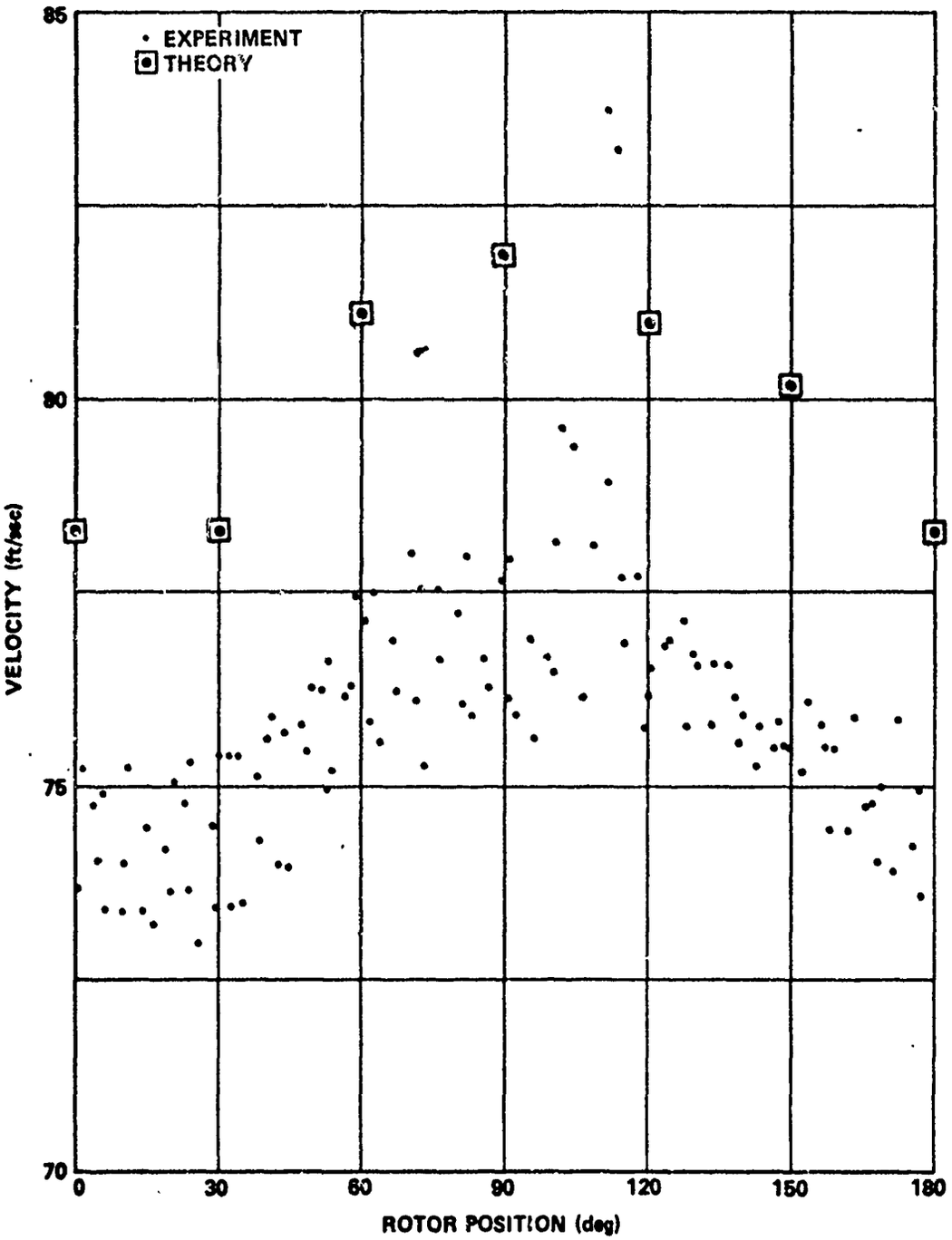

Figure 6. Folded comparison - 7.7 ft/sec airspeed, sensor No. 1, and trial period 0.094500.

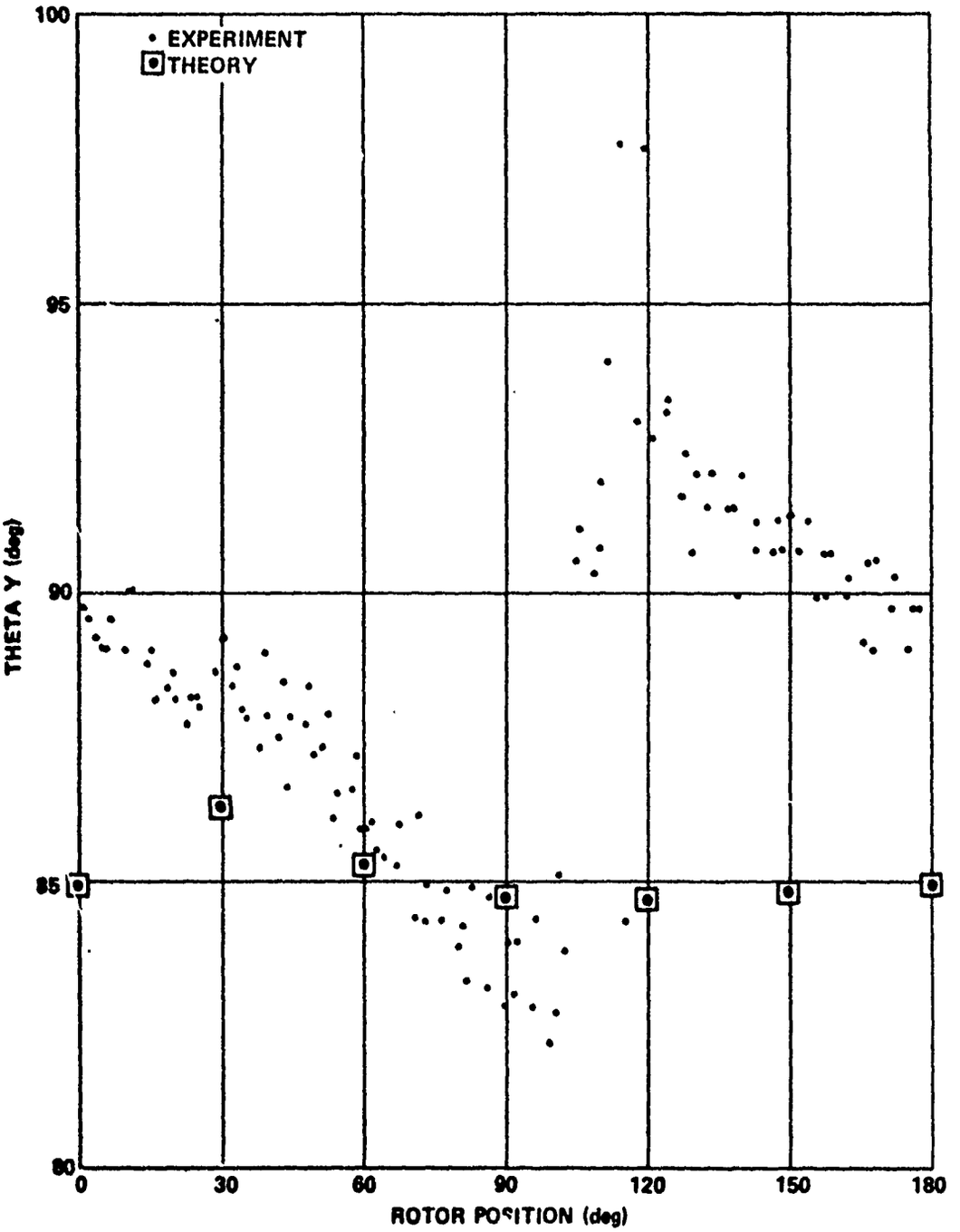

Figure 7. Folded comparison - 7.7 ft/sec airspeed, sensor No. 1, and trial period 0.094500.

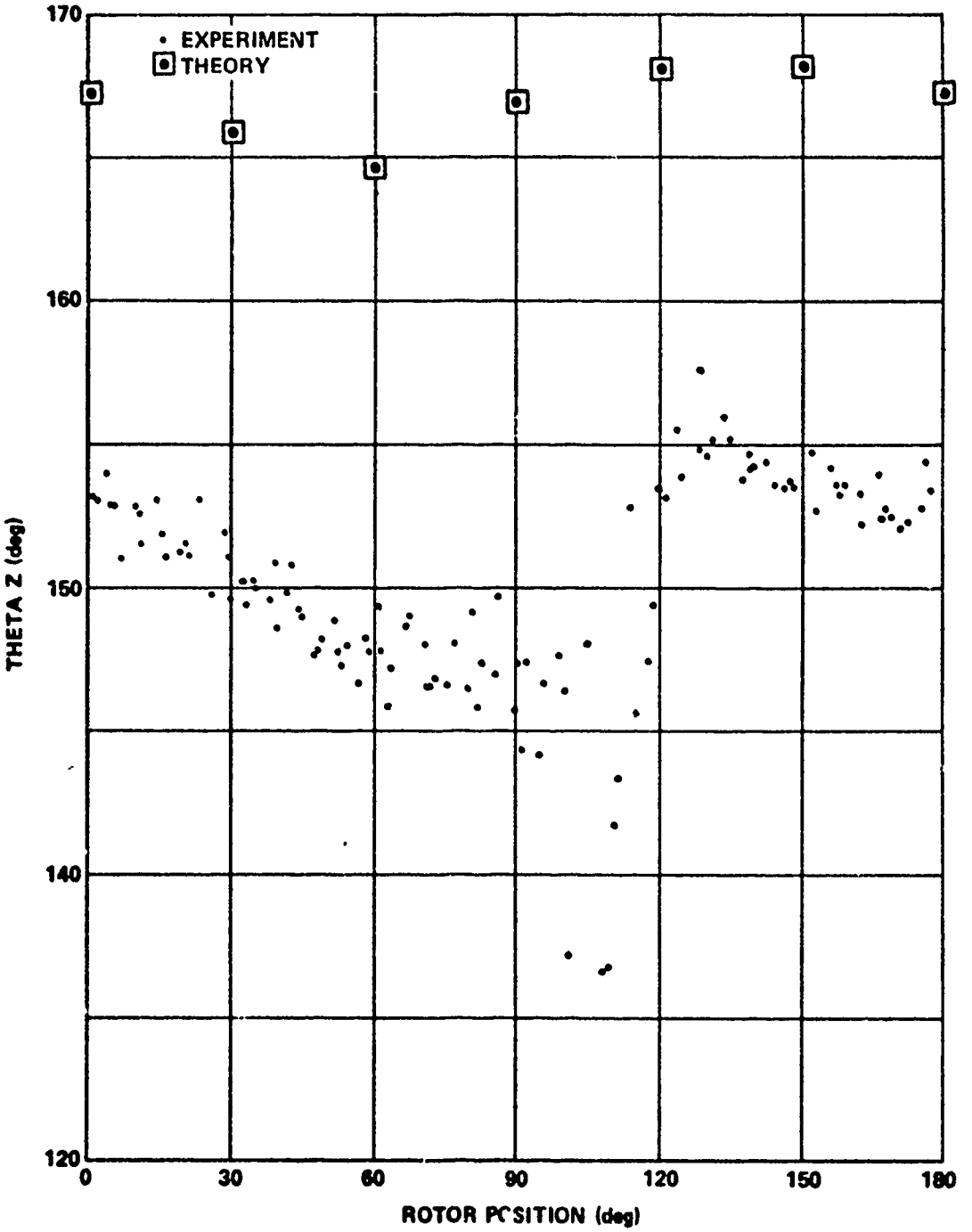

Figure 8. Folded comparison - 7.7 ft/sec airspeed, sensor No. 1, and trial period 0.094500.

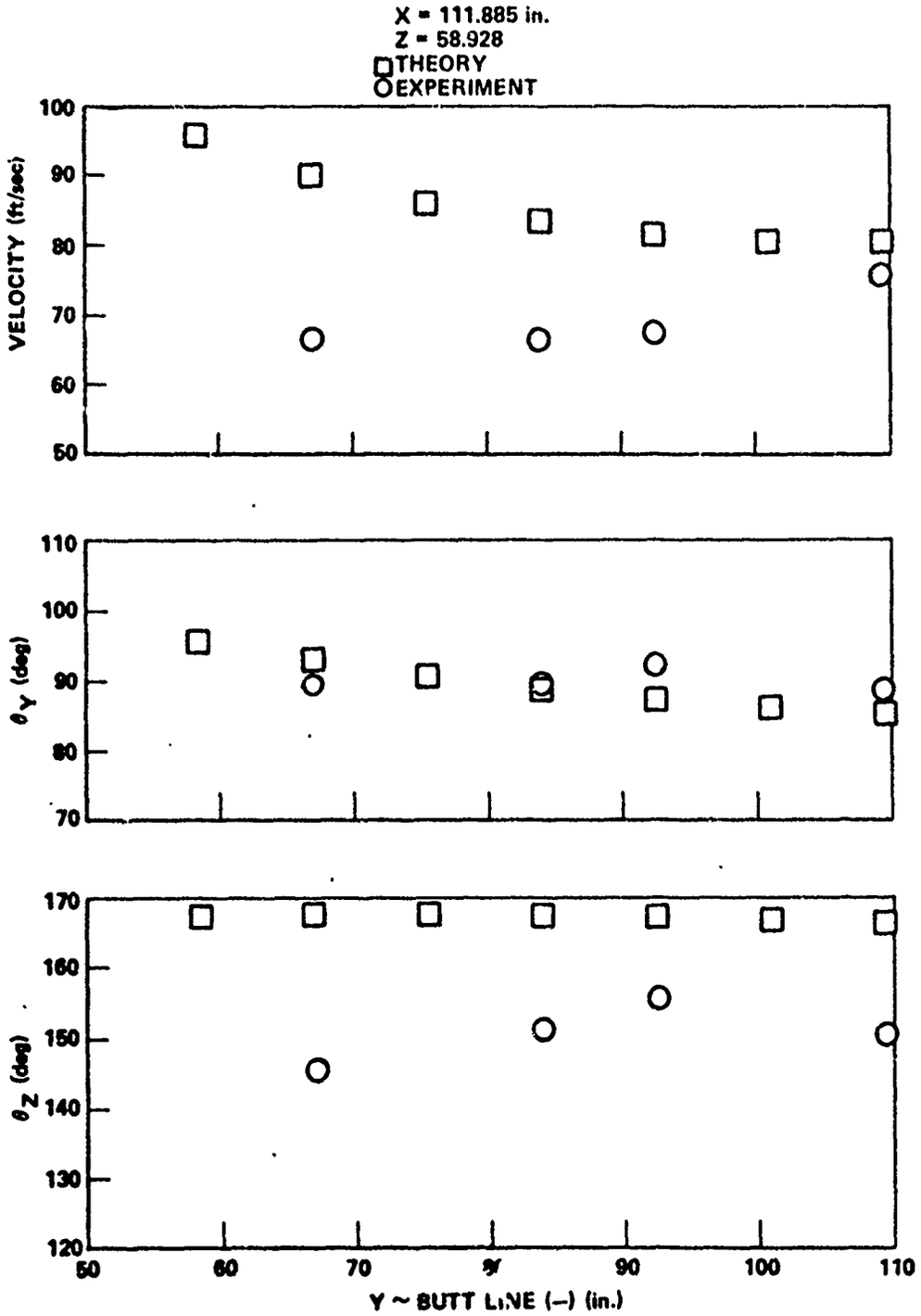

Figure 9. Comparison of time averaged velocity predictions with experiment, 7.7 ft/sec airspeed.

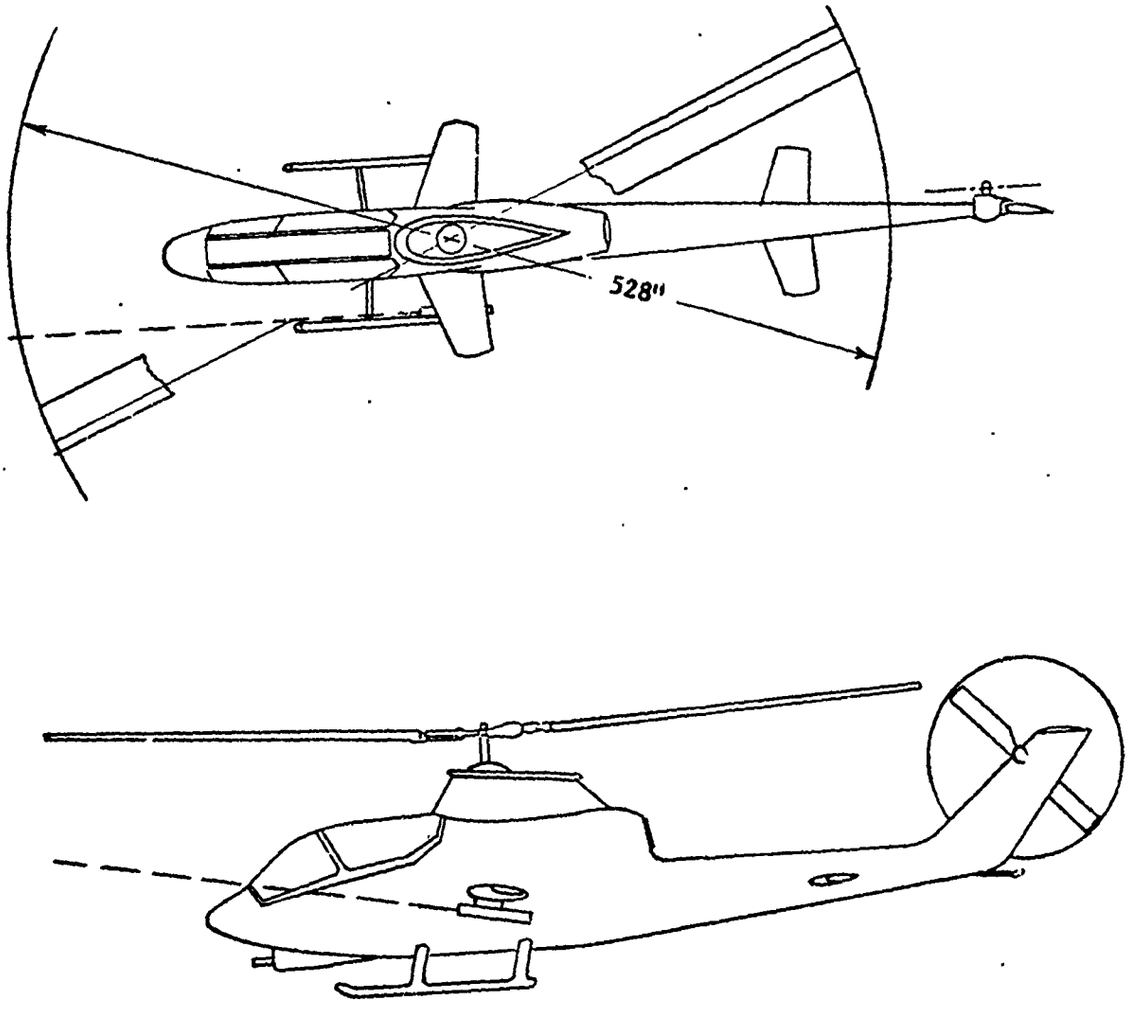

Figure 10. AH-1G aircraft showing typical 2.75" rocket flight path.

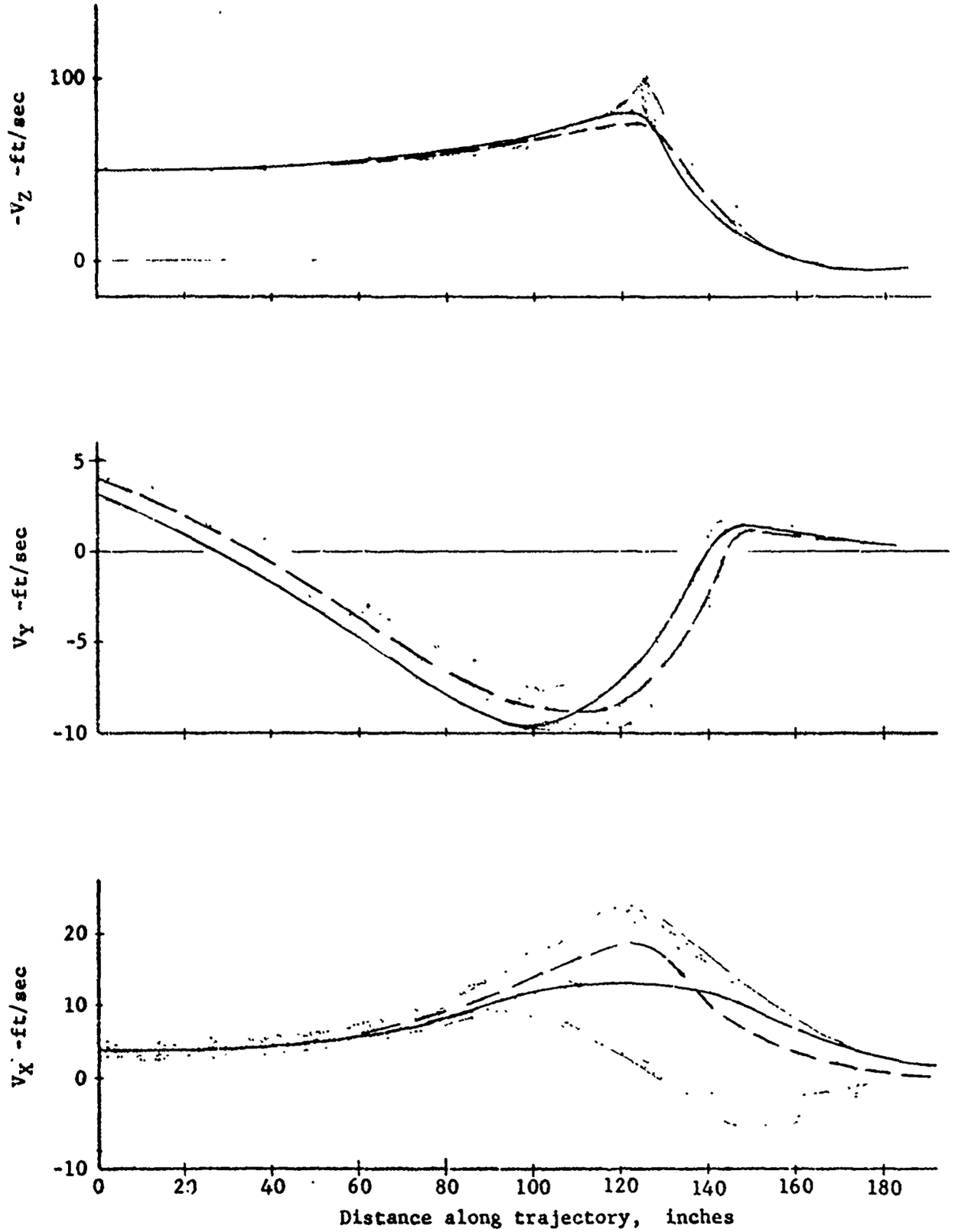

Figure 11. Downwash induced velocity components along a typical 2.75" rocket flight path.

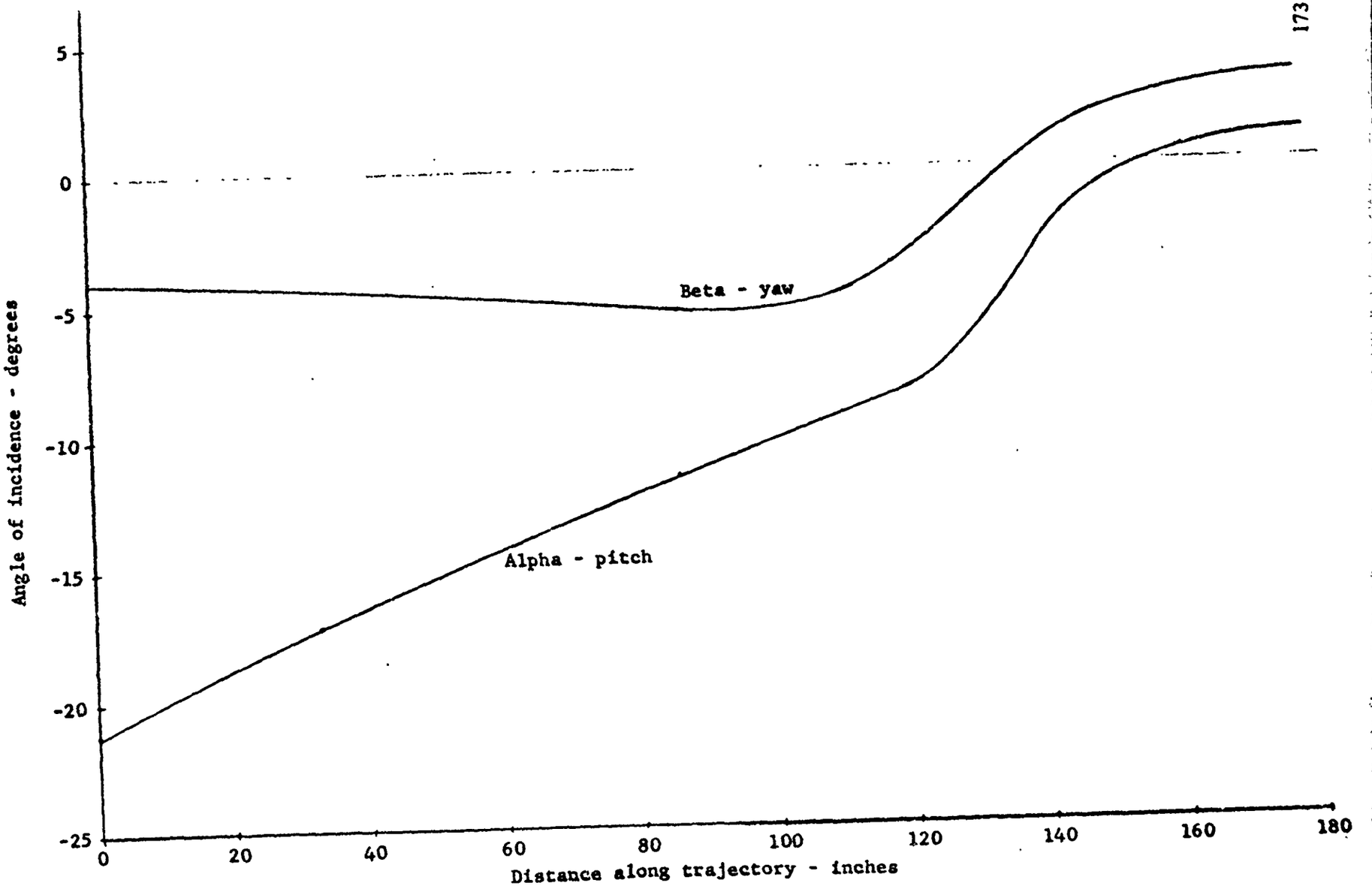

Figure 12. Typical incidence angle history of 2.75" rocket immersed in helicopter downwash.

PAPER NO. 20

A SIMPLE METHOD FOR STUDYING SOME AERODYNAMIC HEATING PROBLEMS*

By

Tse-Fou Zien

Naval Surface Weapons Center

White Oak Laboratory

Silver Spring, Maryland

*This work was supported by NAVSURFWPNCEN/WOL Independent Research Program, IR 199.

ABSTRACT

A simple, analytical method is presented in this paper for the approximate solution of a variety of problems related to aerodynamic heating. The method is basically an integral approach, and represents a refinement of the classical Karman-Pohlhausen momentum integral technique in the boundary-layer theory. Representative applications of the method are presented which include calculations of skin friction and wall heat flux of boundary-layer flows, and calculations of one-dimensional transient heat conduction with a phase transition. The approximate solutions are compared with existing exact solutions, and the remarkable combination of simplicity and accuracy is found to be the principal merit of the method.

1. INTRODUCTION

Problems of aerodynamic heating associated with high-speed vehicles, such as re-entry bodies, are generally quite complicated. The complications stem mostly from the severity of heating and the resulting melting, ablation, etc., of the aerodynamic body. Thus, the existence of various heat-transfer mechanisms and their coupling must be properly accounted for in the overall analysis. To study problems of such complexity, it is often desirable to have an analytical understanding of the heat-transfer processes involved. Such an understanding would usually provide considerable insight into the heating phenomenon under investigation without having to perform extensive computations. The proper coupling of various heating mechanisms involved can thus be effected with great facility.

To provide such analytical tools, simple, approximate methods need to be developed. In this paper, an analytical method is presented which is capable of providing approximate solutions to a variety of heat-transfer problems with remarkable simplicity. Areas of application of this method described in this paper include skin friction and heat transfer in a forced-convection, transpired boundary layer and one-dimensional transient heat conduction with phase transitions. The purpose here is not to present solutions to any new problems. Rather, it is to show how simply some old solutions can be reproduced with good accuracy by the present method. Therefore, examples are chosen for which exact solutions, analytical or numerical, are available so that the accuracy of the present approximate solutions can be tested.

The basic ideas underlying the method are essentially those used earlier in the author's skin-friction calculations[1,2]. The method is basically a refined version of the classical Karman-Pohlhausen (K-P) momentum integral technique in the boundary-layer theory. The ideas for the refinement were originally proposed by Volkov[3]. The generalized version and simplified use of these ideas form the basis of the p esent method for calculating surface properties in boundary-layer flows and the transient heat conduction in the presence of phase changes.

The paper begins with an exhibition of the essential ideas of the present method by means of a simple example in skin-friction calculations for the laminar boundary layer over a circular cylinder. The application to heat-transfer calculations in forced-convection boundary layers is next illustrated, and a special limiting flow is solved as an example. Finally, the one-dimensional transient heat conduction with phase transitions is studied, and some idealized, but representative, models of melting and ablation are treated. For a more comprehensive account of the entire development, the reader is referred to the author's previous publications[1,2,4,5,6].

2. DESCRIPTION OF THE METHOD AND SKIN-FRICTION CALCULATIONS

The essential ideas of the present method can most conveniently be described by means of an example in skin-friction calculations. For simplicity, we shall consider the incompressible, laminar boundary layer on a circular cylinder in crossflow. The inviscid flow outside the boundary layer is assumed to be the potential flow, and separated flow is thus ruled out by implication.

The integrated version of the general laminar boundary-layer equation has the following form:

$$\frac{\tau_w}{\rho} = yu_1 \frac{du_1}{dx} + \nu\frac{\partial u}{\partial y} + u \frac{\partial}{\partial x}\int_0^y u\,dy - uv_w - \frac{\partial}{\partial x}\int_0^y u^2\,dy \quad (1)$$

where (x,y) forms an orthogonal coordinate system with x measuring the distance along the cylindrical surface ($x = a\phi$, see Fig. 1), and (u,v) is the corresponding velocity vector.

τ, ρ, and ν signify, respectively, the shear stress, fluid density and kinematic viscosity. Conditions at the wall and the outer edge of the boundary layer are represented by w and 1, respectively.

Passing the upper limit of the integrals in (1) to the edge of the boundary layer, $y = \delta(x)$, we have the classical K-P equation, i.e.,

$$\frac{\tau_w}{\rho} = \delta u_1 \frac{du_1}{dx} + u_1 \frac{d}{dx}\int_0^\delta u\,dy - u_1 v_w - \frac{d}{dx}\int_0^\delta u^2\,dy \qquad (2)$$

Equation (2) expresses the momentum balance across the entire boundary layer at station x.

In the classical K-P technique, Equation (2) is the sole equation to be solved; the skin friction, τ_w, is directly taken from the derivative of the assumed velocity profile, u, i.e., $\rho\nu\frac{\partial u}{\partial y}\Big|_w$. Since the assumed profile can only be approximate, taking its local derivative is likely to incur significant error.

In the present approach, Equation (2) is merely used as an expression for the skin friction, and it is essentially an integral representation involving the assumed profile. A second equation is generated for the determination of the basic profile parameter, δ. The second equation is the second integration of the original momentum equation across the entire boundary layer. Physically speaking, the present method calculates the skin friction by considering the momentum balance in the entire boundary layer at a local flow

station, based on an assumed velocity profile. Thus, integrating Equation (1) again, we have

$$\frac{1}{2}\delta^2 u_1 \frac{du_1}{dx} + u_1\delta \frac{d}{dx}\int_0^\delta u\,dy - u_1 v_w \delta - \delta \frac{d}{dx}\int_0^\delta u^2\,dy$$

$$= \nu u_1 + \int_0^\delta u\,dy \frac{\partial}{\partial x}\int_0^y u\,dy - v_w \int_0^\delta u\,dy - \int_0^\delta dy \frac{\partial}{\partial x}\int_0^y u^2\,dy = 0 \quad (3)$$

The present procedure is to assume a velocity profile of the form

$$u = \sum_n k_n \eta^n \quad ; \quad \eta \equiv y/\delta \quad , \quad (4)$$

and substitute this profile into Equation (3). A first-order ordinary differential equation for the quantity δ results. The solution of δ is then used in Equation (2) to yield the skin friction through an algebraic process.

In all applications of the method to the calculation of surface properties, the profiles (velocity or temperature) are deliberately chosen to be simple in order to simplify the calculations. Thus, the coefficients in the polynomial, Equation (4), are constants in most cases. These profiles are obviously crude and oversimplified inasmuch as they presume similarity for general cases. However, it will be demonstrated that the present method can tolerate such improperly chosen profiles and still produce results with good accuracy. In fact, the simplified use of the method in the present development represents a full exploitation of the principal merits of the method.

We now specialize the above general formulation to the case of flow over an impermeable circular cylinder. Here we

have $u_1 = 2u_\infty \sin\phi$ and $v_w = 0$, where the subscript "∞" signifies the free-stream unperturbed state. For the present calculation, we use a simple polynomial for the velocity profile, i.e.,

$$\frac{u}{u_1} = 2\eta - 2\eta^3 + \eta^4 \tag{4a}$$

Note that this profile does nothing more than satisfying the essential boundary conditions of $u(x,0) = 0$ and $u(x,\delta) = 1$.

Substituting Equation (4a) into Equation (3) and introducing the following dimensionless quantities, $\bar{\delta} \equiv \delta/a$ and $A \equiv u_\infty a/\nu$, we can readily solve Equation (3) and express the solution for $\bar{\delta}$ in terms of the following quadrature:

$$A\,\bar{\delta}^2 = 16.3 \int_0^\phi \sin^{4.467}\phi \; d\phi/(\sin^{5.467}\phi) \tag{5}$$

The skin friction then follows readily from Equation (2),

$$\frac{1}{2} C_f A^{1/2} = (A^{1/2}\,\bar{\delta} \sin\phi)[0.8553 \cos\phi + 3.8292/(A\bar{\delta}^2)] \tag{6}$$

where $C_f \equiv \tau_w/(\frac{1}{2}\rho u_\infty^2)$ is the skin-friction coefficient.

Equations (5) and (6) represent the solution of skin-friction distribution on the cylindrical surface. The results are plotted in Figure 1 along with the results of previous calculations[2] using a linear profile, $f = \eta$. Exact (numerical) solutions due to Terrill[7] are also included in the figure for establishing the accuracy of the present solutions.

It is clear that the present solutions are remarkably accurate from the stagnation point to the point of separation ($\tau_w = 0$). However, it must be stressed here that the prediction

of separation point has only limited practical significance in view of the idealized flow model used. Of equal importance is the apparent weak dependence of the solution on the chosen profile, as indicated by the close agreement between the two solutions corresponding to two different profiles. This property represents another attractive feature of the present method, and is believed to be the result of using integral representations for the skin friction. The insensitivity has been previously noted and discussed by Zien[1,8] for the porous-plate configuration in light of the improvements on the classical K-P method achieved by the present refinement. The present new results serve to indicate that such insensitivity prevails in the case with pressure gradients.

An interesting comparison of the present and other approximate methods for skin-friction calculations is given by Inger[9].

3. CONVECTIVE HEAT TRANSFER

The basic ideas presented in the last section will now be applied to the calculation of heat transfer in a transpired boundary layer. The procedure is basically the same except that attention is now focused on the thermal boundary layer. Thus, the double integration scheme is applied to the original energy equation. The first integration gives an equation for the energy balance across the entire thermal boundary layer, and this equation is used as the expression for the wall heat flux. A second integration then provides the basic differential equation for the determination of the

parameter characterizing the assumed temperature profile. In order to present a self-consistent development of the calculation procedure, we shall also use the approximate solution for the velocity by the present method in the solution of the energy equation.

For easy demonstration of the procedure, we again consider the simple case of two-dimensional, laminar boundary layers. Only the results for an asymptotic flow corresponding to large Prandtl number and small surface mass transfer will be presented in this paper. The analytical derivation of such asymptotic limits is representative of the unique advantages of analytical methods. The derivation enhances physical understanding of the flow field and brings out similarity parameters to facilitate parametric studies. Results for moderate Prandtl numbers can be found in Reference 4, where a compressible case is also treated.

Neglecting the frictional heating, the first integration of the original energy equation in the direction normal to the wall gives

$$\frac{\partial}{\partial x}\int_0^y u^*\theta \, dy + \varepsilon(\theta - 1) - \theta \frac{\partial}{\partial x}\int_0^y u^* dy = \frac{\alpha}{u_\infty}\left(\frac{\partial \theta}{\partial y} - \frac{\partial \theta}{\partial y}\bigg|_w\right) \qquad (7)$$

where dimensionless temperature, θ, and velocity, u^*, are used, i.e., $\theta = (T - T_\infty)/(T_w - T_\infty)$ and $u^* = u/u_\infty$. ε is the mass transfer parameter defined as v_w/u_∞, and α is the thermal diffusity of the fluid.

Letting the limits of integration in Equation (7) cover the entire thermal boundary-layer thickness, δ_T, we get an expression for the Stanton number,

$$St \equiv \frac{N_x}{R_x P_r} = \frac{d}{dx}\int_0^{\delta_T} u^*\theta \, dy - \varepsilon \quad , \tag{8}$$

where $N_x = q_w x/k(T_w - T_\infty)$ is the Nusselt number, $R_x = u_\infty x/\nu$ is the Reynolds number, and $P_r = \nu/\alpha$ is the Prandtl number (k is the thermal conductivity of the fluid).

Equation (7) is integrated again across the entire thermal boundary layer to yield an equation for the determination of the basic profile parameter, δ_T. Thus, we have

$$\int_0^{\delta_T} dy \, \frac{\partial}{\partial x}\int_0^y u^*\theta dy + \int_0^{\delta_T} (\varepsilon - \frac{\partial}{\partial x}\int_0^y u^* dy)\theta \, dy$$

$$= \delta_T \frac{d}{dx}\int_0^{\delta_T} u^* \, \theta dy - \frac{\alpha}{u_\infty} \quad . \tag{9}$$

Since the momentum equation is decoupled from the energy equation for incompressible flows, u^* can be assumed known in the present calculation. Then Equations (8) and (9) combine to give the solutions of δ_T and St once a temperature profile, for example,

$$\theta = g(\eta_T) \quad , \quad \eta_T \equiv y/\delta_T \quad . \tag{10}$$

is introduced.

As an example of application of this method, let us consider the limit of large Prandtl number. In this limit, δ_T becomes vanishingly small relative to δ. Thus, heat transfer takes place in a very narrow region near the porous wall where the velocity distribution can be approximated by a

linear form, i.e.,

$$u^* = \frac{1}{2} C_f R_T \eta_T \tag{11}$$

where $R_T \equiv u_\infty \delta_T / \nu$.

Substitution of Equations (10) and (11) into Equation (9) leads to

$$\tilde{\alpha} R_T \frac{d}{dR_x} \left(\frac{1}{2} C_f R_T^2\right) = \frac{1}{P_r} + \tilde{\beta} \varepsilon R_T \tag{12}$$

The constants $\tilde{\alpha}$ and $\tilde{\beta}$ are profile-parameters defined as

$$\tilde{\alpha} = \int_0^1 \eta_T g(\eta_T) d\eta_T + \frac{1}{2} \int_0^1 \eta_T^2 g(\eta_T) d\eta_T - \int_0^1 d\eta_T \int_0^{\eta_T} \eta_T g(\eta_T) d\eta_T$$

and

$$\tilde{\beta} = \int_0^1 g(\eta_T) d\eta_T \ .$$

In Equation (12), the three terms from left to right represent, respectively, the effect of convection, conduction and mass transfer. As $P_r \to \infty$, an interesting limit exists in which these three mechanisms of heat transfer still remain in balance. Such a distinguished limit can easily be deduced from Equation (12) by requiring

$$R_T^3 R_x^{-3/2} \sim P_r^{-1} \sim \varepsilon R_T \ , \tag{13}$$

from which it follows that

$$\varepsilon R_x^{1/2} = 0(P_r^{-2/3}) \to 0 \tag{13a}$$

and

$$\varepsilon R_T = 0(P_r^{-1}) \to 0 \tag{13b}$$

Therefore, the transpiration rate, $\varepsilon R_x^{1/2}$, must be small compared to that allowed in the usual boundary-layer flows. Physically, this limit corresponds to the heat transfer in a nearly stagnant layer of fluid close to the solid surface with a small porosity.

In view of Equations (13a) and (13b), the following variables are appropriate for the study of this limiting flow:

$$\Lambda = P_r^{2/3} \varepsilon R_x^{1/2} = 0(1) \tag{14a}$$

and

$$\Lambda_1 = P_r \varepsilon R_T = 0(1) \tag{14b}$$

Thus, P_r and $\varepsilon R_x^{1/2}$ combine to form a single parameter, Λ, which characterizes the asymptotic heat transfer.

In the present integral formulation, the asymptotic solutions can readily be obtained by applying the limit process, Equations (14), to Equation (12).

We shall confine our discussion here to the case of a porous plate with similarity blowing (or suction). First of all, C_f takes on its value for a nonporous plate as the leading approximation. For the sake of self-consistency, we use the result given by Zien[1]. Thus, we have

$$\frac{1}{2}C_f = \frac{1}{3}R_x^{1/2} \quad , \tag{15}$$

corresponding to a linear velocity profile. We note that the results corresponding to a variety of profiles are virtually indistinguishable (see Zien[1,2]).

For the case of similarity flow, εR_T is constant, and Equation (12) can be easily integrated. The solution is

expressed in the parametric (closed) form:

$$\Lambda_1^3 = 6\Lambda^3(1 + \tilde{\beta}\Lambda_1)/\tilde{\alpha} \tag{16a}$$

and

$$N_x/(R_x^{1/2}P_r^{1/3}) = 6^{-1/3}\,\tilde{\gamma}\tilde{\alpha}^{-2/3}(1 + \tilde{\beta}\Lambda_1) - \Lambda \tag{16b}$$

where $\tilde{\gamma} = \int_0^1 \eta_T g(\eta_T)\,d\eta_T$ is another profile-parameter.

Two temperature profiles are used in the present calculation, i.e.,

$$\theta = g_1(\eta_T) = 1 - \eta_T \tag{17a}$$

and

$$\theta = g_4(\eta_T) = 1 - 2\eta_T + 2\eta_T^3 - \eta_T^4 \tag{17b}$$

which are again crude and oversimplified. $(\tilde{\alpha}, \tilde{\beta}, \tilde{\gamma})$ for g_1 and g_4 are (1/8, 1/2, 1/6) and (1/28, 3/10, 1/15), respectively.

The present solutions corresponding to g_1 and g_4 are plotted in Figure 2. Exact solutions to a class of self-similar flows in the same asymptotic limit have recently been obtained independently by Gersten[10], using a different approach. Figure 2 also includes the exact solution for comparison. Good accuracy and weak profile-dependence of the present solutions are again in evidence over a wide range of Λ. The present solutions can also be shown to reduce to the exact limit for large suction. Appreciable deviations from the exact solution occur only near thermal layer blow-off where the heat-transfer rate is very small. This is reminiscent of the

difficulty encountered in the skin-friction calculations near the blow-off point[1,2].

Solutions to a nonsimilar flow in the same limit as well as solutions for small Prandtl number flows appear in Reference 5.

The remarkable combination of simplicity and accuracy of the present method in the heat-transfer calculations is thus demonstrated. Application to compressible flows, though not yet extensively investigated, is a straightforward extension of the present procedure, and should not pose any essential difficulties.

4. TRANSIENT HEAT CONDUCTION WITH PHASE TRANSITION

In this section, the same basic ideas will be further developed to form an approximate method for studying a class of nonlinear problems in transient heat conduction. The problems considered in this paper are certain idealized models of melting and ablation which are the predominant features of re-entry heating. These simplified models of the problem have also been used by Goodman[11,12] in his application of the usual K-P method to nonlinear heat-conduction problems. A direct comparison of the results is thus possible, and the relative merits of the present method can be readily assessed.

4.1 Melting of Solid with Given Boundary Temperature

Consider first the problem of melting of a semi-infinite solid with the boundary temperature, T_o, held fixed at a constant value higher than the melting temperature of the solid. As a further simplification, assume that the solid is

initially maintained at the melting temperature, T_p, so that the temperature distribution in the solid after melting takes place need not be considered. This is usually a good approximation since the heat conductivity of a material is much greater in the solid phase than in the liquid phase.

The governing equation and the boundary conditions that describe the temperature distribution in the molten solid can be written as

$$\frac{\partial T}{\partial t} = \alpha \frac{\partial^2 T}{\partial x^2} \quad , \quad 0 < x < X(t) \quad , \quad t > 0 \tag{18}$$

$$T(0,t) = T_o \tag{19a}$$

$$T(X,t) = T_p \tag{19b}$$

$$-k \left.\frac{\partial T}{\partial x}\right|_X = \rho Q_L \frac{dX}{dt} \tag{19c}$$

and

$$T(x,0^-) = T_p \tag{19d}$$

In the above system, $x = X(t)$ denotes the location of the melting line which is unknown in advance, and α is the thermal diffusivity of the melt. Equation (19c) states the condition at the melting line that the heat flux into the solid portion provides the heat of fusion required to melt the solid. ρ and Q_L denote, respectively, the density and latent heat, and it is implicitly assumed that the density change associated with the phase change is negligible.

It is characteristic of the conduction problems involving a change of phase that a third boundary condition, i.e., Equation (19c), appears in the differential system which is of

second order. This is necessary because the boundary line, $X(t)$, is an additional unknown in the system.

Introducing the dimensionless temperature, θ, and a dimensionless parameter, μ, defined as

$$\theta \equiv \frac{T - T_p}{T_o - T_p} \tag{20a}$$

and

$$\mu \equiv 2\,\frac{k(T_o - T_p)}{\alpha \rho Q_L} = 2\,\frac{C_p(\Delta T)}{Q_L} \quad , \tag{20b}$$

we can rewrite the system, Equations (18) and (19), as follows:

$$\frac{\partial \theta}{\partial t} = \alpha\,\frac{\partial^2 \theta}{\partial x^2} \tag{21}$$

$$\theta(0,t) = 1 \tag{22a}$$

$$\theta(X,t) = 0 \tag{22b}$$

$$-\left.\frac{\partial \theta}{\partial x}\right|_X = \frac{2}{\alpha\mu}\,\frac{dX}{dt} \quad . \tag{22c}$$

The nonlinearity of the system can be made explicit by recognizing that Equation (22b) is equivalent to

$$\frac{D\theta}{Dt} \equiv \left.\frac{\partial \theta}{\partial t}\right|_X + \frac{dX}{dt}\left.\frac{\partial \theta}{\partial x}\right|_X = 0 \tag{23}$$

Thus, combining Equations (23) and (22c) and applying the original partial differential equation, (21), at $x = X(t)$ lead to an alternate boundary condition, i.e.,

$$\frac{\partial^2 \theta}{\partial x^2} = \frac{\mu}{2}\left(\frac{\partial \theta}{\partial x}\right)^2 \quad \text{at} \quad x = X(t) \quad , \tag{24}$$

where the nonlinearity is obvious.

We choose the same quadratic profile for θ as the one used by Goodman[11] so that a direct comparison of the results can be made,

$$\theta = a\left(1 - \frac{x}{X}\right) + (1 - a)\left(1 - \frac{x}{X}\right)^2 \qquad (25a)$$

with

$$a = \frac{2}{\mu}\left(-1 + \sqrt{1 + \mu}\right) \quad . \qquad (25b)$$

This profile satisfies the genuine boundary conditions, Equations (22a), (22b) and (24).

The first and second integrations of Equation (21) lead to the following equations:

$$-\alpha \left.\frac{\partial\theta}{\partial x}\right|_0 = \frac{d}{dt}\left(\int_0^X \theta\, dx + \frac{2}{\mu} X\right) \qquad (26)$$

and

$$\frac{d}{dt}\left[X\int_0^X \theta\, dx - \int_0^X dx \int_0^x \theta\, dx + \frac{1}{\mu} X^2\right] = \alpha \quad . \qquad (27)$$

The present formulation then provides three equations, i.e., Equations (22c), (26) and (27) for three unknowns, $X(t)$, $\left.\frac{\partial\theta}{\partial x}\right|_0$ and $\left.\frac{\partial\theta}{\partial x}\right|_X$, once Equation (25) is used as the profile. The problem is well-defined, and the heat fluxes at the boundary and the melting line are all to be obtained from the physical consideration of heat balance instead of the derivatives of the assumed profile. It should be noted that three equations are actually uncoupled, and their solutions pose no more difficulty than the solution of a single equation for a single unknown.

The solution for $X(t)$ is easily obtained by solving Equation (27) alone. It is case into the following form:

$$X(t)/2\sqrt{\alpha t} = \left[2\left(\frac{2}{\mu} + \frac{1}{3}a + \frac{1}{24}\mu a^2\right)\right]^{-1/2} \quad , \qquad (28)$$

where $a = a(\mu)$ is given by Equation (25b).

The heat flux, q_w, at the boundary x = 0 follows from Equation (26) with X(t) given by Equation (28). Thus, we have

$$q_w/(\rho Q_L \sqrt{\frac{\alpha}{t}}) = \frac{1}{2}\mu(\frac{X}{2\sqrt{\alpha t}})(\frac{1}{2}a + \frac{1}{12}\mu a^2 + \frac{2}{\mu}) \qquad (29)$$

Finally, the heat flux at the melting line, q_X, is given in terms of the melting speed, $\dot{X}(t)$, through Equation (22c).

Exact solution to the problem is available[13] in analytic form, thanks to the existence of similarity in the solution. This similarity structure is a result of the lack of a characteristic length in the given problem. A characteristic length would be present if the heat flux was prescribed at the boundary instead of the temperature (see Zien[6]).

The present solution for X(t), as given by Equation (28), is plotted in Figure 3(a) along with the corresponding exact solution from Carslaw and Jaeger[13], and the solution by Goodman[11] using the usual K-P method with the same temperature profile.

The accuracy of the present solutions is excellent, and is generally better than that of the usual K-P method, as is shown in Figure 3(a). The improvement is especially pronounced in the region where μ is moderately large. In re-entry applications, ΔT is very large, and μ is usually on the order of one or greater. Therefore, the improvement is of practical value.

It should be pointed out that in the usual K-P formulation of this problem, the quantities, $\left.\frac{\partial\theta}{\partial x}\right|_0$ and $\left.\frac{\partial\theta}{\partial x}\right|_X$ are all

obtained directly from the derivatives of the assumed profile. The only basic unknown is X(t). However, two equations, Equations (26) and (22c) are available for the solution of X(t), resulting in a difficult chcice. This annoying difficulty was also recognized by Goodman[11], and he has actually presented solutions from the two different equations. The difference is quite appreciable in the region of moderate values of μ. To remedy this difficulty, Goodman[11] proposed a third-degree polynomia. with an additional parameter to be determined by the extra equation. The profile has the form shown below:

$$\theta = b\left(1 - \frac{x}{X}\right) + \frac{\mu}{4} b^2 \left(1 - \frac{x}{X}\right)^2 + \left(1 - b - \frac{\mu}{4} b^2\right)\left(1 - \frac{x}{X}\right)^3 \quad , \qquad (30)$$

where b is the additional profile parameter.

The present approach is obviously free from such a difficulty. However, for the purpose of testing the sensitivity of results to the variation of profiles, we have also calculated the results for the profile given in Equation (30). In this calculation, we use the derivative of the assumed θ profile for $\left.\frac{\partial\theta}{\partial x}\right|_X$ in Equation (22c) so that the three equations, (22c), (26) and (27), define the solutions for the three unknowns, b, X(t) and $\left.\frac{\partial\theta}{\partial x}\right|_0$.

Thus, we obtain from Equations (22c) and (27) the solutions for b and X(t) as follows:

$$b^3\mu^2 + 2(7b + 3)\, b\mu + 120(b - 1) = 0 \qquad (31a)$$

and

$$X/2\ \sqrt{\alpha t} = \frac{1}{2}\ \sqrt{\mu b} \qquad (31b)$$

The result is also plotted in Figure 3(a). It is seen that in the region of μ covered in the figure, the result is virtually indistinguishable from that corresponding to the quadratic profile, Equation (25). Therefore, the highly desirable property of the approximate solution, i.e., the insensitivity of results to profiles, is again in evidence. This property constitutes a significant improvement to the classical K-P method. The comparison of the results for q_w is very similar to that shown in Figure 3(a), and can be found in Reference 6.

Another approximate method for solving the melting problem has been proposed by Sharma, Rotenberg and Penner[14] based on a partial satisfaction of the differential equations and boundary conditions. Depending on the degree these original equations are satisfied, the method can provide higher approximations (not in a systematic sense) but with increasing complexity. Kulyapin[15], apparently unaware of the work of Reference 14, alsc proposed a method recently which is basically equivalent to the lowest approximation of Sharma, et al.[14]. The solutions by the method of References 14 and 15 for the melting problem considered here are compared with the present solutions in Figure 3(b). It can be seen that only the highest approximation of Reference 14 has an accuracy close to the present method. The large discrepancy of the results corresponding to different degrees of approximation in Reference 14 is to be noted.

4.2 Idealized Model for Ablation

Consider the problem of melting of a semi-infinite solid due to a constant heat flux, q_o, applied at the boundary, with the melt instantaneously and completely removed upon formation. This is an idealized model of aerodynamic ablation usually encountered in the flight of high-speed vehicles. For example, during re-entry the aerodynamic shear force on the body could effectively wipe away the melt upon its formation. The solid is assumed to have a uniform initial temperature, T_∞, before the application of q_o. The problem actually consists of two parts: a pre-ablation period during which the boundary is being heated up to the melting temperature, and a post-ablation period during which the melting is progressing with the melting line acting as the new, moving boundary. For the pre-ablation part, the problem is linear and can be treated either exactly by standard techniques or approximately by the present method. The post-ablation part is the primary subject of study here.

Historically, Landau[16] was the first to present numerical solutions to this idealized ablation problem. Using the usual K-P method, Goodman[11] obtained approximate solutions to this problem with a polynomial form of temperature profile. Most recently, Vallerani[17] studied the more general case of a heat flux of the form $q_o \sim t^m$ by the usual K-P method, but with an exponential form for the temperature profile.

We shall apply the refined K-P method here to the idealized problem with a temperature profile identical to that used by Goodman[11], and introduce a thermal penetration depth, $\delta(t)$.

The post-ablation period is considered here. At $t = 0$ the melting line begins to proceed in the x direction, i.e., $X(0) = 0$. However, the thermal penetration depth is finite and equal to δ_p, due to the pre-ablation heating effect.

The basic differential system describing heat conduction in the solid is as follows:

$$\frac{\partial T}{\partial t} = \alpha \frac{\partial^2 T}{\partial x^2} \quad ; \quad X < x < \delta \quad , \quad t > 0 \tag{32}$$

$$T(X,t) = T_p \tag{33a}$$

$$T(\delta,t) = T_\infty \tag{33b}$$

$$q_o = -k \left.\frac{\partial T}{\partial x}\right|_X + \rho Q_L \frac{dX}{dt} \tag{33c}$$

The last equation states the fact that the heat input, q_o, is equal to the heat flux into the solid plus the rate of heat absorption in the melting process. Strictly speaking, an initial temperature distribution immediately before ablation is needed to complete the formulation. In the integral approach, this initial condition is implicitly specified by the form of the prescribed profile used in the calculation.

From the parameters appearing in the system, Equations (32) and (33), a characteristic length, ℓ_c, and a characteristic time, t_c, can be found, i.e.,

$$\ell_c = \frac{k(\Delta T)}{q_o} \quad , \quad t_c = \frac{\rho k (\Delta T) Q_L}{q_o^2}$$

where $\Delta T \equiv T_p - T_\infty$. Following the notations of Goodman[11], we shall use the dimensionless quantities defined below in the ensuing calculations:

$$\theta \equiv \frac{T - T_\infty}{T_p - T_\infty}$$

$$\tilde{\nu} \equiv \frac{Q_L}{C_p(\Delta T)} \quad , \quad \zeta \equiv \frac{q_o(\delta - X)}{k(\Delta T)} \quad , \quad \lambda \equiv \frac{q_o X}{k(\Delta T)}$$

together with dimensionless length and time defined as

$$\xi \equiv \frac{x}{\ell_c} \quad \text{and} \quad \tau \equiv \frac{t}{t_c}$$

In the dimensionless formulation, the equation and boundary conditions take the form given below.

$$\frac{\partial \theta}{\partial \tau} = \tilde{\nu} \frac{\partial^2 \theta}{\partial \xi^2} \quad , \lambda < \xi < \lambda + \zeta \tag{34}$$

and

$$\theta(\lambda, \tau) = 1 \tag{35a}$$

$$\theta(\zeta + \lambda, \tau) = 0 \tag{35b}$$

$$\left.\frac{\partial \theta}{\partial \xi}\right|_\lambda + 1 = \frac{d\lambda}{d\tau} \tag{35c}$$

The temperature profile is assumed to be

$$\theta = \left(1 - \frac{x - X}{\delta - X}\right)^2 = \left(1 - \frac{\xi - \lambda}{\zeta}\right)^2 \tag{36}$$

which has two parameters, $\delta(t)$ and $X(t)$, and satisfies the genuine boundary conditions, Equations (35a) and (35b), and an additional condition of $\left.\frac{\partial \theta}{\partial x}\right|_\delta = 0$.

Proceeding with the refined K-P method of solution, we obtain from the first and second integration of Equation (34) the following two equations:

$$\frac{d}{d\tau}\left[\frac{1}{3}\zeta + (1 + \tilde{\nu})\lambda\right] = \tilde{\nu} \tag{37}$$

and

$$\zeta \frac{d}{d\tau}(\zeta + 2\lambda) = 6\tilde{v} \tag{38}$$

The limits of integration here are from $\xi = \lambda$ to $\xi = \lambda + \zeta$. Also, Equation (35c) has been used in deriving Equation (37).

Equations (35c), (37) and (38) are to be solved for the three unknowns, $\zeta(\tau)$, $\lambda(\tau)$ and $\left.\frac{\partial\theta}{\partial\xi}\right|_{\lambda}$.

Equations (37) and (38) are first easily integrated to give the following parametric solutions for $\lambda(\tau)$ and $\xi(\tau)$:

$$\tau = -\frac{1}{3}\frac{1 + 3\tilde{v}}{2\tilde{v}}\left[\zeta - \zeta_p + 3(1 + \tilde{v})\ell n \frac{\zeta - 3(1 + \tilde{v})}{\zeta_p - 3(1 + \tilde{v})}\right] \tag{39}$$

and

$$\lambda = \frac{1}{1 + \tilde{v}}\left[\tilde{v}\tau - \frac{1}{3}(\zeta - \zeta_p)\right] \quad , \tag{40}$$

where the conditions $\lambda(0) = 0$ and $\zeta(0) = \zeta_p$ have been imposed, ζ_p being the initial thermal penetration depth determined from the pre-ablation solution. The solution of the heat flux into the solid at the melting line, $\sim \left.\frac{\partial\theta}{\partial\xi}\right|_{\lambda}$, can be obtained from Equation (35c) using $\lambda(\tau)$ given by Equations (39) and (40). For the present discussion, we only need solutions for $\lambda(\tau)$ and $\zeta(\tau)$.

The exact solution for the steady state can be easily derived as follows. We seek a solution of the ablation problem in which the ablation line moves at a constant velocity, V (dimensionless), and the temperature field appears steady in a coordinate system (ξ',τ') moving with the ablation line. The transformation from (ξ,τ) to (ξ',τ') is simply $\xi' = \xi - V\tau$ and $\tau' = \tau$. Therefore, Equation (34) transforms into (ξ',τ') system as

$$-V \frac{\partial \theta}{\partial \xi'} = \tilde{\nu} \frac{\partial^2 \theta}{\partial \xi'^2} \qquad 0 < \xi' < \infty \tag{41}$$

The exact boundary conditions (see Eqns. (35a-c)) become $\theta(0,\tau') = 1$, $\theta(\infty,\tau') = 0$ and $\frac{\partial \theta}{\partial \xi'}(0,\tau') = V - 1$.

Therefore, integrating Equation (41) from $\xi' = 0$ to $\xi' = \infty$ gives

$$V = \frac{\tilde{\nu}}{1 + \tilde{\nu}} \tag{42}$$

which is the limiting solution given by Landau[16].

The steady-state solution can also be readily obtained by letting $\tau \to \infty$ in the present solutions. It can be shown that this limit corresponds to $\tau \to 3(1 + \tilde{\nu})$, and that the limiting solution is independent of ζ_p and is given by

$$\frac{\lambda}{\tau} = \frac{\tilde{\nu}}{1 + \tilde{\nu}} \quad . \tag{43}$$

which is identical to Equation (42).

For solution near $\tau = 0$, the controlling parameter is ζ_p, the initial thermal penetration depth. The approximate solution in this initial period is very critically dependent on ζ_p.

The solutions of $\lambda(\tau)$ have been calculated using two values of ζ_p. First, we use the approximate solution of the present method with a quadratic profile, and we get $\zeta_p = 8/3$. The second choice of ζ_p is based on the combined use of exact solution of the pre-ablation problem and the present solution for the penetration depth corresponding to the quadratic profile. For this choice, we have $\zeta_p = \sqrt{2\pi}$. (See Ref. 6 for details.)

Solutions of $\lambda(\tau)$ are plotted in Figures 4 and 5 for $\tilde{v} = \frac{\sqrt{\pi}}{2}$ and $\tilde{v} = \frac{\sqrt{\pi}}{10}$, respectively, for which the corresponding solutions of Landau[16] (exact in numerical sense) are available for comparison. Goodman's solutions[11] are also included in the figures for reference. We note that Landau's results were presented in graphical form in Reference 16. For the present purpose, these results are carefully replotted, using an interpolator. It is clear that the present approximate solutions are generally better than Goodman's approximate solutions, especially for moderate and large values of τ. For small τ, both approximate solutions are sensitive to ζ_p. The second choice of ζ_p, i.e., $\zeta_p = \sqrt{2\pi}$, gives much improved results for the present method. This finding seems to suggest that it is advisable to use the exact solution for the pre-ablation part of the problem if a high accuracy in the small time solution is desired. This should not be difficult because the pre-ablation problem is linear. Therefore, exact solution can usually be obtained by standard methods with ease.

The accuracy in the ablation rate, $\frac{d\lambda}{d\tau}$, can be inferred from Figures 4 and 5. It is noted here that the accuracy of the present solutions is generally good except very near $\tau = 0$. The present solutions predict a finite initial ablation rate, whereas the exact solution[16] gives zero initial rate but an infinite acceleration for $\tilde{v} > 0$.

5. CONCLUDING REMARKS

The primary objective of this paper is to present a simple method for the approximate calculation of aerodynamic properties, particularly aerodynamic heating. Representative applications of this method given in the paper include calculations of skin friction, convective heat transfer in transpired boundary layers and transient heat conduction in the presence of a phase transition.

The analytical nature of the method provides considerable physical insight into various problems in the solution process, and thus facilitates the understanding of the physical phenomena under investigation. The remarkable combination of simplicity and accuracy represents the principal merit of the method. The general weak profile-sensitivity of the solution is equally significant. It allows accurate solutions to be generated without an advance knowledge of the structure of the exact solution, and thus makes the method practical.

Although applications of the method have been made only to idealized problems, the essential features of the general and realistic problems are all retained in the idealized models. Therefore the applicability, as well as limitations, of the method can be assessed on reasonably general grounds, based on the results obtained for these idealized cases.

The applications illustrated in this paper constitute the basic elements of an approximate procedure for the entire aerodynamic heating analysis. From the simplicity associated with each individual element, the practicality of the

integrated procedure can be inferred. This approximate method should be particularly useful for parametric studies in the preliminary design of various high-speed vehicles.

REFERENCES

1. Zien, T. F., "A New Integral Calculation of Skin Friction on a Porous Plate," AIAA Journal, Vol. 9, Jul 1971, pp. 1423-1425
2. Zien, T. F., "Skin Friction on Porous Surfaces Calculated by a Simple Integral Method," AIAA Journal, Vol. 10, Oct 1972, pp. 1267-1268
3. Volkov, V. N., "A Refinement of the Karman-Pohlhausen Integral Method in Boundary-Layer Theory," Inzhenerno-Fizicheskii Zhurnal, Vol. 9, No. 5, 1965, pp. 583-588 (English translation in Journal of Engineering Physics, Vol. 9, No. 5)
4. Zien, T. F., "An Approximate Calculation of Heat Transfer in Transpired Boundary Layers," NOLTR 73-17, Feb 1973
5. Zien, T. F., "Approximate Analysis of Heat Transfer in Transpired Boundary Layers at Limiting Prandtl Numbers," NOLTR 74-121, Jul 1974 (to appear in INT. Journal of Heat Transfer)
6. Zien, T. F., "An Integral Approach to Transient Heat-Conduction Problems with Phase Transition, NSWC/WOL/TR 75-37, Mar 1975
7. Terrill, R. M., "Laminar Boundary-Layer Near Separation With and Without Suction," Philosophical Transactions of the Royal Society, London, Vol. A253, Sep 1960, pp. 55-100

8. Zien, T. F., "Reply by Author to D. A. MacDonald," AIAA Journal, Vol. 10, No. 12, Dec 1972, pp. 1724-1725

9. Inger, G. R., "Comment on 'Skin Friction on Porous Surfaces Calculated by a Simple Integral Method,'" AIAA Journal, Vol. 11, No. 9, Sep 1973, pp. 1356-1357

10. Gersten, K., "Wärme- und Stoffübertragung bei großen Prandtl-bzw. Schmidtzahlen," Wärme- und Stoffübertragung, Vol. 7, 1974, pp. 65-70

11. Goodman, T. R., "The Heat-Balance Integral and Its Application to Problems Involving a Change of Phase," Trans. ASME, Vol. 80, Feb 1958, pp. 335-342

12. Goodman, T. R., "Application of Integral Methods to Transient Nonlinear Heat Transfer," Advances in Heat Transfer, Vol. 1, 1964, pp. 51-122

13. Carslaw, H. S. and Jaeger, J. C., Conduction of Heat in Solids, 2nd edition, Oxford University Press, London, 1959

14. Sharma, O. P., Rotenberg, M. and Penner, S. S., "Phase-Change Problems with Variable Surface Temperatures," AIAA Journal, Vol. 5, No. 4, Apr 1967, pp. 677-682

15. Kulyapin, V. M., "Some Problems of Heat Conduction with Phase Transitions," Journal of Engineering Physics, Vol. 20, No. 3, Sep 1973, pp. 362-367

16. Landau, H. G., "Heat Conduction in a Melting Solid," Quart. Appl. Math., Vol. 8, 1950, pp. 81-94

17. Vallerani, E., "Integral Technique Solution to a Class of Simple Ablation Problems," Meccanica, Vol. 9, Jun 1974, pp. 94-101

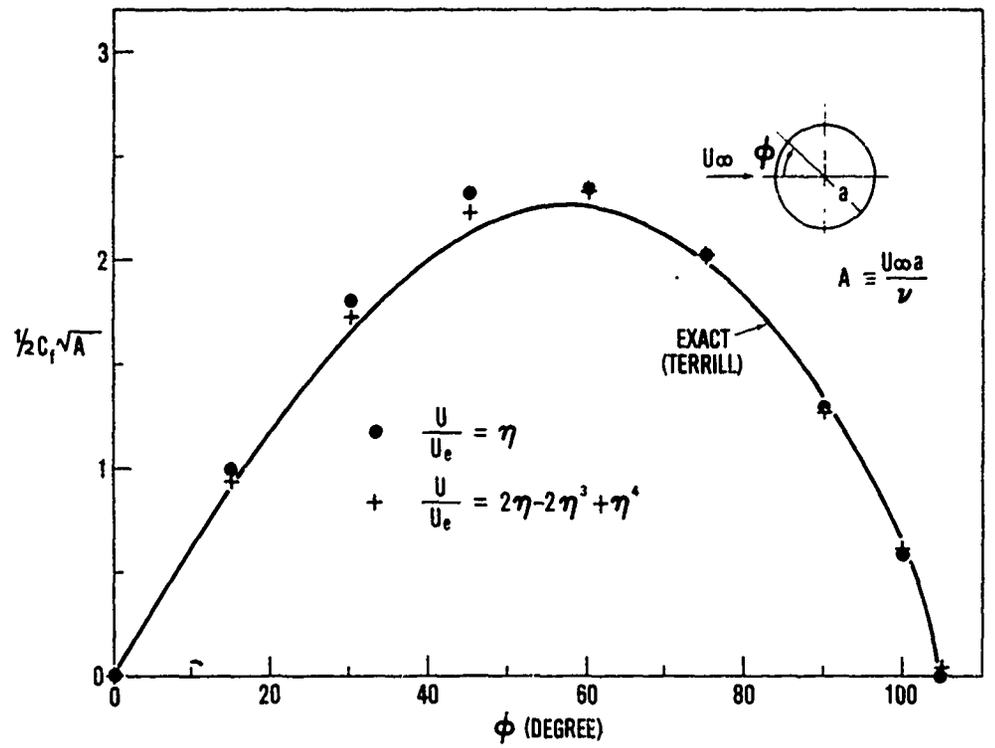

FIG. 1 SKIN FRICTION ON AN IMPERMEABLE CIRCULAR CYLINDER

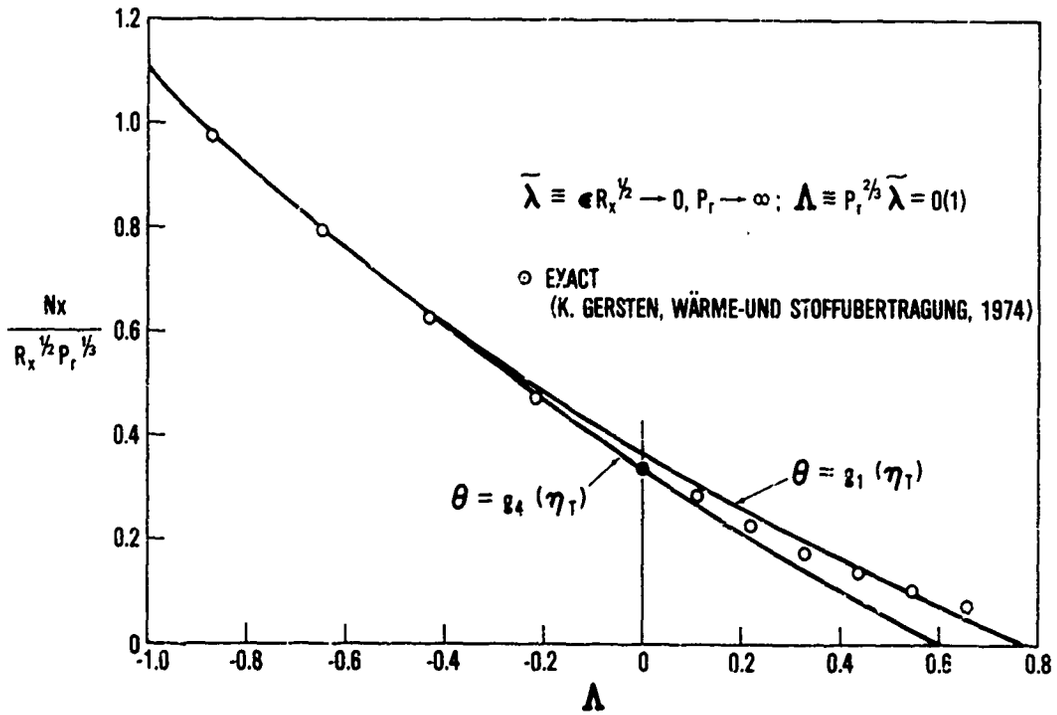

FIG. 2 ASYMPTOTIC HEAT TRANSFER ON A POROUS PLATE

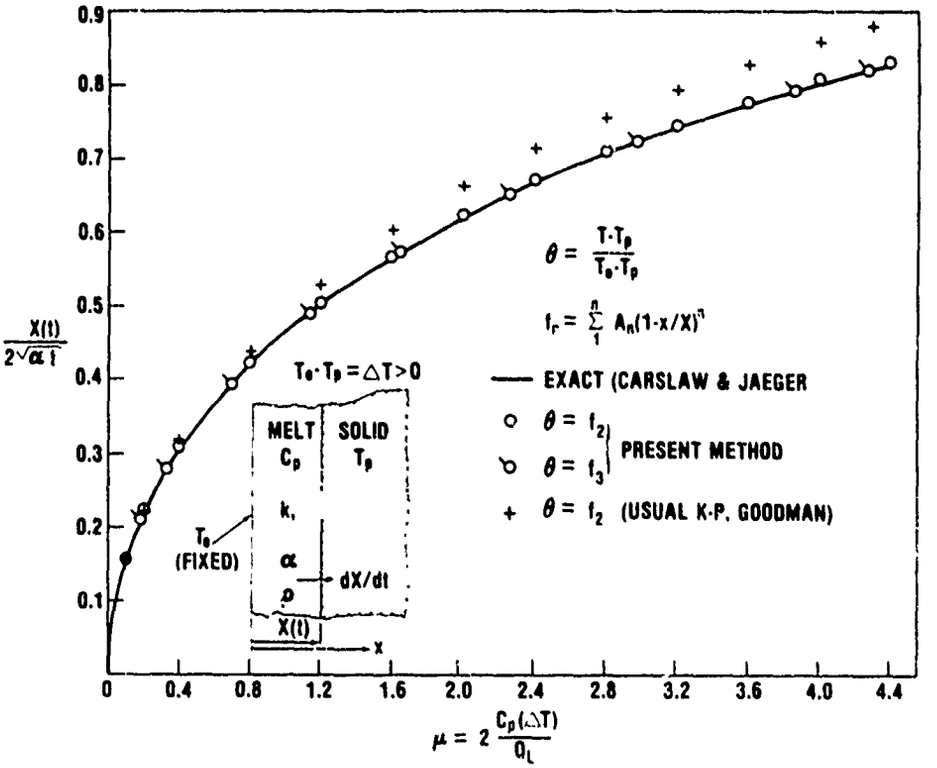

FIG. 3(a) MELTING OF SEMI-INFINITE SOLID - LOCATION OF MELTING LINE

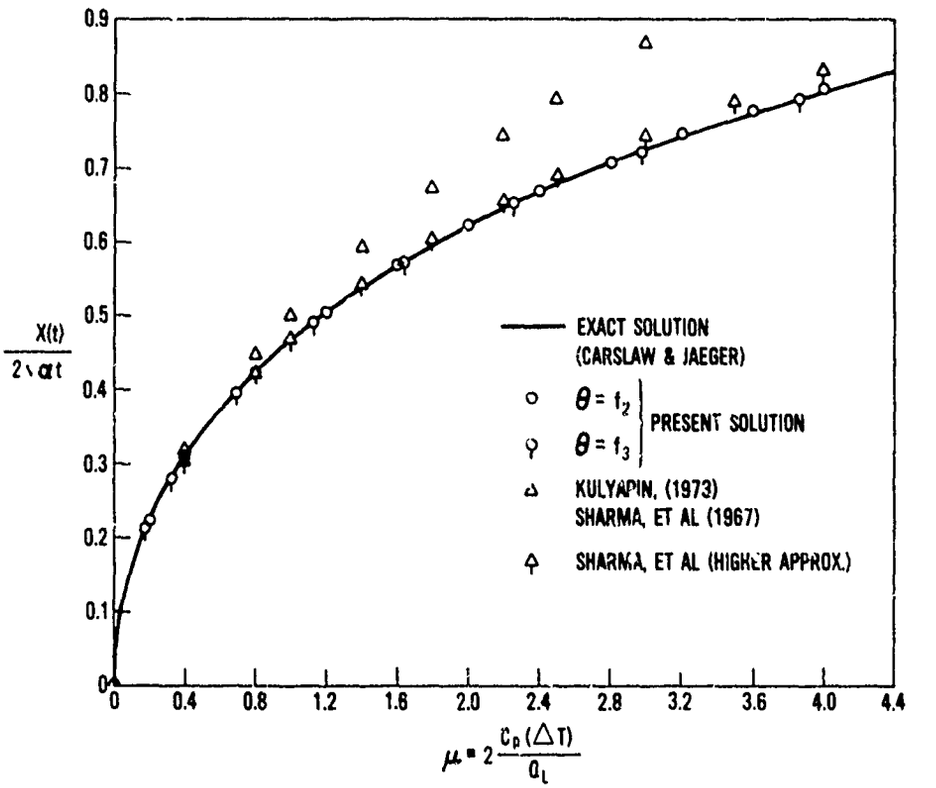

FIG. 3(b) MELTING OF SEMI-INFINITE SOLID - LOCATION OF MELTING LINE

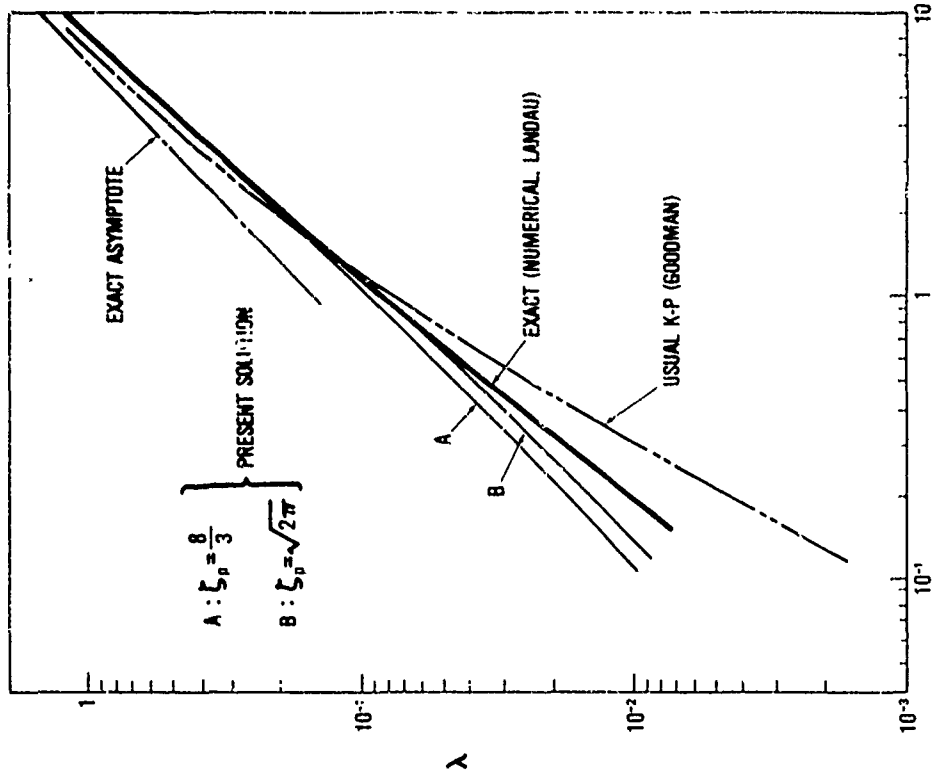

FIG. 5 IDEALIZED ABLATION - SURFACE LOCATION
($\tilde{v} = \sqrt{\pi}/10$)

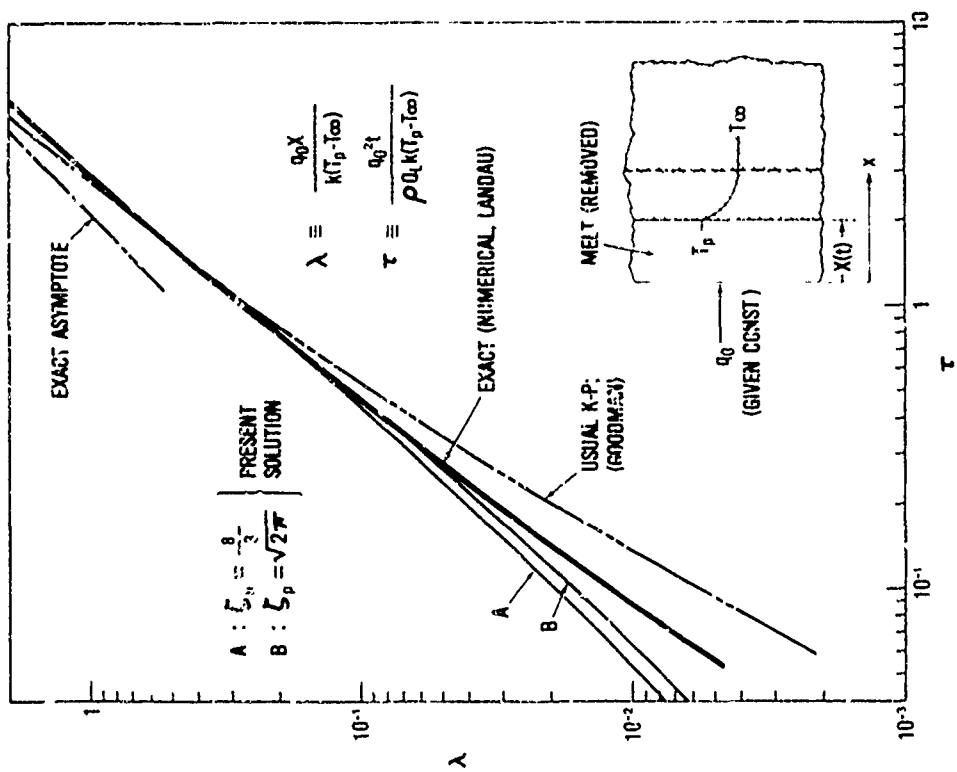

FIG. 4 IDEALIZED ABLATION - SURFACE LOCATION
($\tilde{v} = \sqrt{\pi}/2$)

PAPER NO. 21

For

The Tenth Navy Symposium on Aeroballistics

July 15, 1975

Structural Studies of Rough Wall Boundary Layers

by

Dr. Robert J. Moffat
Department of Mechanical Engineering
Stanford University
Stanford, California

Supported by
The Office of Naval Research
Contract N00014-67-A-0112-0072

Foreword

The study reported here is experimental: its output consists of approximately 200 pages of tabular and graphical data. It is the intent of the present paper to outline the range of available data and to illustrate the principal trends. To this end, most of the figures in the present paper are line representations of the data, for compactness, clarity, and economy. Serious users are invited to obtain copies of the complete report either by writing directly to the author, or by referring to the doctoral thesis of Marcos de Mattos Pimenta, Stanford, 1975, through University Microfilms, Ann Arbor, Michigan. Your inquiries will be most welcome.

Acknowledgements

The present program was begun under the auspices of Dr. W. H. Thielbahr, China Lake Naval Weapons Center and has been extended in scope and continued under the support of the Office of Naval Research, Power Section, through the efforts of Mr. James Patton and Dr. Ralph Roberts under contract N00014-67-A-0112-0072.

Nomenclature

$c_f/2$	Friction factor, $g_c\tau_w/\rho_\infty U_\infty^2$
c_p	Specific heat at constant pressure
δ	Thickness of the velocity boundary layer, $\bar{U} = 0.99$
δ_1	Displacement thickness, $\int_0^\infty (1 - \frac{\rho U}{\rho_\infty U_\infty})dy$
δ_2	Momentum thickness, $\int_0^\infty \frac{\rho U}{\rho_\infty U_\infty}(1 - \frac{\rho U}{\rho_\infty U_\infty})dy$
Δ_2	Enthalpy thickness, $\int_0^\infty \frac{\rho U}{\rho_\infty U_\infty}(\frac{i_\infty - i}{i_\infty - i_w})dy$
ε_H	Eddy diffusivity for heat
ε_M	Eddy diffusivity for momentum
F	Blowing fraction, $\rho V/\rho_\infty U_\infty$
G	Shape factor, Clauser sense, see Eq'n. (3)
g_c	Gravitational constant
h	Heat transfer coefficient
H	Shape factor, Karman sense, δ_1/δ_2
i	Enthalpy, here taken as c_pT
i_w	Enthalpy at wall temperature, $c_p T_w$
i_∞	Enthalpy at free stream temperature, $c_p T_\infty$
κ	Mixing length constant, $\ell = \kappa y$
ℓ	Mixing length
Pr_t	Turbulent Prandtl number, $\varepsilon_M/\varepsilon_H$
q^2	Turbulence kinetic energy, $(\overline{u'^2} + \overline{v'^2} + \overline{w'^2})$
r	Radius of spherical surface elements
ρ_∞	Density of the free stream fluid

St	Stanton number, $h/\rho_\infty U_\infty c_p$
$\overline{T}$	Dimensionless temperature, $(T_w - T)/(T_w - T_\infty)$
t'	Temperature fluctuation
T_τ	Dimensionless temperature, $(T_w - T_\infty)St/\sqrt{c_f/2}$
τ	Shear stress
τ_w	Wall value of shear stress
U	Velocity in x-direction
U_∞	Free stream velocity
U_τ	Shear velocity, $\sqrt{g_c \tau_w/\rho_\infty}$
$\overline{U}$	Dimensionless velocity, U/U_∞
u'	Velocity fluctuation, x-direction
V	Velocity in the y-direction, normal to the plane of the wall
v'	Velocity fluctuation, y-direction
w'	Velocity fluctuation, z-direction
x	Downstream
y	Perpendicular to the wall
y^+	Dimensionless y-position, yU_τ/ν

STRUCTURAL STUDIES OF A ROUGH WALL BOUNDARY LAYER

This paper summarizes an experimental study of the structure of the turbulent boundary layer on a deterministically rough surface subject to heat transfer and transpiration. Data are presented for the heat transfer and friction behavior, as well as profiles of mean velocity and mean temperature and turbulence quantities including the turbulent shear stress and heat flux.

The heat transfer and friction behavior of surfaces is strongly affected by roughness. The difference between smooth and rough values can reach a factor of 3 or 4, or even more depending upon the situation. System design studies aimed at predicting drag or cooling requirements are subject to large uncertainties because no generally valid model of rough surface behavior is as yet available. One reason for the lack of a general model is that the problem is very complex. Surface roughness can take many forms and the shape of the roughness elements affects the interaction, as well as their size. A second reason, however, is that the bulk of the roughness data now in the literature does not include the kind of information needed as input to the modern boundary layer prediction programs. Most of the roughness data in the literature were taken prior to the emergence of finite difference methods. The overall effects of roughness were noted, but not the sort of data needed to deduce the closure relationships. Existing data were, for the most part, aimed at supporting integral methods, or purely correlative efforts. Modern methods are mainly finite-difference equation solvers, and require empirical "closure" schemes to calculate the turbulent transports. The

existing data do not, therefore, provide as good a basis for comparing two models as would be desired, or for developing a new one. Many different models could yield the same heat transfer or friction behavior over a small range of conditions (matching available data) and yet predict widely different results under system design conditions (predicting service behavior). A better test of the validity of a turbulence model would be to require it to satisfactorily predict not only the surface heat transfer and friction behavior, but also the distributions of mean velocity and temperature and other, "higher order", properties of the flow. This requires an extensive data set containing information at different levels concerning the same flow situation.

The present data set is aimed at this problem. The intent was to compile an in-depth picture of the behavior of a reproducible test case, permitting evaluation of models of different levels of sophistication.

The present program at Stanford envisages use of closure models up to and including the various two-equation turbulence models and some examples of Reynolds stress closure. To support these efforts, it was deemed necessary to acquire data at each of the levels of information shown in Figure 1: Stanton number, friction factor, mean velocity distribution, mean temperature distribution, integral parameters, turbulent Prandtl number variation, and first and second levels of turbulence quantities. We have not, at present, proposed a model. The effort has been to collect a coherent and complete set of data and make this data available as a reference set against which to test future models. The complete work upon which this summary is based is by Pimenta [1].

The Physical Situation

The surface used in these studies is shown in Figure 2. It consists of spherical particles 1.25 mm in diameter brazed together in a most dense array with the crests of the balls all lying in one plane. A total of 8.5 million balls were brazed into plates 12.8 mm thick. These were arranged to make a test plate 2.4 meters long and 0.46 meters wide, divided into 24 segments each 0.1 meter in the flow direction. Each of the 24 segments comprised an independent test unit, equipped with imbedded electric heaters, controllable transpiration flow, and temperature instrumentation. The apparatus has been described in detail by Healzer [2].

The test plate was installed as the bottom surface in a closed loop wind tunnel capable of attaining wind speeds up to 75 m/s. A secondary blower provided transpiration flow at up to 0.75 m/s. Both the main flow and the transpiration flow were air.

Heat transfer from the surface was measured by energy balance, using the measured electrical power to the plate heaters and correcting for heat losses by radiation and conduction. Boundary layer data were acquired using one hot wire anemometer probe for both velocity and temperature data, with two separate electronic channels: one for the velocity data and one for the temperature data. This sequential technique eliminates positional ambiguity in matching temperature and velocity profiles.

Friction Factor and Heat Transfer

Figures 3 and 4 show friction factor and Stanton number data for the rough surfaces, in two different coordinates: x-Reynolds number and boundary layer thickness. Note that in x-Reynolds number coordinates the rough wall behavior is markedly velocity-dependent, for both friction factor and

Stanton number. For the present surface, velocities above about 15 m/s produce "fully rough" behavior with the result that friction factor and Stanton number become independent of free stream velocity, varying only with the boundary layer thickness. The same data shown plotted versus boundary layer thickness shows no velocity dependence once the fully rough state is attained. Velocities higher than 40 m/s have been run in other studies, and the results coincide with the data shown here for 27 and 40 m/s. The choice of ball-radius, r, as the relevant scaler was arbitrary.

The behavior shown in these two figures is typical of fully rough and transitionally rough behavior. Values derived from previous work on sand grain or "k"-type roughness, accepted in the literature, support these results. It can therefore be accepted that the structural details reported in the following sections are, in fact, the structural details of a fully rough boundary layer flow of a conventional nature. The structures found here can be regarded as typical of "sand grain" type roughnesses.

Friction factor is seen to be a function only of the boundary layer thickness, in the fully rough state. The velocity profiles are invariant in velocity defect coordinates and friction factor has been shown, by these studies and others, to be a unique function of momentum thickness, for a given surface.

A good approximation to $C_f/2$ for the present surface is:

$$\frac{C_f}{2} = 0.00328\left(\frac{\delta_2}{r}\right)^{-0.175} \qquad (1)$$

This is one of many relationships which fit the data in Figure 3: its coefficient and exponent were selected to best match the behavior at large values of δ_2.

Stanton number is also a function only of the boundary layer thickness, and can again be approximated by a simple form involving the enthalpy thickness:

$$St = 0.00317\left(\frac{\Delta_2}{r}\right)^{-0.175} \qquad (2)$$

These results apply only within the range of boundary layer thickness shown in Figures 3 and 4. There is evidence within these figures, and in the turbulence structure data, to suggest that the boundary layer over a given rough surface might be capable of attaining a truly asymptotic state (constant friction factor and constant Stanton number) if allowed to run long enough along the surface. Such behavior has been predicted for certain types of roughness ("d"-type, according to Perry and Joubert [3] but not previously attributed to "k"-type roughness.

Distribution of Mean Velocity and Temperature

Figure 5 shows three views of the mean velocity distribution in a rough wall boundary layer. In 5a, the smooth wall "Law of the Wall" is compared with rough-wall behavior, in inner region coordinates suitable for discussion of the rough-wall problem. In this figure the distance "y" is measured from the crests of the balls and no correction has been applied. One may, if desired, add a correction, Δy, to the value of y to simulate the effect of a plane wall submerged Δy beneath the crests of the balls. Such an exercise will result in straightening out the curvature of the profile shown in Figure 5a and the slope of the resulting straight line agrees with the "law of the wall" slope. In velocity-defect coordinates typical rough and smooth profiles are identical in the outer region, from y/δ of 0.01 to 1.0 as shown in Fig. 5b.

Use of a y-shift of 0.006 in. conceals one aspect of the data: the absence of viscous effects above the crests of the balls. The data point at $y/\delta = 0.01$ actually lay at $y/\delta = 0.005$ measured from the crests of the balls. The third view shows the general shape of smooth and rough profiles, compared at the same x-Reynolds number. Note, in particular, the absence of the knee in the velocity profile. There is no region of large velocity gradient visible within the layer above the roughness elements.

Figure 6 shows the mean temperature distribution in a typical rough-wall boundary layer. The distribution of temperature is similar to the distribution of velocity but does not extrapolate to zero at the same y-location. This is shown in Figure 6b which plots $\overline{T}$ versus $\overline{U}$ directly. The line is straight everywhere inside $\overline{U} = 0.9$ but flies above $\overline{U}$ in the inner region. At the location where $\overline{U}$ extrapolates to zero, $\overline{T}$ is still nearly 0.1 instead of zero. This is distinctly different from the behavior of a smooth-wall boundary layer, also shown, where $\overline{T}$ lies below $\overline{U}$ in the inner region, and approaches zero with $\overline{U}$.

This behavior of the $\overline{T} - \overline{U}$ plot lends support to the idea of modeling the rough-wall heat transfer using a "stagnant film" or "conduction-layer" within the roughness elements. It is in this region that molecular effects can be found: below the crests of the roughness elements.

Shape Factor, Mixing Length, and Turbulent Prandtl Number

The shape factor for the fully rough boundary layer can be discussed either in the Karman sense, $H \triangleq \delta_1/\delta_2$, or the Clauser sense, G, as defined below

$$G \triangleq \frac{\sqrt{C_f/2}}{\delta_1} \int_0^\infty \left(\frac{U_\infty - U}{U_\tau}\right)^2 dy \approx 6.7 \qquad (3)$$

or

$$H \triangleq \frac{\delta_1}{\delta_2} \approx 1.45 \tag{4}$$

The factors G and H are related by

$$H = \frac{1}{1 - G\sqrt{\frac{C_f}{2}}} \tag{5}$$

Measured variations of H with length are shown in Figure 7a for two different velocities, both in the fully rough regime. The shape factor H is shown to be a very weak function of x, therefore a very weak function of thickness.

The Prandtl mixing length can be used to describe the fully rough boundary layer. The outer region ($y/\delta > 0.1$) seems the same as a smooth layer. The inner region follows a straight Prandtl formulation, $l = \kappa y$ with no damping, and $\kappa = 0.41$ as shown in Figure 7b. A typical smooth wall result is shown for comparison, as well as a sample from a transitionally rough case (U_∞ = 52 fps on this same surface). A "y"-shift of 0.15 mm was used with these data, being the value of "y"-shift which resulted in the longest straight line log region in Law of the Wall coordinates.

The turbulent Prandtl number was calculated from measured turbulent shear stress and measured turbulent heat flux and is shown in Figure 7c. Compared to smooth-wall behavior, the values tend to be lower, near the wall, and slightly high in the outer region. Again, this reflects the absence of a "near wall region" which behaves differently from the outer region.

Turbulence Quantities

Rough wall boundary layers have different distributions of turbulence quantities than do smooth wall layers. Figure 8 shows measured distributions for smooth, transitionally rough, and fully rough conditions. Of primary importance are the disappearance of the u'-peak very near the wall and the rise in level far from the wall. For a smooth wall, the peak occurs at about $y^+ = 15$, in the region of maximum production of turbulent energy. In the present fully rough case, there is no maximum in turbulence production above the crests of the balls: the production rises monotonically, having its largest measured value at the nearest point to the wall. The level of turbulence does show a maximum, however. Values of $\sqrt{\overline{u'^2}}/U_\tau$ decrease very near the wall, perhaps due to pressure interactions, while a higher degree of isotropy seems to hold in the very near wall region, extracting more energy from the axial fluctuation than in the smooth-wall case and delivering it to the transverse components.

The turbulent shear stress distribution is shown in Figure 9 in different formats. Of particular importance is the fact that the $\overline{u'v'}$ correlation coefficient seems to be uniform through the layer, with a value of 0.45 (the same as expected for a smooth layer) and the ratio of Reynolds stress to turbulent kinetic energy is uniform at 0.15 (again, the same value as in a smooth-wall layer). Thus it appears that both of these important relationships are the same in rough and smooth wall boundary layers.

Figure 10 shows the distributions of $\sqrt{\overline{u'^2}}$ and $\sqrt{\overline{t'^2}}$ versus y/δ to illustrate the similarity in their behavior. Figure 11 shows the correlation coefficients for $\overline{u't'}$ and $\overline{v't'}$ to be uniform through the layer and the turbulent heat flux to vary with $U_\tau T_\tau$ just as turbulent shear

stress varied with U_τ^2.

Figure 12 shows the turbulent shear stress and turbulent heat flux distributions through a fully rough boundary layer. The distributions are nearly identical.

The Effect of Blowing

Roughness is frequently accompanied by blowing through the surface (as in a charring ablator). Figure 13 shows Stanton number and friction factor data for the present program, as a function of the blowing fraction, F. There is no velocity dependence in the data: for a given value of F, St and $C_f/2$ are functions of boundary layer thickness only. Thus even the blown layers are "fully rough" even though the values of roughness Reynolds number become very small. One hypothesis regarding this suggests that the pressure field on the surface, induced by the small jets of injected fluid, have some of the same effects on the flow as would solid protuberances. Thus, as the blowing increases, the surface seems to become physically rougher, and in such a way that its net behavior remains fully rough. It has been shown by Healzer [2] that the changes in friction factor and Stanton number caused by blowing can be calculated using the same relationship used for a smooth wall, providing the comparison is made using rough-wall baselines and parameters.

Figure 13 also shows the effect of blowing on the velocity profiles. In particular note that blowing through a smooth wall results in a profile which is indistinguishable from that of a rough wall.

Figure 14 shows the way in which blowing affects the turbulence quantities in the boundary layer, both in the outer region and the inner region. Blowing decreases the values near the wall and increases the values far

from the wall. The distribution of turbulence in a smooth-wall boundary layer with blowing looks not unlike that of a rough-wall boundary layer without blowing. Blowing through a rough-wall layer simply accentuates this effect. Figure 15 shows the correlation coefficients, the mixing length distributions, and the turbulent Prandtl number distributions measured in fully rough boundary layers with blowing. It is apparent that none of these are significantly affected by the presence of blowing. The outer region of the rough-wall boundary layer with blowing seems governed by the same transport mechanisms as the outer region of a smooth-wall flow without blowing.

Concluding Remarks

The data summarized here are available either from University Microfilms, Ref [1], or directly from the author as Report HMT-21 to eligible users. None of the material is classified.

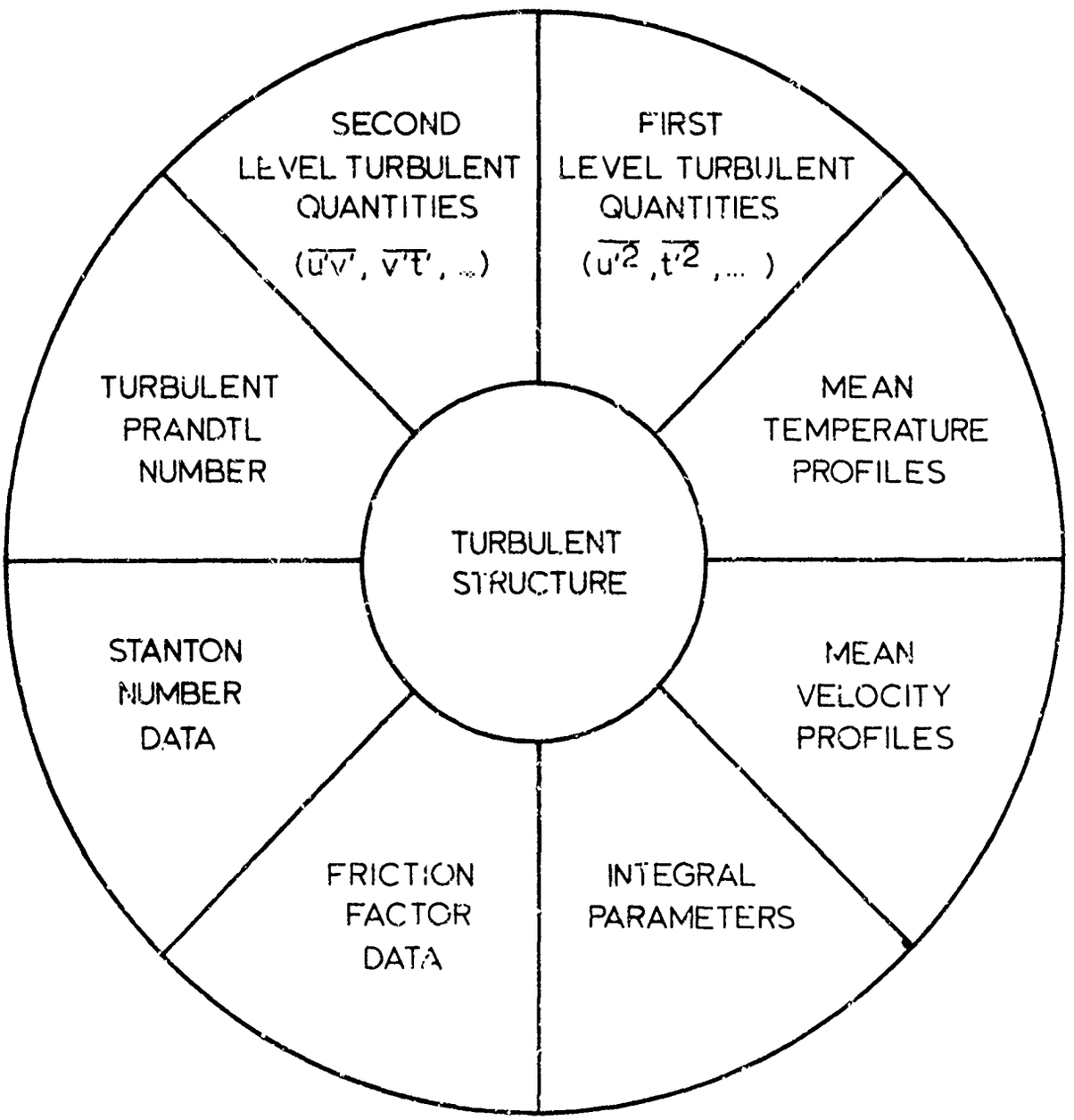

1. Descriptors of the turbulence structure.

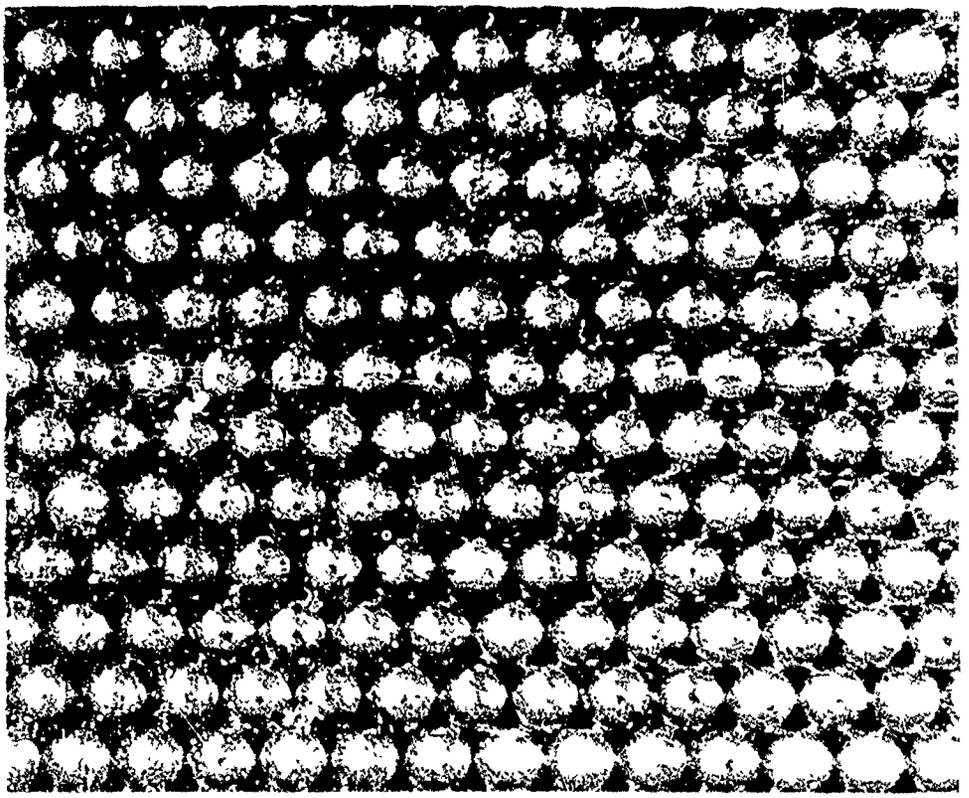

2. The surface used in the present tests: densely nested spheres.

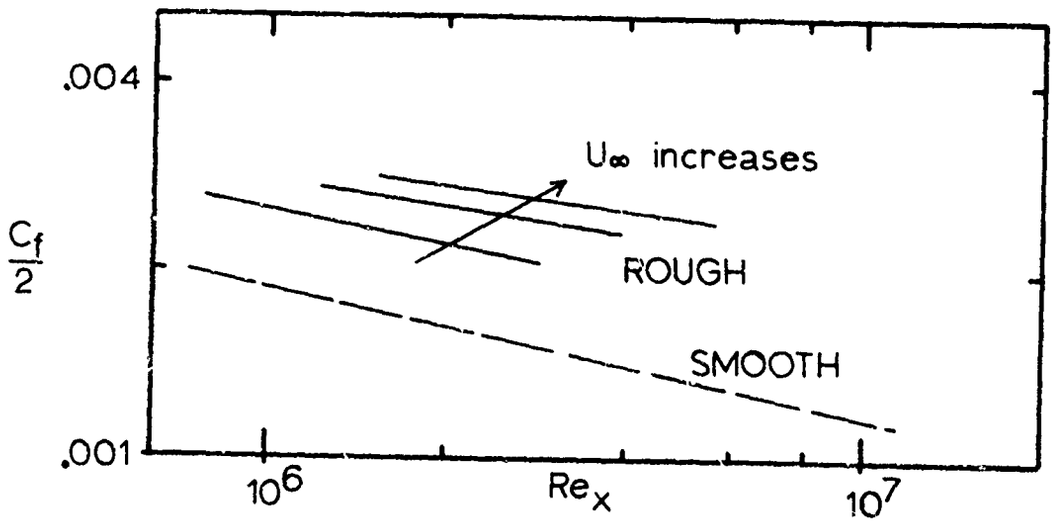

3a. Effect of velocity upon rough-wall friction factor, shown in x-Reynolds number coordinates.

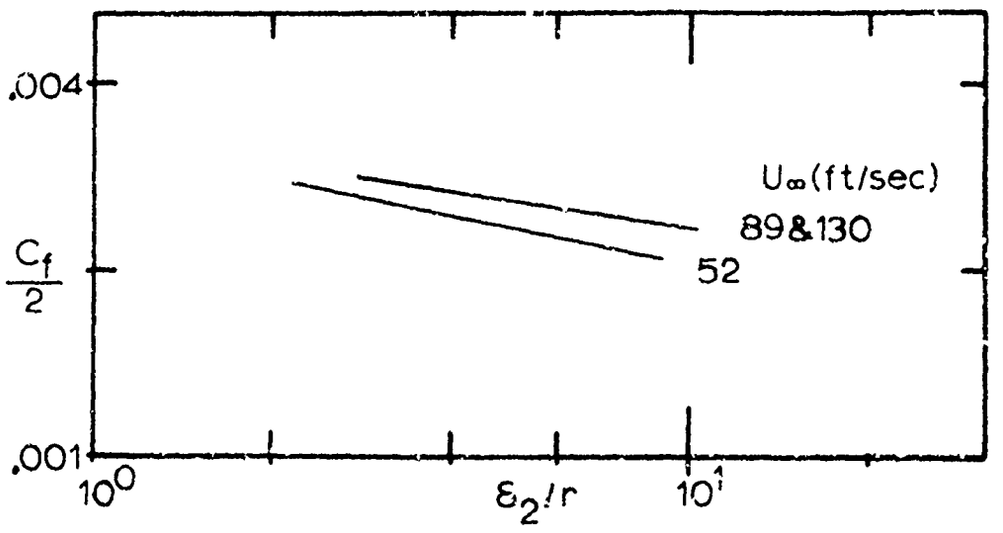

3b. Effect of velocity upon rough-wall friction factor, shown in momentum thickness coordinates.

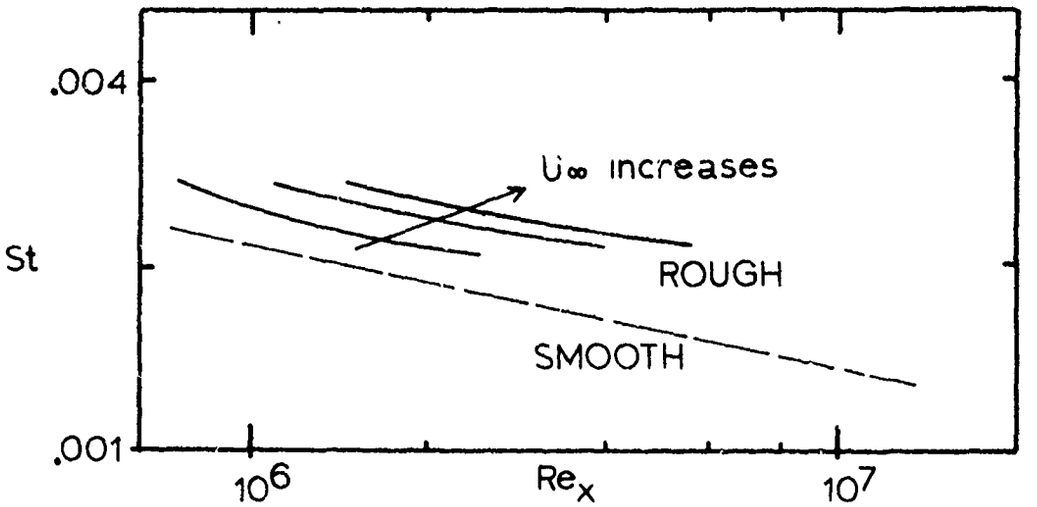

4a. Effect of velocity upon rough-wall Stanton number, shown in x-Reynolds number coordinates.

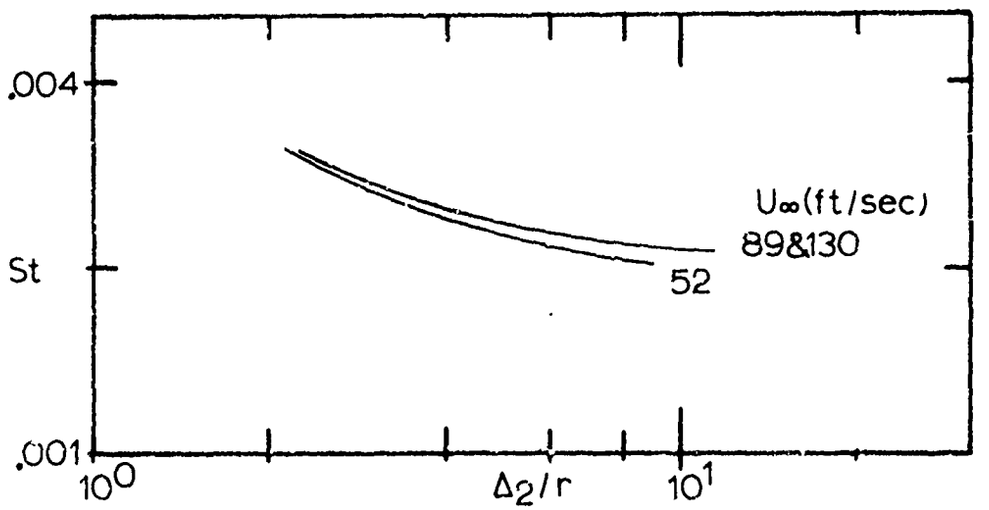

4b. Effect of velocity upon rough-wall Stanton number, shown in enthalpy thickness coordinates.

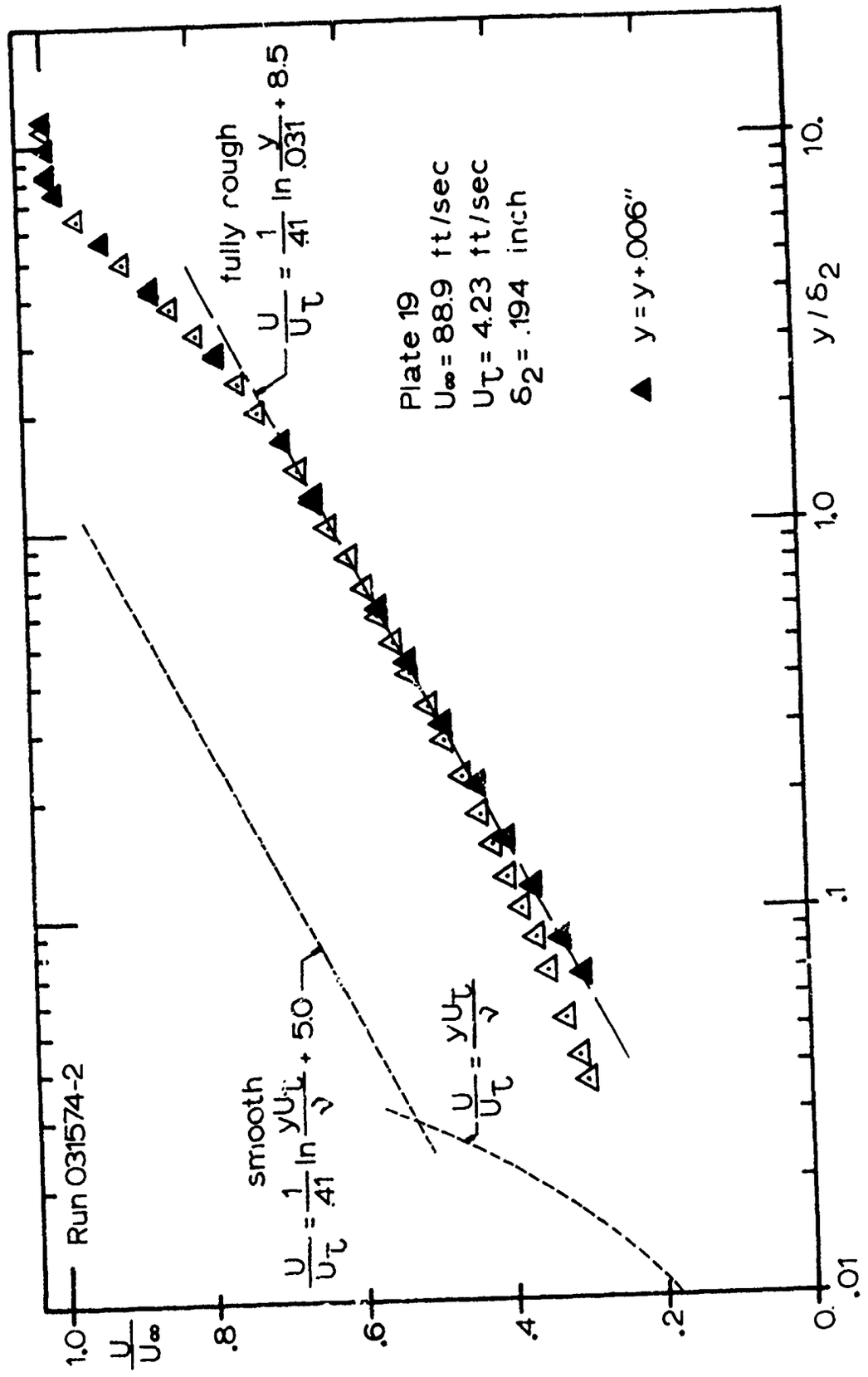

5a. Velocity distribution in a fully-rough boundary layer, shown in inner region coordinates, compared with the smooth wall behavior.

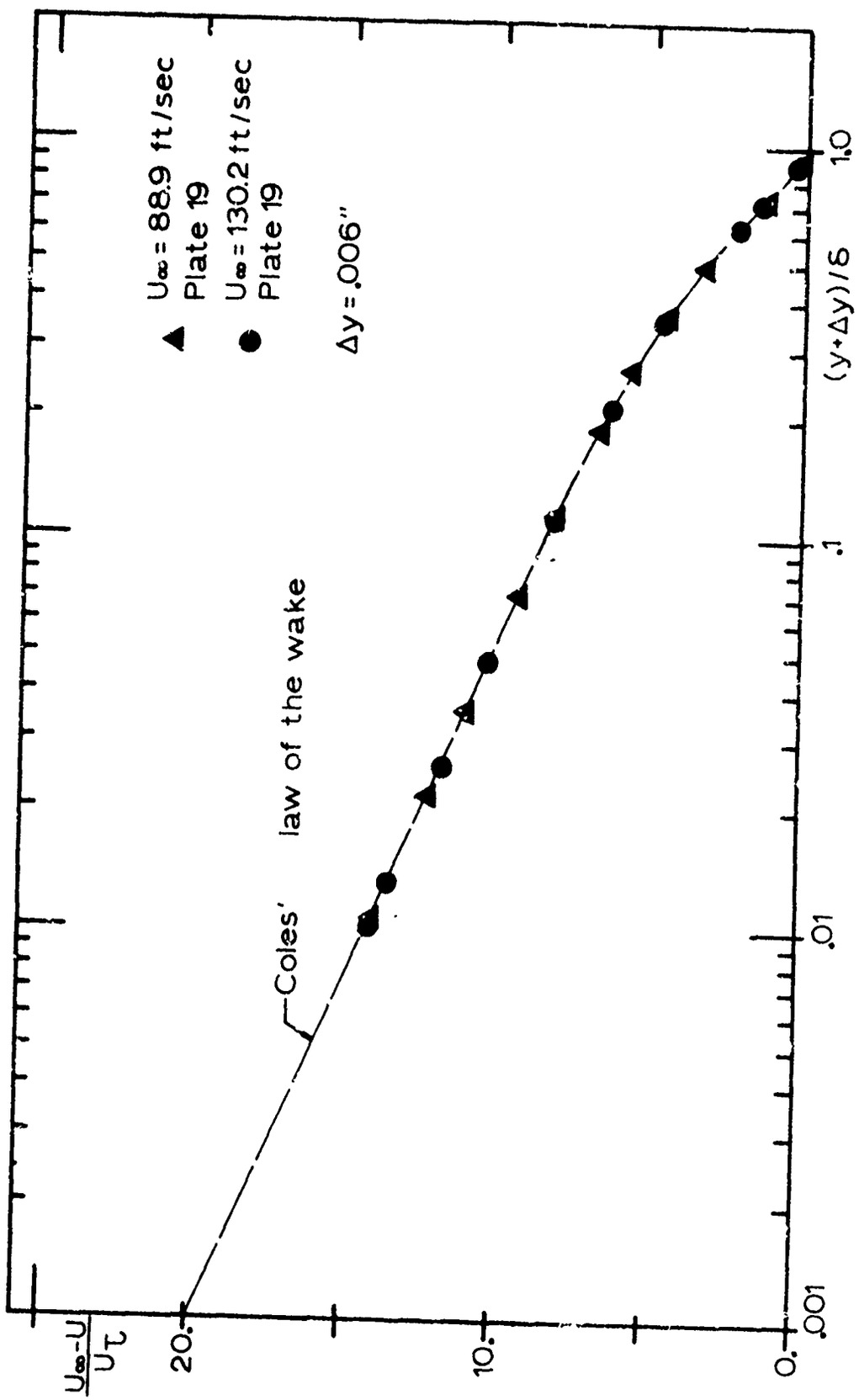

5b. Velocity distribution in a fully-rough boundary layer, shown in velocity-defect coordinates, compared with the smooth wall behavior.

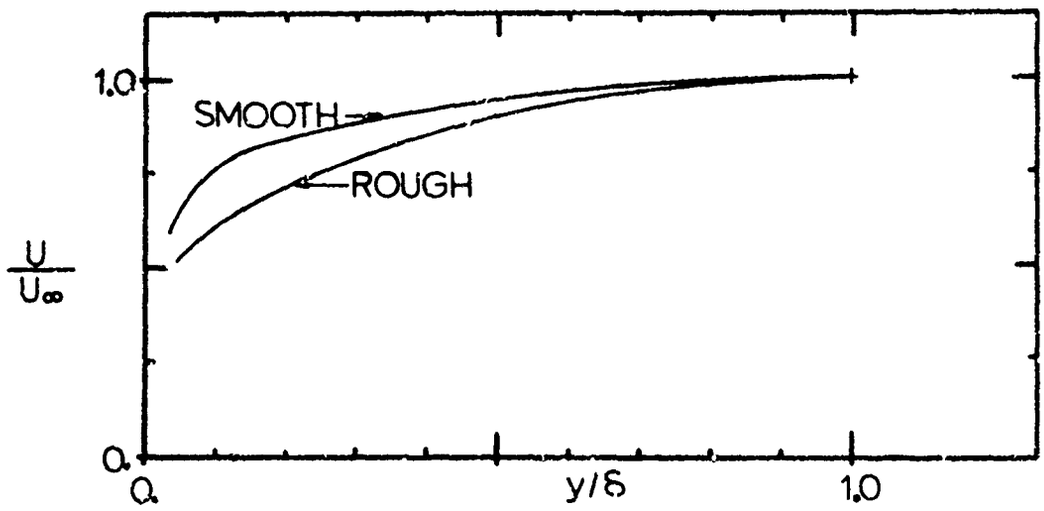

5c. Velocity distributions of smooth and rough-wall boundary layers, compared in outer-region coordinates.

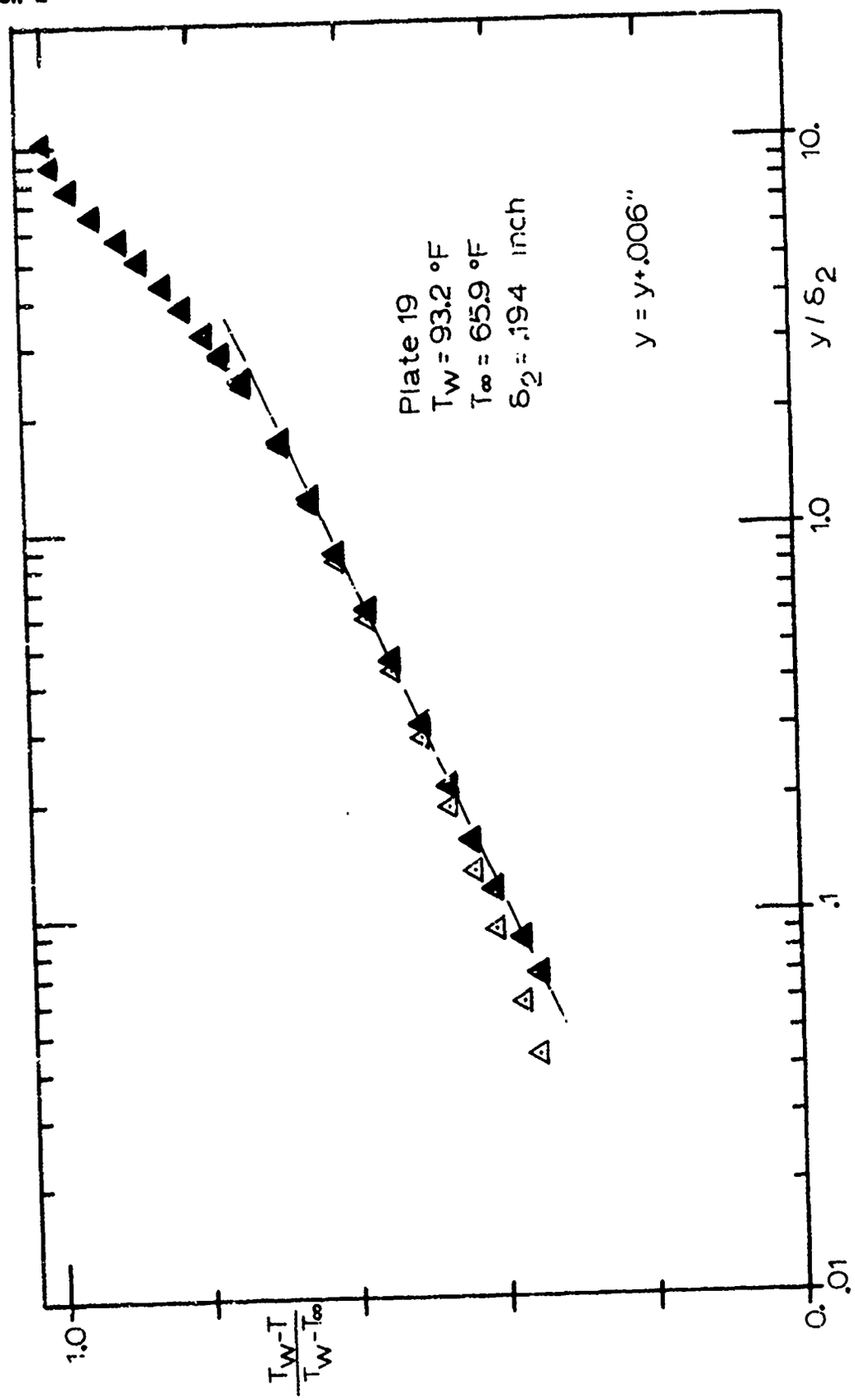

6a. Temperature distribution in a fully-rough boundary layer, shown in inner region coordinates.

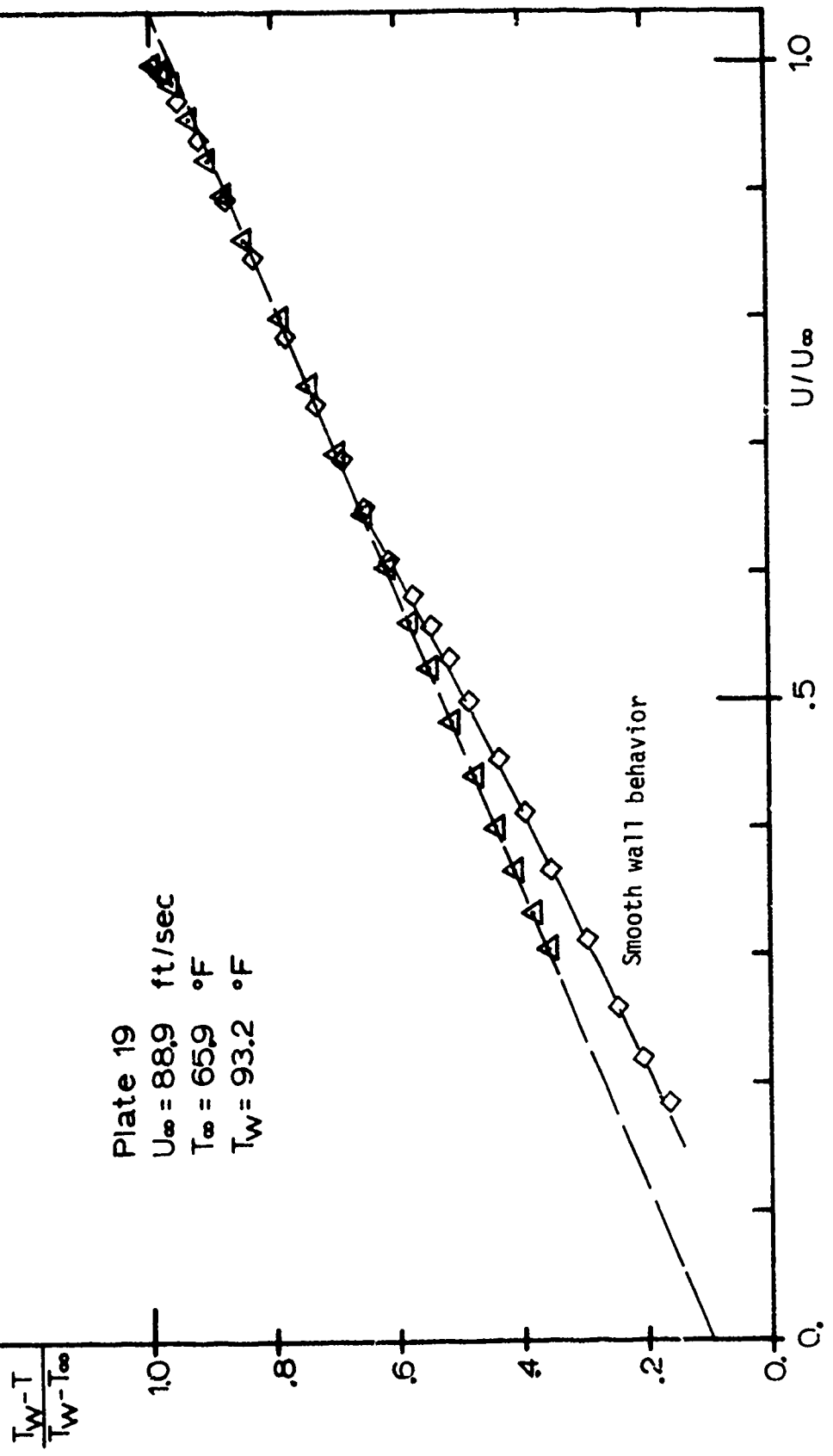

6b. Temperature distribution in a fully-rough boundary layer, plotted against local velocity, point by point through the layer.

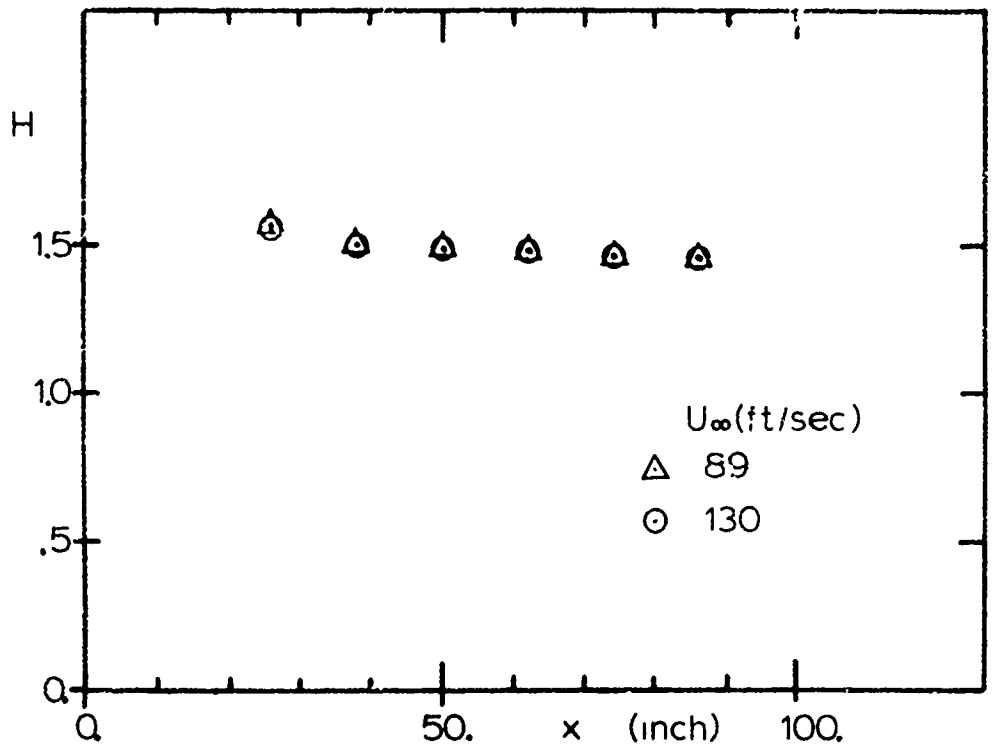

7a. Shape factor versus length for fully-rough flow.

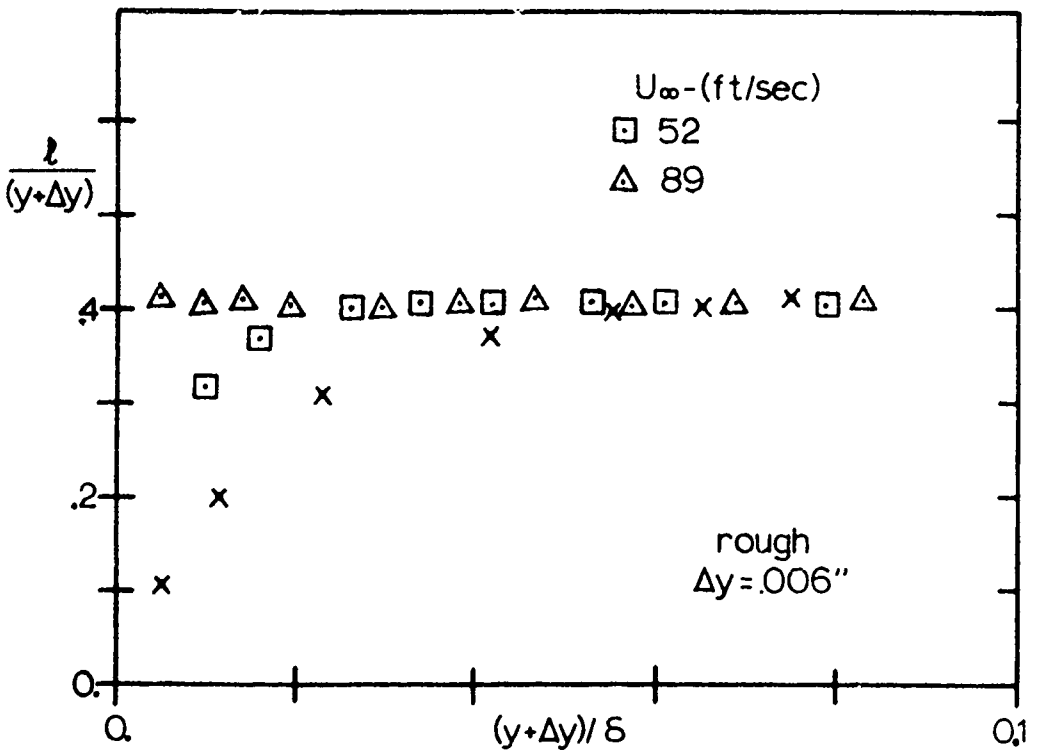

7b. Prandtl mixing length distributions for smooth, transitionally rough and fully rough layers.

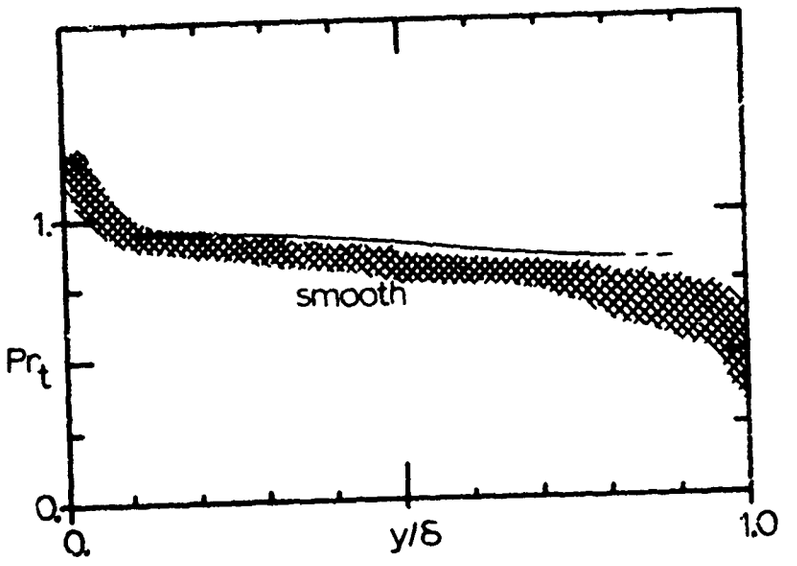

7c. Comparison of turbulent Prandtl number distributic for a fully rough flow with the range of values reported for smooth walls.

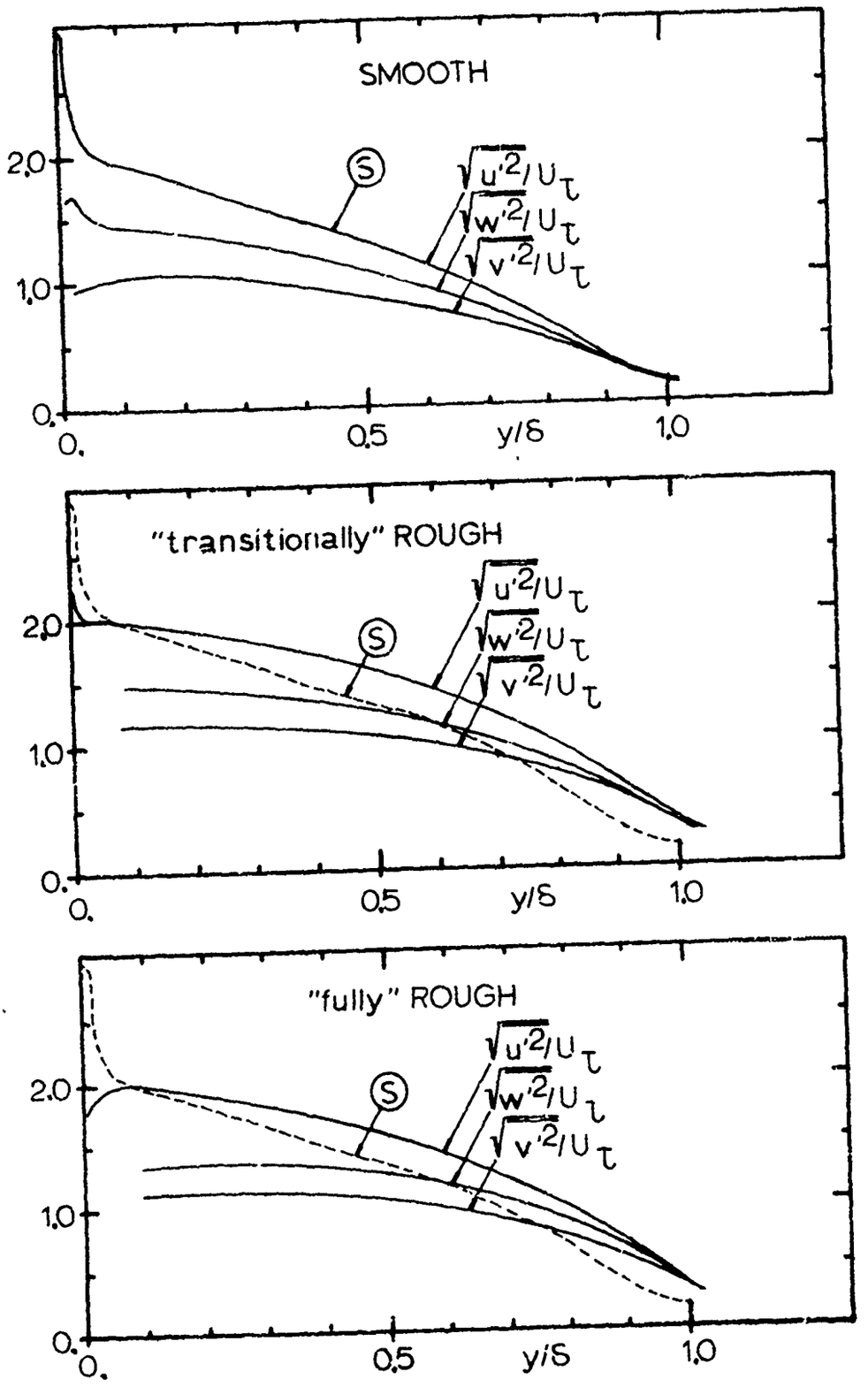

8a,b,c. Distributions of turbulence quantities for smooth (a), transitionally rough (b), and fully rough (c) boundary layer flows.

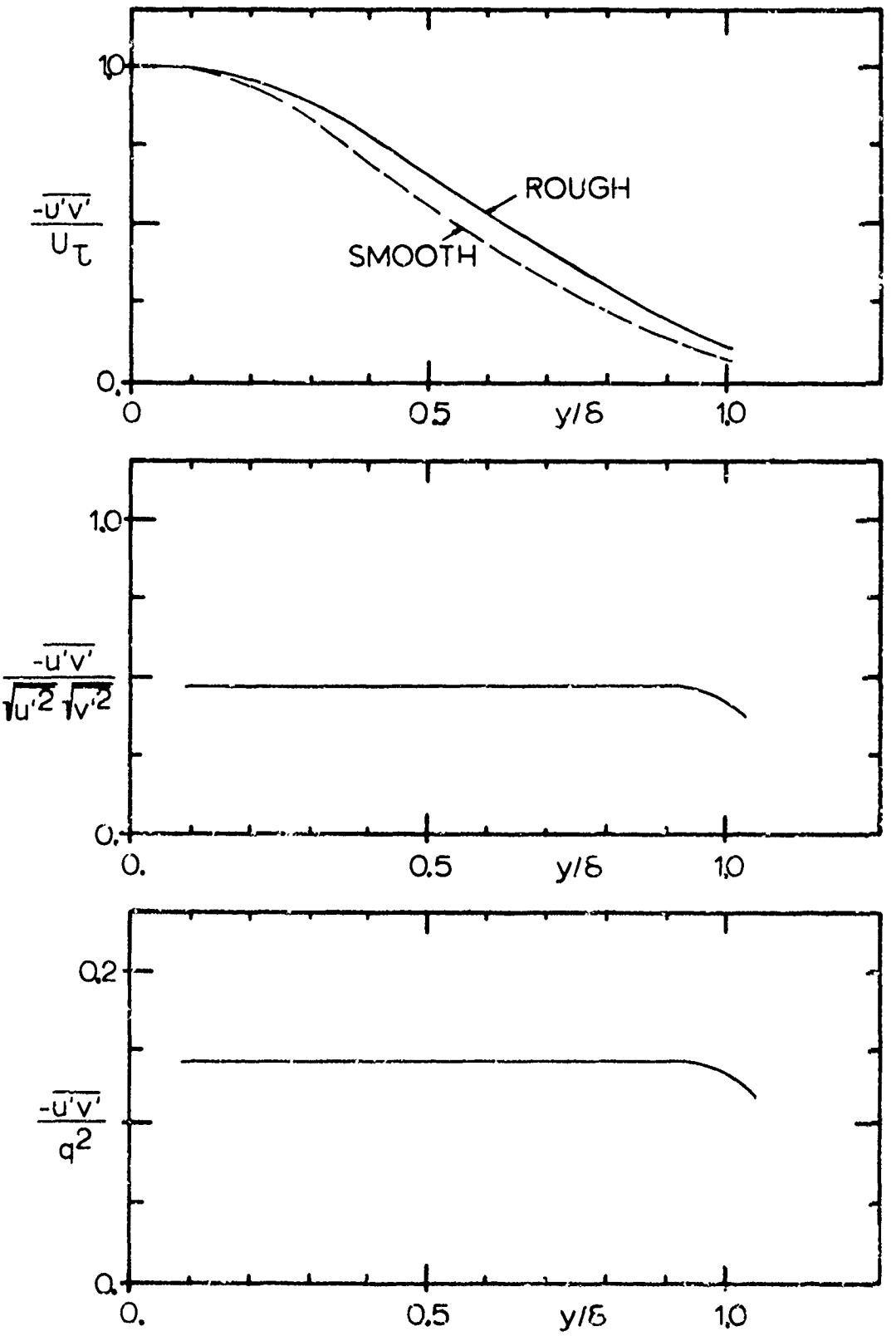

9a,b,c. Turbulent shear stress correlation coefficients.

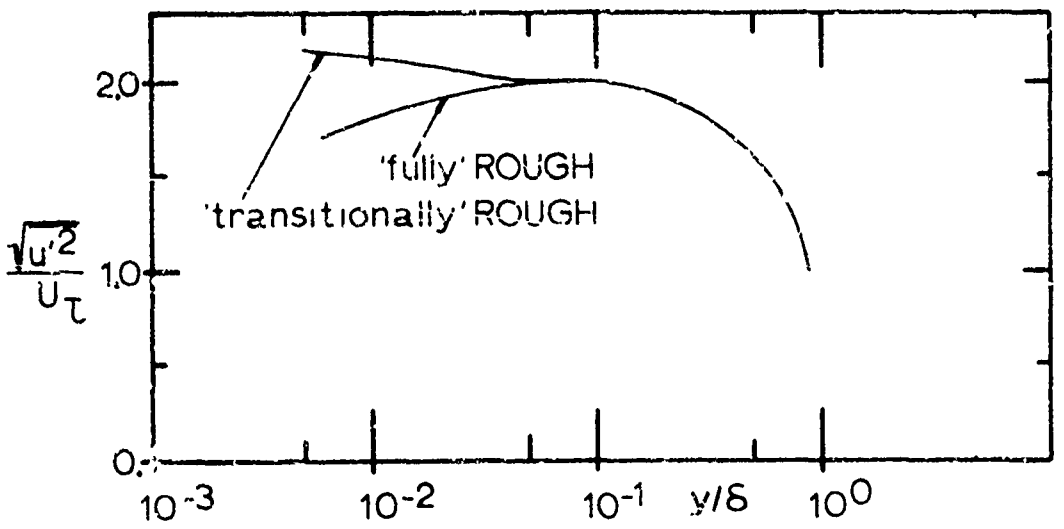

10a. Comparison of U-component fluctuations for transitionally rough and fully rough flows.

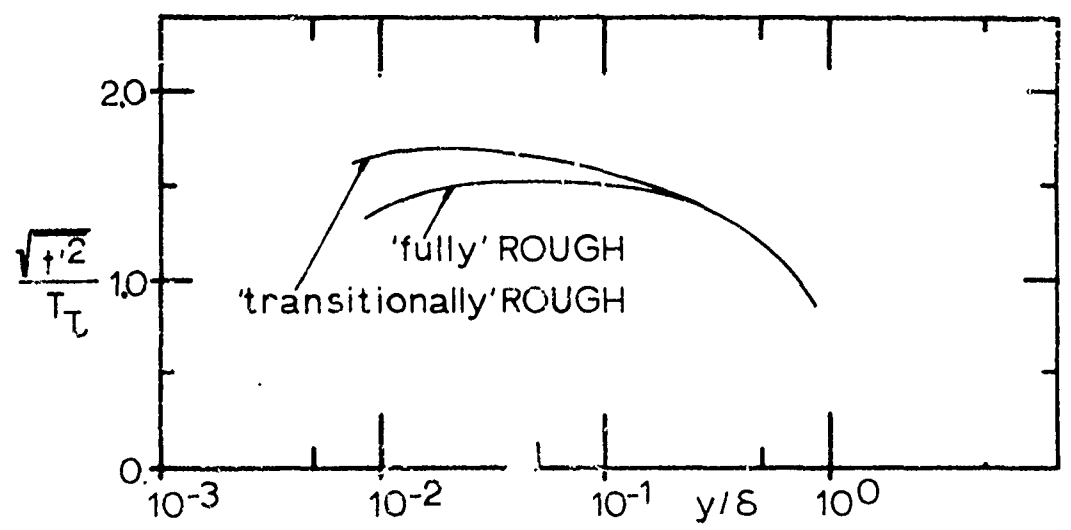

10b. Comparison of temperature fluctuations for transitionally rough and fully rough flows.

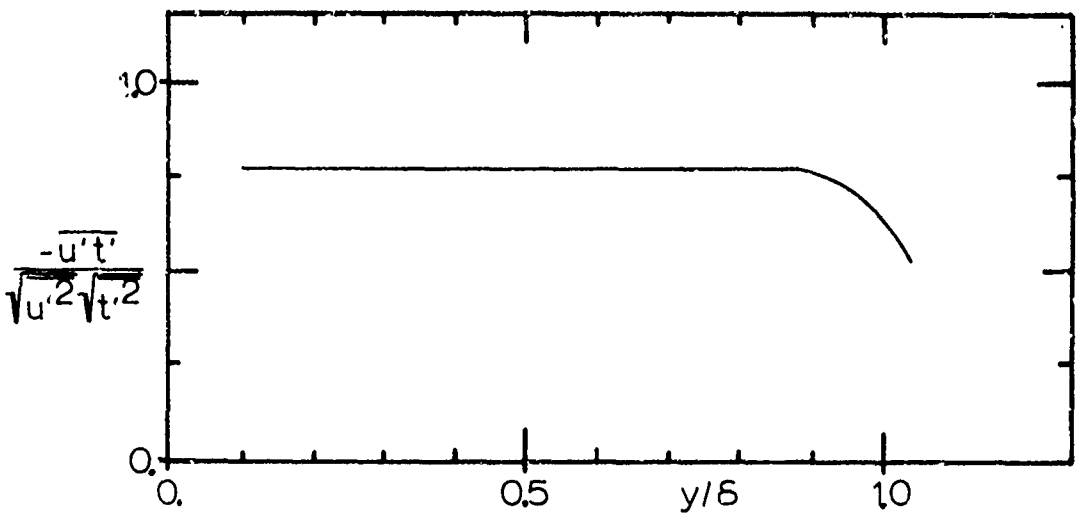

11a. Correlation of the U-component velocity fluctuation with the temperature fluctuation.

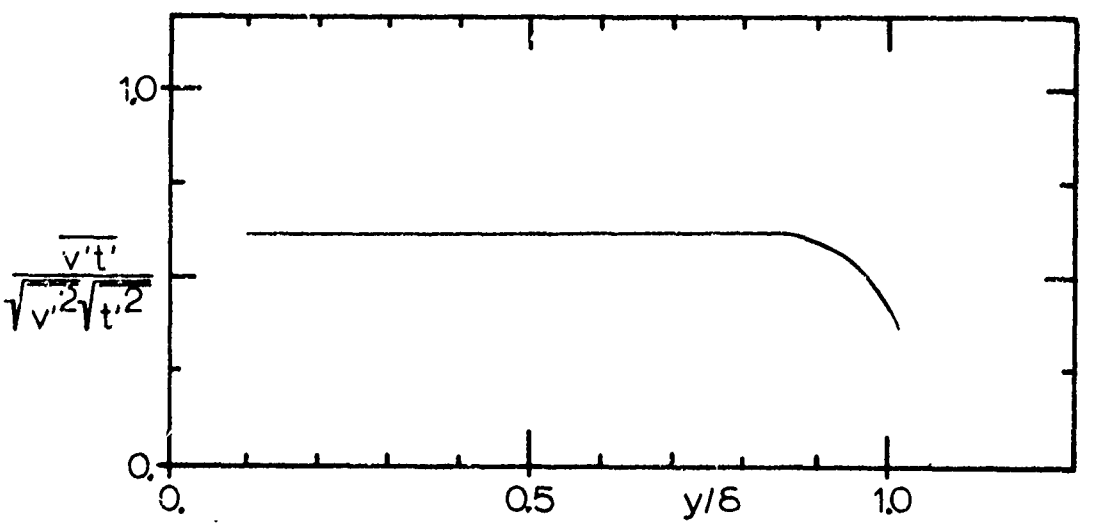

11b. Turbulent heat flux correlation coefficient.

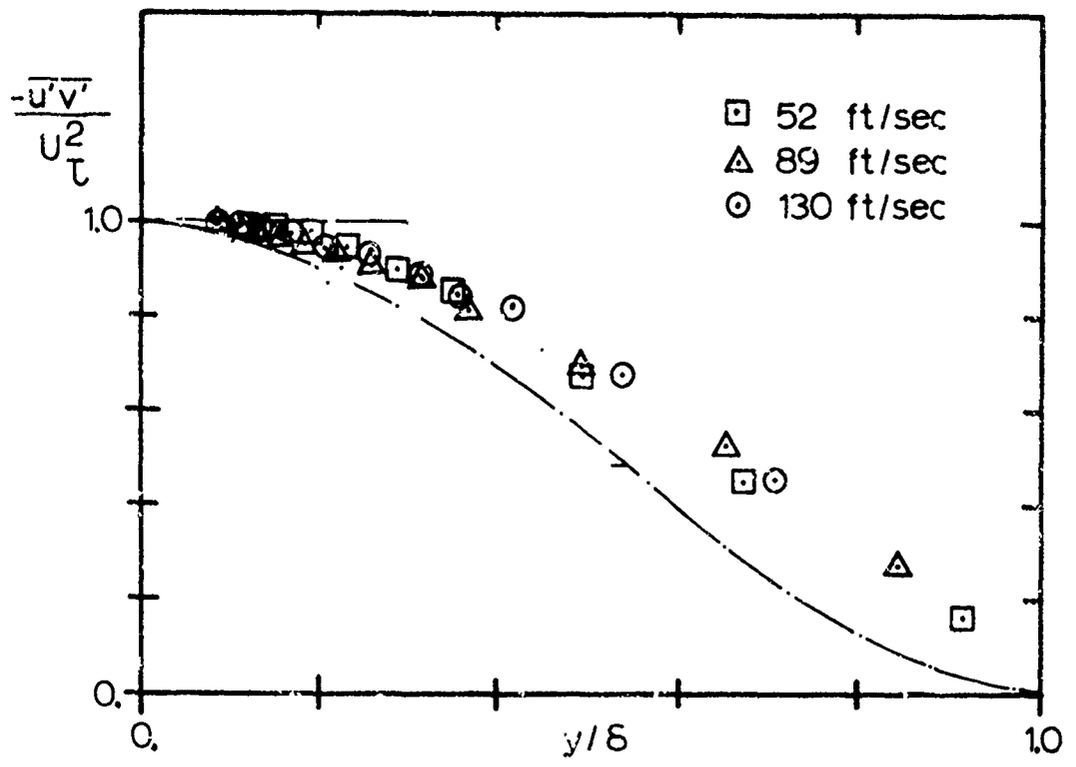

12a. Distribution of the turbulent shear stress.

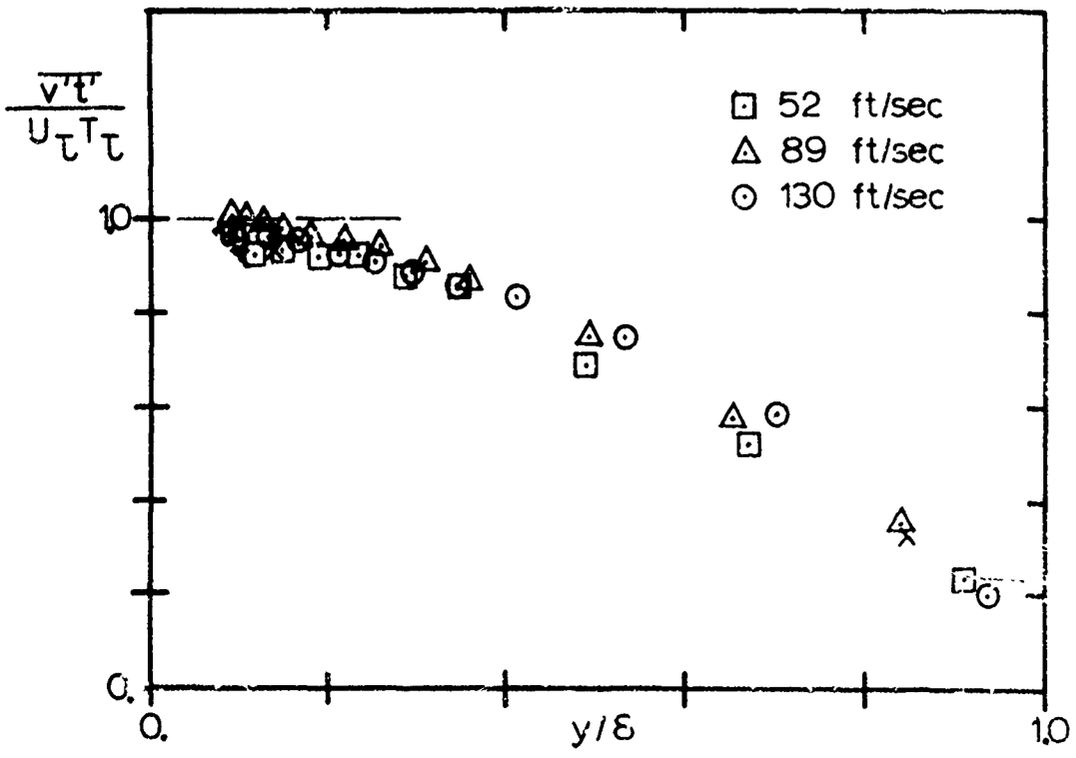

12b. Distribution of the turbulent heat flux.

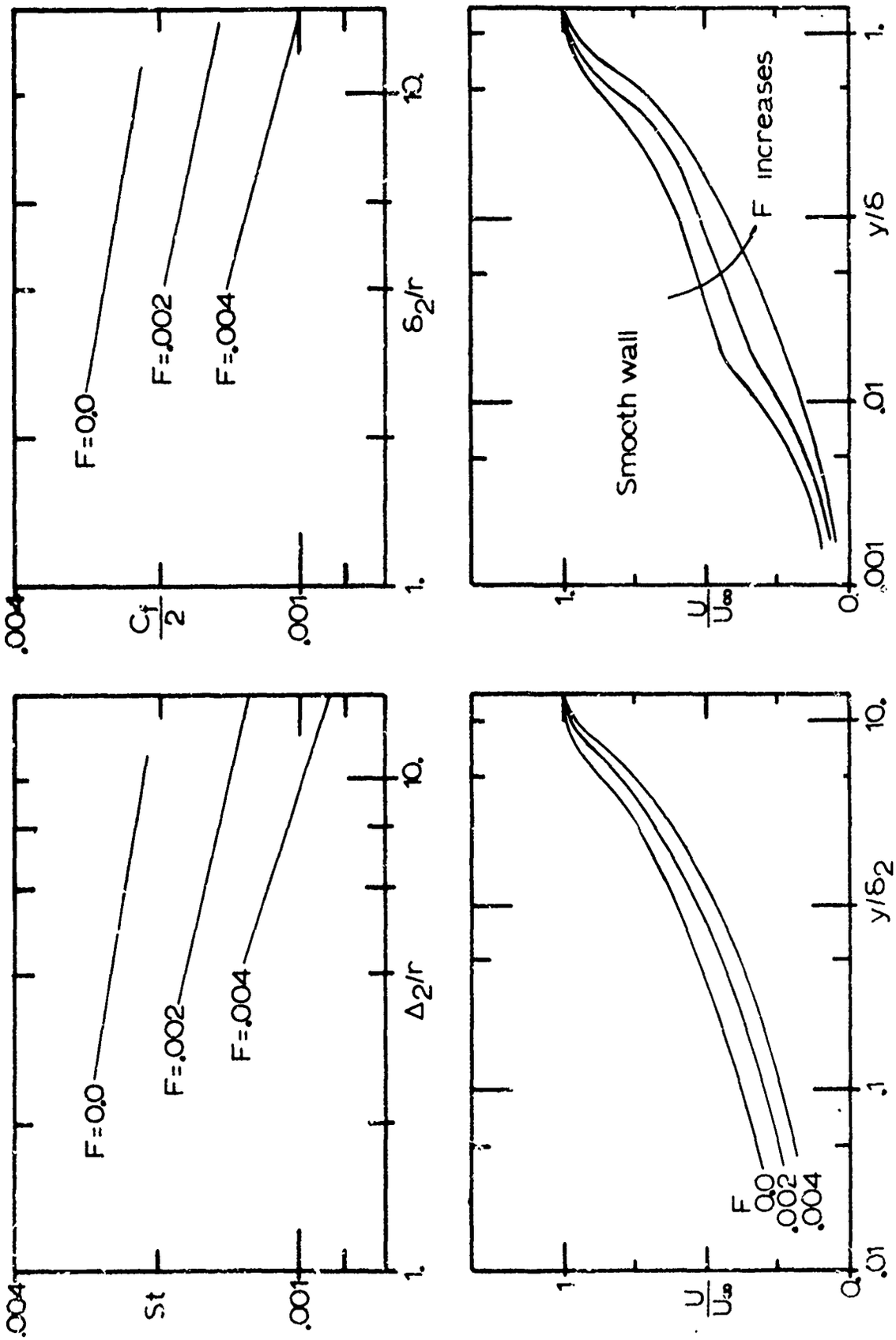

13a,b,c,d. Effects of blowing on Stanton number, friction factor, and velocity distributions.

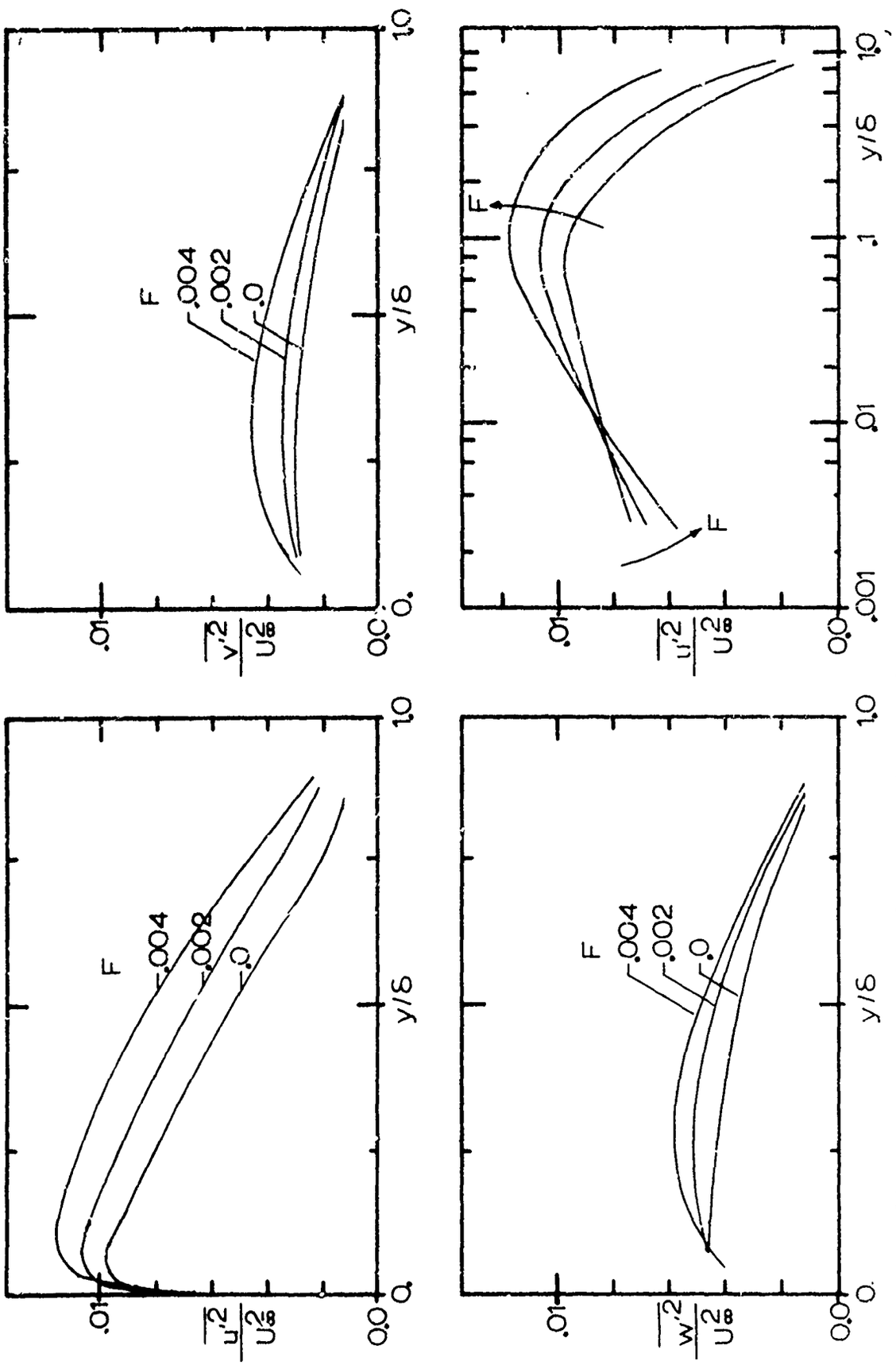

14a,b,c,d. Effects of blowing on the turbulence quantities in a rough-wall boundary layer

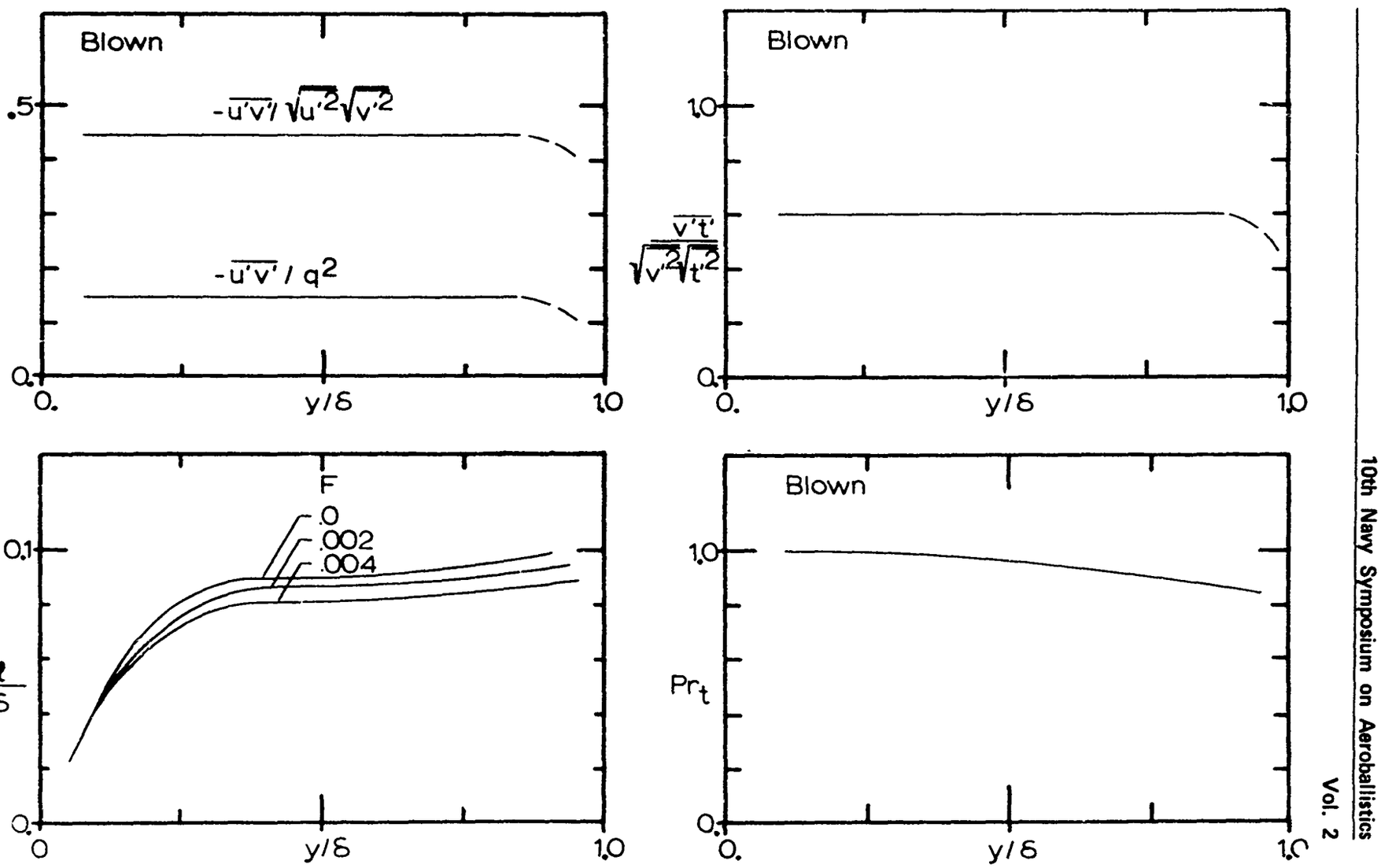

15. Effects of blowing on turbulence correlations, mixing length, and turbulent Prandtl number.

PAPER NO. 22

HEAT TRANSFER FROM A TURBULENT BOUNDARY LAYER ON A POROUS HEMISPHERE

Robert H. Feldhuhn

Naval Surface Weapons Center
White Oak Laboratory
Silver Spring, Maryland 20910

ABSTRACT

Heat transfer distributions have been measured in a wind tunnel on a porous spherically blunted, 2-inch radius sphere cone at a Mach number of 5 and a free stream unit Reynolds number per foot of 17.6×10^6. For this condition, turbulent flow exists on the hemisphere. In addition to the measurements of heat transfer on the porous surface, heat transfer data were also obtained on an impermeable conical aft body ($\theta_c = 5°$). The experimental data are compared with calculated results from the BLIMP program and previous heat transfer correlations obtained on porous flat plates.

NOMENCLATURE

C_p	specific heat, BTU/lb-°R
dv	differential volume, in^3
dA	differential area, in^2
ΔH	total enthalpy difference, BTU/lb
h	heat transfer coefficient, BTU/sec-in^2-°R
P	pressure, psia
$\dot{Q}$	heat transfer rate, BTU/sec-ft^2
R_n	nose radius, in
Re_θ	local Reynolds number based upon momentum thickness
S	distance along model surface, in
T	temperature, °R
t	time, sec
V_w	injectant velocity, in/sec
$\dot{W}$	mass flux, lb/sec-ft^2
ρ	density, lbs/in^3

Subscripts

g	injectant gas properties
m	model material properties
o	without mass addition
o_∞	free-stream stagnation conditions
t_2	stagnation condition behind normal shock-wave

I. INTRODUCTION

It has long been recognized that transpiration cooling[1-4] and/or ablation[5,6] techniques can be employed to thermally protect regions with high heat transfer rates on vehicles traveling at hypersonic velocities. In view of the fact that both of these thermal protection techniques rely in part upon a transfer of material from the surface into the viscous boundary layer which surrounds the vehicle, it is important to understand how the convective heating varies with mass addition. Uncertainties remain concerning the effect of the mass transfer upon boundary layer transition from laminar flow to turbulent flow, the local reduction of heat transfer as a function of mass transfer and the downstream cooling effect of upstream mass transfer.

The dependency of convective heat transfer upon mass transfer has received attention in previous experimental and theoretical studies. Comprehensive studies which provide an overview of previous programs concerning mass addition effects on turbulent boundary layers were presented by Jeromin,[7] Baronti, Fox and Soll[8] and Kays.[9] Discussions of some calculations of turbulent boundary layers with mass transfer are presented by Anderson and Kendall,[10] Landis and Mills,[11] and Lubard and Fernandez.[12] The effect of mass transfer

upon boundary layer transition for sharp cones has been experimentally illustrated by Marvin and Akin.[13] Mass addition effects upon the laminar boundary layer on a blunted cone were experimentally addressed by Pappas and Lee.[14] A review of the previous studies indicate that while laminar and turbulent boundary layer calculations can apparently be performed for compressible flows with mass transfer, pressure gradient and heat transfer effects included, there is a scarcity of experimental data which can be employed to validate the calculations.

In view of the fact that mass addition and pressure gradients exist in the vicinity of nose tips and leading edges of hypervelocity vehicles, an experimental program was initiated to obtain some heat transfer data which could be compared with previously developed calculations and correlations in order to assess the predictive accuracy of these techniques.

II. EXPERIMENTAL CONSIDERATIONS

A. Model Design

In order to obtain heat transfer data for compressible turbulent boundary layers with both mass transfer and pressure gradient effects present, the model illustrated in Figures 1 and 2 was constructed. The model features

a porous beryllium-copper hemisphere-cone forebody, .085 inch thick, with an impermeable stainless steel aftbody, .025 inch thick. A two-inch nose tip radius was chosen in order to be confident of obtaining turbulent flow on the hemispherical portion of the model. Beryllium-copper was chosen as the material for the porous forebody because of the high strength and thermal conductivity properties which are evidenced by the impermeable beryllium-copper alloys.[15] Such properties were required for these experiments in order that thin wall heat transfer data reduction techniques could be employed with large models that contain pressures on the order of 300-400 psia. A tabulation of the properties of the porous beryllium-copper material are provided in Table I.

The porous section was fabricated from two billets of porous beryllium-copper in order to obtain a model with one permeability for chamber #1 and another permeability for chambers #2 and #3. This design option was chosen in order to insure that the mass flow through the porous surface would be relatively independent of model surface pressure and yet would not require prohibitively large internal pressure to satisfy the maximum mass flow requirements. These materials of different permeability were joined by a

circumferential electron beam weld. For the purposes of this investigation, only dat with mass addition from the hemispherical section of the porous model (chamber #1 and #2) will be presented. Heat-transfer data were obtained on the conical section for conditions that included mass transfer from the porous conical section (chamber #3). These data are not being presented at this time because of large scale permeability variations (permeability 1 $\sigma \approx \pm$ 35 percent) on this section of the model. On the hemispherical section of the model, the 1 σ variations in permeability are approximately 10 percent and 15 percent for sections of the model covering chambers #1 and #2, respectively. These variations were determined by sampling flow rates through an O-ring tipped tube with an effective diameter of 0.170 inch.

The porous nose tip and impermeable aft-body were instrumented with copper-constantan and chromel-alumel thermocouples, respectively. A high pressure seal for the thermocouple wires was fabricated for each of the three chambers illustrated in Figure 2. Furthermore, each chamber had an independent injectant gas feed line and pressure monitoring line.

B. Facility and Test Conditions

The experiments were conducted at a free stream Mach number of 5 in the Hypersonic Tunnel at the Naval Surface Weapons Center, White Oak Laboratory. This facility is an open jet wind tunnel with a run time capability on the order of minutes for these test conditions. A two dimensional contoured nozzle with a test section height of approximately 16 inches was utilized. Dried air is the free stream test medium, while nitrogen was the transpired injectant gas.

Heat transfer measurements were obtained at a nominal free stream Reynolds number per foot of 17.6×10^6 with the model at zero degrees angle of attack. For this condition, typical free stream stagnation pressures and temperatures were 735 psia and 500°F, respectively.

C. Test and Data Reduction Technique

Prior to the test, the model was located beneath the open jet test section. The desired nitrogen gas injection rate for each chamber was independently established by regulating the pressure upstream of a choked nozzle. The mass flow rate is determined from the measured upstream stagnation pressure, stagnation temperature and calibrated discharge coefficient for the nozzle. A transient heating condition was established around the model by injecting it into th center of the uniform wind tunnel stream. A typical

transit time from the bottom of the nozzle to the nozzle axis is 0.11 sec. As the model was injected into the stream the wall temperatures were recorded every 0.04 second on magnetic tape. Typical test durations lasted about 5 seconds, but only temperature data obtained within the first 0.64 second after the model reached the nozzle axis were used for transient heat transfer data reduction purposes.

Heat transfer data for the porous and impermeable sections was obtained by the transient thin skin calorimeter technique.[13,14,16,17] This technique assumes a heat balance of the form

$$h[T_o - T_w] = (\rho_m C_{p_m})(\frac{dv}{dA})\frac{dT_w}{dt}\Bigg|_{t=0+} + \rho_w V_w C_{p_g}(T_w - T_g)$$

The recorded wall temperatures were curve fitted and differentiated with respect to time in order to determine the initial derivative of temperature with respect to time. With the exception of the stagnation point, all of the experimental data obtained on the hemisphere, that will be documented herein, represent an average of reduced data from two different size thermocouples (30 and 36 gage wire) displaced from

from each other by 180 degrees. On the frustum, the data, excepting that obtained at $S/R_n = 5.02$, represent an average of reduced data from at least two thermocouples. Based upon an inspection of the data, it is believed that the uncertainty in the experimental data due to random errors are less than ±10 percent on the hemisphere and ±20 percent on the frustum.

III. NUMERICAL CALCULATIONS

A limited number of boundary-layer calculations were conducted for the model geometry, Figure 2, and test conditions of interest. These calculations were obtained with the Boundary-Layer Integral Matrix Procedure (BLIMP) developed by Kendall and his co-workers.[10] The BLIMP code utilizes an integral strip method for solving the multi-component, nonsimilar, laminar, and turbulent boundary-layer equations. For turbulent boundary-layer flows, the time averaged equations of motion are solved utilizing an eddy viscosity model to describe the "Reynolds stress" term plus constant turbulent Prandtl and Schmidt numbers in the energy and species conservation equations. At the time the boundary-layer computations were performed, the pressure distribution was modeled by a Newtonian approximation. This approximation is compared with a more exact finite difference calculation[18] in Figure 3.

Tabulations of the input mass flow rates and calculated heat-transfer rates for these calculations are provided in Tables II and III. Case number 1 represents a laminar boundary-layer solution with zero mass addition. Case numbers 2 through 13 represent turbulent solutions with mass addition. For the purposes of the turbulent calculation, turbulent flow is assumed to occur when the local momentum thickness Reynolds number is greater than 100. Comparison of the tabulated results for case numbers 2, 3, 4 and 5 at an S/R_n of 0.192 indicates that increasing mass transfer initially decreases the heat-transfer rate and then increases it over the zero mass addition value. Inspection of the results of the calculation indicates that this reversal is due to a forward movement of transition due to the increase in the momentum thickness with increased mass transfer. However, for those stations where transition does not occur, these results indicate that increasing the mass flow rate decreases the heat-transfer rate to the surface.

Case numbers 7 through 13 were intended to numerically demonstrate the effects of discontinuous mass addition. Comparing the results at stations $S/R_n = 0.663$ and 0.681 for case numbers 12 and 13, one notes a predicted variation in heat-transfer rate of the order of 60 percent to 150 percent over a physical distance of approximately 0.04 inch.

An attempt was made to correlate the calculated laminar and turbulent heat-transfer rates as a function of the mass transfer in terms of previously suggested nondimensional parameters.[2,4,6,19] This result, illustrated in Figure 4, shows that the previously developed empirical correlations based upon flat plate data provide a reasonable approximation to the calculations. However, closer examination of the mass-transfer and heat-transfer rates tabulated in Tables II and III for case numbers 3, 4, 5 and 6 indicates that the greatest departures from the Leadon and Scott empirical correlation curve appear at an $S/R_n = 1.484$, the sphere cone tangency point, where the pressure gradient is the largest. These results indicate that a more conservative prediction scheme such as that attributed to Arne should be employed in regions of large pressure gradient and high mass flow rate.

IV. EXPERIMENTAL RESULTS

A tabulation of experimental conditions for 14 different combinations of mass flow rates from the hemispherical portion of the model are provided in Table IV. A tabulation of experimentally determined heat-transfer coefficients and test conditions for these 14 experiments is provided in Table V. Test numbers 66, 68, 73 and 79 were conducted in order to demonstrate the effect of increasing mass addition

over a spherical segment from the stagnation point to a $S/R_n = 0.52$. Tests 67, 74 and 82 were conducted in order to demonstrate the effect of local mass addition, without upstream effects, on the hemispherical portion of the nose tip where the pressure gradients are greatest. Tests 69, 75, 83, 80, 81 and 84 provide local data with upstream mass addition effects present. Comparison of the magnitude and distribution of the mass flow rates tabulated in Tables II and IV indicates that the data obtained in experiments 1, 67, 69 and 82 can be compared with film coefficients defined for case numbers 2, 7, 5 and 8, respectively, if one neglects the numerical calculations for $S/R_n > 1.484$ in case number 5 as this calculation included mass transfer on the frustum. These results are plotted in Figures 5, 6, 7 and 8, respectively.

The experimental data without mass addition, illustrated in Figure 5, show very good agreement with the BLIMP calculation in which one assumes that boundary-layer transition occurs at an $Re_\theta = 100$. From the experimental viewpoint, this agreement between experiment and theory for the baseline case of zero mass transfer is interpreted as a reflection of the fact that a turbulent boundary layer exists on the hemisphere to within approximately 20 degrees of the stagnation point ($S/R_n = .30$).

Examination of the hemisphere data ($S/R_n \leq 1.484$) in Figures 5, 6, 7 and 8 shows the largest experimental uncertainty about the average value exists at an $S/R_n = 0.63$. It is believed that this uncertainty is due to a systematic error of approximately 20 percent as each of the two thermocouples which are located at this station consistently provided data either above or below their common average reading. Mass addition caused a reduction in the heat transfer coeffficient calculated from the thermocouple output in either case. The lower value of the two readings generally shows closer agreement with the calculation. Possible sources of the systematic error might be due to local surface roughness or local material inhomogenieties in the porous material.

Generally speaking, one observes in Figures 6, 7 and 8 that the BLIMP calculation provides satisfactory local heat transfer predictions in regions of turbulent flow with mass injection. The experimental turbulent heat transfer data tabulated in Table V are replotted in Figure 9 in terms of the non-dimensional parameters utilized to correlate previous turbulent heat transfer data. As was noted in the discussion of the BLIMP calculations, one observes in regions of pressure gradient for conditions of high mass transfer that the experimental data show good correlation with the empirical predictions of Arne [2]

Whereas, one notes general agreement between predicted trends and measured turbulent data on the hemisphere, Figure 7 illustrates that the measured stagnation point heat transfer data is not satisfactorily predicted by a laminar calculation when there is mass addition. This discrepancy between measured and calculated heat transfer rates to a stagnation point is graphically displayed in Figure 10 whereby the measured heat transfer film coefficients at the stagnation point tabulated in Table V and the measured mass transfer rates tabulated in Table IV have been normalized by measured data in the absence of mass transfer. These results illustrate that the measured heat transfer rate initially decreases and then increases to a value essentially equal to the measured laminar heating rate without mass transfer. This latter observation occurs at a mass transfer rate at which a laminar stagnation point boundary layer calculation predicts that the heat transfer should be approximately 30 percent of the initial value.

One conjectural explanation for this observation is that mass addition introduces disturbances that cause boundary layer transition to occur at the stagnation point. In this case, the reduction in heat transfer due to mass addition effects is offset by the augmentation in heat transfer due to the appearance of turbulent flow. Furthermore,

one might hypothesize that the disturbances which create the turbulence propagate upstream in the subsonic stagnation point flow field. Alternatively, one might propose that experimental uncertainties associated with angle of attack and thermocouple placement might displace the point of measurement from the actual stagnation point. Consequently, there might be a small but finite length of laminar and transitional flow prior to the onset of turbulent flow. Assuming an uncertainty in angle of attack of 0.25° and an uncertainty in thermocouple location approximately 0.040 inch, one might conject that the thermocouple is measuring the temperature at a point approximately 0.050 inch away from the actual stagnation point. While one cannot entirely dismiss this possibility, one should note that the local wetted Reynolds number based upon a length of 0.050 inch and local properties behind the normal shock wave is approximately 15,000. In either event, one requires additional theoretical developments, numerical calculations and experimental data before any firm conclusions can be made concerning mass addition and heat transfer effects at a stagnation point.

A final observation, which is illustrated in Figure 8, is that there are significant discrepancies between the measured and predicted heat transfer

rates immediately following abrupt changes in the mass addition rates. One observes, in Figure 8, that the predicted heat transfer rates are approximately 50 to 100 percent greater than the measured heat transfer rates to the porous conical frustum. Whether this discrepancy is due to a failure of the turbulence modeling technique employed in the BLIMP code or the inapplicability of the boundary layer equations to flows where there are abrupt changes or the mere fact that the experimental flow rate is approximately 10 percent greater than that used in the calculations is not at all clear at the present time.

V. CONCLUDING REMARKS

The results presented herein have provided data that can be utilized to assess the adequacy of predictive techniques for turbulent boundary layers with heat and mass transfer. This study generally confirms the adequacy of the BLIMP code for predicting heat transfer in regions where the boundary layer is turbulent and the mass transfer is uniform. These results also illustrate some potential problems in predicting heat transfer in the vicinity of discontinuous mass addition. Furthermore, the experimental measurements can be interpreted to reflect the fact that mass transfer promoted boundary layer transition at the stagnation point of the test configuration.

In the near future some additional efforts will be completed in or'er to provide some additional insight to the problems discussed herein. These efforts will include:

1. obtaining additional experimental data at lower Reynolds number per foot,

2. obtaining additional calculations for conditions which match the other experiments,

3. obtaining additional calculations to assess the effect of specified pressure distribution, and

4. obtaining additional calculations with transition closer to the stagnation point.

REFERENCES

1. Schuster, J. R. and Lee, T. G., "Application of an Improved Transpiration Cooling Concept to Space Shuttle Leading Edges," AIAA Paper No. 72-389, AIAA/ASME/SAE 13th Structures, Structural Dynamics, and Materials Conference, San Antonio, Texas, April 1972

2. Lee, T. G., "Active Nosetip Evaluation Study," McDonnell Douglas MDCG4795, SAMSO-TR-73-74, November 1972

3. Epes, A. G., "Active Nosetip Evaluation Study,"Aerojet Liquid Rocket Company, SAMSO-TR-73-75, April 1973

4. Gold, H., Mascola, R. E., and Smith, P. C., "Flow Characteristics of Porous Media and Surface Liquid Film Interactions," AIAA Paper No. 70-152, AIAA 8th Aerospace Sciences Meeting, New York, New York, January 1970

5. Schneider, P. J., Teter, R. D., Coleran, W. D., and Heath, R. M., "Design of Graphite Nosetips for Ballistic Re-Entry," Journal of Spacecraft and Rockets, Vol. 10, No. 9, September 1973

6. Baker, R. L., "Low Temperature Ablator Nosetip Shape Change at Angle of Attack," AIAA Paper No. 72-90, AIAA 10th Aerospace Sciences Meeting, San Diego, California, January 1972

7. Jeromin. L. O. F., "The Status of Research in Turbulent Boundary Layers with Fluid Injection," Progress in Aeronautical Sciences, Vol. 10, Küchemann-Editor, Pergamon Press, New York, 1970

8. Baronti, P., Fox, H., and Soll, D., "A Survey of the Compressible Turbulent Boundary Layer with Mass Transfer," Astronautica Acta, Vol. 13, pp. 239-249, 1969

9. Kays, W. M., "Heat Transfer to the Transpired Turbulent Boundary Layer," ASME Paper No. 71-HT-44, ASME-AIChE Heat Transfer Conference, Tulsa, Oklahoma, August 1971

10. Anderson, L. W. and Kendall, R. M., "A Nonsimilar Solution for Multicomponent Reacting Laminar and Turbulent Boundary Layer Flow Including Transverse Curvature," AFWL-TR-69-106, Air Force Weapons Laboratory, Kirtland Air Force Base, New Mexico, October 1969

11. Landis, R. B. and Mills, A. F., "The Calculation of Turbulent Boundary Layers with Foreign Gas Injection," International Journal of Heat and Mass Transfer, Vol. 15, pp. 1905-1932, Pergamon Press, 1972

12. Lubard, S. C. and Fernandez, F. L., "The Turbulent Boundary Layer with Mass Transfer and Pressure Gradient," SAMSO-TR-69-411, January 1970

13. Marvin, J. G. and Akin, C. M., "Combined Effects of Mass Addition and Nose Bluntness on Boundary Layer Transition," AIAA Journal, Vol. 8, No. 5, May 1970

14. Pappas, C. C. and Lee, G., "Heat Transfer and Pressure on a Hypersonic Blunt Cone with Mass Addition," AIAA Journal, Vol. 8, No. 5, May 1970

15. "Proposal for Fabricating a Porous Shell Transpiration Model," McDonnell Douglas Astronautics Co. MDCG3703P, August 1972

16. Scott, C. J., "Transient Response of a Thin-Walled, Transpiration-Cooled Porous Surface," Transactions of the ASME, Journal of Heat Transfer, February 1968

17. Conti, R. J., "Approximate Temperature Distributions and Streamwise Heat Conduction Effects in the Transient Aerodynamic Heating of Thin-Skinned Bodies," NASA TN D-895, September 1961

18. Solomon, J. M., Personal Communication, November 1974

19. Leadon, B. M. and Scott, C. J., "Recovery Dynamics-Heat Transfer at Hypersonic Speeds in a Planetary Atmosphere," Space Technology, Chapter 12, Seifert-Editor, John Wiley and Sons, Inc., 1959 (See also "Transpiration Cooling Experiments in a Turbulent Boundary Layer at M=3, J. Aeronaut. Sci. (No. 8) pp. 798-799, 1956)

TABLE I PROPERTIES OF POROUS BERYLLIUM COPPER

DENSITY:	~ 0.257 LBS/IN^3
ULTIMATE STRENGTH:	$\gtrsim$ 14,000 PSI
ELONGATION AT FAILURE:	$\sim 0.10\%$
ELASTIC MODULUS:	$\sim 7 \times 10^6$ PSI
ROCKWELL HARDNESS:	R_b 62
THERMAL CONDUCTIVITY:*	~ 35 BTU/HR-FT-^{o}F

*ESTIMATED FROM ELECTRICAL RESISTIVITY MEASUREMENTS

TABLE II MASS FLOW RATES [LBS/SEC-FT^2]

H_{wall}=0.57 BTU/lb, H_o=117.5 BTU/lb, T_{wall}=540°R, T_o=1015°R, P_{t_2}=45.41 psia, R_n=2 inches, θ_c=5°

S/R_n \ Case #	1	2	3	4	5	6	7	8	9	10	11	12	13
0	0.000	0.000	0.0425	0.085	0.170	0.000	0.000	0.000	0.000	0.170	0.300	0.600	0.75
0.07													0.90
0.192													
0.297													
0.419							0.170	0.600	0.900				
0.54												0.00	0.00
0.663													
0.681											0.00		
0.70										0.00			
0.715													
0.768													
0.9													
1.14						0.085	0.00	0.00	0.00				
1.484													
1.50													
1.62													
1.80													
2.10													
2.40													
2.70													
3.00													
3.12													
3.24													
$Re_{\theta_{trans.}}$	∞	100	100	100	100	100	100	100	100	100	100	100	100

TABLE III HEAT TRANSFER RATE [BTU/SEC-FT^2]

H_{wall}=0.57 BTU/lb, H_o=117.5 BTU/lb, T_{wall}=540°R, T_o=1015°R, P_{t_2} =45.41 pisa, R_n=2 inches, θ_c=5°

S/R_n \ Case #	1	2	3	4	5	6	7	8	9	10	11	12	13
0	17.3	17.3	14.0	11.0	6.0	17.3	17.3	17.3	17.3	6.0	1.6	0	0
0.07	17.3	17.3	14.1	11.0	6.0	17.3	17.3	17.3	17.3	6.0	1.6	1.31	0.6
0.192	16.3	16.3	13.0	23.7	18.9	16.3	16.3	16.3	16.3	18.9	12.9	5.61	2.13
0.297	16.4	35.2	32.0	29.7	25.1	35.2	35.2	35.2	35.2	25.1	19.1	9.95	4.75
0.419	15.0	38.8	35.9	33.3	28.9	38.8	38.8	38.8	38.8	28.9	23.1	13.4	7.28
0.54	13.6	40.3	37.5	35.0	30.8	40.3	32.7	18.9	12.1	30.8	25.1	15.2	8.66
0.663	12.0	39.3	36.6	34.2	30.2	39.3	31.2	16.9	10.3	30.2	24.7	15.0	8.64
0.681	11.7	39.0	36.3	33.9	29.9	39.0						25.4	20.4
0.70	11.5	38.6	36.0	33.6	29.6	38.6	30.5	16.3	9.8			27.1	22.6
0.715	11.3	38.2	35.6	33.3	29.3	38.2	30.1	15.9	9.5		32.5	28.1	23.9
0.768	10.4	36.7	34.1	31.9	28.0	36.7	28.6	14.7	8.6	34.2	32.7	29.1	25.6
0.9	8.4	31.5	29.0	27.0	23.3	31.5	23.7	11.0	5.9	30.1	29.1	26.8	24.6
1.14	4.68	18.7	16.7	14.9	11.9	18.7	12.1	3.4	1.12	18.1	17.7	16.6	15.6
1.484	1.05	4.80	3.38	2.31	1.0	2.49	4.22	2.97	2.33	4.27	4.16	3.91	3.65
1.50	1.01	4.77	3.33	2.26	0.95	2.43	4.22	2.98	2.34				
1.62	0.96	4.77	3.27	2.18	0.86	2.32	4.26	3.13	2.51				
1.80	0.93	4.76	3.20	2.09	0.77	2.20	4.32	3.29	2.71				
2.10	0.90	4.74	3.13	1.98	0.67	2.07	4.35	3.48	2.96				
2.40	0.87	4.73	3.07	1.91	0.59	1.98	4.41	3.62	3.14				
2.70	0.85	4.71	3.02	1.84	0.53	1.91	4.43	3.73	3.28				
3.0	0.83	4.70	2.98	1.79	0.49	1.85	4.45	3.81	3.40				
3.12	0.83	4.69	2.96	1.78	0.48	1.83	4.45	3.83	3.44				
3.24	0.82	4.69	2.95	1.76	0.45	1.81	4.45	3.86	3.48				

TABLE IV EXPERIMENTAL MASS FLOW RATES [LBS/SEC-FT^2]

M_∞=5.0, $P_{t_2}{}_{nom}$=46 psia, $T_{o}{}_{nom}$=960°R, $T_{wall}{}_{nom}$=530°R

S/R_n \ Test	1	66	68	73	79	67	74	82	69	75	83	80	81	84
0	0.00	0.078	0.160	0.238	0.334	0.00	0.00	0.00	0.163	0.164	0.151	0.336	0.339	0.339
0.30		↓	↓	↓	↓	↓	↓	↓	↓	↓	↓	↓	↓	↓
0.52		0.00	0.00	0.00	0.00	0.162	0.326	0.674	0.162	0.327	0.664	0.163	0.333	0.661
0.63														
0.80														
1.00														
1.20														
1.35						↓	↓	↓	↓	↓	↓	↓	↓	↓
1.48						0.00	0.00	0.00	0.00	0.00	0.00	0.00	0.00	0.00
1.98														
2.45														
2.92														
3.24														
3.52														
4.14														
4.57														
5.02														
5.49														
5.93														
6.37														
6.84														
7.28														
7.72	↓	↓	↓	↓	↓	↓	↓	↓	↓	↓	↓	↓	↓	↓

TABLE V MEAN VALUES OF EXPERIMENTAL HEAT TRANSFER COEFFICIENT ($X10^4$)-BTU/SEC-°R-IN^2

S/R_n \ Test	1	66	68	73	79	67	74	82	69	75	83	80	81	84
0	2.59	1.95	1.91	2.09	2.47	2.58	2.60	2.50	1.92	1.96	2.03	2.39	2.34	2.25
0.30	5.34	4.76	4.00	3.73	3.20	5.35	5.63	5.83	4.05	4.13	4.24	3.29	3.19	3.02
0.63	6.62	6.39	6.22	6.10	5.89	5.77	5.22	4.04	5.42	4.92	4.10	5.14	4.60	3.42
0.80	5.27	5.15	5.03	5.11	4.79	4.20	3.56	2.44	4.12	3.27	2.39	3.93	3.30	2.03
1.00	4.07	3.92	3.88	3.80	3.71	2.88	2.37	1.33	2.83	2.18	1.36	2.78	2.15	1.14
1.20	2.15	2.21	2.08	2.14	1.97	1.32	0.826	0.447	1.29	0.846	0.424	1.28	0.848	0.353
1.35	1.38	1.36	1.35	1.31	1.25	0.753	0.457	0.225	0.723	0.440	0.250	0.682	0.418	0.178
1.98	0.737	0.756	0.776	0.749	0.708	0.593	0.466	0.255	0.599	0.467	0.244	0.583	0.430	0.185
2.45	0.709	0.733	0.727	0.707	0.686	0.603	0.504	0.323	0.588	0.487	0.331	0.599	0.460	0.257
2.92	0.676	0.685	0.696	0.648	0.646	0.583	0.508	0.343	0.608	0.516	0.340	0.588	0.493	0.301
3.52	0.609	0.644	0.610	0.563	0.610	0.517	0.519	0.366	0.510	0.514	0.375	0.567	0.494	0.357
4.14	0.641	0.632	0.634	0.645	0.643	0.589	0.567	0.490	0.584	0.546	0.491	0.604	0.570	0.424
4.57	0.676	0.682	0.692	0.665	0.655	0.619	0.623	0.539	0.634	0.597	0.511	0.621	0.600	0.465
5.02	0.673	0.715	0.733	0.691	0.600	0.679	0.670	0.616	0.679	0.643	0.600	0.676	0.678	0.547
5.49	0.780	0.801	0.807	0.763	0.758	0.756	0.748	0.668	0.746	0.718	0.649	0.754	0.706	0.584
5.93	0.588	0.616	0.645	0.588	0.596	0.582	0.577	0.526	0.617	0.568	0.520	0.555	0.575	0.460
6.37	0.647	0.642	0.653	0.636	0.651	0.583	0.632	0.582	0.631	0.576	0.549	0.597	0.599	0.503
6.84	0.617	0.582	0.644	0.591	0.567	0.570	0.586	0.541	0.613	0.574	0.536	0.566	0.578	0.487
7.28	0.586	0.601	0.607	0.556	0.561	0.595	0.559	0.523	0.597	0.537	0.517	0.557	0.551	0.468
7.72	0.602	0.588	0.513	0.567	0.559	0.565	0.563	0.521	0.591	0.534	0.518	0.571	0.564	0.478
$P_{o\infty}$ (PSIA)	745	737	739	738	743	738	739	743	738	740	744	752	752	711
$T_{o\infty}$ (°R)	975	960	962	962	982	963	957	966	945	954	964	975	974	970

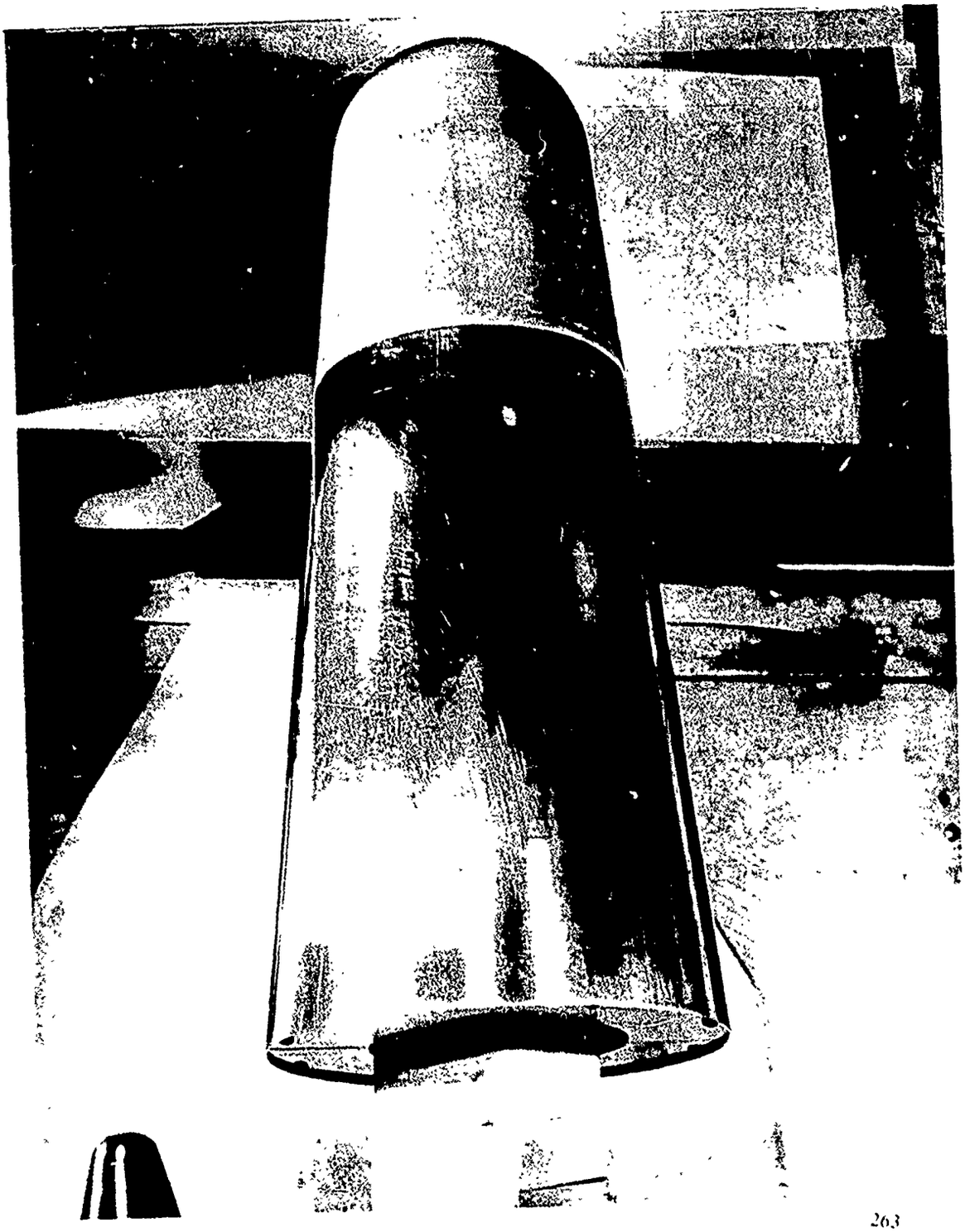

FIG. 1 POROUS SPHERE CONE HEAT TRANSFER MODEL

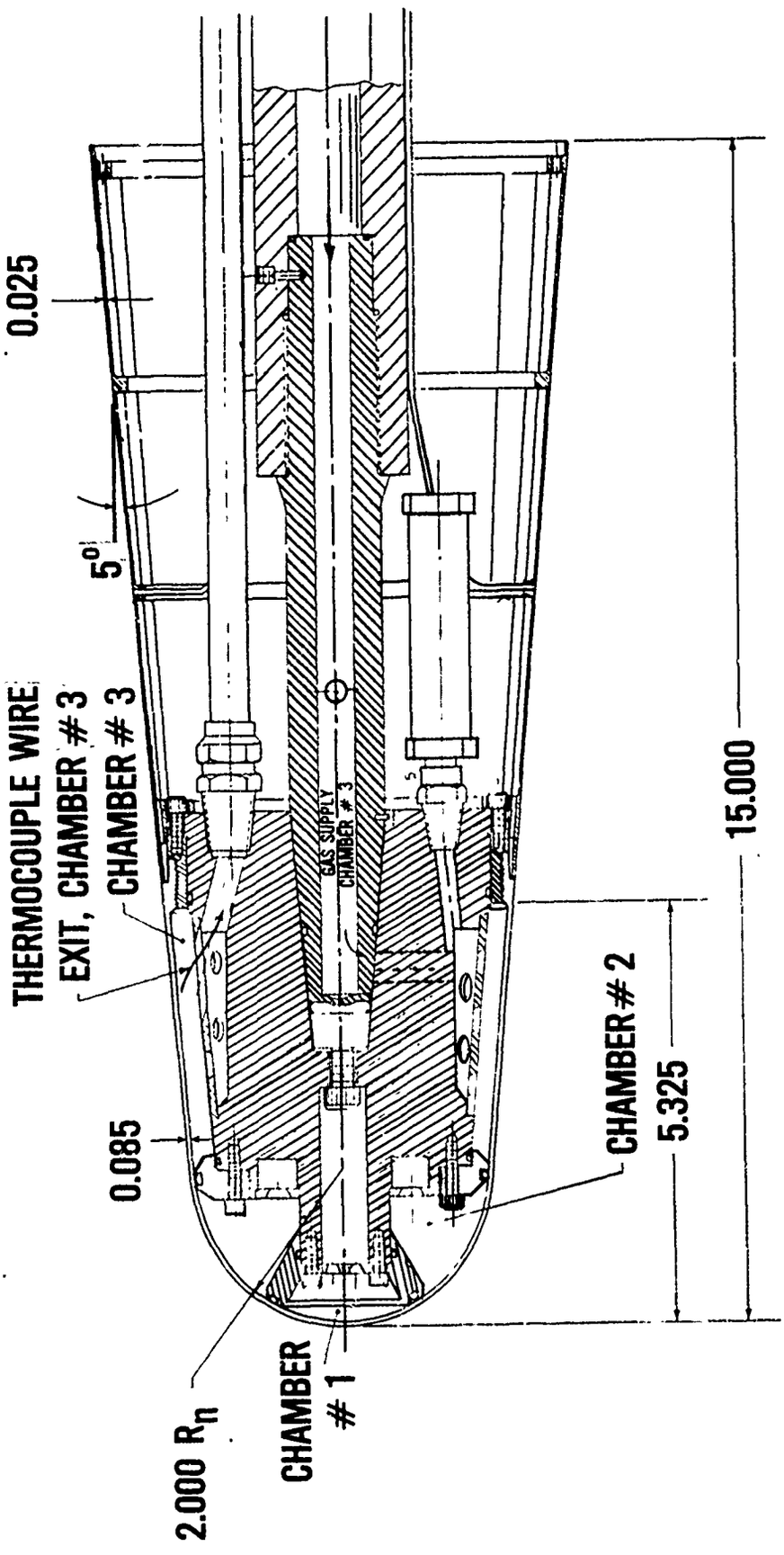

FIG. 2 MODEL SCHEMATIC

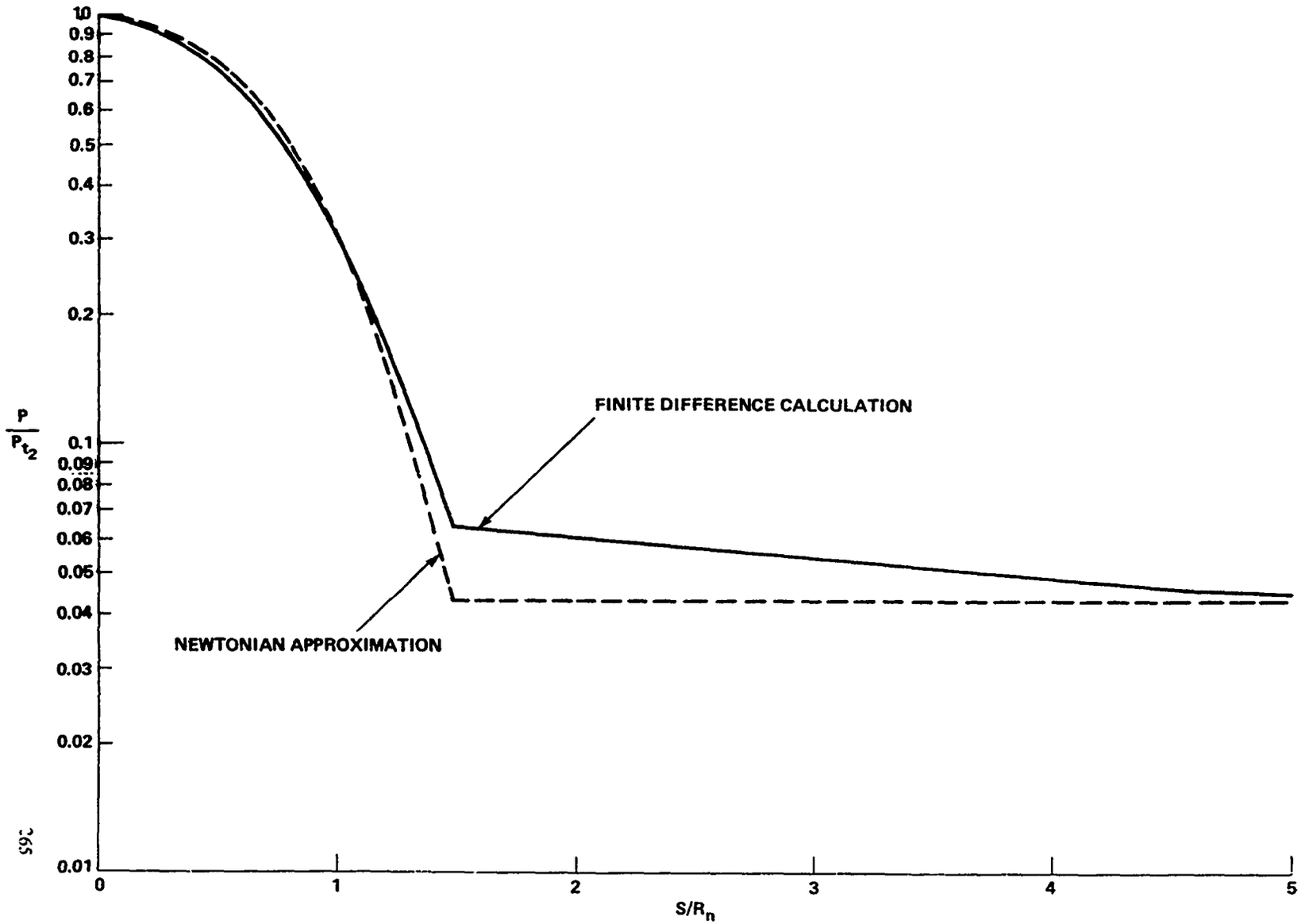

FIG. 3 SPHERE CONE PRESSURE DISTRIBUTION

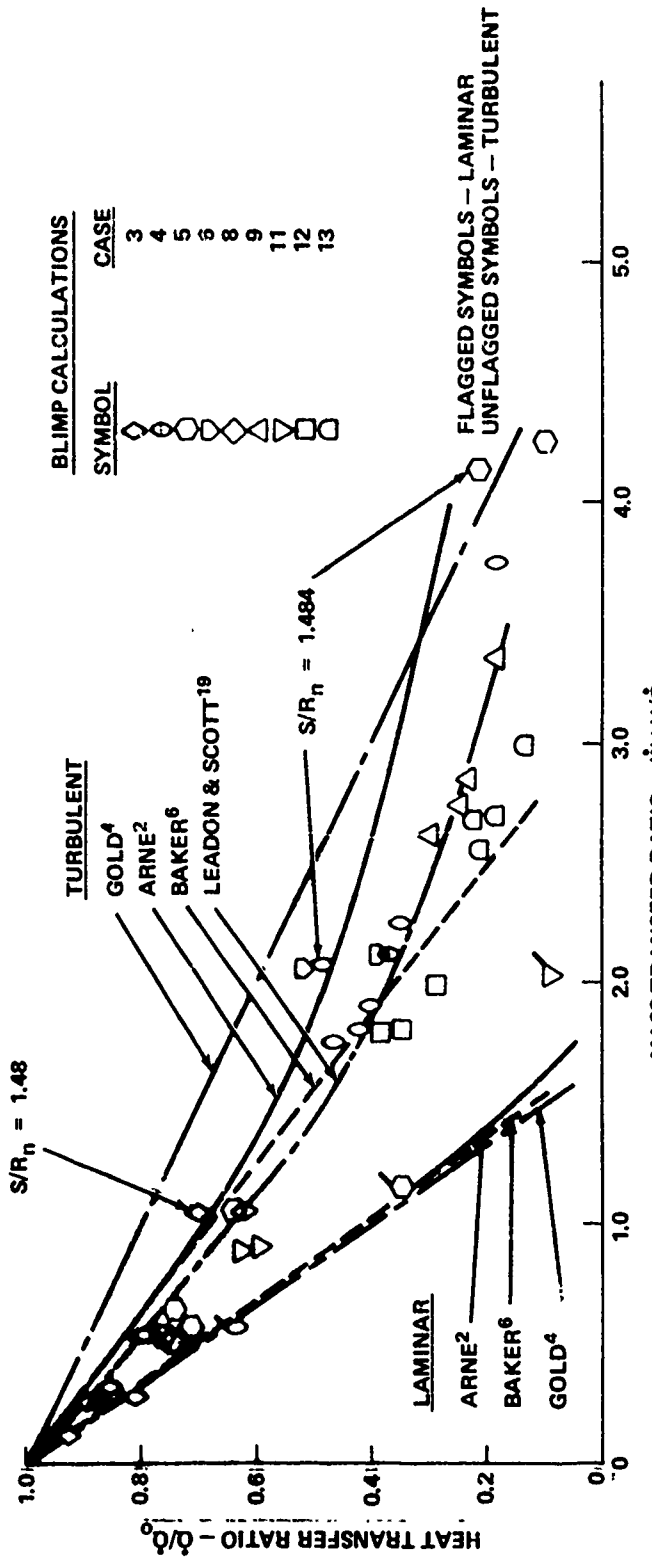

FIG. 4 PREDICTED MASS TRANSFER EFFECTIVENESS

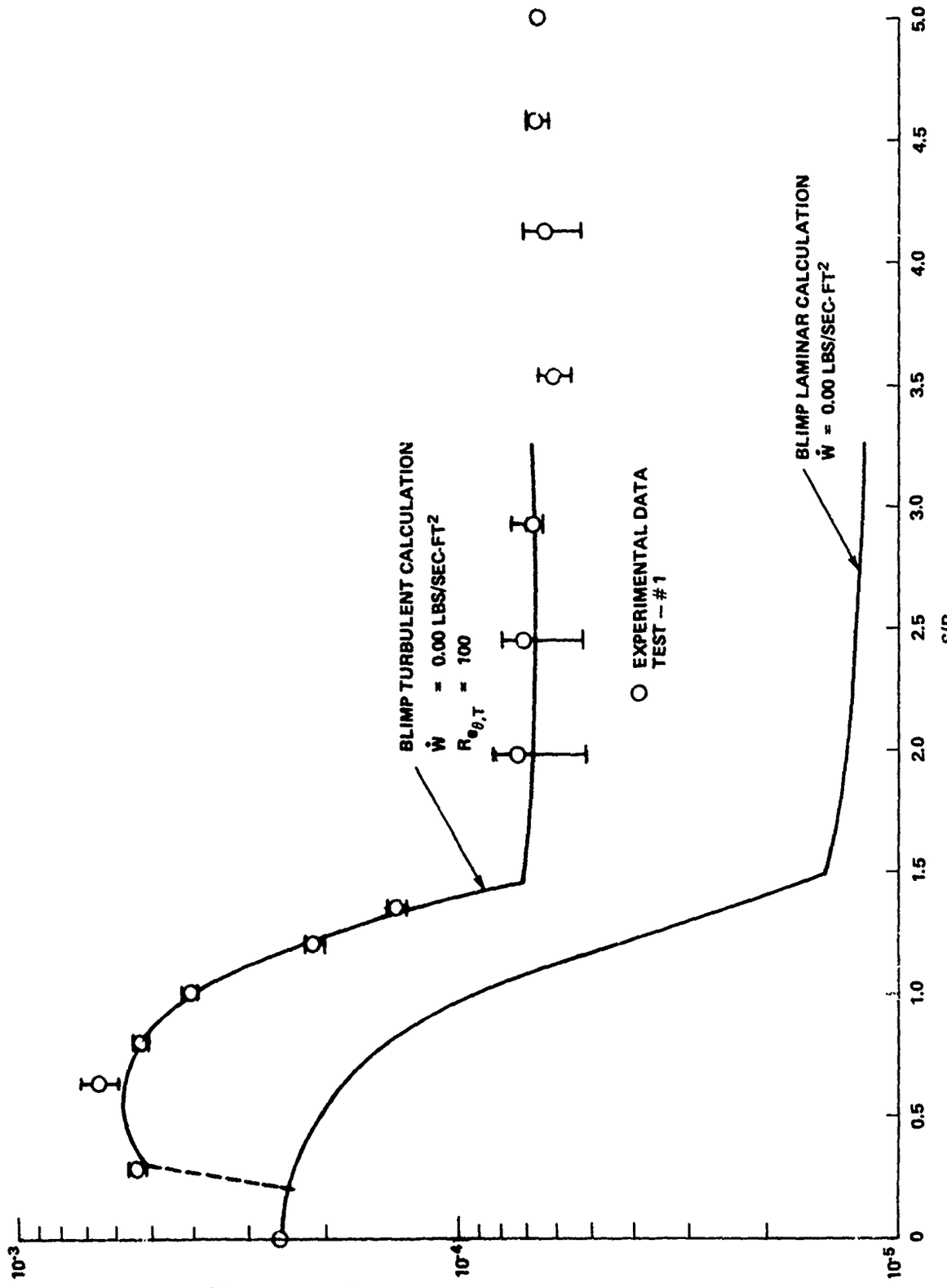

FIG. 5 HEAT TRANSFER DISTRIBUTION – NO MASS ADDITION

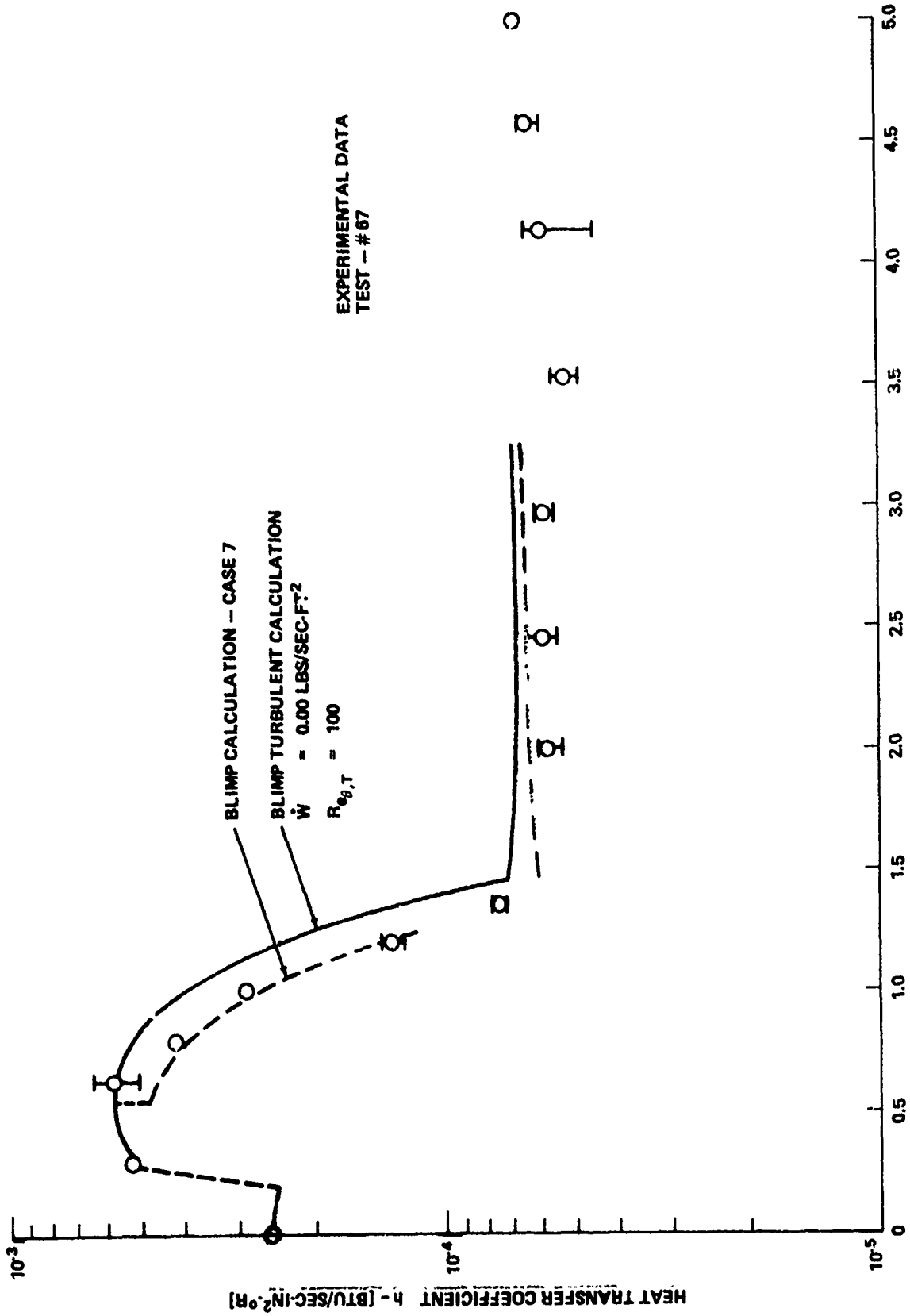

FIG. 6 HEAT TRANSFER DISTRIBUTION – MASS ADDITION

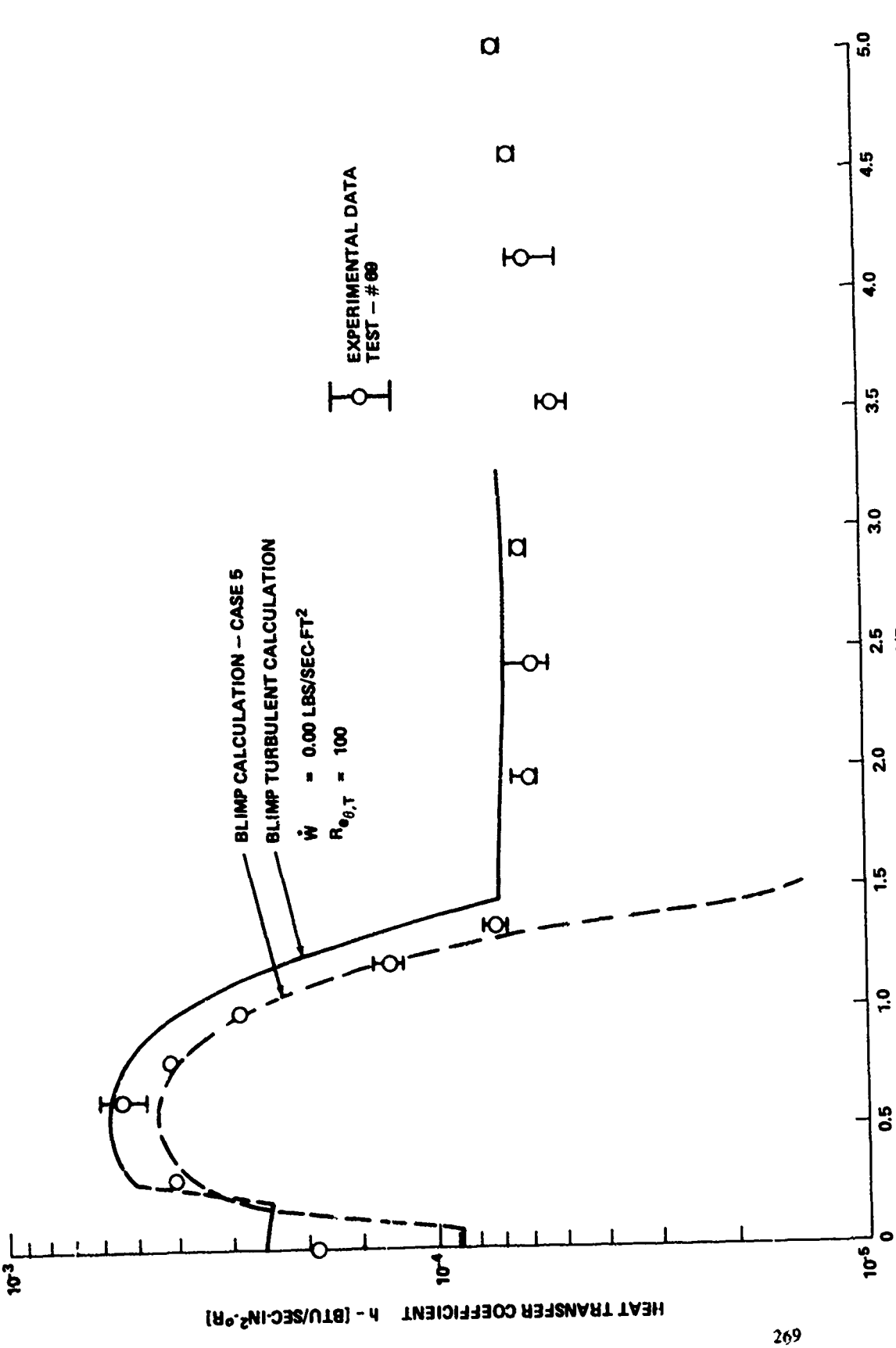

FIG. 7 HEAT TRANSFER DISTRIBUTION – MASS ADDITION

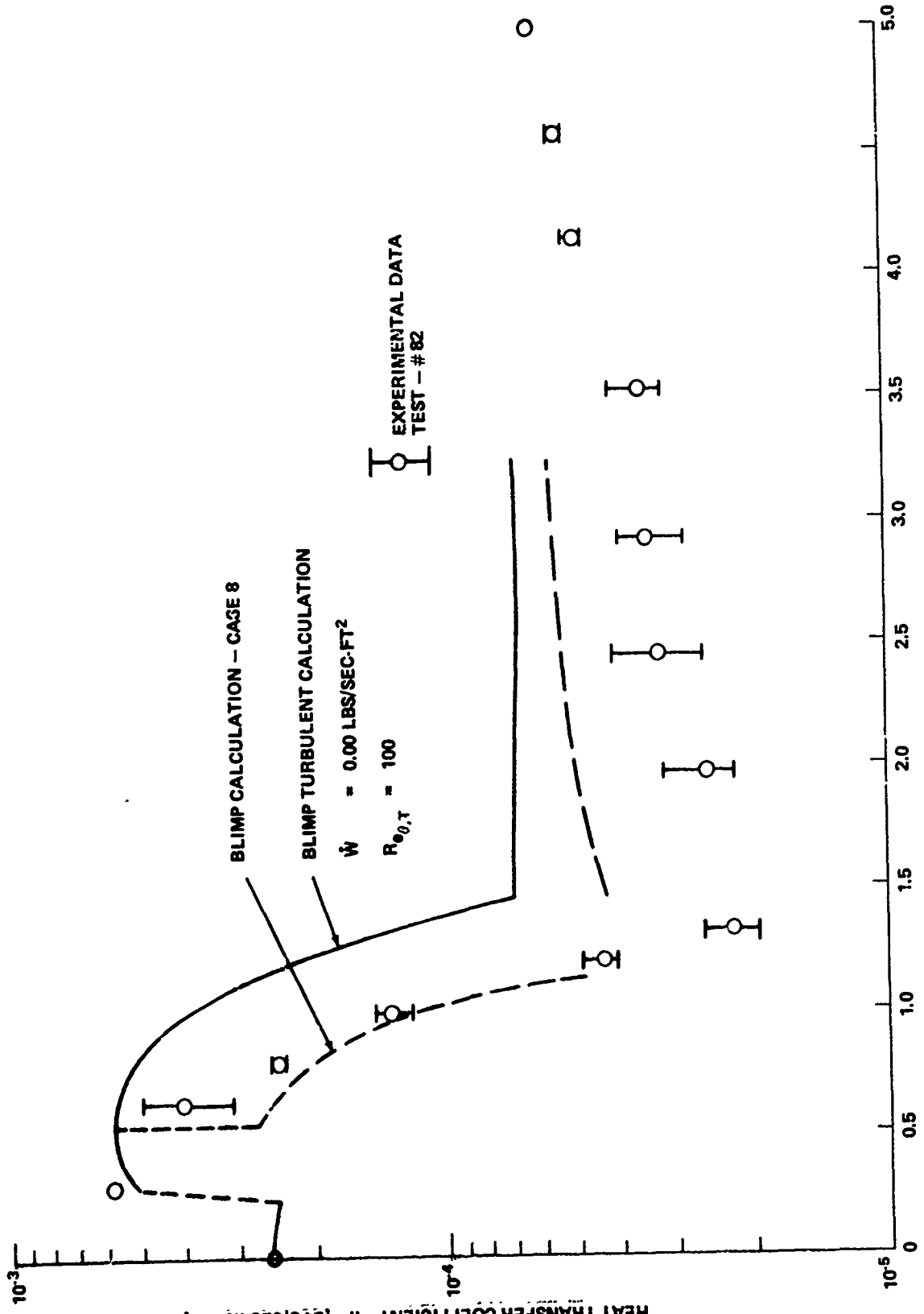

FIG. 8 HEAT TRANSFER DISTRIBUTION – MASS ADDITION

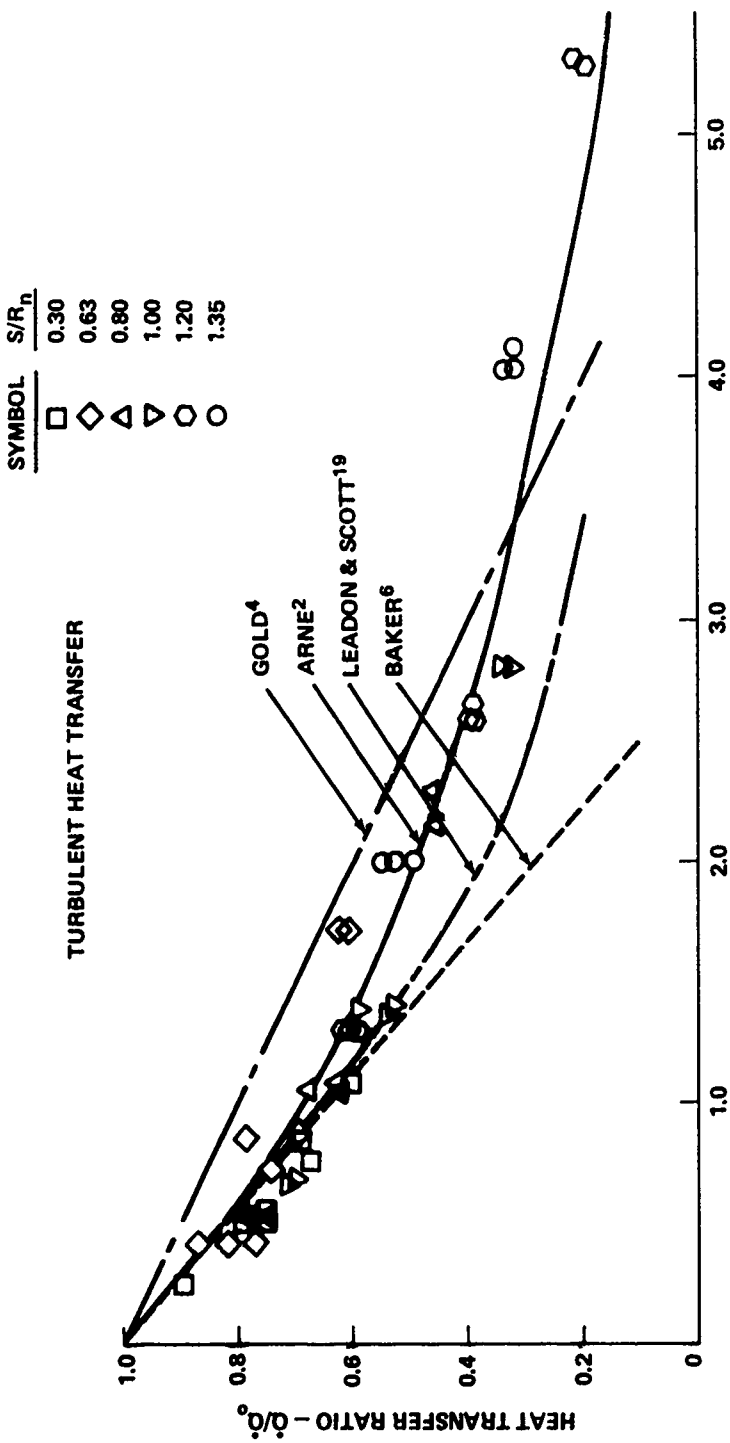

FIG. 9 MEASURED TURBULENT MASS TRANSFER EFFECTIVENESS

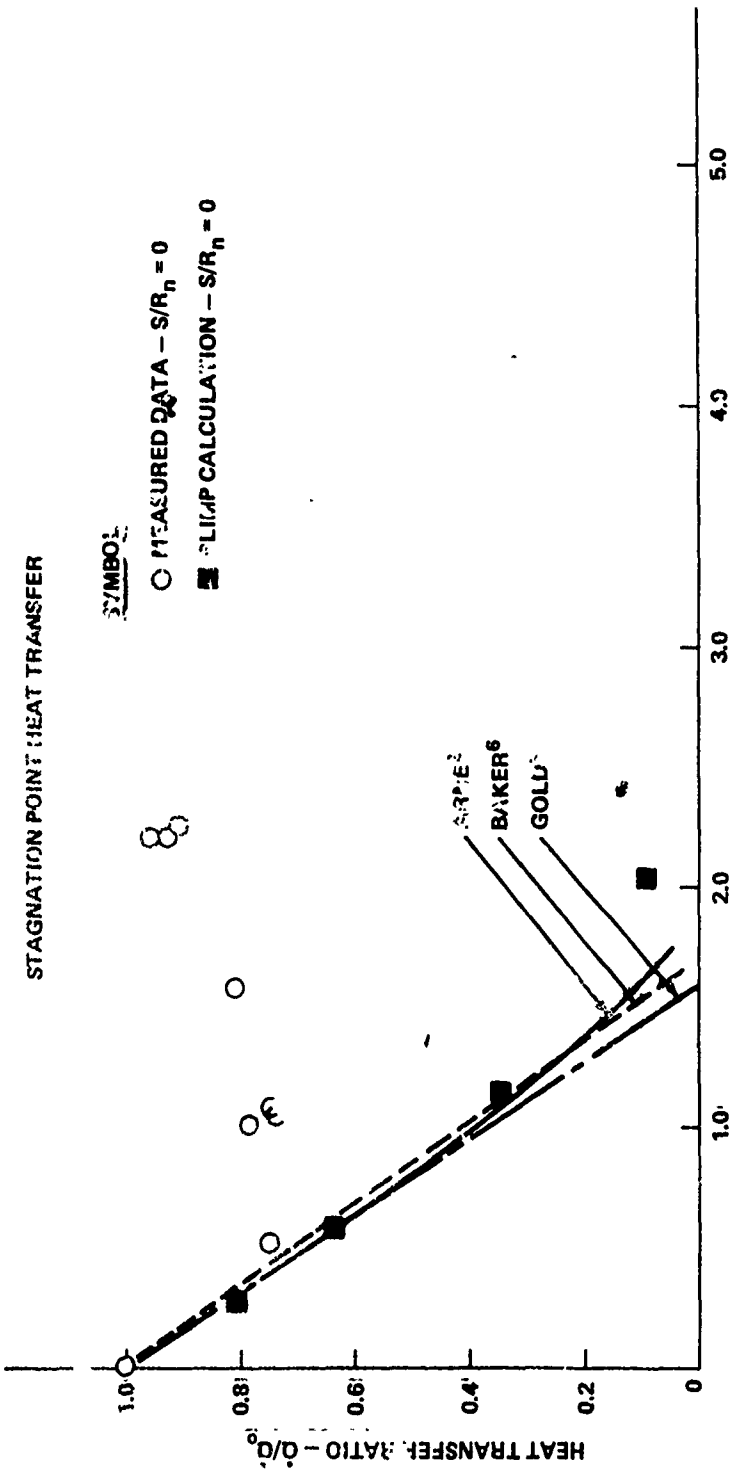

FIG. 10 MEASURED STAGNATION POINT MASS TRANSFER EFFECTIVENESS

PAPER NO. 23

PERFORMANCE CHARACTERISTICS OF TRANSPIRATION NOSE TIPS AT HIGH ANGLES OF ATTACK

J. L. Nardacci
N. C. Campbell
D. Quan
McDonnell Douglas Astronautics Company
Huntington Beach, California

ABSTRACT

Previous studies and flight test programs have shown the feasibility of porous transpiration-cooled nose tips for ballistic reentry vehicle application. This paper presents the results of transpiration-cooled nose tip analysis, ground tests, and flight verification at angle of attack.

A ground test program was performed over a range of angles of attack and thermal environments consistent with flight application. High altitude-low pressure conditions were simulated at the Malta Pit 1 facility. Stagnation pressures of 100 atm and a heating rate of 10,000 Btu/ft^2-sec were simulated in a new Philco Ford facility at El Toro, California. Test results indicated that coolant margins close to theoretical could be used for maneuvering reentry vehicle nose-tip design.

Nose-tip performance was verified in two flight tests. In addition to protecting the nose tip, the coolant decreased heat-shield recession downstream of the nose tip. Postflight predictions using previously developed methodology modified for angle of attack showed good correlation with flight data.

NOMENCLATURE

C_p	Specific heat
f	Mass fraction of coolant
g_c	Gravitational acceleration
h	Enthalpy per mass
H	Enthalpy
Δh	Net enthalpy rise in coolant
ΔH_v	Heat of vaporization
K_s	Thermal conductivity
$\dot{m}$	Coolant mass flux
N_c	Enthalpy heat transfer coefficient
N_{co}	Enthalpy heat transfer coefficient uncorrected for coolant injection
P	Pressure
q_c	Conv ctive heat flux
q_r	Net radiation heat flux
R_N	Nose radius
S	Running length
T	Temperature
V	Velocity
y	Distance
α	Porous matrix viscous flow constant, angle of attack
β	Porous matrix inertial flow constant
ϵ	Emissivity

μ	Viscosity
ρ	Density
σ	Stefan-Boltzmann constant

Subscripts

1	Value at state 1
2	Value at state 2
a	Air
c	Coolant
e	Outer edge of boundary layer
i	Injectant
m	Mixture
L	Liquid
sp	Stagnation point
r	Recovery
R	Reservoir
w	Wall

INTRODUCTION

Previous studies and flight test programs (References 1 through 4) have shown the feasibility of a porous transpiration-cooled nose tip (TCNT) as a heat protection system for reentry vehicle applications. However, all ground and flight tests were conducted at approximately zero-degree angle of attack. The applicability of this concept to maneuvering reentry vehicles is dependent upon the performance characteristics of the nose tip in a high-angle-of-attack environment. Therefore, an analytical and experimental study of these characteristics was made and the findings verified by flight test. The results of this investigation are presented in this paper.

As part of the study, a ground test program was performed over a range of angles of attack and thermal environments consistent with those predicted for maneuvering trajectories. These tests were performed in two facilities which used gas-pressurized liquid-propellant rocket motors to establish the thermal environments. The Malta Pit 1 facility was used to simulate high-altitude, high-angle-of-attack, low-dynamic-pressure conditions. For low-altitude, high-dynamic-pressure conditions, a new facility was constructed by the Aeronutronics Division of Philco Ford (ADP) at El Toro, California. This facility allowed the testing of full-scale flight nose tips at stagnation pressures up to 100 atmospheres and peak heating rates of 10,000 Btu/ft^2-sec.

A thorough calibration program including both pressure and heat flux measurements was performed at each facility to obtain flow-field data. These data were used to analyze the performance of the transpiration test models at various angles of attack. Test results indicated that coolant design margins close to theoretical values could be used for maneuvering reentry vehicle nose tip design.

Two flight tests of the transpiration nose tip were made in which the tips were subjected to a large range of angle-of-attack, stagnation pressure, and heating rates. The nose tips successfully completed the missions, with design margins as low as 25 percent. In addition to protecting the nose tips, the coolant also decreased the recession of the adjacent heat-shield material. This downstream cooling effect was produced both from a liquid film on the vehicle surface and from liquid droplets or vapor in the boundary layer adjacent to the surface. Postflight predictions, using previously developed methodology modified to account for angle-of-attack effects, showed good correlation with the flight data.

GROUND TESTS

The flight environment was divided into two regimes for purposes of defining a ground test program. In general, the highest angles of attack are likely to occur at the higher altitudes where the nose-tip environment is relatively mild. Conversely, at lower altitudes where the nose-tip environment is most severe, the angle of attack will be moderate. Therefore, ground tests were required in both a low-pressure, low-heating environment at high angles of attack and a high-pressure, high-heating environment at moderate angles of attack. Two facilities were chosen to satisfy these diverse requirements. The Malta Pit 1 facility at Ballston Spa, New York was selected to provide the former test conditions while the Philco Ford facility at El Toro, California was selected to provide the latter.

Low-Pressure Tests – Malta

Three calibration tests were conducted to define the heat flux and pressure environments at 0 and 30 degrees angle of attack at the Malta facility. After completion of the calibration tests. four transpiration nose tip tests were conducted to characterize the nose-tip performance at large angles of attack.

Facility Description – The Malta Pit 1 facility utilizes a rocket exhaust gas to simulate the reentry environmental conditions. The oxidizer-fuel combination was liquid oxygen and ethyl alcohol. Propellants were injected through a 3-inch-diameter injector body into a 3-inch-diameter combustion chamber. The resulting gases were exhausted through a 15-degree contoured nozzle with parallel flow at the 5-inch-diameter exit plane. The entire rocket engine combustion chamber and nozzle assembly were mounted on a gimbal arrangement which allows engine initiation and termination away from the model. Nominal conditions for this facility are as follows:

Stagnation Gas Temperature	5,600°R
Combustion Chamber Pressure	258 psia
Exit Mach Number	2.48
Gas Stagnation Enthalpy	2,800 Btu/lb

The coolant expulsion system consisted of a regulated high-pressure gas supply and a flow system panel which contained components to store, filter, and meter coolant (water) to the nose tip. Capability was provided for obtaining four discrete coolant flow rates during a test. During each test, at approximately 3-second intervals from the initiation and occurring at 3, 6, and 9 seconds during the exposure, the coolant flow was decreased in steps by closing a solenoid valve. Total run time was 12 seconds.

Coolant flow rates were controlled in most cases with cavitating venturis made by the Fox Valve Development Company. In some runs the desired incremental flow rates were smaller than could be provided by venturis fabricated by conventional machining techniques. Orifices were used to control the flows under these circumstances. However, in all runs, the lowest flow (which contributes the vast majority of flow at higher flow steps) was set by a cavitating venturi.

Coolant nose tip and expulsion system pressures were measured with Statham strain gage transducers. Coolant flow rates were measured with a Waugh turbine flowmeter. As a secondary determination of flow rates, the pressure drop across the venturis or orifices was correlated to obtain a flow rate. Coolant temperature in the nose-tip cavity was measured with a 0.020-inch-diameter chromel-alumel thermocouple probe.

Surface heat-shield temperatures at the porous nose-tip/heat-shield interface were measured with chromel-alumel thermocouples. One thermocouple was oriented on the windward ray with the second thermocouple in the yaw plane.

Three high-speed color motion pictures were taken during each test. Two Fastax cameras provided close-up pictures of the nose tip; one on the wind side, the other on the lee side. A Hycam camera, located on the wind side, viewed the entire length of the model. All cameras operated at a nominal framing rate of 800 fps. The wind side Fastax camera had a 12-volt light bulb mounted near the lens to provide an indication of solenoid valve closure on the expulsion system. As a valve closed, the light bulb was energized momentarily to indicate a change in flow rate.

Calibration and Transpiration Model Descriptions – The calibration models were sphere-cones with characterizing dimensions of 3/4-inch nose radius, 7-degree cone half-angle, and a base diameter of 3.5 inches. Dimensionally, the calibration models were identical to the transpiration models. Aerotherm/Acurex Corporation fabricated all calibration models for this test series.

In all calibration models, the emphasis was to obtain data on or near the hemispherical portion of the model so that the environment on the porous nose tip could be completely defined. Nose-tip calibration data previously available for the Malta facility consisted of only a stagnation point location and a location several nose radii downstream.

A combined heat flux and pressure calibration model was employed for the 0-degree angle of attack condition. Eleven null-point copper calorimeters and six pressure taps were used as shown in Figure 1a. All pressure tubes were 0.062-inch inside diameter, 0.093-inch outside diameter stainless steel tubes. Separate heat flux and pressure calibration models were used to characterize the model environment at angle of attack of 30 degrees. Each model had 10 null-point calorimeters/pressure taps located as shown in Figure 1b. The separate models were positioned so that the windward ray (0-degree ray) contained the majority of the sensors.

WD2503

STATION NO.	DISTANCE "S", INCHES
1	0
2, 2A, 2B, 2C	0.393
3, 3B	0,720
4, 4A, 4B, 4C	1.086
5, 5B	2.086
6, 6A, 6B, 6C	3.086

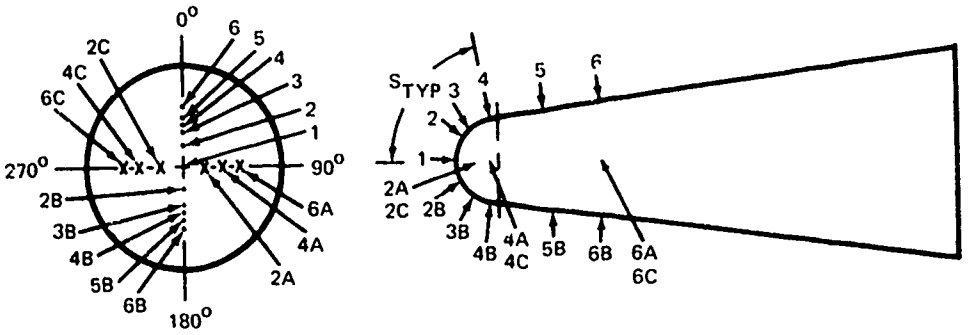

• CALORIMETER

X PRESSURE TAP

A. COMBINED CALIBRATION MODEL, $\alpha = 0^{\circ}$

STATION NO.	DISTANCE "S", INCHES
1	0
2	0.393
3, 3A, 3B	0.785
4	1.336
5, 5A, 5B	2.086
6	3.086

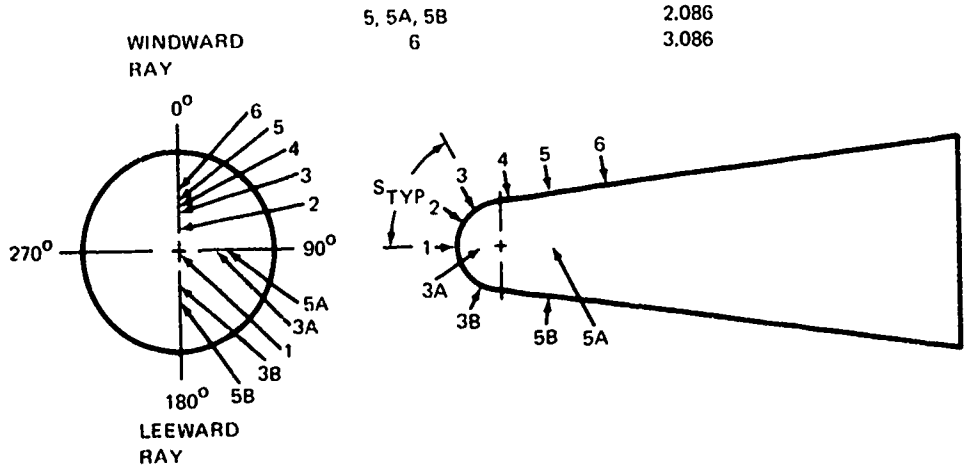

B. SINGLE TYPE CALIBRATION MODEL, $\alpha = 30^{\circ}$

Figure 1. Malta Calibration Models

The overall dimensions of the transpiration nose-tip models were identical to the calibration model. The porous nose tip, fabricated from approximately 86 percent dense sintered stainless steel, consisted of a composite sphere-cone, with the tangent point occurring 83 degrees from the stagnation point. Skirt length, measured along the surface from the tangent point of the porous nose tip, was 0.265 inch.

The porous nose-tip geometry is shown in Figure 2. The inner surface of the nose tip consisted of a hemisphere-cylinder with the junction occurring 44 degrees from the tip axis. Radius of the inner sphere was 0.60 inch and the cylindrical radius of the inner cavity was 0.42 inch. Thus, the region near the stagnation point was a constant 0.150-inch thickness.

The nose tip faired into a phenolic silica conical heat shield. Due to the nature of the model design, the back surface of the porous nose tip was in contact with the leading edge of the heat shield. No coolant flow was allowed to issue from the nose-tip/heat-shield interface. This condition was attained by shot peening of the nose-tip back surface.

WD2503

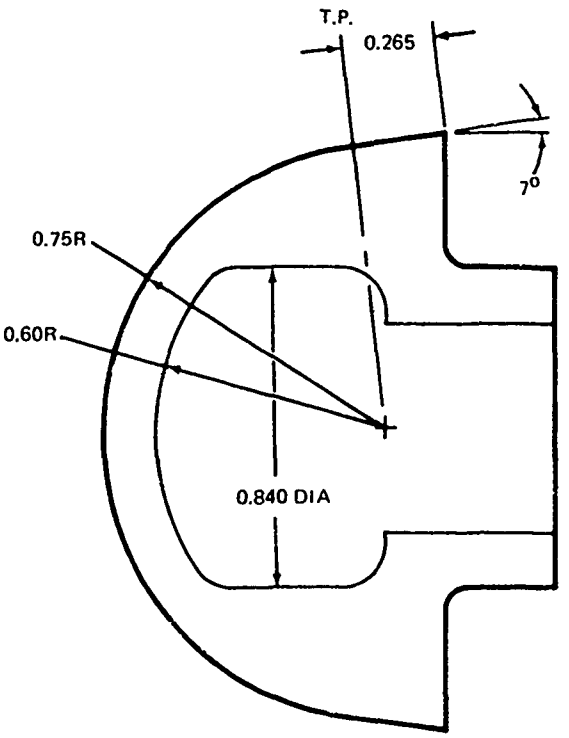

Figure 2. Ground Test Model Nose-Tip Geometry

The calibration and transpiration nose-tip models were protected from transient heating encountered during the gimbaling operation by means of a Teflon cap. The cap was sized to be removed in 0.3 second after gimbaling onto the model. A picture of the test setup with the model in the 30-degree position is shown in Figure 3.

The porous nose tips were flow calibrated prior to testing at Malta to verify the nose-tip flow distribution and permeability. Distributional data were obtained by sampling the flow at the nose-tip surface by means of an 1/8-inch inside diameter probe. Seventeen points on the nosetip were sampled: at the stagnation point and at the 22-, 44-, 66-, and 90-degree stations Four orthogonal points were sampled at each angular position. Data were taken utilizing nitrogen as the flow media. Good agreement between the predicted distribution and the probe data was obtained. Typically, the spread in the four measurements at each station (other than the stagnation point) was less than 15 percent which is close to the accuracy of the probing technique.

Water flow calibration was performed with the expulsion system described previously. Gross permeability values were calculated from these data by a graphical solution of the modified Darcy equation

$$-\Delta P = \frac{(\alpha\mu + \rho\beta V)\overline{V}}{g_c} \qquad (1)$$

Facility Calibration Test Results – Three calibration tests were conducted in Malta Pit 1. These consisted of a combined heat flux/pressure test at 0-degree angle of attack and separate tests for heat flux and pressure at 30-degree angle of attack. The pressure data from the 0- and 30-degree angle of attack calibration tests are summarized in Figure 4a. A stagnation pressure of 8.5 atmospheres was measured. As expected, the pressures on the hemispherical portion of the model are similar for both test conditions and follow a Newtonian distribution.

WD2503

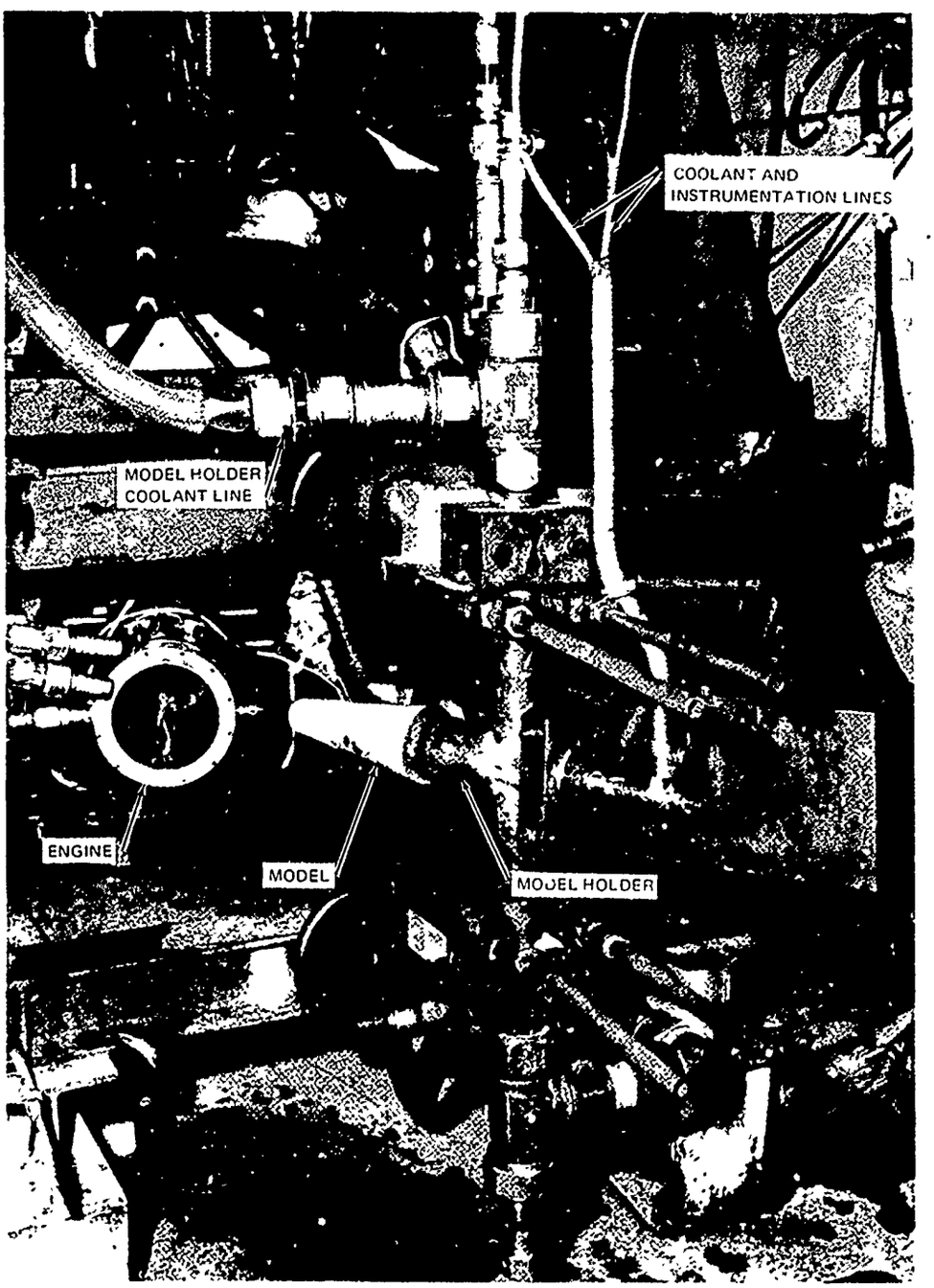

Figure 3 Malta Test Setup

WD2503

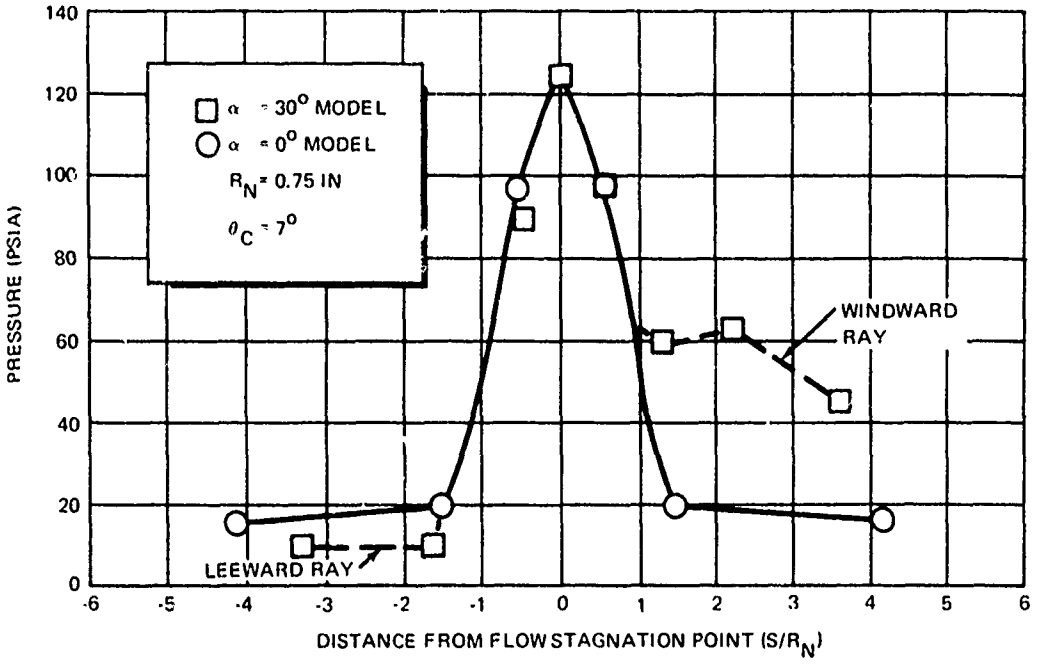

A. PRESSURE DISTRIBUTION

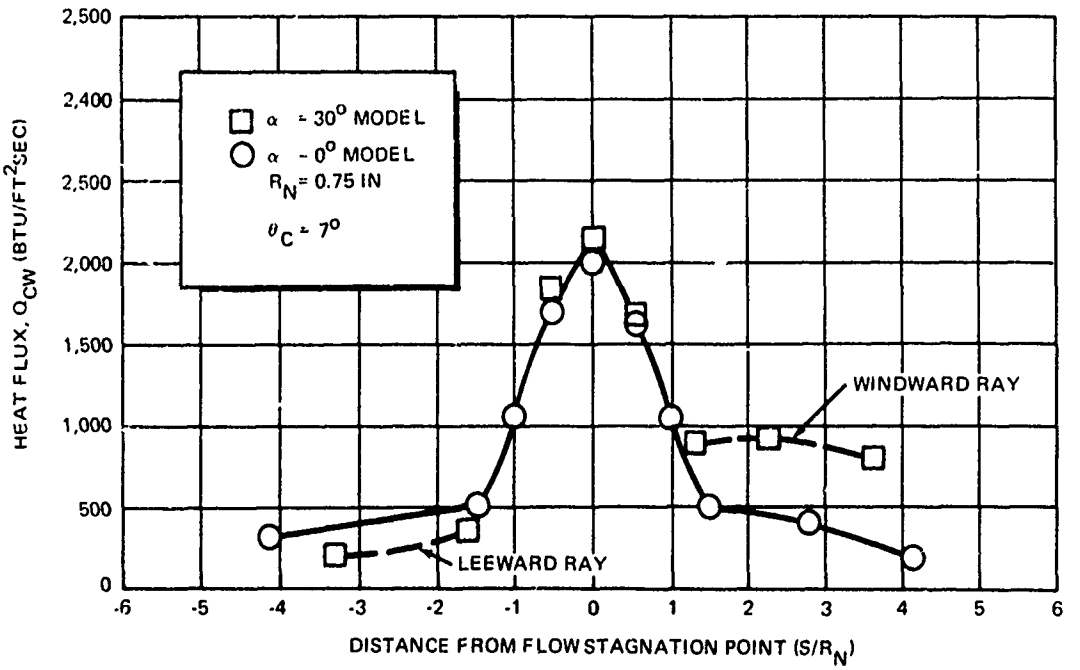

B. HEAT FLUX DISTRIBUTION

Figure 4. Malta Pit 1 Pressure and Heat Flux Distributions

The measured heating distribution is shown in Figure 4b. Average stagnation heat flux between the two test conditions was 2,050 Btu/ft^2-sec. The nose-tip hemispherical heating distribution follows Lee's laminar heating theory (Reference 5), and as was the case with the pressure data, is symmetrical about the axis of symmetry.

With the environment on the nose tip defined, the ideal local coolant mass flux ($\dot{m}_i$) can be calculated. The ideal coolant mass flux is defined as that amount of coolant required to maintain the nose-tip surface at the boiling point temperature of the coolant.

Using the approach given in Reference 6, the ideal coolant flows are determined from the steady-state energy balance

$$q_c - q_r = K_s \left.\frac{dT}{dy}\right|_w = \dot{m}\Delta h \tag{2}$$

In the case where blowing is present

$$q_c = N_{c_o}\left(\frac{N_c}{N_{co}}\right)(H_r - H_w) \tag{3}$$

where the ratio N_c/N_{co} represents the reduction in the heat transfer coefficient due to the alteration of the boundary layer properties caused by the injectant fluid.

The correlation (see Reference 7) for N_{co} is written as

$$\frac{N_c}{N_{co}} = 1 - L\frac{\dot{m}}{N_{co}} \tag{4}$$

where L is a function of both the parameter $\dot{m}/N_{co}$ and the specific heat ratio, C_{p_i}/C_{p_e}.

The term Δh in Equation (2) represents the enthalpy change of the coolant between its storage state and its state at the surface. This enthalpy change includes not only the sensible heats and heats of vaporization, but also the effects of the heat of reaction between the coolant gas and the freestream air. The first step in the calculation of Δh is the definition of a convenient thermodynamic path. The chosen path is illustrated in Figure 5. The overall enthalpy change is from a stored liquid at T_r and P_r to a final state consisting of a real gas mixture at T_2 and P_2 in which reactions have reached equilibrium. The possibility of simply subtracting the enthalpies in the final and stored states is hampered by the difficulty in obtaining data for both states which have the same reference states. Therefore, an alternate path is chosen in which the overall enthalpy change is divided into two parts. The first path consists of the energy required to convert the stored liquid to a saturated vapor at some convenient temperature (T_1) and pressure (P_1). The enthalpy change is given by

$$\Delta h_1 = c_{pL} (T_1 - T_r) + \Delta H_v \qquad (5)$$

WD2503

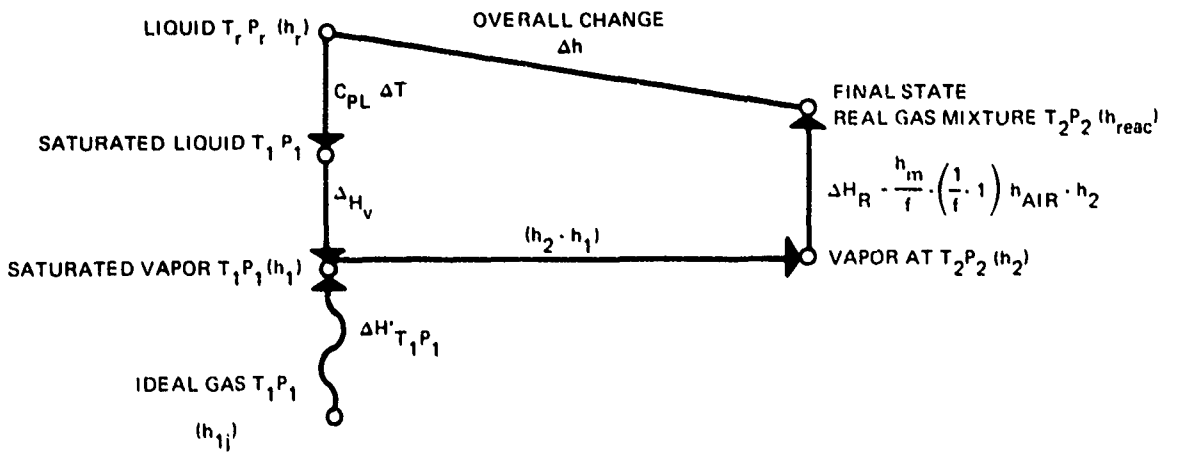

Figure 5. Coolant Thermodynamic Path

The second path consists of the energy required to bring the saturated vapor to the surface temperature and pressure (T_2 and P_2) and includes the heat of reaction between the injectant gas and the freestream air. Since the final state in subsequent calculations is to be based on JANAF property data (which uses the ideal gas at 1 atmosphere as a reference state), it is convenient to use JANAF data to define the enthalpy of the vapor at T_1 and P_1. The real gas enthalpy at T_1 and P_1 can be obtained by subtracting the real gas enthalpy corrections ($\Delta H'_{T_1 P_1}$) at T_1 and P_1 from the JANAF enthalpy value. Thus, the enthalpy change over the second path is

$$\Delta h_2 = (h_2 - h_1) + \Delta H_R \tag{6}$$

where $h_1 = h_{1_j} - \Delta H'_{T_1 P_1}$ = enthalpy of coolant in gas phase at T_1 and P_1 based on the ideal gas enthalpy from JANAF (h_{1_j}) and the real gas correction. The heat of reaction per pound of coolant (ΔH_R) can be obtained by subtracting the enthalpy of the reactants (air and coolant at T_2, P_2) from the enthalpy of the reacted mixture at T_2 and P_2. Thus,

$$\Delta H_R = \frac{h_m}{f} - \left[\left(\frac{1-f}{f}\right) h_a + h_2 \right] \tag{7}$$

Addition of Equations (5) and (6) gives

$$\Delta h = \Delta h_1 + \Delta h_2 = C_{PL} (T_1 - T_r) + \Delta H_V + (h_2 - h_1) + \Delta H_R$$

Substituting for ΔH_R, letting $\lambda = C_{PL} (T_1 - T_r) + \Delta H_v$, and rearranging gives

$$\Delta h = \lambda + \left[\frac{h_m}{f} - \left(\frac{1-f}{f}\right) h_a - h_1 \right] \tag{8}$$

Substitution of Equations (3), (4), and (8) into Equation (2) gives

$$(N_{co} - L\dot{m})\, \Delta H - \sigma \epsilon\, T_2^{\,4} = \left\{ \lambda + \left[\frac{h_m}{f} - \left(\frac{1-f}{f}\right) h_a - h_1 \right] \right\} \dot{m} \tag{9}$$

where $q_r = \sigma \epsilon\, T_2^{\,4}$

Based on Equation (9), Figure 6 presents the laminar and turbulent boundary layer ideal coolant mass flux for water as a function of recovery enthalpy. The curves were generated for an air environment. Comparisons of mass transfer blocking in air and a Malta-type rocket exhaust environment were made and it was found that an increase of approximately 10 percent in mass flux (over the air value) was needed for the Malta environment.

Test Observations – Four transpiration models were tested at the Malta facility. Runs 1719 and 1722 were conducted at 0-degree angle of attack with Runs 1720 and 1721 at 30-degree angle of attack. The nose tip from Run 1719 experienced melting over the entire hemispherical portion of the nose tip. The skirt region of the porous nose tip was virgin although it was covered by solidified stainless steel swept downstream from the hemisphere. Total recession at the stagnation point was approximately 0.050 inch, leaving 0.100 inch of material remaining. The general shape of the nose tip was still hemispherical although the surface had receded to a slightly greater amount at about 60 degrees from the stagnation point.

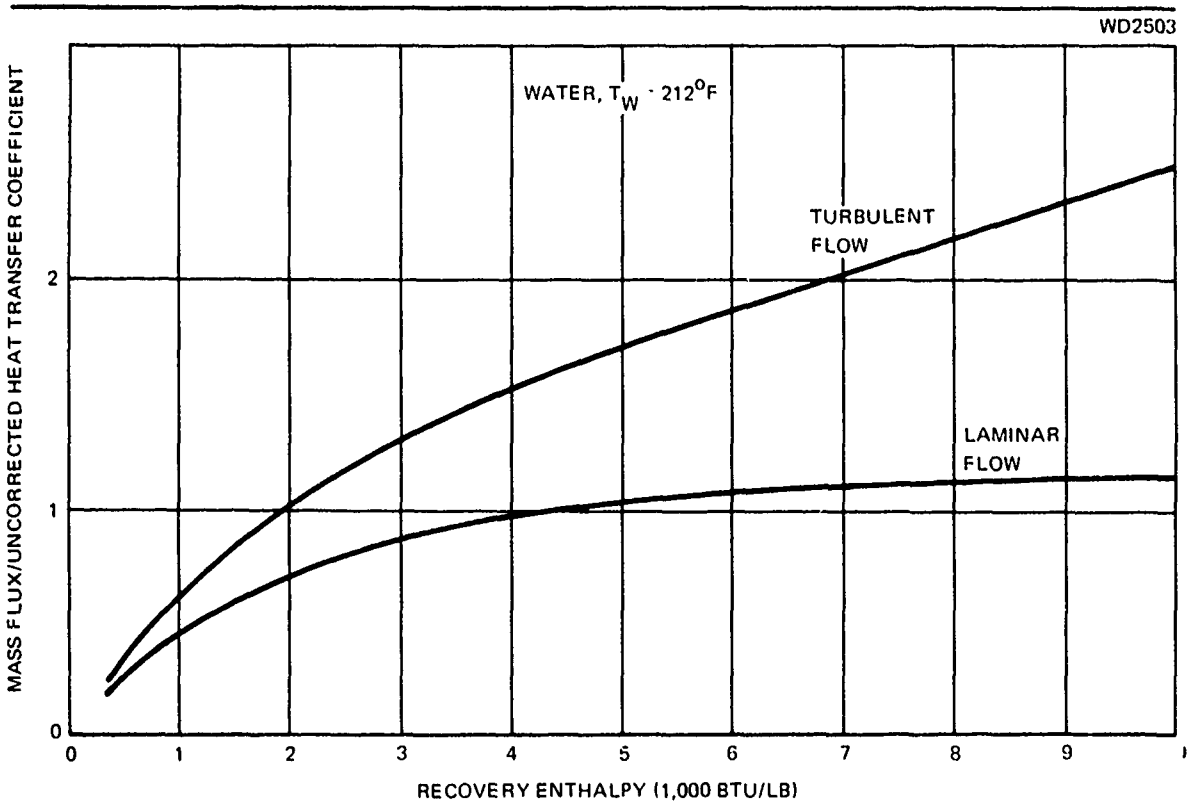

Figure 6. Ideal Transpiration Cooling Requirements

Further evidence of maximum heating at the 60-degree location is given by the post-test appearance (Figure 7a) of Model 517-5 (Run 1722, angle of attack = 0 degrees). Oxidized regions symmetrically located at the 60-degree position were on the nose tip. The nose tip was virgin forward of the sonic line as exemplified in Figure 7b. Even with oxidation occurring over part of the nose tip, no recession was evident.

The only area of nose-tip degradation for the models tested at 30-degree angle of attack occurred on the windward side and adjacent to the phenolic silica heat shield. Little, if any, material was lost from the oxidized regions. As expected, heat-shield ablation materialized only on the windward side. The ablation stopped abruptly 3-1/2 inches downstream of the nose tip indicating the intersection of the flow field boundary with the model. A liquid layer covered the heat shield on the leeward side. Figure 7c presents a photograph of a model tested at angle of attack of 30 degrees.

Details of model performance were clearly shown by the high-speed motion pictures taken during the 0-degree angle of attack tests. The close-up wind side camera, in particular, gave an excellent view of the phenomenon occurring on the surface of the nose tip. In Run 1719, a liquid layer was maintained over the entire nose tip surface for the first three flows. At the beginning of the fourth flow, dry (i.e., loss of liquid film) areas were observed initially at the 60-degree location. Melting started a few hundred milliseconds later at the stagnation region which soon spread over the entire hemisphere. For the remainder of the run, the nose tip receded somewhat uniformly at approximately 0.015 in/sec.

Dry areas were initially observed on the third flow in Run 1722. The dry areas, at about the 60-degree location, spread very slowly for the remainder of the third flow. By the end of the third flow, the center regions of the affected areas were glowing but not melting. During the fourth flow, the dry and oxidized regions expanded symmetrically to an area bounded by the 40- and 70-degree points. No material from the nose tip was ablated. A stable two-phase flow condition existed in the porous matrix. Figure 8 presents a photograph of the nose tip during the test (Run 1722) at each flow rate.

WD2503

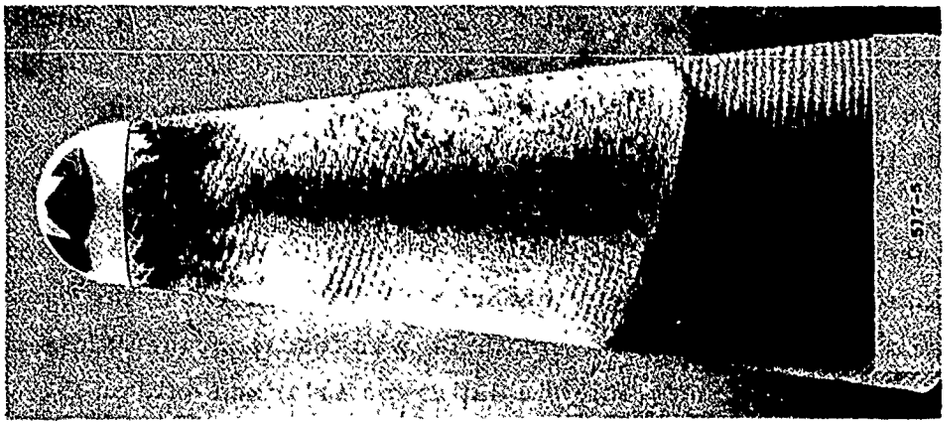

A. MODEL 517-5 (RUN 1722)

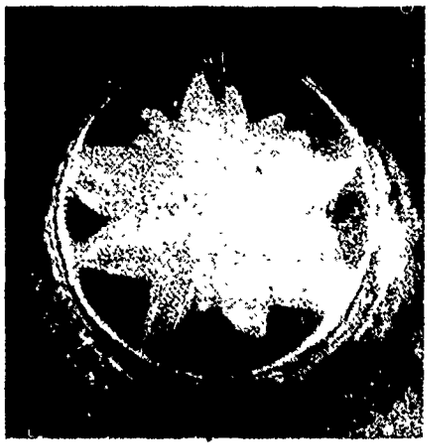

B. HEAD-ON VIEW MODEL 517-5

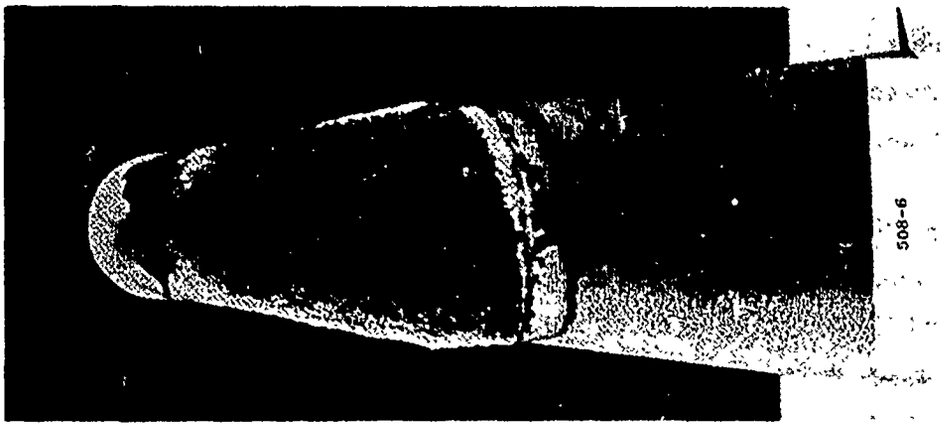

C. WINDWARD VIEW, MODEL 508-6 (RUN 1721)

Figure 7. Post-Test Model Appearance

WD2503

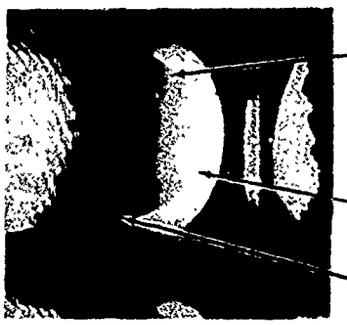

FLOW NO. 1
FLOW RATE: 0.0290 LB/SEC
STAGNATION POINT MARGIN: 80%
MINIMUM MARGIN: -9%

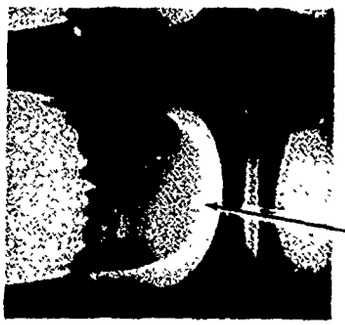

FLOW NO. 2
FLOW RATE: 0.0262 LB/SEC
STAGNATION POINT MARGIN: 60%
MINIMUM MARGIN: -21%

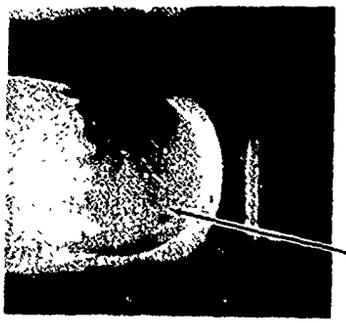

FLOW NO. 3
FLOW RATE: 0.0222 LB/SEC
STAGNATION POINT MARGIN: 35%
MINIMUM MARGIN: -30%

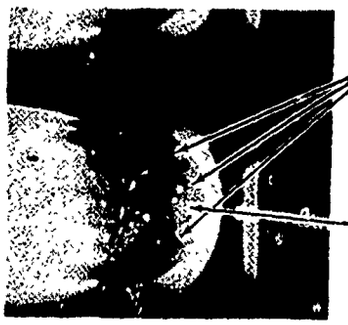

FLOW NO. 4
FLOW RATE: 0.0188 LB/SEC
STAGNATION POINT MARGIN: 8%
MINIMUM MARGIN: -41%

Figure 8. Nose-Tip Appearance During Test

For the 30-degree tests, the windward motion pictures were of lower quality due primarily to the heat-shield brightness. With very little downstream cooling and increased heating over the 0-degree condition, the heat shield became so bright it tended to wash out a picture of the nose tip. On Run 1720, no details of the nose tip were visible. Good pictures were obtained from the lee side cameras but this side of the nose tip was overcooled.

For the second test (Run 1721) at angle of attack, the f-stops on the wind side cameras were increased. Although the drying up of the surface was not distinguishable, the oxidation phase was visible. Oxidation was detected during the middle of flow three and appeared to start from the nose-tip/heat-shield interface. The oxidation zone progressed forward to the 60-degree location by the end of test. No significant amount of melting occurred in the test. As in the previous test, the leeward side remained cool. A summary of the motion picture observations is presented in Table 1.

Nose-Tip Performance – Coolant distributions for every flow rate assuming single-phase coolant flow in the nose tip were determined by a computer program (Reference 8) which calculates three-dimensional coolant distribution within transpiration-cooled nose tips. This program is based on a three-dimensional finite-difference formulation of the modified Darcy equation (Equation 1).

Distributions for Run 1722 (0-degree angle of attack) are plotted in Figure 9. Also shown is the ideal curve based on the measured heat fluxes (laminar distribution). Subtracting the ideal mass flux from the actual and dividing by the ideal, one arrives at the point-to-point coolant margins. When the external flow is laminar and the nose tip is not at angle of attack, the minimum margin always occurs at the stagnation point for the nose tip shown in Figure 2.

Table 1

SUMMARY OF MOTION PICTURE OBSERVATIONS

Run No.	Model No.	Flow	Observations
1719	508-5 angle of attack = 0 deg	1, 2, 3	Liquid layer over entire nose-tip surface
		4	Loss of liquid layer; oxidation and melt over hemispherical surface
1722	517-5 angle of attack = 0 deg	1, 2	Liquid layer over entire nose-tip surface
		3	Loss of liquid layer and oxidation in small region about 60-degree location
		4	Dry and oxidized region spreads. Bounded by 40- to 70-degree location
1720	508-6 angle of attack = 30 deg	1, 2, 3, 4	No details visible from wind cameras. Heat-shield brightness obscures nose tip
1721	517-6 angle of attack = 30 deg	1, 2	No oxidation on nose-tip surface
		3	Oxidation on wind side beginning midway through this flow. Appears to start from nose-tip/heat-shield interface location
		4	Oxidation spreads up to 60-degree location; no significant melting

Referring to Figure 9, flow three in Run 1722 produces a 35-percent margin at the stagnation point and 123 percent at the 60-degree location. The difference in the margins is magnified when downstream cooling effects are included at the 60-degree location. However, recall that oxidation developed at the 60-degree station with virgin material at the stagnation point. This result is not consistent with the laminar heating coolant margins. A more

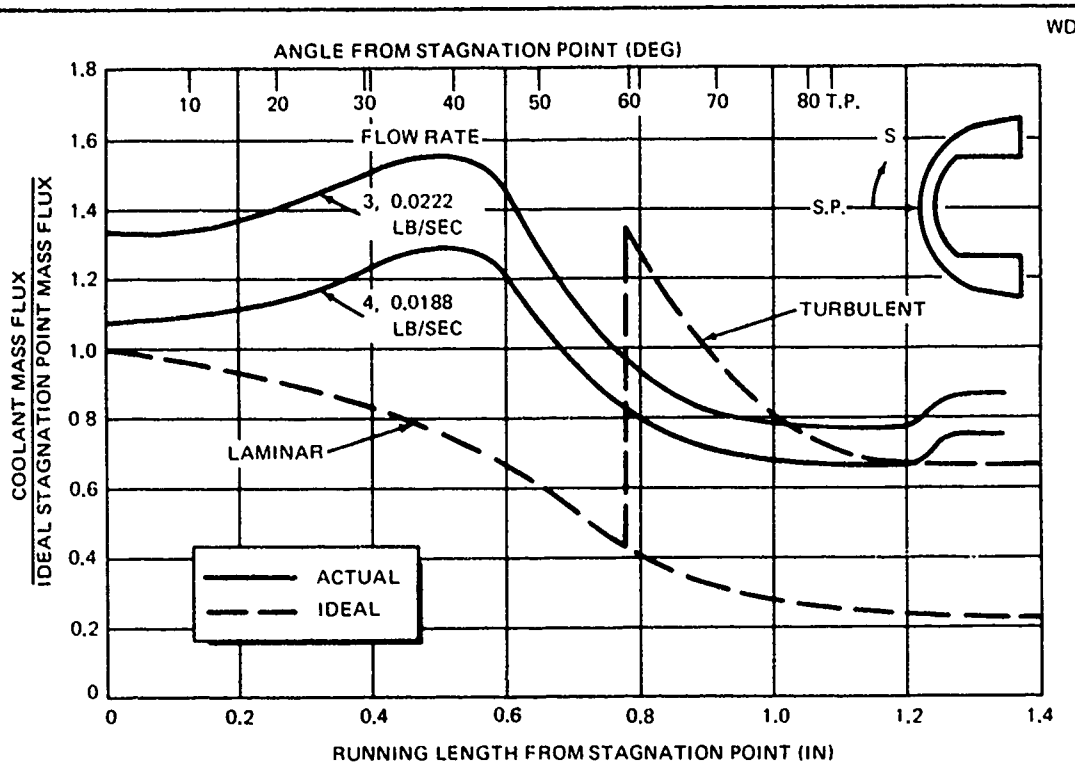

Figure 9. Nose-Tip Coolant Distribution, $\alpha = 0^{o}$ (Run 1722)

plausible explanation is the existence of a turbulent boundary layer beginning at the 60-degree station. Although a laminar boundary layer existed on the calibration models, blowing and/or surface roughness effects apparently caused the tripping of the boundary layer.

With turbulent heating (calculated by the reference enthalpy method, Reference 9) and turbulent blocking, the minimum coolant margin is now minus 30 percent on flow three of Run 1722. Flow four, with oxidation over a significant portion of the nose tip, produces a margin of 8 percent at the stagnation point and minus 41 percent at the 60-degree position. The margins on the fourth flow were not the steady-state values because significant vaporization occurred at the 60-degree position causing a redistribution of flow. An estimate of the steady-state stagnation point margin on the fourth flow can be made by examining the nose-tip coolant pressures. In flow three,

liquid flow existed over a vast majority of the nose tip as indicated by an absence of a rise in the nose-tip pressure. The small amount of oxidation at the 60-degree position did not significantly distort the flow at the stagnation point. On flow four, the nose tip pressure increases from 258 to 268 psig but remains below the pressure of flow three (280 psig). The Darcy equation can be used to estimate the steady-state mass flux at the stagnation point. With the coolant path length, permeability, and coolant temperature unchanged between flow three and four, the stagnation point mass flux is given by

$$\dot{m}_{\text{flow 4}} = \dot{m}_{\text{flow 3}} \times \frac{\left(P_c - P_{sp}\right)_{\text{flow 4}}}{\left(P_c - P_{sp}\right)_{\text{flow 3}}} \qquad (10)$$

With the above equation, the stagnation point coolant margin for flow four is calculated to rise from 8 to 25 percent because of the coolant vaporization at the 60-degree position. A measure of the nose-tip efficiency is the ratio of actual total flow divided by ideal total flow. In Run 1722 an efficiency of 1.15 was attained on the hemispherical portion of the nose tip.

On the other 0-degree test (Run 1719), the margins were minus 5 percent and minus 38 percent for the stagnation point and 60-degree position, respectively. These margins were calculated for the flow rate which produced the melt condition. Steady-state margins cannot be determined for this flow because vaporization and ablation was taking place over the entire hemispherical portion of the nose tip. For both 0-degree tests, the surface temperatures at the leading edge of the heat shield never exceeded the local coolant saturation temperature.

Windward ray flow distributions for the second 30-degree test (Run 1721) are shown in Figure 10. Turbulent flow is predicted on the skirt using the criteria established from the 0-degree tests. Note that the minimum margin in the laminar region now occurs at 36 degrees from the stagnation point. Initial observation of oxidation was detected during flow three; margins during this flow were 34 percent in the laminar zone and minus 33 percent in the turbulent

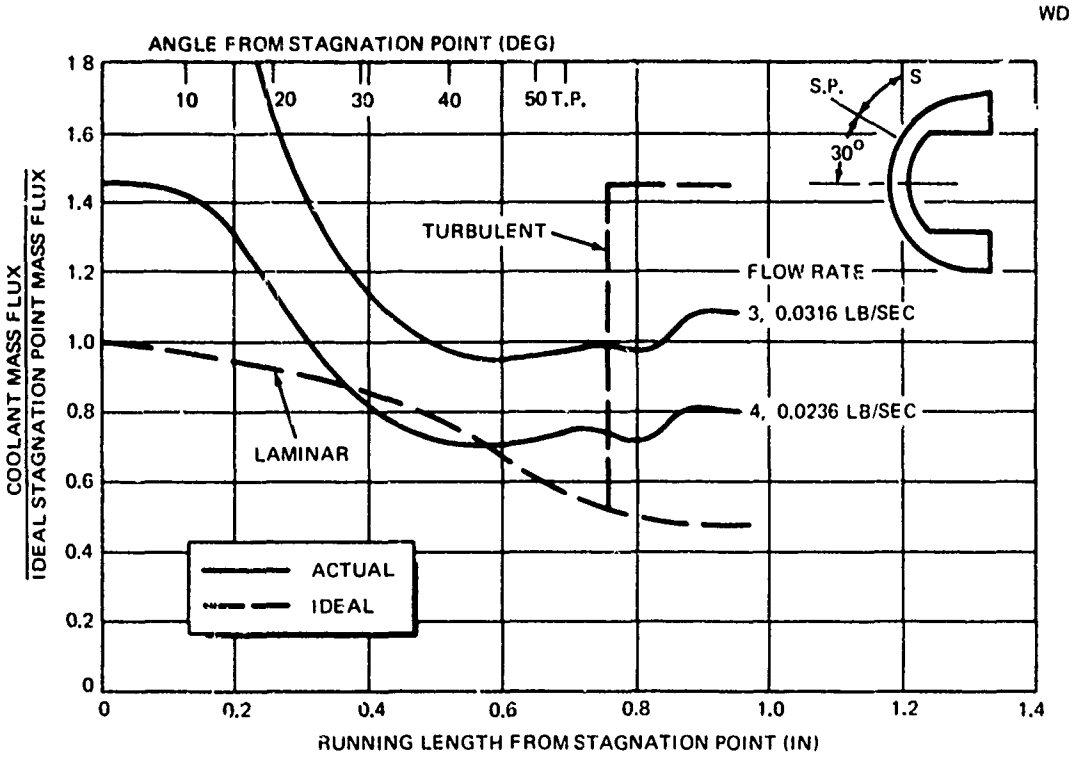

Figure 10. Windward Ray Coolant Distribution, $\alpha = 30^{o}$ (Run 1721)

zone. Margins on the fourth flow were minus 4 percent and minus 50 percent in the laminar and turbulent zones, respectively. Since a very small portion of the total flow rate was vaporized in the matrix, the nose-tip pressures did not increase during any of the flows. The minimum margins in the laminar zone were, therefore, probably not increased because of vaporization at the skirt region.

Oxidation did not occur until the fourth flow of Run 1720 judging by the amount of oxidation relative to Run 1721. The minimum margin obtained on the fourth flow of Run 1720 was minus 38 percent. Table 2 summarizes the coolant point-to-point margins and total flow rates for all four tests. The minimum margin in the tests were -38, -30, -38, and -33 percent at the first indication of oxidation. Although the minimum margin for the angle-of-attack tests

Table 2

SUMMARY OF TEST RESULTS
MALTA PIT 1 TRANSPIRATION NOSE TIP TESTS

Run No.	Angle of Attack (deg)	Test Time (sec)	Coolant Flowrate (lb/sec)	Minimum Margin (%)	Remarks
1719	0	3.09	0.0545	65	Liquid layer removal and melt on flow 4; 0.050-in recession
		3.27	0.0408	25	
		2.79	0.0280	-13	
		4.05	0.0197	-38	
1722	0	3.13	0.0290	-9	Liquid layer loss on flow 3; oxidation on flow 4 - no recession
		3.31	0.0252	-21	
		2.76	0.0222	-30	
		2.81	0.0188	-41	
1720	30	3.09	0.0808	73	Liquid layer loss and oxidation on flow 4
		3.28	0.0575	21	
		2.79	0.0393	-16	
		3.09	0.0288	-38	
1721	30	3.13	0.0565	18	Liquid layer loss and oxidation on flow 3
		3.35	0.0452	-5	
		2.75	0.0316	-33	
		3.07	0.0236	-50	

was consistent with the 0-degree tests, it is entirely possible that oxidation in the angle-of-attack tests may have been triggered by heat transfer from the heat shield. For Run 1721, heat-shield leading edge surface temperatures on the windward ray increased from 1,600°F on flow one to a temperature in excess of 2,500°F on flow 4.

Although the minimum margin for the angle-of-attack tests was similar to the 0-degree tests, the nose-tip at 30-degree angle of attack required approximately 30 percent more total flow than the 0-degree condition. The selected nose-tip geometry was a scaled-up version of a previous design which was configured for a 0-degree condition. At angle of attack, the nose-tip flow is shifted to a less optimum distribution. If an optimum angle-of-attack distribution is desired, the nose-tip flow resistance can be changed to provide a better agreement with the angle-of-attack distribution by internal contouring and/or permeability variation.

The nose-tip performance in the Malta environment is compared to the minimum preflight design margin in Figure 11. Depicted in the figure are margins obtained in the tests at selected points on the nose tip and the local physical condition at the time these margins were attained. The nose tips easily satisfied the flight design minimum margin (50 percent). In all tests, oxidation did not develop until the local margin became negative. Enhancing confidence in the analytical techniques, it was observed that oxidation in downstream cooled regions (downstream of the stagnation point) was initiated at margins from minus 30 to minus 38 percent regardless of whether the nose tip was at 0 or 30 degrees angle of attack.

Conclusions - Malta – The Malta test results indicated that a transpiration nose tip can perform successfully with local coolant mass fluxes close to theoretical values in simulated high-altitude environments. No oxidation developed at the stagnation point with local margins as low as 8 percent. Oxidation did not develop in downstream-cooled regions of the nose tip until margins of minus 30 percent were reached. Margins at which oxidations occurred were independent of angle of attack although higher total flows were provided to the nose tips tested at angle of attack.

Temperatures above the saturation point, i. e., two-phase flow, can be maintained on porous nose tip surfaces downstream of the stagnation point. The local flow is reduced when boiling occurs but if the total flow from the expulsion system is maintained constant, the mass flux at other points must increase. Extra coolant upstream of the boiling zone can then be used to reduce the incident heating downstream. Obviously, as the elevated-temperature zone is closer to the stagnation point, the less likely it is to benefit from the redistribution of flow.

Although a laminar boundary layer existed over the hemispherical portion of the calibration models, turbulent flow over the porous nose tip was indicated by the oxidation pattern. Flowing and/or surface roughness effects apparently

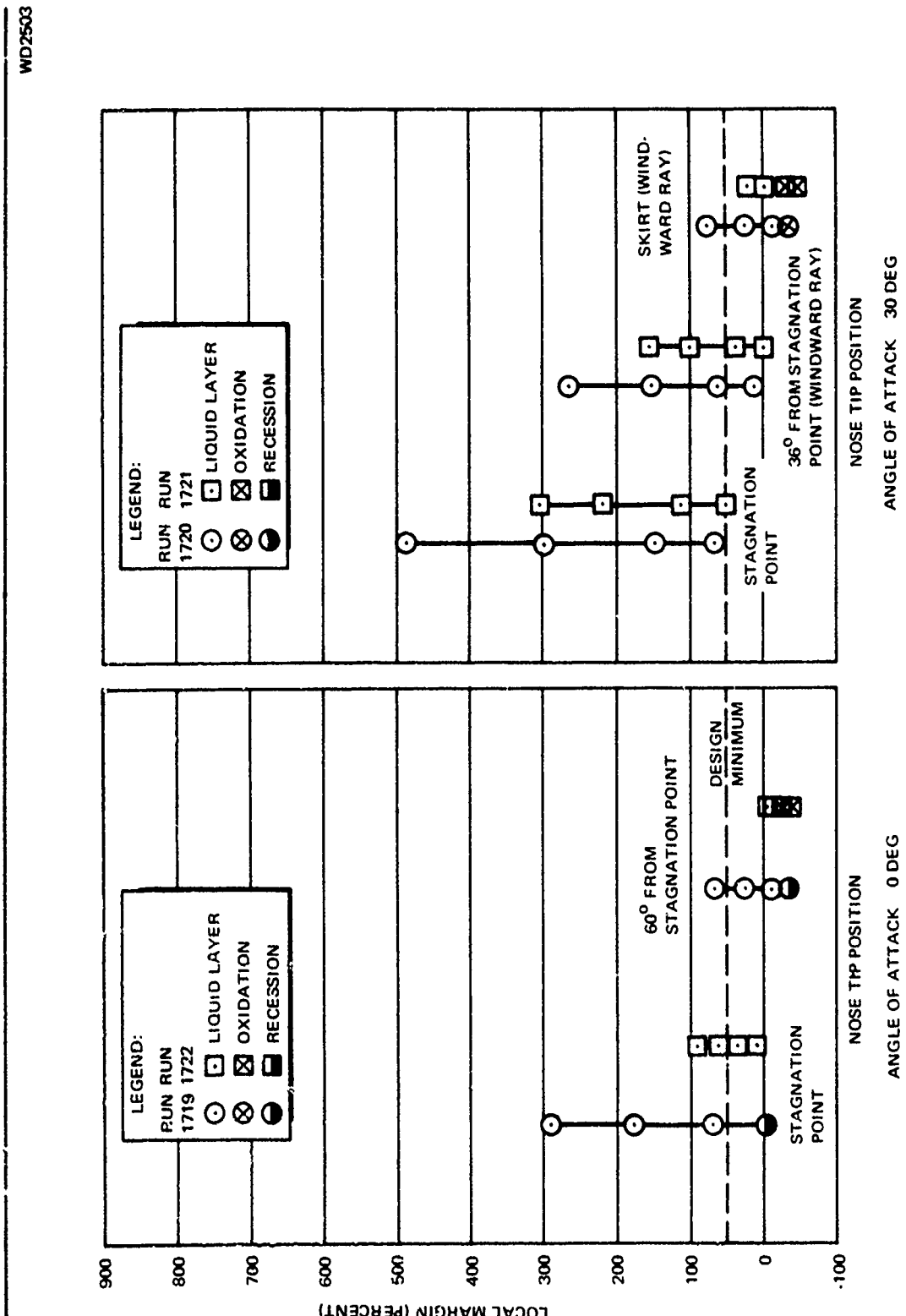

Figure 11. Nose-Tip Coolant Margins

caused the tripping of the boundary layer. A momentum thickness Reynolds number of 130 was calculated at the transition location and is not inconsistent with the transition criteria of $Re_\theta = 150$ used to define the flight transpiration nose tip environment.

Oxidation in the nose tips at angle of attack may have been initiated by heat conduction from the wind side heat shield. To preclude any thermal interaction in future angle-of-attack tests, a small gap between the nose tip and heat shield is recommended.

High-Pressure Tests – ADP

The Malta tests demonstrated the adequacy of the flight design margins under simulated high-altitude conditions. Further tests were required to evaluate the transpiration nose tip in high-pressure, high-heating environments.

Previous transpiration nose tip tests at high stagnation pressures were conducted at the Air Force Flight Dynamics Laboratory, 50 MW arc, the Cornell Wave Superheater, and the AEDC 5 MW arc; however, no facility existed that could provide a test section large enough to immerse a full-scale transpiration nose tip at stagnation pressures in the range of 100 atmospheres. To provide for this need the Aeronutronic Division of Philco-Ford (ADP) was authorized to modify an existing rocket test stand at its El Toro, California, remote test site.

A thorough calibration program was undertaken to obtain flow-field data in the expanded free-jet exhaust for use in the analyses of full-scale nose tip model performance. Heat flux and pressure measurements were made at angles of attack from 0 to 15 degrees, on windward, yaw, and leeward meridians. The calibration program is shown in Table 3 and was completed prior to the start of the transpiration test series. The transpiration test matrix is also presented in Table 3. Three tests were conducted at 0 degrees, two at 7-1/2 degrees, and one at 15 degrees angle of attack.

Table 3
ADP TEST SCHEDULE

Calibration Models			Transpiration Models		
Run No.	Type	Angle of Attack (deg)	Test No.	Model No.	Angle of Attack (deg)
1	Pressure	15	1	521-6	0
2	Heat flux	15	2	520-6	0
3	Pressure and heat flux	0	3	525-5	7-1/2
4	Heat flux	7-1/2	4	524-6	15
5	Pressure	0	5	523-5	0
			6	527-6	7-1/2

Facility Description – The Philco-Ford El Toro High Stagnation Pressure Nose Tip Test Facility, Cell B, is a gas-pressurized, liquid-propellant rocket motor. To minimize contamination, combustion occurs in a water-cooled chamber and the combustion products are expanded in a film-cooled expansion nozzle. The fuel is liquid hydrazine (N_2H_4) and the oxidizer is nitrogen tetroxide (N_2O_4). The oxidizer and fuel, both independently pressurized by nitrogen gas, are metered through a set of cavitating venturis and fed to a water-cooled, copper-impinging, stream-type injector. Nominal combustion chamber pressure is 2,600 psia and the normal operating mixture ratio is 1.2 lb N_2O_4 per lb of N_2H_4.

The combustion gases are exhausted through a nitrogen film-cooled, graphite nozzle with a throat diameter of 1.95 inches and an exit diameter of 3.0 inches. This nozzle produces an exhaust stream of Mach 2.2 at the exit, which yields a recovery stagnation pressure of 100 atmospheres for a nominal 2,600-psia chamber pressure. Nitrogen gas is introduced into the boundary layer of the

nozzle immediately upstream of the throat. This gas remains essentially in the boundary layer and cools the nozzle walls so that no thermochemical reactions occur. The expansion nozzle used for the transpiration test program was a 10-degree half-angle divergent cone. With this conical nozzle design, a test section is available that is 3 inches in diameter by 3 inches long (at the nozzle centerline) within which shock-free flow exists.

The test model is mounted on a 3-inch-diameter steel sting and is held in place by an insulated steel pylon bolted to the concrete firing pad. The model is positioned at the nozzle exit plane. Vernier adjustment of model position and angle of attack is made in a mounting saddle on top of the pylon. The entire pylon can be set at any horizontal angle of attack to the nozzle exit axis up to 30 degrees. The steel sting and pylon are insulated with phenolic silica. A 1-inch-diameter instrumentation hole is provided in the sting which leads to a larger internal cavity within the pylon. The instrumentation wires exit the pylon at the back end and then are routed forward underneath the pylon to the blockhouse. A photograph of the rocket motor with the pylon and a calibration model in place is shown in Figure 12.

The thermodynamic and transport properties of the exhaust gases for the Mach 2.2, 3-inch exit nozzle are given in Table 4. Also given is the equilibrium exhaust gas composition. The expulsion system was the same as used in the Malta series.

A considerable amount of effort was required to obtain high-quality motion pictures of nose tips. Three cameras were used to provide detailed histories of the nose-tip performance. The coverage was planned to yield high-speed overall views and close-up views from two sides of the model. Two side cameras were positioned approximately 10 feet from the model. To minimize movement during the test, the camera tripods were bolted to the concrete floor. Lens extension mounts were attached to the side cameras to obtain the close-up view. The nose tip filled up almost the entire field of view. An overhead camera provided an overall view of the model. Detail features of the nose tip were also captured by this camera.

WD2503

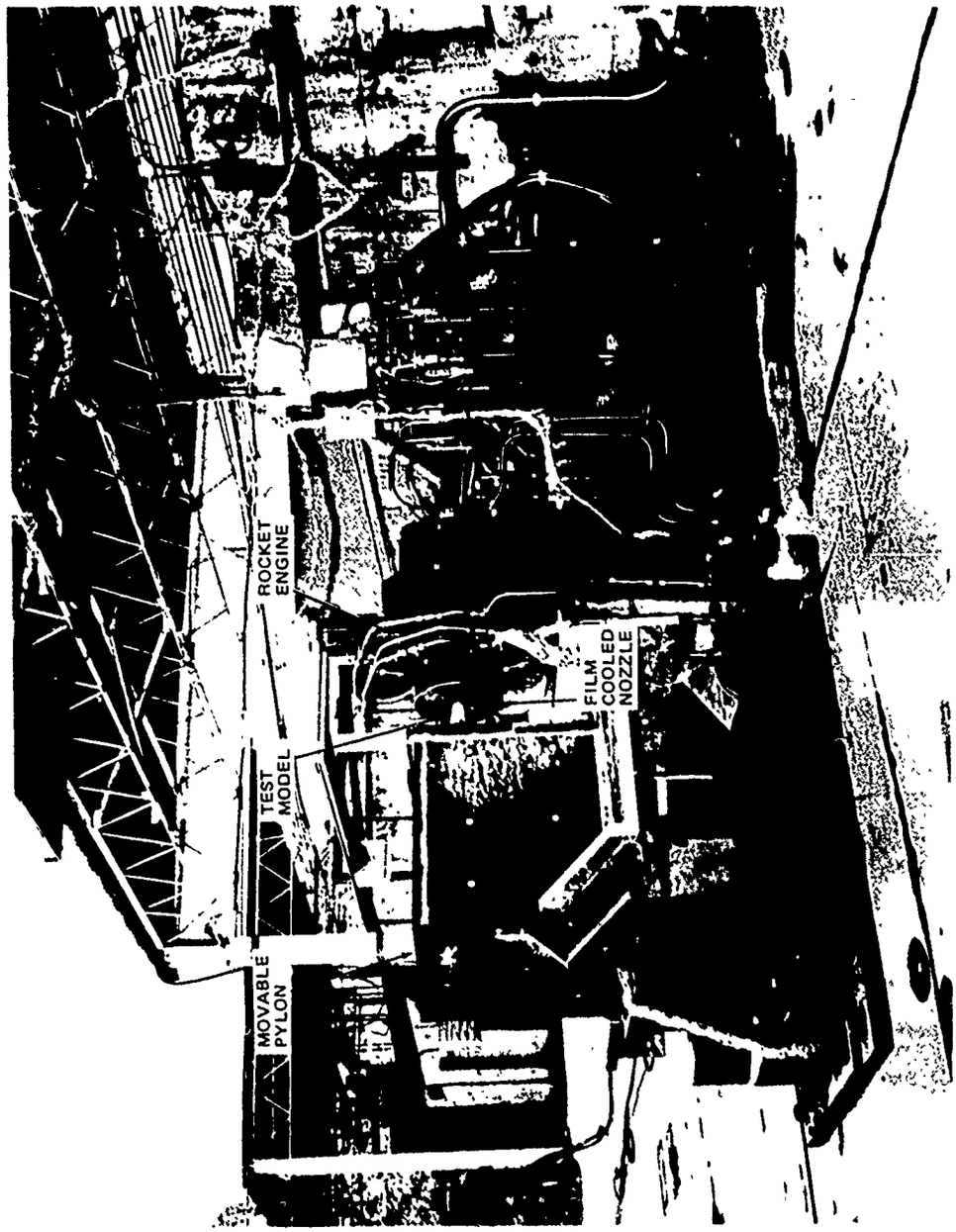

Figure 12. Philco Ford Nose-Tip Test Facility – Cell B

Table 4

ROCKET EXHAUST PROPERTIES
EL TORO HIGH STAGNATION PRESSURE FACILITY

Nozzle Exit Conditions	Static	Total
Exit Mach number	2.2	--
Pressure (psia)	237	1,445*
Temperature (°R)	4,050	5,900
Enthalpy (Btu/lb)	1,830	3,000
Molecular weight	20.6	20.3
Density (lb/ft^3)	0.113	0.471*
Specific heat ratio	1.22	1.22
Prandtl number	0.62	0.62

Gas composition (mole fraction):

H_2O	0.489
N_2	0.415
H_2	0.095
H	0.0006
OH	0.0004
O, O_2, NO, NH_3, NH_2	Trace ($<10^{-4}$)

*Behind normal shock

Two problems were encountered with the camera coverage in the initial transpiration nose tip tests. Camera speeds were either reduced from the initial 1,000 fps or stopped during the run. In addition, the picture was so hazy no details of the nose-tip surface could be seen. Beginning with the third test, power was supplied to each camera separately rather than from a distribution network via a common power supply. As a result of this change, camera speed was maintained at a nominal 1,000 fps on all subsequent tests.

The haze in the pictures presented a problem unrelated to functional performance of the cameras. After some trial-and-error, it was finally determined that recirculation of the exhaust gases was causing the hazy glare in the pictures.

The exhaust gases were being recirculated between the massive pylon and the rocket engine stand. The blunt frontal pylon insulation was contoured to deflect the flow past the pylon rather than recirculating back toward the engine. By the fourth test, the pictures were dramatically improved with details of the nose-tip surface clearly visible.

Calibration and Transpiration Model Description – Five full-scale calibration models were tested. Two of the models were for pressure measurements only, two were for heat flux measurements only, and one was a combined heat flux/pressure model for the 0-degree angle-of-attack calibration. Measurement locations for the single and combined type models were identical to the Malta calibration models except for calorimeter 6B which was deleted from the combined model.

The exterior surfaces of the transpiration models were identical to the Malta models. There was a significant difference in the method of nose-tip attachment. Instead of a threaded attachment as used for Malta tests, the nose tip was welded to the coolant wand. The coolant wand was offset from the axis of symmetry by 0.120 inch to maximize the heat-shield thickness on the windward way. As a result of the Malta tests, each heat shield was custom fitted to a nose tip to provide a small gap at the nose-tip/heat-shield interface. As an additional means of reducing heat transfer from the heat shield to the nose tip, a small fraction of the nose-tip back surface was etched to allow flow. The porous nose tip geometry was identical to the Malta nose tip.

In the first three transpiration nose tip runs, a Teflon boot identical to the Malta design was placed over the porous nose tip to protect the model during the starting transient. These Teflon boots ablated through prior to the

completion of the transient. For the last three transpiration nose tip tests a thick boot, similar to the boots used on the calibration tests, was employed so that the boot would not be removed until steady-state conditions were reached.

Facility Calibration Test Results – Prior to model testing, checkout tests were conducted to optimize and certify the test facility performance. The pressure data from the 0-, 7-1/2-, and 15-degree angle-of-attack calibration tests are summarized in Figure 13. A stagnation pressure of 98 atmospheres was measured at a chamber pressure of 2,600 psia. As expected, the pressures on the hemispherical portion of the model are similar for the several angle-of-attack conditions and follow a Newtonian distribution. Nine pressure readings were obtained over the hemispherical region of the nose tip with a repeatability of better than ±6 percent.

A total of 16 calorimeter measurements were taken on the hemispherical portion of the nose tip from the three calibration tests (0, 7-1/2, and 15 degrees). Stagnation heating of 7,700 Btu/ft^2-sec was measured; peak heating of 10,800 Btu/ft^2-sec occurred on the hemispherical portion of the nose tip. Recovery enthalpy was 2,830 Btu/lb. All data were repeatable to better than ±5 percent and symmetry of environment on the hemisphere was demonstrated. It is believed that these tests represent the most complete calibration of a hemisphere in a severe environment yet made. Since transpiration nose tips maintain shape and are designed specifically for the hemisphere environment, hemispherical environment data are essential in order to properly evaluate their performance. Figure 13 shows the heat flux calibration data to which the nose tip coolant flow rates were matched.

Heat flux data were converted to ideal coolant mass fluxes by the method discussed earlier. Comparisons of mass transfer blocking in air and in the ADP environment showed that an increase of approximately 11 percent in mass flux (over the air value) was needed for the ADP environment.

WD2503

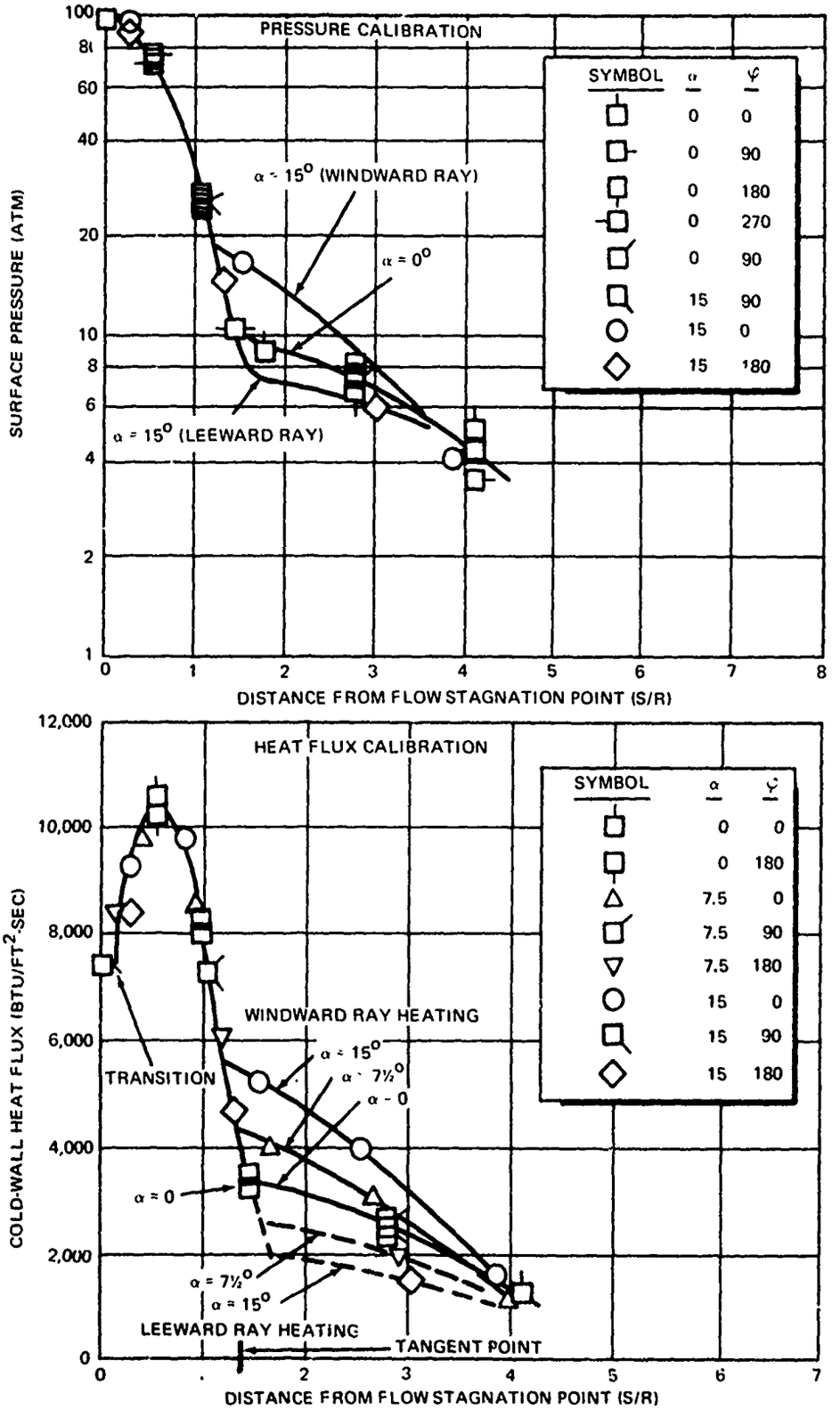

Figure 13. ADP Cell B Nose-Tip Calibration Data

Nose-Tip Performance – Six transpiration nose tip models were tested: 3 at 0 degrees, 2 at 7-1/2 degrees and 1 at 15 degrees angle of attack.

Model 521-6 (0-degree angle of attack), Figure 14A, was heavily eroded after test with approximately one half of the thickness in the stagnation region remaining after the test. The general shape of the nose tip was still hemispherical after the test.

Model 520-6 (0-degree angle of attack), Figure 14B, was eroded over 70 to 80 degrees of the nose tip but the model was not nearly as eroded as Model 521-6. Some minor pitting of the nose tip is visible behind the melted region.

Model 525-5 (7-1/2-degree angle of attack), Figure 14C, has three eroded pits centered about 10 degrees off the stagnation point. Two of the pits are separated by a 1/16-inch unattacked region lying on the windward ray. The deepest of the three pits is about 6 mil deep. This region covers approximately the first 30 degrees from the flow stagnation point. A reddish color is apparent over much of the first 60 degrees of the nose tip and numerous small pits, the size of particles of sand, cover the hemispherical surface. This appearance suggests particle impact. The model surface shows gray-black streaks both concentric and axial about the nose. A gray color extends to the tangency point on the lee side of the nose tip but extends to the heat shield interface between 0 and 90 degrees from the windward ray.

Model 524-6 (15-degree angle of attack), Figure 14D, has the best post-test appearance of all the models. Only one very small melt pocket (1/16-inch diameter) is present about 10 degrees from the stagnation point and near the leeward ray. The reddish color seen on the previous model is apparent as are many small pits suggestive of a surface bombarded with particles. Black rays extend back toward the heat shield over about 1/8th of the model between the windward ray and -95 degrees, extending to the tangency point and starting about 15 degrees from the flow stagnation point. Streaks appear to emanate from oxidized pits.

WD2503

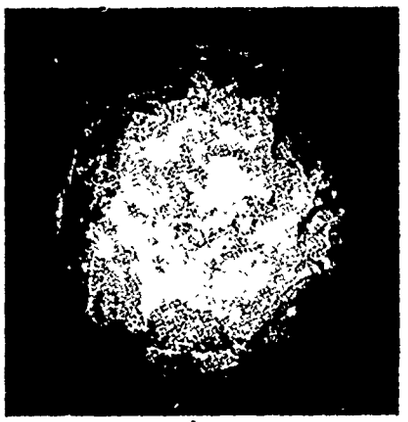

A. MODEL 521-6 $\alpha = 0^{o}$

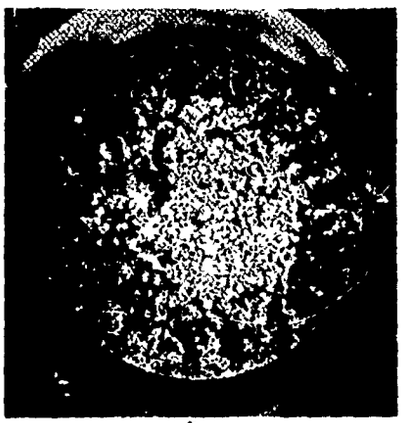

B. MODEL 520-6 $\alpha = 0^{o}$

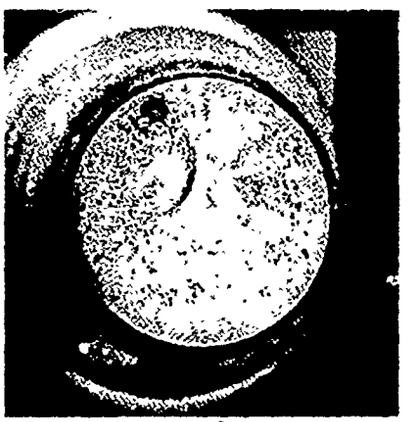

C. MODEL 525-5 $\alpha = 7\text{-}1/2^{o}$

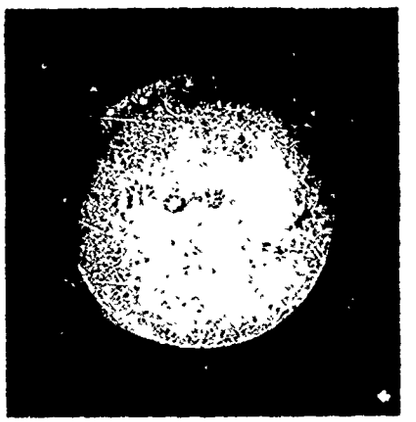

D. MODEL 524-6 $\alpha = 15^{o}$

E. MODEL 523-5 $\alpha = 0^{o}$

F. MODEL 527-6 $\alpha = 7\text{-}1/2^{o}$

Figure 14. High-Pressure Transpiration Nose-Tip Post-Test Photographs

However, an examination of the scales on each model shows the introduction of tramp elements in the ADP model. Scans over relatively large areas of the scale showed silicon as a major element whereas aluminum, chlorine, potassium, and calcium were detected as minor constituents. Examination of discrete particles imbedded in the scale also revealed significant quantities of these constituents.

Chemical analysis techniques substantiated the hypothesis that foreign material was coming in contact with the nose tip during the ADP tests. Analysis of several of the particles indicated the presence of Si, Cl, K, and Ca. In addition, however, there were discrete fibrous particles, a silicon containing compound (probably SiO_2) and discrete apparently ductile particles imbedded deeply in the porous surface which were identified as copper. An examination of the uncontaminated base metal areas showed the typical elemental constituents expected with 316L stainless steel.

Flow rates, nose-tip internal pressures, and coolant temperatures are shown in Table 5. The permeabilities of all nose tips are 15 percent about the mean. Temperature rise in the coolant is a result of flow circulation of the rocket exhaust gases impacting on the coolant delivery tube. Continuing design changes to the pylon resulted in reduction of the problem, but the problem recurred when the pylon was reset to 0-degree angle of attack on test 5.

Greater coolant flow rates are required at angle of attack to achieve the same minimum margin as at 0-degree angle of attack. The same mass transfer blockage factor is used at angle of attack as at 0 degrees; however, the increased flow rate requirement arises from a less efficient distribution of coolant about the nose tip due to the internal nose tip contour being designed for the angle of attack most prevalent during flight, i.e., 0 degrees. In order to achieve a 50-percent minimum margin in the ADP environment, a 14 percent higher coolant flowrate was required at 7-1/2 degrees than at 0-degrees angle of attack, while a 34 percent higher coolant flowrate was required at 15 degrees than at 0 degrees. Specific percentage increases depend on nose-tip permeability, internal contouring, and heat-flux distribution about the nose tip.

Model 523-5 (0-degree angle of attack), Figure 14E, exhibits the brightest red color seen on any model. Red particles are seen rising above the surface of the nose tip. Two melt zones (1/16-inch diameter and 1/8 by 1/4 inch) are present near the tangency point. Concentric markings are seen on the nose tip and dark streaks radiate from several oxidized, minor melt zones located about 10 degrees from the stagnation point in one quadrant. Less severe streaks are present in the adjacent quadrant. Again numerous tiny pits are present.

Model 527-6 (7-1/2-degree angle of attack), Figure 14F, is quite similar in appearance to the other 7-1/2-degree model except that the large pits of the previous model have little material loss on this model. Again gray-black streaks emanate from these zones and radiate back to the tangency point. The model surface is reddish in color and the surface has many discrete pits appearing as would be expected of particle impingement. A yellow-gray color covers the nose tip extending to the tangency point on the leeward ray and to the heat shield interface ±90 degrees from the windward ray.

An investigation of possible contamination from the test facility was initiated because of the anomalous behavior of the first nose tip tested at ADP. Inconsistent test results caused by facility contamination, i.e., bombardment with copper, carbon, etc., has not been uncommon. Visual examination of the damaged area of the first nose tip tested (521-6) showed a significant difference in appearance between this "scale" and that found on other nose tips which had undergone surface melting during environmental tests. A comparison of the melted areas on the ADP test nose tip and a Malta test model (508-6) with a scanning electron microscope (SEM) shows scale on the ADP model is much denser, thicker (verified by cross-section views) and more adherent than that on the typical oxide scale present on the Malta model. Initial conjecture was that the larger amount of melt formation than anticipated was the result of high-temperature chemical corrosion caused by the reaction of the N_2O_4/N_2H_4 combustion products and the 316L stainless steel.

A comparison of predicted and experimental values of the nose-tip pressure was made based on the measured flow rates and coolant temperature. Viscous dissipation through the nose tip was accounted for in the analysis. The effect of temperature change within the nose tip due to a surface at the boiling point of water was not considered. If conduction from the boiling coolants was important, the actual pressure should be less than predicted and diverge with test time. Only in one model, 525-5, does this temperature trend show itself. It is concluded the thermal conduction from the nose-tip surface is not important. The pressure deviations experienced are probably due to uncertainties in nose-tip permeability. The worst-case pressure error was 9 percent; this corresponds to a 5.5 percent error in permeability.

Table 5

ADP TRANSPIRATION TEST SUMMARY

Test/Model	Flow Rate (lb/sec)	Pressure (psia)	Temperature (F°)
1	0.275	3,070	61
(521-6)	0.250	2,470	65
	0.222	Invalid	80
	0.193	data	88
2	0.250	2,980	50
(520-6)	0.225	2,640	55
	0.215	2,300	62
	0.194	2,170	64
3			
(525-5)	0.220	2,370	55
4			
(524-6)	0.300	3,000	64
5			
(523-5)	0.225	2,560-2,000	64-104.5
6	0.314	3,160	64
(527-6)	0.257	2,620	67
	0.225	2,360	68
	0.210	2,160	72

Table 6 shows the minimum coolant margins for each test as well as comments as to the appearance of the model during test based on motion picture coverage. Figure 15 gives the margin distributions for models 524-6 (15 degree), 523-5 (0 degree), and 527-6 (7-1/2 degree); the distributions about the other models are similar.

Camera coverage was not available on either of the first two runs. Therefore, only qualitative conclusions can be drawn. The first model was tested at 0-degree angle of attack and four flow rates. The unexpected 27°F temperature rise of the coolant due to flow-field recirculation onto the coolant delivery tube resulted in margins less than planned. As a result the model experienced negative margins for 4 of the 8.3 seconds of test (-14 percent for 2 seconds, -75 percent for 2 seconds). The model after test is hemispherical but is heavily eroded with a maximum of one-half the nose-tip thickness removed in some places near the stagnation point. A margin distribution plot revealed that the model did experience the most melting in the zone of predicted minimum margin. The second test, Model 520-6, was also run at 0-degree angle of attack using four flow rates. This model experienced much less erosion (~10 mil) than the first model. The fact that the model eroded and that erosion was less than the first model is not surprising when the margins are reviewed. The model was exposed to 2 seconds at a margin of -14 percent. Again, the minimum margin was predicted as being at the stagnation point, and melt did occur in that region.

Since film coverage was not obtainable on the first two tests it was decided to use a single flow at the flight vehicle design margin (50 percent) for the third test, Model 525-5, 7-1/2-degree angle of attack, so that the condition of the model after the test would be the result of the single test condition. The minimum margin achieved on this test was 34 percent. The margin distribution is quite flat such that the first 60 degrees of the nose tip have generally the same margin. The nose-tip appearance is quite good except for several melt pockets near the stagnation point.

Table 6

ADP TRANSPIRATION RESULTS

Test	Angle of Attack (deg)	Margin (%)	Comment
1 (521-6)	0 (4 flows)	94 48 -14 -75	No camera coverage; 50 percent of nose-tip thickness ablated.
2 (520-6)	0 (4 flows)	84 50 30 -14	No camera coverage; 10 mils removed in stagnation region.
3 (525-5)	7-1/2 (1 flow)	34	Nose-tip pitting; 2 melt pockets.
4 (524-6)	15 (1 flow)	45	Nose-tip pitting.
5 (523-5)	0 (1 flow) Variable temperature	31 8 -14 -31	Margins quoted at 2-sec intervals. Model pulses at 8% margin. Pulsing streaks at 0% margin, Material loss at -25%.
6 (527-6)	7-1/2 (4 flows)	90 52 28 2	Slight pulsing at 52%. Significent pulsing at 28%. Pulsing, slight material loss at 2%.

Note: All nose tips structurally sound; pitting on all nose tips due to contamination

Model 524-6 (15 degrees) also employed one flow rate throughout the test. Figure 15 shows the margin distribution for this model. The minimum margin was constant at 45 percent and occurred 0.8 inch (60 degrees) from the geometrical stagnation point. Upstream of the minimum margin location the margin (110 to 140 percent) is considerably greater than the minimum. Therefore, excess coolant upstream of the minimum margin location is available for cooling that location. The streaks on the post-test model are apparent as a pulsing of the model from white hot to cool without material loss at 3.5 sec into the test. The small pits containing melt occur 5.9 sec into the 8.5 sec test.

WD2503

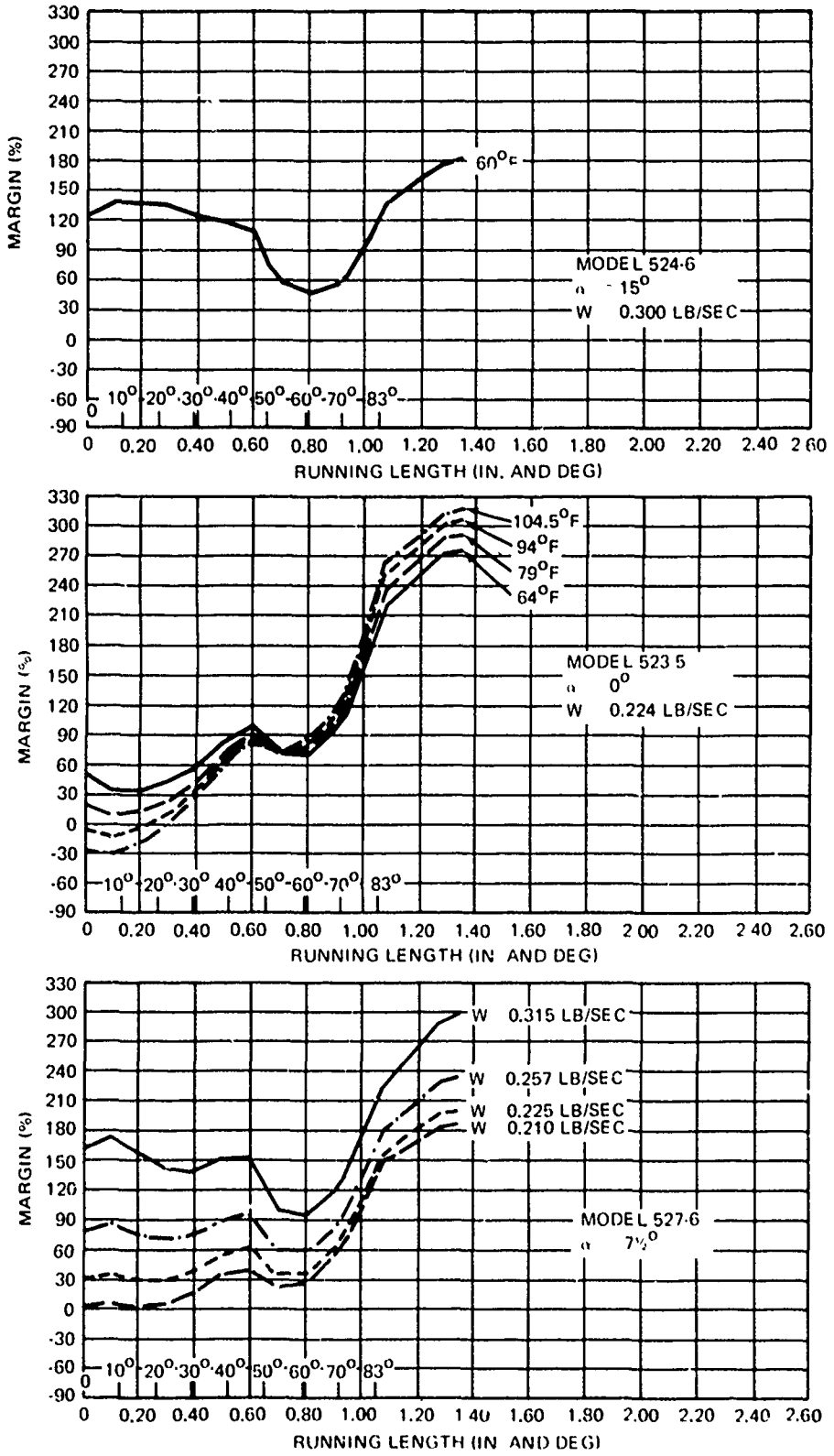

Figure 15. ADP Coolant Margins

Test 5 (Model 523-5, 0-degree angle of attack) was a unique test in that the flow rate was held constant, but the coolant temperature rose from 64 to 104.5°F during the test resulting in a continuous decrease in margin during the test. Figure 15 shows the margin distributions at 2-second intervals in the test. The model had a 31-percent minimum margin after 2 seconds of test, 8 percent after 4 seconds, -14 percent after 6 seconds, and -31 percent at the end of test. Review of the films indicates there is a possible slight pulsing of the nose tip (glowing/cool pulses) at the time of 30 percent margin which becomes a pronounced pulsing cap extending to 30 degrees from the stagnation point at a 8-percent margin. Rays extending toward the heat shield are pulsing vividly at a -5 percent margin. Material loss in the form of a melted pit at the tangency point occurs at a -25 percent margin, 1 second before engine shutdown. A white hot streak on the heat shield occurs simultaneously with the formation of the melt pocket on the nose tip.

The last test (Model 527-6, 7-1/2-degree angle of attack) employed multiple flow rates since camera coverage had improved to the point of meaningful data being c ined from such a test. The minimum margins ranged from 90 to 2 percent and were constant over the first 30 to 45 degrees of the nose tip (Figure 15). Films revealed that slight nose-tip pulsing occurred at a 52 percent margin. A cap over the first 30 degrees of the nose tip pulsed on the third flow rate (28 percent) while pulsing streaks radiating toward the heat shield developed at the 2 percent margin. Slight material loss occurred at this last flow rate.

The nose tips tested at Malta oxidized and melted at the transpiration nose-tip/heat-shield interface at high angle of attack possibly due to contact with the hot heat shield. This problem was eliminated at ADP by imposing a small gap between nose tip and heat shield as a requirement and by allowing a low water flow from the gap between the nose tip and heat shield. No model at ADP experienced oxidation or melt at this interface.

Conclusions – ADP – Tests 3 to 6 are tests from which conclusions relative to flight can be made based on film coverage. These tests show that under the margins tested little or no material was lost by the nose tip.

During flight, the margin drops below a nominal 50 percent for 2 seconds. Three tests used margins less than 50 percent for 8.3 seconds, a condition more severe than flight.

The minimum margins in test are less than flight design margins. In addition, margins at the transpiration nose-tip/heat-shield interface are greater in flight than in ground tests. It is concluded that the flight nose tip would survive reentry heating to impact.

Several technological conclusions can be drawn from the ADP test series. Porous transpiration-cooled nose tips will survive margins of less than 50 percent and approaching 0 percent in high-heating/high-pressure environments including the conditions where the minimum margin occurs at the stagnation point. The nose-tip concept works equally well at all angles of attack up to at least 15 degrees in an ADP type environment. Higher coolant flow rates are required at angle of attack due to the flow distribution characteristics of the nose tip being optimized for 0-degree angle of attack. The use of a constant-flow device (cavitating venturi) to control coolant flow to the models permits the nose tips to operate in stable two-phase flow. Previous tests using a pressure-control device (orifice) resulted in nonstable operation once a hot spot developed on the model. When a hot spot develops on a nose tip downstream of an orifice, two-phase flow occurs, pressure in the nose tip increases pressure drop across the orifice decreases, and coolant flow decreases. The decreasing coolant flow rate results in growth of the hot spot and thus propagation of the failure. The current results indicate that it should be a requirement for any flight coolant flow control concept that it meter coolant flow independent of pressure drop. The g-valve used on the flight vehicle satisfied this requirement.

FLIGHT TEST RESULTS

The flight vehicle transpiration system consisted of the nose tip and the expulsion subsystem. The porous nose tip concept developed by McDonnell Douglas on the ReEntry Systems Environmental Protection (RESEP) program and successfully flown on the RVTO-1A and RVTO-2A vehicles was used for the current flight tests. The nose tips are machined from billets of porous (~85 percent dense) stainless steel which are formed from pressed and sintered stainless steel powder. The material permeability is governed by the powder size coupled with the particular pressing and sintering conditions utilized. The permeabilities used for the current flights were chosen to allow optimum usage of coolant in the different environments for each of the two vehicles.

One vehicle was characterized by relatively low angles of attack (<10 degrees) and high stagnation pressures (100 to 150 atm) during the low coolant margin portions of the flight. Conversely, the second vehicle maintained high angles of attack (>10 degrees) and moderate stagnation pressures (50 to 70 atm) in the low margin regime.

A cold-gas blowdown expulsion system was used to force the coolant through the nose tip. Pertinent features of this subsystem are shown in Figure 16. Coolant contained in the cylindrical reservoir is pressurized using helium which is intially stored at 11,200 psi. The resultant flow of coolant to the nose tip is controlled by an acceleration-sensing flow control valve which regulates the flow as a function of vehicle longitudinal acceleration independently of upstream and downstream pressure variations. Valves for each vehicle were sized to meet a specific flow vs acceleration requirement based upon the flight trajectory.

Nose-Tip Thermal Performance

One means of measuring nose-tip performance is by a point-by-point coolant margin. As described previously, a point-by-point coolant margin is defined as the ratio between the coolant flux actually flowing at a point on the tip minus that thermally required to maintain that point at the boiling temperature (or

WD2503

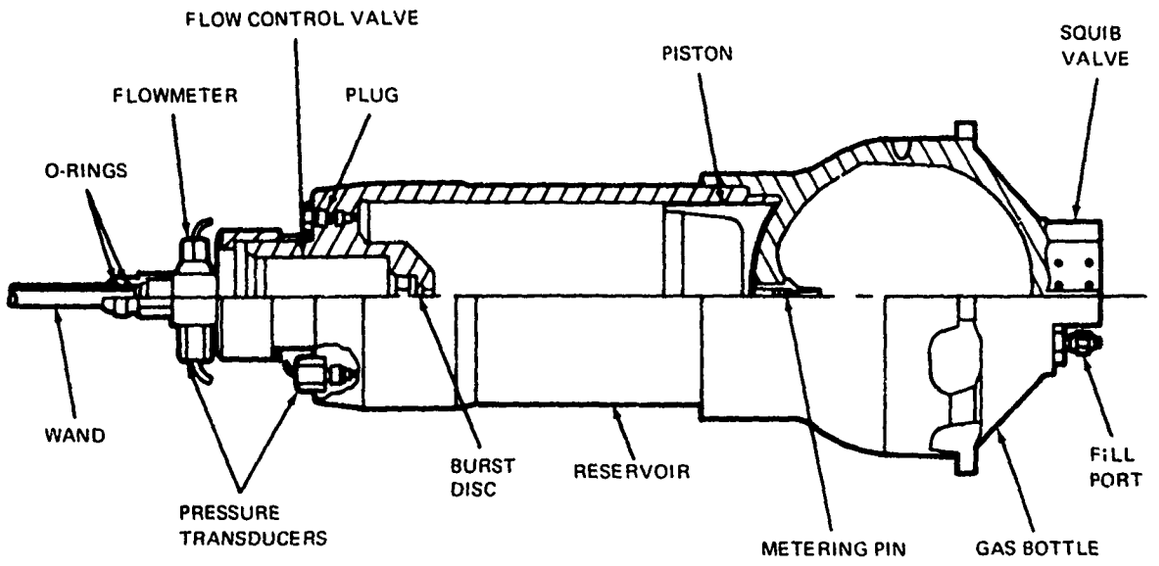

Figure 16. Expulsion System

any other specified temperature) of the coolant divided by the thermally required coolant. This definition is illustrated in Figure 17 which contains the windward ray actual and thermally required coolant mass fluxes for a time point in each of the two trajectories. The thermally required curve represents the amount of coolant necessary at each local running length to balance the thermal environment and maintain a 212°F nose-tip surface temperature. This value of mass flux is dependent only on the local heat transfer coefficient, recovery enthalpy, coolant reservoir temperature, and thermal and thermochemical properties of the coolant. The actual mass flux curve, as the name implies, represents the amount of coolant which will actually be present along the windward ray at this particular time point in the trajectory. This mass flux is a function of the local external pressure, the total coolant flow rate, the coolant reservoir temperature, and the nose-tip material permeability and geometry.

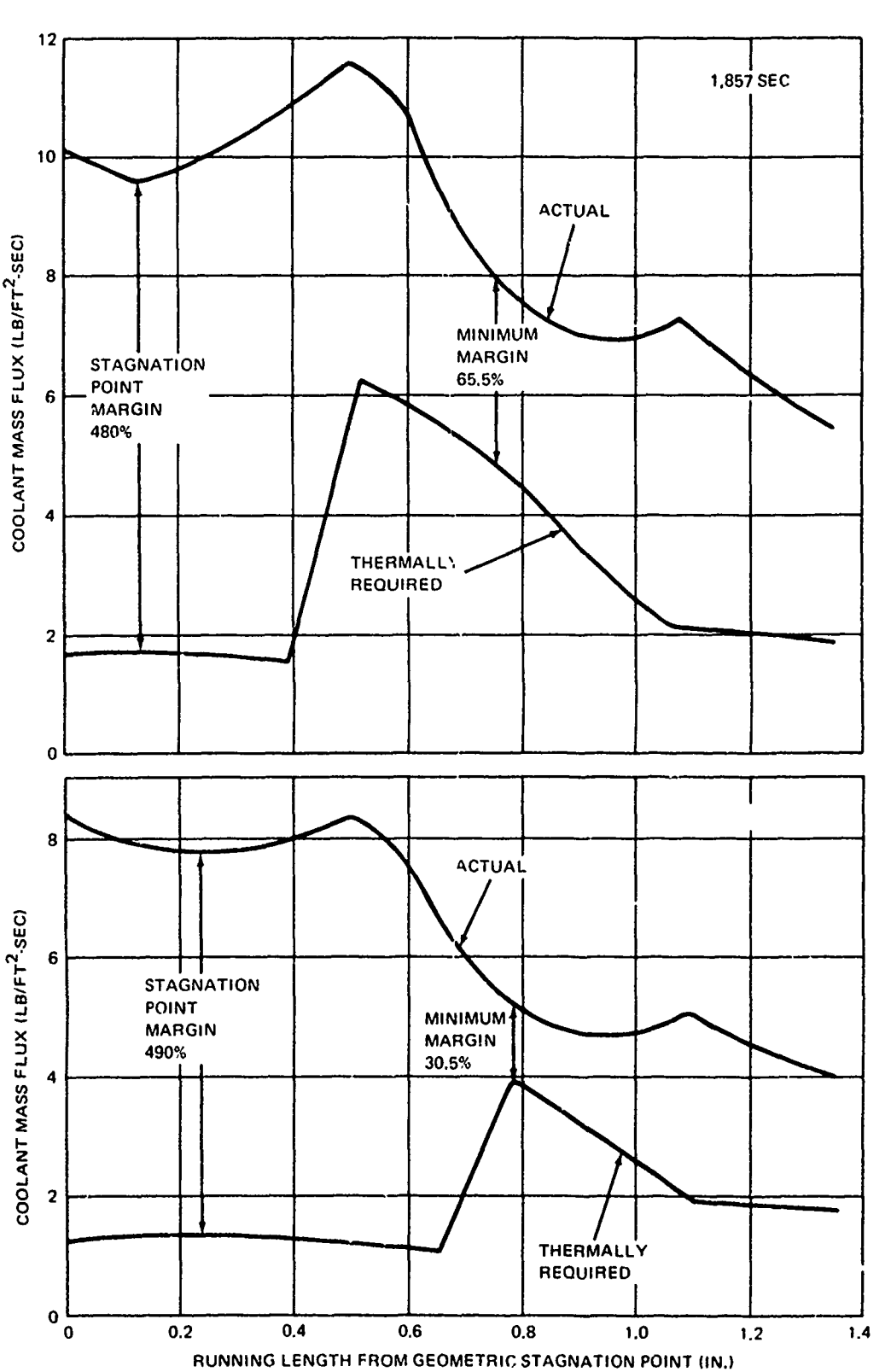

Figure 17. Nose-Tip Coolant Distributions

As shown in the figure, the point-by-point margin varies along the surface of the nose tip, being relatively high in the stagnation region where the flow is laminar and the heating low, and lowest where the flow is turbulent. In addition to varying along the windward ray as shown, the margin also varies circumferentially around the nose tip, reaching a minimum at only one discrete location. Since at each time point the margin distribution is also different, a minimum for the entire flight is reached at only one location and one time.

The relationship between ground and flight margin distributions can be seen from a comparison of Figures 9, 10, 15, and 17. In general, the flight margin distribution is more similar to those from the Malta tests than from the ADP tests, i.e., high margins near the stagnation point and minimum margins on the aft portions of the hemisphere. The reason for this result is due to the fact that the heating distribution in Malta and the flight is characterized by laminar/turbulent flows values while the ADP heating is fully turbulent. This heating condition leads to a higher flow requirement (and thus lower margins) nearer the stagnation point at ADP than in either Malta or flight The ADP test is therefore considered to be a conservative measure of nose-tip performance.

The ground rule used for the flight nose-tip design was to maintain a point-by-point margin of 50 percent or greater during flight. This criterion was based upon the results of ground tests performed on the RESEP program and on RVTO-1A and RVTO-2A flight tests which utilized nose tips similar to the current design. However, results of the current series nose-tip ground tests allowed the use of lower margins later in the program.

The minimum coolant margins attained during each flight, as well as the preflight margin predictions, are contained in Figure 18. As was expected from preflight predictions, the margin is high at high altitude when the aerodynamic flow on the nose tip is fully laminar, and drops off dramatically when turbulent flow moves onto the nose tip between 1, 855 and 1, 856 seconds. A transition momentum Reynolds number of 150 was used in the analysis.

For the first flight, the preflight and postflight predictions show good agreement, with the lowest minimum margin predicted to be 54 percent and occurring at 1, 858 seconds (the "critical point"). However, due to the large oscillations in angle of attack and g's occurring during this portion of the flight, there is considerable doubt in the validity of the flight data used to obtain the postflight margins after 1, 857. 4 seconds. The lowest margin attained prior to the oscillations was approximately 65 percent.

For the other flight, the lowest value of margin attained during flight was approximately 30. 5 percent. In order to assess the accuracy of this margin, an uncertainty analysis was performed for time point 1, 856. 0 seconds. This analysis considered uncertainties in freestream velocity, angle-of-attack, coolant flow rate, and material permeability. The off-nominal trajectory parameter values were obtained from postflight trajectory reconstructions; the flow rate values include a 1. 04 percent instrument error, a 0. 375 percent PCM error, and a 0. 004 lb/sec g-sensitivity error. The permeability uncertainty was assumed to be 7 percent based upon studies made on prior programs (RVTO-1A and RVTO-2A). Since coolant temperature and freestream temperature and pressure variations were extremely small, they were not considered in the analysis.

Each of the parameters was varied independently of the others and a minimum margin calculated. These values were then root sum squared to give a ±0. 1655 variation in minimum margin which at time point 1, 856. 0 gives

$$30.5 \pm 5.05 \text{ percent}$$

This variation is depicted in Figure 18. (Results of a similar analysis for the first flight are also shown in the figure.)

The value of minimum margin calculated above differs from the preflight prediction of 43 percent. The major contributor to the lower value of margin obtained in flight is the difference between the flight flow rate (0. 189 lb/sec)

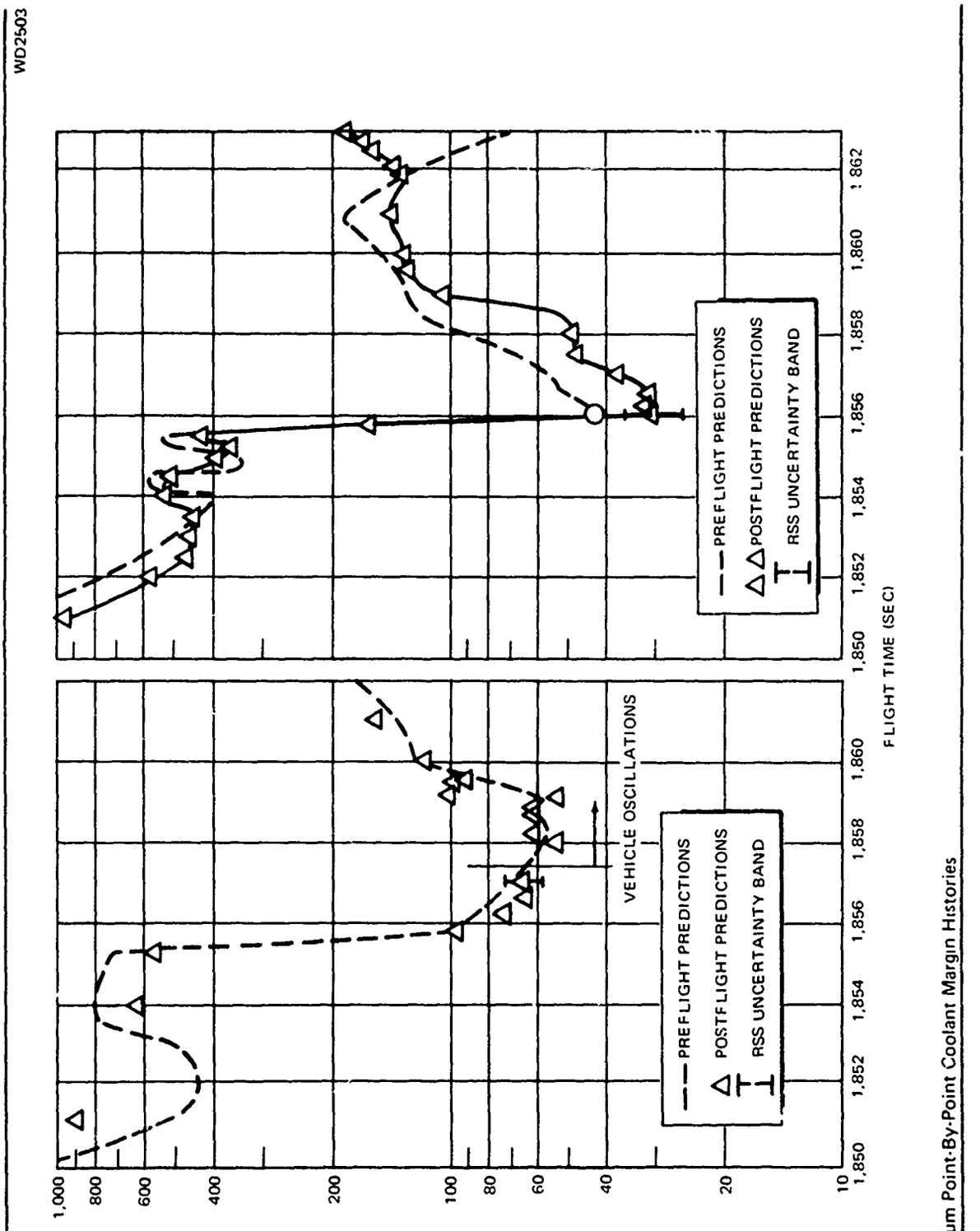

Figure 18. Minimum Point-By-Point Coolant Margin Histories

and the preflight simulated flow rate (0.208 lb/sec) at the critical time point caused by trajectory and g-history differences. This 10 percent difference in flow rate, everything else being equal, gives rise to a 14 to 15 percent increase in minimum margin.

In addition to the coolant margins, the nose-tip internal coolant pressure was also calculated for each flight. A comparison of the measured* post-flight nose-tip pressure and the calculated pressures was made and the results are shown in Figure 19. For both trajectories the calculated pressures are generally equal to or about 10 percent higher (~200 psi) than the measured (or simulated) values which is acceptable for subsystem design.

Downstream Cooling (Near-Nose Ablation)

Coolant minimum margins greater than 30 percent were seen to exist during the bulk of the flight time. A positive margin implies the existence of excess coolant over that required to protect the nose tip which is able to flow downstream and cool the heat shield adjacent to the nose tip. Downstream of the nose tip, the coolant can exist in several forms, either as a liquid film on the vehicle surface or as liquid droplets or vapor in the boundary layer adjacent to the surface.

The existence of a liquid film on the surface of the heat shield can be determined from a surface temperature measurement at the point under examination. If this temperature is equal to or less than the boiling point of the coolant at the local pressure, then a liquid film is present.

Figure 20 shows the temperature traces from surface thermocouples located between the nose tip and heat shield on the windward** and leeward rays at Station 6.33. Included on the plots are coolant boiling-point temperatures calculated at the nose-tip/heat-shield interface local pressure. Since these boiling-point temperatures are generally greater than the measured surface temperatures, it can be concluded that a liquid film of finite thickness existed at these locations during the entire flight.

*Due to a malfunction of the flight nose-tip pressure sensor on the second flight, a pressure simulation based upon the expulsion subsystem performance was used in place of the measured values.

**The windward ray thermocouple was inoperative at launch for the first flight.

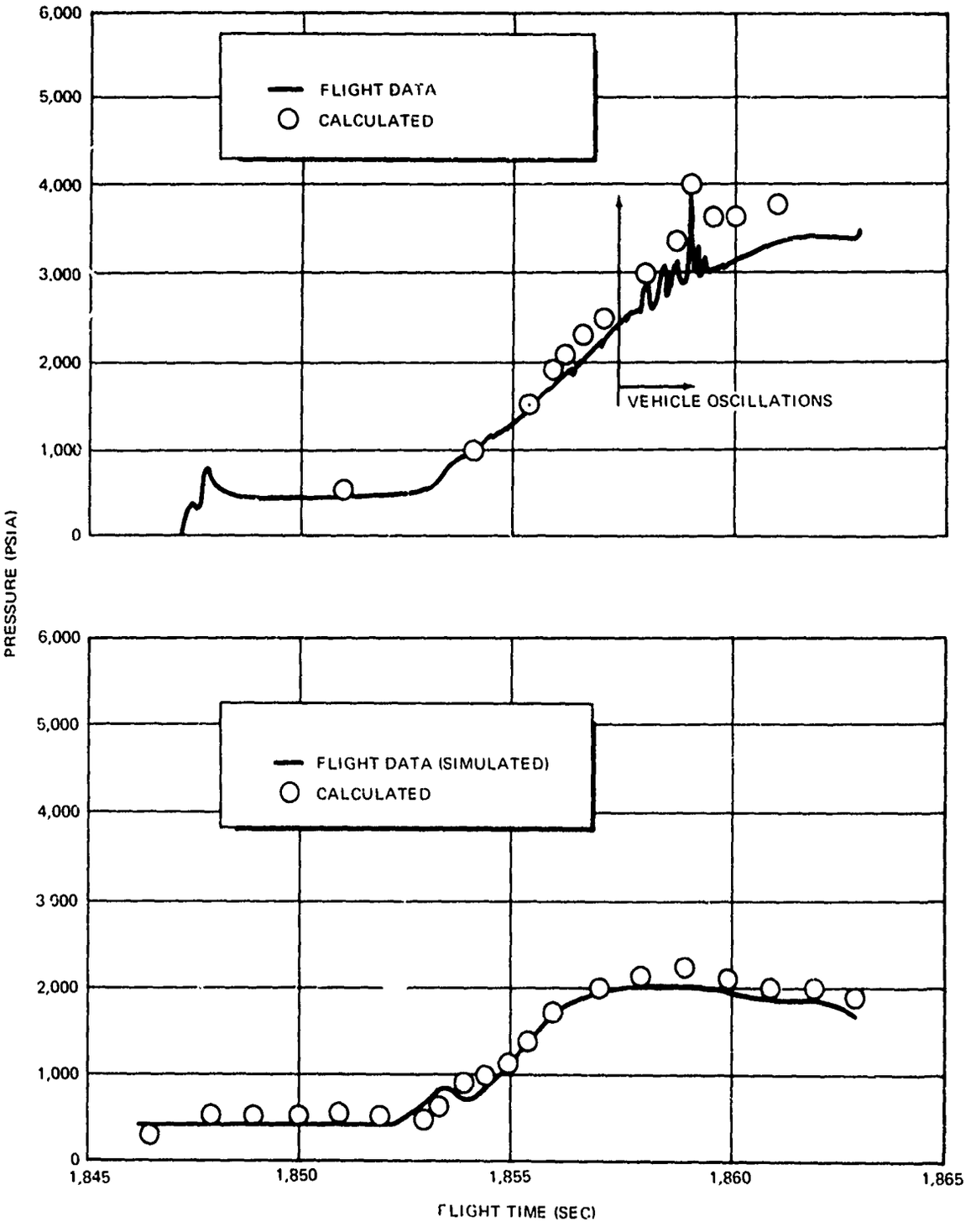

Figure 19. Comparison of Calculated and Measured Nose-Tip Internal Pressure

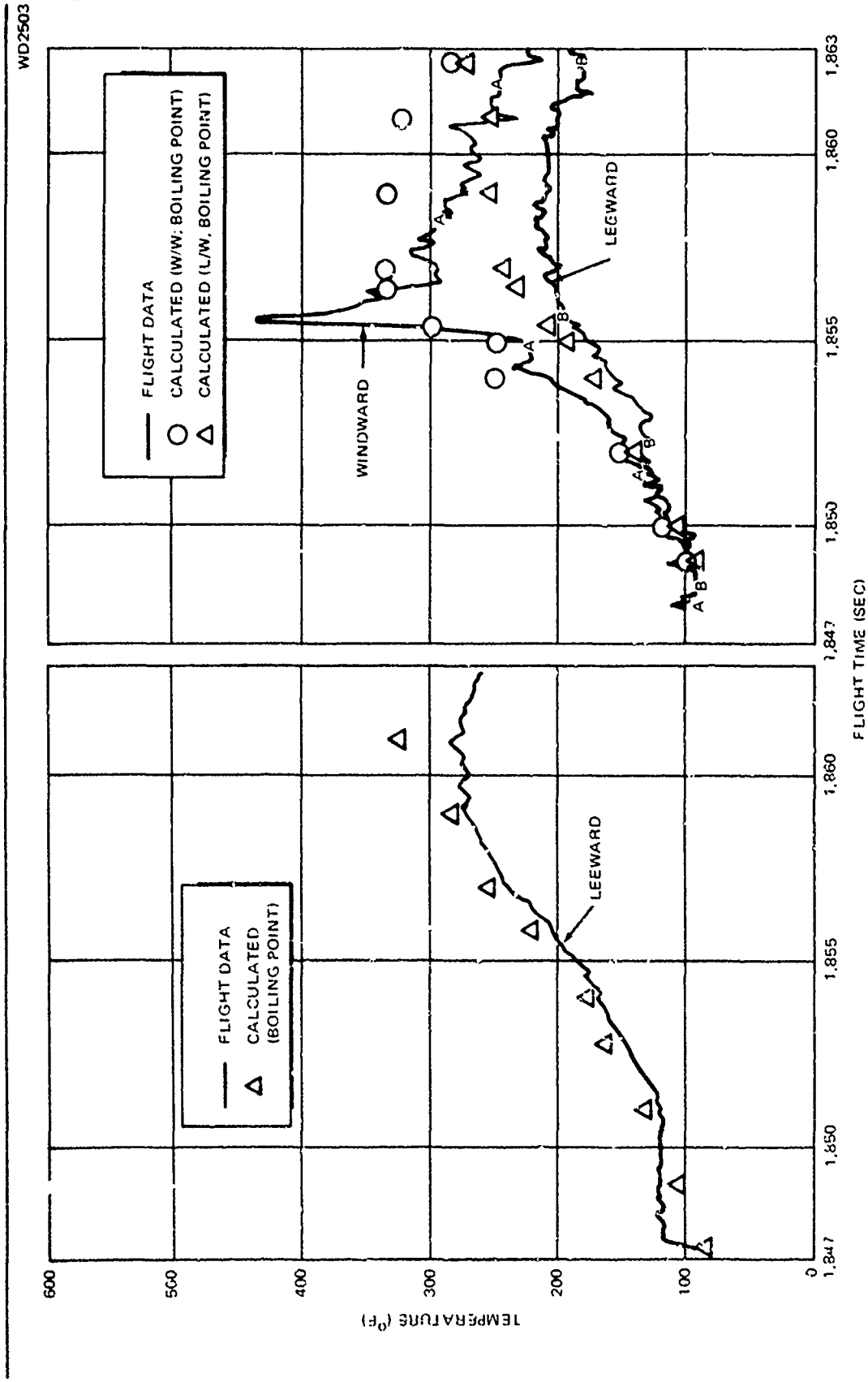

Figure 20. Nose-Tip/Heat-Shield Interface Temperature Response

In a similar manner, the extent of the liquid film downstream of the nose tip can be estimated from heat-shield temperature data. Figures 21 and 22 illustrate the effectiveness of a liquid film in protecting the heat shield downstream of the nose tip. Contained in the figures are temperature data from five locations along the leeward ray at various distances from the nose-tip/heat-shield interface (Station 6.33) for the second flight. Also included in the figures are calculated values of surface thermocouple response in the absence of any downstream cooling effects.

At Station 7.4, the heat-shield surface was covered by a liquid film from the time of coolant onset (~1,847.5 seconds) until impact. Prior to coolant onset, the sensor was covered by a Teflon boot which was used to protect the nose tip at high altitudes.

At Station 12.3, which is not covered by the boot, the temperature at the surface thermocouple rises until coolant onset where it drops to levels indicative of the presence of a liquid film. Late in flight, when the angle of attack drops sharply, the temperature again rises due to the removal of the liquid film.

At Station 20.6 (14.3 inches behind the nose tip), the surface temperature is seen to oscillate, roughly in conjunction with the rise and fall of the vehicle angle of attack. This behavior is indicative of the liquid film being swept back and forth across the sensor during the course of the flight.

Comparison with the no downstream cooling predictions at all three locations shows very clearly the cooling effect of the excess coolant from the nose tip. These predictions were made using the standard transition criterion of momentum Reynolds number equal to 150.

At Stations 48 and 72 (Figure 22), the liquid film has disappeared. The amount of downstream cooling (caused by boundary layer cooling) present at these locations is dependent upon the existence of vortex heating along

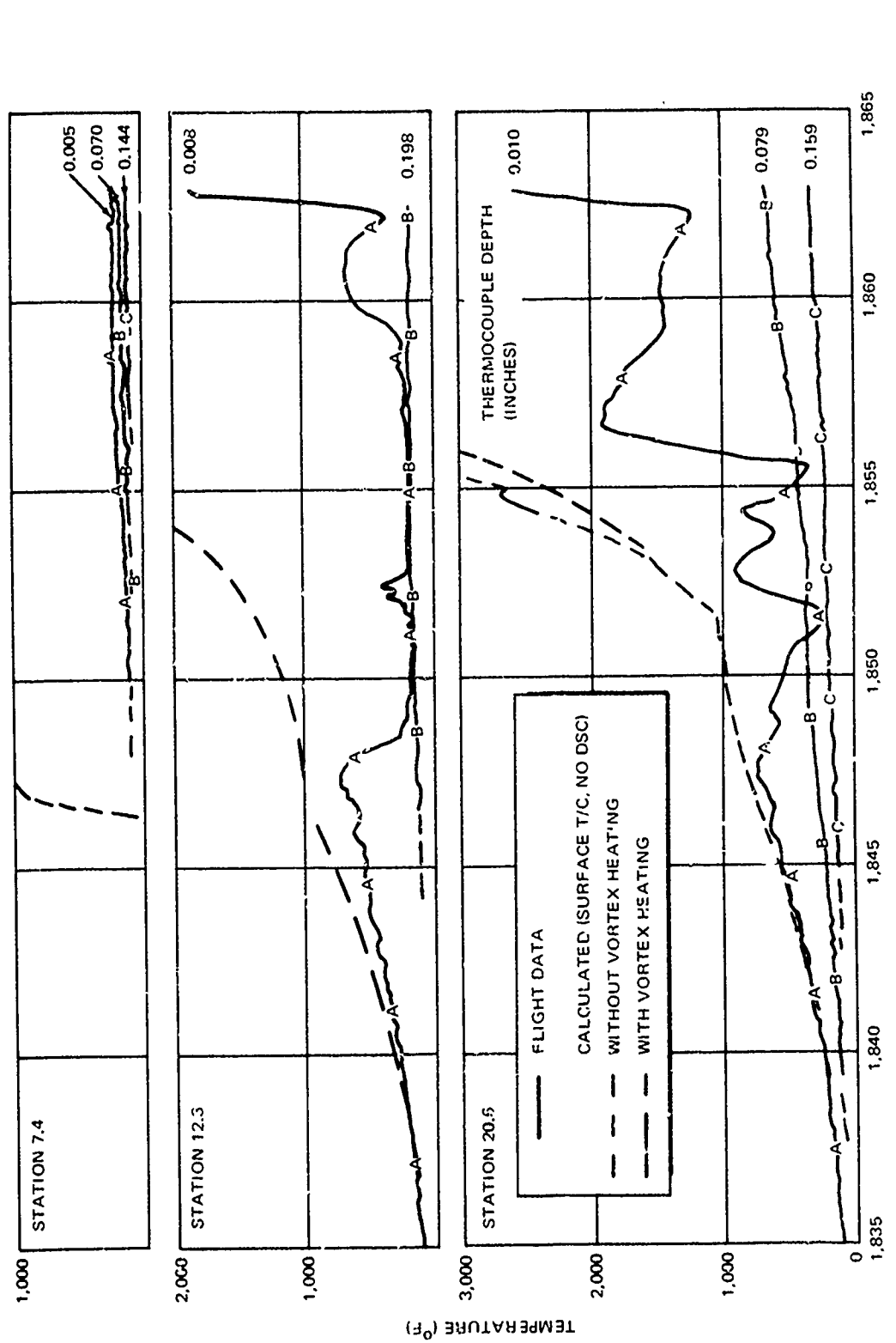

Figure 21. Effect of Liquid Film on Leeside Heat-Shield Performance, Forward Stations

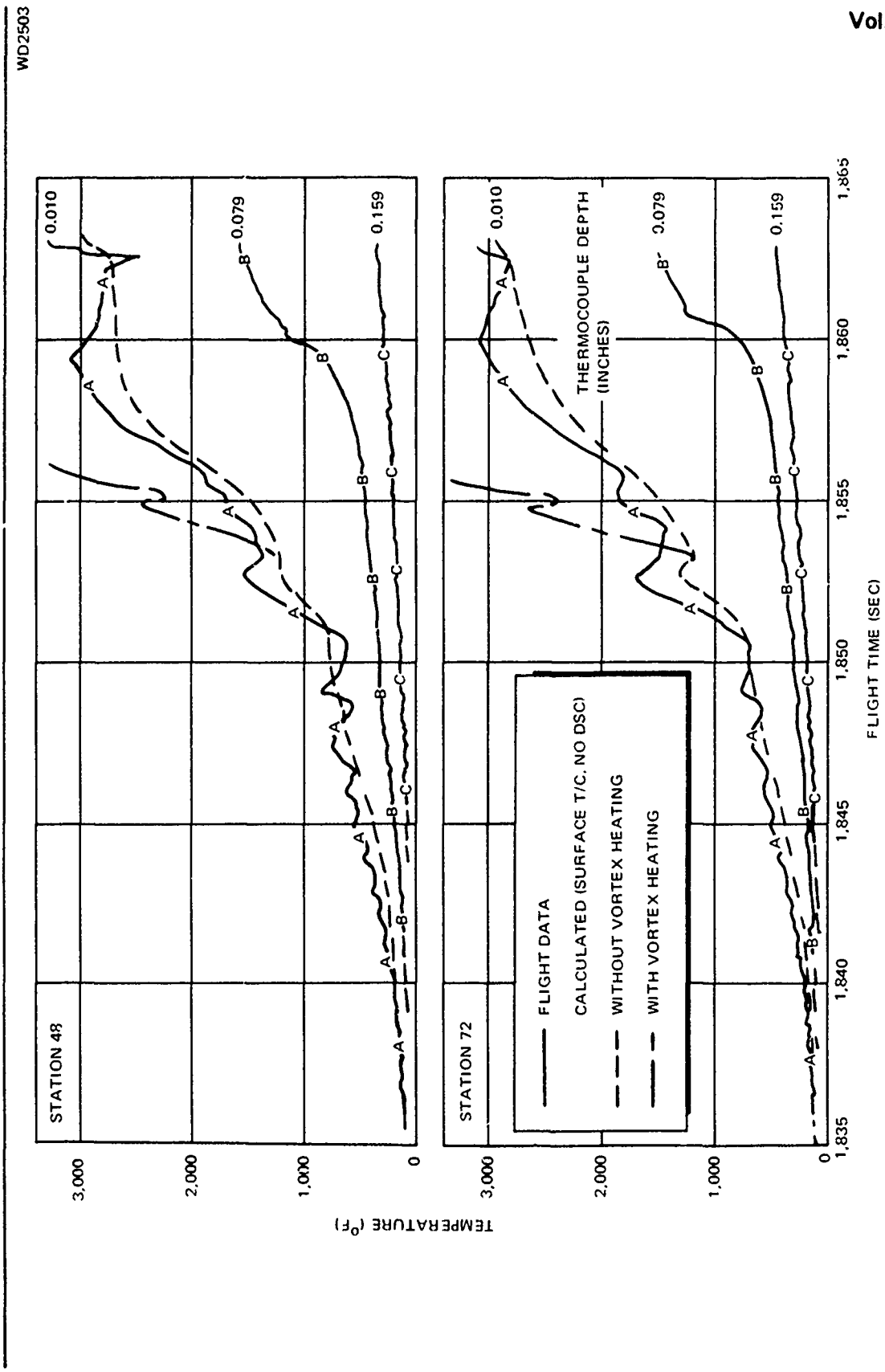

Figure 22. Effect of Liquid Film on Leeside Heat-Shield Performance, Aft Stations

the leeward ray. As can be seen from the curves, if vortex heating does not exist, then the heat-shield behavior is accurately predicted without the benefit of downstream cooling. However, if vortex heating is present, then downstream cooling is indicated to exist at the later times in flight.

So far the discussion has centered around the leeward ray. Liquid films are also present on the windward ray although, as might be expected, to a much lesser extent. Figure 23 shows the flight data on the windward ray at Station 7.18. As can be seen, a liquid film existed until 1,852.8 seconds, at which time the angle of attack rose sharply and resulted in the film being swept to the leeside. However (as will be discussed later), even in the absence of the liquid film, boundary layer cooling resulted in large reductions in near-nose heating and resultant ablation.

Downstream of the liquid film, the heat shield is cooled by the presence of liquid droplets and/or vapor in the adjacent boundary layer. The ultimate effect of this phenomenon is to lower the heat transfer to the vehicle surface and thus reduce the heat-shield temperatures and recession. In order to assess the magnitude of the cooling downstream of any liquid films, a detailed postflight analysis was performed for both flights which consisted in the calculation of heat-shield temperature and recession using various transition criteria both with and without a downstream cooling assumption, followed by a comparison to the flight data at each near-nose sensor location. A discussion of the calculations performed at Station 7.18 for the second flight will serve to illustrate the analysis procedures as well as some important features of the results.

Two methods are available to obtain the estimates of downstream cooling effectiveness. The first method was developed from flight data obtained from both the RVTO-1A and RVTO-2A flight tests (Reference 4). The method is empirically derived and consists of relating the reduction in heat transfer coefficient due to downstream cooling to a calculated ideal liquid film length (zero shear condition). This method is referred to as the "reduced N_c" method.

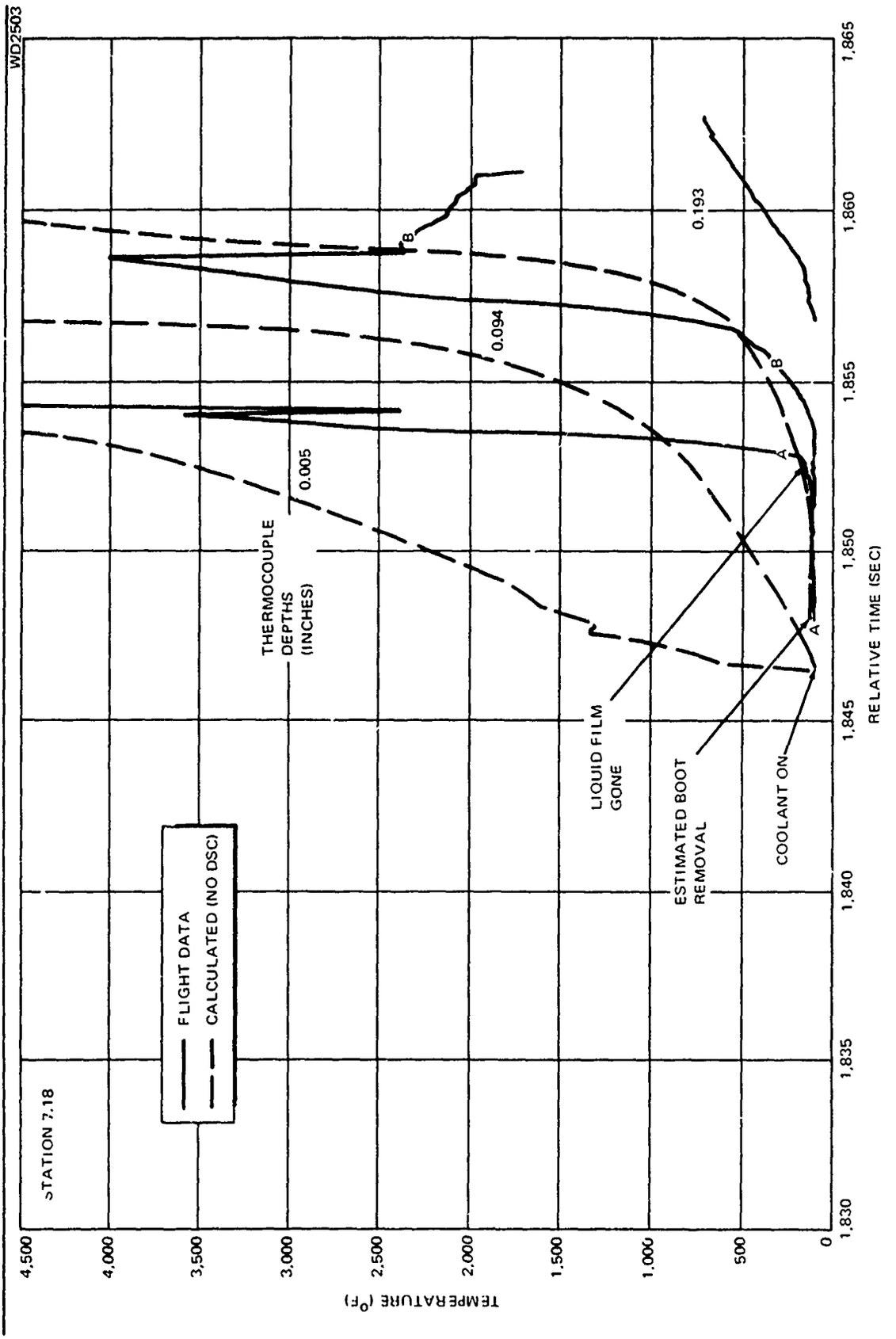

Figure 23. Effect of Liquid Film on Windward Heat-Shield Performance

The second method is analytical in nature and assumes that the excess coolant reduces the boundary layer temperature (enthalpy) while the heat transfer coefficient remains unchanged. This method is referred to as the "reduced H_R" method.

Figure 23 contained a comparison of the flight data at Station 7.18 with heat-shield in-depth temperatures calculated without any downstream cooling and with a transition altitude of 75,000 feet (determined from $Re_\sigma = 150$). Figure 24 contains the same flight data compared with calculations assuming all laminar flow with no downstream cooling, and also calculations using 75,000-foot transition altitude with downstream cooling determined from the reduced N_c method.* Since, in the absence of downstream cooling, even the all laminar case overpredicts the in-depth temperatures, it is evident that downstream cooling was in fact present. In addition, the shape of the laminar temperature response for the middle thermocouple, when compared to the flight data, also suggests that the flow was turbulent at the lower altitudes. The calculations performed using downstream cooling methodology show an improved agreement with the flight data over those with no downstream cooling. The largest discrepancies occur when the surface is covered by a liquid film (since the method was derived from flight data which included a negligible liquid film) and prior to the onset of transition (1,855 seconds).

Figure 25 contains recession predictions (normalized to the windward ray total heat-shield thickness) and flight data for Station 7.18. As can be seen, the measured recession falls far below the amount which would be expected in the absence of downstream cooling and with a nominal transition altitude. Comparison with the all-laminar case seems to indicate that simply reducing the transition altitude in the absence of downstream cooling would allow the prediction to match the data. However, from the in-depth temperature predictions discussed previously, use of any transition altitude between 75,000 and 0 feet would result in an overprediction in in-depth temperature.

*Temperatures determined with the reduced H_R method were similar but somewhat more conservative.

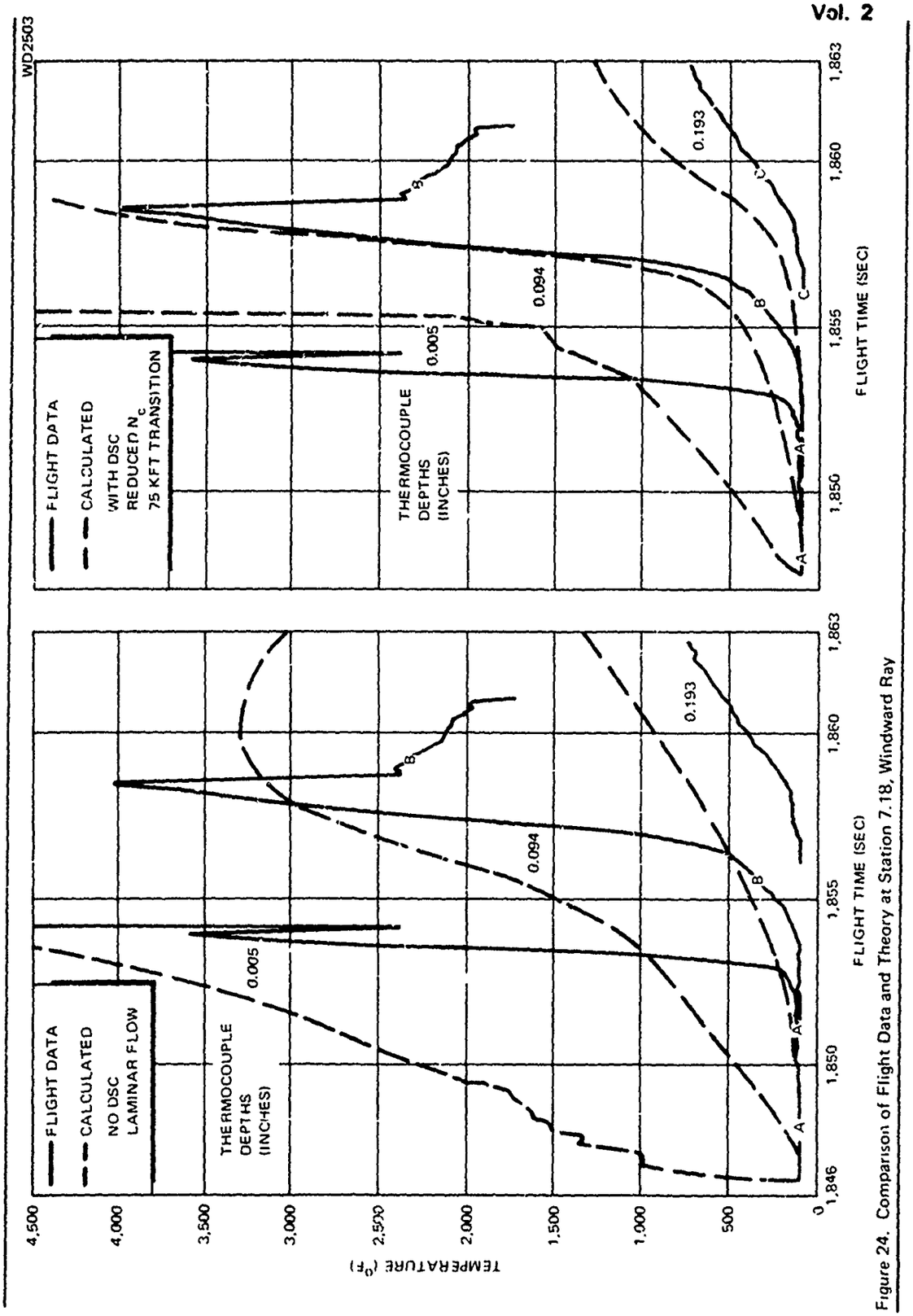

Figure 24. Comparison of Flight Data and Theory at Station 7.18, Windward Ray

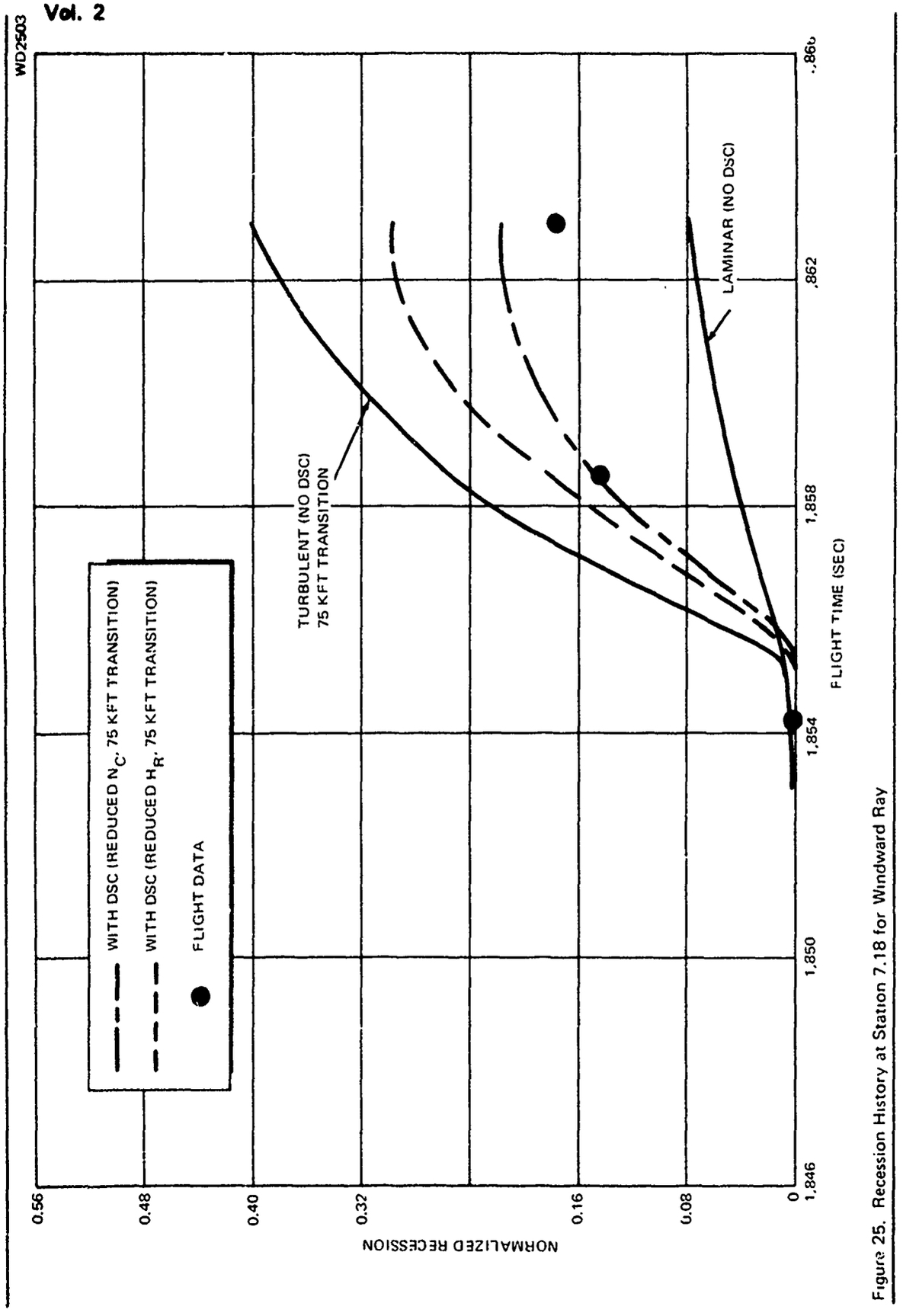

Figure 25. Recession History at Station 7.18 for Windward Ray

Therefore, downstream cooling must be present. The recession prediction with a 75,000-foot transition altitude in the presence of downstream cooling and carbon-water reactions is also shown in the figure. The agreement with data is good with the reduced N_c method and fair with the reduced H_R method.

Analyses similar to those for Station 7.18 were performed at each forward frustum sensor location and the results in terms of normalized recession are shown in Figure 26 for the windward ray (Stations 7.18 and 12.2) and in Figure 27 for the leeward ray* (Stations 7.4 and 12.3). On the windward ray, the downstream cooling is effective for approximately 1 foot aft of the nose tip with reductions in recession of up to 50 percent under the no downstream cooling prediction. On the leeward ray, the effect of the downstream cooling is to eliminate all recession on the forward frustum. On both rays, the predicted and measured recession show good agreement.

Flight Test Results Summary

Several pertinent observations were made from the flight data:

- Flight test data confirmed the ability of the nose tip to survive in a high-angle-of-attack flight environment with coolant margins at least as low as 25.5 percent, which is approximately half of the previously used design value of 50 percent.

- The accuracy of the nose-tip flow prediction techniques was verified by the good correlation between the measured and calculated internal nose-tip pressure using the measured coolant flow rate as an input to the analysis.

*Sensors were also located at the 45 degree (Station 7.93) and 315 degree (Station 8.68) rays. Results at Station 7.93 indicated approximately a 33 percent reduction in recession due to downstream cooling while at Station 8.68 the reduction was on the order of 10 to 15 percent.

WD2503

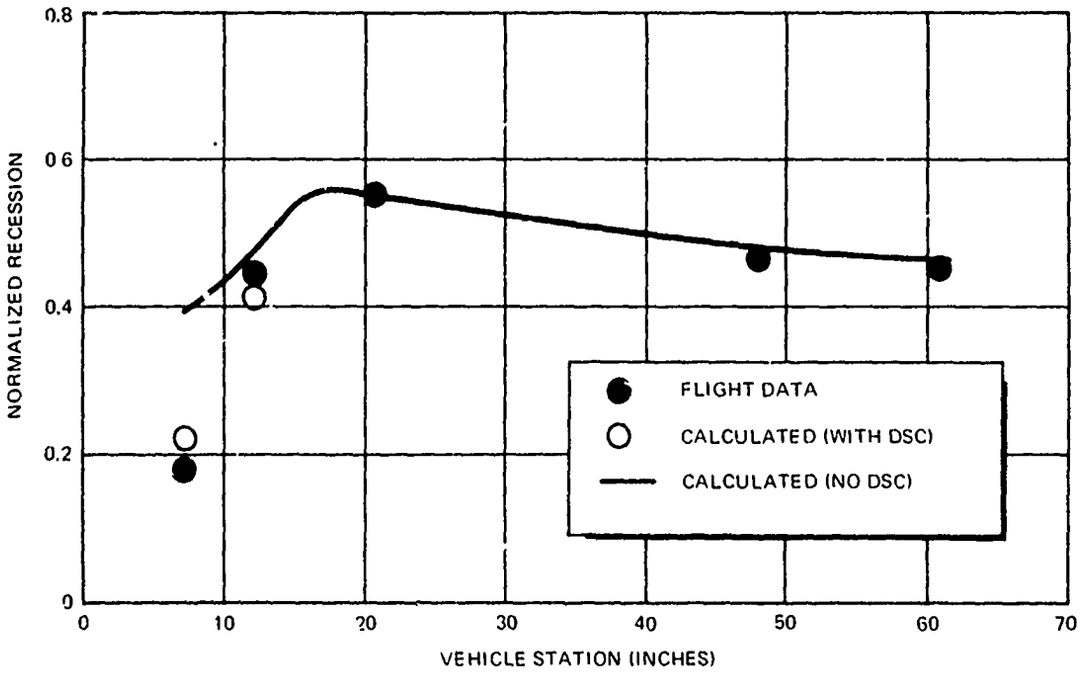

Figure 26. Frustum Recession at Impact, Windward Ray

WD2503

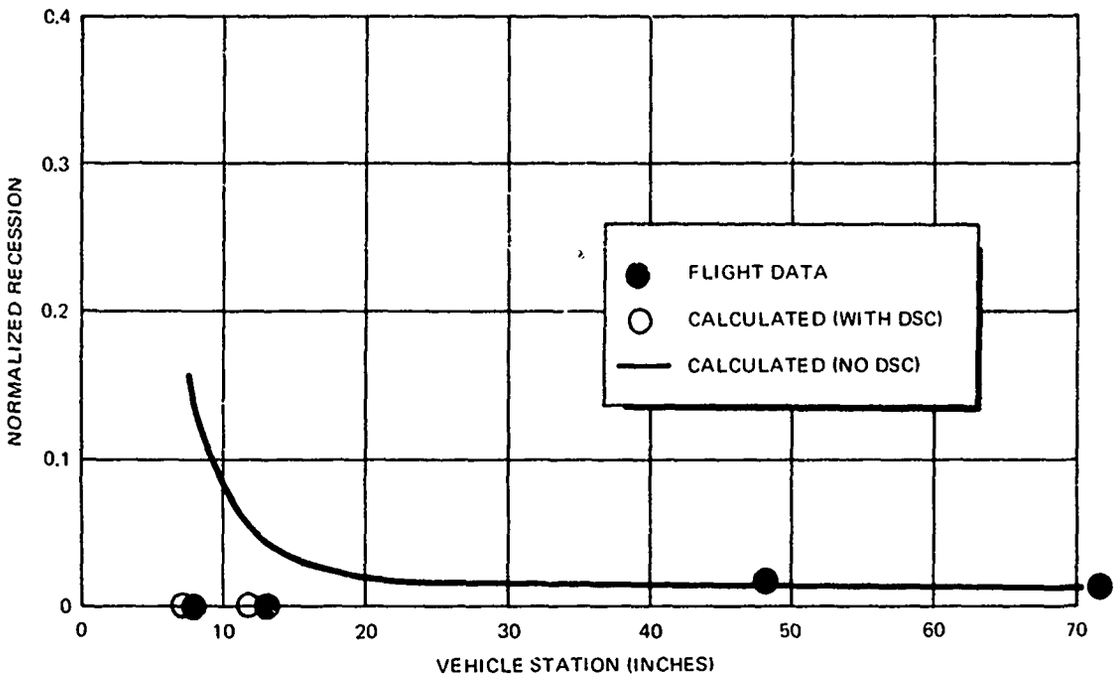

Figure 27. Frustum Recession at Impact, Leeward Ray

- Results from both flights were qualitatively similar with the downstream cooling being strongly affected by the vehicle oscillations on the first flight.
- Significant liquid film lengths were observed downstream of the nose tip. These films were especially long on the lee side.
- Data from the near-nose instrumentation indicate the presence of downstream cooling aft of, or in the absence of, liquid films; in general, current downstream cooling calculation techniques give a good estimate of near-nose heating but require the addition of a liquid film model for greater accuracy.
- Current downstream cooling techniques can be used for vehicle near-nose heat-shield design, but will be conservative in the presence of liquid films.
- Near-nose heat-shield recession reflects the presence of downstream cooling, i.e. measured recession values are significantly lower than those predicted in the absence of cooling.*

REFERENCES

1. J. L. Nardacci and N. C. Campbell. Re-Entry Systems Environmental Protection (RESEP) Program I, Final Report, Task 5, Transpiration Cooled Heat Shields. SAMSO-TR-68-463, March 1969.

2. N. C. Campbell. Re-Entry Systems Environmental Protection (RESEP) Program II, Final Report, Task 10.4, Transpiration Cooled Heat Shields. SAMSO-TR-70-248, August 1970.

3. B. G. Leonard. Re-Entry Systems Environmental Protection (RESEP), Task 5 RVTO-1A Flight Experiment, Final Technical Report. SAMSO-TR-70-87, March 1970.

4. RVTO-2A Final Report, Vol I, Flight Evaluation Report for WT2A-L21 and WT2A-S21 Vehicles, Part I – Analysis. SAMSO-TR-71-118, April 1971.

5. L. Lees. Laminar Heat Transfer Over Blunt Nosed Bodies at Hypersonic Flight Speeds. Jet Propulsion, April 1956.

*An exception to these conclusions is Station 12.2, windward ray. At this station (approximately 6 inches behind the nose tip), the use of a downstream cooling model caused about a 15 to 20 percent underprediction in recession.

6. N. C. Campbell, J. L. Nardacci, and D. Quan. Semi-Annual Technical Progress Report, RESEP Task 5, Transpiration Cooled Heat Shields. BSD-TR-66-369, July 1967 (Classified Confidential).

7. C. L. Arne. Ablative Materials Subject to Combustion and Thermal Radiation Phenomena. Douglas Paper 1851, January 1964, McDonnell Douglas Corp., Santa Monica, Calif.

8. J. R. Schuster. MDAC Computer Program H589, Coolant Flow in Transpiration Cooled Nose Tips. MDC G2287, April 1971.

9. E. R. G. Eckert. Survey of Boundary Layer Heat Transfer at High Velocities and High Temperatures. WADC TR-59-624, April 1960.

PAPER NO. 24

SURFACE TEMPERATURE MEASUREMENTS IN HYPERSONIC FREE FLIGHT

By
Daniel C. Reda, Robert A. Leverance,
and William G. Dorsey, Jr.

Naval Surface Weapons Center
White Oak Laboratory
Silver Spring, Maryland

ABSTRACT

Combined experimental and analytical programs are being conducted at the Naval Surface Weapons Center, White Oak Laboratory, in support of current and future strategic re-entry systems. This paper reports on present White Oak Laboratory capabilities for creating free-flight re-entry environments within the 1000-foot Hyperballistics Range and for accurately measuring surface temperature contours on models exposed to such environments. Details of an electrooptical pyrometer system, recently adapted for use at the White Oak Laboratory, are described, and limiting assumptions in data reduction and interpretation are discussed. Surface temperature contours measured on a re-entry vehicle nose-tip configuration are presented and comparisons made with calculations generated by a currently utilized nose-tip design code.

NOMENCLATURE

C	speed of sound
$E_b\ (\lambda)$	black body radiation
$E_G\ (\lambda, T, \rho)$	gas radiation
H	enthalpy
k	characteristic microroughness
$k\ (o)$	initial surface roughness
$k_J\ (t)$	local surface roughness as a function of time
K_L	augmentation factor applied to local laminar heat-transfer rate
p	pressure
$R_{e_\infty}/_{FT}$	free-stream unit Reynolds number, $\frac{\rho_\infty V_\infty}{\mu_\infty}$
R_{e_θ}	momentum thickness Reynolds number, $\left(\frac{\rho V}{\mu}\right)_{EDGE} \cdot \theta$
R_N	nose-tip radius
R_N'	effective nose-tip radius after ablation
$\Delta r_J\ (t)$	local normal recession at time t
S	arc length, measured from geometric stagnation point
$S_{11}\ (\lambda)$	image converter tube response
T	temperature
t	time, measured from muzzle exit
V	velocity
V_e	re-entry velocity
$W_{12}\ (\lambda)$	cut-off filter response
$\Delta x_J\ (t)$	local axial recession at time t

Δy_J (t)	local radial recession, normal to body axis, at time t
β	ballistic coefficient
γ_e	re-entry angle
Δ (ψ, V_∞, p_∞, R_N)	local shock stand-off distance
δ^*	smooth wall, boundary-layer mass displacement thickness
ε	surface emissivity
θ	smooth wall, boundary-layer momentum thickness
λ	wave length
μ	viscosity
ρ	density
ρ_{STD}	standard reference density, .08073#m/ft^3
ψ	angle measured from geometric stagnation point

Subscripts

edge, e	at boundary-layer edge
i	at muzzle exit
J	at local body surface point J
STAG	at the stagnation point
TANK	in blast tank
w	at the wall or surface
∞	free stream
2	behind normal shock

INTRODUCTION

Design of advanced re-entry vehicle nose tips and heat shields requires a detailed understanding of viscous and inviscid flow fields, heat transfer, and ablation phenomena (shape change) within hypersonic real gas environments. Codes used for such design calculations must accurately model such key elements as boundary-layer transition onset conditions, transition zone location and extent, roughness augmented heat transfer, and ablation thermochemistry.

Experimental information required for the correct modeling of such complex phenomena is often generated under wind-tunnel and/or arc-jet environments which are incapable of achieving complete simulation of actual re-entry conditions, i.e., Mach number, Reynolds number, and total enthalpy levels simultaneously. Semiempirical correlations based on such data must, therefore, be verified through atmospheric flight tests or through short duration free-flight tests within ballistics ranges, wherein actual re-entry conditions can be achieved.

Due to severe model launch loads and short test times encountered in ballistics range research, essentially all data acquisition are accomplished through optical techniques. It is the objective of the present paper to describe a recently created optical technique[1] for the measurement of surface temperature contours on models in hypersonic free flight, to present experimental data so measured on a hemispherical nose tip of a carbonaceous material, and to compare

such measurements with transient surface temperature predictions generated with a state-of-the-art nose-tip design code.

EXPERIMENTAL APPARATUS

Facility

The facility employed in the current study of nose-tip thermal response in clear air re-entry environments is the White Oak Laboratory 1000-foot Hyperballistics Range (a brief description of which is presented below).

In order to create valid re-entry simulations, hypersonic launch velocities must be achieved. This requirement dictates the use of a two-stage light-gas gun (a schematic of which is shown in Figure 1). An explosively driven Teflon piston is used to compress hydrogen gas in the first-stage driver section. This gas is contained within the pump tube by a metallic diaphragm until a preselected pressure level is reached. The diaphragm bursts and the low molecular weight gas rapidly accelerates the model/sabot package down the launch tube, or second stage, to hypersonic velocities while the piston is decelerated and stopped through deformation in the converging portion of the high-pressure section. Muzzle velocities achievable with the White Oak Laboratory 2.0-inch inside diameter launcher are shown in Figure 2 as a function of package weight.

Once the package clears the muzzle, it is exposed to a low static pressure environment (~0.1 atm) within the blast tank. Here, the sabot, comprised of four separate fingers or petals, is aerodynamically stripped from the model. The model

traverses the blast tank and enters the 1000-foot range tube through a quick opening valve port, while the sabot sections diverge from the model flight path due to aerodynamic lift and are destroyed on impact with a series of metal plates.

Since the range tube can be independently maintained at any desired static pressure level from atmospheric down to ~0.5mm Hg (effective altitudes based on density from sea level to ~170,000 feet), various re-entry environments can be achieved through appropriate combinations of range pressure and launch velocity. Figure 3 shows free-stream unit Reynolds number, stagnation pressure, and stagnation enthalpy levels attainable as a function of launch velocity with range static pressure as the parameter. Figure 4 shows the operating envelope of this facility in comparison with typical re-entry trajectories for slightly blunted sphere/cones, illustrating that actual re-entry conditions can indeed be simulated.

The range tube is fully instrumented with a variety of optical instrumentation, including electrooptical pyrometers (discussed in detail in the subsequent section), lasers for both frontlighted and backlighted model contour photography as well as flow field (shadowgraph) photography of high-luminosity models, dual plane spark shadowgraphs for flow field definition about low-luminosity models, and dual plane X-ray stations for model angle-of-attack and structural integrity information. Accurate measurements of model roll rates, angle-of-attack histories in pitch and yaw, and shape change due to ablation and/or erosion can thus be made.

Electrooptical Pyrometer

At present two electrooptical pyrometer stations are installed and operational within the 1000-foot Hyperballistics Range at axial distances of 37.8 and 198.2 feet from the range tube entrance; a third station is planned for installation early in FY76 and will be located at a position dictated by future programs.

The physical arrangement utilized in adapting this system to the 1000-foot range is shown schematically in Figure 5. The basic operating principle of electrooptical pyrometry is to record film densities of known temperature sources (here the end-on filtered and unfiltered images of a carbon arc electrode) and an unknown temperature source (e.g., a nose tip in free flight) and, through the experimentally defined calibration relationship between source brightness temperature and film density, determine apparent brightness temperature distributions on the unknown temperature source.

To obtain the required calibration of film density versus source temperature, a specially designed carbon arc is incorporated (Mole-Richardson Company, Hollywood, California). Electrodes of this unit are positioned to yield a 120-degree included angle between them, thereby allowing end-on observations of the positive graphite electrode via proper alignment of the planar mirror in the range tube. The crater of the positive electrode, when operated under properly chosen voltage and current conditions, provides a source of high temperature radiation of exceptionally high reproducibility (3806°

± 10°K). A series of calibration filters (traceable to the National Bureau of Standards) allows effective black body temperatures from ~2400°K to ~3800°K (the unfiltered temperature) to be generated; effective temperatures above 3800°K are achievable by photographing the unfiltered image at reduced camera f/numbers (i.e., larger apertures) than are used for recording actual free-flight data. A useable temperature range of ~2400°K to ~4400°K (~4300°R to ~8000°R) can thereby be attained.

At the receiving end of the optical path is an image converter camera which consists of a planar photocathode (S-11), a planar phosphor screen (P-11), a relay lense, and a sliding film back (four-inch x five-inch negatives). When a high voltage pulse is applied across the photocathode/phosphor screen region, any light image incident on the photocathode surface is transferred, via accelerated electrons, to the phosphor screen; the recreated light image is then relayed to the exposed film surface and recorded. Since the number of electrons released per unit area is proportional to the number of photons impinging on the photocathode per unit area, the electron image density distribution on the phosphor screen is directly proportional to the original light image brightness distribution. Further, since electron image propagation is effectively maintained only in the presence of a high voltage acceleration field, an effective electronic shutter time can be set by preselecting the time duration of the voltage pulse. Exposure times of the order of 0.1 microsecond and less can

thereby be attained, minimizing motion blur (i.e., ~20 mil axial translation in 0.1 microsecond at 18,000 feet per second, coupled with an essentially head-on view, yields no adverse effects on image resolution).

One problem encountered during calibration, but not during actual data recording, concerns the small but finite off/on ratio of light transmitted by the image converter tube. During free-flight observations, the model image is rapidly swept through the prescribed field of view due to its high velocity, thereby serving to limit the total amount of light received at the photocathode surface. Since the calibration arc is stationary, its long duration signal would, despite the short absolute shutter time of the image converter camera, result in noticeable bleed through of light, i.e., a fogging of the film. This is countered by sweeping the arc image across the photocathode field of view by means of a rotating mirror while limiting its impingement on the tube surface to a single pass via a light detector/electronic delay circuit/ mechanical shutter arrangement.

All calibration images are recorded on a single negative via a sliding film back arrangement. At the completion of calibration, the planar mirror is rotated (onto an identical optical path) to view the approaching flight path; final optical alignment is accomplished with a CW laser. Standard test procedures are then initiated, culminating with model launch and data acquisition. The nose-tip brightness image is always recorded on the same negative used for calibration in order to eliminate film development inconsistencies.

Figure 6 shows component and overall system response as a function of incident light wavelength. Use of a cut-off filter ($W_{12}(\lambda)$) coupled with the photocathode tube response ($S_{11}(\lambda)$) serves to limit monitored wavelengths to the range $0.50 \leq \lambda \leq 0.65$ micron due to the overall $S_{11}(\lambda) \cdot W_{12}(\lambda)$ system response. By monitoring only a narrow 0.15 micron wavelength band, overall system performance is improved in two areas: first, within this wavelength regime, the calibration source exhibits true black body characteristics, and second, contributions to the data signal from gas cap radiation are greatly reduced (calculation of and correction for the gas cap contribution are discussed under limiting assumptions).

Overall system accuracy was investigated in reference (1) by placing a second calibration source in the range tube and treating it as an unknown temperature source. Using standard calibration and data acquisition procedures, ten separate tests were conducted. Measured arc electrode temperatures were, in all cases, within ± 2 percent of the unfiltered value (i.e., a maximum data band of $\pm 75^{\circ}K$ about the nominal value of $3806^{\circ}K$).

DATA REDUCTION PROCEDURES

The four-inch x five-inch film sheet, containing all calibration images plus the model image, is developed. Calibration images on the resulting negative are scanned with a microdensitometer and relative film density levels are simultaneously plotted by an isodensitracer (see Figure 7). In this procedure, all film densities are measured relative to

a reference density generated by scanning a separate piece of high quality uniform density film, referred to here as the reference filter. Use of a reference filter is dictated by possible requirements for shifting the density scale limits higher or lower in order to accommodate nose-tip density levels within available plotting space; a rescan of this reference filter under any new density scale constraints supplies a repeatable reference level from which nose-tip density levels may be measured. An example of a pyrometer calibration curve generated in this manner is shown in Figure 8, where the reference filter for this test corresponds to an effective brightness temperature of 3320°K. As noted, calibration curves are linear above ~3000°K (~5400°R).

Having defined the film density to source temperature relationship, a scan of the nose-tip image is then made. A scan sensing area of 1.0 x 1.5mm is utilized on the nose-tip image as magnified by the microdensitometer optics (see Figure 9). In physical coordinates, this corresponds to a sensing area of 8.6 x 12.8 mils for pyrometer #1 (37.8-foot station) or 18.1 x 27.2 mils for pyrometer #2 (198.2-foot station).

Nose-tip film density levels are plotted in two distinct ways. First, a complete scan of the entire nose-tip image is made and color coded isodensity contours of this end-on view are simultaneously plotted by the isodensitracer (a black and white recreation of one such plot is shown in Figure 10). After this overall scan is complete, selected cross cut planes are rescanned, and relative film density is plotted as a function

of physical location (such cross cuts are usually taken on a major diameter, i.e., one through the geometric stagnation point). Figure 11 shows such a plot taken on a horizontal cut through the stagnation point of the isodensity contour plot of Figure 10. These analog plots of relative film density versus physical displacement along a major diameter can be digitized through use of appropriate scale factors (i.e., calibration curve and optical/mechanical magnification factors) and results replotted as nose-tip surface temperature versus nondimensional arc length (S/R_N) along the nose-tip surface.

LIMITING ASSUMPTIONS IN DATA INTERPRETATION

Strictly speaking, the pyrometer calibration procedure relates relative film density to source brightness temperature. In order to equate brightness temperatures measured by the electrooptical pyrometer system to model surface temperatures certain limiting assumptions must be invoked. These are discussed below.

First, it is required that within the monitored wavelength regime surfaces under observation radiate incandescently according to Planck's equation, i.e., radiate with black on grey body characteristics. This assumption is justifiable for bulk graphites and carbonaceous ablation chars (i.e., nose-tip materials of current interest) which possess smooth near unity emissivity versus temperature curves throughout the visible spectrum[2]. For such materials, the system calibration procedure is most valid since both the calibration arc electrode and the nose tip are carbonaceous and both radiate as black or near-black body sources.

Second, ablation phenomena at or near the model surface must not measurably influence recorded brightness images. Surface thermochemistry is a function of nose-tip material and the gaseous environment to which it is exposed. Violent chemical reactions (e.g., combustion), which can occur at various metallic surfaces exposed to high temperature oxidating environments and melt layers which can occur on certain ablating surfaces (e.g., quartz phenolic) would most likely attenuate, i.e., add to or detract from, surface radiation. However, subliming and/or charring carbonaceous ablators which yield gaseous products of ablation are felt to meet this second restriction.

Thirdly, it must be assumed that the flow field itself does not attenuate the surface radiation signal. At hypersonic velocities, a strong bow shock wave forms ahead of the blunt nose tip. Between this bow wave and the model surface there exists a thin, dense, real gas shock layer. This region, referred to here as the gas cap, contains, depending on flight conditions and range tube gas, various dissociated and/or ionized species. Effects of both gas cap absorption and emission on the surface radiation signal must be ascertained.

Gas cap absorption effects can be neglected if the product of absorption coefficient times local shock layer thickness is small compared to unity. Based on reported absorption coefficients of Gilmore[3] at maximum density and temperature conditions experienced under present test conditions, this product was computed to be of the order of 10^{-2}.

Figure 12, also based on calculations of Gilmore[3], shows the energy radiated into spherical space by a unit volume of air at temperature and density conditions bracketing most ballistics range environments of interest as a function of wavelength. If at any point on the nose tip one calculates the local shock wave stand-off distance (i.e., the local depth of radiating gas) and subsequently computes the integral listed at the bottom of Figure 12, a measure of the local gas cap radiation (energy/unit area) can be derived. In this calculation, the one-half factor accounts for that portion of the radiant energy per unit volume directed towards the sensing instrument. A computer code for performing the above calculations was developed in reference (4) and has been applied here.

Having calculated the energy per unit area radiated by the gas cap to the image converter camera, it remains to devise a procedure whereby corrections for this contribution to the data signal can be made. A relationship between energy per unit area sensed by the pyrometer and brightness temperature of the radiating source is thus required.

Figure 13 shows the energy radiated into hemispherical space by a unit area of a black ($\varepsilon = 1.0$) and a grey ($\varepsilon < 1.0$) surface, each at $7000^{o}R$, as a function of wavelength (recall that $1\mu = 10^{-4}$cm). Photocathode tube response and overall pyrometer system response to the grey body energy input are also shown. An integration with respect to wavelength of these lower two curves yields the energy per unit area sensed

by the electrooptical pyrometer system with and without the cut-off filter for a grey body at the specified surface temperature. Such calculations were made for both black and grey ($\varepsilon = 0.9$) surfaces over the full operating temperature range of the present pyrometer system, and results are shown in Figure 14. Several points concerning this figure should be made.

First, the present system is represented by the lower two curves, i.e., the $[S_{11}(\lambda) \cdot W_{12}(\lambda)]$ response. Second, an uncertainty in surface emissivity of the order of ten percent results in only a 50 to 100°R uncertainty in surface brightness temperature. Third, an equivalent black body brightness temperature can be defined for any computed gas cap radiation level. Fourth, and finally, corrections to measured surface temperatures for gas cap contributions can be made as noted below. For any specified position on the nose tip, Figure 14 defines a radiant energy level corresponding to the observed brightness temperature. An independent calculation of local gas cap radiant energy per unit area is made, and this value is subtracted from the experimentally defined energy level. The resulting net energy level is attributed to surface radiation, and a corrected model surface temperature is thus defined. Experience has shown that such corrections are generally small, as will be demonstrated under data analysis.

DATA ANALYSIS

As stated in the introduction, one primary element of the present research is to determine the aerothermodynamic prediction

capabilities of currently utilized nose-tip design codes through comparisons with surface temperature data obtained under controlled re-entry conditions. The present section is thus divided into two subsections: the first outlines principle features of a computer code used for predicting the aerothermal response of ablating bodies exposed to hypersonic real gas environments and statements concerning recent updates to this code are made; the second subsection presents a detailed analysis of a graphite nose tip launched in the 1000-foot Hyperballistics Range on which surface temperature measurements were made.

Code

The nose-tip shape change and thermal response computer code currently utilized at the White Oak Laboratory was developed under government sponsorship by the Aerotherm/Acurex Corporation and is described in detail in reference (5). The primary purpose of this code is to numerically model the surface and in-depth transient thermal response and shape change history of an ablating nose tip subjected to an actual or simulated re-entry environment. Figure 15 presents a flow chart of the overall calculation procedure.

In general terms, the required inputs for a calculation consist of the following:

a. Nose-tip environment, e.g., $V_\infty(t)$, $\rho_\infty(t)$, $p_\infty(t)$, and free-stream gas composition.

b. Nose-tip initial geometry.

c. Grid network for internal heat conduction calculations.

(1) Surface layer or implicit/radial grid network for

calculations in the large temperature gradient region near the surface; this constant thickness surface layer and its nodal network recede with the surface as shape change occurs.

(2) Fixed or explicit/rectangular grid network for calculations throughout the remainder of the nose-tip interior.

d. Nose-tip material(s), their surface roughness characteristics, and thermal properties as functions of temperature.

e. Ablation thermochemistry information, e.g., tabular listings relating ablation rate, surface temperature, and surface pressure for the material(s) of interest; such inputs are generated by a separate computer code, e.g., reference (6).

Engineering codes such as the one under discussion rely on a series of approximations and assumptions to calculate the desired overall results of nose-tip shape change and thermal response. Approximations take the form of semiempirical correlations relating various quantities of interest (e.g., shock shape to body geometry, boundary-layer transition onset and location to various surface and flow field variables, etc.) while assumptions invoked center on requirements to simplify complex mathematical expressions (e.g., the boundary-layer momentum integral equation which describes the growth of the viscous layer along the surface).

Given the required inputs and the assumption of zero angle of attack, the code computes the bow shock shape, surface pressure distribution, and axisymmetric inviscid flow field about the initial body geometry. Real gas effects are

accounted for through incorporation of a Mollier diagram for high temperature air. Boundary-layer edge conditions for subsequent viscous flow computation are thus defined.

Boundary-layer heat and mass transport are modeled using a film coefficient approach (see reference (7)). The momentum integral equation is solved assuming that zero pressure gradient relations between skin friction and momentum thickness apply in the presence of pressure gradients. Reynolds analogy and compressibility corrections are applied to obtain the smooth wall, nonablating heat-transfer coefficient distribution. Effects of blowing (mass addition) are accounted for as a function of local ablation rate, where the mass-transfer coefficient is related directly to the heat-transfer coefficient.

Transition from laminar to turbulent flow is dictated by a recent semiempirical correlation of the form

$$R_{e_\theta}\left[\frac{k}{\theta}\cdot\frac{T_e}{T_w}\right]^{0.7} = \begin{cases} 255, \text{ onset} \\ 215, \text{ location} \end{cases}$$

where a value of 255 must be reached or exceeded by the sonic line location[8]; if this condition is satisfied, then the transition zone physically begins at a location where this parameter reaches a value of 215.

Effects of surface roughness on both laminar and turbulent flow heat-transfer distributions are modeled by semiempirical correlations which relate an augmentation factor to some roughness parameter which depends on both surface conditions and smooth wall flow field variables. The present

code was recently updated with a correlation suggested by Phinney[9] for effects of surface roughness on blunt body laminar heat-transfer rates. This correlation takes the form

$$K_L = 1 + \left[\frac{\rho_2 V_2 R_N'}{\mu_2}\right]^{\frac{1}{2}} \left[f\left(\frac{k}{\delta^*}\right)\right]$$

where

$$f\left(\frac{k}{\delta^*}\right) = \begin{cases} .00166\left(\frac{k}{\delta^*}\right), & \left(\frac{k}{\delta^*}\right) \leq 2.41 \\ .004, & \left(\frac{k}{\delta^*}\right) > 2.41 \end{cases}$$

and $(\rho_2 V_2) = (\rho_\infty V_\infty)$ by conservation of mass across a normal shock wave. This correlation was assumed to hold at all points on the nose tip where the flow remained laminar, with δ^* being evaluated locally. Effects of surface roughness on turbulent heat-transfer rates were modeled in the code (based on the work of Powars[10]) and this semiempirical correlation was applied to present analyses in its original form.

For each instantaneous body shape, once the surface heat-transfer distribution has been computed, finite difference numerical techniques are employed to solve the heat conduction equations written for both implicit and explicit nodal network coordinate systems.

Ablation rate and surface temperature at all points on the nose tip are determined by accounting for energy, mass, and species conservation at the ablating surface. A surface

energy balance of the convective transfer coefficient type is employed (see reference (11)), and an iterative solution, coupled to the input ablation thermochemistry for the material of interest, is generated. Recession rates (e.g., inches/second) normal to the surface at each body calculation point are thereby defined. Based on the computational time interval, each surface point is moved a distance corresponding to its computed recession rate, and a new body contour is defined. The inviscid flow field over this new contour is computed, and the above listed computational procedure is reinitiated.

One additional feature has been added to this code by the present author which mathematically allows for local surface roughness development as a function of time, based on computed recession of the mean surface contour (see Figure 16).

In actual re-entry applications, a nose tip experiences laminar ablation under high altitude/low free-stream density conditions. An initially hemispherical contour is further blunted with maximum recession occurring at the stagnation point (for zero angle-of-attack trajectories). This ablation process replaces the initial near-uniform surface roughness of the material, k (o), imposed by manufacturing/machining specifications, with a microroughness, k, characteristic of the nose-tip material and independent of the trajectory flown. It is this microroughness which eventually trips the nose-tip boundary layer to a turbulent state, creating increased surface heat-transfer rates, increased ablation rates, accelerated shape change, and the possible formation

of an increased macroroughness scale downstream of transition (e.g., cross hatching and/or scalloping) with roughness element dimensions dependent on both material and trajectory parameters, as well as elapsed time of flight.

In present ballistics range research, two options are of interest: (1) a nose tip launched with an initially polished surface finish ($k(o) \ll k$), its characteristic microroughness forming as a result of ablation ($k(o) \leq k_J(t) \leq k$), and (2) a nose tip launched with a preconditioned surface roughness ($k(o) = k_J(t) = k$) formed by sufficient time exposure of the material to a low-pressure, high enthalpy, laminar flow, arc jet environment simulating high altitude re-entry.

It is assumed in the present model that the maximum surface roughness scale which can form, or be maintained, during a ballistics range test is equal to the material's characteristic microroughness. This assumption is justifiable for nose-tip dimensions and trajectories under current investigation (R_N = .375 inch, $V_\infty \leq$ 18,000 feet per second, $p_\infty \leq$ .35 atm) where maximum predicted surface recession up to the final data monitoring station is of the order of the microroughness dimension (~3k or less, as compared to experimentally observed minimum macroroughness dimensions of the order of 10k).

Graphite Nose-Tip Thermal Response

This subsection presents a detailed analysis of the transient thermal response of a solid ATJ-S graphite nose tip on which surface isotherms were measured (recall Figures 10

and 11). This particular nose tip was launched as part of a model/sabot development effort (the results of which will ultimately be applied in an investigation of nose-tip boundary-layer transition). Certain key requirements were met during this test which are essential to any well defined aero-thermal analysis.

First, the nose tip was fully enclosed in a sabot which possessed a smooth Teflon interior machined to exactly match the nose-tip contour. This served to protect the initial polished surface finish and overall structural integrity of the nose tip during launch acceleration (~100,000g's), as well as to shield the nose tip from heat transfer within the launch tube, thereby ensuring a known uniform initial temperature distribution throughout the graphite upon its exposure to the free-flight environment.

Second, both the initial surface finish and characteristic microroughness of this bulk graphite material were accurately measured and documented under a supporting contract effort[12], wherein established material characterization techniques[13] were employed. Results of this effort are shown in Figures 17 and 18.

Figure 17 shows cross sectional views magnified 320 times of both polished and preconditioned (via laminar ablation) ATJ-S graphite surfaces. Figure 18 shows fractional percentage distributions of roughness element height, width, and peak-to-peak spacing as measured on the ablated sample. Intersection of the fiftieth percentile line with the roughness element

height distribution defines a mean height of 8.9 microns; applying a factor of $\left(\frac{4}{\pi}\right)$, which approximately accounts for the failure of the cross sectional plane to pass through the true peak of the roughness elements[12], results in a characteristic ATJ-S graphite microroughness of 11.3 microns (i.e., k = 0.45 mil). The polished surface was found to possess only widely spaced roughness elements of the order of 1.5 microns in height or less, thereby defining a nominal k (o) value of .05 mil.

Figure 19 shows the aerothermodynamic environment experienced by the nose tip along its flight path from muzzle exit through blast tank conditions to a point downrange of the second data monitoring station. This model was aerodynamically stable (static margin of the order of 14 percent) and measured angle-of-attack oscillations were within ± 4 degrees over its entire trajectory.

Consistent with previous discussions, data of Figure 11 (on two rays, 180 degrees apart, emanating from the stagnation point) were digitized, arithmetically averaged, corrected for gas cap radiation and replotted as a function of nondimensional arc length $\left(\frac{S}{R_N}\right)$ around the nose-tip contour. The resulting surface temperature distribution is shown in sections (a) of Figures 20 through 22. A computed gas cap equivalent black body temperature distribution is also shown for comparison purposes; note that the maximum correction for gas cap radiation was of the order of one percent of the observed brightness temperature level.

Three separate computations of nose-tip transient thermal response were made for the ballistics range environment of Figure 19; differences between these computations center on assumptions concerning material surface roughness and the calculation of laminar heat-transfer rates in the presence of surface roughness. Results are shown in Figures 20 through 22.

The first computation assumed that surface roughness develops according to the model proposed in Figure 16 and that surface roughness does not influence laminar heat-transfer rates. Results are shown in Figures 20(a) through 20(c), where Figure 20(a) shows surface temperature distributions around the nose tip with time as the parameter; Figure 20(b) shows surface temperature versus time for two discrete points on the nose tip; and Figure 20(c) shows surface roughness distributions around the nose tip with time as the parameter. A general lack of agreement with the experimental results is observed. Predicted surface temperatures in the laminar flow stagnation point region are ~37 percent below measured values, and the general shape of the predicted surface temperature distribution at the time of data acquisition (14.76 milliseconds) does not correspond to that observed experimentally. Predicted peak surface temperatures occurred at the sonic point, while maximum surface temperatures observed experimentally occurred at the stagnation point. Utilization of unaugmented laminar heat-transfer rates resulted in a low predicted surface roughness growth rate (i.e., recession rate)

which delayed the attainment of a surface roughness dimension sufficient to cause boundary-layer transition until the 10-millisecond station.

The second computation also incorporated the roughness growth model of Figure 16, but here laminar heat-transfer rates were assumed to be influenced by surface roughness according to Phinney's correlation, as previously discussed. Results are shown in Figures 21(a) through 21(c). The postulated interaction between surface roughness and laminar heat-transfer rates resulted in a more rapid development of a roughness scale sufficient to cause nose-tip boundary-layer transition (7 milliseconds here versus 10 for the previous calculation). Roughness augmented laminar heat-transfer rates increased predicted surface temperatures in the near stagnation point region, resulting in a surface temperature distribution at the data acquisition station which qualitatively agreed quite well with the experimentally observed distribution, i.e., relatively uniform between the stagnation and sonic points with the maximum occurring at the stagnation point. Quantitatively, agreement was quite reasonable with maximum variations between theory and experiment of the order of +15 to +20 percent for $0 \leq \frac{S}{R_N} \leq \sim .8$.

Results of a third computation are presented in Figures 22(a) through 22(b) which demonstrate the predicted transient thermal response of a preconditioned ATJ-S nose tip ($k(o) = k_J(t) = k = 0.45$ mil) to the same ballistics range trajectory flown by the present (initially polished) nose tip. Transition onset

for a preroughened model is predicted to occur instantaneously upon exposure to the free-flight environment. Turbulent heating creates peak surface temperatures at the sonic point with sonic point and stagnation point values approaching a common steady-state limit after ~15 milliseconds of flight. Such trends are of course inconsistent with present experimental results obtained on an initially polished model.

SUMMARY

The present paper has focused on current capabilities at the White Oak Laboratory for creating valid free-flight simulations of re-entry aerothermodynamic environments, for accurately measuring surface temperature contours on nose-tip configurations exposed to such environments, and for conducting detailed thermal analyses of these ablating bodies under highly transient ballistics range conditions.

Application of electrooptical pyrometry to the measurement of surface temperature distributions in hypersonic free flight was discussed and limiting assumptions in data reduction and interpretation were reviewed. Isotherms measured on a solid ATJ-S graphite nose tip were reported.

Updates to a currently utilized nose-tip design code were made to account for surface roughness development as a function of time and to account for effects of surface roughness on laminar heat-transfer rates. Predictions generated with this modified code were found to qualitatively match the shape of the experimentally observed surface temperature distribution in the stagnation-to-sonic point region; reasonable quantitative

agreement was also observed with predicted surface temperatures a maximum of 15 to 20 percent above experimentally determined values.

REFERENCES

1. Dugger, P. H., Bock, O. H., Enis, C. P., and Gilley, B. W., "Photographic Pyrometry in an Aeroballistics Range," presented at Society of Photooptical Instrumentation Engineers 16th Annual Technical Meeting, San Francisco, CA, Oct 1972
2. Wilson, R. G., and Spitzer, C. R., "Visible and Near-Infrared Emittance of Ablation Chars and Carbon," AIAA Journal, Vol. 6, No. 4, Apr 1968, p 665-671
3. Gilmore, F. R., "Approximate Radiation Properties of Air Between 2000^{o} and 8000^{o}K," Rand Corporation Memo RM-3997-ARPA, Mar 1964
4. Miller, J. T., "Development of an Aeroballistics Range Testing Capability for Blunt Body Boundary-Layer Transition Studies," AEDC-TR-73-117, Jul 1973 (CONF)
5. Rafinejad, D., and Derbidge, T. C., "User's Manual: Sandia Nose-Tip Analysis Procedure (SNAP)," Aerotherm/ Acurex Corp. Report UM-74-57, Dec 1974
6. Powars, C. A., and Kendall, R. M., "User's Manual: Aerotherm Chemical Equilibrium (ACE) Computer Program," Aerotherm/Acurex Corp. Report, May 1969
7. Putz, K. E., and Bartlett, E. P., "Heat-Transfer and Ablation-Rate Correlations for Re-entry Heat-Shield and Nose-Tip Applications," AIAA Journal of Spacecraft and Rockets, Vol. 10, No. 1, Jan 1973, p 15-22

8. Anderson, A. D., "Boundary-Layer Transition on Nose Tips with Rough Surfaces," Appendix A, Second Interim Report on Passive Nose-Tip Technology (PANT) Program, Vol. II, Summary of Experimental Results, Aerotherm/ Acurex Corp. Report 74-100 (II), Feb 1975

9. Phinney, R. E., "Mechanism for Heat Transfer to a Rough Blunt Body," Letters in Heat and Mass Transfer Journal, Vol. 1, No. 2, p 183-188

10. Pc [illegible], C. A., "Surface Roughness Effects on Re-entry H[illegible]ng," Aerotherm Technical Memo TM-71-10, Jul 1971

11. Kendall, R. M., Rindal, R. A., and Bartlett, E. P., "A Multicomponent Boundary Layer Chemically Coupled to an Ablating Surface," AIAA Journal, Vol. 5, No. 6, Jun 1967, p 1063-1071

12. Dirling, R. B., Jr., "Graphite Microroughness and Material Characterization Tests," McDonnell Douglas Contract Report MDCG-5788, Apr 1975

13. Kratsch, K. M., Dirling, R. B., Jr., Johnson, G. P., and Swain, C. E., "Erosion Mechanisms and Improvement of Graphitic Materials, Vol. II, Hyperthermal Erosion Tests and Surface Roughness Characterization," AFML-TR-70-307, Vol. II, Jun 1972

BALLISTICS RANGE SCHEMATIC

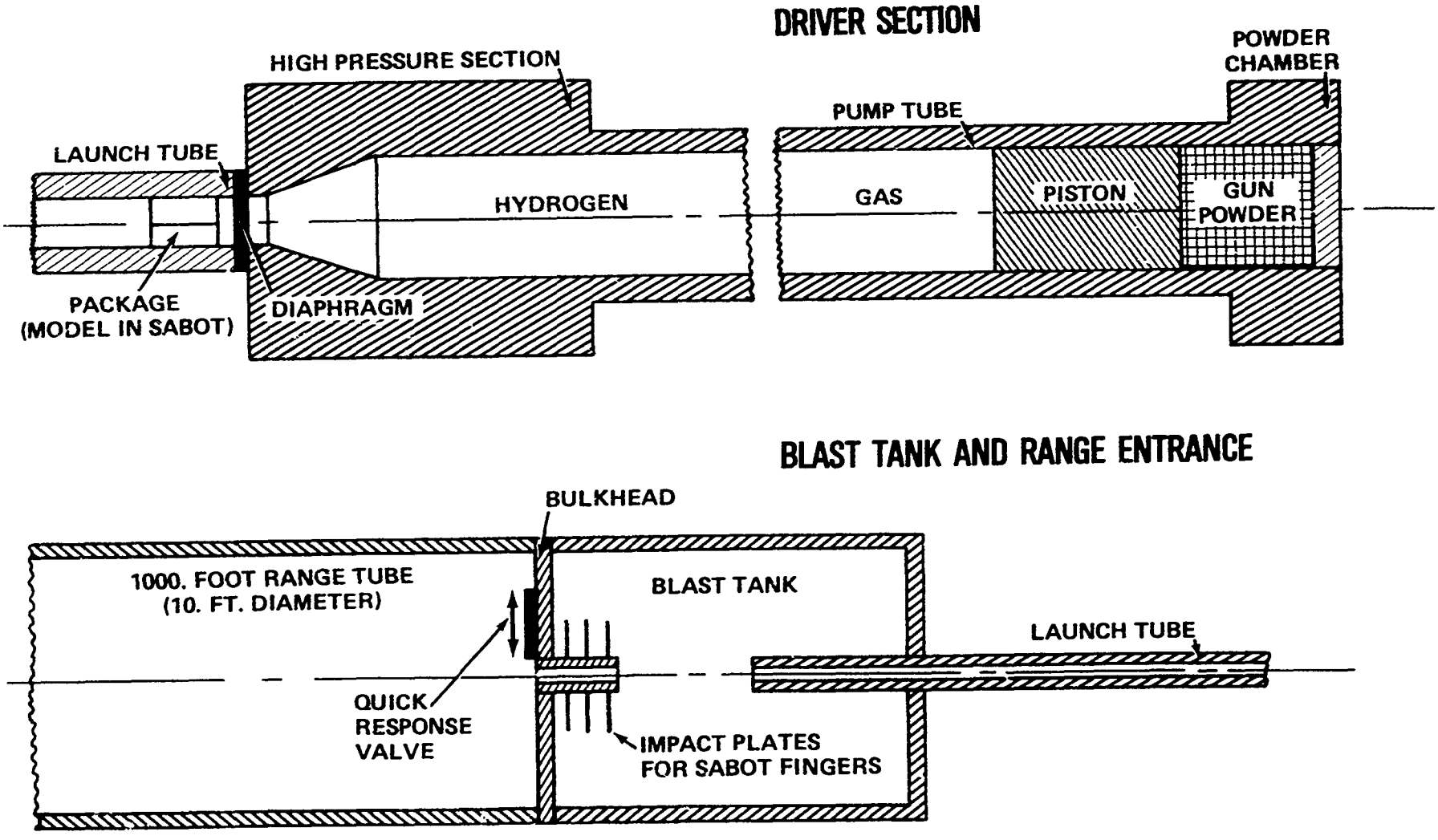

FIG. 1 BALLISTICS RANGE SCHEMATIC

N.S.W.C./W.O.L.
2.0" DIAMETER LAUNCHER

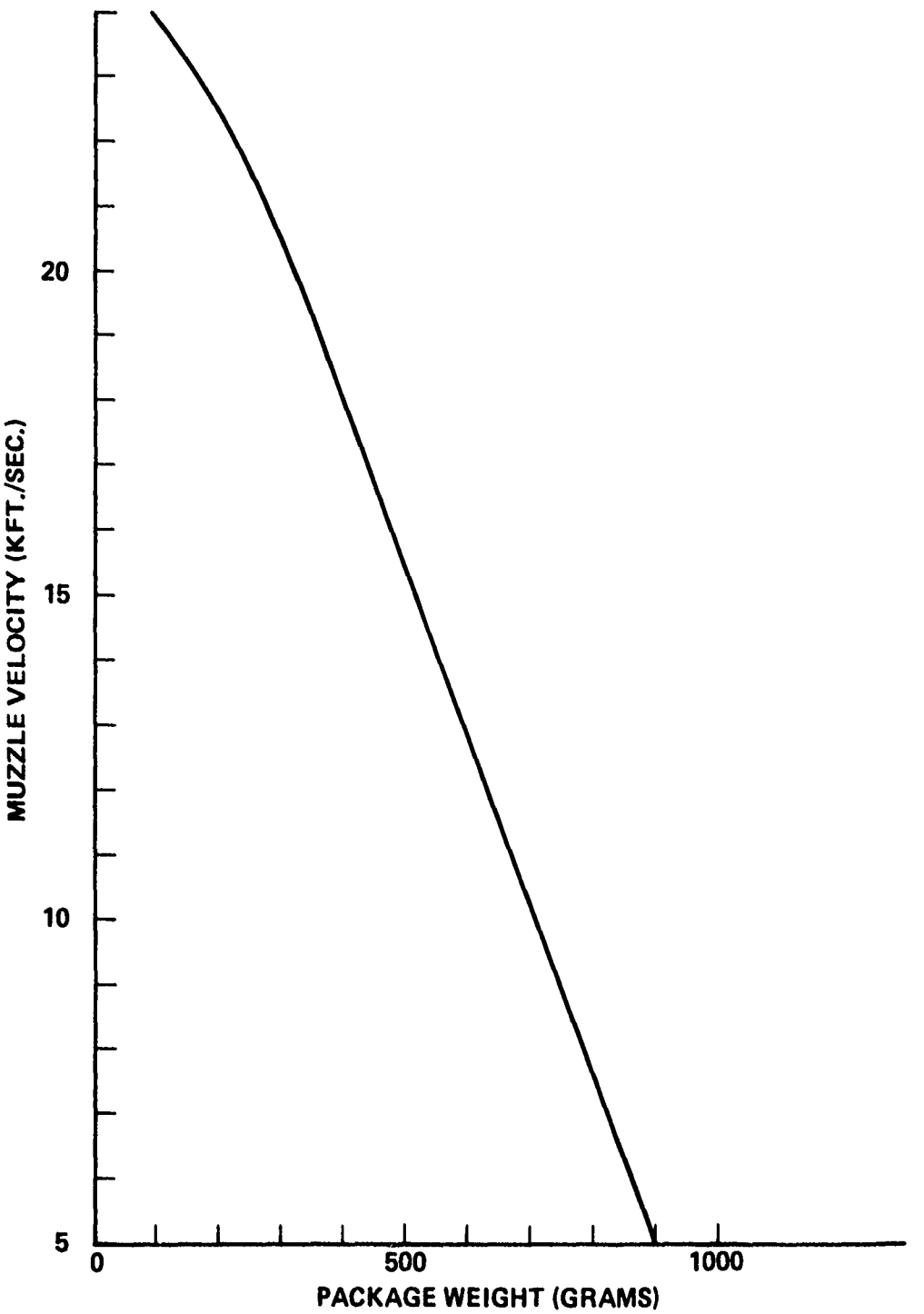

FIG. 2 LAUNCHER PERFORMANCE

N.S.W.C./W.O.L.
1000–FT. BALLISTICS RANGE

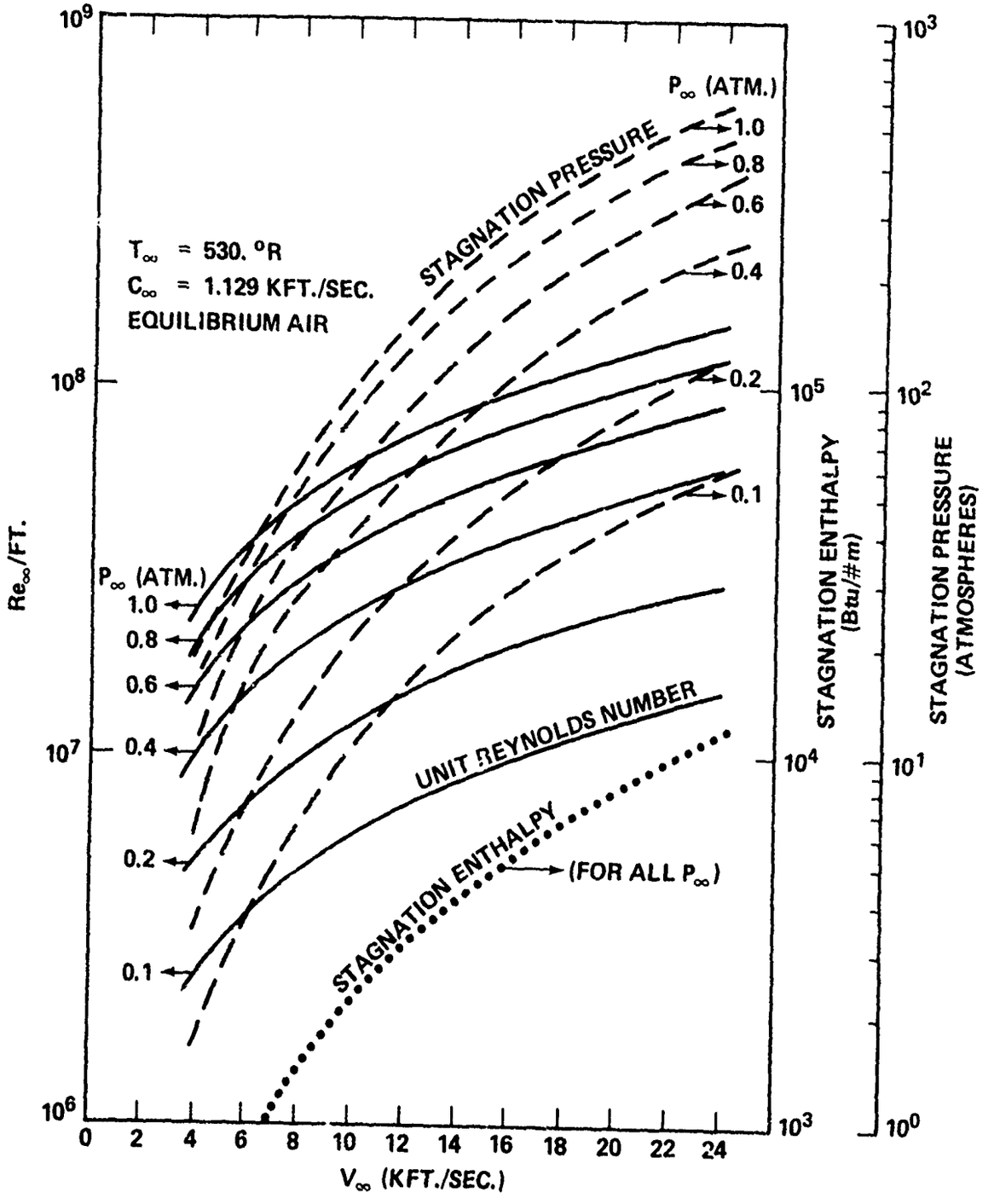

FIG. 3 BALLISTICS RANGE ENVIRONMENTS

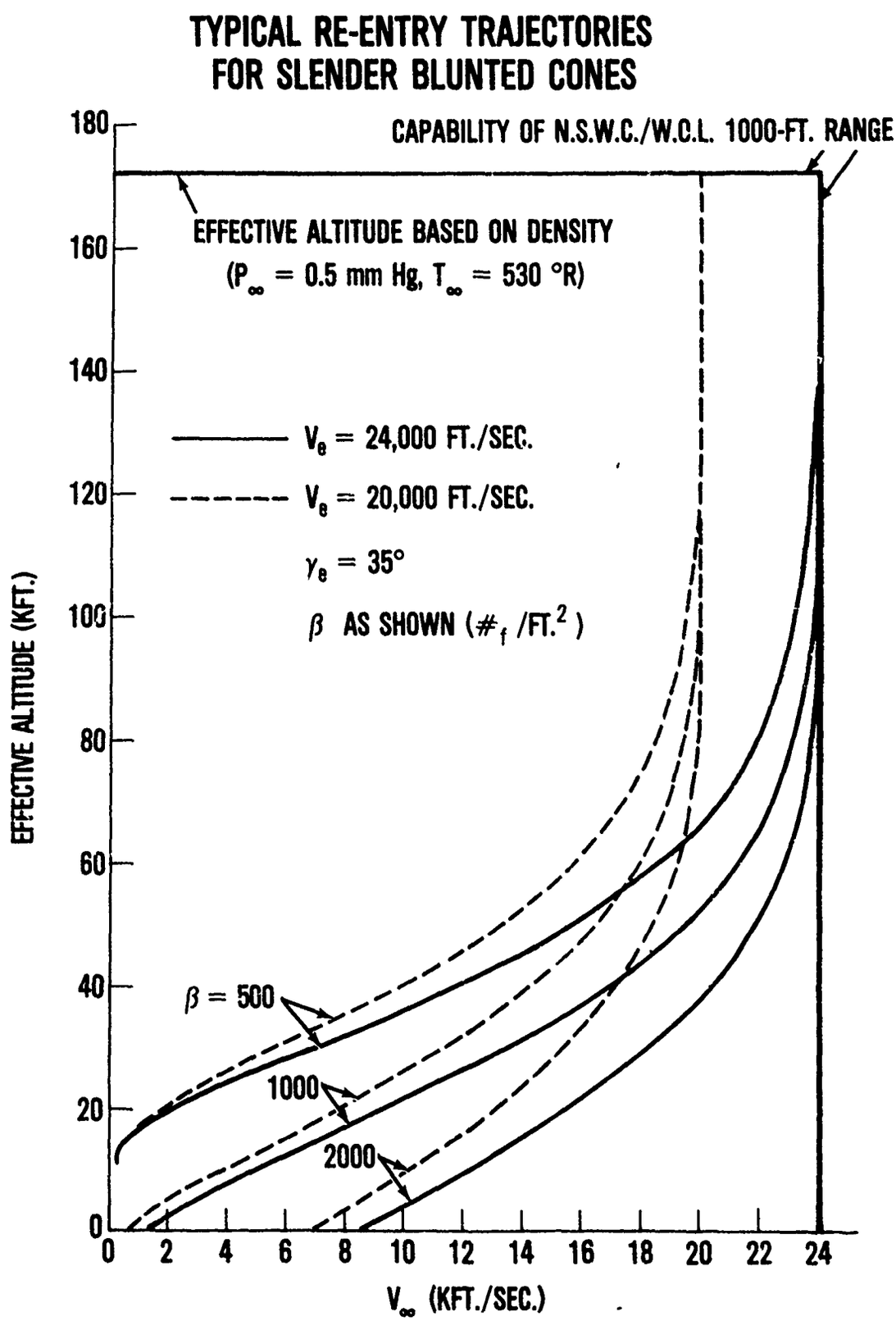

FIG. 4 EFFECTIVE ALTITUDE - VELOCITY OPERATING ENVELOPE OF BALLISTICS RANGE

ELECTROOPTICAL PYROMETER SYSTEM SCHEMATIC

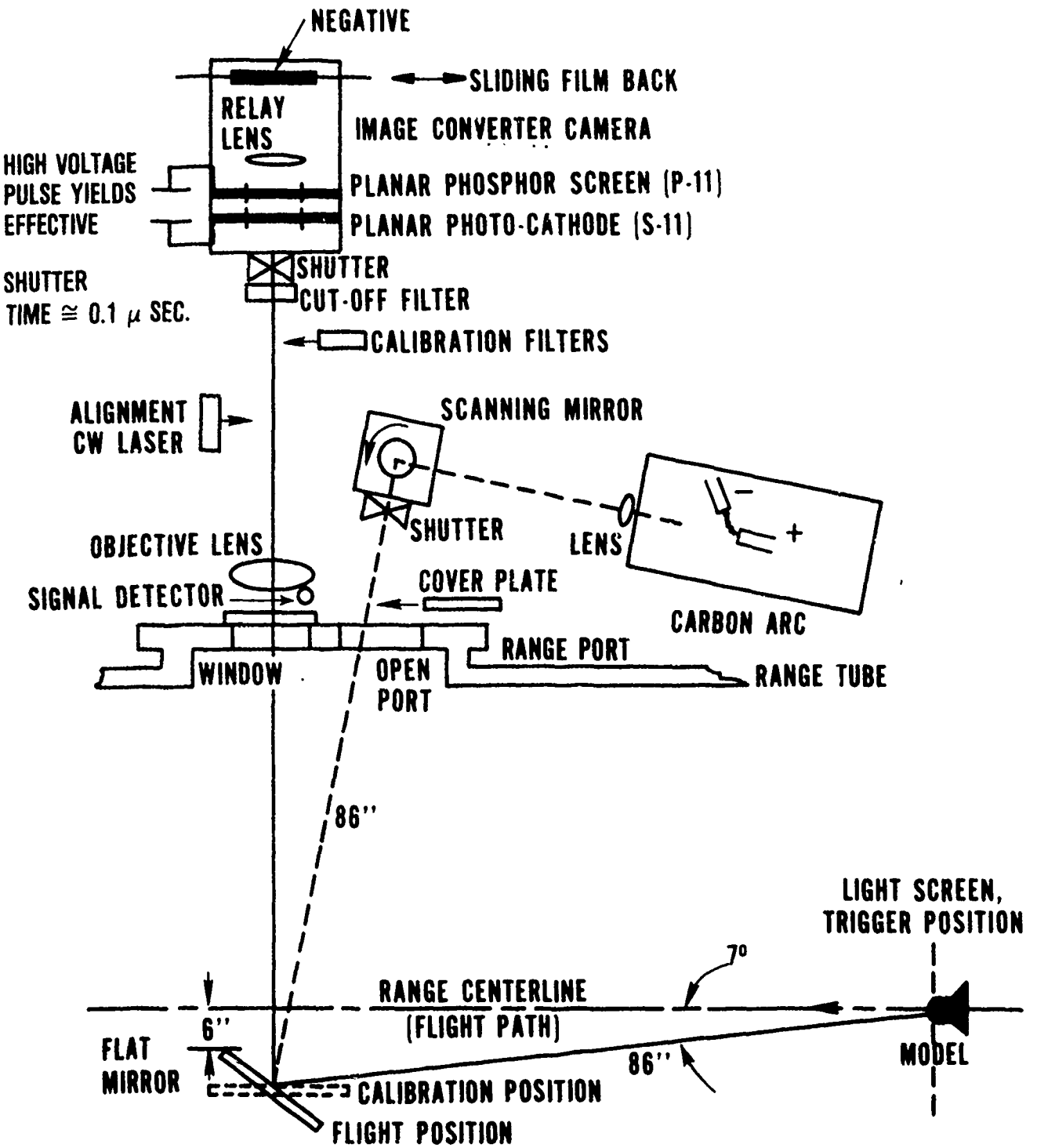

FIG. 5 ELECTROOPTICAL PYROMETER SYSTEM SCHEMATIC

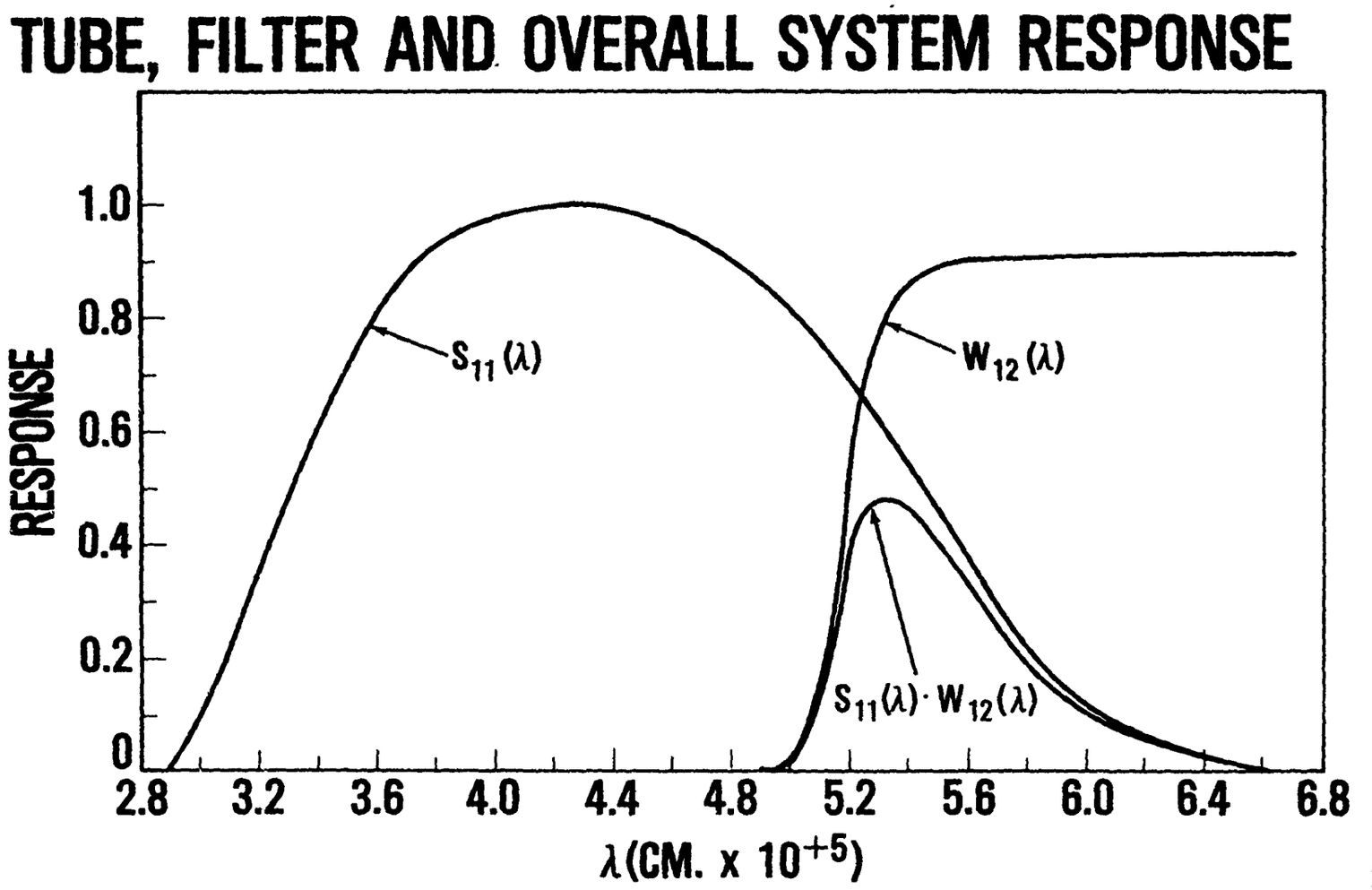

FIG. 6 IMAGE CONVERTER CAMERA, CUT-OFF FILTER, AND OVERALL PYROMETER SYSTEM WAVE LENGTH RESPONSE

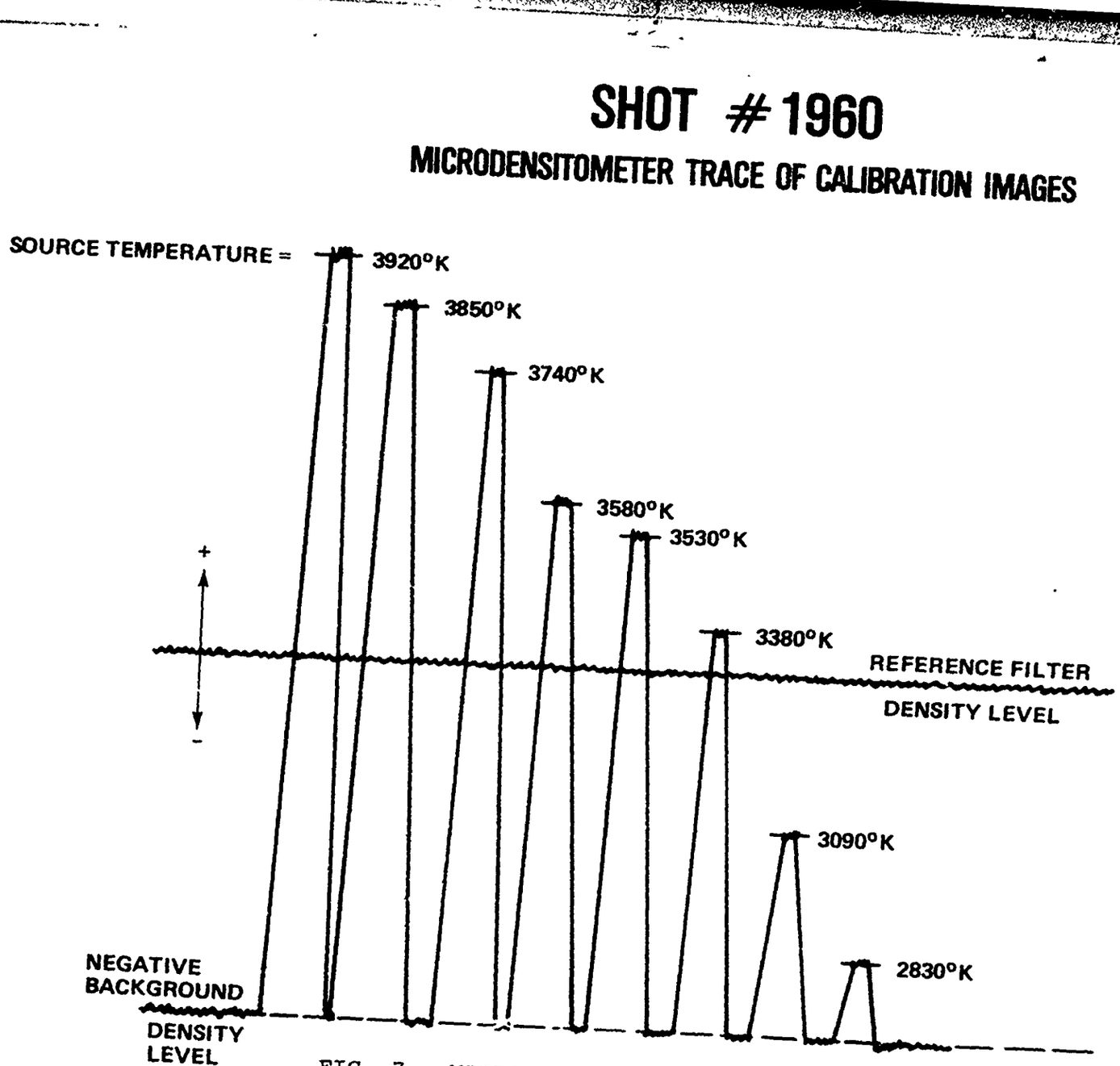

FIG. 7 MICRODENSITOMETER TRACE OF CALIBRATION IMAGES

PYROMETER CALIBRATION
SHOT #1960

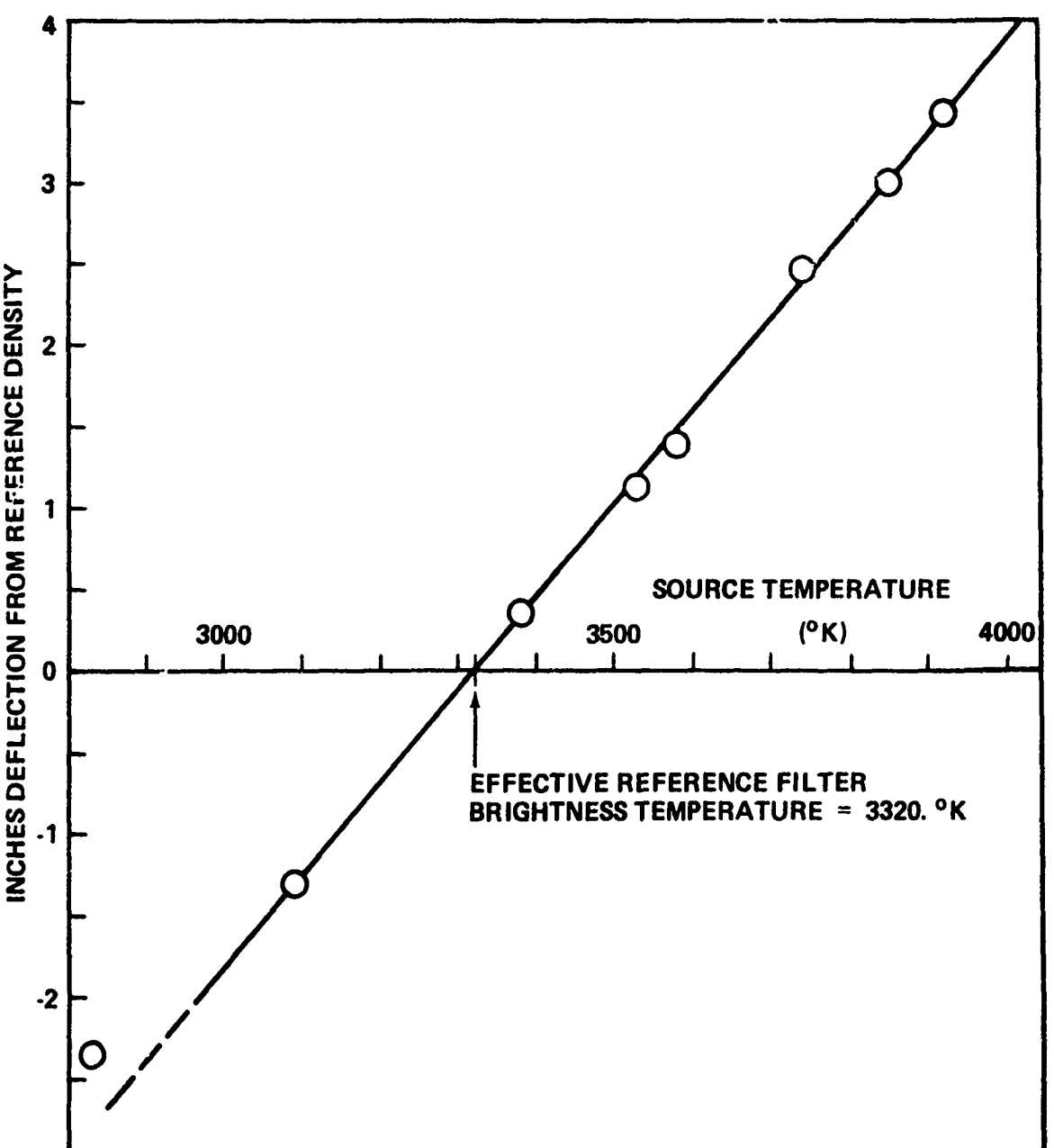

FIG. 8 PYROMETER CALIBRATION CURVE

SCHEMATIC OF OPTICAL AND MECHANICAL MAGNIFICATION FACTORS

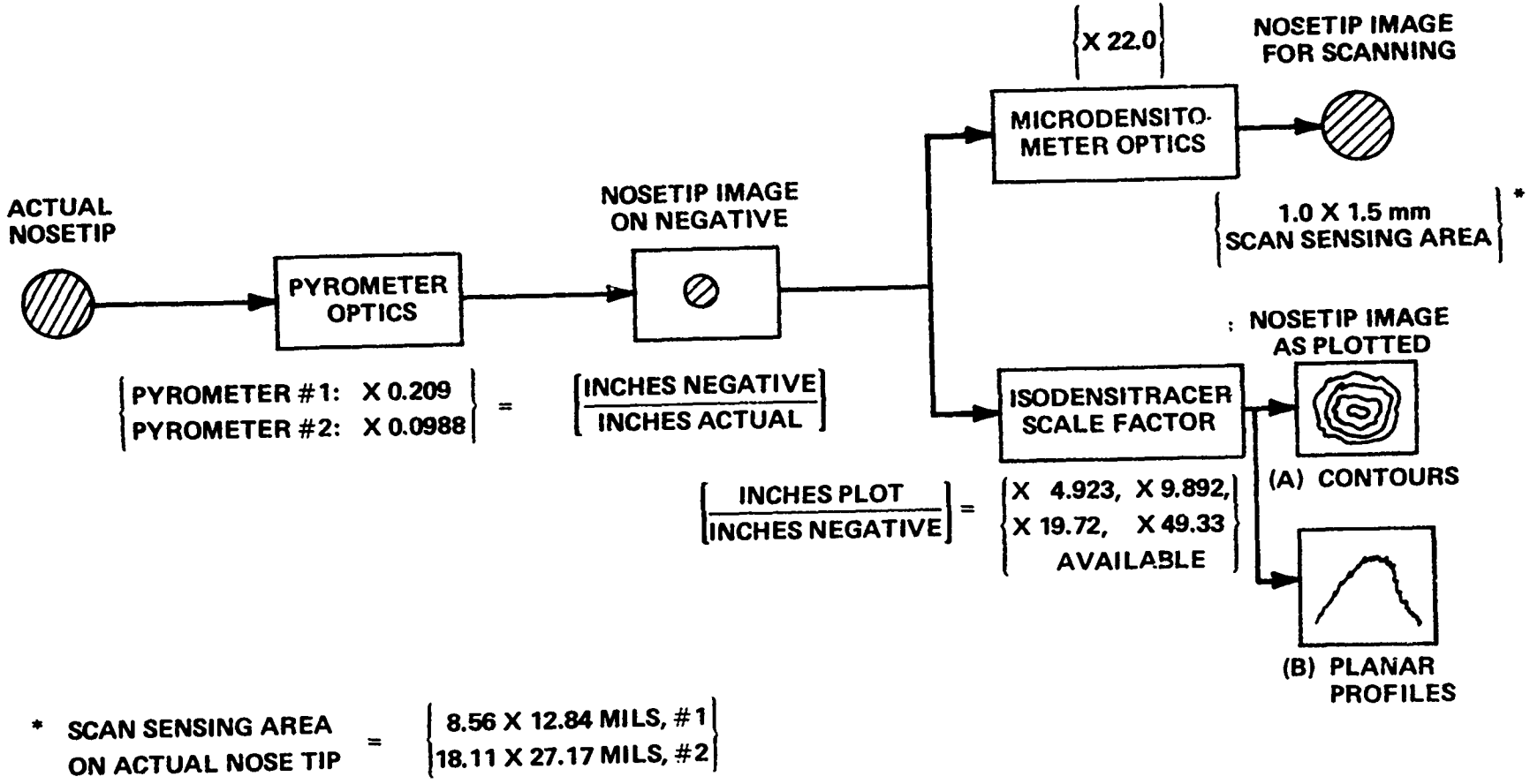

FIG. 9 SCHEMATIC OF OPTICAL AND MECHANICAL MAGNIFICATION FACTORS

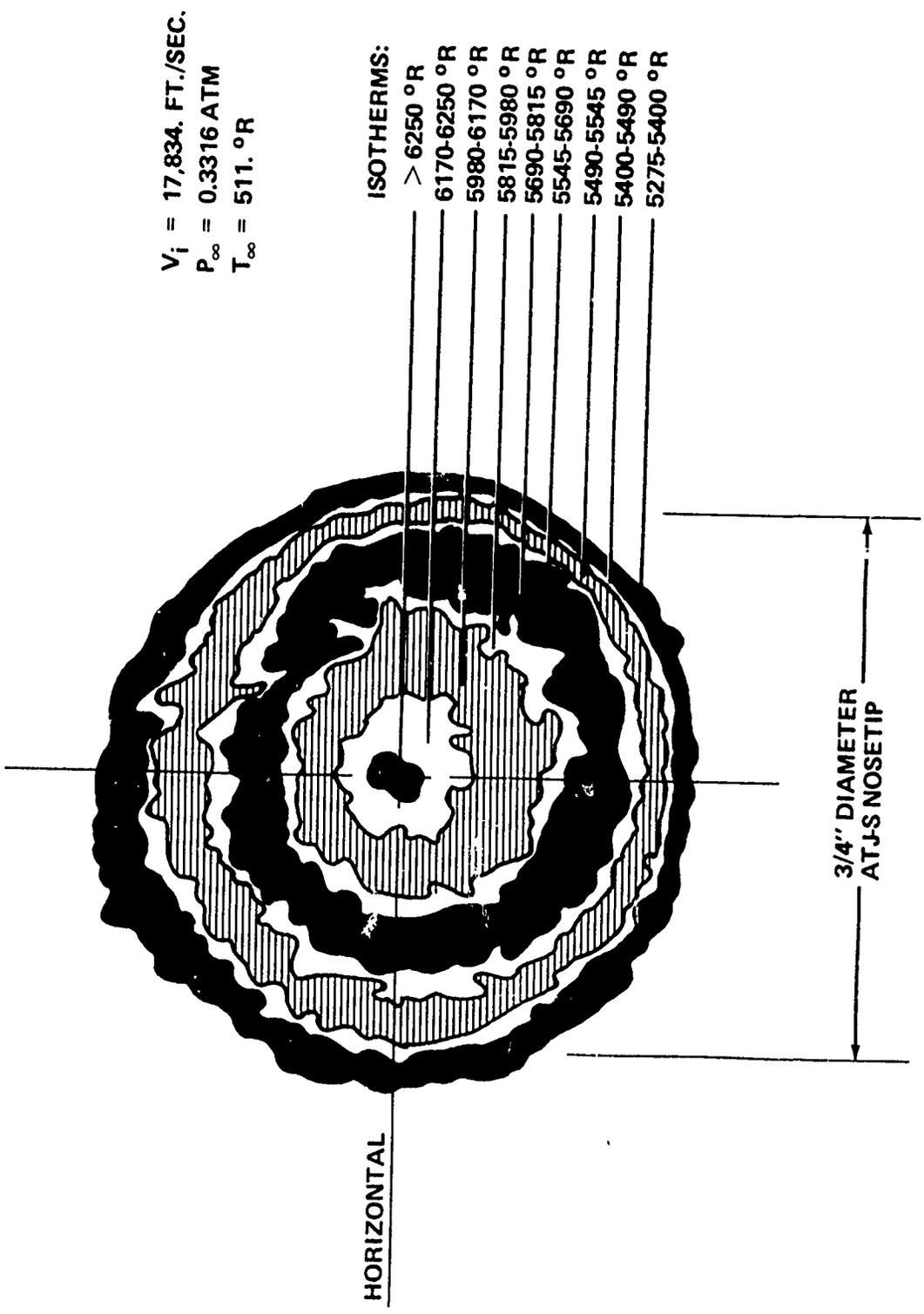

FIG. 10 ISOTHERMS ON GRAPHITE NOSE TIP

SHOT # 1960

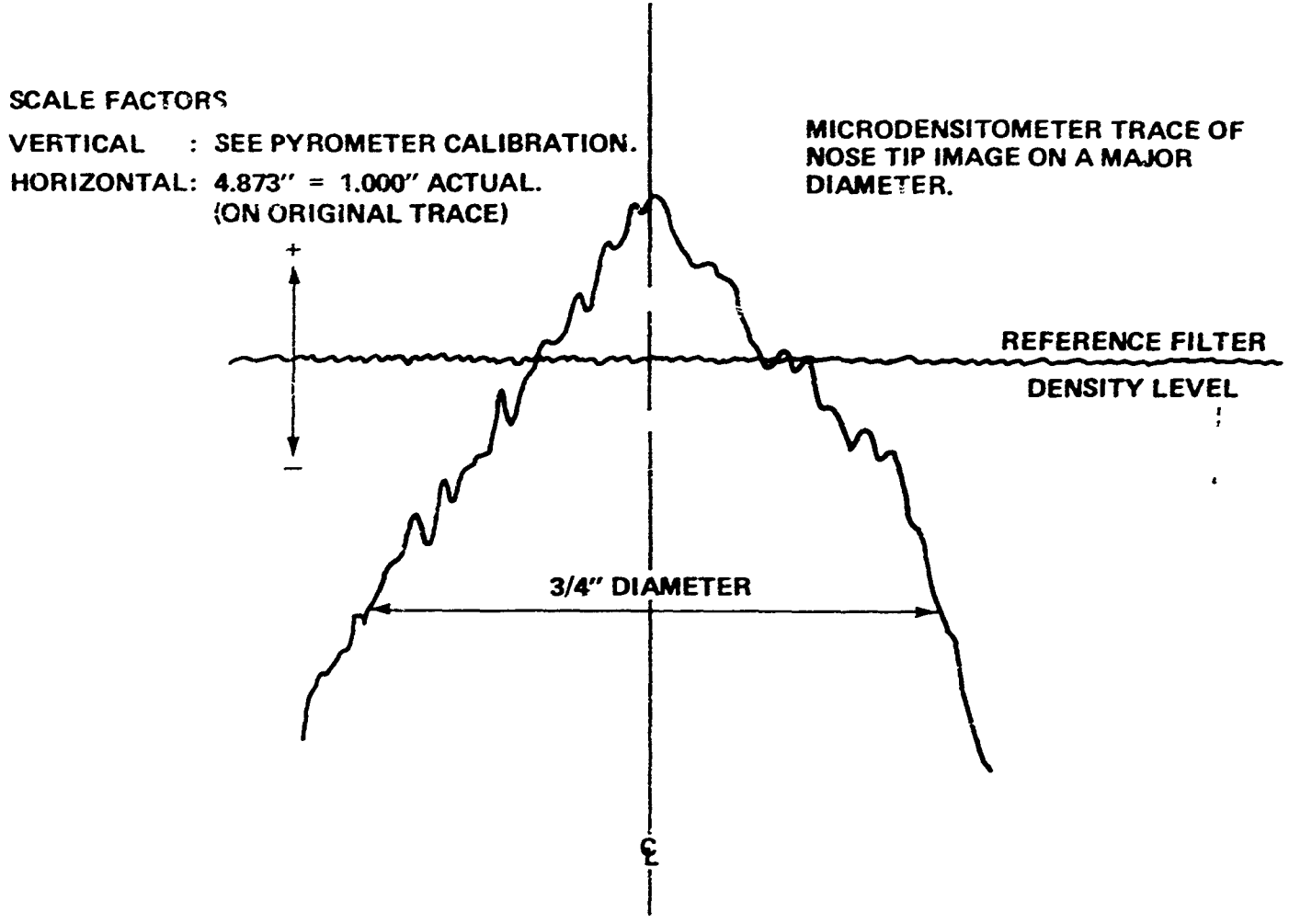

FIG. 11 MICRODENSITOMETER TRACE OF NOSE-TIP IMAGE ON A MAJOR DIAMETER

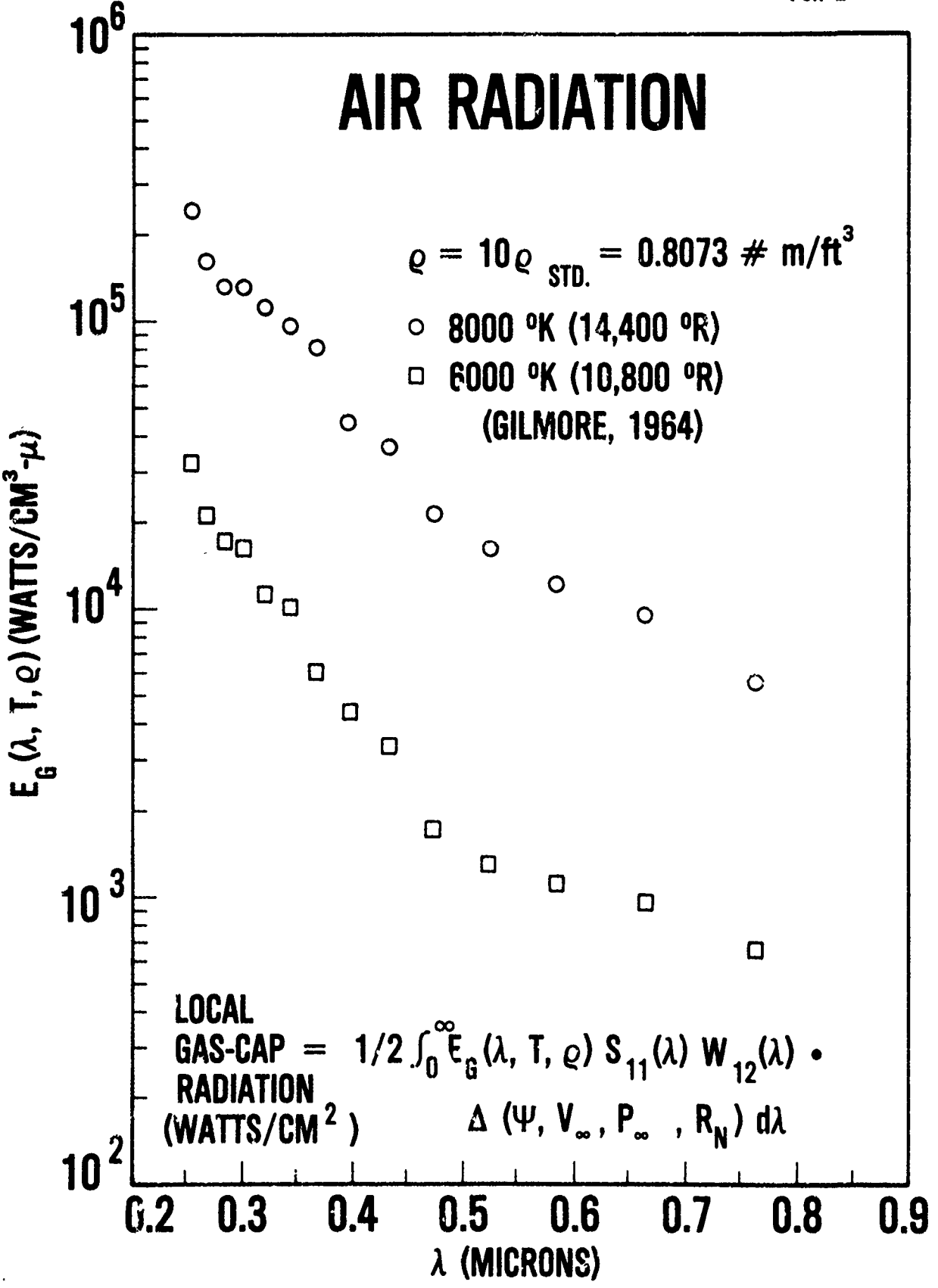

FIG. 12 HIGH TEMPERATURE AIR RADIATION VERSUS WAVE LENGTH

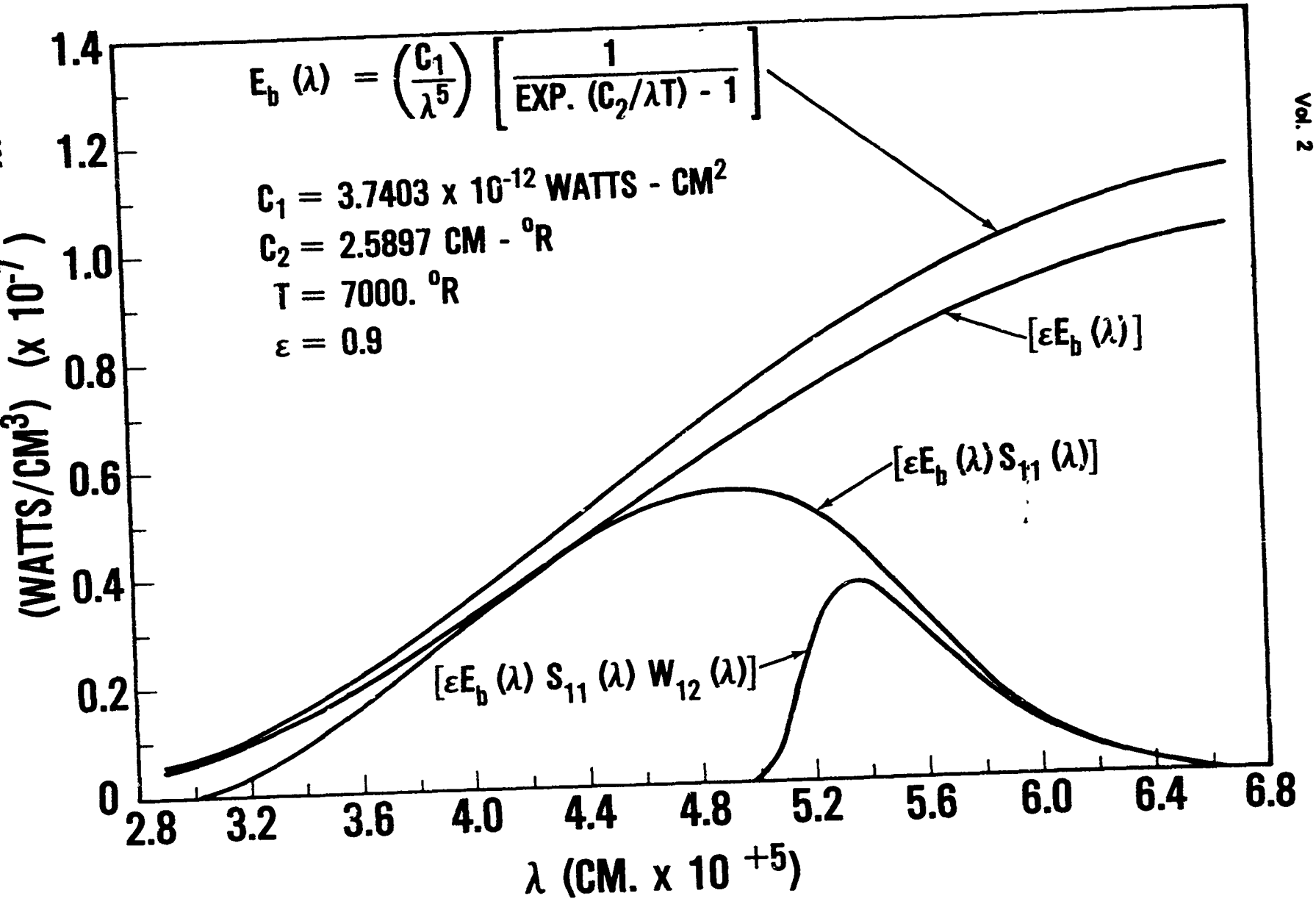

FIG. 13 SYSTEM RESPONSE TO BLACK BODY RADIATION

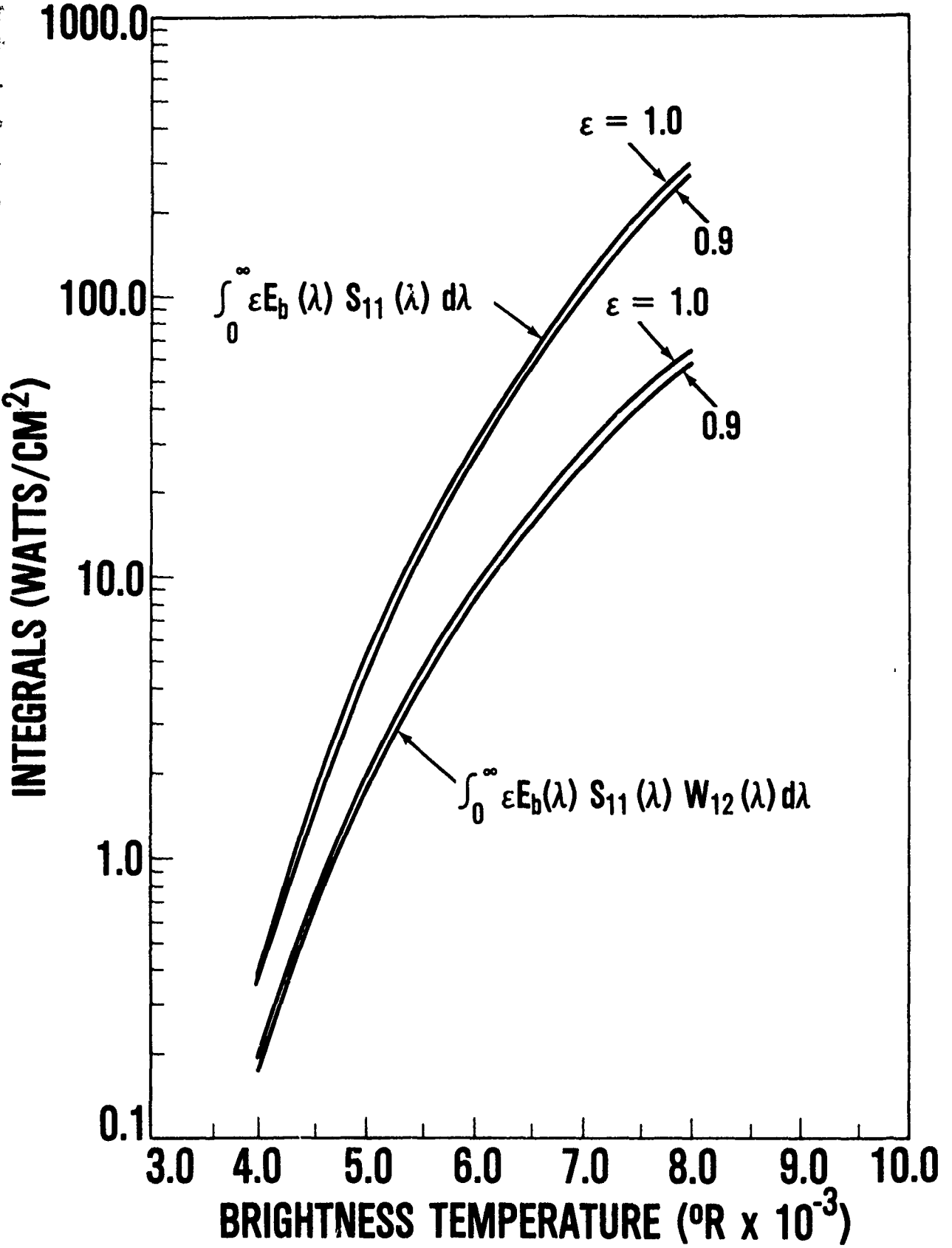

FIG. 14 ENERGY PER UNIT AREA SENSED BY PYROMETER VERSUS SOURCE BRIGHTNESS TEMPERATURE

NOSETIP THERMAL RESPONSE AND SHAPE CHANGE CALCULATION PROCEDURE

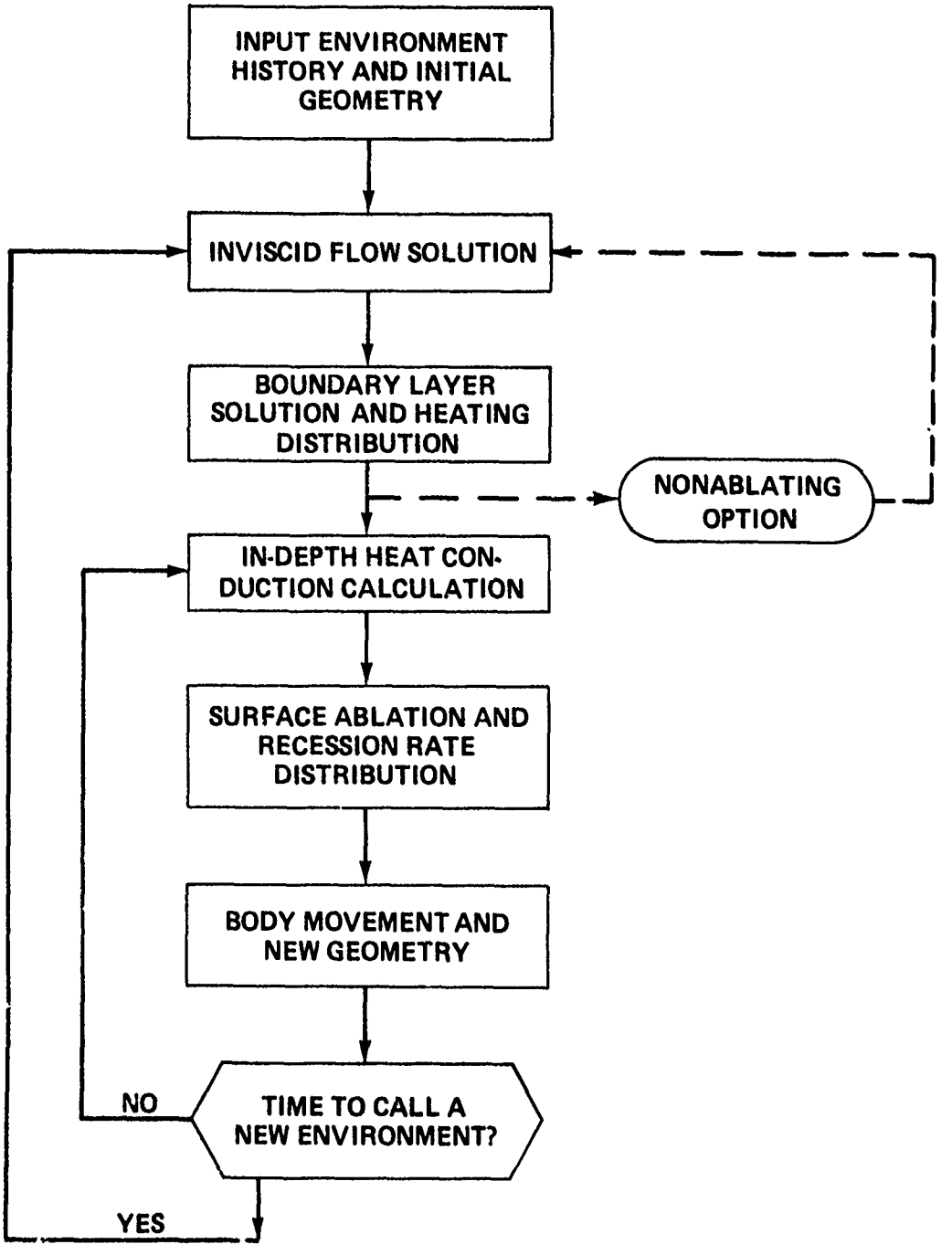

FIG. 15 NOSE-TIP THERMAL RESPONSE AND SHAPE CHANGE CALCULATION PROCEDURE

MICROROUGHNESS DEVELOPMENT MODEL

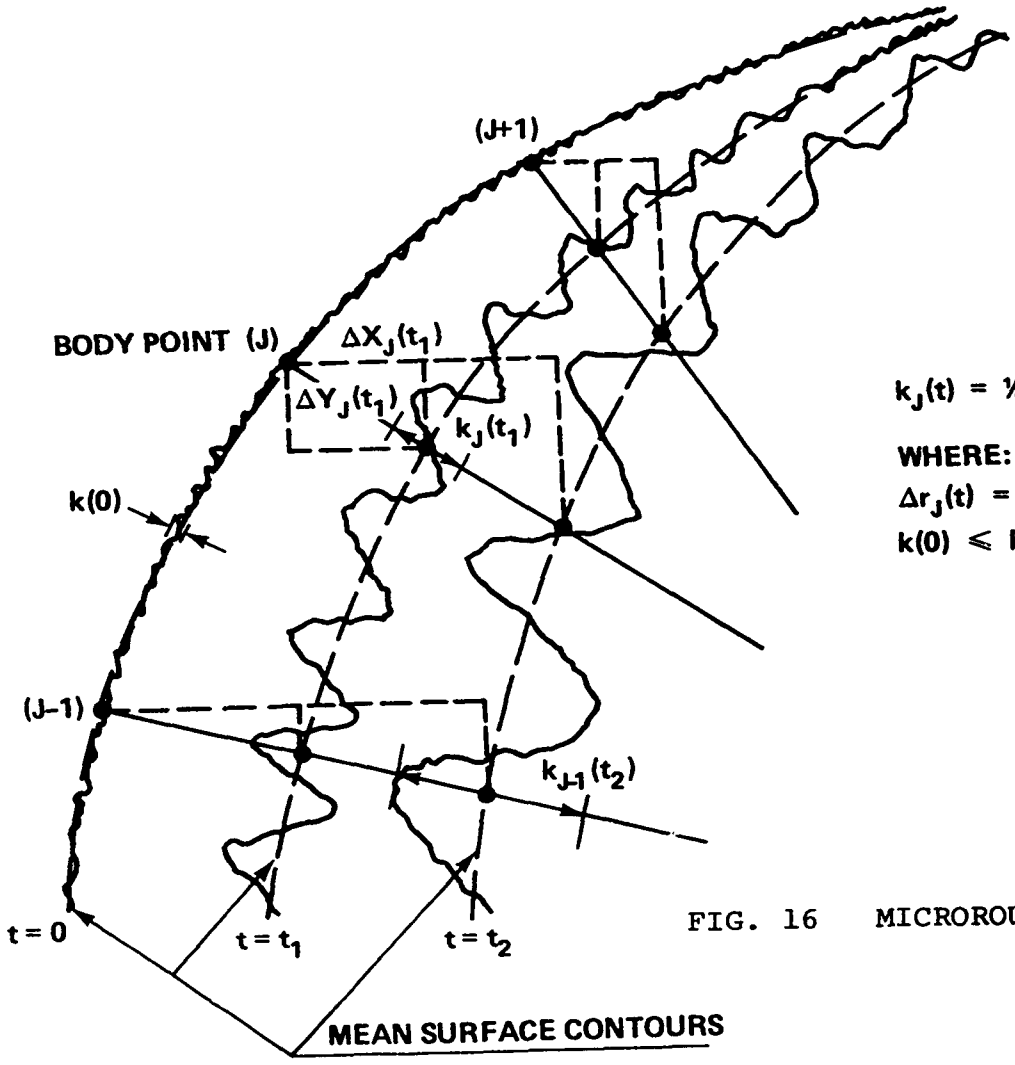

$$k_J(t) = \tfrac{1}{2}\Delta r_J(t)$$

WHERE:

$$\Delta r_J(t) = \sqrt{\Delta X_J^2(t) + \Delta Y_J^2(t)}$$

$$k(0) \leq k_J(t) \leq k$$

FIG. 16 MICROROUGHNESS DEVELOPMENT MODEL

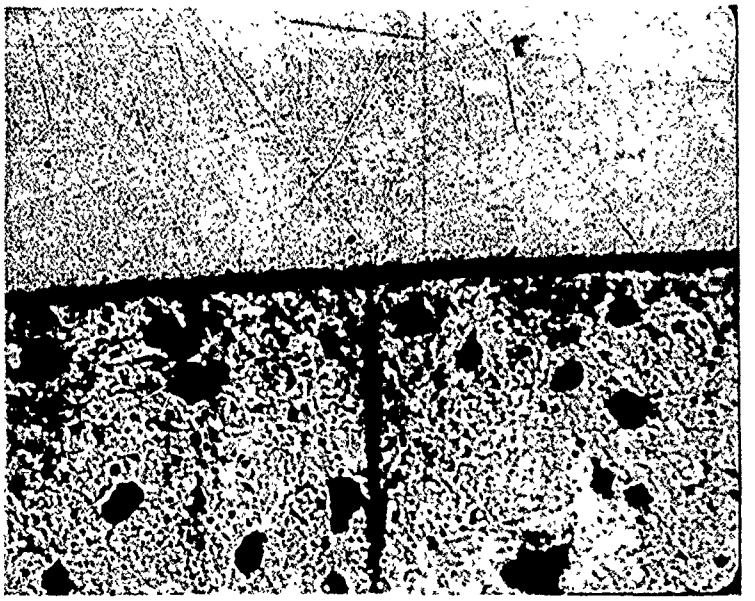

(a) POLISHED

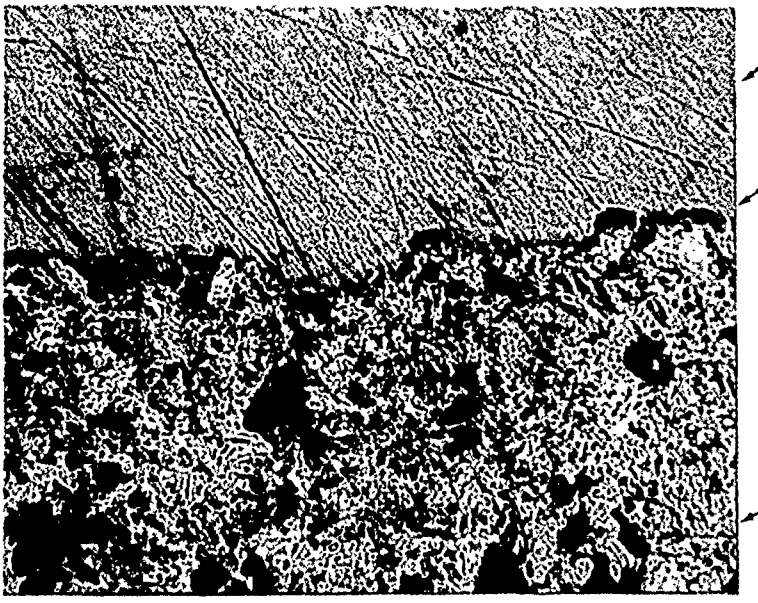

(b) PRECONDITIONED

FIG. 17 320X CROSS SECTIONAL VIEWS OF POLISHED AND PRECONDITIONED ATJ-S GRAPHITE SURFACES

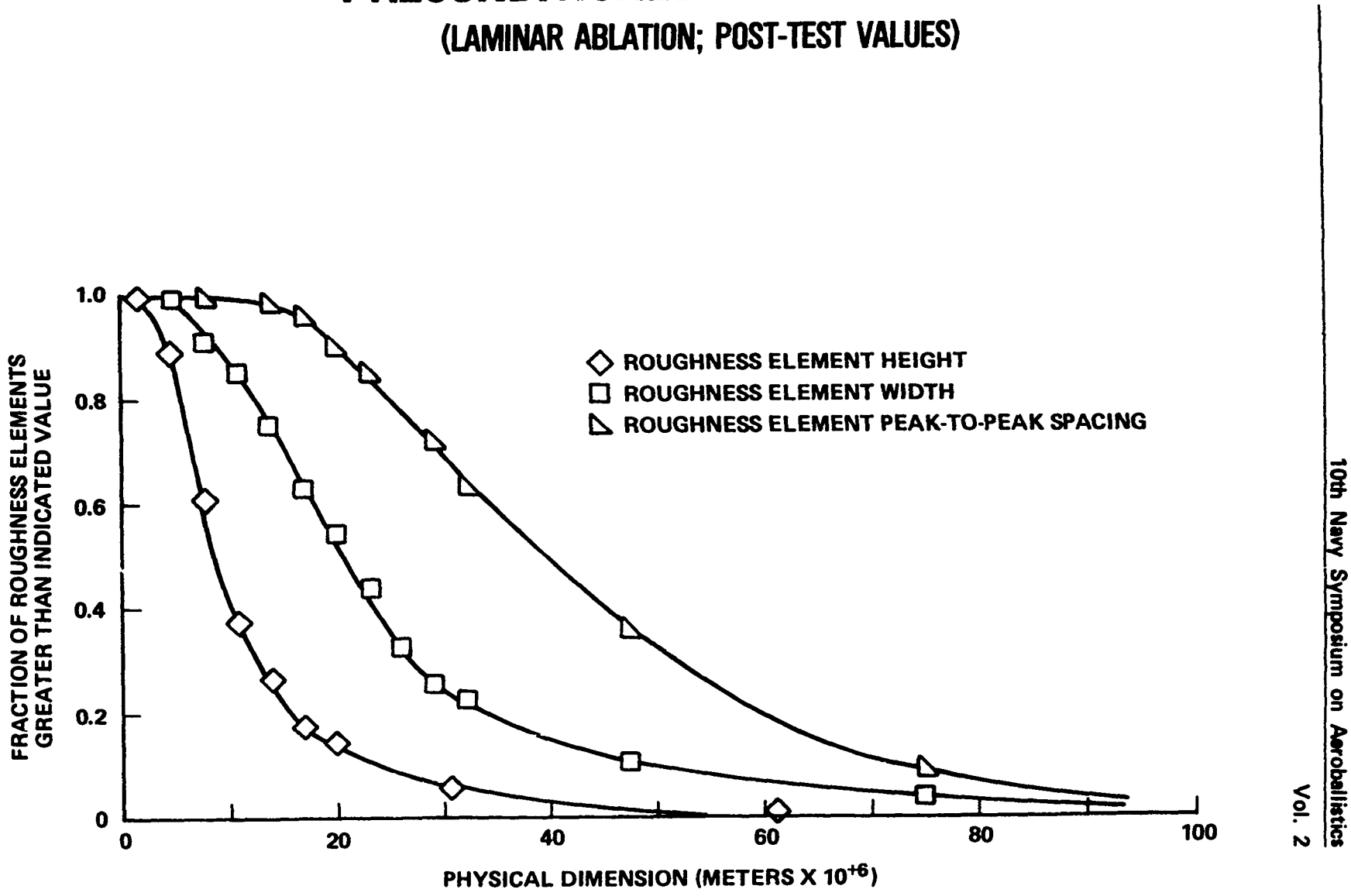

FIG. 18 ROUGHNESS ELEMENT HEIGHT, WIDTH, AND PEAK-TO-PEAK SPACING DISTRIBUTIONS FOR PRECONDITIONED ATJ-S GRAPHITE

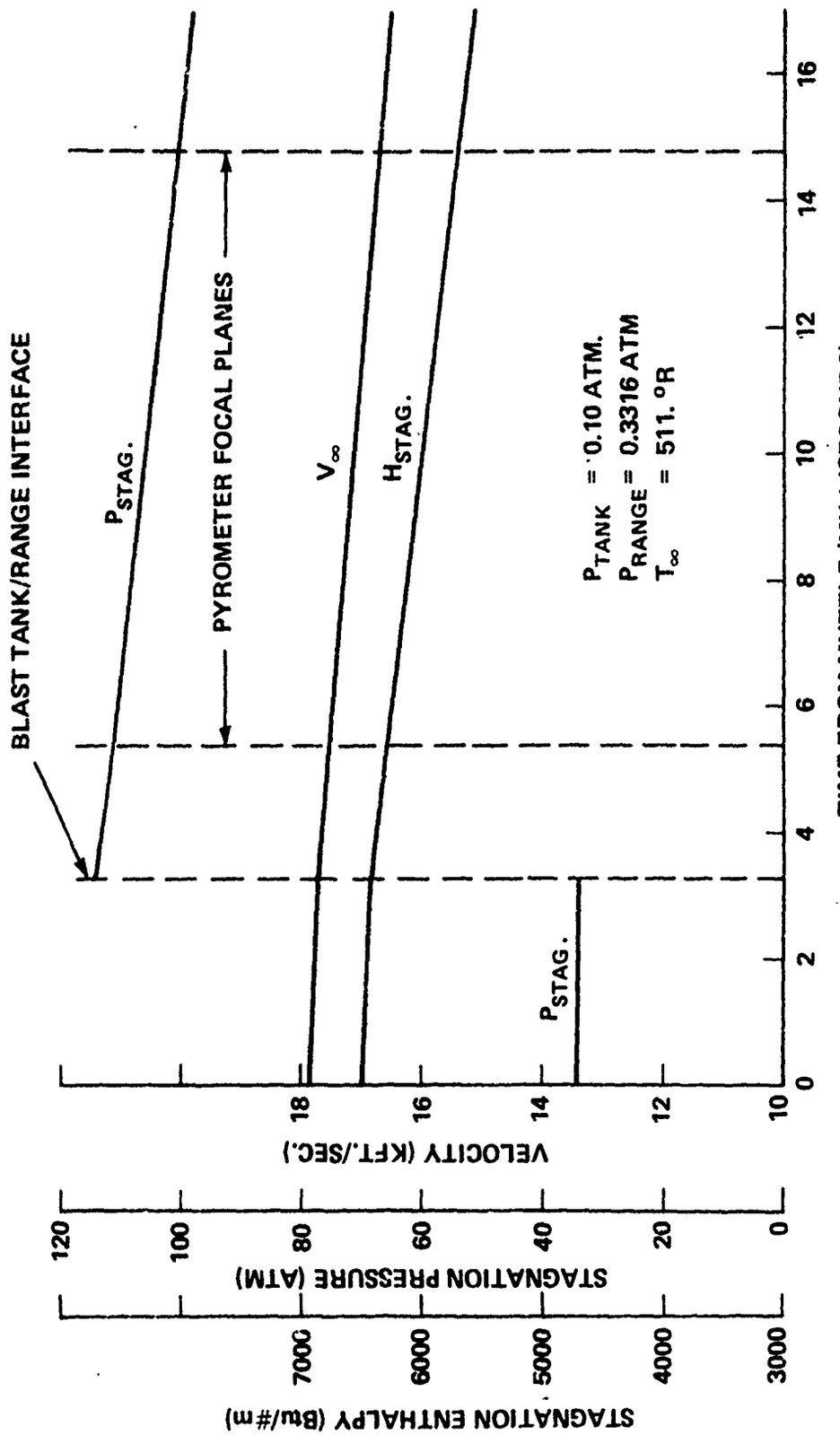

FIG. 19 BALLISTICS RANGE AEROTHERMODYNAMIC TRAJECTORY

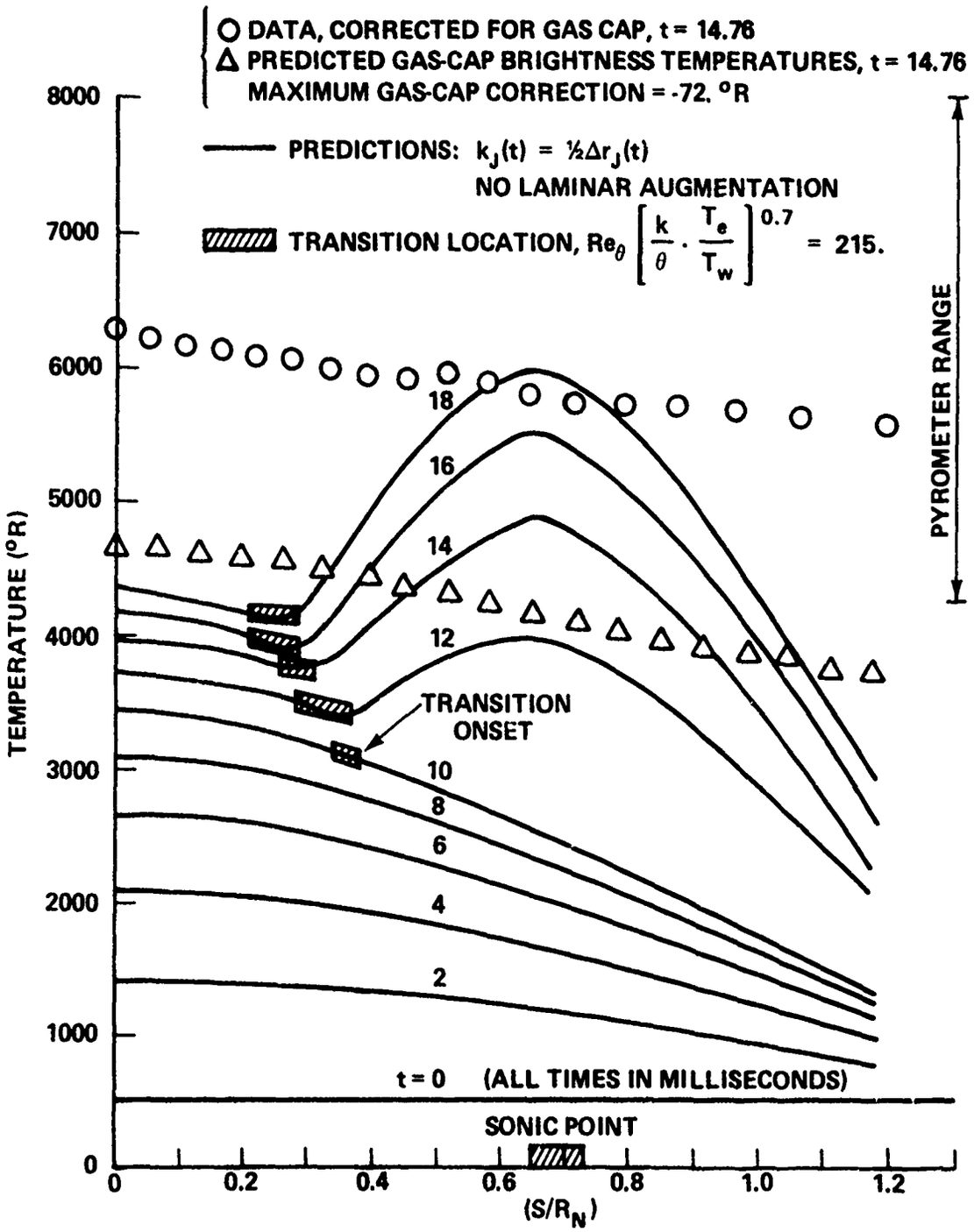

FIG. 20(a) SURFACE TEMPERATURE VERSUS $\left(\frac{S}{R_N}\right)$ FOR MICROROUGHNESS DEVELOPMENT MODEL AND NO LAMINAR AUGMENTATION

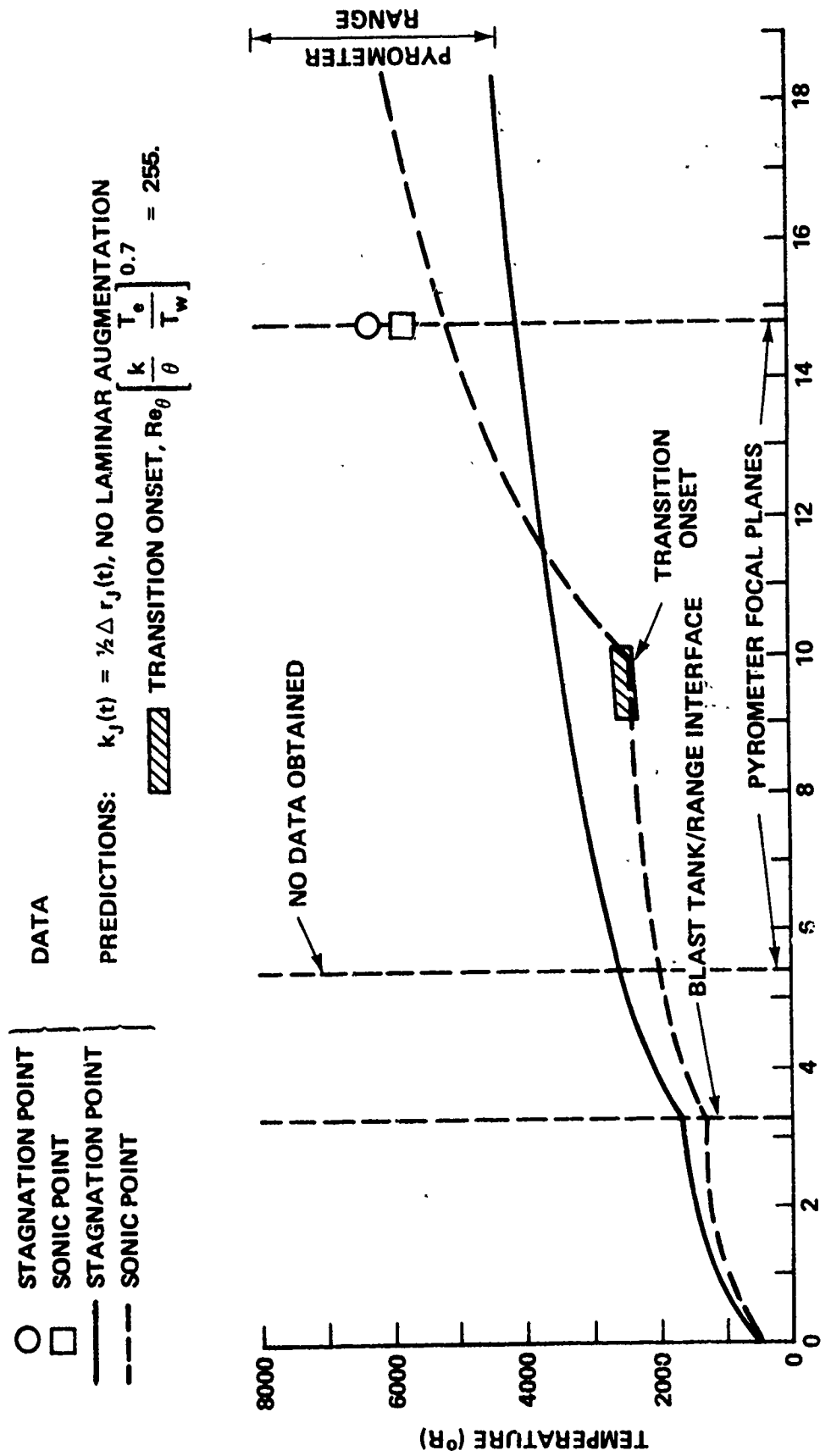

FIG. 20(b) SURFACE TEMPERATURE VERSUS TIME FOR MICROROUGHNESS DEVELOPMENT MODEL AND NO LAMINAR AUGMENTATION

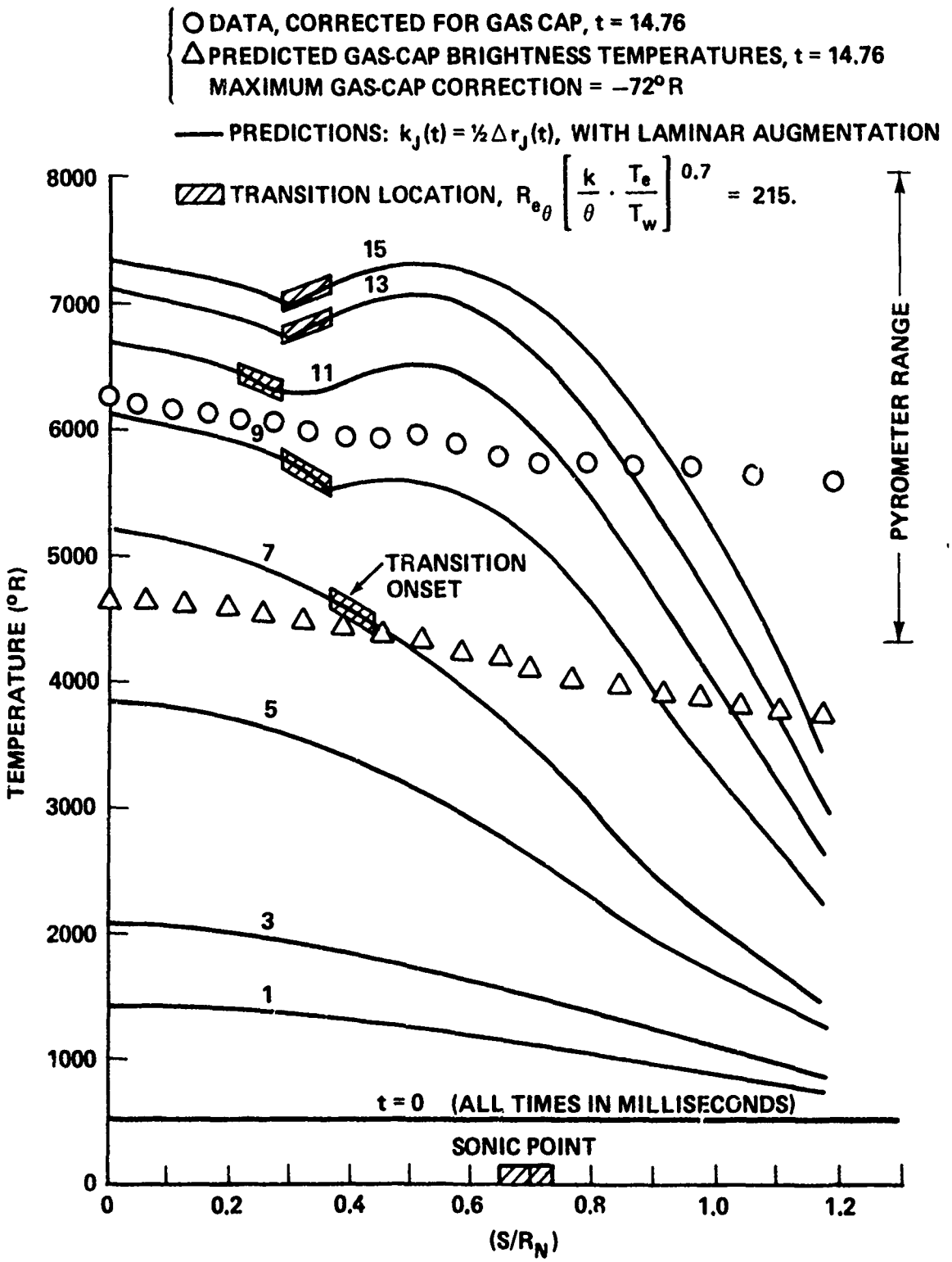

FIG. 21(a) SURFACE TEMPERATURE VERSUS $\left(\frac{S}{R_N}\right)$ FOR MICROROUGHNESS DEVELOPMENT MODEL WITH LAMINAR AUGMENTATION

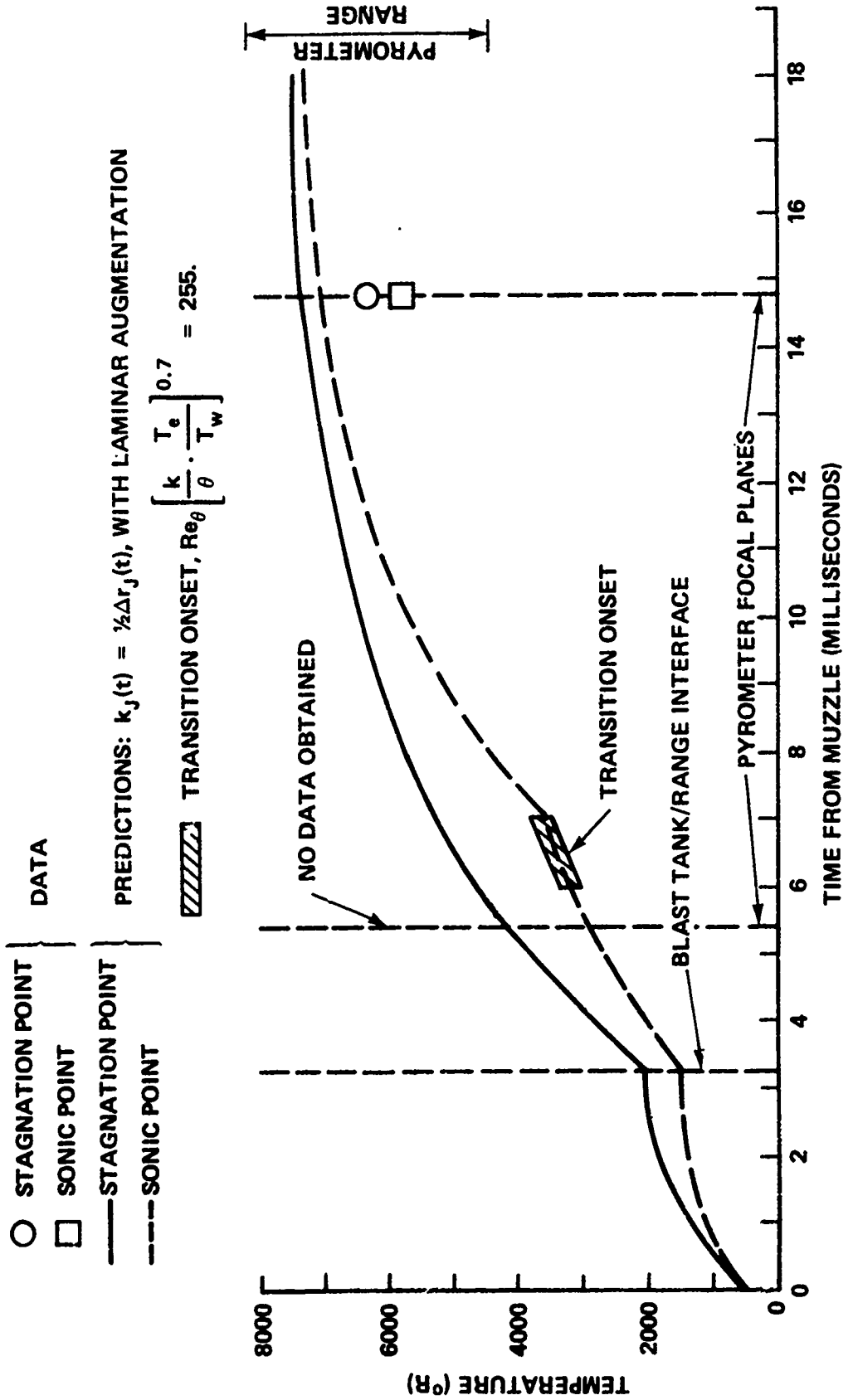

FIG. 21(b) SURFACE TEMPERATURE VERSUS TIME FOR MICROROUGHNESS DEVELOPMENT MODEL WITH LAMINAR AUGMENTATION

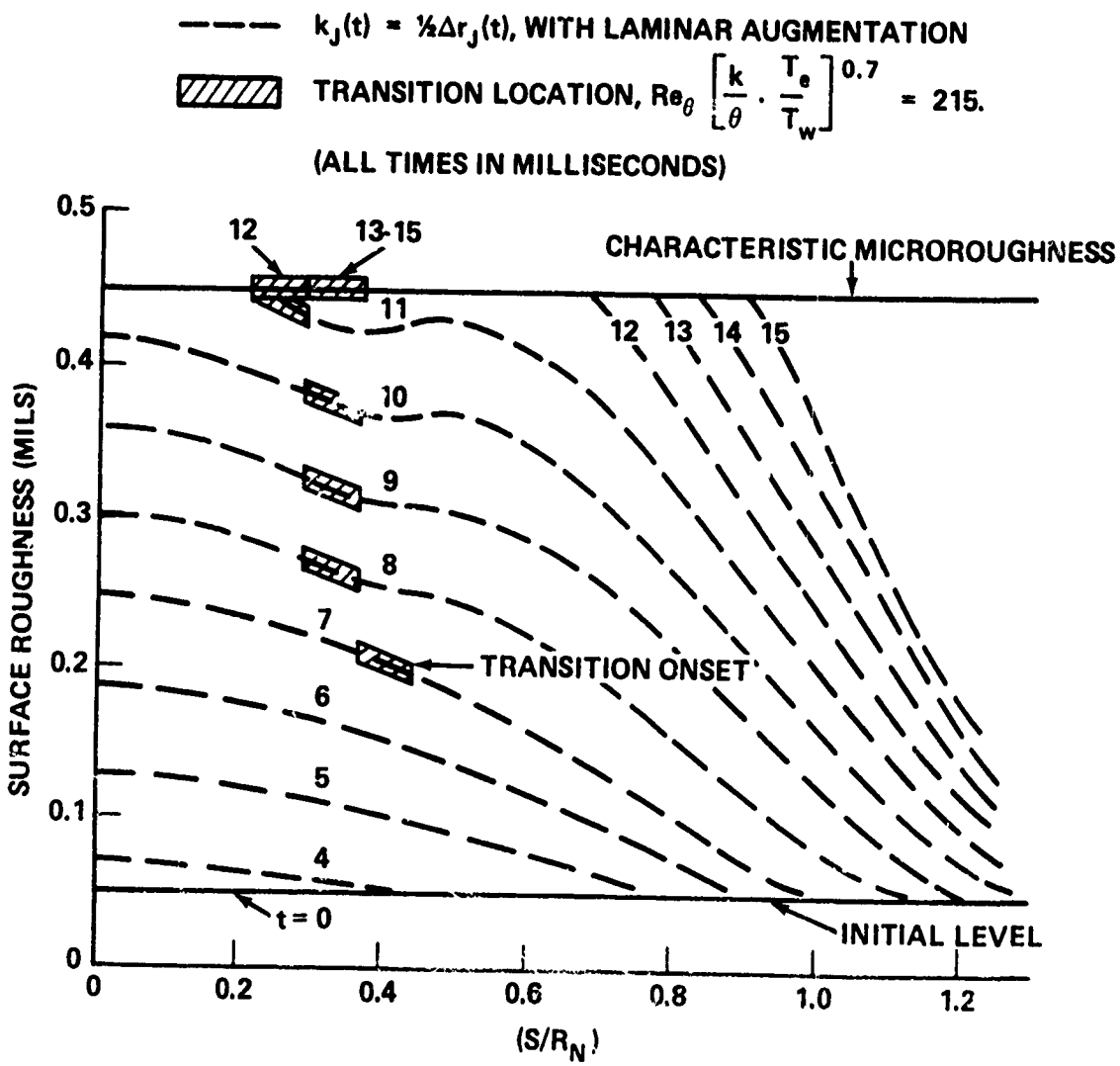

FIG. 21(c) SURFACE ROUGHNESS VERSUS $\left(\frac{S}{R_N}\right)$ FOR MICROROUGHNESS DEVELOPMENT MODEL WITH LAMINAR AUGMENTATION

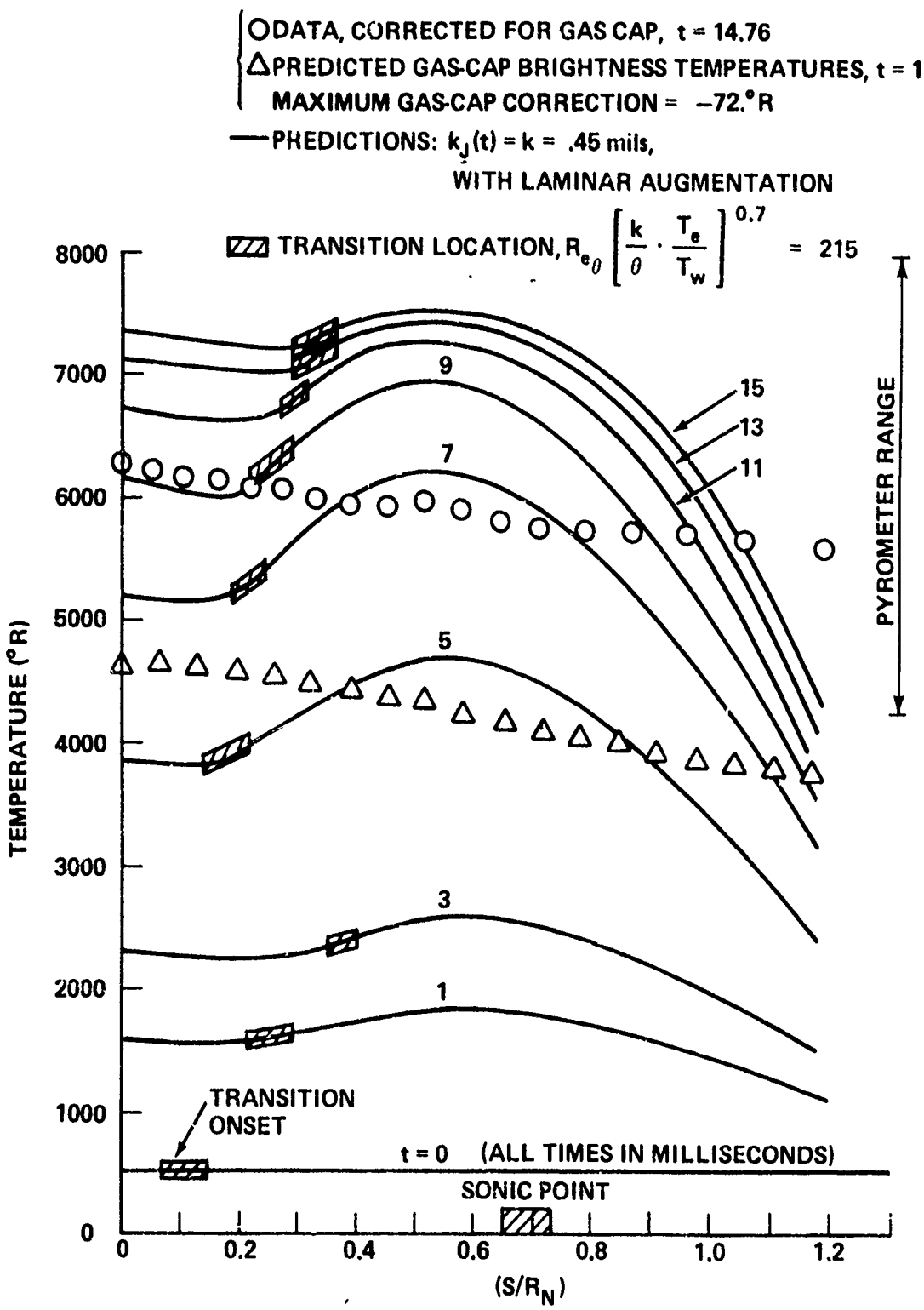

FIG. 22(a) SURFACE TEMPERATURE VERSUS $\left(\frac{S}{R_N}\right)$ FOR A PRECONDITIONED SURFACE WITH LAMINAR AUGMENTATION

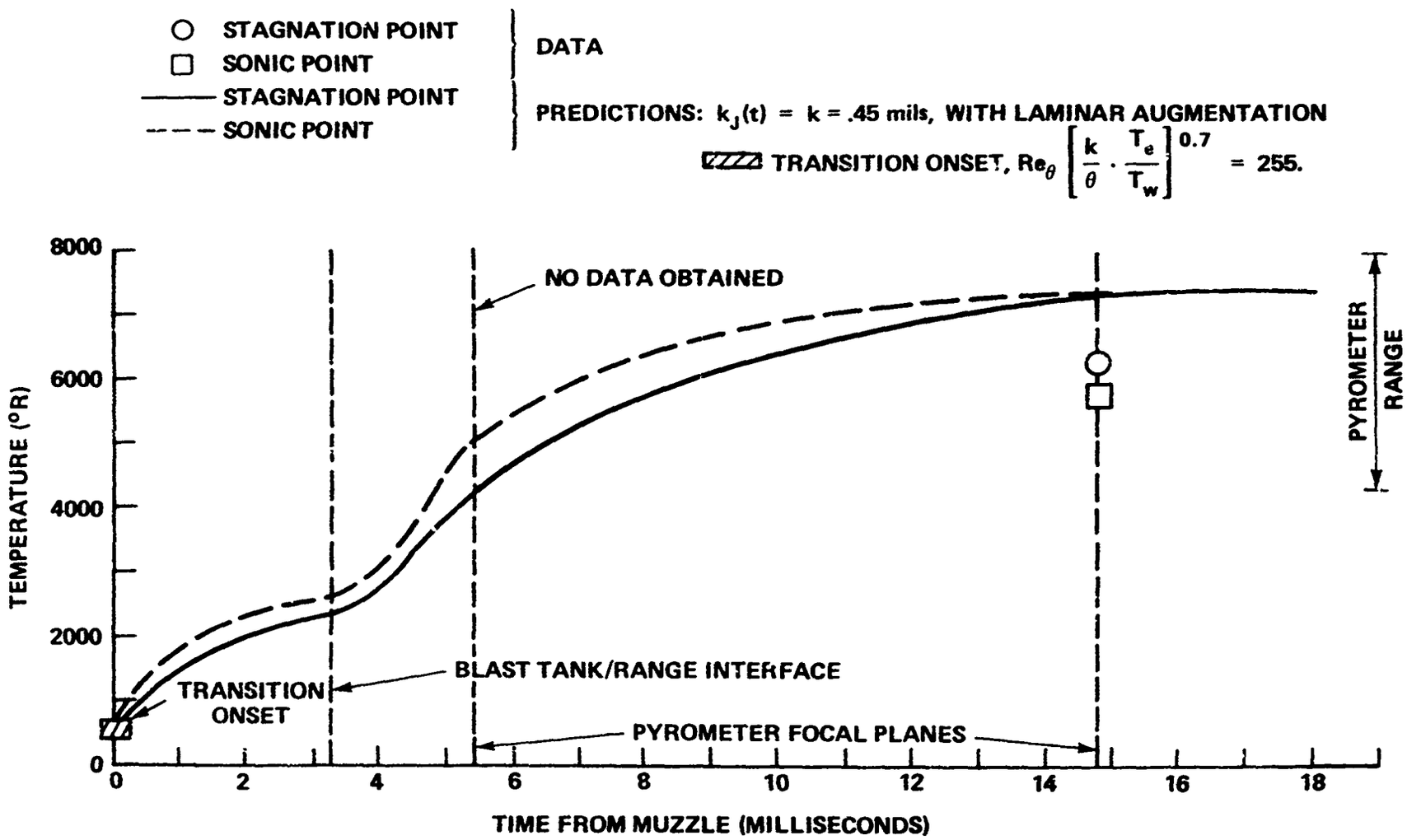

FIG. 22(b) SURFACE TEMPERATURE VERSUS TIME FOR A PRECONDITIONED SURFACE WITH LAMINAR AUGMENTATION

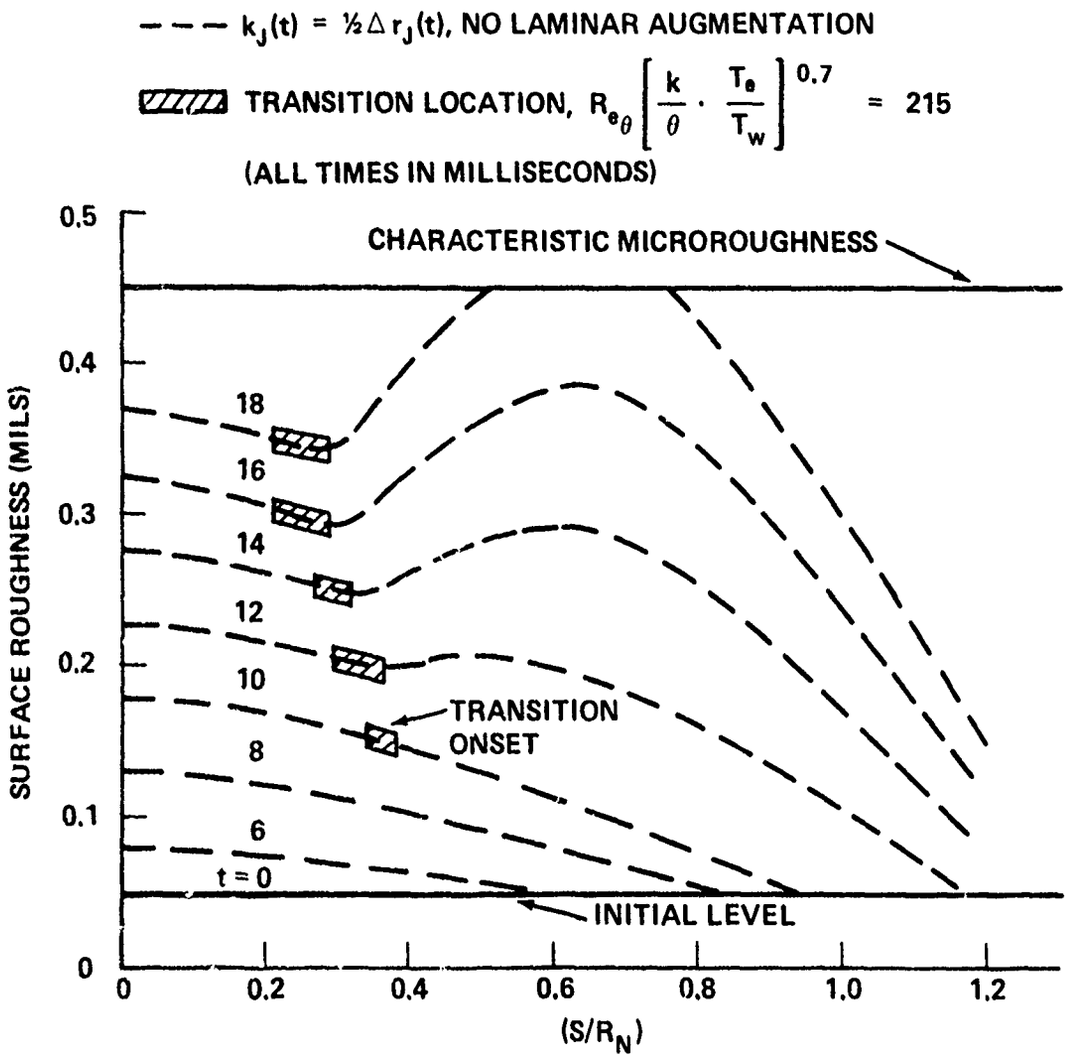

FIG. 20(c) SURFACE ROUGHNESS VERSUS $\left(\frac{S}{R_N}\right)$ FOR MICROROUGHNESS DEVELOPMENT MODEL AND NO LAMINAR AUGMENTATION

PAPER NO. 25

THE AUGMENTATION OF STAGNATION POINT HEAT TRANSFER BY PARTICLE-FLOW INTERACTIONS

W. J. GRABOWSKI

PAPER WITHDRAWN

PAPER NO. 26 Vol. 2

HEAT TRANSFER TO A CIRCUMFERENTIAL GAP ON A CONE AT ANGLE OF ATTACK*

D.E. NESTLER
Aerothermophysics Laboratory
Re-entry Systems Department
General Electric Company
P.O. Box 8555
Philadelphia, Pa. 19101

ABSTRACT

Results are presented of an investigation of heat transfer to a circumferential gap on a cone at angle of attack in hypersonic turbulent flow. Tests were conducted in AEDC Tunnel B at M_∞ = 8.0 and Re_∞ = 3.5 million per foot. Detailed heating distributions are presented for gap widths of .04 to 0.32 inches, gap depths of 1.6 and 0.8 inches, and angles of attack from 0 to 20 degrees. Simple engineering correlations for gap heating are developed for the gap mid-depth and floor locations. Phase change paint "flow pictures" are included which support the multi-vortex gap flow model suggested by the heating distributions.

* This research was performed for the Air Force Space and Missile Systems Organization under Contract F04701-71-C-0081.

INTRODUCTION

Re-entry vehicle construction frequently requires the existence of a circumferential gap between the nosetip and frustum sections. If the vehicle re-enters at angle of attack, the aerodynamic heating received by the gap will be increased above gap heating levels for zero angle of attack, for two reasons: (1) windward surface heat transfer upstream of the gap is increased due to angle of attack, and (2) the ratio of gap heat transfer to external surface heat transfer upstream of the gap is increased due to crossflow effects.

At the outset of this study, gap heat transfer data and correlations were limited to two-dimensional flow conditions. Correlations for heat transfer at the base of a gap in two-dimensional turbulent flow were available, e.g., Nestler, et al, Reference 1; however the application of such correlations to the case of a circumferential gap at angle of attack was felt to be unconservative due to the neglect of crossflow effects. The objective of this study thus was to obtain experimental heat transfer data to a circumferential gap on a cone at angle of attack in hypersonic turbulent flow, and to develop an engineering correlation of such data.

APPROACH

Prior to planning an experimental program, a conceptual model of a circumferential gap on a cone at angle of attack was developed, in order to provide insight into the relations among the physical parameters. As shown in Figure 1, it was hypothesized that inflow into the gap would exist wherever the local external pressure P_1 exceeded the

gap internal pressure P_2, while outflow from the gap would develop wherever $P_1 < P_2$. By means of the continuity equation, and assuming one-dimensional channel flow relations for frictional pressure drop and heat transfer in the circumferential direction, the circumferential distribution of gap pressure and heat transfer were determined in terms of external circumferential pressure variation. Due to uncertainties in the selection of flow coefficients for the gap inflow and outflow computations, this analysis was used to provide preliminary estimates only. Nevertheless, the analysis was valuable in demonstrating that a crossflow component of gap flow should exist, which could potentially lead to a maximum gap heat transfer away from the windward meridian.

An experimental program was then planned and conducted in Tunnel B of the Arnold Engineering Development Center at a Mach number of 8 and a free stream Reynolds number of up to 3.6×10^6/ft. Sharp and blunt-nosed cones having a circumferential gap were tested at angles of attack up to 25 degrees. The program included an initial exploratory phase using the phase change paint technique, followed by a densely instrumented thin skin heat transfer and pressure model. Results of these tests are given in the following sections.

EXPLORATORY TESTS

These tests were conducted on a six degree half-angle cone having a nose radius of 1.5 inches. The gap depth was fixed at 0.80 inch, while the gap width was varied from .080 to 0.32 inch by means of spacer rings. Turbulent flow at the gap was provided by boundary layer trips located on the nose. Time lapse photography was used to provide

a record of paint melt line progression on the gap sidewalls, from which the heat transfer distribution was computed by standard one-dimensional transient conduction solutions. Typical heat transfer coefficient contours are shown in Figure 2, for the downstream gap face.

Figure 3 shows gap heating distributions for the windward meridian of the 0.32 inch gap for an angle of attack α of 18 degrees. In this and subsequent figures, results are presented as normalized heat transfer coefficients h/h_o, where:

h = local heat transfer coefficient based on external total temperature

h_o = local heat transfer coefficient immediately upstream of gap on the windward meridian (again based on external total temperature)

In Figure 3, the maximum gap heating occurs at the reattachment corner of the downstream wall. Ratios of h/h_o approaching 4.0 at the corner were estimated from melt-line transient development early in the run, indicating an extremely severe gradient over the upper .05 inches of the downstream wall. The results for $\alpha = 0$ (also shown in Figure 3) show that the relative gap heating is significantly increased by crossflow. Noting that h_o is the external reference heating for the respective test conditions for each value of α, Figure 3 shows e.g. that at a location of 0.14 inches down the downstream wall, the value of h/h_o with crossflow is over 4 times the value of h/h_o without crossflow.

The decrease in h/h_o along the downstream wall levels out somewhere below the gap half-depth, followed by a rise in heating near the gap

floor. In contrast, the variation in h/h_o along the upstream wall is just the opposite, exhibiting an increase where a decrease occurred on the downstream wall, and a decrease where an increase occurred on the downstream wall. Indeed, the maximum heating on the upstream wall appears to occur directly opposite the location of the minimum heating on the downstream wall.

Consideration of the windward gap heating distributions such as those of Figure 3 suggests the flow model of Figure 4, in which a multi-vortex flow is induced within the gap. This flow model is appropriate for either an annular gap at $\alpha = 0$ or a windward gap cross-section at finite α, since the crossflow velocity is zero in the windward plane. The effect of angle of attack is to cause P_2 to be lower than P_1, resulting in an initial shear layer expansion with higher energy flow circulation within the gap. Hot spot regions are associated with jet-like impingement of shear layers; the location of these hot spots depends on the aspect ratio of the vortices.

Further confirmation of the flow model of Figure 4 was provided by the post-test photographs of the gap inserts for certain tests in which the melted paint froze on the lower heating regions of the gap sidewalls, thus providing a flow visualization technique. Thus, Figure 5 illustrates the type of flow pattern obtained for selected gap surfaces which is consistent with the flow directions postulated in Figure 4. These paint flow pictures showed a strong crossflow circulation away from the windward meridian, especially for the smaller gaps (see Figure 6).

Prediction of maximum crossflow heating for the wind tunnel conditions using the approximate analysis described above yielded values below the threshold levels which could be measured in the paint tests. This result is consistent with the measured circumferential heating distributions, which indicated the windward meridian to be the location of maximum gap heat transfer. The crossflow heating component is zero at the windward meridian, increases to a maximum near 60 degrees off windward, then decreases to zero at the leeward meridian (Figure 7). The gap heating component corresponding to longitudinal-flow-induced vortex circulation is maximum at the windward meridian, decreasing to a minimum at the leeward meridian.

THIN-SKIN MODEL TESTS

Extensive heat transfer and pressure data within circumferential gaps at angle of attack were obtained on the model shown in Figure 8. The model was designed and fabricated by Ellco Engineering, Inc., acting as vendor to AEDC. Spacer rings allowed gap widths of .040, .080, .120, and .160 inches, and gap depths of 0.80 and 1.60 inches. Vertical translation of forward frustum relative to rear frustum provided for forward and rearward facing steps of 0.10 and 0.20 inches at the gap location. Either sharp nose or 1.50 inch radius blunt nose could be tested; however, most tests used the sharp nose to promote turbulent flow.

Separate gap inserts provided for 98 thin-wall thermocouple heat flux and 56 pressure measurements within the gap. Gardon gages measured heat flux to the floor of the 0.8 inch depth gaps of .12 and .16 inch widths. Test conditions are shown in Table 1.

Typical heat transfer distributions within a gap at α = 10 degrees are presented in Figure 9, for several peripheral stations. The windward meridian received the highest gap heating, with a monatonic decrease toward leeward, in agreement with the exploratory paint tests. Exceptions to this trend occurred near the bottom of the .040 inch gap. For values of $\alpha \leqq 5$ degrees, maximum heating was measured between 30 and 60 degrees off the windward meridian, as shown in Figure 10.

The effect of gap width on windward meridian gap heat transfer for α = 10 degrees is shown in Figures 11 and 12 for gap depths of 1.6 and 0.8 inches, respectively. In general, gap heating increases as gap width increases, although some crossover trends are apparent in the upper half of the deeper gap. The wider gaps are seen to exhibit heating maxima part way down the walls, presumably due to the multi-vortex flow pattern postulated in Figure 3. Careful study of Figures 11 and 12 indicates that heating levels are similar for the two gaps at a given absolute distance down the gap wall from the corner in the upper portion of the gap, but that from mid-depth to floor, heating levels are similar at a given relative distance from the corner. The different behavior is probably associated with three-dimensional flow effects; the paint "flow pictures" (such as Figure 6) implied strong crossflow in the lower half of the gap.

The effect of body angle of attack on windward meridian gap heat transfer for a gap width of 0.16 inches is shown in Figures 13 and 14 for a gap depth of 1.6 and 0.8 inch, respectively. In general, gap

relative heating h/h_o increases as α increases, except for some reduction on the upstream wall as α exceeds 10 degrees. Significant increase in h/h_o occurs as α changes from 0 to 5 degrees, with less increase as α increases above 5 degrees.

At this point, it is worth noting that the values of h/h_o on the gap floor shown in Figures 11 and 13 are significantly higher than sidewall values in the lower half of the gap. This increased heating is indicative of a stagnation effect due to wall boundary layer impingement on the floor as it negotiates a 90 degree turn.

The effect of forward and rearward facing steps on windward meridian gap heat transfer for a 0.16 x 0.80 inch gap at α = 10 degrees is shown in Figure 15. As anticipated, large reductions in heating are caused by the rearward facing step, while large increases in heating are caused by the forward facing step. For α = 5 and 10 degrees, little difference in h/h_o occurred for blunt vs. sharp nose. For α = 10 degrees, h/h_o was slightly less for the sharp nose configuration. These results imply that gap heat transfer ratios at angle of attack are relatively insensitive to variations in local Mach and Reynolds number upstream of the gap, over the range of the present tests.

Typical static pressure distribution within the 0.32 inch gap is shown in Figure 16. As expected, gap pressure decreased from windward to leeward in a similar fashion as the external pressure. The reattachment corner pressure exceeded the external cone pressure over the windward sector for the widest gap (0.32 inches); otherwise, gap pressures were less than external pressure for $0 < \phi < 90$ degrees. The floor

pressure exceeded the sidewall pressure, confirming the strong floor stagnation effect implied by the heating data. Although large variations in pressure were noted within the 0.32 inch gap in the windward sector, more uniform pressures were observed for the smaller gaps. This is consistent with the lower gap velocities expected for smaller gaps, for which the upstream boundary layer velocity defect prevents attainment of asymptotic shear layer development across the gap prior to reattachment.

The non-similar character of the gap sidewall heating distributions precluded the development of simple correlation functions for the spatial distribution of gap heat transfer. Hence, emphasis was placed on three locations within the gap, for the windward meridian: gap mid-depth, gap floor, and reattachment corner. Figure 17 shows the variation of h/h_o at the mid-depth. It was possible to obtain a reasonable collapse of the portion of this data for which $5 \leq \alpha \leq 20$ degrees, as well as the corresponding data for the 0.8 inch gap depth, by plotting h/h_o vs. a/δ (Figure 18). Here, "a" is the gap width and δ is the theoretical turbulent boundary layer thickness upstream of the gap. Values of δ were computed by the empirical method of Copper and Shaw (Reference 2):

$$\delta/\delta_{\alpha=o} = \exp\left[-2 + 2\exp\left(-0.3\,\alpha/\theta_c\right)\right] \qquad (1)$$

in which θ_c is the cone half-angle and $\delta_{\alpha=o}$ is the value at $\alpha = 0$, as determined by the following approximation for sharp cones:

$$\delta_{\alpha = 0} \approx 0.2\, S / Re_S^{0.2} \qquad (2)$$

in which S is the wetted length from the effective origin of the turbulent boundary layer. The use of a/δ as the correlating parameter is not derivable directly from theory, but appears to (fortuitously) allow for both the effect of decreased boundary layer thickness and increased crossflow as angle of attack increases.

A similar correlation for the gap floor is shown in Figure 19. Comparison with the sidewall mid-depth correlation shows that the heat transfer coefficient on the floor is on the order of 50 percent higher than at the mid-depth sidewall location.

An attempt to derive a similar correlation for the reattachment corner was not as successful, as seen in Figure 20. Despite the large scatter, a clear trend exists for increased heating as the ratio a/δ increases. For values of $a/\delta > 1$, reattachment heating is seen to exceed the conical heating level.

The application of the preceding correlations to the prediction of heat shield gap sidewall recession requires an estimate of the true local heat transfer coefficient within the gap based on the gap local recovery temperature. Since the recovery temperature within a gap is less than the total external flow temperature, the true value of h will be greater than the value based on T_o. An approximate analysis was performed to estimate the variation of T_R/T_o within the gap with a/δ. The analysis assumed a Prandtl-Meyer expansion of streamlines at various

heights within the upstream boundary layer, based on the Crocco temperature distribution and a 1/7th power law velocity profile. The pressure ratios for the expansion were obtained from test measurements. The recovery temperature of the streamline which just impinged at the reattachment corner was selected as a representative gap recovery temperature. This approximate method neglects the opposing effects of shear layer mixing across the gap and heat loss from the gap boundary layer to the wall. The predicted variation of T_R/T_o is shown in Figure 21, as an enthalpy ratio H_R/H_o for real gas application, and represents an average of calculations at several angles of attack and gap depths. The corresponding adjusted heat transfer coefficient correlation is also shown in Figure 21, where it is compared with the correlation based on H_o.

CONCLUSIONS

The principal conclusions which have evolved as a result of this study are summarized below:

- In general, gap heat transfer is maximum on the windward meridian, being several times greater than would be predicted by equivalent cone application of two-dimensional gap heat transfer correlations.
- For certain combinations of gap dimensions and angle of attack, heat transfer near the bottom of the gap can be maximum away from the windward meridian, due to strong crossflow effects. This condition is promoted by small gap width and small angle of attack.
- Gap heat transfer increases as gap width and angle of attack increase; gap width should be minimized to avoid significant heating rates to the gap floor.

- The ratio of gap heat transfer to external surface heat transfer can be correlated as a function of the simple parameter a/δ (where a = gap width and δ = boundary layer thickness) for a wide range of gap sizes, angle of attack, and local Mach and Reynolds numbers.

- The downstream edge of the gap receives extremely high reattachment heating, exceeding cone surface heating rate for gap widths greater than the local cone boundary layer thickness.

The results presented are believed to be unique in providing experimental data, conceptual flow models, and prediction techniques for a basic aerothermodynamic problem which previously has not been treated in the aerospace literature.

REFERENCES

1. Nestler, D.E., Saydah, A.R., and Auxer, W.L., "Heat Transfer to Steps and Cavities in Hypersonic Turbulent Flow", AIAA Paper No. 68-672, June 1968. Also included in: "Supersonic Flows with Imbedded Separated Regions", Advances in Heat Transfer (1970).

2. Copper, J.A., and Shaw, W.J., Jr., "Turbulent Boundary Layer Thicknesses on Yawed Cones", AIAA Journal, Vol. 8, No. 6, June 1970, pp. 1138-1140.

TABLE 1: GAP HEAT TRANSFER TEST MATRIX

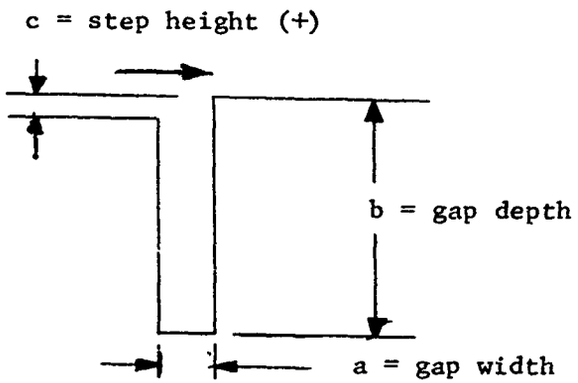

Test Conditions:

M_∞ = 8.0

Re_∞ = 3.5 x 10^6/ft.

T_w/T_o = 0.39

b in.	a in.	c in.	α deg.	Nose
1.6	0.320	0,-0.1,-0.2	0, 5, 10, 20	Sharp
↓	0.160	0	↓	Sharp, blunt + trip
	0.080	0,-0.1		Sharp
	0.040	0 0,-0.1,-0.2		Sharp, blunt + trip
0.8	0.320	0,-0.1,+0.1	0, 5, 10, 20	Sharp
↓	0.160	0	↓	Sharp
	0.080	0		Sharp
	0.040		0, 2, 5, 10, 20	Sharp

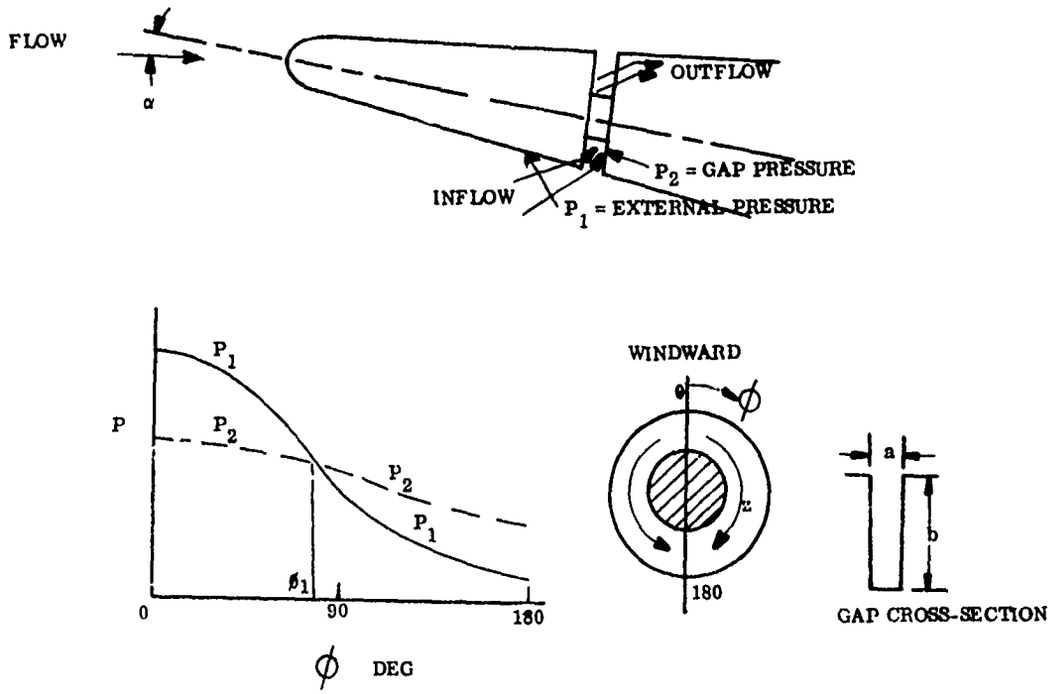

Figure 1. Conceptual Model of Circumferential Gap at Angle of Attack

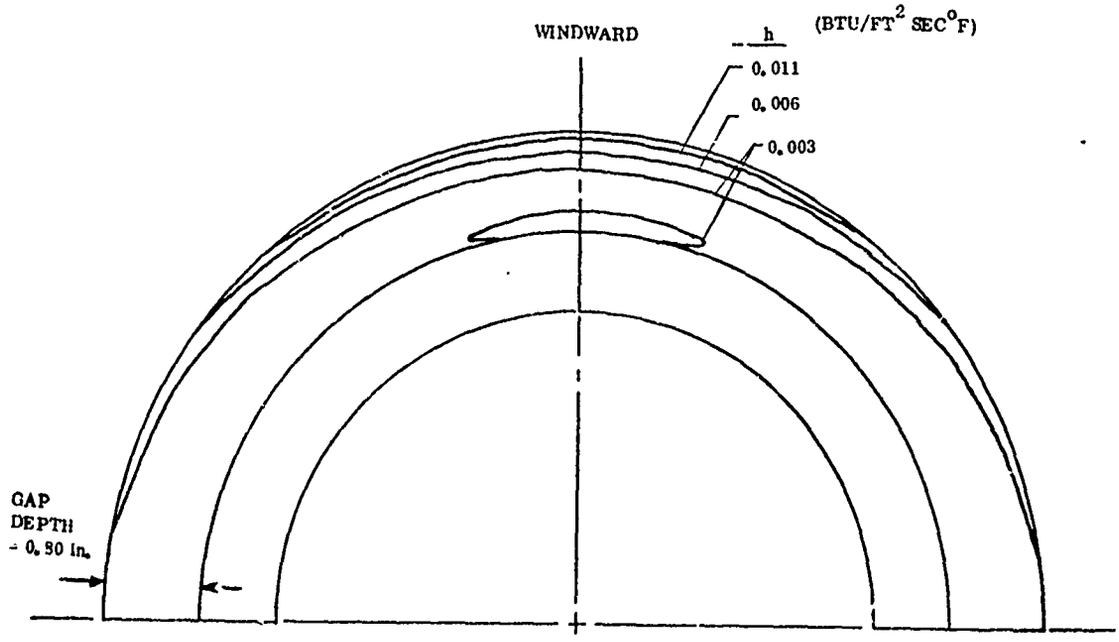

Figure 2. Typical Gap Heating Distributions - Phase Change Paint Technique, a = 0.32 in., b = 0.80 in., $\alpha = 18^{o}$

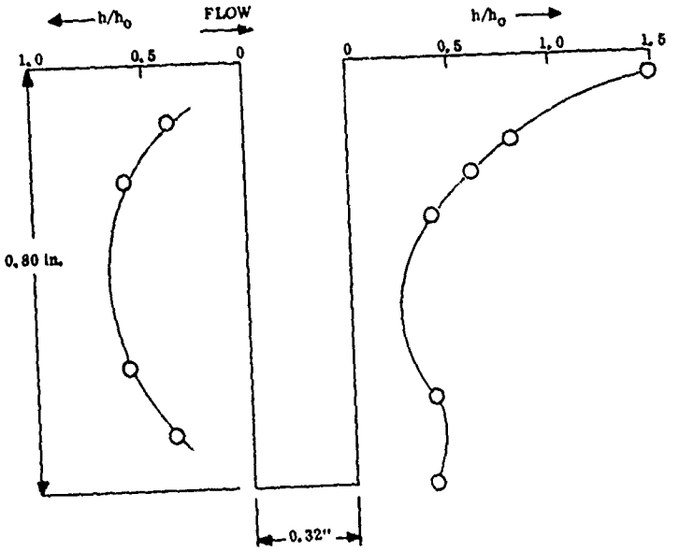

Figure 3. Gap Heat Transfer Distribution - Windward Meridian, Phase Change Paint Technique, a = 0.32 in., b = 0.80 in., $\alpha = 18^{0}$

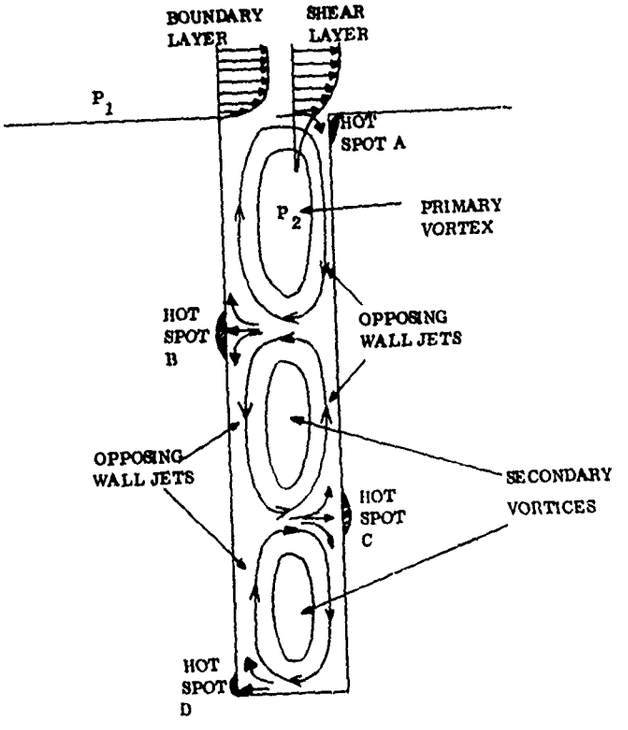

Figure 4. Flow Model for Deep Gap

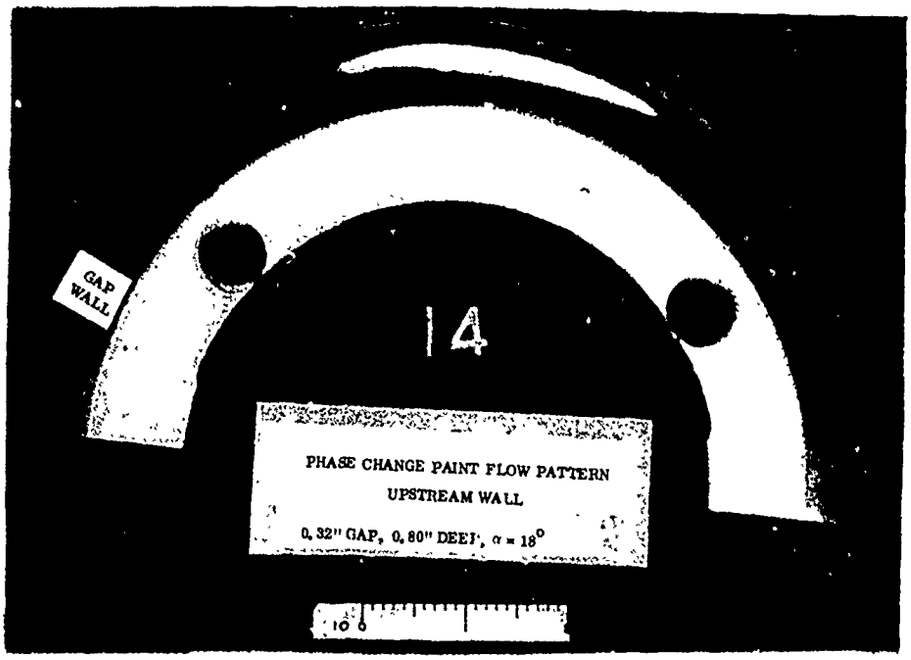

Figure 5. Phase Change Paint Flow Pattern - Upstream Wall

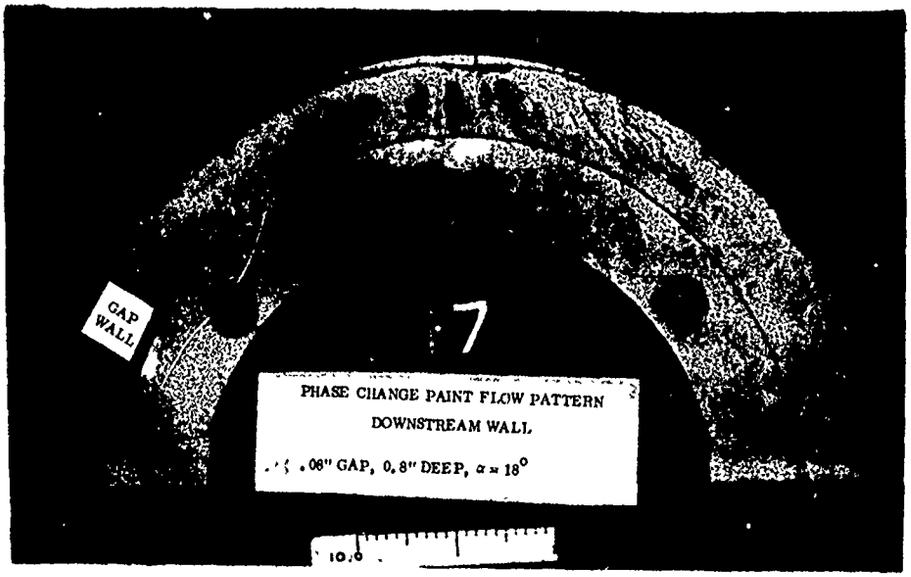

Figure 6. Phase Change Paint Flow Pattern - Downstream Wall

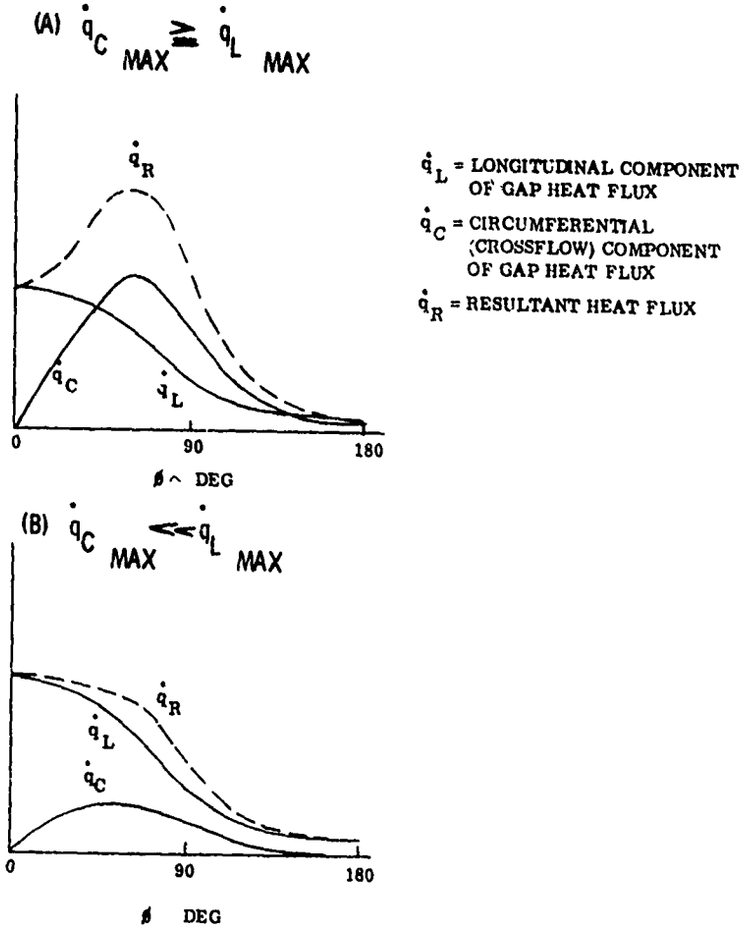

Figure 7. Schematic Representation of Crossflow Effects on Gap Heating

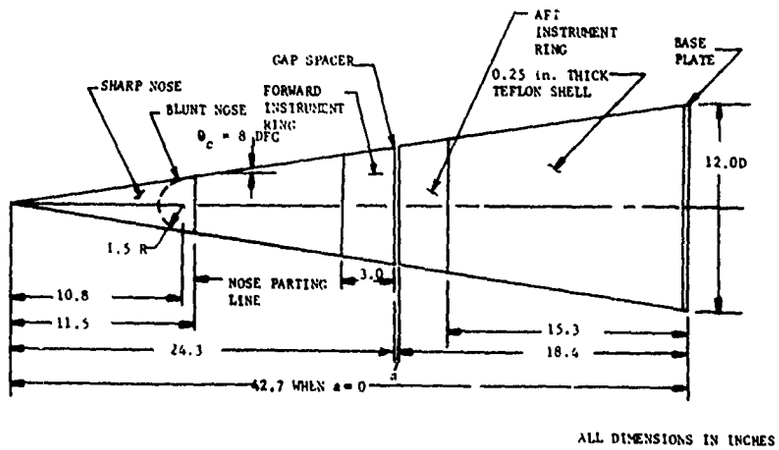

Figure 8. Thin-Skin Gap Test Model

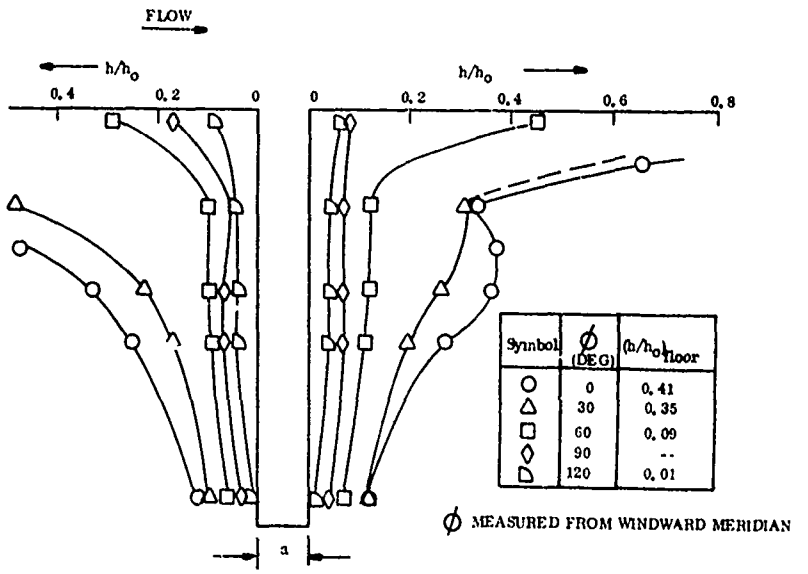

Figure 9. Gap Heat Transfer Distributions. $\alpha = 10^{o}$, a = 0.16 in., b = 1.6 in.

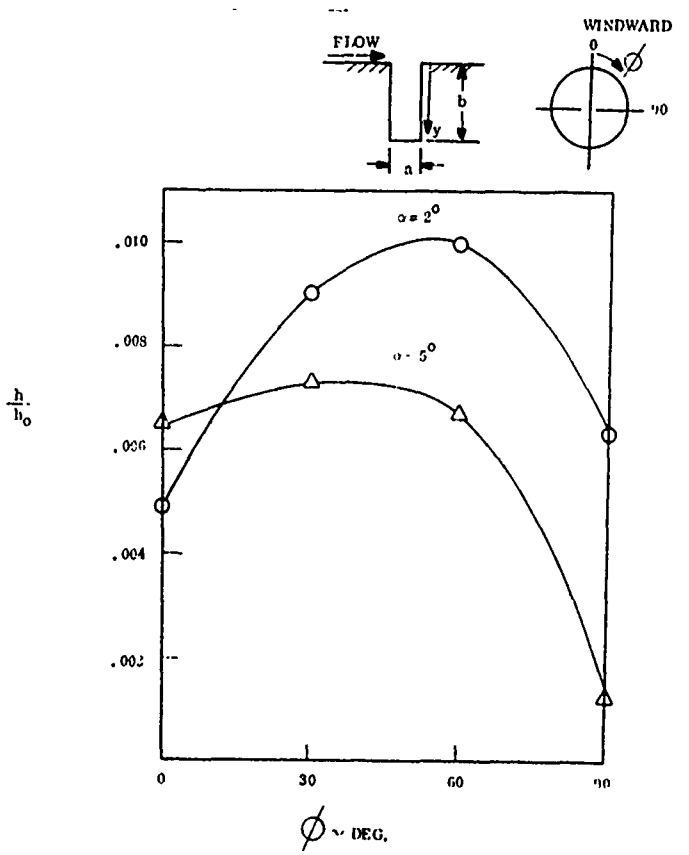

Figure 10. Examples in which Maximum Gap Heating Occurs off Windward Meridian

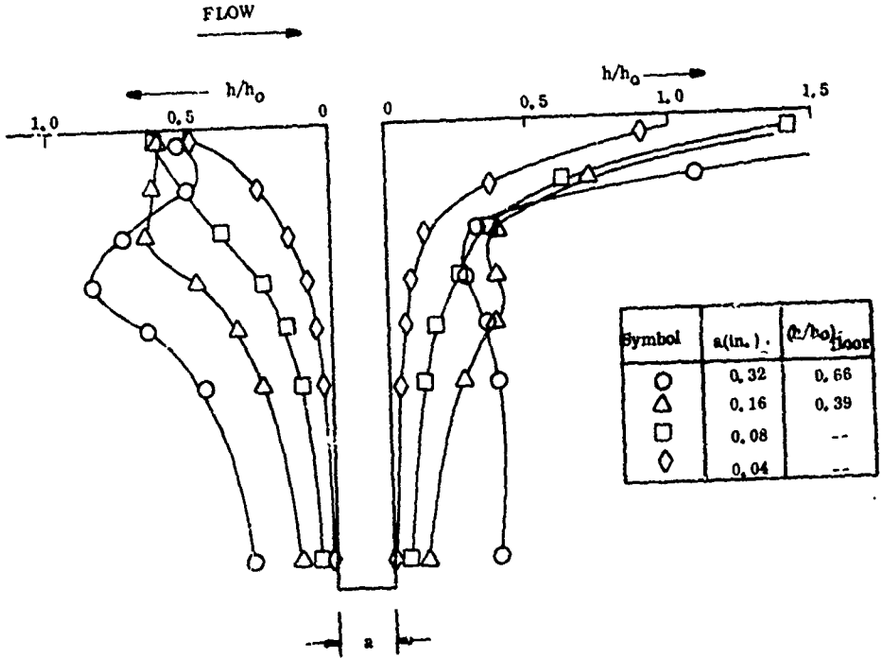

Figure 11. Effect of Gap Width on Gap Heat Transfer Distribution. Windward Meridian, $\alpha = 10^o$, b = 1.6 in.

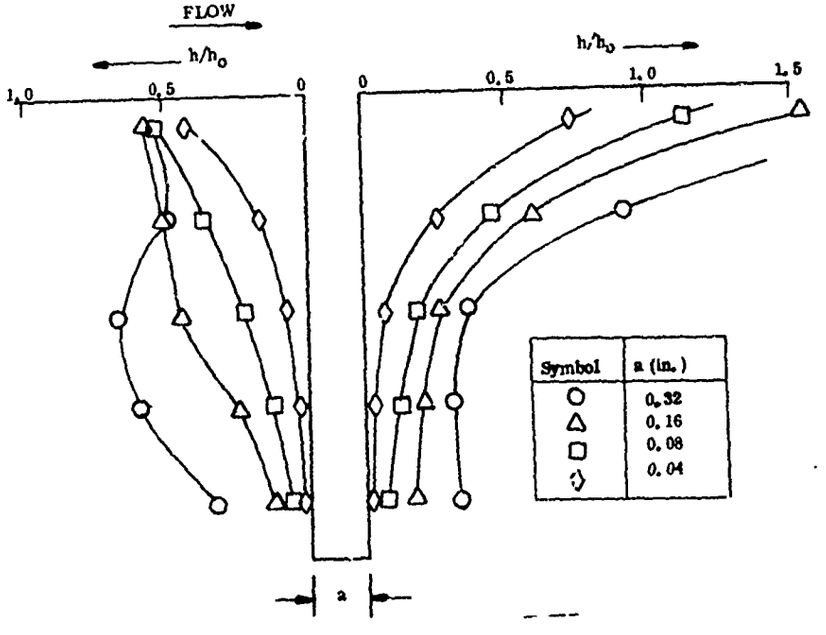

Figure 12. Effect of Gap Width on Gap Heat Transfer Distribution. Windward Meridian, $\alpha = 10^o$, b = 0.8 in.

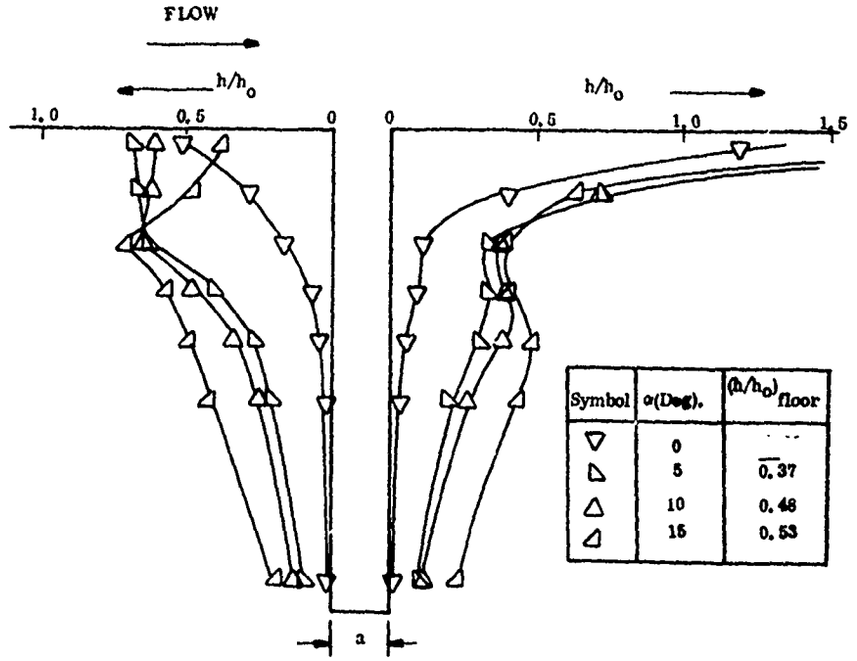

Figure 13. Effect of Angle of Attack on Gap Heat Transfer Distribution. Windward Meridian, a = 0.16 in., b = 1.6 in.

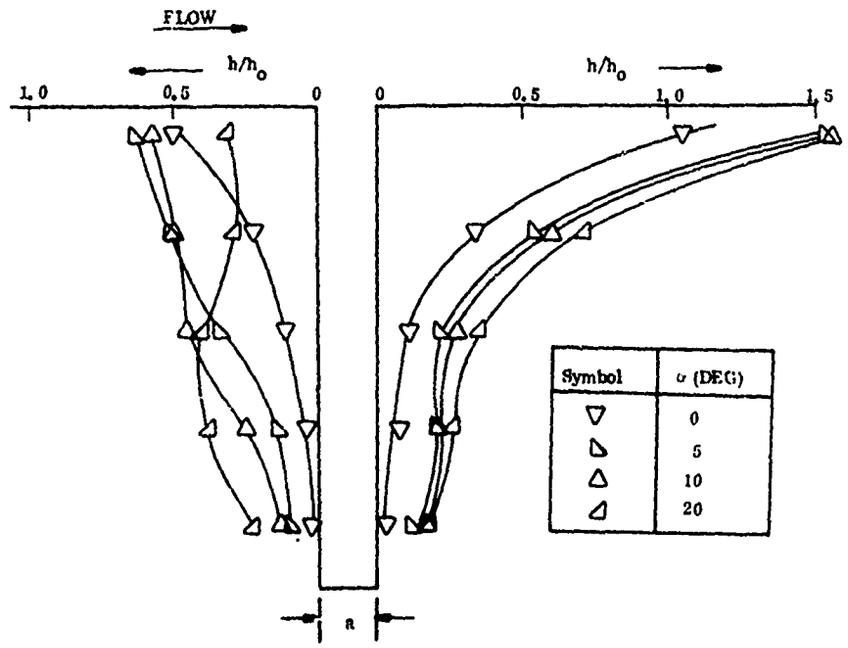

Figure 14. Effect of Angle of Attack on Gap Heat Transfer Distribution. Windward Meridian, a = 0.16 in., b = 0.8 in.

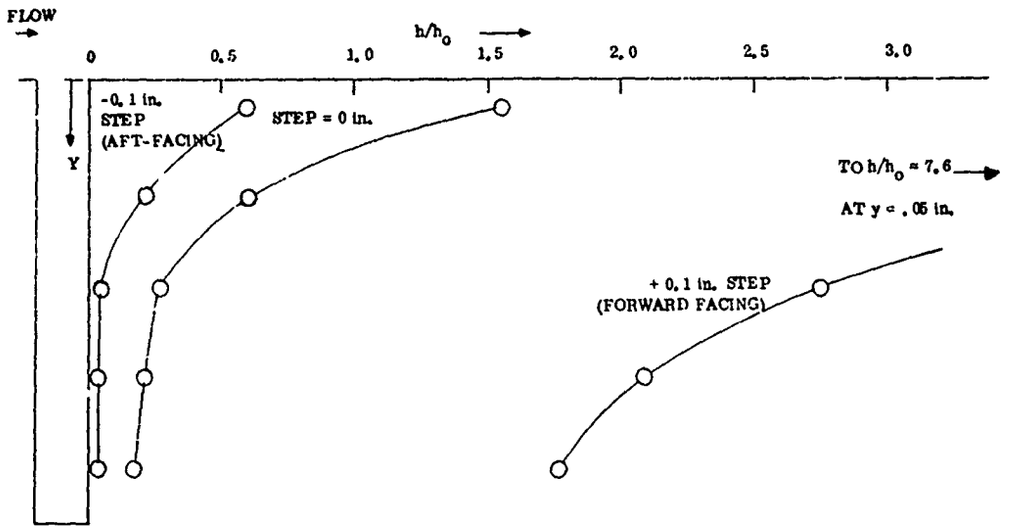

Figure 15. Effect of Step on Gap Heat Transfer. Windward Meridian, $\alpha = 10^{o}$, a = 0.16 in., b = 0.8 in.

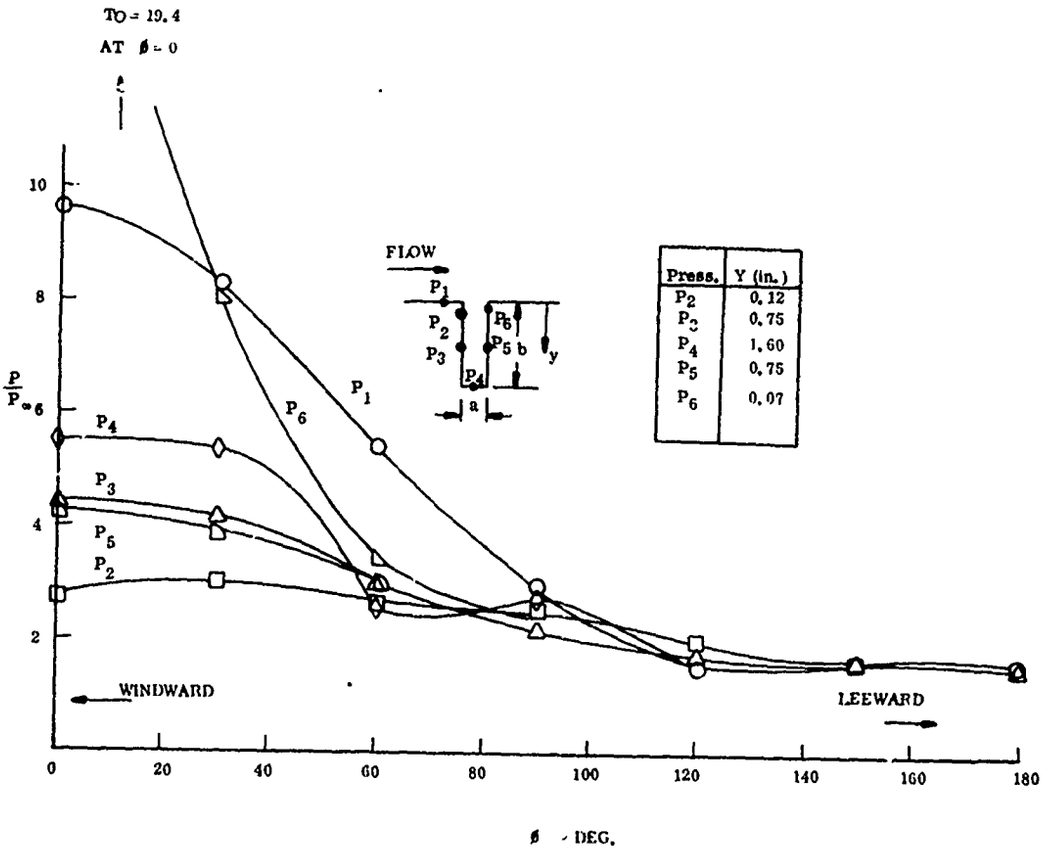

Figure 16. Gap Pressure Distribution. $\alpha = 10^{o}$, a = 0.32 in., b = 1.6 in.

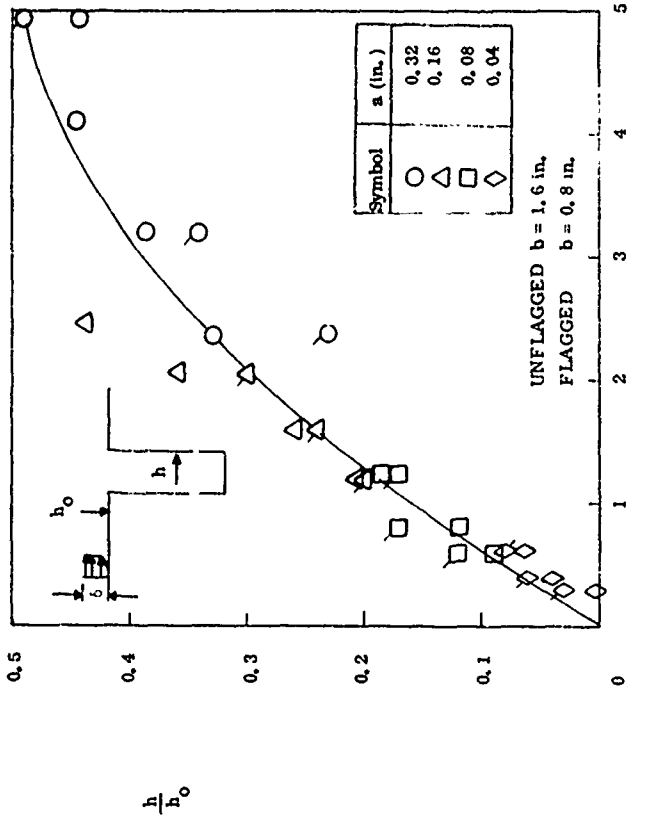

Figure 18. Correlation of Gap Heat Transfer. Midheight Location, 5 Ⅶ α 20°, Windward Meridian

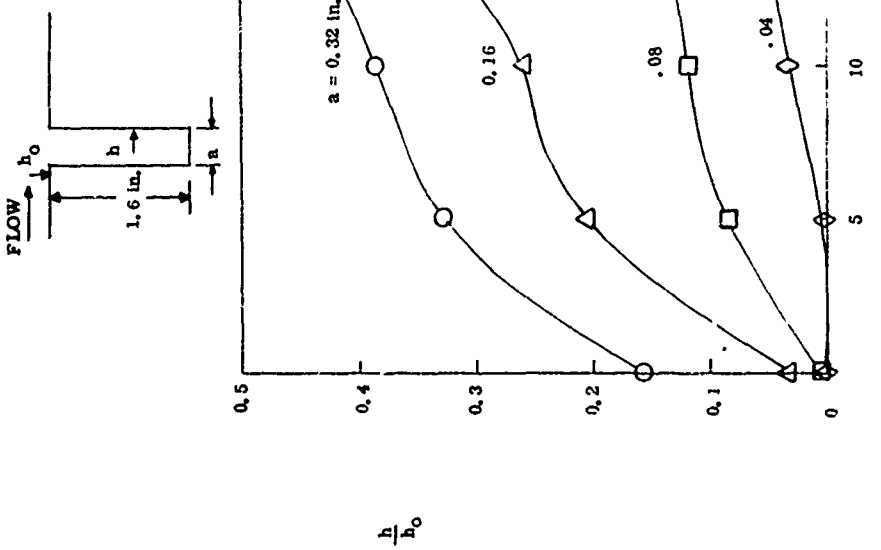

Figure 17. Effect of Gap Width and Angle of Attack on Mid-Depth Heating in Gap

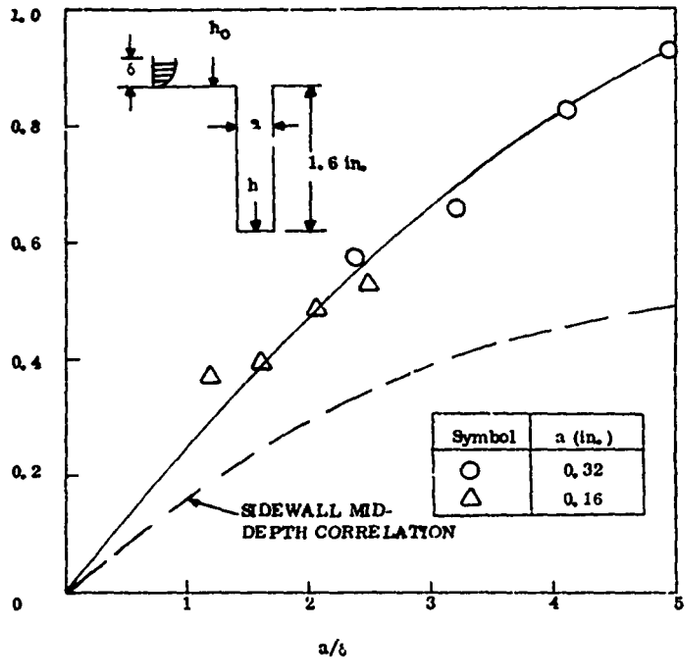

Figure 19. Correlation of Gap Heat Transfer. Floor Location, $5 \leq \alpha \leq 20^{o}$, Windward Meridian

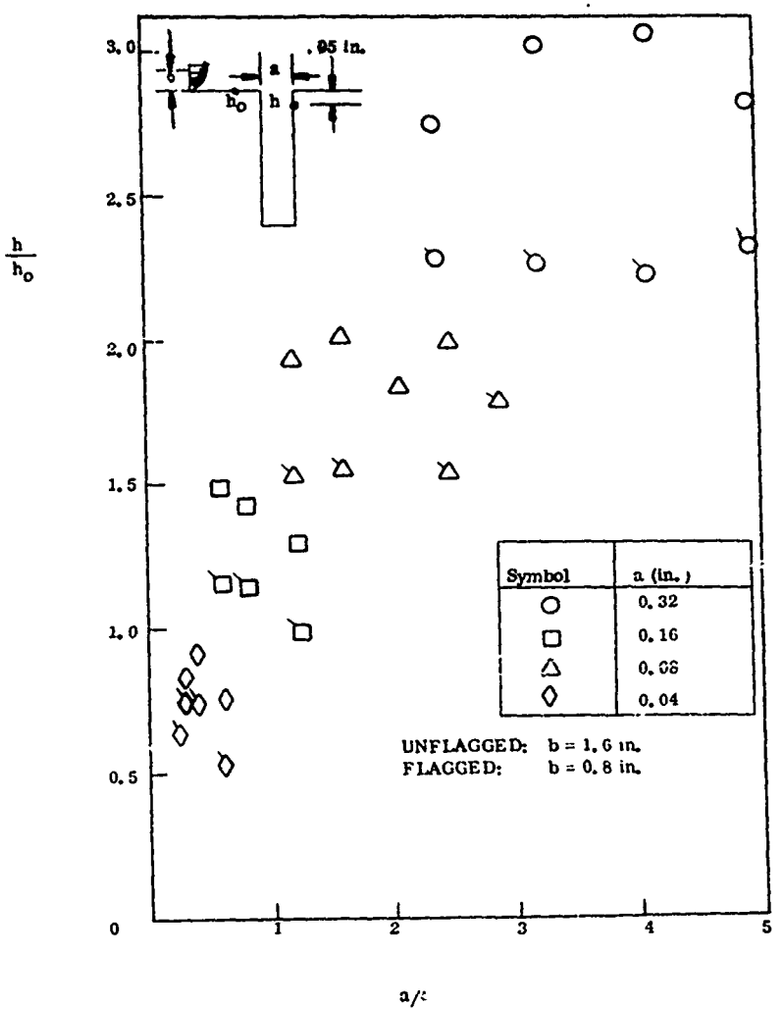

Figure 20. Correlation of Gap Heat Transfer. Reattachment Corner, $5 \leq \alpha \leq 20^{o}$, Windward Meridian

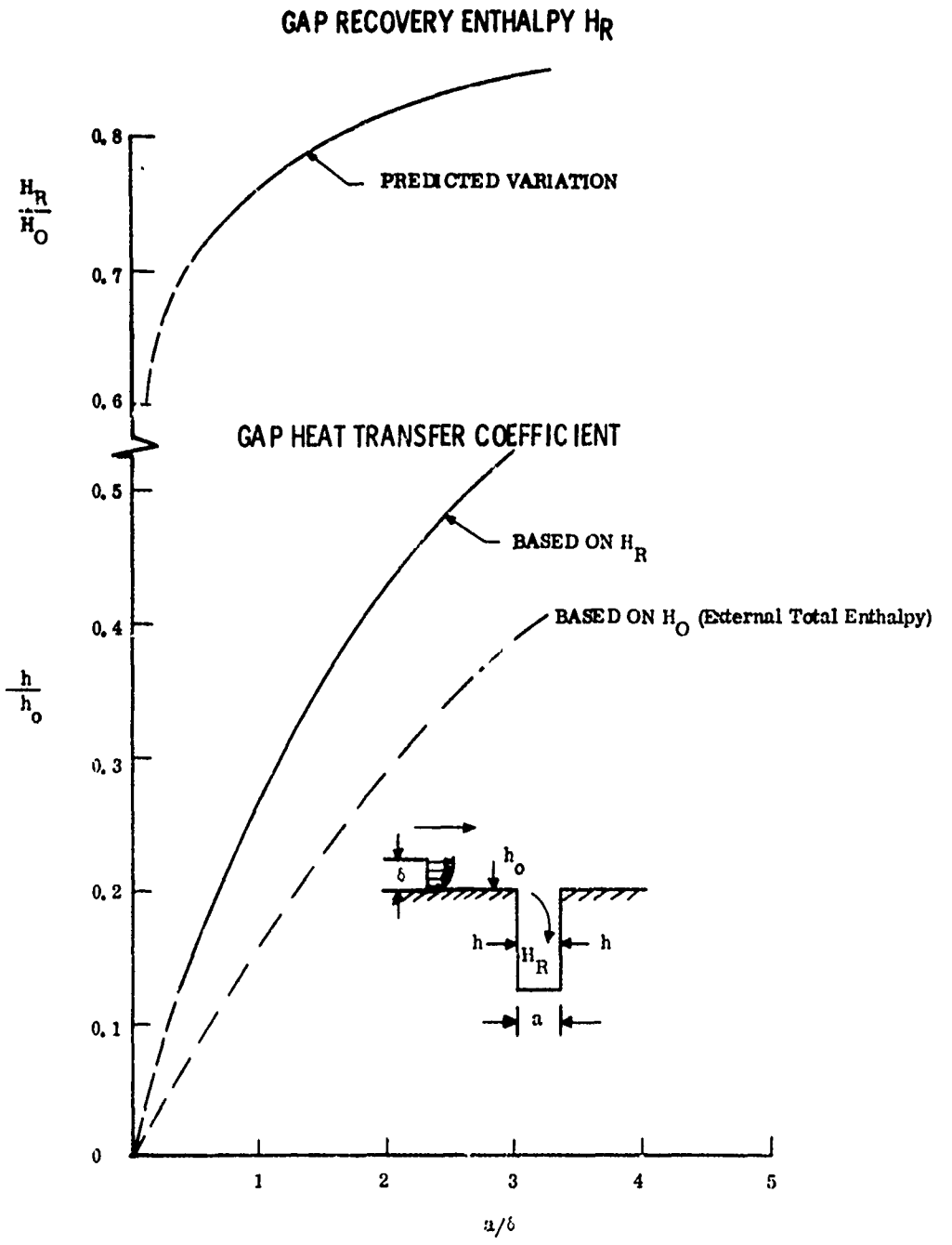

Figure 21. Adjustment of Mid-Depth Correlation for Effect of Gap Recovery Enthalpy Deficit

PAPER NO. 27

EXPERIMENTAL INVESTIGATION OF A FIN-CONE INTERFERENCE FLOW FIELD AT MACH 5*

By

Joseph D. Gillerlain, Jr.

Naval Surface Weapons Center

White Oak Laboratory

Silver Spring, Maryland

*This work was supported by the Naval Air Systems Command, AIR 320

ABSTRACT

The general purpose of this investigation was to study the separated flow field associated with a fin-body juncture. Specific objectives included: (a) determining the severity and extent of aerodynamic heating, (b) providing flow visualization results to illustrate the flow structure, and (c) obtaining a data base of heat-transfer and surface-pressure measurements upon which to develop future analytical relations to predict peak interference heating levels.

Tests were conducted at Mach 5 over a unit Reynolds number range of 4.5 to 26 million per foot. A fin-cone model was used. The data consist of surface-pressure distributions, heat-transfer measurements using the phase-change paint technique, and schlieren and oil-flow photographs. Results are presented for several fin-cone geometries to include fin sweep and fin-cone gap. The flush-mounted, unswept fin results are emphasized because they are the most dramatic. Where possible, comparisons are made with fin-flat plate data.

NOMENCLATURE

d	fin leading-edge diameter, fin thickness
h	heat-transfer coefficient
M_∞	free-stream Mach number
p	static pressure
po	total or supply pressure
p_∞	free-stream static pressure
Re_∞/Ft	free-stream unit Reynolds number (per foot)
To	total or supply temperature
x	distance along cone ray
z	distance along cone surface normal

INTRODUCTION

Advanced high-speed flight vehicles which utilize fins as control surfaces may be subject to loss of control effectiveness due to flow separation or to possible loss of structural integrity as the result of fin-body interference flow phenomena. Depending on such geometrical factors as fin leading-edge sweep and bluntness, the bow shock of a control fin will interact strongly with the centerbody surface boundary layer, which is typically turbulent. The fin shock may cause the boundary layer to separate well upstream of the fin leading edge, resulting in an extensive separated flow region. Areas of substantially increased surface pressures accompanied by corresponding regions of high heat transfer may occur in the separated flow region. Designing around these problems usually results in overdesign with its consequential weight penalties. It would, therefore, be helpful to the designer to have information necessary to make reasonable estimates of peak pressure levels, peak heating rates, and the extent of flow separation.

References (1) and (2) cite over 900 studies of problems related to separated flow phenomena. Most investigations of the fin-body problem to date have dealt with fin-flat plate configurations; for examples, see References (3)-(5). More recently, Bramlette (6) and Coleman and Lemmon (7) have investigated aeroheating phenomena associated with small roll-control fins on conical vehicles. In spite of these numerous studies, the ability to predict separated flow phenomena either by means of analytical solutions or on the basis of subscale tests is still very limited.

The general purpose of this investigation was to study the separated flow field associated with a general fin-body or wing-body

juncture. Specific objectives included: (a) determining the severity and extent of interference heating, (b) providing flow visualization experiments to illustrate the flow structure, and (c) gathering a data base of heat-transfer and surface-pressure measurements upon which to develop future analytical relations to predict peak interference heating and peak pressure levels. A fin-cone configuration was tested at Mach 5 over a range of several Reynolds numbers. Heat transfer in the interference flow field was measured using the phase-change paint technique. Surface pressures were measured on the fin leading edge and on the cone ahead of the fin. These quantitative measurements were used in conjunction with both schlieren and oil-flow photographs in an effort to characterize the fin-cone interference flow field.

MODELS AND TEST PROCEDURES

Tests were conducted in the NAVSURFWPNCEN, White Oak Laboratory Hypersonic Tunnel (Reference (8)) at a nominal free-stream Mach number of 5 over a range of free-stream unit Reynolds numbers of about 4.5, 13, and 26 million per foot. Two geometrically identical fin-cone models were fabricated from existing conical models, one made of teflon with a metal insert and a stainless-steel tip and the other of stainless steel. Both models consisted of a sharp, five-degree half-angle cone with two aft-mounted, cylindrically blunted fins 180 degrees apart, one unswept and one swept 60 degrees with respect to the cone surface normal. A schematic diagram of the models is shown in Figure 1. Photographs of both models are provided in Figures 2 and 3. The fins are adjustable by means of setscrews in a direction normal to the cone surface to simulate a control hinge configuration. For all test conditions, the cone was maintained at zero angle of attack and zero

yaw and the fins were at zero cant. In all of the tests the models were injected into the flow rapidly using the hydraulic ram feature of the Hypersonic Tunnel after the desired test conditions had been established in the test cell. The teflon model was utilized in the phase-change paint heat-transfer tests and in the oil-flow visualization experiments. The extension and fins were made of dark gray teflon to provide better contrast with the paints, many of which dry to a light opaque color. The stainless-steel model was used in the pressure distribution tests.

Heat-Transfer Measurements

Heat transfer in the interference flow field was measured by means of a temperature-sensitive paint method, specifically the phase-change paint technique pioneered by Jones and Hunt (9) at the NASA-Langley Research Center. In recent years the technique has evolved into a useful diagnostic tool which is considered capable of providing reliable quantitative heat-transfer data. It is especially applicable to complex geometries with interference heating patterns of unknown severity and extent. The phase-change paint technique and extensions of the method are well documented; for example, see References (9) and (10). Use of the technique at NAVSURFWPNCEN, White Oak Laboratory is documented in Reference (11). Basically, the method consists of coating a model with a paint which is rated to change phase, i.e., melt, from a dry crystalline opaque solid to a clear liquid irreversibly at a specific rated temperature. The model is injected into the flow and progression of the melt line location is recorded on movie film. This time input used in conjunction with the thermophysical properties of the model material determines the heat-transfer coefficient,

h, in the data reduction scheme. The model is assumed to behave like a semi-infinite slab and to undergo a step increase in heat transfer to a constant value of heat-transfer coefficient at any given point on its surface upon being exposed to the flow. The data reduction is based further on the assumption that the coating and the model surface are at the same temperature at the same time. That is, there is no latent heat of melting associated with the phase-change coating. Therefore, only a very thin (0.001 inch or less) coating is necessary. To achieve this condition, the paints were thinned using a special thinner specified by the manufacturer (Tempilaq Thinner and Tempilaq Phase-Change Paints by the Tempil Corporation), and were applied fairly uniformly to the model by means of an airbrush. These particular temperature-sensitive paints are considered well suited for short-duration high-speed wind-tunnel tests. They have been found to be insensitive to ambient pressures or heating rates in exhibiting their rated melting temperatures (9). Calibration checks (11) at NAVSURFWPNCEN, White Oak Laboratory showed the paints to melt at temperatures in good agreement with those specified by the manufacturer.

Another necessary input for the phase-change paint data reduction scheme is the initial temperature of the model. This information was provided by four embedded thermocouples in the teflon model, one in each fin and one in the cone ahead of each fin. Secondarily, these thermocouples provided a check on when the semi-infinite slab approximation was violated.

Teflon was chosen as the model material partly because of its low thermal diffusivity which enhanced its semi-infinite slab behavior. In addition, teflon was strong enough to withstand the loading

associated with rapid injection of the model, and it had a fairly high melting temperature. Also, lateral conduction effects were minimized due to its thermophysical properties.

Pressure Measurements

The stainless-steel model was instrumented with pressure taps on the fin leading edges and on the cone ahead of the fins extending about six fin thicknesses (leading-edge diameter) upstream on the fin center-line. Each tap had its own strain-gage-type pressure transducer mounted in a multiple transducer bank. Selected pressure taps were monitored during a test run to assure that the data reflected full response of the taps.

Oil-Flow Tests

Oil-flow tests provide visual data on surface shear directions on a model surface. A 350-centistokes silicone oil was used with titanium oxide powder in suspension to provide white pigmentation. The oil mixture was applied to the model in a direction transverse to the free-stream flow direction. The model was rapidly injected into the flow and photographs were taken with the tunnel running once the desired patterns had developed.

Schlieren Photographs

Schlieren photographs were obtained using the flow visualization system of the Hypersonic Tunnel (8).

Further details on all of these test conditions and procedures are available in References (11) and (12).

EXPERIMENTAL RESULTS AND DISCUSSION

Results are presented for two fin-cone configurations, namely for the fins mounted flush on the cone and for the fins gapped 0.125-inch

off the cone surface. The low Reynolds condition is represented the most, mainly because it comprises a very complete set of data overall. The reader is referred to Reference (12) for additional data at the higher Reynolds numbers and at an intermediate fin-cone gap of 0.060 inch.

Examination of the flow visualization data provides insight to the heat-transfer and pressure distribution patterns to be presented subsequently. Schlieren photographs are shown in Figure 4 for the flush-mounted fins and in Figure 5 for a 0.125-inch fin-cone gap. The cone bow shock did not impinge on the fins in any of the tests, by design. Figure 4 shows that the flush-mounted unswept fin with its strong bow shock causes a separation-induced shock wave which impinges on the fin leading edge. The flush 60-degree-swept fin is sufficiently swept that very little upstream separation is apparent. When the fins are gapped off the surface as they might be in a control-hinge configuration, it appears that in Figure 5 the flow displays complex inlet flow patterns in the gap. The unswept fin shows a very complex pattern of reflected shocks. The swept fin displays flow attachment at its leading tip followed by some reflected shocks. In both schlieren photographs, weak shock waves are seen to propagate from the interface of the original cone and the finned extension.

Figure 6 shows a side-view oil-flow photograph for the flush-mounted fins. Recall that the oil is swept away in regions of high shear and pools along lines of flow separation. The lateral extent of the separated flow region associated with the unswept fin is immediately obvious. An oil accumulation line on the side of the unswept fin indicates flow separation associated with a corner vortex pattern. Figures 7 and 8 provide additional visual information for this

fin-cone geometry by showing top views of the unswept and swept fin, respectively. The viewing angle is along a cone surface normal. In Figure 7, the existence of two separation lines is apparent. The primary separation line occurs about 2.2 fin leading-edge diameters (fin thickness, d) upstream of the unswept fin's leading edge. This line marks the initial flow separation of the cone boundary layer due to the adverse pressure gradient caused by the fin bow shock. This behavior of separation about 2d upstream appears to be characteristic of turbulent boundary-layer separation ahead of blunt fins of height and thickness greater than the local boundary-layer thickness over a Mach number range of about 1.2 to 2.1 independent of Reynolds number (13). The behavior apparently carries over from fin-plate to fin-cone geometries for the conditions indicated.

In Figure 7 a secondary separation line occurs about 0.7d upstream. The region between the primary and secondary separation lines is usually called "separated flow" while the region between the secondary separation line and the fin is called "reattached flow" (5, 14). A local spot from which there is apparent outward flow occurs about 1d upstream. A similar flow attachment point was observed by Winkelmann (4, 5), and will be noted later in the heat-transfer data. Lastly, in Figure 7 there is evidence of herringbone oil-flow patterns outboard of the fin. These patterns are indicative of vortical patterns trailing off downstream from the fin centerline interaction region which includes horseshoe vortices (3, 4).

In Figure 8 both primary and secondary separation occur within about 0.3d upstream of the swept fin. (Evident in the figure is an epoxy-plaster plug in the fin leading edge, which was necessitated

by loss of a teflon plug in an earlier test. The plug had originally provided access to the fin thermocouple.) The reduced lateral extent of outboard disturbance is evident by merely sweeping the fin a sufficient amount.

Figure 9 shows the oil-flow side view for the 0.125-inch gap. The flow interacts strongly with fin-hinge corner resulting in pronounced regions of high shear on the sides of both fins. In Figure 10, which is a top view of the gapped unswept fin, primary separation now occurs only about 1d upstream. The secondary separation line is not well defined near the fin leading edge due to the complex flow pattern associated with the gap. When the flow in the gap interacts with the fin hinge, a separation line appears which has a very interesting and unusual changing curvature as it moves outboard. Once again the herringbone patterns are very evident. The changing curvature of this hinge separation line is probably the result of its interaction with the vortical patterns from the upstream separation regions. The top-view oil-flow photograph for the gapped swept fin, Figure 11, shows clearly how the flow now interacts with the fin hinge, creating an outboard disturbance region comparable to that of the unswept flush-mounted fin. Also note that primary separation did not occur until the flow was in the gap.

Heat-Transfer Measurements

Keeping in mind the oil-flow patterns, consider now the heat-transfer results. The reduced phase-change paint data are presented as lines of constant heat-transfer coefficient, h, so-called isoheating contours. Figures 12 and 13 show side and top views, respectively, of the flush-mounted unswept fin. In Figure 13 the viewing angle is

about 10-degrees forward of a normal to the cone surface at the fin leading edge. (This angle view was an attempt to obtain more detail about the leading-edge heating. The slight inclination was a physical constraint of the tunnel windows and model position. The additional leading-edge detail was not achieved due to the rapid heating rates.) Regions of high heating comparable to that near the leading edge (as shown in Figure 12) are shown to occur in a crescent-shaped region at the fin "foot" and at the flow reattachment point about 1d upstream. High heating at this point 1d upstream identifies it as a high-shear region, or as a point where flow is entrained and brought into contact with the cone surface. This appears to be contrary to Winkelmann's conclusion (5) that this reattachment point is a low-shear or "dead air" region.

Isoheating contours for the swept fin are shown in side and top views in Figures 14 and 15, respectively, for the same flow conditions. Both the level of and extent of interference heating are greatly reduced. The dotted lines on the leading edge of the fin in Figure 14 indicate where the plug was located. The maximum h-value is down about 25 percent on the leading edge and that on the cone is down about 40 percent from the unswept fin case. This is purely a sweep effect.

Figures 16 and 17 show isoheating contours for the gapped unswept fin. The fin hinge clearly shows up as having an interaction flow field with heat transfer as severe as that on and around the fin leading edge. The heating level at primary separation remains at about the same level as for the flush-mounted fin. Now, both the fin "foot" region (a misnomer since the fin is gapped here) and the hinge region

are areas of high interference heating of the same level as that shown in Figure 13 at the fin "foot".

Heat-transfer data for the gapped swept fin are shown in Figures 18 and 19. From Figure 18 it may be seen that the immediate leading-edge segment and the hinge have heating levels comparable to the unswept fin case. In contrast, however, Figure 19 indicates a marked decrease in the interference heating level on the cone to about 60 percent of that for the gapped unswept fin.

The general conclusion to be drawn from Figures 12-19 is that sufficient leading-edge sweep alone produces less lateral disturbance in the form of a separated flow region and results in lower interference heating levels in the disturbed region on the centerbody. The values of heat-transfer coefficient are considered to be accurate to within about 20 percent based on analyses presented in Reference (11).

Cone Surface-Pressure Distribution

Again recalling the oil-flow patterns of Figures 6-11, consider the surface-pressure distributions measured on the cone ahead of the fins. Figure 20 shows the flush-mounted unswept fin. The surface pressures are normalized by the undisturbed cone value, which was sensed generally by several of the most upstream taps. The abscissa is distance along the fin-centerline cone ray referenced to the fin leading edge and normalized by the fin leading-edge diameter (fin thickness, d). Data are shown for three Reynolds numbers. The pressure begins to rise a little more than 2d upstream, corresponding to the point where primary separation occurs. It rises to a slight peak, then dips, and rises again to a high peak in the fin foot region about 0.25d upstream of the leading edge. The peak pressure in the fin

foot region is about 10 times the undisturbed level. Winkelmann (4) observed peak pressure ratios about six times the undisturbed value for his fin-flat plate configuration. The peak pressure region corresponds to the crescent-shaped peak heating region of Figure 13. The reattachment zone 1d upstream, which had earlier been found to be a high heating region, corresponds here only to a point where the pressure dips after the initial rise. The pressure ratios at the point of separation and the curves in general are not construed to represent a definite Reynolds number effect. Rather, the differences are thought to be indicative of flow unsteadiness and instability associated with the separated flow region and the likely scavenging action of the horseshoe vortices (3, 4).

Figure 21 shows the corresponding pressure distribution on the cone ahead of the swept fin. As expected, there is almost no upstream disturbance.

Figure 22 shows the gapped unswept fin and Figure 23 shows the gapped swept fin. Pressure taps existed in the fin-cone gap as shown. In both cases the flow moves into the gap and displays its peak pressure in the gap. In Figure 22 the peak pressure level, down from 10 to 8, occurs just inside the gap. In question here is the exact location of the peak with respect to the tap location. After this first pressure peak the flow appears to begin to interact with the hinge, but insufficient data exist. It may be noted that the initial pressure rise is observed to begin about 1d upstream of the unswept leading edge, corresponding to the location of the primary separation line in Figure 10.

In Figure 23 there is no upstream disturbance for the swept fin. An attenuated pressure peak occurs about 2d into the gap. This

lower peak pressure corresponds to the lower peak heating indicated in Figure 19.

Fin Leading-Edge Pressure Distributions

Figure 24 shows the leading-edge pressure distribution for both of the flush-mounted fins. Distance, z, along the cone surface normal at the plane of the leading edge is nondimensionalized by the fin leading-edge diameter. The pressures are normalized by the free-stream static pressure. The relative difference in the pressure levels is explained by oblique shock theory. The bulge in the pressure distribution on the unswept fin's leading edge corresponds to the impingement of the separation-induced shock wave which appears in the schlieren photograph of Figure 4 to occur at about $z/d \approx 0.9$. No pressure tap exists at $z/d = 0.5$ in the swept fin because of physical limitations in fabricating the fin.

The fin leading-edge pressure data for the gapped fins are shown in Figure 25. There is slight evidence of flow interaction on the unswept fin. There is little detail in Figure 5 to identify this bulge. In general, the relative levels remain the same as before.

CONCLUSIONS

The interaction flow field on fin centerline for an unswept, cylindrically blunted fin flush mounted on a cone appears to be qualitatively similar to, but quantitatively different from, fin-flat plate and cylinder-flat plate results for similar flow conditions. The interaction is characterized by peak heating levels and corresponding peak pressures on the centerbody surface in the fin foot region. These peak pressures may be on the order of 10 times the undisturbed levels. The cone surface-pressure distributions scale with fin leading-edge diameter, d.

Separation occurs about two fin leading-edge diameters upstream of a flush-mounted unswept fin independent of Reynolds number. This behavior is characteristic of cylindrically blunted fin-flat plate and cylinder-flat plate results over a wide Mach number range (1.2 to 21) when the fin height and thickness exceed the local boundary-layer thickness (13, 3).

Fin leading-edge sweep alone significantly reduces the severity and extent of interference heating on the centerbody. However, when a swept fin design embodies a control hinge in the form of a circular rod, the flow in the fin-centerbody gap will interact with the control hinge. This interaction results in peak heating on the centerbody comparable to that for a flush-mounted unswept fin. Whereas sweeping the control hinge is not a practical solution, the severity of the flow interaction may possibly be alleviated by providing a control hinge fairing.

Certain aspects of these results indicate that fin-centerbody investigations are in order to investigate Mach number effects rather than simply applying fin-flat plate or cylinder-flat plate results. The separated flow regions outboard the fins appear to exhibit a more vortical nature. Two other cases in point for the flush-mounted unswept fin are the higher peak pressure level in the fin foot region and the high heating level associated with flow attachment about 1d upstream. Both may be indicative of greater three-dimensional scavenging action associated with a fin-centerbody configuration than with a fin-flat plate model.

REFERENCES

(1) Ryan, B. M., "Summary of the Aerothermodynamic Interference Literature," Naval Weapons Center TN 4061-160, April 1969.

(2) Korkegi, R. H., "Survey of Viscous Interactions Associated with High Mach Number Flight," AIAA Journal, Vol. 9, No. 5, May 1971, p. 771.

(3) Kaufman, II, L. G., Korkegi, R. H., and Morton, L. C., "Shock Impingement Caused by Boundary Layer Separation Ahead of Blunt Fins," ARL Report 72-0118, August 1972, and AIAA Paper 73-236.

(4) Winkelmann, A. E., "Experimental Investigations of a Fin Protuberance Partially Immersed in a Turbulent Boundary Layer at Mach 5," NOLTR 72-33, January 1972.

(5) Winkelmann, A. E., "Flow Visualization Studies on a Fin Protuberance Partially Immersed in a Turbulent Boundary Layer at Mach 5," NOLTR 70-93, May 1970.

(6) Bramlette, T. T., "A Study of Fin-Induced Laminar Interactions on Sharp and Spherically Blunted Cones," AIAA Paper 73-235, January 1973.

(7) Coleman, H. W., and Lemmon, E. C., "Prediction of Turbulent Heat Transfer and Pressure on Swept Leading Edges," Journal of Spacecraft and Rockets, Vol. 11, No. 6, June 1974, pp. 376-381.

(8) Baltakis, F. P., "Performance Capability of the NOL Hypersonic Tunnel," NOLTR 68-187, October 1968.

(9) Jones, R. A., and Hunt, J. L., "Use of Fusible Temperature Indicators for Obtaining Quantitative Aerodynamic Heat-Transfer Data," NASA TR R-230, February 1966.

(10) Hunt, J. L., Pitts, J. I., and Richie, C. B., "Application of Phase-Change Technique to Thin Sections with Heating on Both Surfaces," NASA TN D-7193.

(11) Gillerlain, J. D., Jr., "Use of Phase-Change Paints to Study Fin-Body Interference Heating," NSWC/WOL/TR 75-62 (in preparation).

(12) Gillerlain, J. D., Jr., "Experimental Investigation of a Fin-Cone Interference Flow Field at Mach 5," NSWC/WOL/TR 75-63 (in preparation).

(13) Westkaemper, J. C., "Turbulent Boundary-Layer Separation Ahead of Cylinders," AIAA Journal, Vol. 6, No. 7, July 1968, pp. 1352-1355.

(14) Young, F. L., Kaufman, L. G., and Korkegi, R. H., "Experimental Investigation of Interactions Between Blunt Fin Shock Waves and Adjacent Boundary Layers at Mach Numbers 3 and 5," ARL Report 68-0214, December 1968.

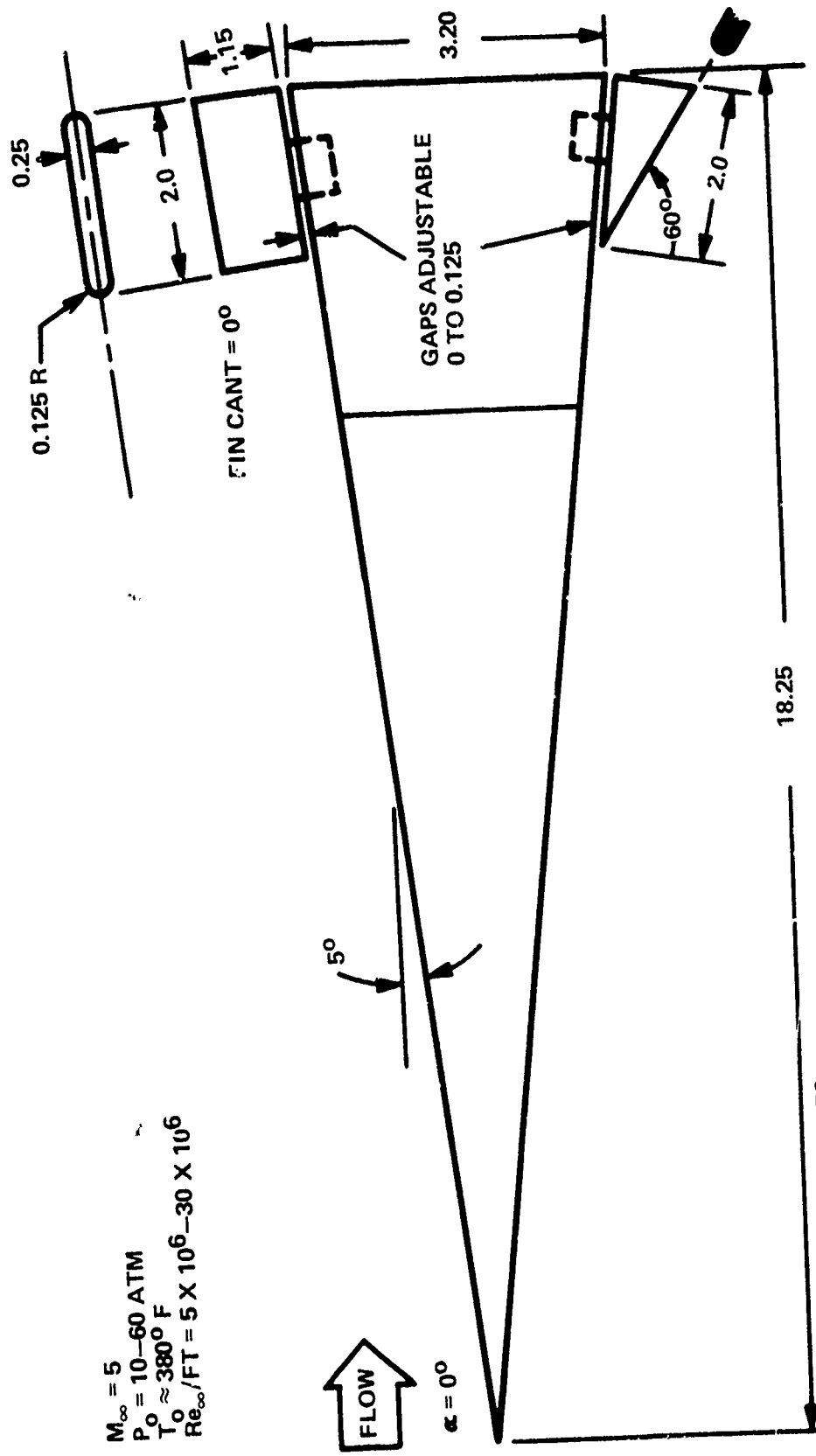

FIG. 1 SCHEMATIC DIAGRAM OF FIN-CONE MODEL

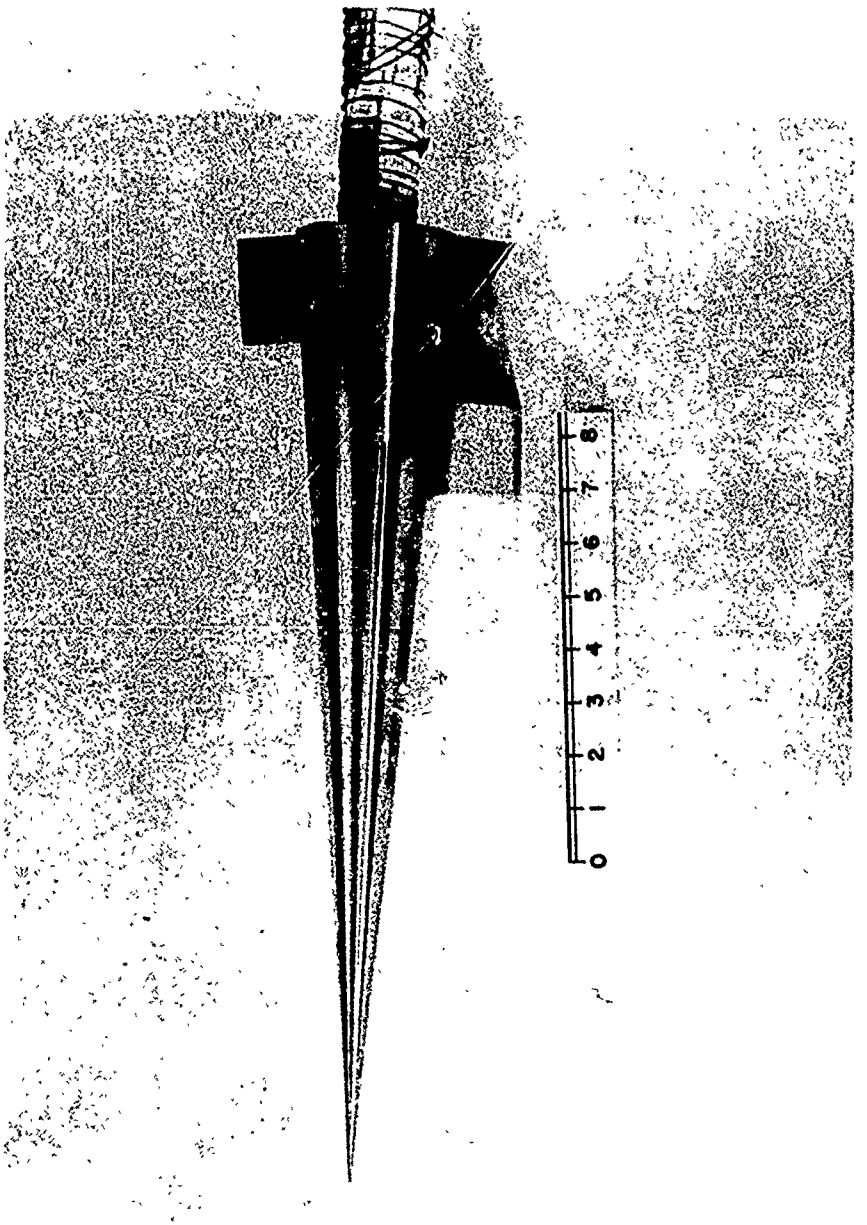

FIG. 2 STAINLESS-STEEL PRESSURE-DISTRIBUTION MODEL (SCALE IN INCHES)

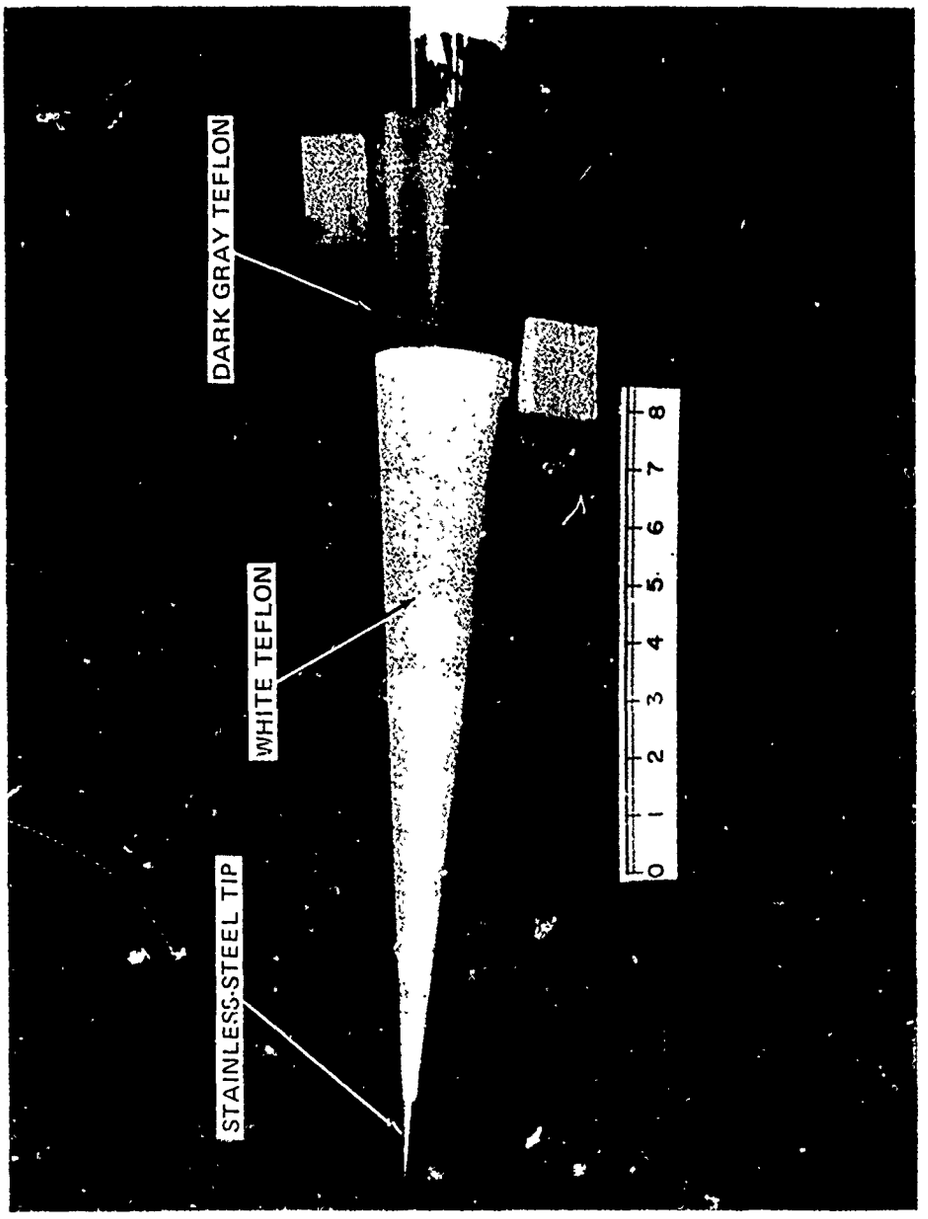

FIG. 3 TEFLON HEAT-TRANSFER AND FLOW VISUALIZATION MODEL (SCALE IN INCHES)

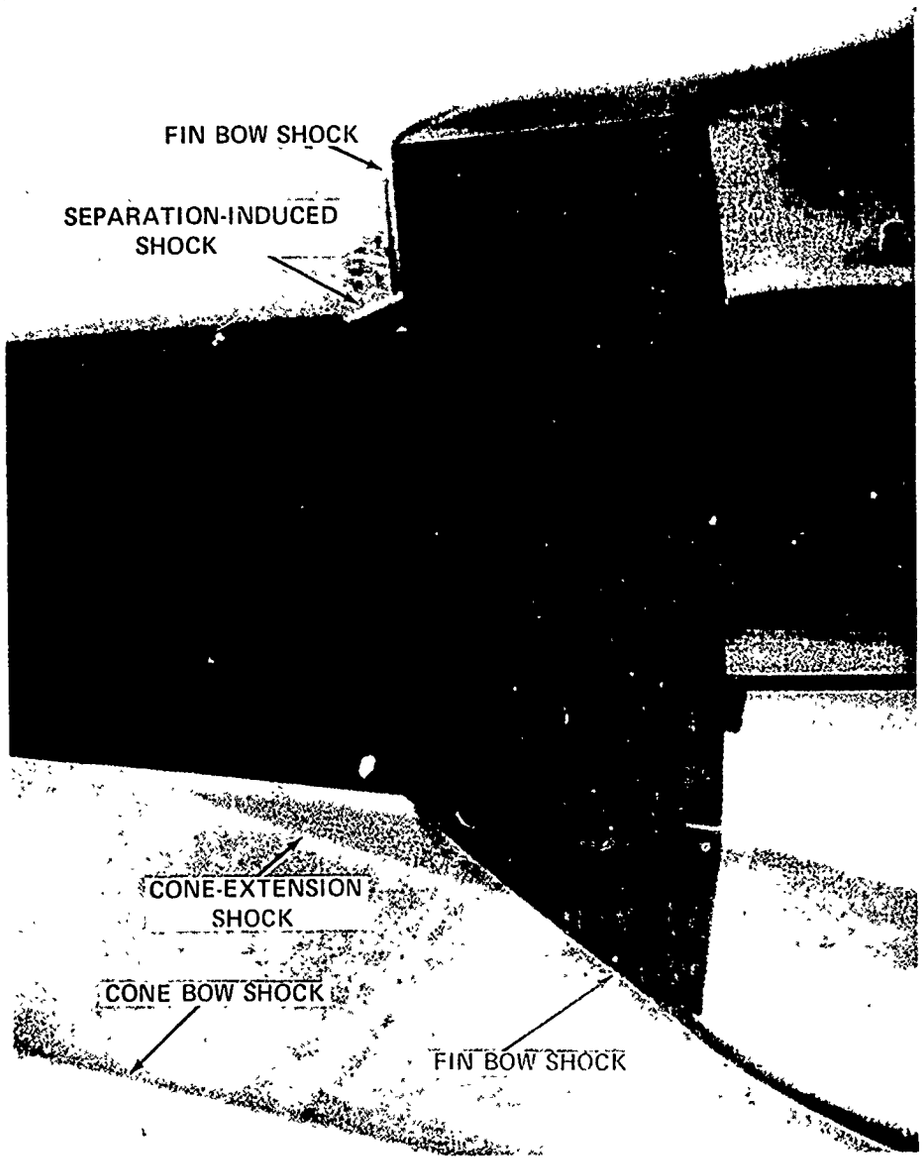

FIG. 4 SCHLIEREN PHOTOGRAPH OF FLUSH-MOUNTED FINS; $M_\infty = 5$, $Re_\infty/FT = 4.5 \times 10^6$

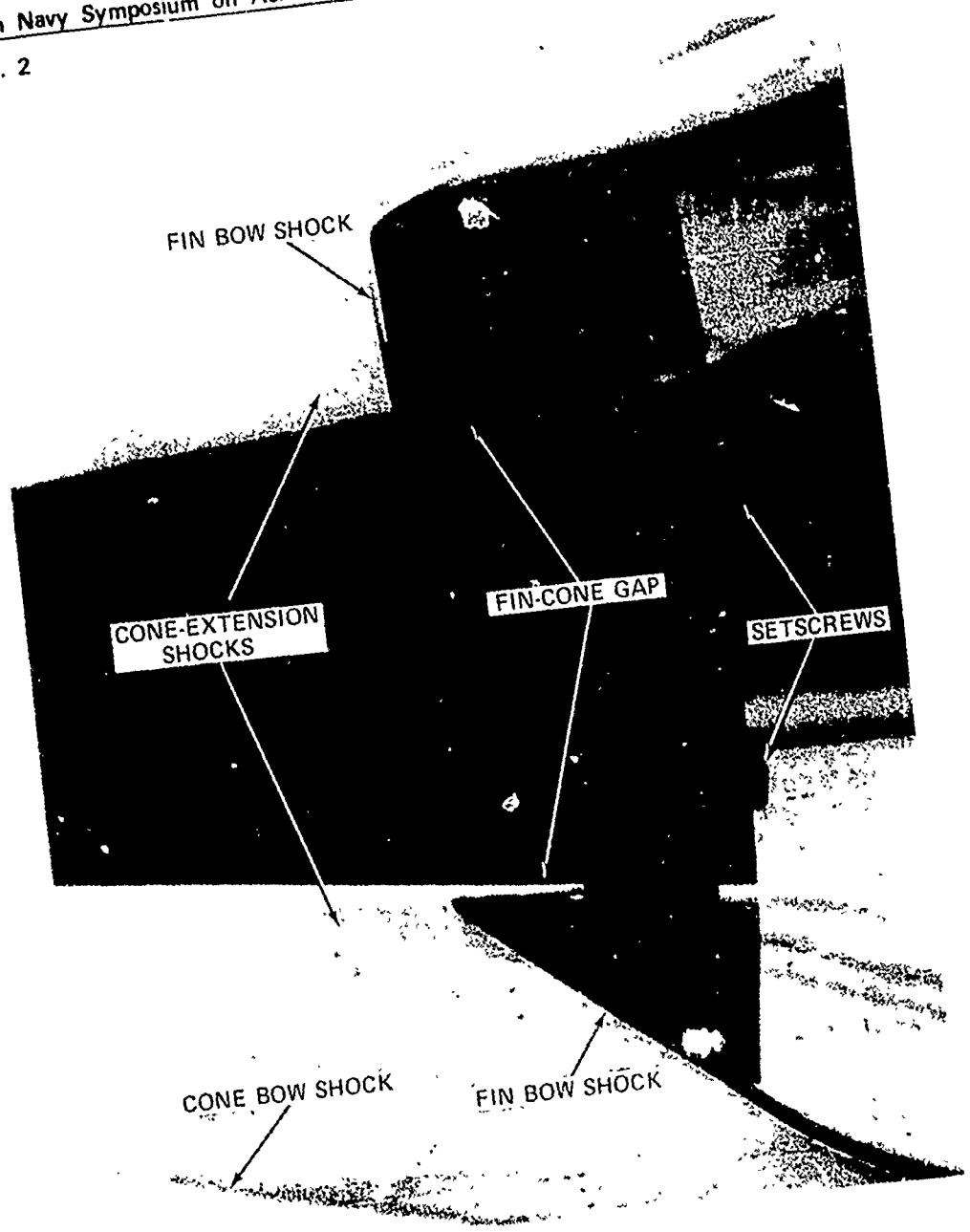

FIG. 5 SCHLIEREN PHOTOGRAPH FOR 0.125-INCH FIN-CONE GAP; $M_\infty = 5$, $Re_\infty/FT = 4.5 \times 10^6$

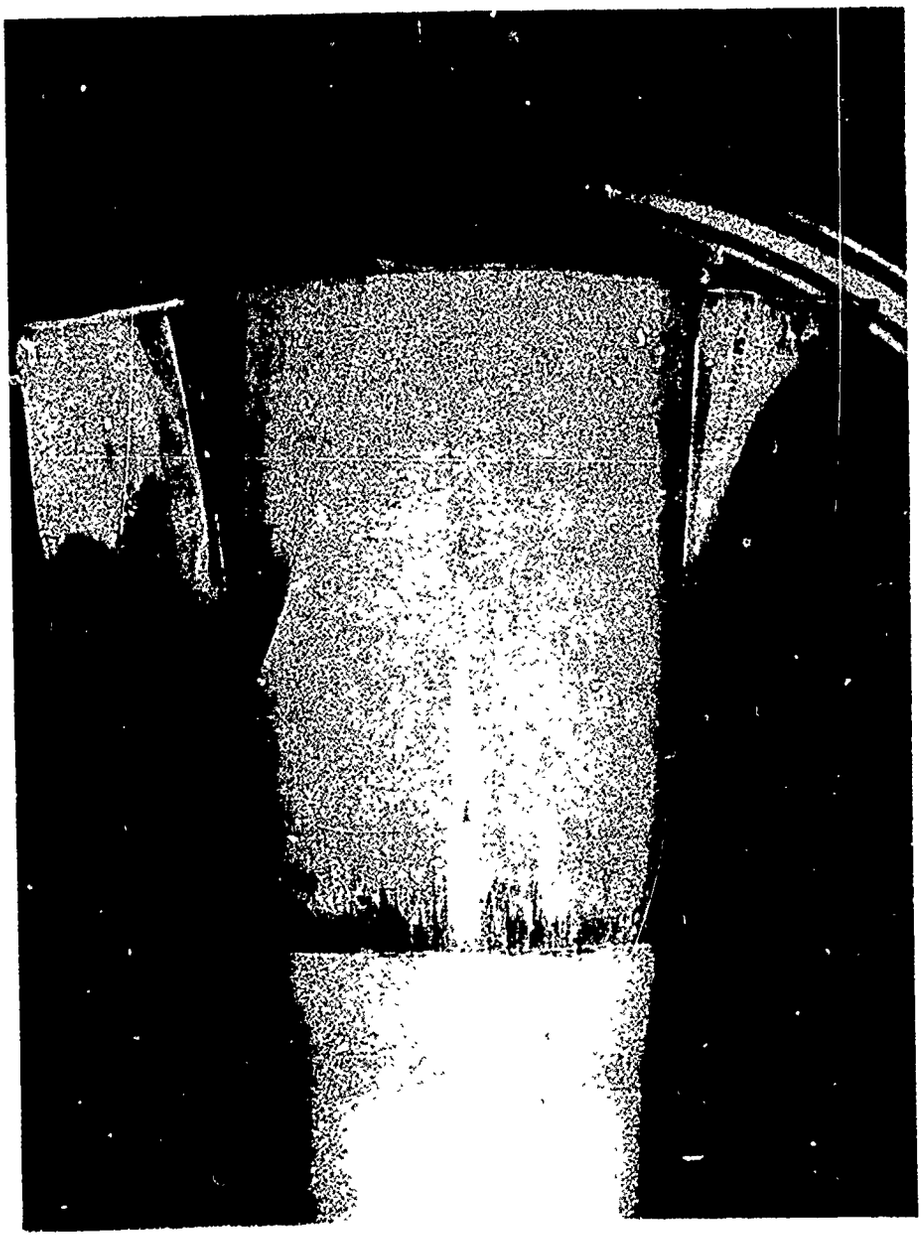

FIG. 6 SIDE-VIEW OIL-FLOW PHOTOGRAPH FOR FLUSH-MOUNTED FINS; $M_\infty = 5$, $Re_\infty/FT = 4.5 \times 10^6$

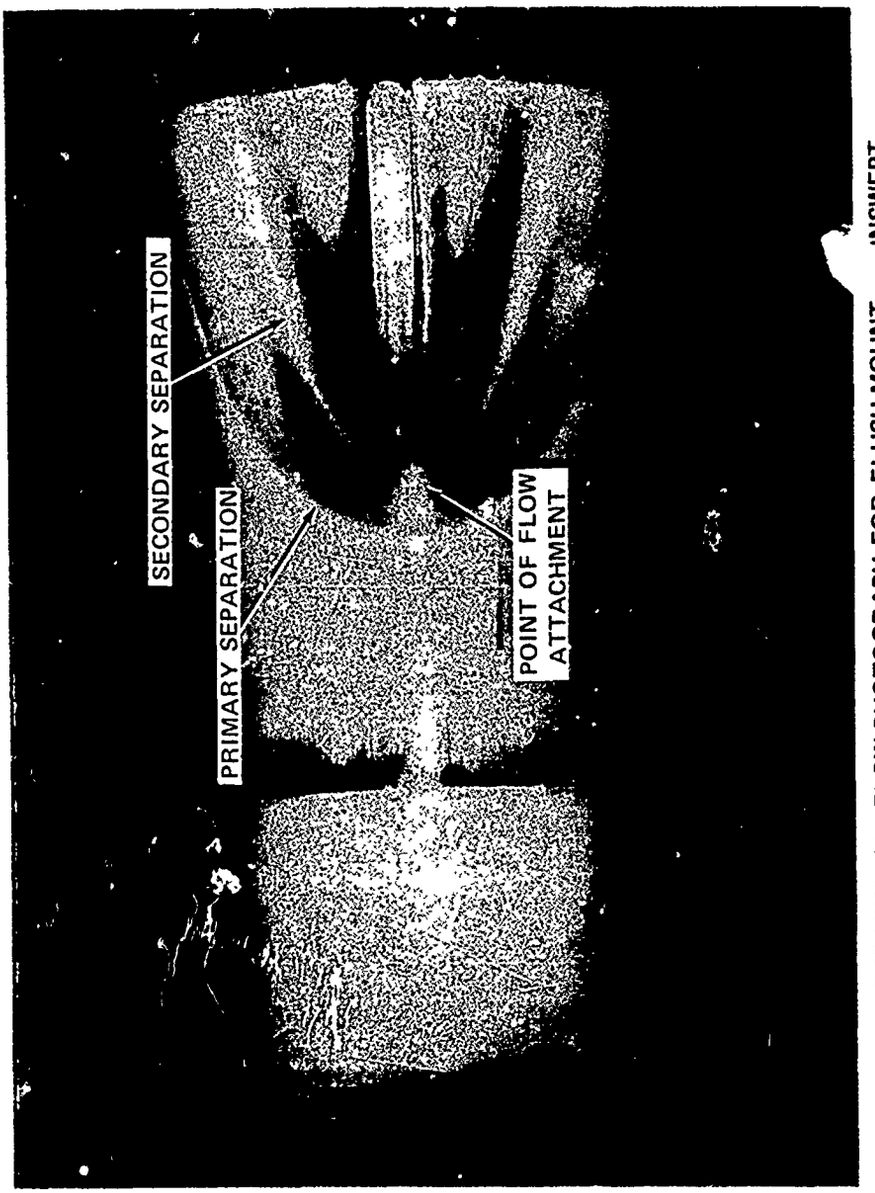

FIG. 7 TOP-VIEW OIL-FLOW PHOTOGRAPH FOR FLUSH-MOUNT, UNSWEPT FIN; $M_\infty = 5$, $Re_\infty/FT = 4.5 \times 10^6$

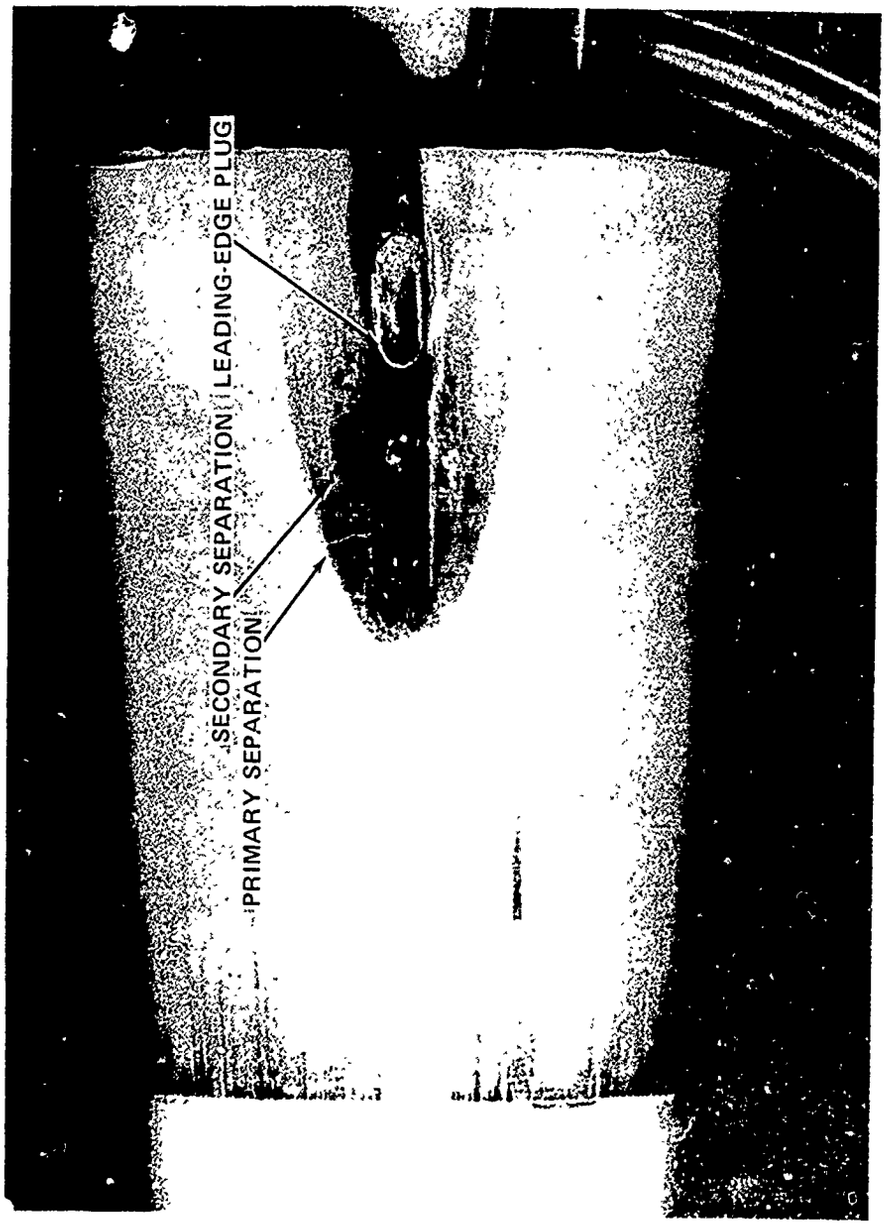

FIG. 8 TOP-VIEW OIL-FLOW PHOTOGRAPH FOR FLUSH-MOUNTED 60°-SWEPT FIN; $M_\infty = 5$, $Re_\infty/FT = 4.5 \times 10^6$

FIG. 9 SIDE-VIEW OIL-FLOW PHOTOGRAPH FOR 0.125-INCH FIN-CONE GAP; $M_\infty = 5$, $Re_\infty/FT = 4.5 \times 10^6$

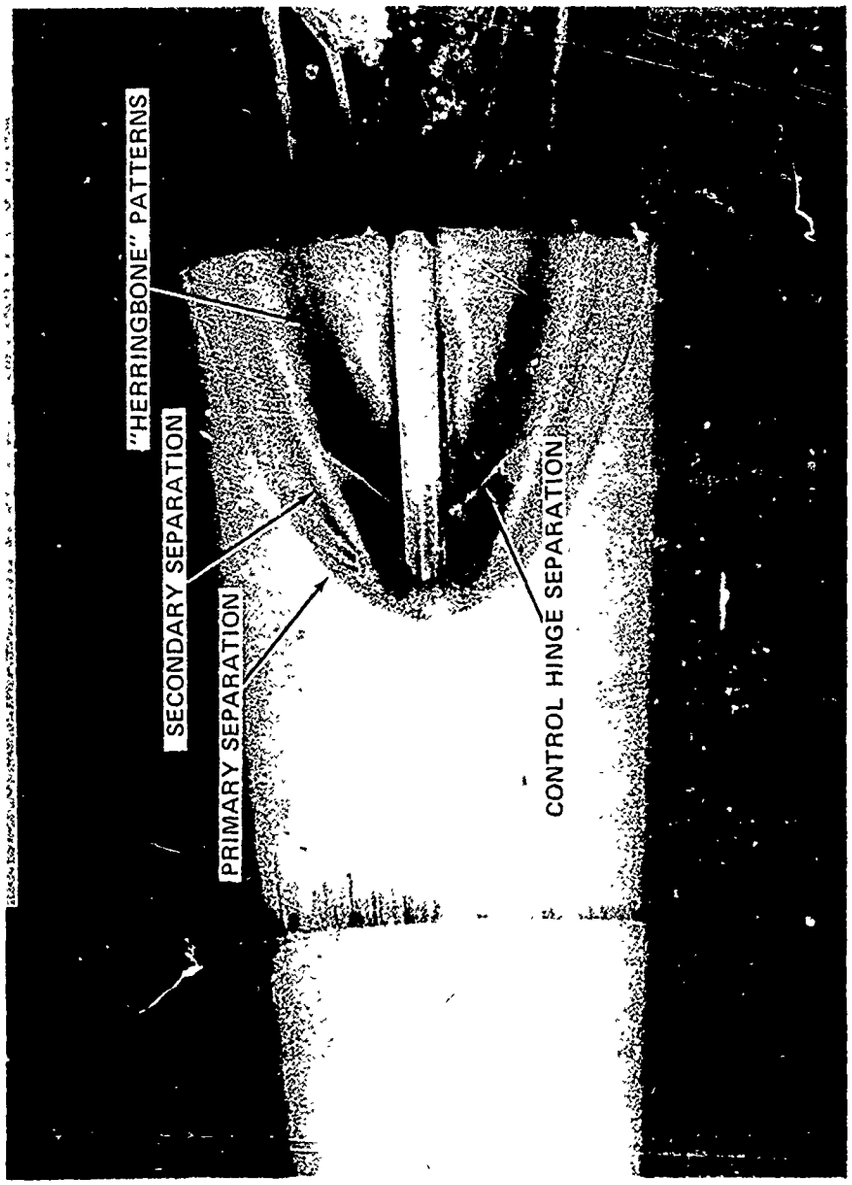

FIG. 10 TOP-VIEW OIL-FLOW PHOTOGRAPH OF UNSWEPT FIN WITH 0.125-INCH FIN-CONE GAP; $M_\infty = 5$, $Re_\infty/FT = 4.5 \times 10^6$

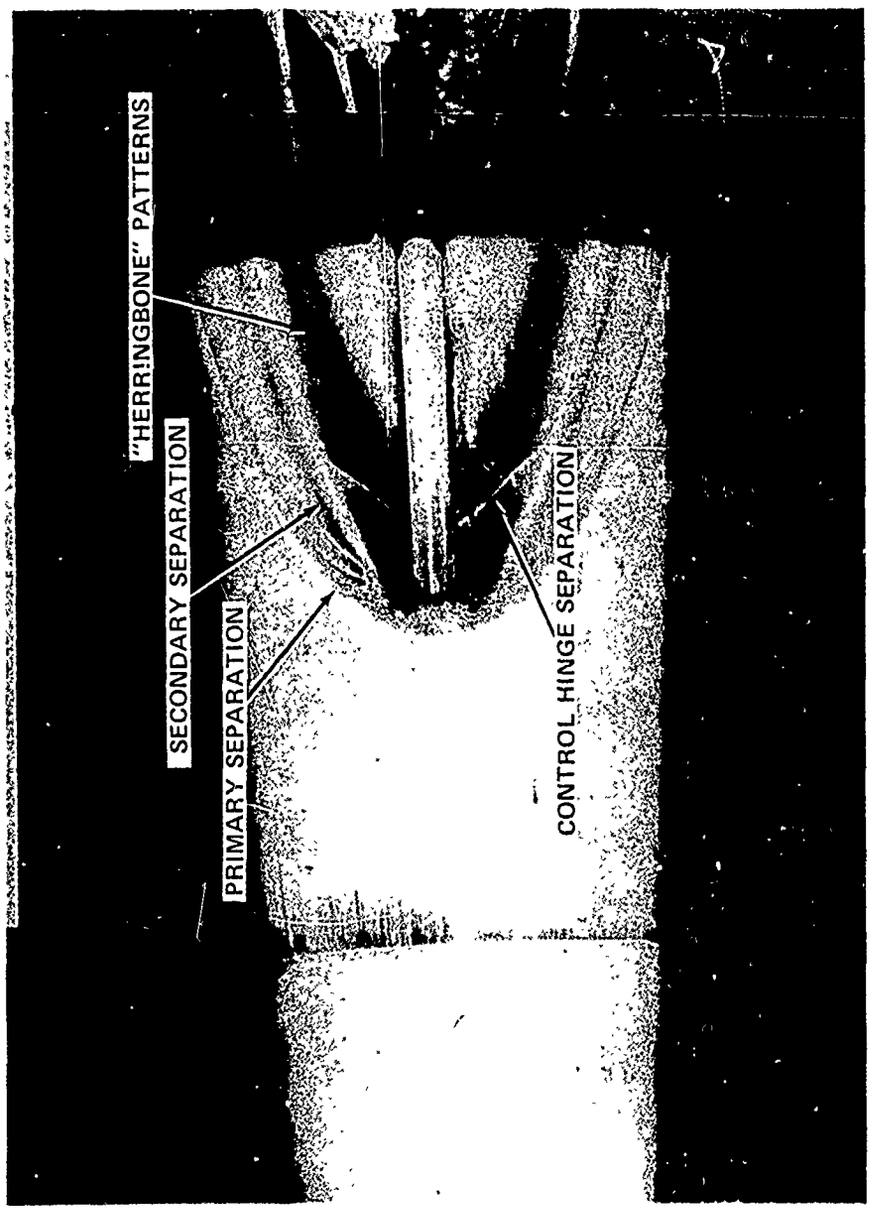

FIG. 10 TOP-VIEW OIL-FLOW PHOTOGRAPH OF UNSWEPT FIN WITH 0.125-INCH FIN-CONE GAP; $M_\infty = 5$, $Re_\infty/FT = 4.5 \times 10^6$

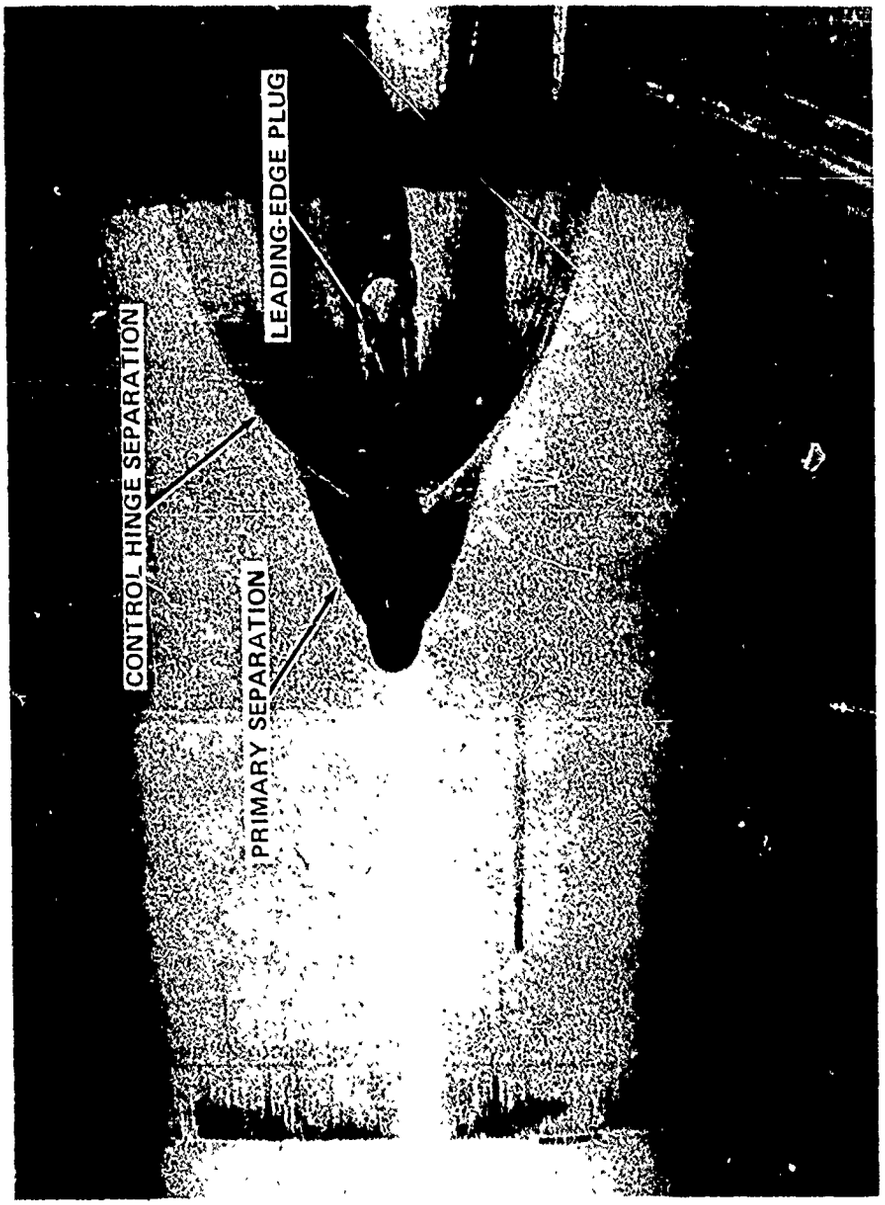

FIG. 11 TOP-VIEW OIL-FLOW PHOTOGRAPH OF 60^{0} SWEPT FIN WITH 0.125-INCH FIN-CONE GAP; $M_{\infty} = 5$, $Re_{\infty}/FT = 4.5 \times 10^{6}$

$M_\infty = 5$
$Re_\infty/FT = 4.5 \times 10^6$
GAP = 0.0"

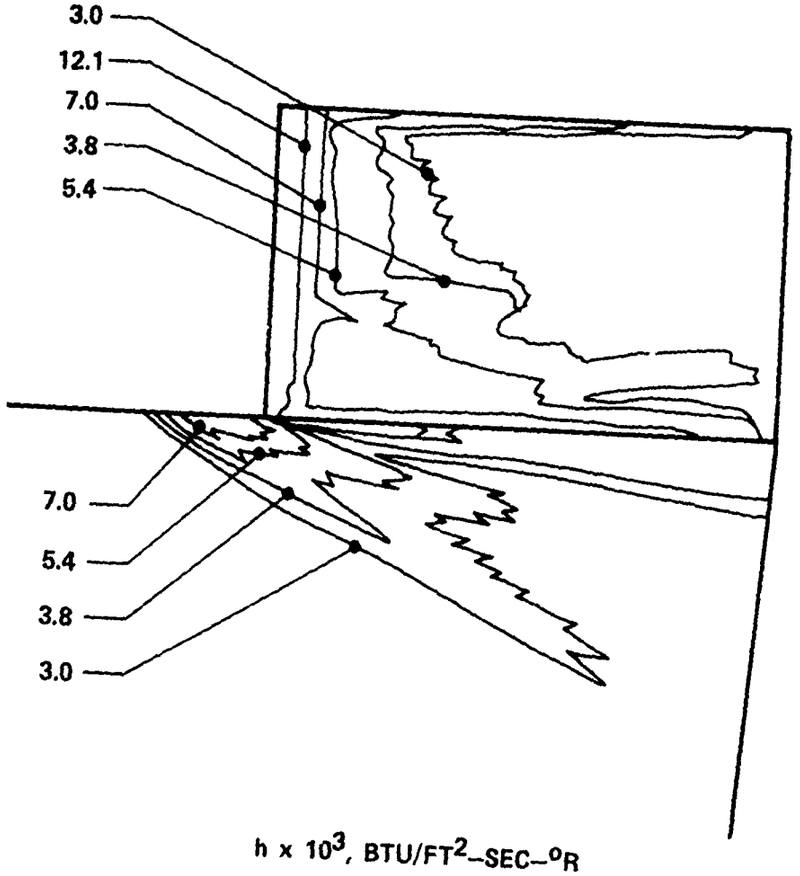

$h \times 10^3$, BTU/FT^2–SEC–^oR

FIG. 12 ISOHEATING CONTOURS FOR FLUSH-MOUNTED UNSWEPT FIN. SIDE VIEW

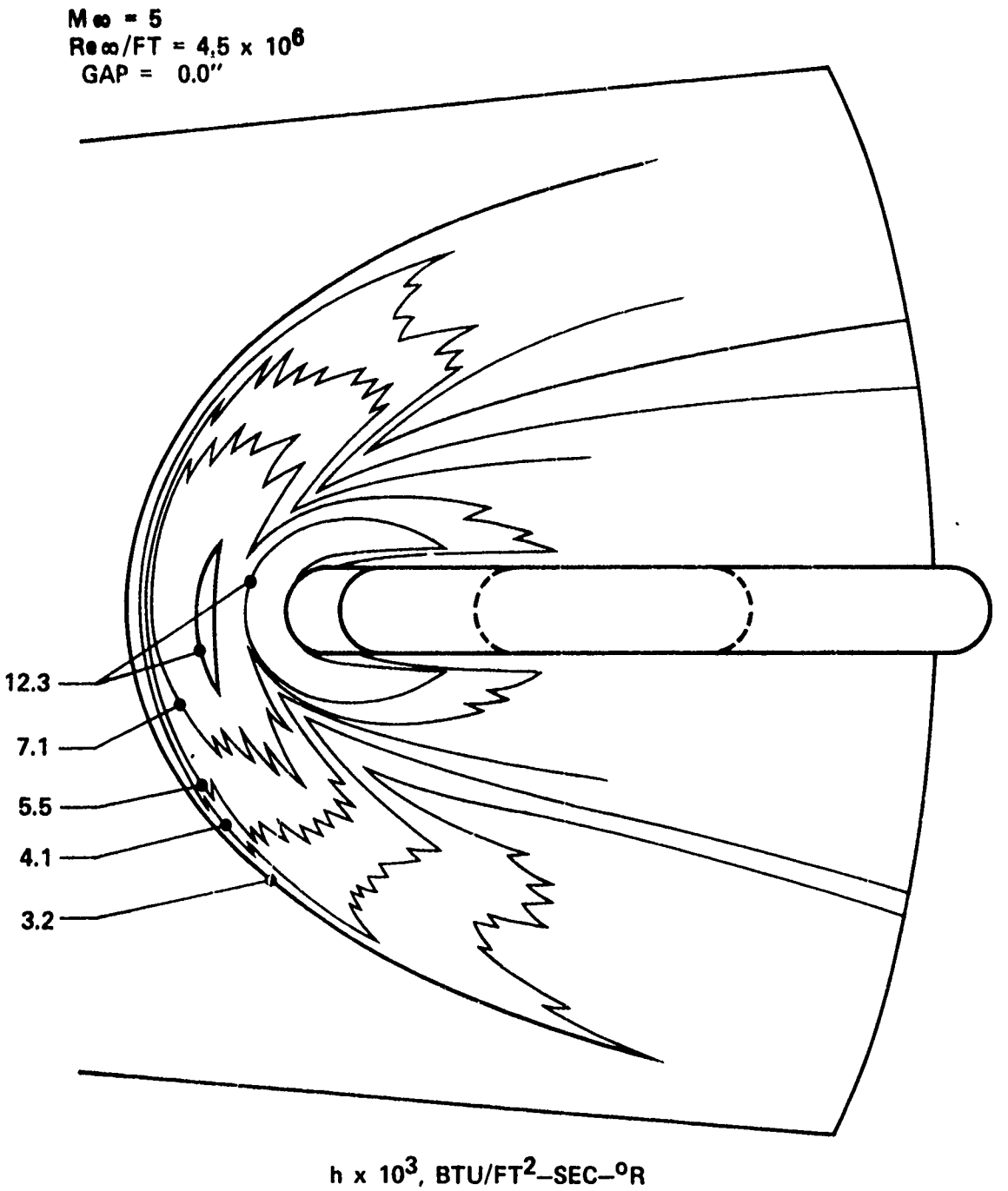

FIG. 13 ISOHEATING CONTOURS FOR FLUSH-MOUNTED UNSWEPT FIN. TOP VIEW, ABOUT 10° FORWARD OF LEADING EDGE

$M\infty = 5$
$Re\infty/FT = 4.5 \times 10^6$
GAP = 0.0"

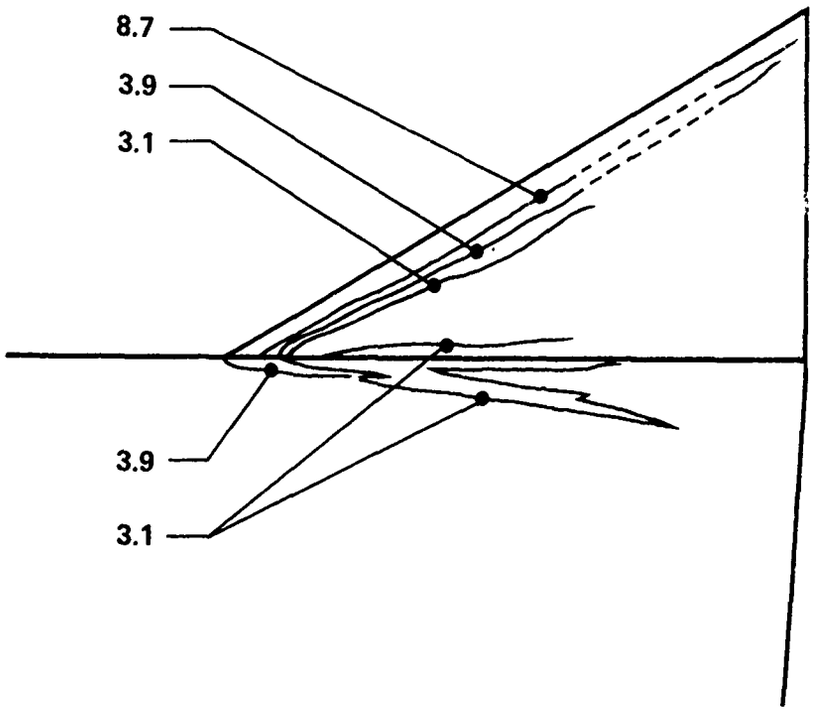

$h \times 10^3$, BTU/FT^2–SEC–^{o}R

FIG. 14 ISOHEATING CONTOURS FOR FLUSH-MOUNTED 60^o-SWEPT FIN. SIDE VIEW.

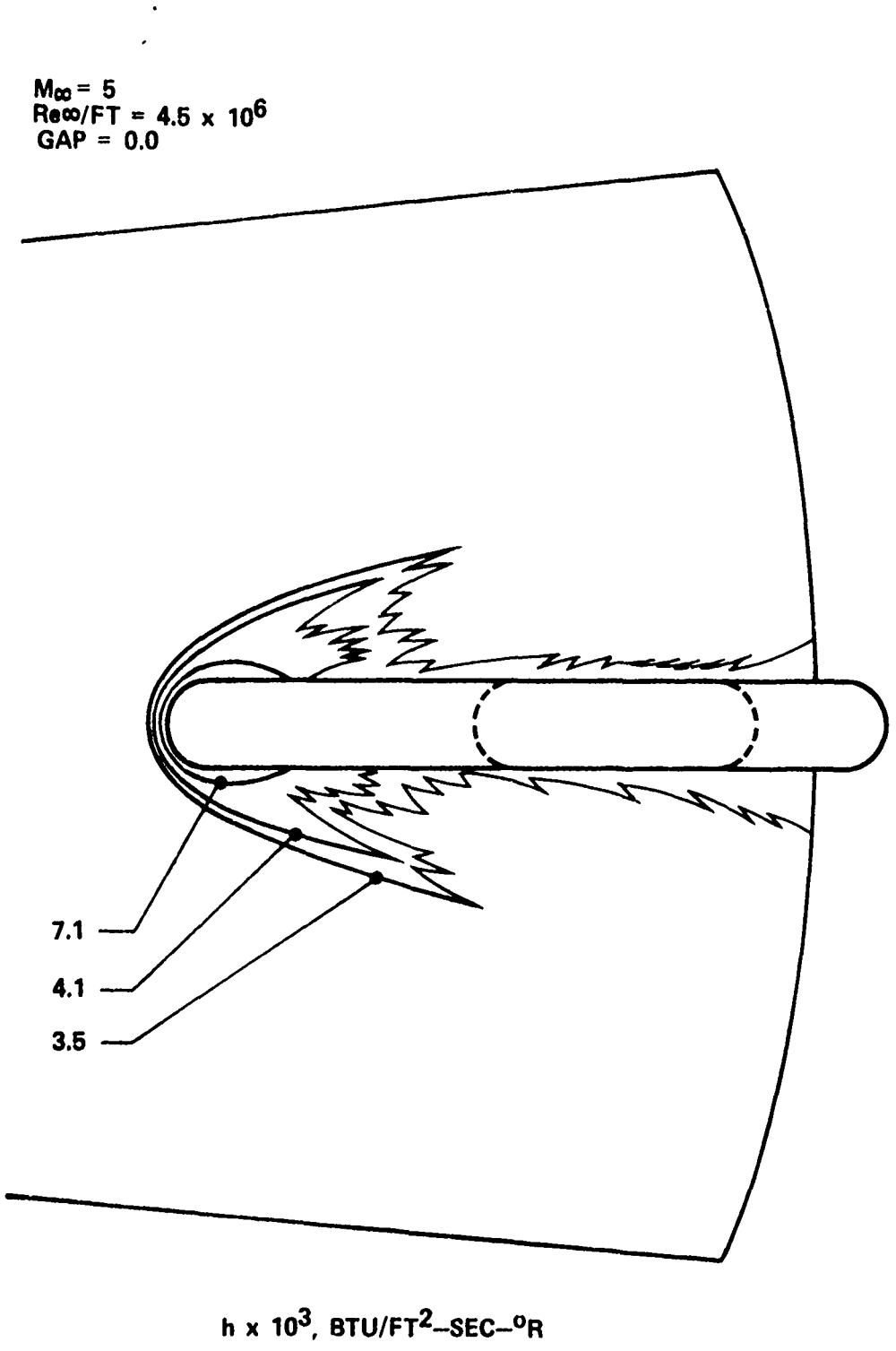

FIG. 15 ISOHEATING CONTOURS FOR FLUSH-MOUNTED 60°-SWEPT FIN. TOP VIEW

$M_\infty = 5$
$Re_\infty/FT = 4.5 \times 10^6$
GAP = 0.125"

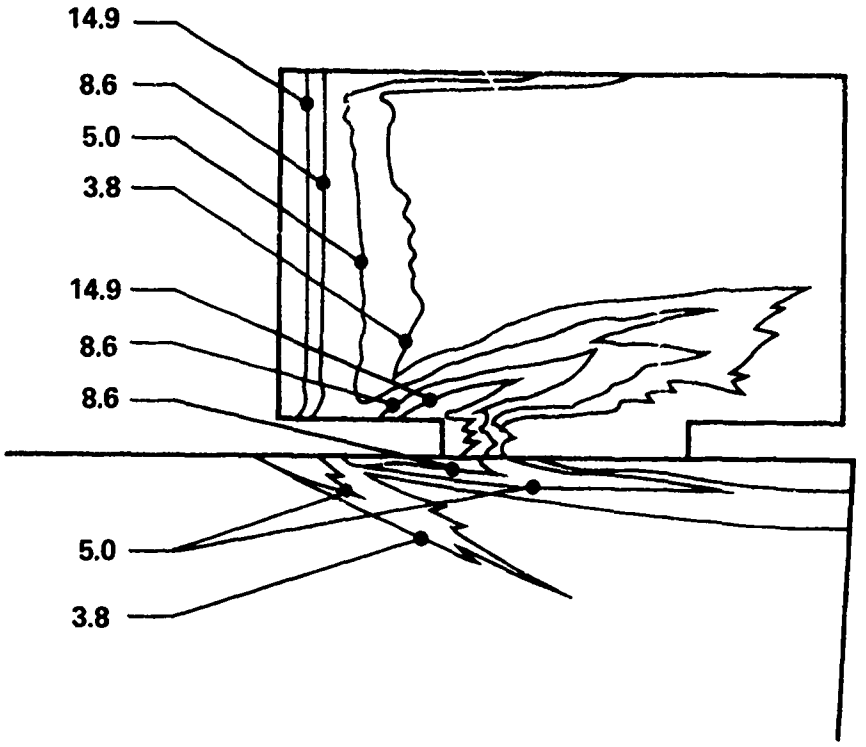

$h \times 10^3$, BTU/FT^2–SEC–^{o}R

FIG. 16 ISOHEATING CONTOURS FOR UNSWEPT FIN WITH 0.125-INCH FIN-CONE GAP. SIDE VIEW

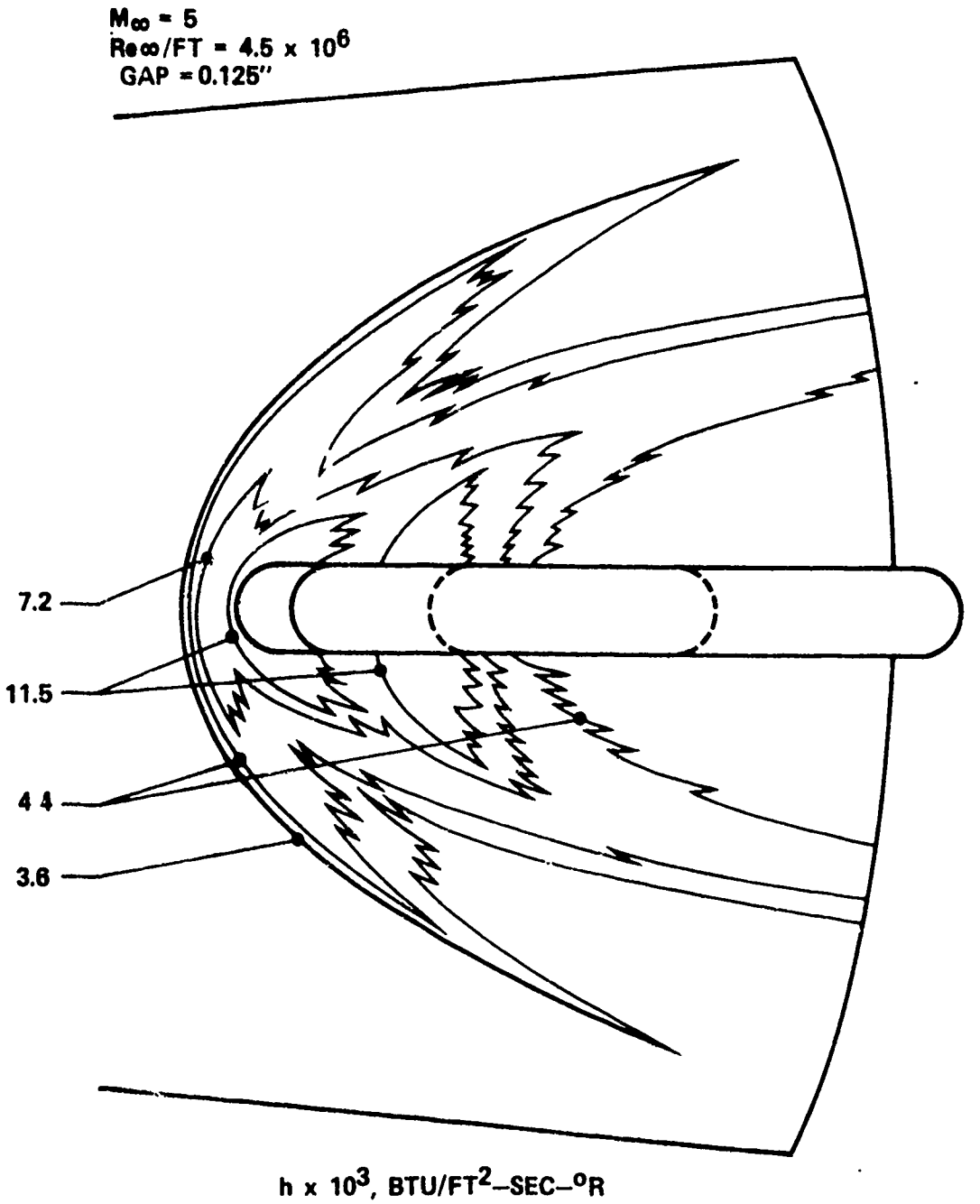

FIG. 17 ISOHEATING CONTOURS FOR UNSWEPT FIN WITH 0.125-INCH FIN-CONE GAP. TOP-VIEW, ABOUT 10^o FORWARD OF LEADING EDGE

$M_\infty = 5$
$Re_\infty/FT = 4.5 \times 10^6$
GAP = 0.125"

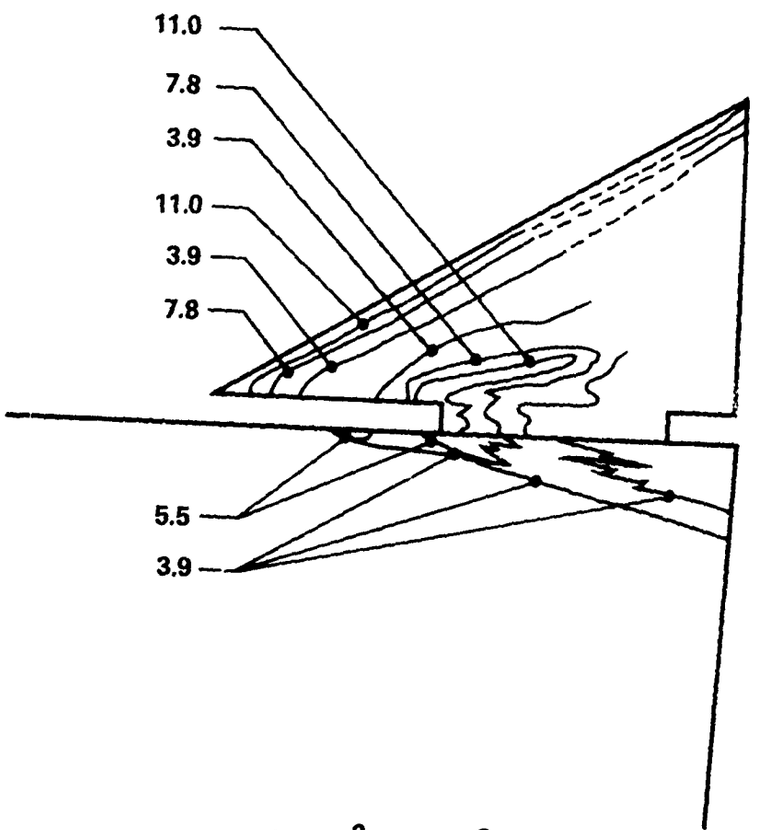

$h \times 10^3$, BTU/FT^2–SEC–^oR

FIG. 18 ISOHEATING CONTOURS FOR 60°-SWEPT FIN WITH 0.125-INCH FIN-CONE GAP. SIDE VIEW

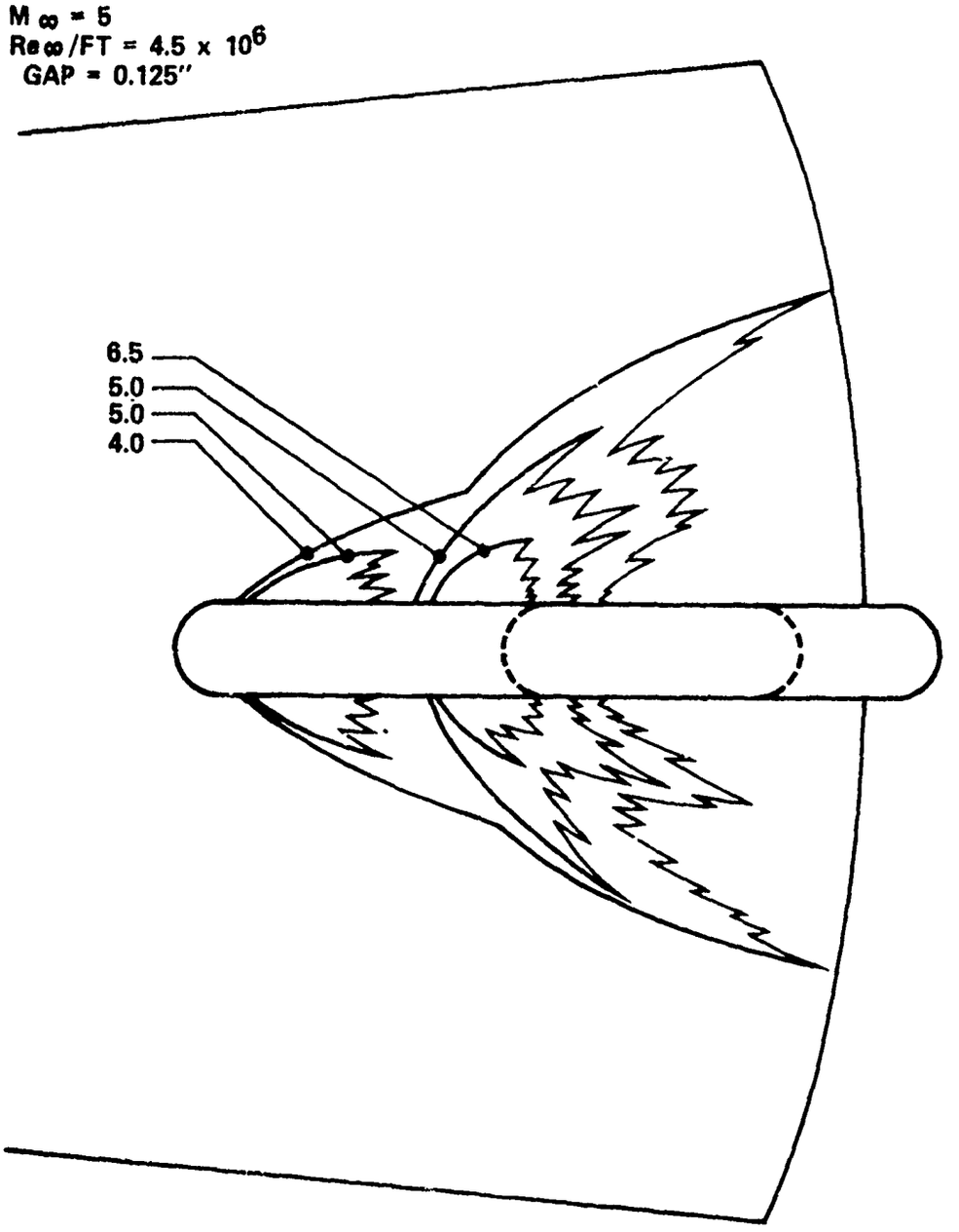

FIG. 19 ISOHEATING CONTOURS FOR 60°-SWEPT FIN WITH 0.125-INCH FIN-CONE GAP. TOP VIEW

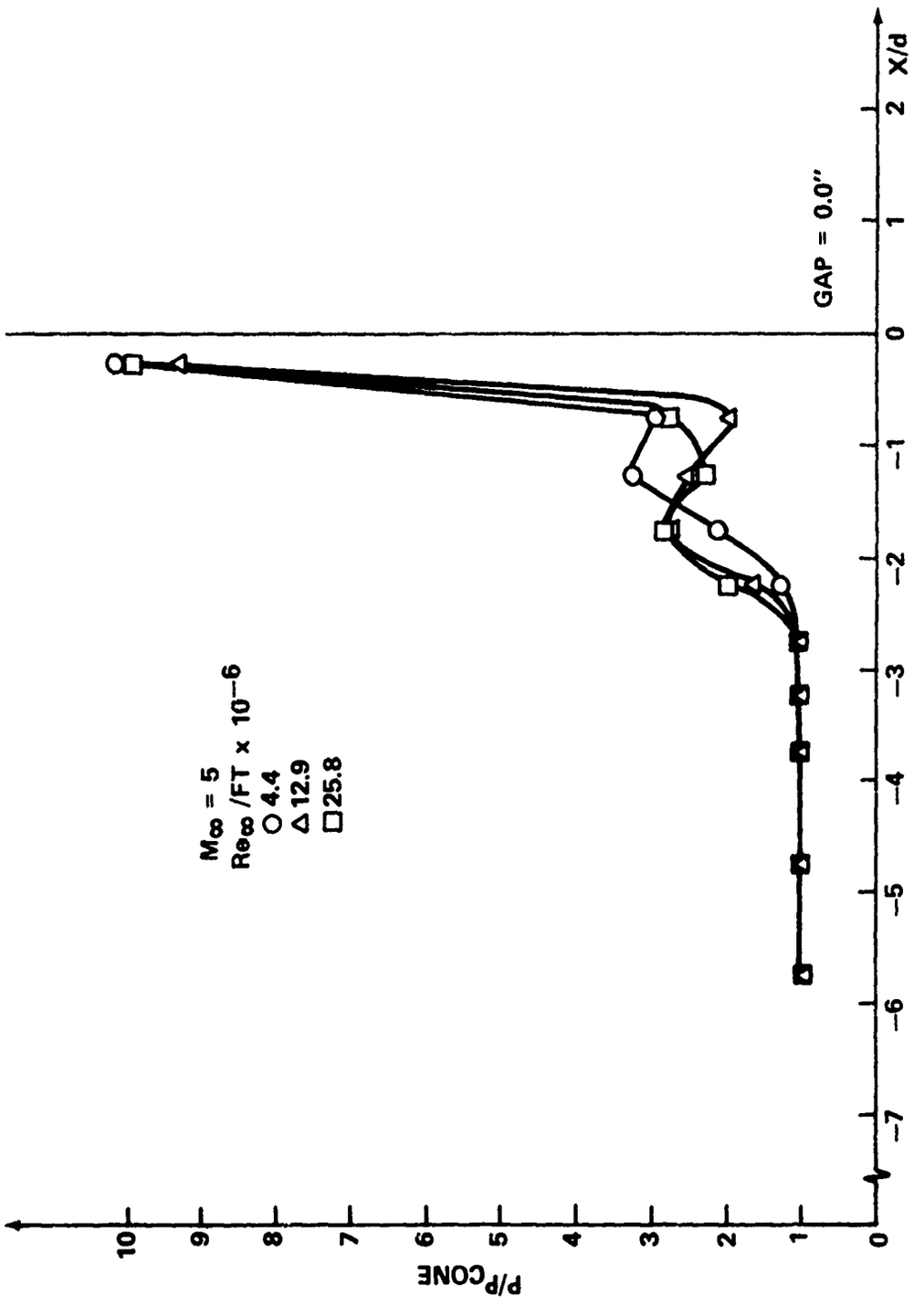

FIG. 20 PRESSURE DISTRIBUTION ON CONE AHEAD OF FLUSH-MOUNTED UNSWEPT FIN

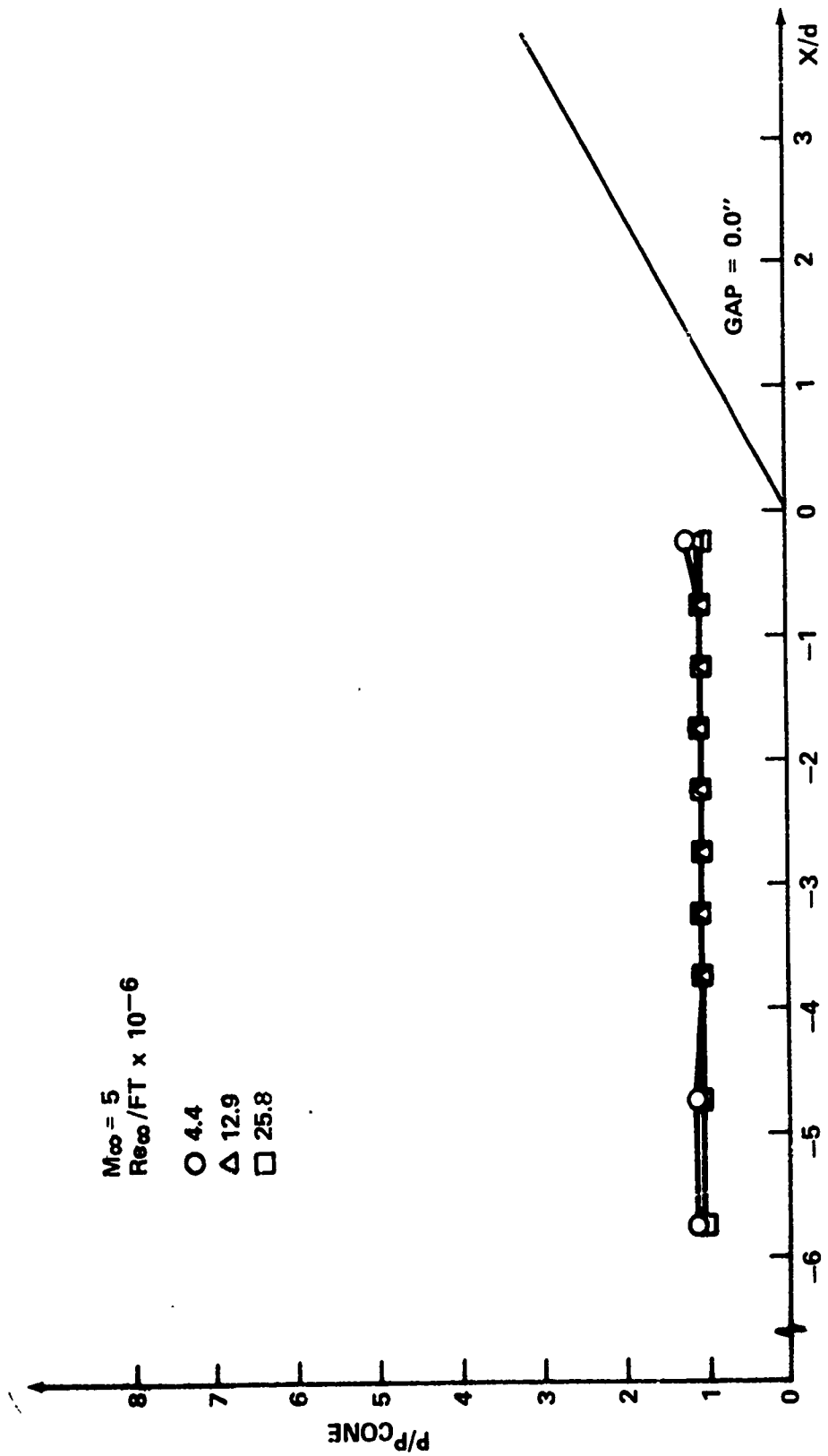

FIG. 21 PRESSURE DISTRIBUTION ON CONE AHEAD OF FLUSH-MOUNTED 60°-SWEPT FIN.

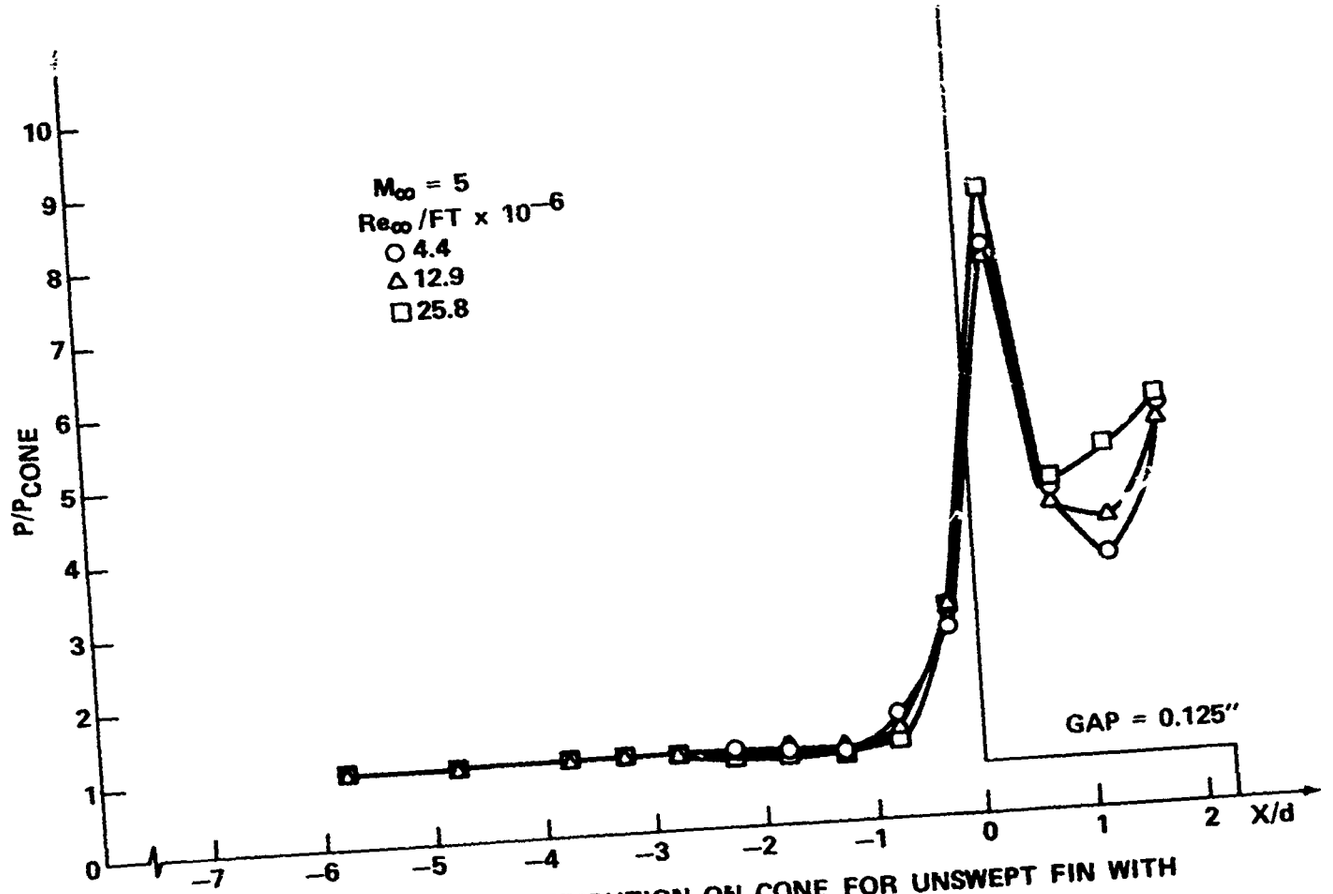

FIG. 22 PRESSURE DISTRIBUTION ON CONE FOR UNSWEPT FIN WITH 0.125-INCH FIN-CONE GAP.

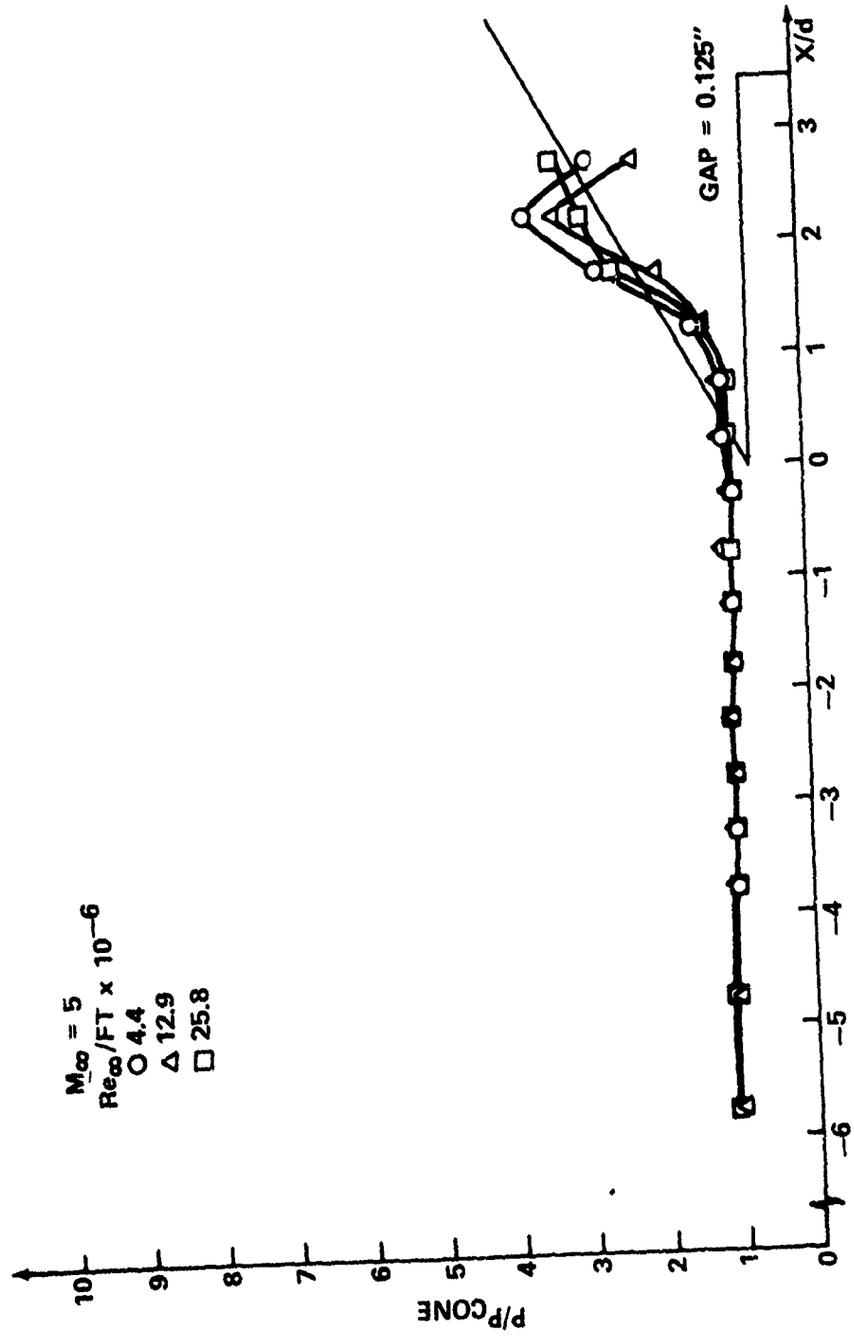

FIG. 23 PRESSURE DISTRIBUTION ON CONE FOR 60°. SWEPT FIN WITH 0.125-INCH FIN-CONE GAP.

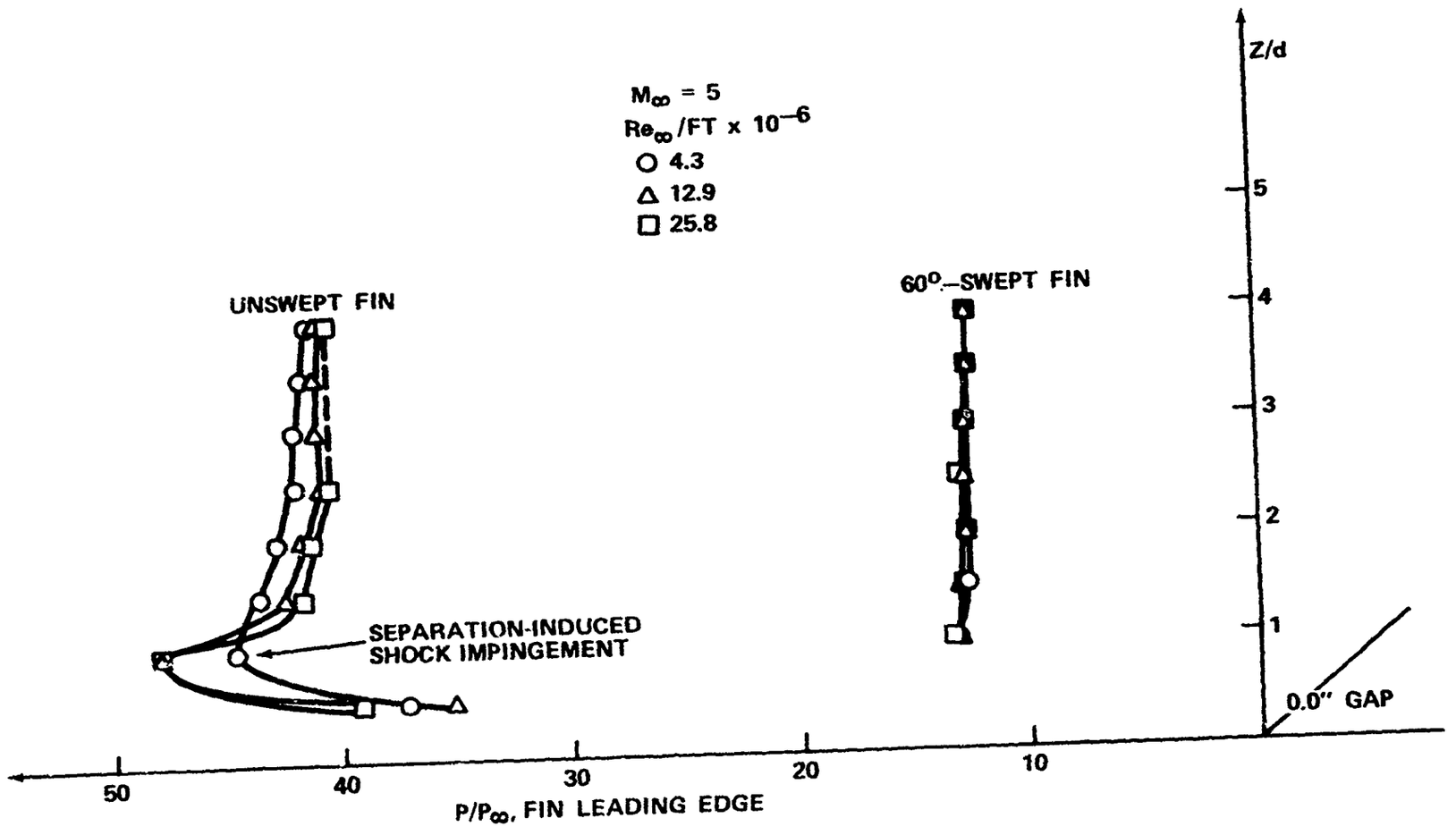

FIG. 24 LEADING–EDGE PRESSURE DISTRIBUTIONS FOR FLUSH-MOUNTED FINS

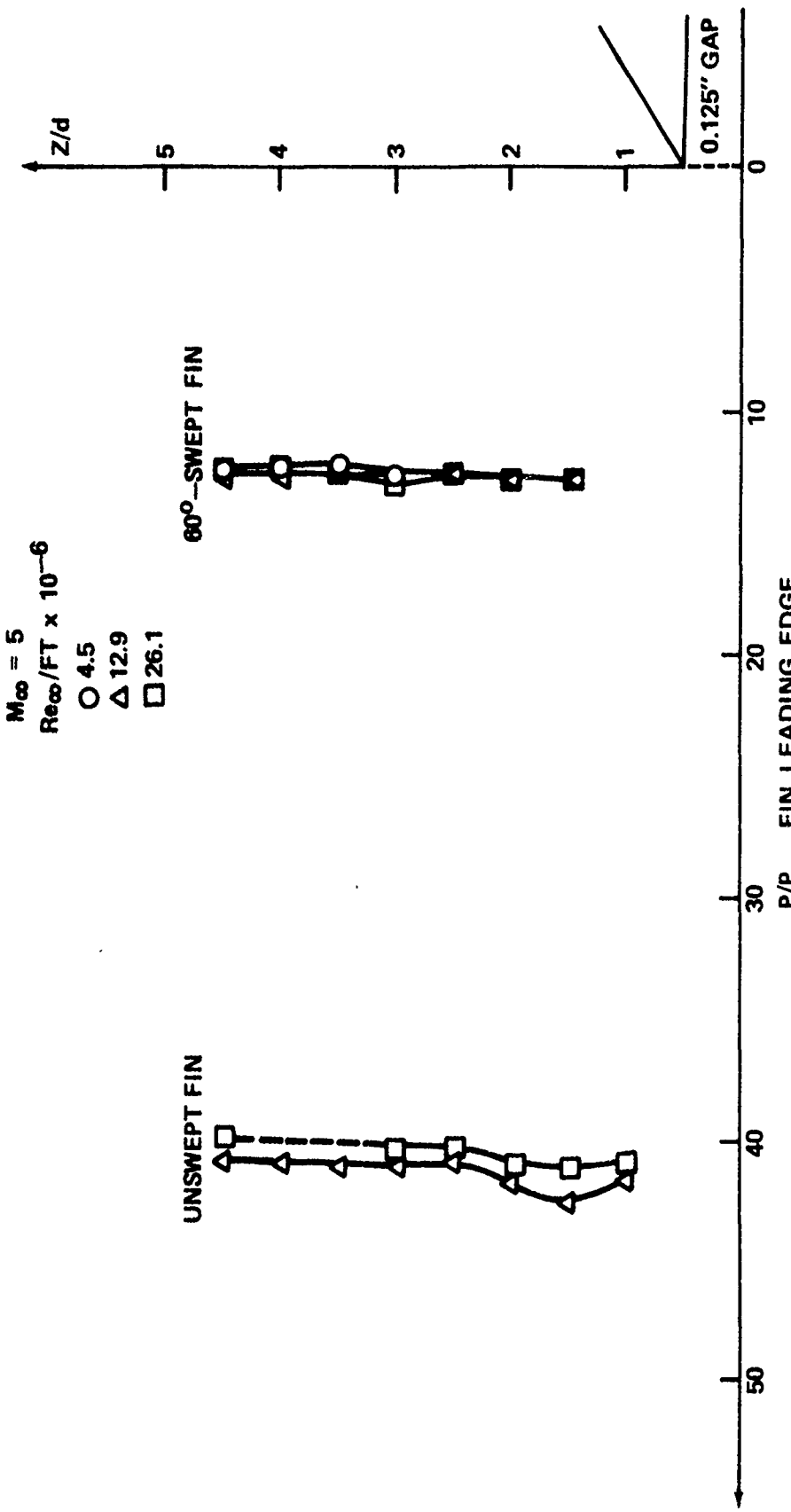

FIG. 25 LEADING-EDGE PRESSURE DISTRIBUTIONS FOR FINS WITH 0.125-INCH FIN-CONE GAP.

PAPER NO. 29

AERODYNAMIC CHARACTERISTICS OF A MISSILE CONFIGURATION HAVING A FORWARD LOCATED INLET

M. LEROY SPEARMAN
CLYDE HAYES

PAPER WITHDRAWN

PAPER NO. 30

ANALYSIS AND DESIGN OF EJECTOR DIFFUSER FOR OPTIMUM THRUST

Tsze C. Tai

Naval Ship Research and Development Center

Bethesda, Maryland

Abstract

An analytical inverse approach is presented in which the pressure distribution along the diffuser wall of an ejector is defined for a given entrance flow condition and the contour of the desired diffuser wall is determined by using a finite difference technique. The prescribed pressure distribution is first optimized by a modified Stratford criterion for incipient separation of turbulent boundary layers; this optimization makes it applicable to compressible two-dimensional and axisymmetric flows. Application of the method is illustrated for the case of a thrust-augmenting ejector in which a primary high-speed flow mixes with the ambient air in the upstream and then diffuses in the downstream. Numerical results indicate that the newly derived ejector is considerably shorter and has a higher thrust augmentation ratio than conventional ejectors. The present procedure can readily be extended to three-dimensional cases and thus is applicable to practical vehicles.

This work was sponsored by the Naval Air Systems Command (AIR-320). The author wishes to thank R. F. Siewert, Jr., for suggesting the problem and R. H. Liebeck for helpful discussions.

Nomenclature

A	Functional coefficient
a	Constant given by Eq. (7)
B	Constant given by Eq. (10b)
b	Constant given by Eq. (8)
C_p	Pressure coefficient defined by Eq. (4)
$\bar{C}_p$	Pressure coefficient defined by Eq. (3)
ℓ	Overall ejector length
ℓ_D	Length of diffusion section
ℓ_M	Length of mixing section
P	Static pressure
R	Ejector half width
Re_{x_o}	Reynolds number given by Eq. (3)
T	Temperature, ^oF
u_τ	Friction velocity, $u_\tau = \sqrt{2\tau_w/\rho}$
V	Velocity
x,y	Coordinates measured along and perpendicular to the axial direction
ρ	Fluid density
τ_w	Shear stress at wall
ϕ	Thrust augmentation ratio defined in Eq. (1)

Subscripts

c	At centerline
p	Primary flow
s	Secondary flow
o	Initial station
∞	Uniform atmospheric condition

Introduction

Recent advances in jet ejectors operating under static conditions have produced high thrust augmentation that is feasible for application to V/STOL flight. There the primary jet exhaust flow is ejected in a nozzle to entrain a large amount of ambient air. An increased mass flow and diffusion process inside the ejector is responsible for the thrust augmentation. However, because of (a) loss in augmentation in duct flow, (b) ramjet effect, and (c) space limitations, high performance and compactness are required in the design of thrust-augmenting ejectors for V/STOL aircraft.

Previous efforts to increase thrust augmentation have been mainly concerned with improving the mixing process[1,2,3] and the boundary layer control.[4,5] The contours of the ejector wall are generally either straight[6] or conform to the shape of an airfoil segment.[7] No particular attention has been directed to proper design of the diffuser section of the ejector in order to achieve overall high thrust augmentation.

In the present paper, a numerical procedure is developed to provide guidelines for designing the contour of the ejector diffuser with the low exit flow distortion required in a volume-limited vehicle system. Basically, the incipient separation condition of the turbulent boundary layer has been imposed and coupled with a finite difference inverse approach for a compressible internal flow. Because of its numerical nature, the method can readily be extended to axisymmetric and three-dimensional general subsonic diffuser problems.

Theoretical Considerations

Compressible Flow in Two-Dimensional Ejector

The schematic of the compressible flow in a two-dimensional center-nozzled ejector is represented in Fig. 1. The primary flow is expanded isentropically in the nozzle from its reservoir condition to a high velocity, V_p. It then discharges to the mixing duct where it entrains a secondary flow from the ambient atmosphere. The amount of entrainment depends on the effectiveness of the mixing process and on the back pressure at the ejector exit. For a simple nozzle (illustrated here), the mixing efficiency is rather limited compared with more sophisticated hypermixing nozzles.[6,7] The flow is essentially two-dimensional across the duct, and the mechanism of the mixing process may be represented by turbulent eddy viscosity models. Different eddy viscosities may have to be used to characterize various flow zones across the duct. In that stage, the flow is undergoing a diffusion process to recover its static pressure at the exit of the ejector. The mixing continues when the flow diffuses. The pressure rises continuously in the diffusion section, and its gradient values are almost completely dependent on the shape of the diffuser. The wall turbulent boundary layer may remain attached if the diffuser is long enough to yield moderate adverse pressure gradient.[8] Short, flat-walled diffusers, on the other hand, generally cause flow separation which results in considerable performance loss.

The level of thrust augmentation is indicated by the ratio of measured thrust at the ejector exit to the thrust generated by the primary flow alone as it isentropically expands to the speed at the nozzle exit. Mathematically,

$$\phi = \frac{(\int V \, d\dot{m})_{x=\ell}}{V_p \dot{m}_p} \qquad (1)$$

where ϕ is the thrust augmentation ratio; $\dot{m}$ and V are the mass flow rate and velocity at the ejector exit, respectively; and $\dot{m}_p$ and V_p are the mass flow rate and velocity of the primary flow.

Optimization of Diffuser

There is obviously room for improvement in both mixing and diffusion aspects. The latter appears more desirable in that practically no work has been done in this area and yet it is more amenable to theoretical treatment.

The treatment involves the development of an optimization procedure whereby an ejector of maximum thrust or of minimal overall length is derived by using the incipient separation condition of the boundary layer. Such a theory is based on the argument that the boundary layer can withstand a nearly infinite adverse pressure gradient for a very short distance without separation. After the sudden pressure jump, however, the pressure gradient must decrease steadily in order to maintain an attached boundary layer in a state of imminent separation.

The concept is illustrated in Fig. 2 which shows typical pressure distributions with and without incipient separation. In order to achieve the same pressure recovery, the distribution with incipient separation requires a considerably shorter diffusion length. The lower the level of pressure recovery desired, the greater the saving in diffusion length.

The greatest advantage of using incipient separation to recover pressure levels derives when it is incorporated properly for a short distance and at an early stage. There is no practical gain at all when the condition is imposed for a long distance. This is indicated in Fig. 2 when the pressure recovery level amounts to $C_p = 0$.

When a high level of pressure recovery is desired, the incipient separation may have to be applied at an early station, such as curve b in Fig. 3. However, if it is imposed too early, as for curve c in Fig. 3, there is no convergent solution. Therefore, there should be an "optimum" station somewhere between curves a and c.

Theoretical Procedures

Theoretical procedures are developed for optimizing the contour of the diffuser section of the ejector. The primary flow nozzle is aligned with the centerline of the ejector so that the flow will be symmetric with respect to the center plane. This arrangement, which is employed for simplicity, imposes no restriction on the method for handling more general initial velocity profiles. Furthermore, any usual approaches to the mixing process can be coupled with the present procedure to provide the initial condition for diffuser optimization.

Stratford Incipient Separation

The use of the condition of incipient separation of the boundary layer for surface optimization has been applied by Griffith in laminar flow[9] and by Liebeck and Ormsbee in turbulent flow.[10] In the present approach, we will use the concept of incipient separation as the basis for optimization and make necessary modifications to satisfy the ejector flow problems.

The criterion for the incipient separation of turbulent boundary layer was discussed and given by Stratford[11] as:

$$\bar{C}_p \left(x \frac{d\bar{C}_p}{dx} \right)^{0.5} = 0.35 \left(\frac{Re_{x_o}}{10^6} \right)^{0.1} \qquad (2a)$$

or

$$\bar{C}_p = 0.489 \left\{ Re_{x_o}^{\frac{1}{5}} \left[\left(\frac{x}{x_o} \right)^{\frac{1}{5}} - 1 \right] \right\}^{\frac{1}{3}} \tag{2b}$$

for

$$\frac{d^2P}{dx^2} < 0 \quad \text{and} \quad \bar{C}_p \leq \frac{4}{7}$$

where

$$\bar{C}_p = \frac{P - P_o}{\frac{1}{2}\rho V_o^2} \quad \text{and} \quad Re_{x_o} = \frac{V_o x_o}{\nu} \tag{3}$$

The pressure coefficient $\bar{C}_p$ as given by Eq. (3) differs from that of the conventional expression

$$C_p = \frac{P - P_\infty}{\frac{1}{2}\rho_\infty V_\infty^2} \tag{4}$$

They are related as follows

$$C_p = \frac{P_o - P_\infty}{\frac{1}{2}\rho_\infty V_\infty^2} + \frac{P_o V_o^2}{\rho_\infty V_\infty^2} \bar{C}_p \tag{5}$$

Equation (5) can be recast with Eq. (2b) in a form with two constant parameters

$$C_p = a \left[\left(\frac{x}{x_o} \right)^{\frac{1}{5}} - 1 \right]^{\frac{1}{3}} + b \tag{6}$$

where

$$a = 0.489\, Re_{x_o}^{\frac{1}{5}} \frac{\rho_o V_o^2}{\rho_\infty V_\infty^2} \tag{7}$$

and

$$b = \frac{P_o - P_\infty}{\frac{1}{2}\rho_\infty V_\infty^2} \tag{8}$$

The values for a and b are completely determined at the initial point where the condition of incipient separation is imposed. However, a numerical experiment indicates that there are difficulties when Eq. (6) is used to generate the corresponding diffuser shape by means of a finite difference scheme. This is probably because the mechanism of flow mixing outside the boundary layer differs considerably for present ejector flows from that of the original experimental simple duct flow condition postulated by Stratford. Necessary modification of Eq. (6) therefore seems in order.

Modified Stratford Incipient Separation

Physically, when the separation of boundary layer is imminent, the flow is traveling with zero skin friction at the wall. Such a condition implies that the flow must be in a state of neutral stability. Any increase in skin friction would stabilize the flows and prevent separation. Therefore, it is plausible to use the skin friction value as the criterion for incipient separation. This is especially helpful when the theory is to be implemented with numerical schemes.

It is therefore suggested that the Stratford theory, Eq. (6), be modified as follows:

$$C_p = A\left[B\left(\frac{x}{x_o}\right)^{\frac{1}{5}} - 1\right]^{\frac{1}{3}} + b \qquad (9)$$

where

$$A = f(x) \qquad (10a)$$

and

$$B = \text{const. at } x = x_o$$
$$= 1 \quad \text{at } x > x_o \qquad (10b)$$

The form of f(x) is to be determined so that the value of skin friction stays within specified limits above zero. The absolute lower limit, of course, is zero. The value for B is determined by a step function which enables an infinite pressure gradient to be avoided at $x = x_o$. Yet, the gradient value is still kept high enough to permit a pressure jump at the initial point and to force the friction velocity toward a low specified value. The procedure is best illustrated in Fig. 4 which indicates the distributions of friction velocity with and without conditions of incipient separation. The turbulent boundary layer is kept attached at very low skin friction all the way to the exit. The corresponding pressure distributions for curves a and b have been given in Fig. 3.

Variational Problem

With the incipient separation criterion at hand, the problem is now to maximize the thrust augmentation ratio ϕ for a given set of constraints and variational parameters. As indicated in Eq. (1), ϕ can be written in the functional form

$$\phi = \phi [\dot{m}_p, V_p, \dot{m}, V, \ell] \qquad (11)$$

That is, it is desired to find $\dot{m}$ and the distribution of V which maximize ϕ for given values of $\dot{m}_p$ and V_p. The problem, then, is a variational one with variational parameters $\dot{m}$ and V subject to the constraints of the incipient separation condition, represented by Eq. (9), and desired overall length of the ejector ℓ for given values of $\dot{m}_p$ and V_p.

Alternatively, it is desired to minimize the overall ejector length with a fixed ϕ in order to meet the volume-limited design requirement. In this case, it takes the form

$$\ell = \ell [\dot{m}_p, V_p, \dot{m}, V, \phi] \tag{12}$$

The variational problem has variational parameters $\dot{m}$ and V subject to the constraint of Eq. (9) and desired value ϕ for given values of $\dot{m}_p$ and V_p.

In both cases, the variational parameters are $\dot{m}$ and V. Since the total mass flow rate is the sum of the primary and secondary flow rates,

$$\dot{m} = \dot{m}_p + \dot{m}_s \tag{13}$$

With known constant $\dot{m}_p$, the actual variable then is $\dot{m}_s$.

Also, the velocity distribution at the ejector exit V is determined by solving the partial differential equations that govern the ejector flow. This, in turn, depends on the initial condition of the diffusion section at the initial station $x = x_o$. Different values of x_o give different sets of initial conditions, provided that the flow solutions in the mixing section remain valid and continuous. Therefore, V can be considered as function of x_c.

In accordance with the above arguments, Eqs. (11) and (12) can be rewritten as follows

$$\phi = \phi [\dot{m}_p, V_p, \dot{m}_s, x_o, \ell] \tag{14}$$

and

$$\ell = \ell [\dot{m}_p, V_p, \dot{m}_s, x_o, \phi] \tag{15}$$

The optimization for Eqs. (14) and (15) can be carried out either by using a procedure similar to that presented by Liebeck and Ormsbee[10] or directly through a numerical optimization scheme, like that developed by Vanderplaats and Moss.[12] The latter is preferred in the present work.

Numerical Computations

The theoretical procedures described above have to be implemented numerically because of the complexity of the flow in two dimensions. Here we will use an existing computer program for analyzing the flow in the mixing section and we will develop a design program for determining the appropriate contour of the diffuser section.

Analysis Program for Mixing Solution

Gilbert and Hill have developed a finite difference computer program for calculating two-dimensional ejector flows with a symmetric, variable-area mixing section and a coaxial converging primary nozzle.[8] The variation of the surface of the mixing section is assumed to be small so that the static pressure can be considered uniform in each cross section and the effect of wall curvature can be neglected. Different eddy viscosity models are utilized for various flow regions. The coaxial, fixed nozzle allows the primary flow to be expanded to high subsonic or slightly supersonic speeds. For a given mass flow rate $\dot{m}_p$ and velocity V_p of the primary flow, the numerical calculation proceeds with a top-hat velocity distribution with uniform profiles for both primary and secondary flows. The geometry of the mixing section is prescribed. The calculation is then carried out until $x = x_o$ for a specified secondary flow rate $\dot{m}_s$. At $x = x_o$, the output of the mixing section solution becomes the initial design condition for the diffuser section.

Design Program for Diffuser Section

Strictly speaking, however, there is no clear border line which separates the mixing and diffusion section since the flow may undergo a diffusion process without complete mixing. The two sections are so

designated mainly for convenience. A design program for the subject problem has been developed by modifying the Gilbert-Hill program. Modifications are made in the following areas:

(a) The direct solution procedure of the analytical program is converted to an inverse approach in which the pressure gradient values are used as input and the coordinates of the desired diffuser contour are calculated as output along with flow property values.

(b) To implement Eq. (9) in the design program, its A(x) values are determined by a trial-and-error scheme in accordance with the criterion that the friction velocity should approach zero, i.e., $1 \leq u_\tau \leq 4$ ft/sec. Numerically, the above u_τ values correspond to the velocity near the wall and amount to between 0.4 and 0.45 percent of the center velocity, i.e.,

$$0.004 \leq \frac{V_{y \to 0}}{V_c} \leq 0.0045$$

(c) The numerical optimization computer program based on the method of feasible directions originally developed by Vanderplaats and Moses,[12] is incorporated by using variational parameters x_o and $\dot{m}_s$ with constraints described in (b).

Results and Discussions

Numerical results were calculated for given mixing section geometry and flow conditions that enabled comparisons with available two-dimensional theoretical data.

Typical velocity profiles at different longitudinal stations along the ejector are shown in Fig. 5 for $\dot{m}_p = 0.075$ lb_m/sec-in and $\dot{m}_s = 0.2763$ lb_m/sec-in. The y/R = 0 coincides with the centerline of

the ejector. From x = 0 to x = 7 in, the flow undergoes acceleration, mixing, and entrainment. After imposition of the incipient separation condition at x_o = 8.1 in., the flow is decelerated sharply to achieve static pressure gains in the diffusion section. Without this application, the flow would not have diffused so effectively, as indicated in Fig. 6.

The geometry of a newly derived ejector with $\dot{m}_p$ = 0.075 lb_m/sec-in and $\dot{m}_s$ = 0.2763 lb_m/sec-in is compared in Fig. 7 to that of a conventional ejector with the same flow condition. Note that a diffusion length of only 5.6 in. attains the same level of recovery as in the 9.9-in. conventional ejector. The ratio of the two is 0.57. Because the flow travels through the shorter distance at lower friction values, the new ejector experiences less frictional loss and thus gives a higher thrust augmentation ratio. The corresponding pressure distributions for the above two ejectors have been given in Fig. 3 (curves b and d).

The results indicate that with the same primary and secondary flow conditions at the nozzle, different diffuser contours and consequently different thrust augmentation ratios may be achieved by using different x_o values. This is illustrated by Ejectors I and II, as shown in Figs. 7 and 8, respectively. Comparing Ejector II with Ejector I, we find that as the mixing section length ℓ_M ($\ell_M = x_o$) is shortened, so is the ℓ_D. Since the decrease in both ℓ_M and ℓ_D results in less total frictional loss, Ejector II thus offers a higher ϕ value.

Ejector III, shown in Fig. 8, was generated with the same primary flow rate as for Ejector II but with a higher entrained secondary flow. With a fixed ℓ_M, the higher entrainment in Ejector III gives a higher thrust augmentation ratio. The trend is correct in accordance with the ejector principle. Note, however, that attainment of a higher ϕ necessitates a longer diffusion length, as indicated in Fig. 8.

The overall effects of the principal variables, ℓ_M and $\dot{m}_s$, are best assessed by the performance map shown in Fig. 9 where the thrust augmentation ratio ϕ is plotted as ordinate and the overall ejector length ℓ as abscissa. The latter is the sum of the ℓ_M and ℓ_D values. Recall that the optimization effort should be aimed at determining an ejector with highest ϕ and shortest ℓ for which a converged solution can be obtained. For a given secondary flow rate $\dot{m}_s$, these two desirable features can almost always be obtained simultaneously, for the reason discussed previously. However, there is a lower limit for the ℓ_M (and thus ℓ) values in order to establish proper mixing and thus maintain a continuous unseparated flow throughout the ejector. The upper left end of each curve implies such a limit. Indeed, the figure provides some guidelines for design purposes. For a desired ϕ, one uses lower $\dot{m}_s$ values in order to minimize ℓ or for a fixed ℓ, one uses higher $\dot{m}_s$ values to maximize ϕ.

Conclusions

The diffusion section of thrust-augmenting ejectors can be optimized for maximum thrust or for minimum overall ejector length by applying the modified Stratford criterion for incipient separation of turbulent boundary layers. In general, it was found that

(a) The incipient separation criterion should be applied at an early stage and for a short distance in order to achieve maximum gain in pressure recovery. Prolonged use of the criterion yields little or no advantage.

(b) For given flow conditions at the ejector nozzle, the ejector diffuser can (1) be optimized for maximum thrust subject to a fixed

overall ejector length or (2) be optimized for minimum overall ejector length subject to a possible desired thrust augmentation ratio.

References

1. Bevilaqua, P. M., "Evaluation of Hypermixing for Thrust Augmenting Ejectors," Journal of Aircraft, Vol. 11, No. 6, Jun 1974, pp. 348-354.

2. Quinn, B., "Compact Ejector Thrust Augmentation," Journal of Aircraft, Vol. 10, No. 8, Aug 1973, pp. 481-486.

3. Fancher, R. B., "Low Area Ratio Thrust Augmenting Ejectors," Journal of Aircraft, Vol. 9, No. 3, Mar 1972, pp. 243-248.

4. McCormick, B. W., Jr., "Aerodynamics of V/STOL Flight," Academic Press, New York, 1967, pp. 280-288.

5. Ambrosiani, J. P. et al., "Lift Augmenting Ejectors for V/STOL Aircraft," North American Rockwell Report NR71H-532, Dec 1971.

6. Quinn, B., "Recent Developments in Large Area Ratio Thrust Augmentors," AIAA Paper 72-1174, New Orleans, La., Nov-Dec 1972.

7. Brown, S. L. and R. D. Murphy, "Design and Test of Ejector Thrust Augmentation Configurations," AGARD CP-143, Oct 1974.

8. Gilbert, G. B. and P. G. Hill," Analysis and Testing of Two-Dimensional Slow Nozzle Ejectors with Variable Area Mixing Sections," NASA CR-2251, May 1973.

9. Lachmann, G. V., "Boundary Layer and Flow Control," Pergamon Press, New York, 1961.

10. Liebeck, R. H. and A. J. Ormsbee, "Optimization of Airfoil for Maximum Lift," Journal of Aircraft, Vol. 7, No. 5, Sep-Oct 1970, pp. 409-415.

11. Stratford, B. S., "The Prediction of Separation of the Turbulent Boundary Layer," Journal of Fluid Mechanics, Vol. 5, 1959, pp. 1-6.

12. Vanderplaats, G. N. and F. Moses, "Structural Optimization by Methods of Feasible Directions," in "Computers and Structures," Vol. 3, Pergamon Press, London, 1973, pp. 739-755.

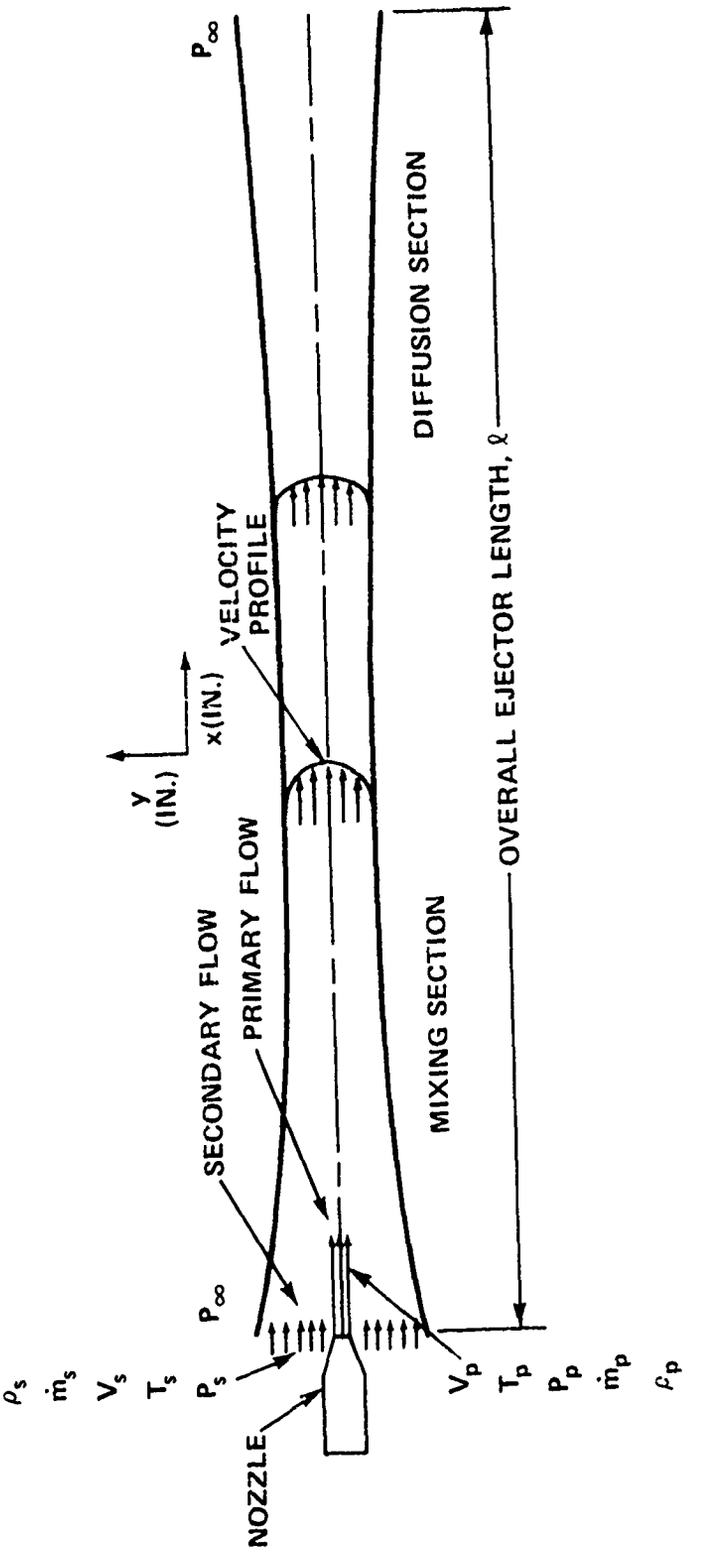

Figure 1 – Schematic of Two-Dimensional Ejector Flow

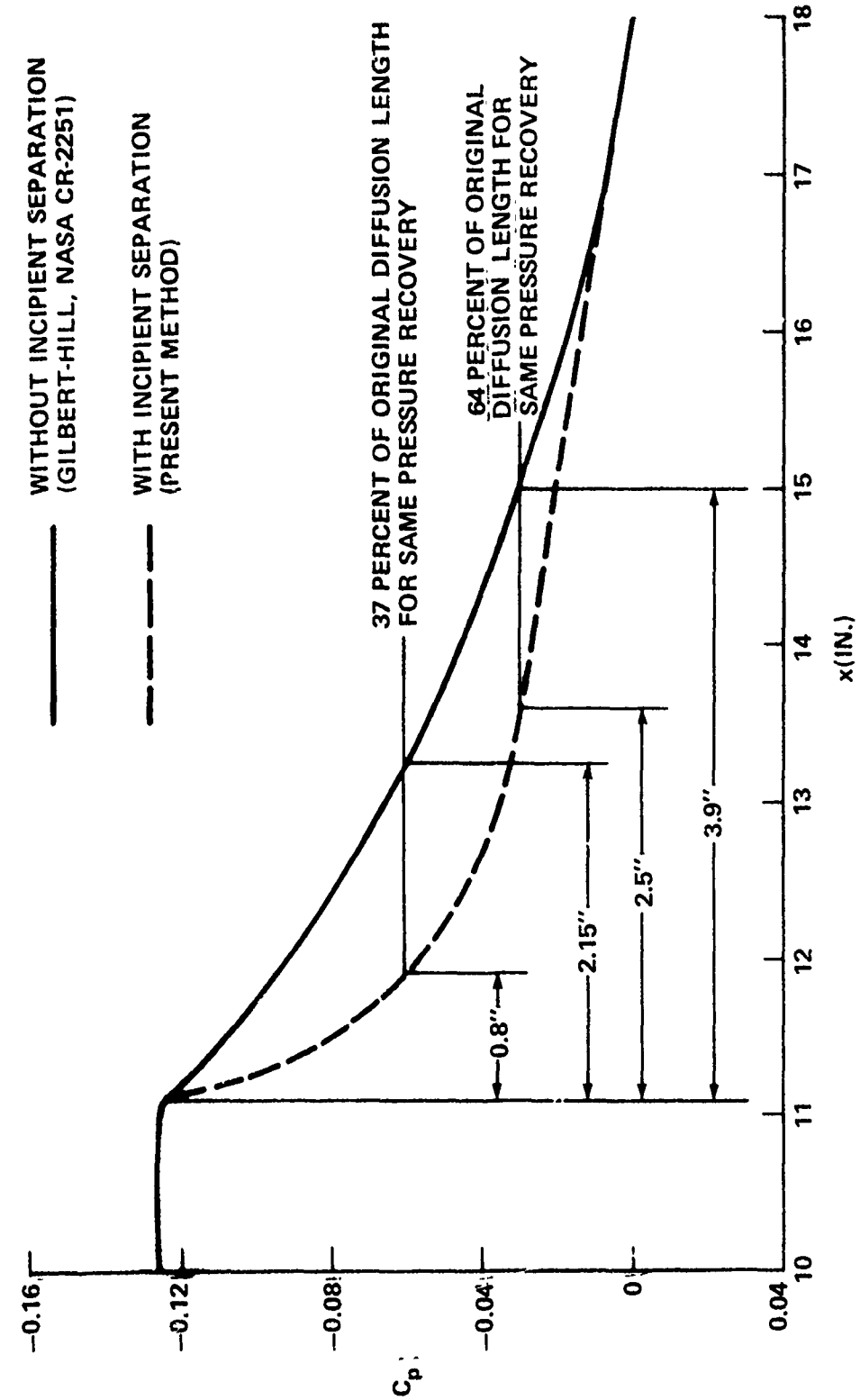

Figure 2 – Typical Pressure Distributions in an Ejector Diffuser

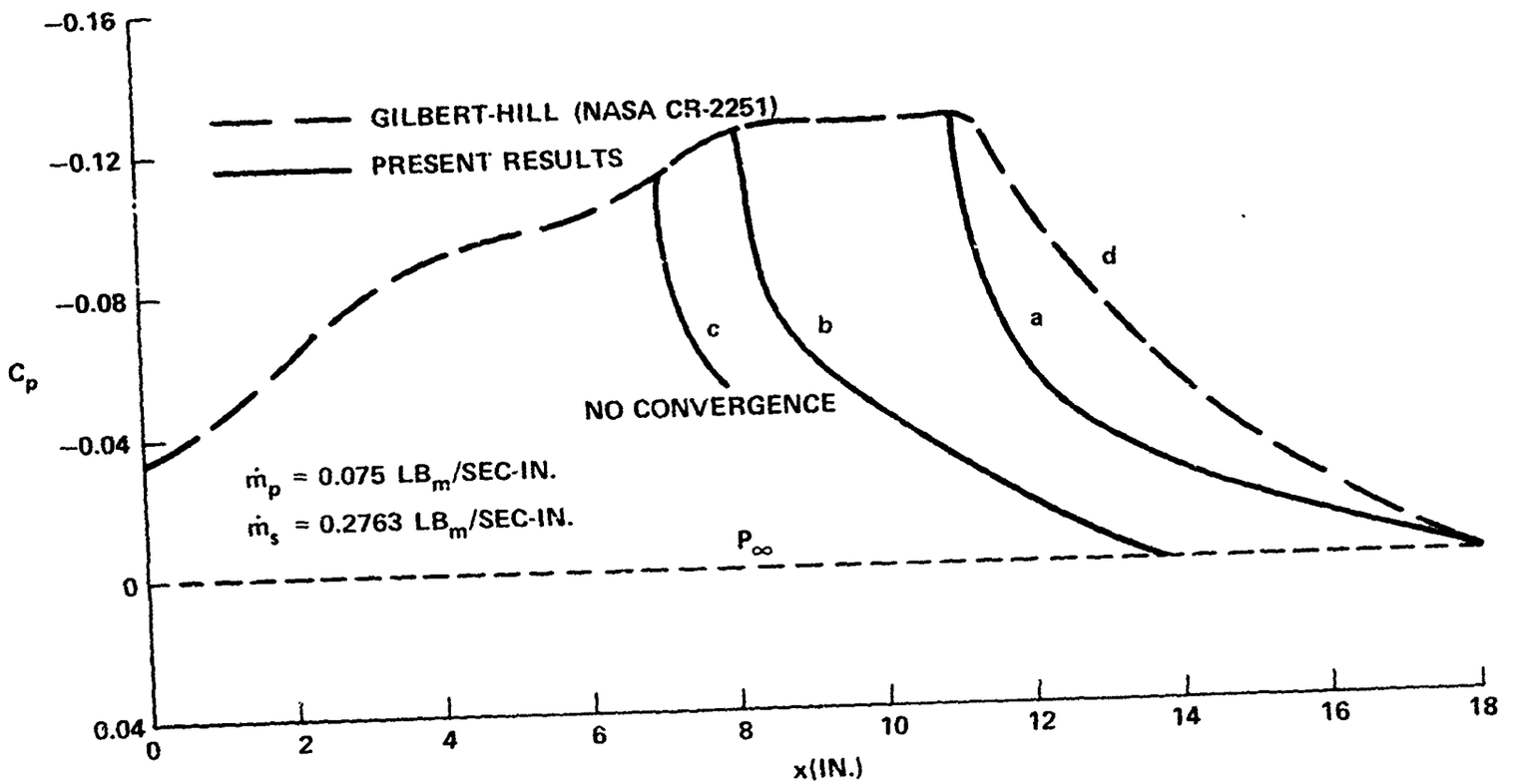

Figure 3 – Pressure Distributions in Ejector with $\dot{m}_s$ = 0.2763 LB_m/SEC-IN.

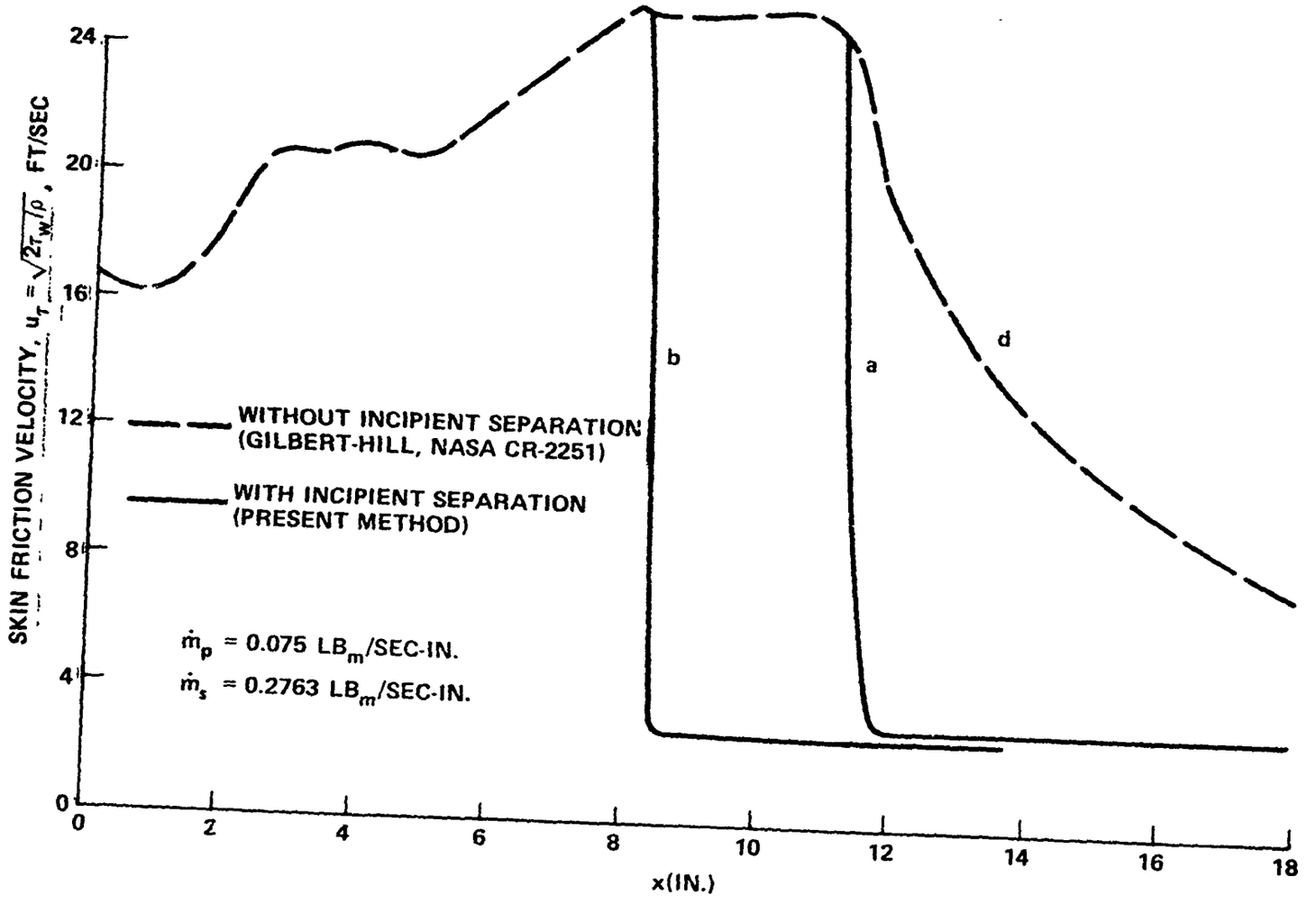

Figure 4 – Distribution of Friction Velocity on Ejector Wall

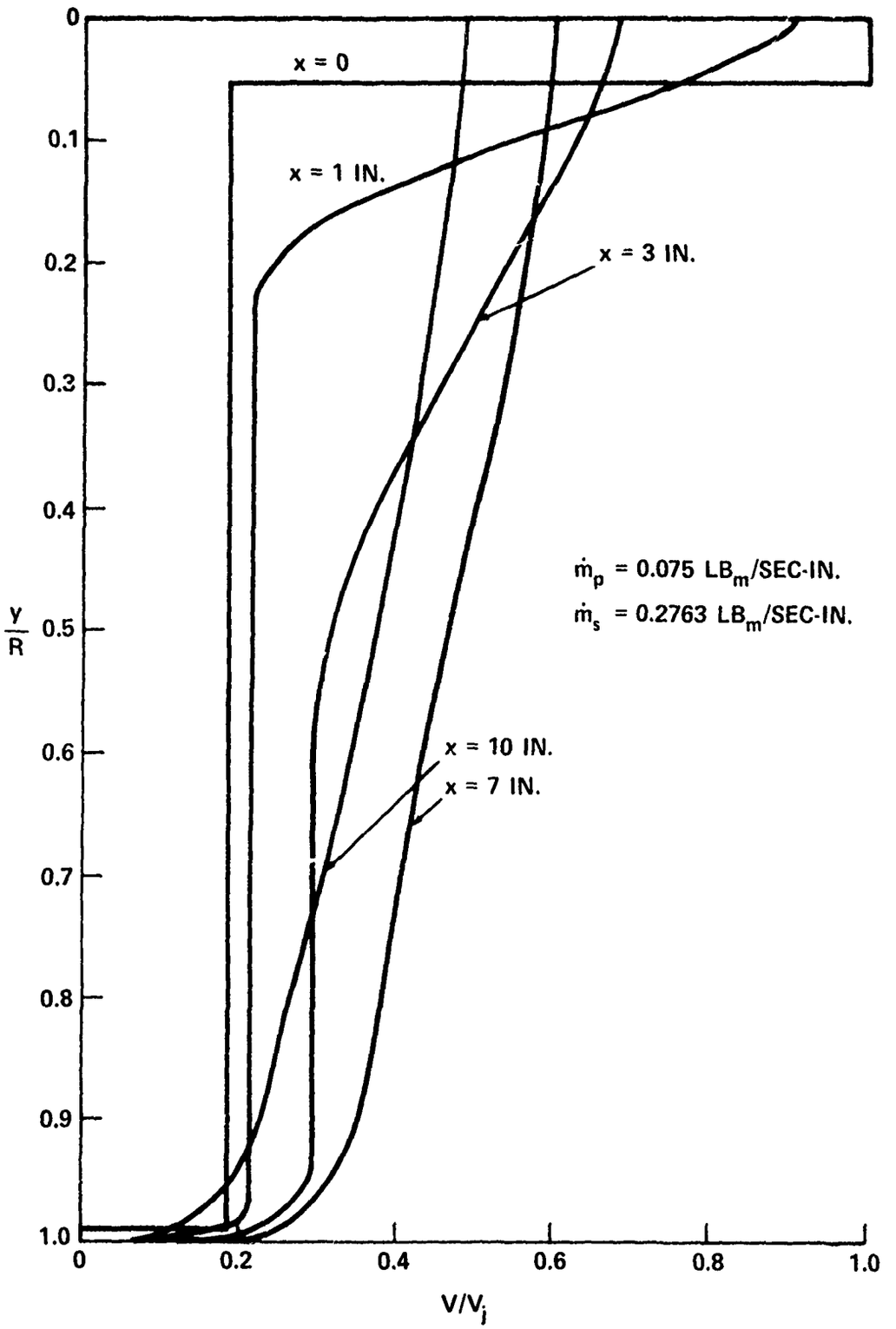

Figure 5 – Velocity Profiles in an Ejector

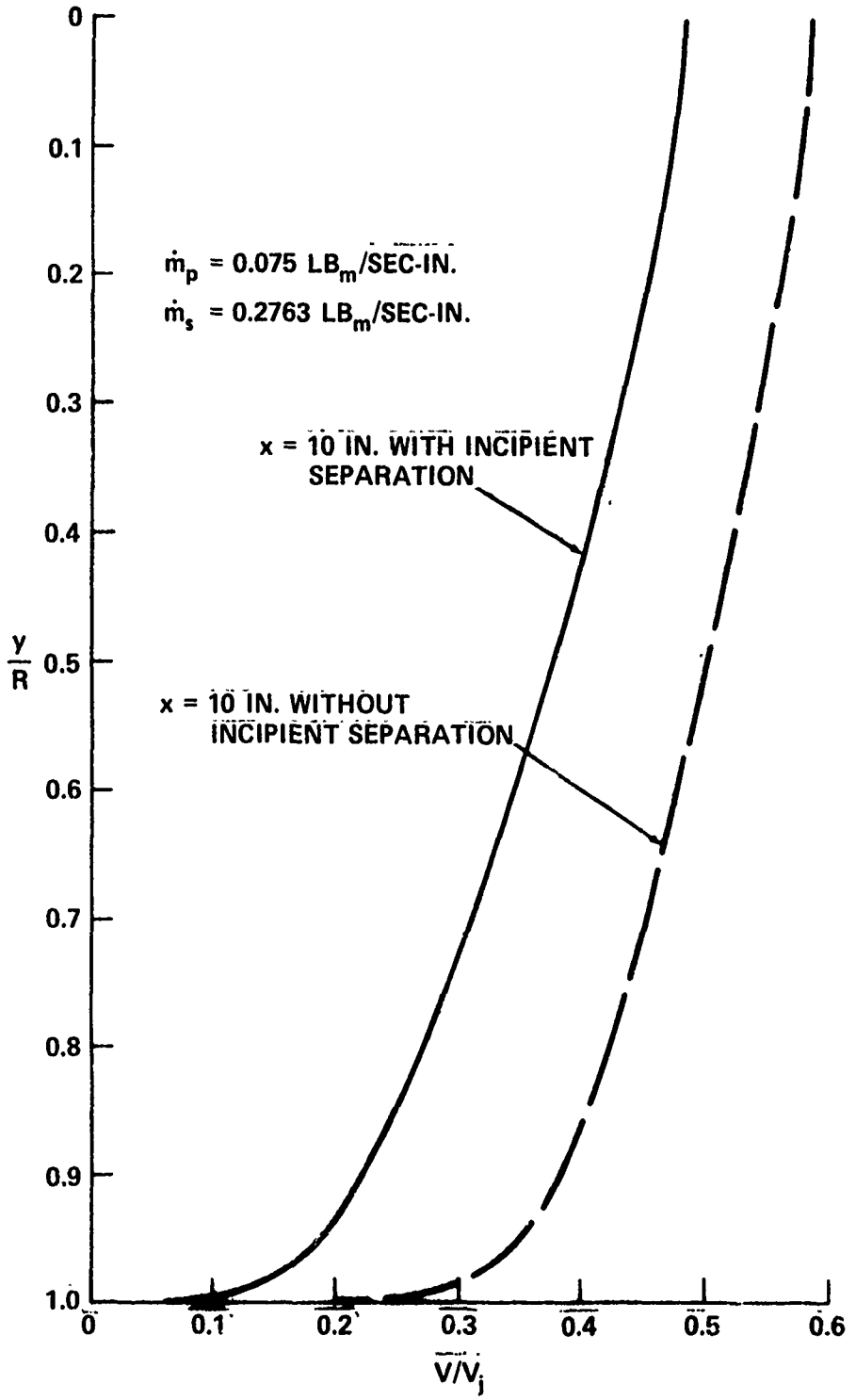

Figure 6 – Velocity Profiles With and Without Optimization

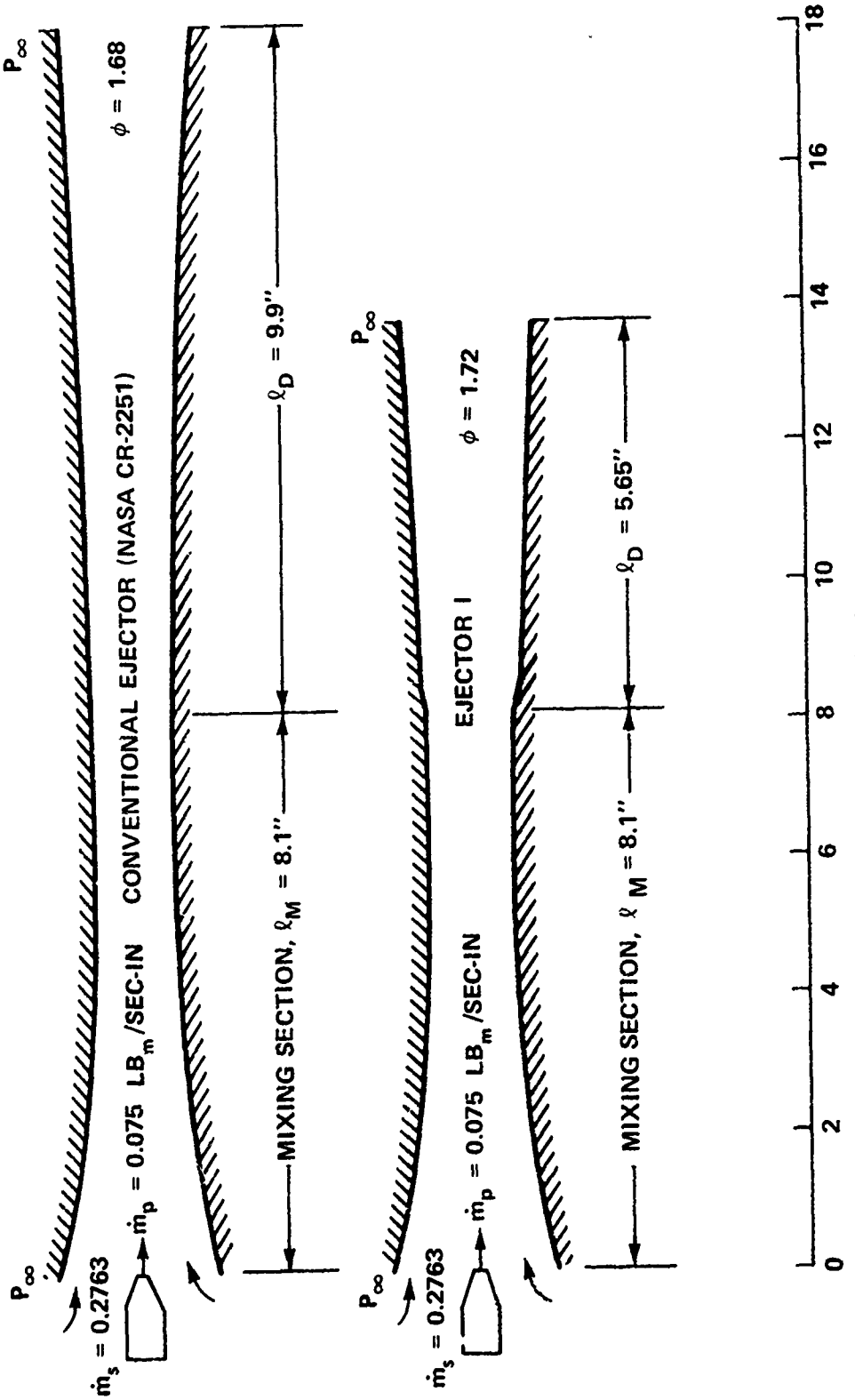

Figure 7 – Ejectors With and Without Optimization

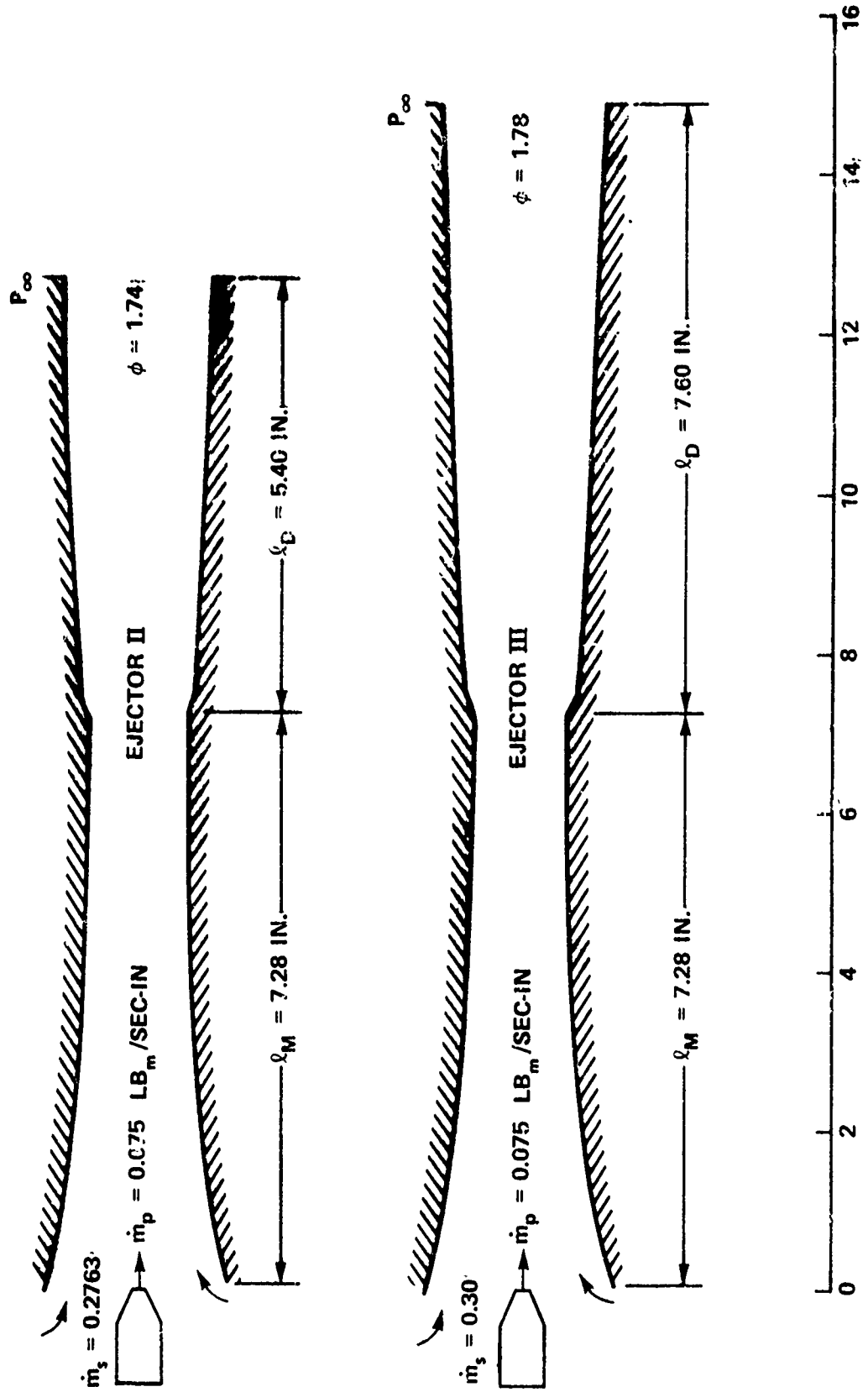

Figure 8 – Optimum Ejectors with Various Secondary Flow Rates

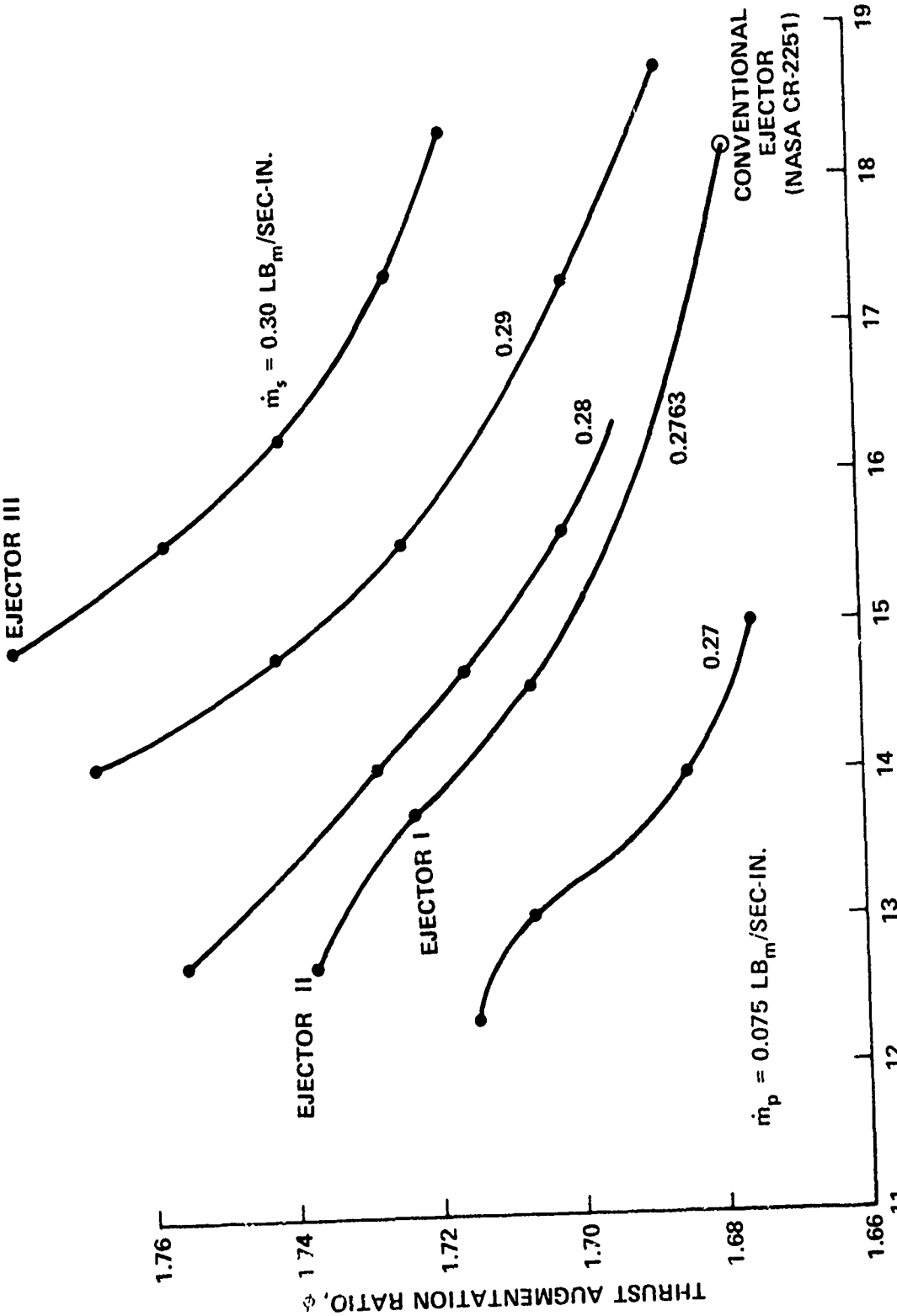

Figure 9 – Performance Map for Ejector Design

PAPER NO. 31

EVALUATION OF A COAXIAL GAS FLOW CHAMBER

R. E. LEE

PAPER WITHDRAWN